



HAL
open science

Fast Electron Transport Study for Inertial Confinement Fusion

Michaël Touati

► **To cite this version:**

Michaël Touati. Fast Electron Transport Study for Inertial Confinement Fusion. Instrumentation and Methods for Astrophysic [astro-ph.IM]. Université de Bordeaux, 2015. English. NNT : 2015BORD0076 . tel-01238782

HAL Id: tel-01238782

<https://theses.hal.science/tel-01238782>

Submitted on 7 Dec 2015

HAL is a multi-disciplinary open access archive for the deposit and dissemination of scientific research documents, whether they are published or not. The documents may come from teaching and research institutions in France or abroad, or from public or private research centers.

L'archive ouverte pluridisciplinaire **HAL**, est destinée au dépôt et à la diffusion de documents scientifiques de niveau recherche, publiés ou non, émanant des établissements d'enseignement et de recherche français ou étrangers, des laboratoires publics ou privés.



THESIS

SUBMITTED TO

UNIVERSITÉ DE BORDEAUX

ÉCOLE DOCTORALE DES SCIENCES PHYSIQUES ET DE L'INGÉNIEUR

by **Michaël TOUATI**

for the degree of

DOCTOR in ASTROPHYSICS, PLASMAS AND NUCLEAR

Fast Electron Transport Study

for Inertial Confinement Fusion

Defended on June 10, 2015 at Talence (France)

Board of examiners:

A.P.L. Robinson	Professor, SFTC RAL (United Kingdom)	Reviewer
G. Bonnaud	Professor, CEA-Saclay INSTN (France)	Reviewer
P. Mora	Research Director, École Polytechnique CPHT (France)	Examiner
L. Gremillet	Research Engineer, CEA-Bruyères-le-Châtel DPTA (France)	Examiner
E. d'Humières	Researcher, Université de Bordeaux CELIA (France)	Examiner
V.T. Tikhonchuk	Professor, Université de Bordeaux CELIA (France)	Supervisor
J.-L. Feugeas	Research Engineer, CEA-Cesta CELIA (France)	Supervisor
Ph. Nicolai	Research Engineer, CEA-Cesta CELIA (France)	Supervisor

Dedicated to my grandmother Louise Halimi Laloum who died the 1st of february 2015 at the age of 95 years old still without knowing how to write nor read.

Dedicated also to my friend Jonathan Sandler (30 years old), his two sons Aryeh (3 years old) and Gabriel (6 years old) and their little friend Myriam Monsonogo (8 years old) murdered at the entrance of their school Ozar Hatorah in Toulouse (France) that horrible March 19, 2012, just because they were Jews.

”It can be said that anti-Semitism is one particular case of intolerance; that for centuries it had a prevailing religious character; that in the Third Reich it was exacerbated by the nationalistic and military predisposition of the German people and by the “differentness” of the Jewish people; that it was easily disseminated in all of Germany—and in a good part of Europe—thanks to the efficiency of the fascist and Nazi propaganda, which needed a scapegoat on which to load all guilts and resentments; that the phenomenon was heightened to paroxysm by Hitler, a maniacal dictator.

But these commonly accepted explanations do not satisfy me. They are reductive-not commensurate with, nor proportionate to, the facts that need explaining. In rereading the chronicles of Nazism, from its murky beginnings to its convulsed end, I cannot avoid the impression of a general atmosphere of uncontrolled madness. Thus I prefer the humility with which some of the most serious historians confess to not understanding the furious anti-Semitism of Hitler and of Germany back of him. [...]

For this reason, it is the duty of everyone to meditate on what happened. Everybody must know, or remember, that Hitler and Mussolini, when they spoke in public, were believed, applauded, admired, adored like gods. They were “charismatic leaders”; they possessed a secret power of seduction that did not proceed from the credibility or the soundness of the things they said, but from the suggestive way in which they said them. And we must remember that their faithful followers, among them the diligent executors of inhuman orders, were not born torturers, were not (with a few exceptions) monsters: they were ordinary men. Monsters exist, but they are too few in number to be truly dangerous; more dangerous are the common men, the functionaries ready to believe and to act without asking questions.

Since it is difficult to distinguish true prophets from false, it is well to regard all prophets with suspicion. Yet it is clear that this formula is too simple to suffice in every case. A new fascism, with its trail of intolerance, abuse, and servitude, can be born outside our country and imported into it, walking on tiptoe and calling itself by other names; or it can loose itself from within with such violence that it routs all defenses. At that point, wise counsel no longer serves, and, and one must find the strength to resist. But then, too, the memory of what happened in the heart of Europe, not very long ago, can serve as support and warning.”

Primo Levi

Publications related to this thesis

Some results from this PhD research work have given or are going to give rise to the following publications:

1. M Touati, J-L Feugeas, Ph Nicolai, J J Santos, L Gremillet and V T Tikhonchuk. *A reduced model for relativistic electron beam transport in solids and dense plasmas*. New J. Phys 16, 073014 (2014)
2. S Gus'kov, X Ribeyre, M Touati, J-L Feugeas, Ph Nicolai and V T Tikhonchuk. *Ablation Pressure Driven by an Energetic Electron Beam in a Dense Plasma*. Phys. Rev. Lett. 109, 255004 (2012)
3. J J Santos, B Vauzour, M Touati, L Gremillet, J-L Feugeas, T Ceccotti, R Bouillaud, F Deneuille, V Floquet, C Fourment, M Hadj-Bachir, S Hulin, A Morace, Ph Nicolai, P d'Oliveira, F Reau, A Samaké, O Tcherbakov, V T Tikhonchuk, M Veltcheva and D Batani. *Ultra-high pressure hydrodynamics driven by fast electrons in solid targets*. To be submitted
4. X Vaisseau, J J Santos, M Touati, J-L Feugeas, Ph Nicolai, V Tikhonchuk et al., *Laser-generated fast electron beam collimation in laser-shocked vitreous carbon foils*. To be submitted

The model has also been used by colleagues for studies that have given or are going to rise to the following publications:

1. Ph Nicolai, J-L Feugeas, M Touati, X Ribeyre, S Gus'kov, V T Tikhonchuk. *Deleterious effects of nonthermal electrons in shock ignition concept*. Phys. Rev. E 89, 033107 (2014)
2. L Volpe, J-L Feugeas, Ph Nicolai, J J Santos, M Touati, J Breil, D Batani, and V Tikhonchuk. *Controlling the fast electron divergence in a solid target with multiple laser pulses*. Phys Rev E 90, 063108 (2014)
3. D Del Sorbo, J-L Feugeas, Ph Nicolai, M Olazabal-Loumé, B Dubroca, S Guisset, M Touati and Vladimir T. Tikhonchuk. *Reduced Entropic Model for Studies of Multidimensional Nonlocal Transport in High-Energy-Density Plasmas*. Submitted to Phys. of Plasma
4. A Colaitis, G Duchateau, X Ribeyre, Y Maheut, G Boutoux, L Antonelli, Ph Nicolai, D Batani and V Tikhonchuk. *A multiscale model for laser-plasma interaction*. Submitted to Phys. Rev. Letter

Finally, some results have been partially presented in the following conferences

1. Fast ignition workshop, Napa Valley, California, United-States, 2012 (oral)

-
2. Laser Plasma Institute (ILP) conference, Île de Ré, France, 2012 (poster)
 3. Laser Plasma Institute (ILP) conference, Orsières, France, 2013 (poster)
 4. Anomalous Absorption Conference (AAC) 2014, Estes Park, Colorado, United States (poster)
 5. Fast ignition workshop, Oxford, United Kingdom, 2014 (oral)

and in the following graduate summer schools:

1. APPEPLA Summer School, Rethymno, Crete, Greece, 2011 (poster)
2. ERICE Summer School, Erice, Sicily, Italy, 2013 (poster)

Contents

0	Introduction	21
0.1	Thermonuclear Plasma Fusion as the Solution for the XXIth century Energy Production	22
0.1.1	World Energy Balance	22
0.1.2	Thermonuclear Fusion	24
0.1.3	Lawson Criterion	27
0.2	Inertial Confinement Fusion (ICF)	28
0.2.1	Conventional ICF Schemes	28
0.2.2	Problems facing the ICF Conventional Schemes	30
0.2.3	Fast Ignition and Shock Ignition Alternative Schemes	31
0.3	Fast Electron Generation in the context of ICF	35
0.3.1	Role of Fast Electrons in the Shock Ignition Scheme	35
0.3.2	Fast Electron Beam Divergence in the context of Fast Ignition	36
0.3.3	Existing Simulation Methods for Fast Electron Transport Modeling	38
0.4	Objectives of the thesis and Plan of the Manuscript	39
I	State of the Art of Fast Electron Generation and Fast Electron Transport in the context of Inertial Confinement Fusion	43
1	Fast Electron Generation	45
1.1	Laser-Solid Interaction at High Intensities	46
1.1.1	Collisional versus "Collisionless" Absorption mechanisms	46
1.1.2	Resonant Absorption	51

1.1.3	Ponderomotive Force and Parametric Instabilities	52
1.1.4	Simplified Scheme of Electron Acceleration by Landau Damping in strong Electron Plasma Waves	55
1.2	Laser solid interaction at Ultra-High Intensities	56
1.2.1	Single Electron Motion in an Ultra-High Intense Laser Pulse	56
1.2.2	Cold Plasma Approximation	59
1.2.3	Relativistic Ponderomotive Force and $\mathbf{j} \times \mathbf{B}$ heating	61
1.2.4	Brunel Effect and Vacuum heating	65
1.2.5	Anharmonic Resonant Absorption	66
1.2.6	Stochastic heating	68
1.3	Particle-in-Cell method for Laser-Plasma Interaction simulations	71
1.3.1	Phase-Space Discretization for the Vlasov Equation	71
1.3.2	Binary Collision Modelling	73
1.3.3	Computational Constraints	74
1.4	Brief Summary of Laser Solid Interaction and Laser-Generated Relativistic Electron Beam Properties	75
2	Electromagnetic Neutralization of a Laser-generated Relativistic Electron Beam	81
2.1	Electric Field Generated by a Monoenergetic, Collimated and Homogeneous Semi-infinite Relativistic Electron Beam Propagating in Vacuum	82
2.2	Electric Neutralization of a Monoenergetic, Collimated and Homogeneous Rigid Relativistic Electron Beam Propagating in Solids or Dense Plasmas	87
2.2.1	Electric Neutralization of a Monoenergetic, Collimated and Homogeneous Rigid Relativistic Electron Beam Propagating in a Conductor	87
2.2.2	Electric Neutralization of a Monoenergetic, Collimated and Homogeneous Rigid Relativistic Electron Beam Propagating in a Dielectric	94
2.3	Magnetic Neutralization of a Monoenergetic, Collimated and Homogeneous Rigid Relativistic Electron Beam Propagating in a Conductor	96
3	Collective Effects of Relativistic Electron Beam Transport in Solids and Dense Plasmas	101
3.1	Quasi-static Approximation	102

3.1.1	Background Electrons Dynamics after the Beam Electromagnetic Neutralization	102
3.1.2	Electric and Magnetic Fields Radial Profiles	105
3.2	Beam-Plasma Instabilities	107
3.2.1	Linear Theory of Collisionless Instabilities	107
3.2.2	Non-linear Evolution and Saturation Effects	112
3.2.3	Resistive Filamentation Instability	113
3.3	Temperature Dependence of Fast Electrons Transport	117
3.3.1	Temperature Dependence of the Background Electrical Resistivity and Ionization State	117
3.3.2	Heat Equations	121
3.3.3	Plasma Heating by an Electron Beam	123
4	Collisional Effects in Relativistic Electron Transport through Solids and Dense Plasmas	127
4.1	Binary Collisions of a Relativistic Electron with Background Particles	128
4.1.1	Electron-Electron Binary Collisions	128
4.1.2	Electron-Ion Binary Collisions	130
4.2	Slowing Down of a Relativistic Electron in Solids and Dense Plasmas	131
4.2.1	Stopping Powers of relativistic Electrons	131
4.2.2	Range of a Relativistic Electron Propagating in a Dense Plasma	136
4.3	Angular Scattering of a Relativistic Electron in Solids and Dense Plasmas	137
4.3.1	Multiple Scattering Theory by Lewis	138
4.3.2	Multiple Scattering Theory by Moliere	139
4.4	Belyaev-Budker Collision Integral	141
5	Existing Simulation Methods for Fast Electron Transport	145
5.1	Particle-In-Cell methods	146
5.1.1	Full Particle-in-Cell methods	146
5.1.2	Hybrid Particle-in-Cell methods	148
5.2	Vlasov-Fokker-Planck methods	149

5.2.1 Full Vlasov-Fokker-Planck methods 149

5.2.2 Distribution Function Expansion methods 151

5.3 Conclusion 159

II Development, Implementation and Validation of a New Reduced Model for Fast Electron Transport in Solids and Dense Plasmas **163**

6 Development of a Reduced Model for Laser-generated Relativistic Electron Beam Transport in Solids and Dense Plasmas **165**

6.1 Kinetic Description of Relativistic Electron Beam Transport in Solids and Dense Plasmas 166

6.1.1 The Relativistic Vlasov-Belyaev-Budker Equation Applied to Relativistic Electron Beam Transport 166

6.1.2 Collisional Effects of Relativistic Electron Transport in Solids and Dense Plasmas 169

6.1.3 Background Electrons Dynamics in the "Hybrid" Assumption 172

6.2 M1 Model for Relativistic Electron Beam Transport 174

6.2.1 Spherical Harmonic and Cartesian Tensor Scalar Product Expansions 174

6.2.2 M1 closure 175

6.2.3 Properties of the M1 closure 179

6.3 Physics of the Background Material 189

6.3.1 Ionization State Z^* and Thermal Capacities $C_{V,\alpha}$ 189

6.3.2 Two-Temperature Electron Transport Coefficients η and κ_e 193

6.3.3 Electron-Ion/Lattice Coupling Term G 200

6.4 Conclusion 201

7 Numerical Implementation of the Model **205**

7.1 M1 equations 209

7.1.1 Second Order Explicit HLL Scheme for the Fast Electron Advection in Space and Fast Electron Slowing Down due to the Self-Generated Electric field 210

7.1.2 Downwind Explicit Scheme for the Fast Electron Collisional Slowing Down 216

7.1.3 Explicit Scheme for the Fast Electron Angular Deviations 216

7.1.4	Summary of the Full Explicit Scheme	218
7.1.5	First order Implicit Scheme for the Collisional Terms in the case of Very Dense Plasmas	218
7.1.6	Fast Electron Injection and Escaping Boundary Conditions	219
7.2	Self-Generated Electromagnetic Fields	221
7.2.1	Second Order Implicit Scheme describing the Self-Generated Magnetic Fields Diffusion and Second Order Explicit Schemes describing the Self-Generated Magnetic Fields Sources	223
7.2.2	Deduction of the Self-Generated Electric Field from the Magnetic Fields	228
7.2.3	Boundary Conditions	229
7.3	Second order Explicit Schemes for the Heat Equations	229
7.4	Summary	232
8	Validation of the Model	237
8.1	2D-3V Academic Case	238
8.1.1	Introduction	238
8.1.2	Plasma Heating and Self-generated Electromagnetic Fields	239
8.1.3	Kinetic evolution of the electron beam	242
8.1.4	Summary	247
8.2	2D-3V Realistic Simulation of Laser-generated Relativistic Electron Beam Transport	248
8.2.1	Introduction	248
8.2.2	Comparison with the Hybrid PIC Simulation	253
8.2.3	Conclusion	256
III	Applications to the Study of Laser-Generated Fast Electron Beam Transport in the Context of ICF	257
9	Application to the $K\alpha$ emission during Fast Electron Transport in Solid Targets	259
9.1	Computational Methods for Estimating the Emission of $K\alpha$ Photons	262
9.1.1	Fast Electron Recirculation and M1 Model for Fast Electron Transport	262

9.1.2	Emission of $K\alpha$ Photons in Hybrid Models due to Laser-generated Fast Electron Beam	266
9.1.3	K-shell Hole Density Dynamics	269
9.2	Application to the Saclay UHI100 Experiment	273
9.2.1	Preliminary 2D-3V Simulation - Effects of Solid State Corrections	275
9.2.2	Refluxing Dependence on the Target Thickness	280
9.2.3	Comparison of Time Integrated $K\alpha$ Emission of with the Experimental Data	289
9.2.4	Three-Dimensional Effects	293
9.2.5	Photoionization Effects	301
9.2.6	Summary and Conclusion	303
10	Application to the Generation of Shock Waves by Fast Electron Energy Deposition	307
10.1	Role of Laser-generated Fast electrons in the Shock Ignition Scheme	314
10.1.1	Theoretical predictions	314
10.1.2	Coupling of the Reduced Model for Fast Electron Transport with the Radiation Hydrodynamic CHIC code	318
10.1.3	Electron driven shock waves	321
10.1.4	Conclusion	324
10.2	Blast Wave generation in solid targets by the quasi-isochoric heating by laser-generated Electron Beam	325
10.2.1	Analytical Estimates	325
10.2.2	Radiation Hydrodynamic Simulations	330
11	Conclusion	337
IV	Résumé en Français	343
12	Étude du transport d'Electrons Rapides pour la Fusion par Confinement Inertiel	345

V	Appendix	359
A	Classical Plasma Kinetic Theory	361
A.1	BBGKY Hierarchy	364
A.1.1	Vlasov Equation	364
A.1.2	Liouville Theorem	365
A.1.3	BBGKY Hierarchy	365
A.1.4	Vlasov-Boltzmann Equation	366
A.1.5	Properties of the Boltzmann equation	368
A.2	Vlasov-Fokker-Plank-Landau Equation	372
A.2.1	Differential Rutherford Cross Section	372
A.2.2	Small-angle Collisions	374
A.2.3	Coulomb Logarithm $\ln \Lambda_{e\alpha}$	377
A.2.4	Properties of the Landau equation	379
A.3	Simplified Forms of the Collision Integral	380
A.3.1	BGK Approximation	380
A.3.2	Lorentzian Plasmas	380
B	Classical Plasma Hydrodynamic Theory	383
B.1	Two fluids Hydrodynamic Equations	385
B.1.1	Definitions	385
B.1.2	Local Thermodynamic Equilibrium	386
B.2	Plasma Transport Coefficients	388
B.2.1	Lorentz Approximation	388
B.2.2	Electron-electron Collision Contribution to the Hydrodynamic Fluxes	390
B.2.3	Transport Coefficients in an External Magnetic Field	391
B.2.4	Electron Degeneracy Corrections	393
B.3	Radiation Hydrodynamic Code CHIC	395
B.3.1	Monofluid Hydrodynamic Equations	395
B.3.2	Radiation Hydrodynamic Code CHIC	397

CONTENTS

B.3.3 CHIC MHD Package	400
----------------------------------	-----

List of symbols used

Physical Constants (the manuscript is written in the cgs units)

Physical quantity	Symbol	Value	Units
Boltzmann constant	k_B	$1.3807 \cdot 10^{-16}$	erg.K ⁻¹
Elementary charge	e	$4.8032 \cdot 10^{-10}$	statcoulomb
Speed of light in vacuum	c	$2.9979 \cdot 10^{10}$	cm/sec
Electron mass	m_e	$9.1094 \cdot 10^{-28}$	g
Proton mass	m_p	$1.6726 \cdot 10^{-24}$	g
Standard atomic weight	A	depends on the material	dimensionless
Atomic number	Z	depends on the material	dimensionless
Ion mass	m_i	Am_p	g
Planck constant	h	$6.6261 \cdot 10^{-27}$	erg.sec
	$\hbar = h/2\pi$	$1.0546 \cdot 10^{-27}$	erg.sec
Permittivity of free space	ϵ_0	$1/4\pi$	dimensionless
Permeability of free space	μ_0	$4\pi/c^2$	dimensionless
Fine-structure constant	$\alpha = e^2/\hbar c$	$1/137.038$	dimensionless
Electronvolt	eV	$1.6022 \cdot 10^{-12}$	erg

Linear algebra notations

Let us note a a scalar, \mathbf{A} , \mathbf{B} and \mathbf{C} three vectors in a 3-dimensional space (x, y, z) , \mathbf{D}_2 , \mathbf{E}_2 and \mathbf{F}_2 second order tensors (or 3×3 -dimensional matrices) and \mathbf{G}_3 a third order tensor in the same 3-dimensional space.

Scalar product

$$\mathbf{A} \cdot \mathbf{B} = \sum_{i=x,y,z} A_i B_i.$$

Linear transformations

$$\begin{aligned} \mathbf{B} &= \mathbf{D}_2 \cdot \mathbf{A} \quad \text{implies} \quad \forall i \in \{x, y, z\}, & B_i &= \sum_{j=x,y,z} D_{2,ij} A_j, \\ \mathbf{C} &= \mathbf{A} \cdot \mathbf{D}_2 \quad \text{implies} \quad \forall j \in \{x, y, z\}, & C_j &= \sum_{i=x,y,z} A_i D_{2,ij}, \\ \mathbf{D}_2 &= \mathbf{E}_2 \cdot \mathbf{F}_2 \quad \text{implies} \quad \forall (i, j) \in \{x, y, z\}^2, & D_{2,ij} &= \sum_{k=x,y,z} E_{2,ik} F_{2,kj}, \\ \mathbf{D}_2 &= \mathbf{G}_3 \cdot \mathbf{A} \quad \text{implies} \quad \forall (i, j) \in \{x, y, z\}^2, & D_{2,ij} &= \sum_{k=x,y,z} G_{3,ijk} A_k \quad \text{and} \\ \mathbf{E}_2 &= \mathbf{A} \cdot \mathbf{G}_3 \quad \text{implies} \quad \forall (j, k) \in \{x, y, z\}^2, & E_{2,jk} &= \sum_{i=x,y,z} A_i G_{3,ijk}. \end{aligned}$$

Transposition

$\mathbf{A} = \mathbf{B}^T$ is the transposition of \mathbf{B} and
 $\mathbf{D}_2 = \mathbf{E}_2^T$ is the transposition of \mathbf{E}_2 .

Vectorial product

$$\mathbf{A} \times \mathbf{B} = \begin{pmatrix} A_y B_z - A_z B_y \\ A_z B_x - A_x B_z \\ A_x B_y - A_y B_x \end{pmatrix}.$$

Tensorial products

$\mathbf{T}_2 = \mathbf{A} \otimes \mathbf{B}$ implies $\forall (i, j) \in \{x, y, z\}^2$, $\mathbf{T}_{2,ij} = A_i B_j$ and
 $\mathbf{T}_3 = \mathbf{A} \otimes \mathbf{B} \otimes \mathbf{C}$ implies $\forall (i, j, k) \in \{x, y, z\}^3$, $\mathbf{T}_{3,ijk} = A_i B_j C_k$.

Twice contracted product

$$a = \mathbf{D}_2 : \mathbf{E}_2 = \sum_{i=x,y,z} \sum_{j=x,y,z} D_{2,ij} E_{2,ji}.$$

Differential operators notations

Let us note $\mathbf{x} = (x, y, z)^T$ a vector expressed in 3-dimensional Cartesian coordinates in the basis $(0, \mathbf{e}_x, \mathbf{e}_y, \mathbf{e}_z)$, $\mathbf{r} = (z, r, \theta)^T$ a vector expressed in 3-dimensional cylindrical coordinates in the basis $(0, \mathbf{e}_z, \mathbf{e}_r, \mathbf{e}_\theta)$ and $\mathbf{p} = (p, \theta, \varphi)^T$ a vector expressed in 3-dimensional spherical coordinates in the basis $(0, \boldsymbol{\Omega} = \mathbf{p}/p, \mathbf{e}_\theta, \mathbf{e}_\varphi)$. Also, we note $f = f(\mathbf{x})$, $g = g(\mathbf{r})$ and $h = h(\mathbf{p})$ scalar functions of \mathbf{x} , \mathbf{r} and \mathbf{p} , respectively, $\mathbf{A} = A_x(\mathbf{x})\mathbf{e}_x + A_y(\mathbf{x})\mathbf{e}_y + A_z(\mathbf{x})\mathbf{e}_z$, $\mathbf{B} = B_z(\mathbf{r})\mathbf{e}_z + B_r(\mathbf{r})\mathbf{e}_r + B_\theta(\mathbf{r})\mathbf{e}_\theta$ and $\mathbf{C} = C_p(\mathbf{p})\boldsymbol{\Omega} + C_\theta(\mathbf{p})\mathbf{e}_\theta + C_\varphi(\mathbf{p})\mathbf{e}_\varphi$ vectorial functions of \mathbf{x} , \mathbf{r} and \mathbf{p} , respectively and $\mathbf{D} = [D_{ij}(\mathbf{x})]$, $(i, j) \in \{x, y, z\}^2$, $\mathbf{E} = [E_{ij}(\mathbf{r})]$, $(i, j) \in \{z, r, \theta\}^2$ and $\mathbf{F} = [F_{ij}(\mathbf{p})]$, $(i, j) \in \{p, \theta, \varphi\}^2$ 2nd order tensorial functions of \mathbf{x} , \mathbf{r} and \mathbf{p} , respectively. Also, we note $\mathbf{v} = (v_x, v_y, v_z)^T$, $(v_z, v_r, v_\theta)^T$ or $(v_p, v_\theta, v_\varphi)^T$ a velocity in the chosen system of coordinates.

Gradient

$$\frac{\partial f}{\partial \mathbf{x}} = \begin{pmatrix} \frac{\partial f}{\partial x} \\ \frac{\partial f}{\partial y} \\ \frac{\partial f}{\partial z} \end{pmatrix}, \quad \frac{\partial g}{\partial \mathbf{r}} = \begin{pmatrix} \frac{\partial g}{\partial z} \\ \frac{\partial g}{\partial r} \\ \frac{\partial g}{\partial \theta} \end{pmatrix} \quad \text{and} \quad \frac{\partial h}{\partial \mathbf{p}} = \begin{pmatrix} \frac{\partial h}{\partial p} \\ \frac{\partial h}{\partial \theta} \\ \frac{\partial h}{\partial \varphi} \end{pmatrix}.$$

It may happen in the text that $(\partial/\partial\mathbf{x}) = (\partial_x, \partial_y, \partial_z)^T$, $(\partial/\partial\mathbf{r}) = (\partial_z, \partial_r, (1/r)\partial_\theta)^T$ or $(\partial/\partial\mathbf{p}) = (\partial_p, (1/p)\partial_\theta, (1/p\sin\theta)\partial_\varphi)^T$ are used as vectors in expressions such as presented previously in the paragrah **Linear algebra notations** (see for example *curl*)

Infinitesimal volume

$$d^3\mathbf{x} = dx dy dz, d^3\mathbf{r} = rdz dr d\theta \text{ and } d^3\mathbf{p} = p^2 \sin\theta dp d\theta d\varphi.$$

Divergence of a vectorial function

$$\begin{aligned} \frac{\partial}{\partial\mathbf{x}} \cdot \mathbf{A} &= \frac{\partial A_x}{\partial x} + \frac{\partial A_y}{\partial y} + \frac{\partial A_z}{\partial z}, \\ \frac{\partial}{\partial\mathbf{r}} \cdot \mathbf{B} &= \frac{\partial B_z}{\partial z} + \frac{1}{r} \frac{\partial}{\partial r} (rB_r) + \frac{1}{r} \frac{\partial B_\theta}{\partial \theta} \text{ and} \\ \frac{\partial}{\partial\mathbf{p}} \cdot \mathbf{C} &= \frac{1}{p^2} \frac{\partial}{\partial p} (p^2 C_p) + \frac{1}{p \sin\theta} \frac{\partial}{\partial \theta} (\sin\theta C_\theta) + \frac{1}{p \sin\theta} \frac{\partial C_\varphi}{\partial \varphi}. \end{aligned}$$

Divergence of a tensorial function

$$\begin{aligned} \frac{\partial}{\partial\mathbf{x}} \cdot \mathbf{D} &= \begin{pmatrix} \frac{\partial D_{xx}}{\partial x} + \frac{\partial D_{yx}}{\partial y} + \frac{\partial D_{zx}}{\partial z} \\ \frac{\partial D_{xy}}{\partial x} + \frac{\partial D_{yy}}{\partial y} + \frac{\partial D_{zy}}{\partial z} \\ \frac{\partial D_{xz}}{\partial x} + \frac{\partial D_{yz}}{\partial y} + \frac{\partial D_{zz}}{\partial z} \end{pmatrix}, \frac{\partial}{\partial\mathbf{r}} \cdot \mathbf{E} = \begin{pmatrix} \frac{\partial E_{zz}}{\partial z} + \frac{1}{r} \frac{\partial}{\partial r} (rE_{rz}) + \frac{1}{r} \frac{\partial E_{\theta z}}{\partial \theta} \\ \frac{\partial D_{zr}}{\partial z} + \frac{1}{r} \frac{\partial}{\partial r} (rE_{rr}) + \frac{1}{r} \frac{\partial E_{\theta r}}{\partial \theta} - \frac{E_{\theta\theta}}{r} \\ \frac{\partial D_{z\theta}}{\partial z} + \frac{1}{r} \frac{\partial}{\partial r} (rE_{r\theta}) + \frac{1}{r} \frac{\partial E_{\theta\theta}}{\partial \theta} + \frac{E_{\theta r}}{r} \end{pmatrix} \\ \text{and } \frac{\partial}{\partial\mathbf{p}} \cdot \mathbf{F} &= \begin{pmatrix} \frac{1}{p^2} \frac{\partial}{\partial p} (p^2 F_{pp}) + \frac{1}{p \sin\theta} \frac{\partial}{\partial \theta} (\sin\theta F_{\theta p}) + \frac{1}{p \sin\theta} \frac{\partial F_{\varphi p}}{\partial \varphi} - \frac{F_{\theta\theta} + F_{\varphi\varphi}}{p} \\ \frac{1}{p^2} \frac{\partial}{\partial p} (p^2 F_{p\theta}) + \frac{1}{p \sin\theta} \frac{\partial}{\partial \theta} (\sin\theta F_{\theta\theta}) + \frac{1}{p \sin\theta} \frac{\partial F_{\varphi\theta}}{\partial \varphi} + \frac{F_{\theta p} - \cot\theta F_{\varphi\varphi}}{p} \\ \frac{1}{p^2} \frac{\partial}{\partial p} (p^2 F_{p\varphi}) + \frac{1}{p \sin\theta} \frac{\partial}{\partial \theta} (\sin\theta F_{\theta\varphi}) + \frac{1}{p \sin\theta} \frac{\partial F_{\varphi\varphi}}{\partial \varphi} + \frac{F_{\varphi p} + \cot\theta F_{\varphi\theta}}{p} \end{pmatrix}. \end{aligned}$$

Curl

$$\begin{aligned} \frac{\partial}{\partial\mathbf{x}} \times \mathbf{A} &= \begin{pmatrix} \frac{\partial A_z}{\partial y} - \frac{\partial A_y}{\partial z} \\ \frac{\partial A_x}{\partial z} - \frac{\partial A_z}{\partial x} \\ \frac{\partial A_y}{\partial x} - \frac{\partial A_x}{\partial y} \end{pmatrix}, \frac{\partial}{\partial\mathbf{r}} \times \mathbf{B} = \begin{pmatrix} \frac{1}{r} \frac{\partial}{\partial r} (rB_\varphi) - \frac{1}{r} \frac{\partial B_r}{\partial \varphi} \\ \frac{1}{r} \frac{\partial B_z}{\partial \varphi} - \frac{\partial B_\varphi}{\partial z} \\ \frac{\partial B_r}{\partial z} - \frac{\partial B_z}{\partial r} \end{pmatrix} \text{ and} \\ \frac{\partial}{\partial\mathbf{p}} \times \mathbf{C} &= \begin{pmatrix} \frac{1}{p \sin\theta} \frac{\partial}{\partial \theta} (\sin\theta C_\varphi) - \frac{1}{p \sin\theta} \frac{\partial C_\theta}{\partial \varphi} \\ \frac{1}{p \sin\theta} \frac{\partial C_r}{\partial \varphi} - \frac{1}{p} \frac{\partial}{\partial p} (pC_\varphi) \\ \frac{1}{p} \frac{\partial}{\partial p} (pC_\theta) - \frac{1}{p} \frac{\partial C_p}{\partial \theta} \end{pmatrix}. \end{aligned}$$

Laplacian of a scalar function

$$\begin{aligned}\frac{\partial^2 f}{\partial \mathbf{x}^2} &= \frac{\partial^2 f}{\partial x^2} + \frac{\partial^2 f}{\partial y^2} + \frac{\partial^2 f}{\partial z^2}, \\ \frac{\partial^2 g}{\partial \mathbf{r}^2} &= \frac{\partial^2 g}{\partial z^2} + \frac{1}{r} \frac{\partial}{\partial r} \left(r \frac{\partial g}{\partial r} \right) + \frac{1}{r^2} \frac{\partial^2 g}{\partial \theta^2} \text{ and} \\ \frac{\partial^2 h}{\partial \mathbf{p}^2} &= \frac{1}{p^2} \frac{\partial}{\partial p} \left(p^2 \frac{\partial h}{\partial p} \right) + \frac{1}{p^2 \sin \theta} \frac{\partial}{\partial \theta} \left(\sin \theta \frac{\partial h}{\partial \theta} \right) + \frac{1}{p^2 \sin^2 \theta} \frac{\partial^2 h}{\partial \varphi^2}.\end{aligned}$$

Laplacian of a vectorial function

$$\begin{aligned}\frac{\partial^2 \mathbf{A}}{\partial \mathbf{x}^2} &= \begin{pmatrix} \frac{\partial^2 A_x}{\partial \mathbf{x}^2} \\ \frac{\partial^2 A_y}{\partial \mathbf{x}^2} \\ \frac{\partial^2 A_z}{\partial \mathbf{x}^2} \end{pmatrix}, \quad \frac{\partial^2 \mathbf{B}}{\partial \mathbf{r}^2} = \begin{pmatrix} \frac{\partial^2 B_z}{\partial \mathbf{r}^2} - \frac{2}{r^2} \frac{\partial B_\theta}{\partial \theta} - \frac{B_r}{r^2} \\ \frac{\partial^2 B_\theta}{\partial \mathbf{r}^2} + \frac{2}{r^2} \frac{\partial B_r}{\partial \theta} - \frac{B_\theta}{r^2} \\ \frac{\partial^2 B_r}{\partial \mathbf{r}^2} - \frac{2}{r^2} \frac{\partial B_\theta}{\partial \theta} - \frac{B_r}{r^2} \end{pmatrix} \text{ and} \\ \frac{\partial^2 \mathbf{C}}{\partial \mathbf{p}^2} &= \begin{pmatrix} \frac{\partial^2 C_p}{\partial \mathbf{p}^2} - \frac{2}{p^2} \frac{\partial C_\theta}{\partial \theta} - \frac{2}{p^2 \sin \theta} \frac{\partial C_\varphi}{\partial \varphi} - \frac{2 C_p + \cot \theta C_\theta}{p^2} \\ \frac{\partial^2 C_\theta}{\partial \mathbf{p}^2} + \frac{2}{p^2} \frac{\partial C_p}{\partial \theta} - \frac{2 \cos \theta}{p^2 \sin^2 \theta} \frac{\partial C_\varphi}{\partial \varphi} - \frac{C_\theta}{p^2 \sin^2 \theta} \\ \frac{\partial^2 C_\varphi}{\partial \mathbf{p}^2} + \frac{2}{p^2 \sin \theta} \frac{\partial C_p}{\partial \varphi} + \frac{2 \cos \theta}{p^2 \sin^2 \theta} \frac{\partial C_\theta}{\partial \varphi} - \frac{C_\varphi}{p^2 \sin^2 \theta} \end{pmatrix}.\end{aligned}$$

Components of advection terms

In Plasma Hydrodynamic Theory, the relation

$$\frac{\partial}{\partial \mathbf{x}} \cdot (n \mathbf{v} \otimes \mathbf{v}) = n \left[\left(\frac{\partial}{\partial \mathbf{x}} \cdot \mathbf{v} \right) \mathbf{v} + \left(\mathbf{v} \cdot \frac{\partial}{\partial \mathbf{x}} \right) (\mathbf{v}) \right]$$

describes the convection term. Therefore, we will note :

$$\begin{aligned}\left(\mathbf{v} \cdot \frac{\partial}{\partial \mathbf{x}} \right) (\mathbf{A}) &= \begin{pmatrix} v_x \frac{\partial A_x}{\partial x} + v_y \frac{\partial A_x}{\partial y} + v_z \frac{\partial A_x}{\partial z} \\ v_x \frac{\partial A_y}{\partial x} + v_y \frac{\partial A_y}{\partial y} + v_z \frac{\partial A_y}{\partial z} \\ v_x \frac{\partial A_z}{\partial x} + v_y \frac{\partial A_z}{\partial y} + v_z \frac{\partial A_z}{\partial z} \end{pmatrix}, \\ \left(\mathbf{v} \cdot \frac{\partial}{\partial \mathbf{r}} \right) (\mathbf{B}) &= \begin{pmatrix} v_z \frac{\partial B_z}{\partial z} + v_r \frac{\partial B_z}{\partial r} + \frac{v_\theta}{r} \frac{\partial B_z}{\partial \theta} \\ v_z \frac{\partial B_r}{\partial z} + v_r \frac{\partial B_r}{\partial r} + \frac{v_\theta}{r} \frac{\partial B_r}{\partial \theta} - \frac{v_\theta B_\theta}{r} \\ v_z \frac{\partial B_\theta}{\partial z} + v_r \frac{\partial B_\theta}{\partial r} + \frac{v_\theta}{r} \frac{\partial B_\theta}{\partial \theta} + \frac{v_\theta B_r}{r} \end{pmatrix} \text{ and} \\ \left(\mathbf{v} \cdot \frac{\partial}{\partial \mathbf{p}} \right) (\mathbf{C}) &= \begin{pmatrix} v_p \frac{\partial C_p}{\partial p} + \frac{v_\theta}{p} \frac{\partial C_p}{\partial \theta} + \frac{v_\varphi}{p \sin \theta} \frac{\partial C_p}{\partial \varphi} - \frac{v_\theta C_\theta + v_\varphi C_\varphi}{p} \\ v_p \frac{\partial C_\theta}{\partial p} + \frac{p}{v_\theta} \frac{\partial C_\theta}{\partial \theta} + \frac{p \sin \theta}{v_\varphi} \frac{\partial C_\theta}{\partial \varphi} + \frac{v_\theta C_p - v_\varphi \cot \theta C_\varphi}{p} \\ v_p \frac{\partial C_\varphi}{\partial p} + \frac{p}{v_\theta} \frac{\partial C_\varphi}{\partial \theta} + \frac{p \sin \theta}{v_\varphi} \frac{\partial C_\varphi}{\partial \varphi} + v_\varphi \frac{C_p + \cot \theta C_\theta}{p} \end{pmatrix}.\end{aligned}$$

Symbols related to the laser pulse characteristics

Physical quantity	Symbol	SI Unit	cgs Unit	Practical Unit
Intensity	I_L	W.m^{-2}	$\text{erg.sec}^{-1}.\text{cm}^{-2}$	W.cm^{-2}
Wavelength	λ_L or λ	m	cm	μm or c/ω
Wave number	$k = 2\pi/\lambda_L$	rad.m^{-1}	rad.cm^{-1}	ω/c
Temporal period	$T = \lambda/c$	s	sec	$1/\omega$
Frequency	$f = 1/T$	Hz	sec^{-1}	ω
(angular) Frequency	ω, ω_0 or $\omega_L = 2\pi f$	rad.s^{-1}	rad.sec^{-1}	ω
Electrostatic potential	Φ	V	statvolt	$m_e c^2/e$
Vector potential	\mathbf{A}	V.s.m^{-1}	gauss.sec	$m_e c/e$
Electric field	$\mathbf{E} = -\frac{\partial\Phi}{\partial\mathbf{r}} - \frac{\partial\mathbf{A}}{\partial t}$	V.m^{-1}	statvolt/cm	$m_e c\omega/e$
Magnetic field (induction)	$\mathbf{B} = c\frac{\partial}{\partial\mathbf{r}} \times \mathbf{A}$	T	gauss	$m_e c\omega/e$

(Here

\mathbf{r} is the vector position expressed in whatever the coordinates system)

Symbols of fundamental plasma parameters

The electron temperature T_e is expressed in eV, the electron and ion densities n_e and n_i in cm^{-3} .

Physical quantity	Symbol	Formula	order of magnitude (cgs)
Plasma ionization state	Z^*	$Z^* = n_e/n_i$	$0 \leq Z^* \leq Z$
Electron-ion Coulomb logarithm	$\ln \Lambda_{ei}$	Annexe A.2.3	> 2
Electron Thermal velocity	$v_{T,e}$ or $v_{Th,e}$	$\sqrt{k_B T_e/m_e}$	$4.19 \cdot 10^7 \sqrt{T_e}$
Ion sound velocity	c_s	$\sqrt{Z^* k_B T_e/m_i}$	$4.19 \cdot 10^7 \sqrt{T_e}$
Electron plasma frequency	ω_p, ω_e or $\omega_{p,e}$	$\sqrt{4\pi n_e e^2/m_e}$	$5.64 \cdot 10^4 \sqrt{n_e}$
Electron gyrofrequency	ω_c or ω_{ce}	$eB/m_e c$	$1.76 \cdot 10^7 B$
Electron-ion collision rate	$\bar{\nu}_{ei}, \nu_{ei}$ or ν	Annexe A.3.2	$3.9 \cdot 10^{-6} n_i Z^{*2} \ln \Lambda_{ei} T_e^{-3/2}$
Coulomb explosion time	τ_e	ν_{ei}/ω_p^2	$1.2 \cdot 10^{-15} Z^* \ln \Lambda_{ei} T_e^{-3/2}$
Electron De Broglie wave length	λ_{DB} or $\lambda_{\text{De Broglie}}$	$\hbar/2m_e v_{T,e}$	$1.38 \cdot 10^{-8} T_e^{-1/2}$
Electron-electron Landau length	λ_L or λ_{Landau}	$e^2/k_B T_e$	$1.44 \cdot 10^{-7} T_e^{-1}$
Debye screening length	λ_D or λ_{Debye}	$v_{T,e}/\omega_p$	$7.43 \cdot 10^2 (T_e/n_e)^{1/2}$
Mean ions distance	r_i	$(3/4\pi n_i)^{1/3}$	$0.6 n_i^{-1/3}$
Electron Larmor radius	r_L or R_L	$v_{T,e}/\omega_c$	$2.88 T_e^{1/2} B^{-1}$
Electron inertia length	λ_e	c/ω_p	$5.31 \cdot 10^5 n_e^{-1/2}$

Relativistic electron beam transport

The electron temperature T_e of the plasma, where the beam propagates through, is expressed in eV, the plasma ion density n_i is in cm^{-3} , the beam density n_b is in [10^{21} cm^{-3}], the beam radius r_b is in [$10 \mu\text{m}$], the electron velocity v and the beam electrons mean velocity v_b of a collimated and monoenergetic electron beam (*) are in cm.s^{-1} and the thermal Maxwell-Juttner (M-J) beam temperature T_b is in keV.

CONTENTS

Physical quantity	Symbol	Formula	order of magnitude (cgs)
Electron velocity	β	v/c	$\lesssim 1$
Electron Lorentz factor	γ	$1/\sqrt{1-\beta^2}$	≤ 1
Electron momentum	p	$\gamma m_e v$	
Electron kinetic energy	ε	$(\gamma - 1)m_e c^2$	
Electron gyrofrequency	ω_c	$eB/\gamma m_e c$	$1.76 \cdot 10^7 B/\gamma$
Larmor electron radius	λ_L	v/ω_c	$1.7 \cdot 10^3 \gamma \beta B^{-1}$
Electron De Broglie wave length	λ_{DB}	$\hbar/2p$	$1.9 \cdot 10^{-11}/\gamma \beta$
Beam* electrons velocity	β_b	v_b/c	$\lesssim 1$
Beam* electrons Lorentz factor	γ_b	$1/\sqrt{1-\beta_b^2}$	≤ 1
Beam* electrons momentum	p_b	$\gamma_b m_e v_b$	
Beam* electrons kinetic energy	ε_b	$(\gamma_b - 1)m_e c^2$	
Beam (M-J) thermal velocity	$\beta_{T,b}$	$\sqrt{2k_B T_b/\gamma_b m_e c^2}$	$0.06 T_b^{1/2}$
Beam* neutralization time ($\omega_p/\nu_{ei} \gg 1$)	$\bar{\nu}_{ei}^{-1}$	Chapter 2.2	$2.6 \cdot 10^5 T_e^{3/2}/n_i Z^{*2} \ln \Lambda_{ei}$
Beam* neutralization time ($\omega_p/\nu_{ei} \ll 1$)	τ_e/γ_b	Chapter 2.2	$1.2 \cdot 10^{-15} Z^* \ln \Lambda_{ei}/\gamma_b T_e^{3/2}$
Beam* diffusion time	τ_d	Chapter 2.2	$9 \cdot 10^{-13} r_b^2 T_e^{3/2}/Z^* \ln \Lambda_{ei}$
Beam (* and M-J) plasma frequency	ω_b	$\sqrt{4\pi n_b e^2/\gamma_b m_e}$	$1.78 \cdot 10^{15} (n_b/\gamma_b)^{1/2}$
Beam (M-J) Debye screening length	λ_D	$\sqrt{k_B T_b/4\pi\gamma_b n_b e^2}$	$7.43 \cdot 10^{-7} (T_b/\gamma_b n_b)^{1/2}$
Beam (* and M-J) electrons inertia length	λ_b	c/ω_b	$1.68 \cdot 10^{-5} \gamma_b/n_b^{1/2}$
Alfven-Lawson limit*	I_A	$-\gamma_b \beta_b m_e c^3/e$	$-17 \gamma_b \beta_b$ kA

Chapter 0

Introduction

"Physics is like sex: sure, it may give some practical results, but that's not why we do it."

Richard P. Feynman

0.1 Thermonuclear Plasma Fusion as the Solution for the XXith century Energy Production

0.1.1 World Energy Balance

All experiments and observations carried out until today show that there is a universal quantity which is conserved during all evolutions and all transformations of matter and fields : the energy. According to Noether's theorem, conservation of energy is a direct mathematical consequence of the translational symmetry of the quantity conjugate to the energy, namely the time. In other words, it is nothing else than the intuition we have that physics laws do not change with time. In 1845, this quantity has been introduced by James Prescott Joule in order to understand the link between mechanical work and generation of heat. In order to pay homage to him, one calls "Joule" and one notes "J" the SI energy unit, based on the amount transferred to an object by the mechanical work of moving it 1 m against a force of 1 N. Since the development of the thermodynamics theory in the XIXth century, the energy conservation principle has become an indispensable element of understanding of any physical process. All developments of modern physics are related to studying different ways of converting energy from one form into another. To give an order of magnitude, the nuclear reactions of fission of 0.01 g of Uranium provide approximatively 1 kWh ($1 \text{ kWh} = 3.6 \text{ MJ}$) of heat energy in a nuclear power plant. The same amount of heat energy can be obtained by burning approximatively 100 g of oil, coal or gas (1 million of tonnes of oil or oil equivalent produces about 4.4 TWh of electricity on a modern power station), by condensing 1.6 kg of water vapor or by capturing solar radiations energy on a surface of 1 m^2 during one hour (The sun light intensity on Earth is about 0.1 W.cm^{-2} during a sunny day). 1 kWh represents also the gravitational potential energy of 3 tonnes of water falling from 100 m of altitude in a hydroelectric power plant or the kinetic energy of 20000 m^3 of air moving with a velocity of 60 km.h^{-1} in a wind power plant or the energy needed by a human being of 65 kg to climb a mountain peak of 3000 m. In addition to this important concept of energy conservation, the thermodynamic theory has also led to the Industrial Revolution : little by little, a manual labor has been replaced by machines, a horse-drawn carriage has been replaced by steam powered or thermal engines transportation vehicles and a lot of new manufacturing have been developed. In the XXth, thanks to this concept, a technological and scientific knowledge has exponentially grown up and has led to incredibly improved quality of human life, allowing the world population to considerably increase (see the World Population estimates of the United Nations). It is striking to notice how the Gross National Product of a today country is strongly correlated with its energy "consumption". The fossil fuels such as oil, gas and coal are used today mainly for energy "production" and represent $\approx 90\%$ in the world energy "consumption" as shown in **Figure 1**. The nuclear and hydroelectrical energy represent each one only $\approx 6\%$ of the world energy "consumptions". Even if other renewable energies from wind, biomass, waste, solar and geothermal power plants are more and more used thanks to

governments subsidies, their contribution is still negligible.

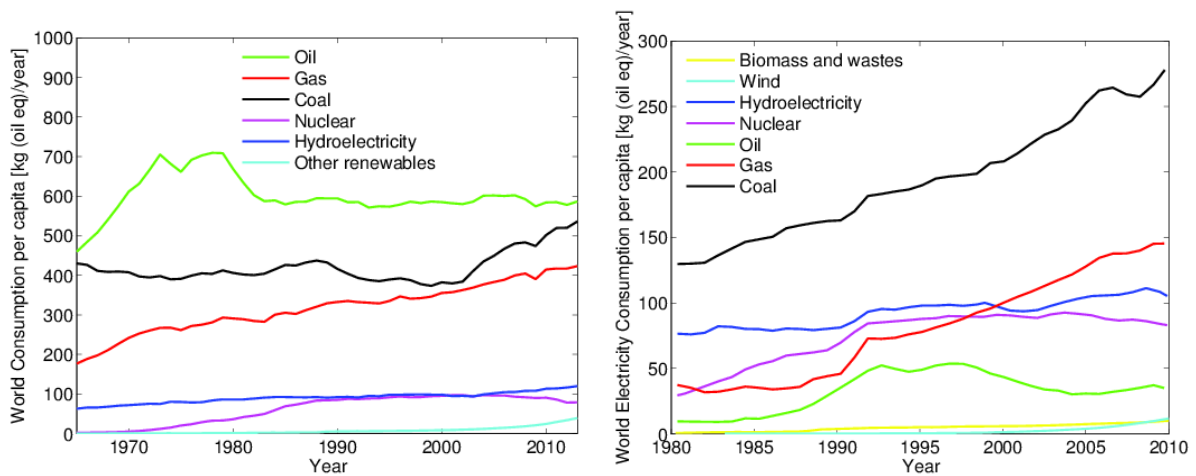


Figure 1: World consumption per capita (left) estimated from the *BP Statistical Review of world energy 2014 workbook* and World Electricity Consumption per capita (right) estimated from data published by the World Bank and the International Energy Agency. The world population is estimated from *the United Nations Revision of the World Population*

One must say that the expressions such as energy "consumption" or "production" are misused. Indeed, by definition, the energy is conserved during all transformations/evolutions. The sense that we attribute to the words "production" and "consumption" of energy is that one converts one amount of energy which already exists in a certain form into the same quantity of energy in another form. In this way, there is no "clean energy", the energy "production"/"consumption" is nothing else than the pure modification of our environment. Thus, like all continuous functions, one can show that each energy resource extraction from Earth will attain its maximum at a certain time and then will decrease until the resource will totally disappear from Earth. The *BP Statistical Review of world energy 2014* estimates that the oil and natural gaz reserves-to-"production" ratios are available for about 50 years, while the coal reserves-to-"production" ratio will be available for about 100 years. These evaluations are probably underestimated because of financial reasons but, on the other hand, these estimates are based on the 2013 data of the World population, while it is expected to grow up to more that 11 billions of people in ≈ 2100 (compared to ≈ 7.1 billions in 2013) according to extrapolations carried out by the United Nations in 2012. In addition, this strong population growth is expected to happen in developing countries where the resource demands will be the higher than average. One understands easily, according to **Figure 1**, which highlights our huge consumption of coal, gaz and oil, that the cost of energy consumption will be continuously increasing until each of them disappears if one does not find an alternative. Even if it is the more efficient way of producing energy and the less harmful for the environment, the governments policy is expected to limit the use of nuclear power plants due to the long life time of the radioactive waste and the growing public opposition -which plays an important role during elections- due to disasters such as Fukushima (2011), Chernobyl (1986) and Three Mile Island (1979). However, the reality is quite opposite. One can easily demonstrate that nuclear power

plants are responsible for less human deaths than fossil fuel burning plants if one takes into account the induced skin and lung cancers and the death of mine workers.

In addition, each way of "producing" or "consuming" energy produces actually entropy due to the irreversible modifications it operates in the Nature. The entropy is also a physical quantity which has been defined during the development of thermodynamics in the XIXth century. It is a measure of the number of specific ways in which a thermodynamic system may be arranged. It can therefore be understood as the measure of the system disorder. According to the second law of thermodynamics, the entropy of an isolated system never decreases and such systems spontaneously evolve towards thermodynamic equilibrium, that is to say, the configuration with a maximum entropy. The Earth is not an isolated system due to its continuous irradiation by Cosmic Rays and its self-emission of thermal infrared radiations. Besides, one can show according to the second principle of Thermodynamics taking into account these processes, that the World "Entropy consumption/production" is responsible for the rise of the Earth temperature ($\approx +1^\circ$ since the beginning of the XXth century). Indeed, since 1965, the carbon dioxide emission, known to be one of the major factor responsible for the Earth greenhouse effect, has increased from ≈ 3500 kg/year/capita to ≈ 5000 kg/year/capita according to the *BP Statistical Review of world energy 2014 workbook* and the United nations world population estimates. Consequently, even if the hydro power plants are the most efficient way of "producing" energy among all ecologically friendly ones, it will also be affected by the climate changes due to the droughts induced by this increase of temperature. For example, Europe is expected to lose 20 – 30% of precipitations until 2100 leading to a smaller hydroelectricity production efficiency (The majority of European hydro power plants does not work well yet at summer). Finally, other "renewable energies" such as wind power plants or photovoltaic panels are insufficient to supply the World demand especially in the industrial zones. As a conclusion, there is an important and challenging Energy issue for the Humanity in the XXIth century and will surely lead to important conflicts between Nations if one does not find an alternative (or reduce our consumption which seems to be impossible).

0.1.2 Thermonuclear Fusion

Four fundamental interactions have been discovered by physicists : the Gravitational, the Electromagnetic, the Strong Nuclear and the Weak Nuclear interaction. Effective only at a distance of a few fm, the Strong Nuclear force is 137 times stronger than the Electromagnetic one, 10^{25} times stronger than the Weak Force interaction and 10^{38} times stronger than the Gravitational interaction. This ensures the stability of ordinary matter, in confining the elementary particles quarks into hadrons such as proton and neutron both called nucleons, the largest components of the mass of ordinary matter. Most of the mass-energy of a common proton $m_p c^2$ or neutron $m_n c^2$ is in the form of the Strong Force Field Energy; the individual quarks provide only about 1% of the mass-energy of a proton. Also, experiments show that the mass of an atomic nucleus M is always smaller than the sum of its nucleons

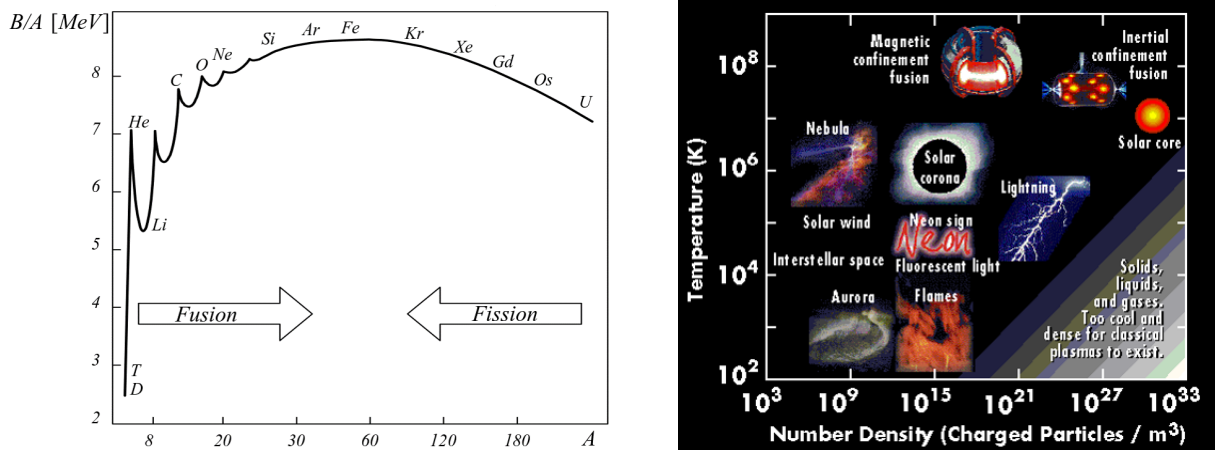
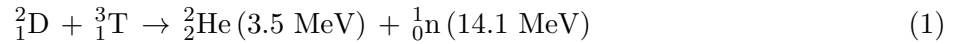


Figure 2: The Aston curve of the strong nuclear binding energy per nucleon $B(Z, N)/A$ (left) and a NASA density-temperature map of existing plasmas

mass $Nm_n + Zm_p$ taken separately. This mass energy deficit $[M - (Nm_n + Zm_p)]c^2$ is converted into strong nuclear binding energy according to the famous Einstein equation, and it is consequently responsible for the stability of atoms. Besides, not all combinations of $A = Z + N$ nucleons are necessary stable. Only 282 nuclei are known to be stable on the Earth (see the Aston curve on the left panel of **Figure 2**). Lightweight atoms are stable when the number of their neutrons N approximately equals the number of protons Z which defines the nucleus electrical charge. The atoms heavier than iron ($A > 54$) are stable if $N \approx 1.5Z$. Again according to the Aston curve, two kinds of nuclear reactions are exoenergetic : the nuclear fission of one heavy nucleus, which is a process already used in fission nuclear power plants, but also the nuclear fusion of two lightweight nuclei. In the 1950's, the idea of controlling thermonuclear combustion of lightweight atoms for Energy "production" was born shortly after the development of a theoretical model of the fusion reactions of lightweight elements to explain the conversion of nuclear binding energy into heat in stars [Bethe, 1939]. Since then, "bringing the star power on Earth" has been the dream of many physicists and seems to be a promising solution to solve the World Energy issue of the XXIth century. The problem is that while the Gravitational and Electromagnetic forces act over potentially infinite distance, the another two Nuclear forces act over minuscule subatomic distances and are more difficult to access. According to the Electromagnetic theory, an energy of about 1 MeV is needed to counteract the Coulomb barrier between two nuclei and make them getting close enough to fuse. Actually, an energy of about 10 keV is sufficient thanks to the quantum tunneling effect [Gamow, 1928]. The fusion of two nuclei has been achieved many times thanks to particle accelerators and a lot of stable nuclei have been discovered thanks to them. Recently, the yet-unnamed element 117 have been created by physicists at the GSI Helmholtz Center for Heavy Ion Research, an accelerator laboratory located in Darmstadt, Germany. But, concerning the energy "production", the quantity of accelerated isotopes is too small to generate more energy than the energy needed to accelerate them. Also, even if the cold fusion or muon-catalyzed fusion is a well known process since the 1980's [Jones et al., 1983], it does not allow to get high gains. Indeed,

a net energy production is impossible because of a high energy required to create muons, their short $2.2 \mu\text{s}$ life time and a high probability that a muon will bind to a new alpha (He) particle.

The only way to "produce" energy thanks to fusion reactions consists in creating a thermonuclear plasma in order to achieve high reaction rates and consequently high gains like in the Stellar Temperature-Density conditions (see the right panel of **Figure 2**). In addition to this constraint, there are other requirements : the nuclear reaction must be exothermic, it must employ the lightest possible nuclei to limit the Coulomb barrier, which is proportional to their atomic number Z , it must have a large cross section (probability), implying consequently only 2 nuclei, it must conserve the proton and neutron numbers in order to limit the weak nuclear interaction and finally it must produce at least one neutron in addition to the heavier nucleus in order to heat the blanket coolants and to produce electricity. 80 fusion reactions satisfy these criteria but the most probable one is the fusion reaction of the two Hydrogen isotopes :



due to the existence of an intermediate resonant nuclear state in this reaction. In **Figure 3**, the reaction rate of such a $\text{T(d,n)}^4\text{He}$ fusion nuclear reaction $\langle \sigma v \rangle$ is plotted. Here, σ is the fusion reaction cross section i.e. the effective area of a targeted Deuterium (or Tritium) nuclei seen by a projectile Tritium (Deuterium, respectively), v is the relative velocity of the projectile in a collision and the angle brackets mean that the rate is averaged over a Maxwell-Boltzmann distribution function (thermodynamic equilibrium). One can see that the reaction probability is maximum for a thermonuclear DT plasma at a temperature $T \approx 100 \text{ keV}$, which is not yet achievable with the today technology. However, a plasma temperature of 10 keV can be achieved and would be sufficient. Three other fusion nuclear reactions can also occur at this temperature but with smaller probabilities : ${}^3\text{He(d,p)}^4\text{He}$, D(d,p)T and $\text{D(d,n)}^3\text{He}$. Their reaction rates are also shown in **Figure 3**.

From a practical point of view, concerning the energy "production", there is an almost infinite quantity of Deuterium ${}^2_1\text{D}$ on the Earth with 33 g in each tons of sea water; That is why one calls the DT fusion the *blue energy*. The Tritium ${}^3_1\text{T}$ can be produced in a fusion reaction between the escaping neutrons ${}^1_0\text{n} (14.1 \text{ MeV})$ and lithium nuclei ${}^6_3\text{Li}$ or ${}^7_3\text{Li}$ which are abundant on Earth. So, contrary to the fission nuclear power plants, which are using limited resources of Uranium, Plutonium and Thorium, there is no resources problems. Also, the DT fusion presents no risk of a runaway chain reactions and no long life time radioactive waste. The fusion reaction products are stable and only activation of construction materials by fast neutrons is expected. As a conclusion, an eventual nuclear fusion power plant would have all the pros of the nuclear fission ones without its cons that is to say, without polluting the environment, without eventual nuclear catastrophes and not facing the problem of limited terrestrial resources.

0.1.3 Lawson Criterion

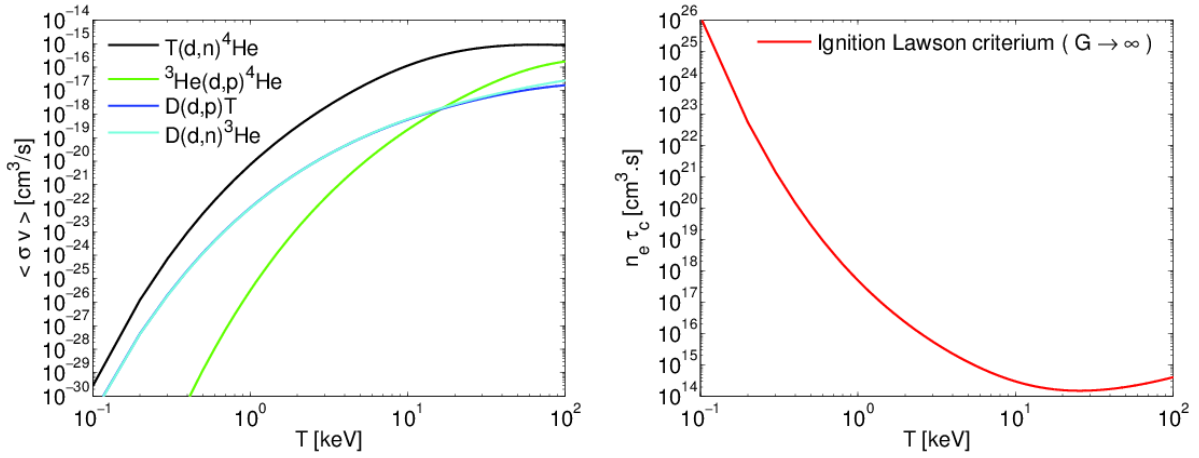


Figure 3: Reaction rate $\langle \sigma v \rangle$ of the different fusion nuclear reactions (left panel) and Lawson criterion for the Ignition (right panel) both estimated from [Bosch and Hale, 1992]

Even more than 99% of visible matter in the universe can be found in the plasma state and it has been studied for many decades. However, it is still difficult to create and maintain a thermonuclear plasma today. In order to evaluate the conditions needed to create and control such an equimolar DT plasma, one has to take into account on the one hand the plasma power losses P_{loss} and on the other hand the total power gain P_{gain} . By definition, a plasma is made of a large number of charged particles and it is characterized by a collective behavior of particles due to the long distance electromagnetic forces. Therefore, the total power losses consist in the thermal, mechanical and radiation losses (every accelerated charged particles lose energy by emitting light). The total power gain consists in the external energy brought by the "driver", that is to say, the external power needed to create and maintain the plasma P_{ext} and the fraction $P_{\alpha} = F_{\alpha}(3.5/17.6)P_{\text{fus}}$ released by the fusion reactions P_{fus} in a form of alpha particles (^2_2He), as only alpha-particles are depositing their energy. The neutrons are electrically neutral and are consequently leaving from the plasma without collisions. Their energy is recovered in the blanket and used to produce the Tritium and heat. By considering a stationary energy balance $P_{\text{loss}} = P_{\text{gain}} = P_{\alpha} + P_{\text{ext}}$ and assuming that all α particles deposit their energy inside the plasma ($F_{\alpha} = 1$), one may define the energy gain $G = P_{\text{fus}}/P_{\text{ext}}$. Then, by evaluating the plasma life time or confinement time by the ratio of its internal energy divided by the total power losses $\tau_c = 3n_e k_B T / P_{\text{loss}}$ where n_e is the plasma electron density and T the plasma temperature, one finds a criterion to achieve the ignition of such a little star on Earth defined by $G \rightarrow \infty$ of an equimolar DT plasma [Lawson, 1957]

$$n_e \tau_c > \frac{12}{3.5 \text{ MeV}} \frac{k_B T}{\langle \sigma_{DT} v \rangle} \approx 10^{15} \text{ cm}^{-3} \cdot \text{s} \text{ at } T \approx 10 \text{ keV}. \quad (2)$$

Due to chaotic motion of charged particles at a temperature of $T \approx 10 \text{ keV}$, the plasma tends

0.2. INERTIAL CONFINEMENT FUSION (ICF)

naturally to expand and it is difficult to maintain it during the needed time τ_c with a sufficiently high density n_e , because these two parameters T and τ_c are linked according to the Lawson criterion. In the star cores, the plasma confinement is accomplished naturally thanks to the Gravitational attraction. For example, the mass of the Sun (about 10^{30} kg) is sufficiently high to attract and compress matter to densities up to 10^{32} cm $^{-3}$ during its whole life of about 10 billion years, which corresponds to the time it needs to consume all its fusion fuel. The fact that plasma particles are electrically charged has naturally led to the idea of using strong magnetic fields in order to confine the thermonuclear plasma. In the 1950's, the Soviet physicists Igor Tamm and Andrei Sakharov proposed a device called *tokamak* in the shape of a torus allowing to confine a thermonuclear plasma thanks to a toroidal magnetic field produced by magnetic coils that surround the torus. In addition, a poloidal magnetic field which is created by a toroidal electric current that flows inside the plasma allows to heat it. The international project ITER is currently building the world's largest experimental tokamak nuclear fusion reactor and aims to make the long-awaited transition from experimental studies of plasma physics to full-scale electricity-producing fusion power plants. In 2003, the ITER prototype Tore Supra has obtained the world record by confining a thermonuclear plasma of $n_e \approx 10^{15}$ cm $^{-3}$ more than 6 minutes and 30 seconds during which time, energy on the order of 300 kWh was injected and extracted.

0.2 Inertial Confinement Fusion (ICF)

Inertial confinement fusion (ICF) is an alternative way to control fusion reactions. It is based on scaling down a thermonuclear bomb explosion to a small size, applicable for a power production. In this approach, achieving the energy gain through fusion reactions relies firstly on a fast compression to a high density (up to 1000 g.cm $^{-3}$ in the fuel) of a mm-scale capsule filled with a mixture of Deuterium and Tritium by the use of an ablative rocket effect. Then, a conversion of the implosion kinetic energy into the internal energy results in heating of the central zone called "hotspot" up to temperatures $T > 5$ keV, allowing to initiate the fusion reactions of the DT fuel in agreement with the Lawson criterion. Thus, instead of magnetic fields, here, the plasma is confined by its own inertia. Besides, this process lasts only a few ns so that this approach presents significant technological difficulties due to a high repetition rate of 10 Hz needed to continuously produce electricity. However, by reaching very high densities during a short confinement time, the ICF approach would be much more efficient in terms of gain, than magnetic confinement fusion, which aims to fuse the DT fuel at low densities but long confinement times.

0.2.1 Conventional ICF Schemes

Since the invention of lasers [Maiman, 1960], it came naturally the idea to use many laser pulses to strongly compress DT fuel capsules. In the 1970's, scientists began experimenting with powerful laser

beams in France [Colin et al., 1968], in the United States of America (USA) [Nuckolls et al., 1973] and in the Union of Soviet Socialist Republics (USSR) [Basov et al., 1968]. In the “direct drive” approach to ICF, powerful beams of laser light are focused on a small spherical pellet containing micrograms of Deuterium and Tritium (see **Figure 4**). A rapid heating caused by the laser driver makes the outer layer of the target explode. According to the momentum conservation law, the remaining portion of the target is driven inwards in a rocket-like implosion, causing compression of the fuel inside the capsule and the formation of a shock wave. The latter heats the fuel in the very center and results in ignition of fusion reactions which are propagating the fusion burn wave and release of more nuclear energy than was initially deposited. In the “indirect drive” method, the lasers heat the inner walls of a gold cavity called a hohlraum containing the pellet, creating a hot plasma which radiates a uniform “bath” of soft X-rays (see **Figure 4**). The X-rays rapidly heat the outer surface of the fuel pellet, causing a high-speed ablation, or “blowoff,” of the surface material and the fuel capsule implosion as if it had been hit with the lasers directly. In both approaches (direct drive and indirect drive), symmetrically compressing the capsule with radiations creates a central “hot spot” where fusion processes set in, the plasma is self-heated and the fusion burn propagates outward through the cooler, outer regions of the capsule much more rapidly than the capsule can expand.

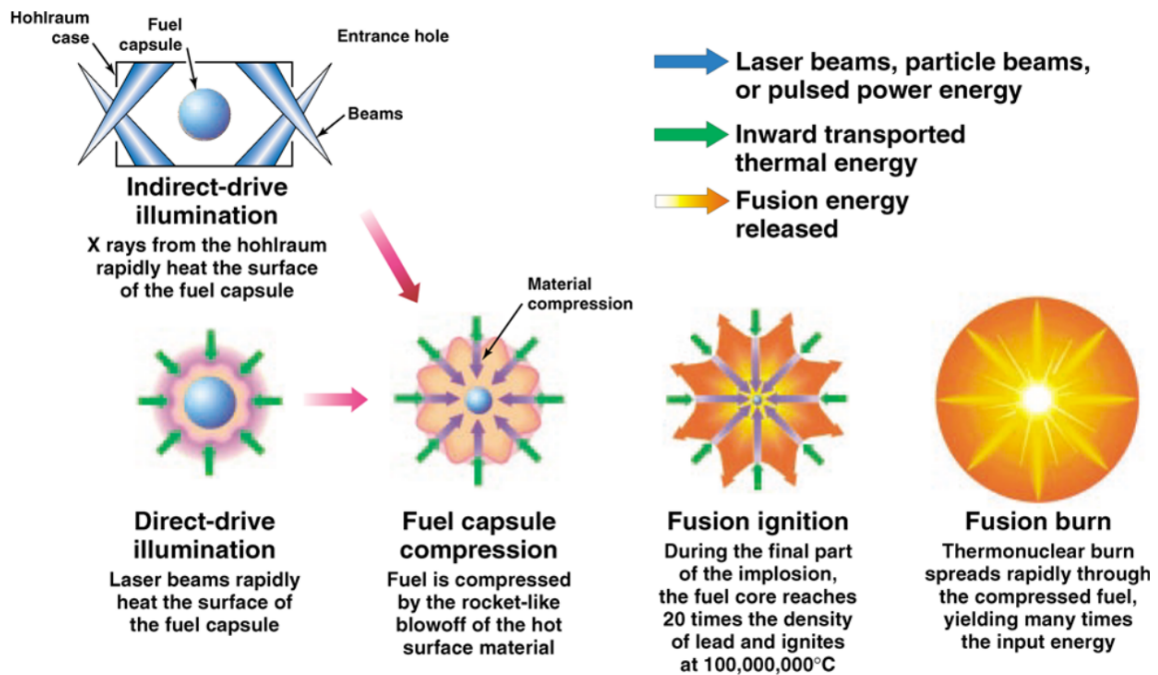


Figure 4: Classical ICF schemes : The Direct and Indirect drive approaches [Campbell and Hogan, 1999]

Direct and indirect drive schemes have their advantages and drawbacks. The former has a higher laser-target coupling efficiency but is less uniform in laser irradiation due to the use of discrete laser beams. Beam smoothing techniques have a key role in the direct drive. The indirect drive by soft X rays, which are generated at the inner surface of a hohlraum, may produce a better uniformity.

This allows to reduce the growth of perturbations due to Rayleigh-Taylor instabilities. The soft X ray drive has much higher ablation rates and is less sensitive to hot electron preheat. A potential disadvantage of indirect drive is the larger scale of the plasma crossed by the laser beam from the inlet hole to the hohlraum wall. Parametric instabilities (i.e. the unstable decomposition of the incoming laser radiation into two daughter waves) in hohlraums are responsible for a significant energy loss and production of energetic electrons. One of the most important advantages of the indirect drive approach is a radiation drive concept which allows to use another drivers such as Z-pinch of heavy ions.

The National Ignition Facility (NIF) at the Lawrence Livermore National Laboratory (LLNL) is operational since March 2009 and a variety of experiments have already been completed. The NIF is a Nd : Glass laser facility, which is now routinely operating at 1.6 MJ of ultraviolet (3ω) light on target with a very high reliability. It recently reached its design goal of 1.8 MJ laser energy and 500 TW power of 3ω light on target, and has performed experiments with 1.9 MJ at peak powers of 410 TW [Moses, 2009]. In addition to this impressive success, the National Ignition Campaign (NIC) on the NIF has allowed to achieve the world record indirect-drive neutron yield of $6.1 \cdot 10^{15}$ neutrons representing a gain G of few % during one indirect-implosion [Hurricane O. A. et al., 2014]. Even if the primary break-even goal ($G > 1$) has not been achieved yet, the NIC allowed to obtain new experimental results and code developments, generating a large body of knowledge and corrections of the previous models. In France, the Laser MegaJoule (LMJ) is under construction near Bordeaux at the Cesta center of the "Commissariat à l'Énergie Atomique et aux Énergies Alternatives" (CEA). The project implies a construction of 176 laser beam lines (instead of 240 at the beginning) delivering more than 1 MJ to a DT target using, as the NIF, the indirect drive method. The first laser shots with 8 beam lines were successfully delivered in the end of 2014. The laser lines of LMJ will be assembled in quads of four beams. Each quad will deliver more than 30 kJ of energy within a few ns. Direct drive ICF has been studied with smaller pellets at sub-ignition scale for many years, in particular, at the University of Rochester (USA), on the Omega laser (60 beams delivering a total of 30 kJ on target) and at the University of Osaka (Japan), on the Gekko laser (12 beams delivering 15 kJ on target).

0.2.2 Problems facing the ICF Conventional Schemes

The conventional schemes rely on the ignition of an isobaric hotspot where the DT fuel must reach a temperature of $T \approx 7$ keV and an areal density of $\rho R \approx 0.25$ g.cm⁻² during a confinement time of $\tau_c \approx 40$ ps. In order to achieve this extreme conditions, many ns laser pulses representing a total energy of $E_L \approx 1$ MJ are needed to uniformly irradiate the solid shell. From irradiation by laser pulses (direct approach) or x-rays (indirect approach), the outer shell layers are ablated and the resulting laser-generated plasma expands. The time evolution of the laser pulses is chosen according to the Nuckolls-Kidder law such that the ablation pressure launches a spherically converging shock wave

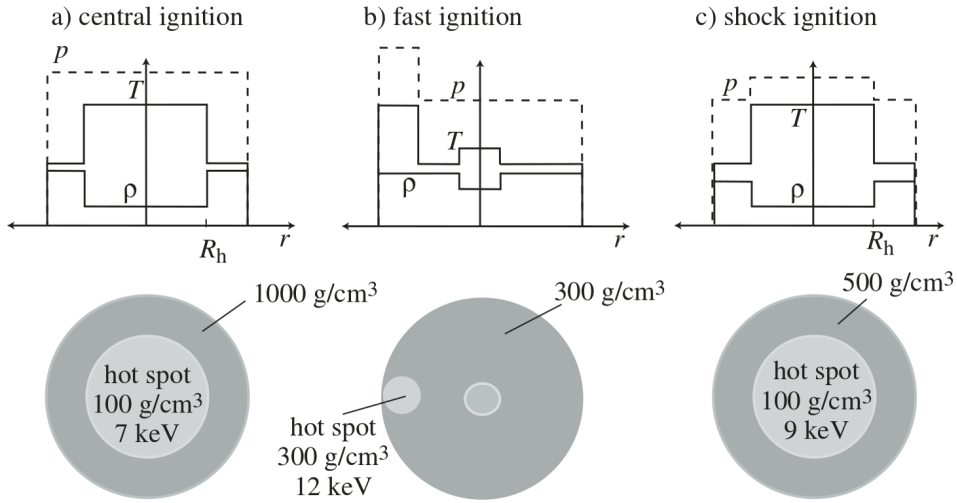


Figure 5: Fuel configuration at ignition for the conventional scheme a), the fast ignition scheme b) and the shock ignition scheme c) [Atzeni, 2009]

followed by a continuous succession of spherically converging compressional waves, which arrive at the same time on the internal surface of the shell. At that moment, a shock wave is transmitted in the DT gas, while a rarefaction wave is reflected in the shell. When the latter arrives at the ablation surface, the shell undergoes a strong acceleration and the capsule implodes. Due to its spherical symmetry, the DT fuel in the shell is compressed to the desired density. A conversion of the imploded target's kinetic energy into internal energy results in the creation of an isobaric hotspot, where a self-sustained reaction of Deuterium and Tritium fusion is initiated. The fusion reactions generate a spherically diverging thermonuclear combustion wave followed by a detonation, which burns the denser part of the shell. The confinement time τ_c corresponds to the hotspot lifetime before its hydrodynamic expansion.

Thus, the simultaneous compression and heating processes of the fuel impose several constraints on the target and driver designs which make it difficult to obtain significant energy gains. These constraints are multifactorial. Firstly, parametric instabilities may reduce the conversion efficiency of laser energy deposited in the target and create the pressure inhomogeneities. Secondly, the generation of fast electrons due to laser-plasma interaction processes results in the target preheat, which leads to the increase of the target entropy and limits the shell compression. Finally, the hydrodynamic instabilities may mix the hot and cold fuel and can break the shell during its implosion.

0.2.3 Fast Ignition and Shock Ignition Alternative Schemes

Since the discovery of the Chirped Pulse Amplification (CPA) by [Strickland and Mourou, 1985], short pulse laser technology has grown steadily. In the 1990's, the threshold intensity value of $10^{18} \text{ W.cm}^{-2}$ has been attained, allowing to reach the relativistic laser-matter interaction regime where high currents of relativistic electrons can be generated. In order to relax the constraints on the driver and the target

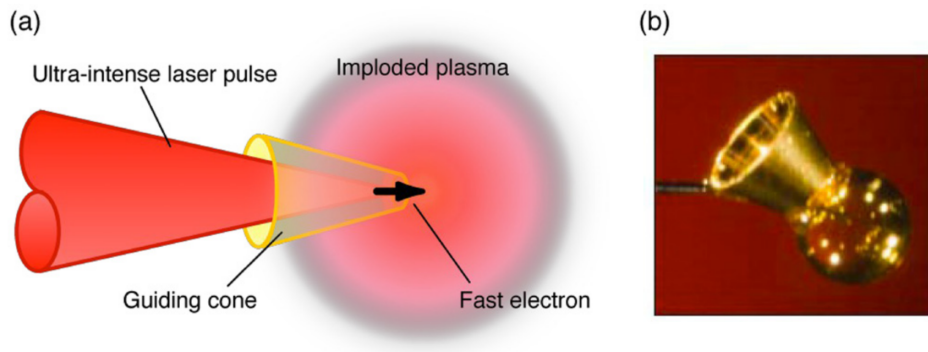


Figure 6: Schematic of cone-guided fast ignition (a) and photograph of cone-attached shell target used for integrated experiments on OMEGA (b). [Norreys et al., 2014]

imposed by the simultaneous compressing and heating processes, it was thus proposed to separate the target compression and fuel heating phases. In this scheme, the shell is imploded at a lower velocity in a more stable regime. The ignition is achieved by using such a relativistic laser pulse generating a fast electron beam, which creates a hot spot in the dense part of the fuel just after the end of the compression phase at the capsule stagnation [Tabak et al., 1994]. In this **fast ignition** scenario, the required density is much smaller (300 g.cm^{-3} instead of 1000 g.cm^{-3}) due to the fact that the hot spot is not created anymore in the center of the target but in the lateral denser region due to the heating by the fast electrons, as shown in **Figure 5**. Thus, the constraints on the shock wave convergence and on the implosion symmetry are reduced. Furthermore, the compression phase needs much less energy ($200 - 300 \text{ kJ}$) than in the conventional scheme and the compression driver cost is consequently lower. This is definitely an advantage for a future fusion power plant. The shell implosion velocity is also much smaller than in the conventional scenario. This allows a greater tolerance concerning the hydrodynamic instabilities and a lower risk of breaking the shell. Moreover, a laser-produced relativistic electron beam may provide a more efficient heating of the dense material and one may expect much higher gains than in the conventional scenario. Finally, the fast ignition has the advantage of creating a much denser isochoric hot spot due to the fact that the heating time by the fast electrons is much less than the hot spot hydrodynamic expansion time.

However, the fast ignition opens new problems to resolve. Due to the fact that the Ultra-High Intense (UHI) laser pulse cannot propagate beyond the critical density n_c of the plasma, there is a problem to transport the electron beam to the dense fuel. Moreover, it has been demonstrated that the generated relativistic electron beam is divergent and cannot deliver the energy into a sufficiently small hot spot. Two approaches have been proposed to compensate the beam divergence. First, one may use a first ultra intense laser pulse to create a channel through the process of hole boring letting a second UHI laser pulse to generate the ignitor electron beam as close as possible to the dense area. However, an efficient hole boring was not demonstrated so far. Another approach relies on a cone inserted in the target as shown in **Figure 6**. It allows to reduce the distance to $\approx 100 \mu\text{m}$ between

the electron beam generation zone and the dense part of the fuel. The parameters required to reach ignition have been estimated thanks to hydrodynamic simulations assuming the fast electron beam energy being deposited in a spherical zone of a compressed fuel [Atzeni, 1999]

$$\begin{aligned} E_{\text{ign}} &= 18 \left(\frac{\rho}{300 \text{ g.cm}^{-2}} \right)^{-1.85} \text{ kJ}, \\ \tau_{\text{ign}} &= 21 \left(\frac{\rho}{300 \text{ g.cm}^{-2}} \right)^{-0.85} \text{ ps and} \\ r_{\text{ign}} &= 20 \left(\frac{\rho}{300 \text{ g.cm}^{-2}} \right)^{-0.97} \mu\text{m}. \end{aligned} \quad (3)$$

It was found that, assuming a fuel density $\rho = 300 \text{ g.cm}^{-3}$, one needs to deposit the energy of $E_{\text{ign}} \approx 18 \text{ kJ}$ during the time $\tau_{\text{ign}} \approx 21 \text{ ps}$ in a sphere of the radius $r_{\text{ign}} \approx 20 \mu\text{m}$. This corresponds to a hot spot areal density of $\rho R = 0.6 \text{ g.cm}^{-3}$. According to numerical simulations, the optimal ignitor energy and pulse duration scale with the density as $E_{\text{ign}} \propto \rho^{-1.85}$ and $\tau_{\text{ign}} \propto \rho^{-0.85}$, while optimal beam radius of the resulting accelerated electrons scales with the density as $r_{\text{ign}} \propto \rho^{-0.97}$. The electrons having a stopping length of $40 \mu\text{m}$ can be generated by a laser pulse with an intensity of [Atzeni et al., 2009b]

$$I_{\text{ign}} = \frac{6.8 \cdot 10^{19}}{\eta_{L \rightarrow e}} \left(\frac{\rho}{300 \text{ g.cm}^{-2}} \right)^{0.95} \text{ W.cm}^{-2} \quad (4)$$

where $\eta_{L \rightarrow e}$ is the laser-to-electron beam conversion efficiency.

Experiments conducted on the Gekko-XII ns laser system coupled with a PW laser beam at the Institute of Laser Engineering of the Osaka University in Japan has already demonstrated a significant increase in the number of neutrons released by the fusion reactions compared to the direct scheme scenario [Kodama R. et al., 2001] [Kodama R. et al., 2002]. In another experiment conducted in 2010 on the Gekko XII laser coupled with the new LFEX PW laser (that can deliver an energy up to 10 kJ in a $0.5 - 20 \text{ ps}$ pulse), the neutron enhancement was confirmed. However, a relatively modest neutron yield of $3.5 \cdot 10^7$ has been obtained with a short pulse laser energy of 300 J on the target, which is smaller than the yield obtained in 2002 [Shiraga et al., 2011]. Some sub-ignition scale Fast-ignition experiments were also performed on the OMEGA/OMEGA EP laser at the University of Rochester in the USA. With optimal timing, the OMEGA EP pulse produced up to $1.4 \cdot 10^7$ additional neutrons, which is a factor of ≈ 4 more than without short-pulse heating [Theobald et al., 2011]. One quad of NIF beams is undergoing conversion to high-intensity picosecond-duration pulses to provide an Advanced Radiographic Capability (ARC). These beams will deliver up to 10 kJ in a 5 ps pulse that can be used as a sub-scale ignitor pulse to study fast electron core heating in integrated fast ignition experiments. In France, the PETAL project consists in coupling the LMJ facility to a PW laser with an energy of 3.5 kJ and a pulse duration of $0.5\text{-}5 \text{ ps}$.

Another method to separate the assembly and ignition phases of the DT fuel is Shock Ignition. It consists in igniting a central hot spot (see **Figure 5**) heated by the ignitor shock generated by an

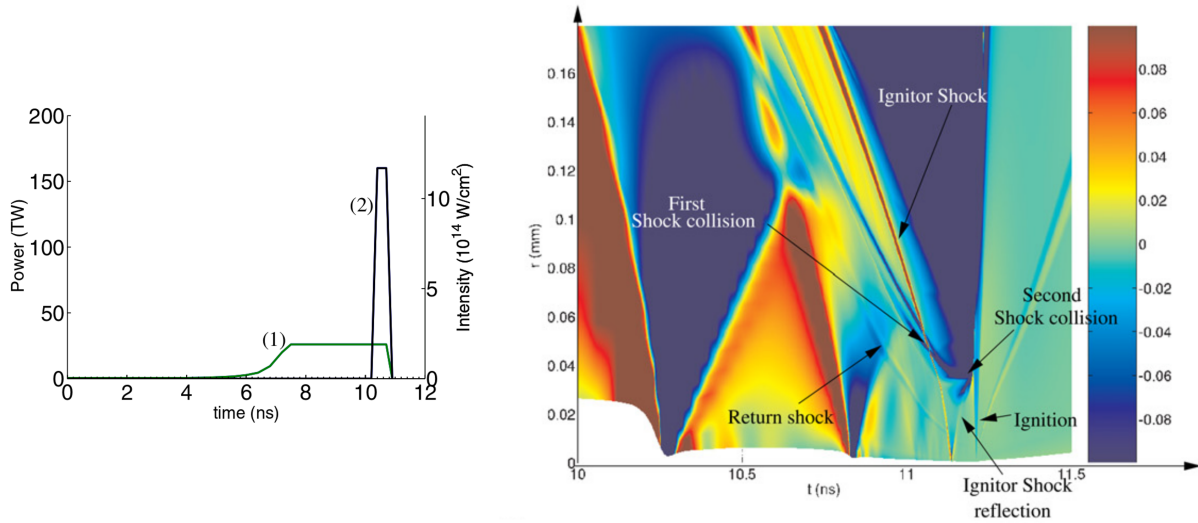


Figure 7: Laser pulses shape for shock ignition : (1) corresponds to the Nuckolls-Kidder law for the compression phase and (2) is the ignitor pulse (left) and the corresponding logarithmic pressure gradients in the target versus space and time (right) [Ribeyre et al., 2009]

ablation pressure of 300 Mbar at the end of compression phase. It increases its strength as it converges in the imploding shell and collides with the return shock [Zhou and Betti, 2005] [Betti et al., 2007]. Massive cryogenic shells at a low implosion velocity and a low adiabat can be used in this shock ignition scheme leading to fuel assemblies with large areal densities. The igniting shock creates the hot-spot pressure greater than the surrounding dense fuel pressure. Such a nonisobaric assembly features a lower energy threshold for ignition than the conventional isobaric one. The ignitor shock can be launched by a spike in the laser power which is compatible with the performance of NIF and LMJ. The thermonuclear gain can be significantly larger than in the conventional isobaric ignition for an equal driver energy. Compared with fast ignition, shock ignition presents the advantages that it does not require any complex cone-in-a-shell targets or high power lasers. Also, the physics at work in this scheme is standard laser driven hydrodynamics, a relatively well-known and proven discipline. Yet the latter observation must be mitigated considering the failure of the NIC. Besides, as it involves low velocity implosions, this scheme is relatively robust with regards to hydrodynamic instabilities during the shell acceleration and it mitigates the Rayleigh–Taylor instability at the stagnation time. The required power for a 300 Mbar shock delivery corresponds to a 120-200 TW final spike, the actual value depending on the ablator material and focal spot dimensions, independently of the irradiation pattern. This power is an order of magnitude lower than the power required by fast ignition and it is achievable with the NIF-LMJ technology. Nevertheless, the coupling of this final pulse to the target presents several unsolved issues such as parametric instabilities, hydrodynamic instabilities or the role of the fast electrons generation in the ignitor shock creation. An ignitor shock generated by an ablation pressure close to the required 300 Mbar has been achieved recently in Omega experiments with $\approx 500 \mu\text{m}$ – diameter solid plastic ball targets and a laser spike of $4 \cdot 10^{15} \text{ W.cm}^{-2}$ laser pulse

[Theobald et al., 2013].

0.3 Fast Electron Generation in the context of ICF

0.3.1 Role of Fast Electrons in the Shock Ignition Scheme

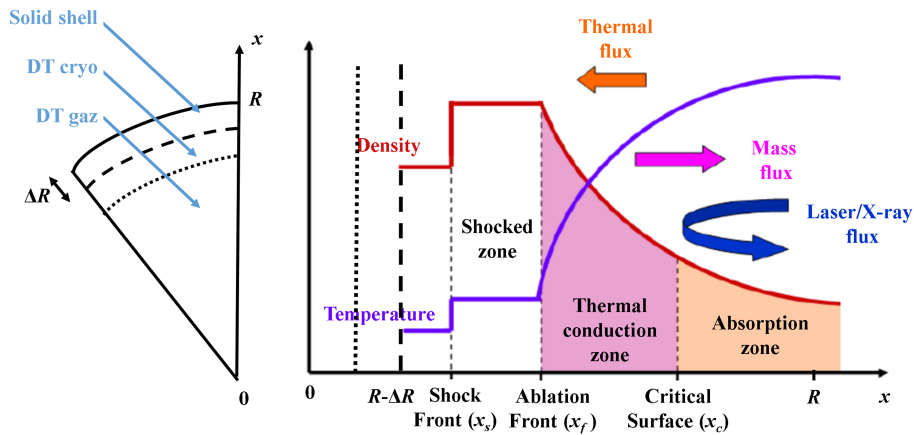


Figure 8: Schematic view of the laser-shell interaction

In the non relativistic regime of laser-plasma interaction where $I_L \lambda^2 \ll 10^{18} \text{ W.cm}^{-2} \cdot \mu\text{m}^2$ (with I_L being the laser pulse intensity and λ its wavelength), the material is ionized by the laser electric field during the first ps of the Laser-Solid-Interaction (LSI) [Keldysh, 1965]. This quasi-instantaneous multi-photon absorption process takes place for laser intensity above $I_L \approx 10^{11} \text{ W.cm}^{-2}$. Due to their low inertia, the electrons rapidly gain a kinetic energy from the laser in collisions with atoms and ions. The laser energy transfer to the ions is done indirectly through the energy exchange in collisions with electrons. While the heated plasma consequently expands, the laser pulse cannot penetrate the plasma where the electron density n_e is above the value of $n_c \approx 10^{21} \text{ cm}^{-3} / \lambda[\mu\text{m}]^2$ called the critical density. Indeed, in this denser part of the plasma, the Langmuir frequency $\omega_{pe} = \sqrt{4\pi n_e e^2 / m_e}$, at which the electrons oscillate, is greater than the laser frequency $\omega = 2\pi c / \lambda$ so that the laser field is screened. Thus, a part of the laser energy is absorbed in the sub-critical region and another part is reflected. The denser part where $n_e \geq n_c$ is heated by the electron thermal conduction launched from the absorption zone, that is to say, by the collisions of hotter electrons with cooler ones. The electron heat conduction transports the absorbed energy to the ablation front where it is transformed into the energy of vapors. The reaction of ejected vapors creates the ablation pressure which is responsible for the rocket effect and the launching of shock/compression waves depending on the laser intensity temporal profile.

Concerning the Shock Ignition scheme, at the moment of the laser peak, the absorption zone called corona has a larger scale and a higher temperature than in the conventional ICF designs. This changes

considerably the conditions of exciting the parametric instabilities. As the laser intensity is higher than in the conventional schemes, more absorbed energy is transported by hot electrons which can reach kinetic energies up to several 10th keV as pointed out by [Klimo et al., 2010] according to kinetic simulations. Thus, one of the main issues of Shock Ignition concerns the transport of hot electrons. At the moment of the ignition spike's arrival, the shell is already compressed, its radius is reduced by a factor of 2-3 and its areal density is increased by a factor of ten or twenty approaching a level of about 10 mg.cm^{-2} . This value is comparable to the range of a 100 keV electron. For this reason, the hot electrons generated in the corona with lower energies than 100 keV may not present a danger for the fuel compression contrary to the conventional scenario [Ribeyre et al., 2009]. Depending on their characteristics (kinetic energy spectrum and number) as well on the target hydrodynamic properties (density gradient and density value) at the moment of the spike arrival, the hot electrons may play an important role in the creation of the ablation pressure $\approx 300 \text{ Mbar}$ required for launching the ignitor shock. Also, the electron transport may affect the implosion symmetry because of a large distance between the zone of electron generation in the underdense corona and the ablation surface. The hot electrons may smooth out the small scale inhomogeneities improving consequently the shell stability and suppressing the fuel mix with the hot-spot material at the internal surface of the shell. All these observations about the role of the fast electrons in the shock ignition scheme need further experimental as well as numerical studies.

0.3.2 Fast Electron Beam Divergence in the context of Fast Ignition

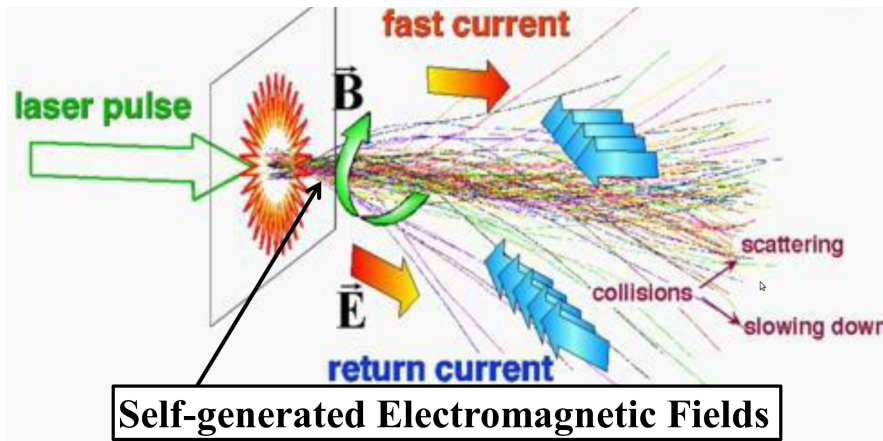


Figure 9: Schematic of the transport of laser-driven fast electrons in a dense plasma [Gremillet et al., 2002]

Interaction of Ultra-High Intensity (UHI) laser pulses, $I_L \lambda^2 \geq 10^{18} \text{ W.cm}^{-2}.\mu\text{m}^2$, with solid targets leads to a forward acceleration of electrons up to several MeV [Beg et al., 1997]. Such a relativistic electron beam of a density n_b and a current density \mathbf{j}_b , propagating through a plasma or a solid having an electron density $n_e \gg n_b$, generates an electric field, which tends to eject the plasma electrons

out of the beam volume in order to equilibrate the total charge. The charge neutralisation proceeds on a timescale of the order of the plasma electron-ion collision time [Hammer and Rostoker, 1970] or the Coulomb explosion time [Cox and Bennett, 1970], depending on the plasma temperature-density conditions. Over the same timescale, the electric field accelerates the plasma electrons thus creating a return current $\mathbf{j}_e \approx -\mathbf{j}_b$, and decelerates the beam electrons in order to cancel the total current density in agreement with Lenz's law [Hammer and Rostoker, 1970]. In case of irradiation of an insulator by a UHI laser pulse, the laser-generated electron beam is electrostatically neutralized [Debayle and Tikhonchuk, 2007]. Electrons of the material are firstly ionized at the beam front by the charge-space electrostatic field generated by the fast escaping electrons. Then, they are accelerated by this electrostatic field thus creating a current density $\mathbf{j}_e \approx -\mathbf{j}_b$. This "return current", ionizing the material through collisions with the bound electrons of the material, leads to the electric neutralization of the fast electron beam. In both cases, metal/plasma or insulator, the return current allows for the propagation of electron currents in excess of the Alfvén-Lawson limit which defines the maximum relativistic electron beam current in vacuum [Alfvén, 1939]. However, due to the imperfect current neutralization, a magnetic field is induced that can deflect the beam electrons. The plasma electron temperature-density crossed gradients, plasma resistivity gradients and the beam current density curl are the main sources of this residual magnetic field. Later, this magnetic field begins to diffuse leading to a separation of the beam and the return current [Lee and Sudan, 1971]. Besides, the resulting system of two counterpropagating high currents is very unstable and may lead to the electron beam resistive filamentation [Bret et al., 2010b]. The collisions of the relativistic electrons with plasma electrons and ions also contribute to the scattering and the slowing down of the beam.

The experimental studies of fast electron generation by a UHI laser pulse have shown a significant beam divergence angle [Green et al., 2008]. Concerning the Fast Ignition scheme, this strong divergence strongly limits the estimates (3) of energy deposition in the hot spot [Bellei et al., 2013]. Several methods have been proposed to collimate the electron beam. It has been noticed that the plasma resistivity gradients naturally induced in the heated material by the electron beam can collimate the beam [Bell and Kingham, 2003]. This self-collimation, however, is not sufficient for the beam guiding because of the radial dependence of the divergence angle [Debayle et al., 2010]. It was also proposed to guide a relativistic electron beam in a magnetic channel created by a relativistically intense, picosecond laser prepulse followed by the main pulse [Robinson et al., 2008] [Scott et al., 2012]. The prepulse serves to create such a collimating magnetic field structure due to the laser-produced electron beam propagation. This magnetic channel then helps guide the fast-electron beam generated by the second pulse. Other methods consist in using targets containing a high-resistivity-core-low-resistivity-cladding structure or a low-density-core-high-density-cladding structure. These field structures can be generated during the beam transport, hence enabling the beam to self-collimate [Cai et al., 2011]. In the high-resistivity-core-low-resistivity-cladding targets, the magnetic field at the interfaces is generated by the resistivity gradients and the fast electron current, while in low-density-core-high-density-cladding targets, the magnetic field is generated by a rapid change of the flow velocity of the background elec-

trons in the transverse direction (perpendicular to the flow velocity) caused by the density jump. A similar idea, based on a more complex array of resistivity gradients consisting of alternating layers of different Z materials have also been proposed [Robinson et al., 2012] [Schmitz et al., 2012a]. Adapted to the Fast Ignition cone-in-shell target, this "elliptical mirror" may improve the coupling efficiency into the hot spot by a factor of 3-4 [Robinson and Schmitz, 2013]. Also, it has been shown that a target composed of resistive filaments with a decreasing background density, adiabatically converts the beam transverse energy into longitudinal energy [Debayle et al., 2013]. Another possibility is to apply an external magnetic field parallel to the beam direction in the fuel [Strozzi et al., 2012]. With a field strength exceeding 2 kT, relativistic electrons are trapped by the magnetic field lines and the lateral transport of these electrons is strongly suppressed. In the paper by [Daido et al., 1986], it has been demonstrated that kilotesla magnetic fields can be generated by using a capacitor-coil target. More recently, a magnetic field of 1.5 kT was generated [Fujioka S. et al., 2013]. Extended double cones have also been proposed to confine the fast electrons escaping from the cone by electrostatic and magnetic fields formed in the vacuum gap region of several micrometres width between the two walls [Johzaki et al., 2011]. It has been shown through numerical simulations of electron transport that an extended double cone may enhance the core heating rate by more than a factor four compared to single cones, under otherwise similar conditions. However, despite these progresses in the understanding of relativistic electron beam transport, there is still a need of further numerical and experimental studies.

0.3.3 Existing Simulation Methods for Fast Electron Transport Modeling

The equation which takes into account both the collisional and collective processes of fast electron transport in the context of shock and fast ignition is the Vlasov-Fokker-Planck (V-F-P) equation for the beam distribution function f_b [Landau and Lifshitz, 1981]. Due to the complexity of fast electron transport imposed by the coupling of the VFP equation with the Maxwell equations and the temperature-dependence of the transport coefficients, numerical tools are needed for preparation and interpretation of experiments. This system of equations has been extensively studied for 30 years and several numerical methods have been developed [Thomas et al., 2012]. Several families of codes can be identified. The first family consists in solving the V-F-P equation by a Particle-In-Cell (PIC) method [Birdsall and Fuss, 1969] and by interpolating the resulting macroparticle positions and velocities to compute the electromagnetic fields. Historically, this method was used to solve physical problems where collisional processes can be neglected. All electrons (both plasma and beam electrons) are sampled by macroparticles which consequently leads to accurate but time-consuming computations. Moreover, in order to limit the non-conservative force associated with the particle-grid mapping which leads to self-heating and numerical instabilities, the space resolution has to be comparable to the Debye screening length. This poses a strong constraint in the case of dense and/or cold plasmas. Collisional

processes are usually treated by Monte-Carlo methods [Takizuka and Abe, 1977]. The second family of codes employs the same method but restricted to the beam electrons, introducing a low-energy cut off [Gremillet et al., 2002]. The plasma electrons are taken into account via hydrodynamic equations of conservation or simplified ones. This approach belongs to the family of hybrid PIC codes. Other authors solve the full V-F-P equation [Yokota et al., 2006] [Duclous et al., 2009] or use a decomposition of the distribution function in the momentum space with their corresponding hybrid versions. It has been shown that a spherical harmonic decomposition of the distribution function enables modeling of arbitrary local anisotropy for large enough expansion orders [Tzoufras et al., 2011]. Besides their accuracy and the rapid progress in high performance computing resources, all these codes are time consuming because of the Courant-Friedrichs-Lewy condition that restricts the time step computation (a fraction of a plasma period) combined with the high resolution needed (a fraction of the Debye length), the large number of the distribution function variables $(x, y, z, v_x, v_y, v_z, t)$ and the large spatial (of the order of mm) and temporal (tens of ps) scales needed to study fast electrons transport in the context of the fast or shock ignition of fusion pellets.

0.4 Objectives of the thesis and Plan of the Manuscript

The goal of this PhD thesis consists in developing a new reduced 3D-3V hybrid relativistic Vlasov-Fokker-Planck model, which must be as accurate and time efficient as possible for the study of fast electron transport in solids and dense plasmas in the context of ICF. Firstly, the model will be applied to interpret experiments of laser-generated fast electron transport in solids or dense plasmas. Secondly, the model will allow us to study the collimation methods for laser-generated electron beams in a fusion pellet. Thirdly, the model will be coupled with a hydrodynamic code for studying of the role of fast electrons in the shock ignition scheme.

In the first part of this manuscript, the state of the art of this problematic is presented:

- Chapter 1 reviews the physics of laser-plasma interaction and the main electron acceleration mechanisms relevant to the Shock and Fast Ignition. We also estimate the laser-to-electron coupling efficiency as well as the spatial, energetic and angular properties of laser-generated fast electron beam.
- Chapter 2 is dedicated to the electromagnetic neutralization of laser-generated relativistic electron beam. Self-consistent electromagnetic fields of a relativistic electron beam propagating through vacuum are derived in order to highlight the need of its electromagnetic neutralization allowing it to overpass the Alfvén-Lawson limit. The electric and magnetic neutralization of fast electron beams are presented separately, showing the main differences between metal/plasma or insulator targets.

- Chapter 3 focuses on the collective effects of electromagnetically neutralized fast electron beam transport. The quasi-static approximation in the Maxwell equations is introduced as well as the instability theory of two counterpropagating currents and the temperature dependence of fast electron beam transport. These collective effects play an important role in the Fast Ignition scheme since the proposed collimation techniques are based on the self-generated electromagnetic field.
- Chapter 4 deals with the collisional effects of fast electron beam transport. The slowing down and scattering of fast electrons from collisions with free electrons, bound electrons and screened free electrons is detailed as well as their angular scattering from collisions with background ions and electrons. These effects play an important role in the Fast Ignition scheme since they are responsible for the fuel heating and the pellet ignition. Finally, we present the relativistic Vlasov-Fokker-Planck (VFP) equation based on the Belyaev-Budker small-angle collision tensor. This equation describes both the collective and collisional processes ruling fast electron transport.
- Chapter 5 presents the numerical methods used to solve the relativistic V-F-P equation. Often, these codes are based on the "hybrid assumption", that is to say, they solve the V-F-P equation only for the high-energy component of the electron population. The dynamics of background particles is computed according to hydrodynamic equations or simplified ones. A comparison between the PIC method, the full "Vlasov-Fokker-Planck" method and other methods, based on the decomposition of the distribution function, is presented. Most of V-F-P (full or expanded) models do not use the Belyaev-Budker collision tensor but a Landau-like relativistic collision operator. Moreover, except for the relativistic V-F-P code of [Yokota et al., 2006], the dependence of Coulomb logarithms on the relativistic mass γm_e is often neglected.

In the second part of the manuscript, a new fast electron model is presented including. Its numerical implementation and its validation are also presented:

- In **Chapter 6**, the Landau-like relativistic collision operator mentioned above is derived from the Belyaev-Budker collision operator in the context of relativistic electron beam transport. It allows us to derive an expression for the relativistic Coulomb logarithm, starting from the fast electron stopping power term, in the V-F-P equation. It thus relates naturally the fast electron angular scattering rate due to the collisions with free, bound and screened free background electrons with the corresponding stopping powers. According to **Chapter 5**, the best compromise between the accuracy and the numerical cost can be obtained with hybrid and expanded relativistic V-F-P methods. As a consequence, the model developed in this PhD thesis consists in solving the two first angular moments of the V-F-P equation in order to make computations as fast as possible. Besides, truncating the distribution function expansion at the first angular harmonic may lead to non-physical results in a case of strong anisotropy. Consequently, a special closure relation based on the Minerbo approach of a maximum angular entropy [Minerbo, 1977] [Minerbo, 1978],

developed for the radiative transfer theory, is adapted here to the fast electron transport. It allows us to close the set of equations by evaluating the 2nd order angular moment of the distribution function needed in the 1st order angular moment equation. Contrary to the largely used approximation of the distribution function with one Legendre polynomial often called P1, this M1 model allows to describe the distribution function with an arbitrary local anisotropy. It is shown that the model is exact in the limits of fully isotropic and fully anisotropic local angular distribution functions. As the laser-generated relativistic electron beams may have a wide energy spectrum and an arbitrary angular distribution functions, the equation of the local angular entropy is derived and the limitations of the model are discussed. Developments of new plasma transport coefficients necessary to model the self-generated electromagnetic fields are also proposed.

- Chapter 7 is dedicated to the numerical tools developed to solve the equations of the model. A key point is the use of a numerical model developed previously for the radiative transfer equations which ensure that the 0th order angular moment stays positive and that the 1st order angular moment stays smaller than the 0th order one for all electron energies, times and space locations.
- Chapter 8 presents a simple academic test case of fast electron transport in a warm and dense Hydrogen plasma, allowing us to present the major features of the model. Analytical expressions are also derived to check the numerical schemes. Then, a comparison with a hybrid PIC simulation is presented to validate the model. It deals with a realistic laser-produced fast electron beam deduced from the PIC simulation of an experiment conducted on the UHI100 laser facility of the CEA (Saclay).

The third part of the manuscript is dedicated to applications of the model in the context of ICF:

- Chapter 9 is dedicated to studies of the $K\alpha$ emission induced in a plasma or in a solid by the fast electron transport. The theory of $K\alpha$ emission is presented and the simulation results are compared to experimental data. It is shown that 3-dimensional effects as well as the photoionization process assuming the specular reflexion of fast electrons at the solid target edges are not sufficient to recover the results obtained experimentally.
- Chapter 10 presents two applications of the model concerning the generation of shock waves by the fast electron energy deposition. The first one deals with the same experimental campaign considered in two previous chapters. It is shown that, in agreement with the target temperature evaluated with the M1 model, a UHI laser pulse with the energy less than 1 J can heat a solid target and generate temperature gradients that drive a blast wave of ≈ 50 Mbar. A theoretical model of such a blast wave generation and transport is proposed and compared with the experiment and hydrodynamic simulations. The second application concerns with the role

0.4. OBJECTIVES OF THE THESIS AND PLAN OF THE MANUSCRIPT

of the fast electrons in the shock ignition scheme. The M1 model is coupled to the radiation hydrodynamic code CHIC using a simplified numerical scheme. The simulation results are in good agreement with theoretical predictions. It is shown that the hot electrons accelerated by the ignitor laser spike can deposit a sufficient energy in the dense shell and generate a 300 Mbar shock required to reach the ignition.

The original results obtained in this thesis are summarized in the **Conclusion**. Perspectives of this present work are also proposed. **Appendix A** is dedicated to the classical plasma kinetic theory while **Appendix B** presents the classical hydrodynamic theory. It introduces the non relativistic kinetic approach as well as the Spitzer, Braginskii and Lee-More transport coefficients. The radiation hydrodynamic monofluid and two-temperatures CHIC code is also presented.

Part I

State of the Art of Fast Electron Generation and Fast Electron Transport in the context of Inertial Confinement Fusion

Chapter 1

Fast Electron Generation

”Philosophy is written in that great book which ever lies before our eyes — I mean the universe — but we cannot understand it if we do not first learn the language and grasp the symbols, in which it is written. This book is written in the mathematical language, and the symbols are triangles, circles and other geometrical figures, without whose help it is impossible to comprehend a single word of it; without which one wanders in vain through a dark labyrinth.”

Galileo Galilei

In the non relativistic regime of laser-plasma Interaction (where $I_L \lambda^2 \ll 10^{18} \text{ W.cm}^{-2}.\mu\text{m}^2$ with I_L being the laser pulse intensity and λ its wavelength), the laser pulses may have temporal durations from several tens of fs with an energy of several mJ to several ns with an energy of several kJ. For long pulse durations like those used in the conventional ICF schemes, the material is ionized by the laser electric field during the first ps of the Laser-Solid-Interaction (LSI) and heat the plasma. While the heated plasma consequently expands, the laser pulse cannot penetrate the plasma where the electron density n_e is above the critical density $n_c \approx 10^{21} \text{ cm}^{-3}/\lambda[\mu\text{m}]^2$. Concerning the Shock Ignition scheme, at the moment of the laser spike's arrival, the sub-critical zone has a larger scale and a higher temperature than in the conventional scheme. This changes considerably the conditions of laser-plasma interaction and it is expected that part of the laser energy is converted into fast electrons. For short laser pulse durations, the plasma has no time to expand so that the laser pulse interacts with a steep gradient density. Since the discovery of the Chirped Pulse Amplification (CPA) by [Strickland and Mourou, 1985], short-pulse laser technology has grown steadily. In the 1990's, the threshold value of a laser intensities with $I_L \lambda^2 \geq 10^{18} \text{ W.cm}^{-2}.\mu\text{m}^2$ has been attained allowing to reach the relativistic laser-matter interaction regime. However, the intense short laser pulse is preceded by a lower intensity prepulse of several ps duration. Therefore, the plasma may have time to expand. The relativistic laser plasma interaction leads to the generation of very energetic electrons. This chapter is dedicated to the description of laser-plasma interaction in general and a special attention is devoted to the different mechanisms responsible for fast electron generation in the context of conventional ICF, shock ignition and fast ignition.

1.1 Laser-Solid Interaction at High Intensities

1.1.1 Collisional versus "Collisionless" Absorption mechanisms

The laser pulse propagation is described by the equation for the electric field \mathbf{E} obtained from the Maxwell equations

$$\left(\frac{\partial^2}{\partial^2 \mathbf{r}}\right)(\mathbf{E}) - \frac{\partial}{\partial \mathbf{r}} \left(\frac{\partial}{\partial \mathbf{r}} \cdot \mathbf{E}\right) - \frac{1}{c^2} \frac{\partial^2 \mathbf{E}}{\partial t^2} = \frac{4\pi}{c^2} \frac{\partial \mathbf{j}_e}{\partial t} \quad (1.1)$$

where $\mathbf{j}_e = -n_e e \mathbf{v}_e$ is the plasma electron current density. The plasma response to electromagnetic fields is described by the plasma electron hydrodynamic equations (see **Appendix B, section B.1.2**). By neglecting the electron viscosity, the electron pressure, the magnetization effects and the thermal force, these equations read

$$\begin{aligned} \frac{\partial n_e}{\partial t} + \frac{\partial}{\partial \mathbf{r}} \cdot (n_e \mathbf{v}_e) &= 0 & (a) \\ \frac{\partial \mathbf{v}_e}{\partial t} + \left(\mathbf{v}_e \cdot \frac{\partial}{\partial \mathbf{r}}\right)(\mathbf{v}_e) &= -\frac{e}{m_e} \left(\mathbf{E} + \frac{\mathbf{v}_e}{c} \times \mathbf{B}\right) - \nu_{ei} \mathbf{v}_e & (b) \\ \frac{3}{2} n_e k_B \left[\frac{\partial T_e}{\partial t} + \left(\mathbf{v}_e \cdot \frac{\partial}{\partial \mathbf{r}}\right)(T_e)\right] - \frac{\partial}{\partial \mathbf{r}} \left(\kappa_e \frac{\partial T_e}{\partial \mathbf{r}}\right) &= \frac{\partial}{\partial \mathbf{r}} (\eta_{\text{abs}} I_L) & (c) \end{aligned} \quad (1.2)$$

where $\nu_{ei} = \nu_0 T_e^{-3/2}$ is the electron ion collision frequency with $\nu_0 = (1/3)\sqrt{2/\pi} Z n_e e^4 \ln \Lambda_{ei} / (\sqrt{m_e} (k_B)^{3/2})$, Z the mean ionization state of the material and $\kappa_e = \kappa_0 T_e^{5/2}$ with $\kappa_0 = 8(2/\pi)^{3/2} k_B^{7/2} / m_e^{1/2} Z e^4 \ln \Lambda_{ei}$ is the Spitzer-Härm transport coefficient (see **Appendix B, section B.2.2**). In all what follows, we neglect the advection term of the temperature in the left hand side of Equation (1.2 c).

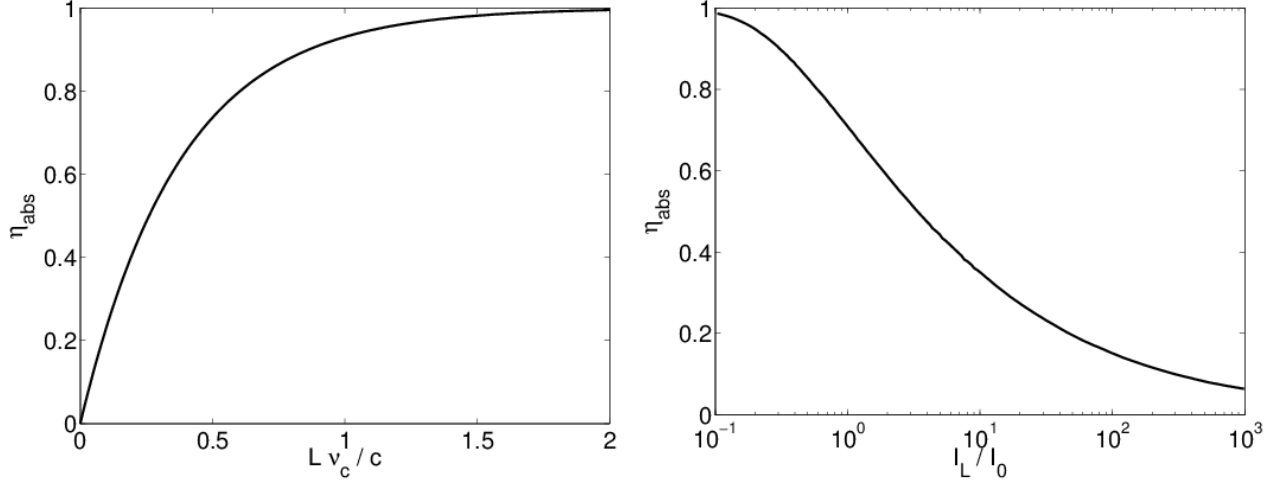


Figure 1.1: Inverse bremsstrahlung absorption coefficient η_{abs} as a function of $\nu_c L/c$ according to Equation (1.4) (left) and I_L/I_0 according to Equation (1.5) (right)

Let us firstly consider the case of a $\omega = 2\pi c/\lambda$ monochromatic laser pulse of linear polarization, normally incident on a flat solid target ($\mathbf{E} = E_y \mathbf{e}_y$). We also assume the coronal plasma to be quasi-neutral ($n_e = Z n_i$), fully ionized with the exponential electron density profile $n_e = Z n_i = n_c \exp[-(x - x_c)/L]$ if $x > x_f$ and $n_e = C^{\text{te}}$ else such that $\nu_{ei} < \omega$ in all the absorption zone $x > x_c$ as illustrated in **Figure 8**. By solving the linearized 1st order equations of $\{(1.1), (1.2)\}$, one finds for the electric field at normal incidence

$$\frac{d^2 \widehat{E}_z}{dx^2} + \frac{\omega^2}{c^2} \epsilon(x, \omega) \widehat{E}_z(x) = 0. \quad (1.3)$$

Here, \widehat{E} is the time Fourier transform of the electric field and $\epsilon(x, \omega) = 1 - \omega_p(x)^2 / [\omega(\omega + i\nu_{ei}(x))]$ is the coronal permittivity. According to the WKB approximation (from the names of its founders G. Wentzel, H. A. Kramers and L. Brillouin), one can derive the laser energy absorption coefficient in the corona [Dawson and Oberman, 1962] [Mora, 1982]

$$\begin{aligned} \eta_{\text{abs}} &= 1 - \exp \left[-2 \int_{x_c}^{\infty} \frac{\nu_{ei}(x) n_e(x)}{c n_c} \left(1 - \frac{n_e(x)}{n_c} \right)^{-1/2} dx \right] \\ &= 1 - \exp \left(-\frac{8 L \nu_c}{3 c} \right). \end{aligned} \quad (1.4)$$

where $\nu_c = \nu_{ei}(x_c)$. The calculation of Integral (1.4) shows that, typically in the conventional ICF schemes, 50 % of the laser absorption takes place in the immediate vicinity of the critical density where

the density is between $0.88 n_c$ and n_c in the case of a low absorption ($L\nu_c \lesssim c$). In the opposite case of an almost total absorption of the laser energy ($L\nu_c \gg c$), more energy is absorbed in the lower density zone. According to the self-similar isothermal expansion, L scales with $c_{st} \propto T_e^{1/2}$ where $c_s = \sqrt{Zk_B T_e/m_i}$ is the sound velocity while $\nu_c \propto n_c T_e^{-3/2}$. Thus, by equating the absorbed energy flux $\eta_{\text{abs}} I_L$ to the energy flux necessary to maintain this self-similar isothermal expansion from the critical density to the vacuum $4n_c T_e c_s$, one finds that the temperature scales with the laser intensity I_L and the laser wavelength λ as $T_e \propto (\eta_{\text{abs}} I_L \lambda^2)^{2/3}$. By injecting this expression in (1.4), one obtains [Mora, 1982]

$$\eta_{\text{abs}} = 1 - \exp \left[- \left(\frac{I_0}{\eta_{\text{abs}} I_L} \right)^{2/3} \right] \quad (1.5)$$

where $I_0 = 4.8 \cdot 10^{11} \text{ W.cm}^{-2} (1.06 \mu\text{m}/\lambda)^5 (2Z/A)^{5/4} [Z (\ln \Lambda_c/6) (t/100 \text{ ps})]^{3/2}$. This laser energy absorption mechanism called **Inverse Bremsstrahlung Absorption** (IBA) is the main absorption mechanism for laser intensities below $10^{15} \text{ W.cm}^{-2}$ used in the conventional ICF schemes. The implicit Equation (1.5) can be solved numerically and the resulting IBA absorption coefficient is plotted in the right panel of **Figure 1.1**. η_{abs} decreases as the intensity increases and is larger for shorter wavelengths.

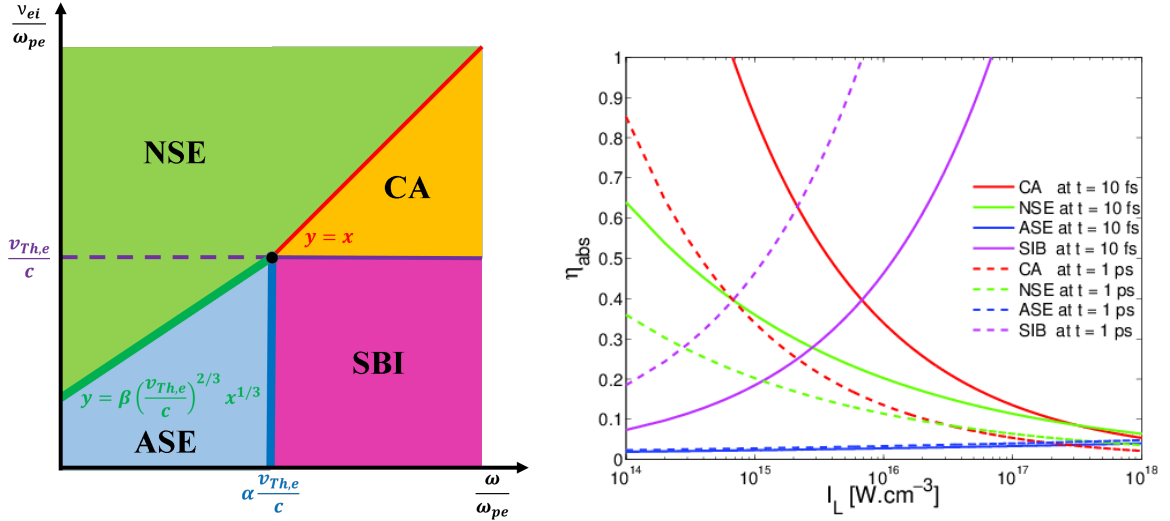


Figure 1.2: (Left panel) Parameters domain in the (ν_{ei}, ω) plane where occurs each absorption mechanism during the LSI with a laser pulse and a step density gradient; $\alpha = [1 + (\pi/2)^{1/4}] / 2 \pm [1 - (\pi/2)^{1/4}] / 2$ and $\beta = [(1/2)^{1/3} + (\pi/2)^{1/6}] / 2 \pm [(1/2)^{1/3} - (\pi/2)^{1/6}] / 2$; the signs \pm come from the uncertainties on frontiers between the different regimes, evaluated according to the conditions of validity of each mechanism. (Right panel) Plot of the corresponding absorption coefficients as a function of the laser pulse intensity I_L evaluated for Copper with $\lambda = 1 \mu\text{m}$ at $t = 10 \text{ fs}$ and $t = 1 \text{ ps}$ after the beginning of the LSI according to Equations (1.9), (1.10), (1.11) and (1.12) (right)

For laser pulse duration Δt_{FWHM} shorter than used in conventional ICF schemes such as $L/c_s \gg \Delta t_{\text{FWHM}}$, the laser-ionized plasma has no time to expand hydrodynamically. Let us as-

sume so that the laser pulse at normal incidence interacts directly with a solid steep density gradient ($L \rightarrow 0$). In this case, the resolution of {(1.1), (1.2)} shows that the laser pulse penetrates the solid over a skin-depth $L_s \approx c/\omega_{pe}$ while a stationary wave consisting in the incident laser pulse and the reflected parts is formed, standing in vacuum. For high electron temperatures and high laser frequencies, the previous model developed for large density gradients can be extended by taking the limit $L \rightarrow 0$ and then by replacing L by the penetration depth L_s in (1.4). This laser energy absorption mechanism is called **Collisional Absorption** (CA). For lower laser frequencies and colder and/or denser solids, the electron collision frequency becomes larger than the laser frequency. In this case, well-known in metal optics, this is the **Normal Skin Effect** (NSE) which is responsible for the laser absorption in the skin-depth. This is what happens for example when a light is reflected by a mirror. These two collisional absorption mechanisms are valid only if the electron mean free path $v_{Th,e}/\nu_{ei}$ and the mean distance travelled by electrons during one laser period $v_{Th,e}/\omega$ are smaller than the skin-depth L_s where $v_{Th,e} = \sqrt{k_B T_e/m_e}$ is the electron thermal velocity. With increasing laser intensities and electron temperatures, "collisionless" absorption mechanisms become dominant. Two "collisionless" mechanisms have been firstly identified : the **Sheath Inverse Bremsstrahlung** (SIB) [Catto and More, 1977] and the **Anormal Skin Effect** (ASE) [Weibel, 1967a]. It has been demonstrated later that they are in fact two limits of the same "collisionless" absorption mechanism [Yang et al., 1995]. Usually discussed separately, the absorption coefficients for these four mechanisms can be derived within a common theory by linearizing Equation (1.1) coupled with the classical kinetic equation expressed within the BGK approximation (for the name of its founders P. L. Bhatnagar, E.P. Gross and M. Krook, see **Appendix A, section A.3.1**)

$$\frac{\partial f_e}{\partial t} + \frac{\partial}{\partial \mathbf{r}} \cdot (\mathbf{v} f_e) - \frac{\partial}{\partial \mathbf{v}} \cdot \left[\frac{e}{m_e} \left(\mathbf{E} + \frac{\mathbf{v}}{c} \times \mathbf{B} \right) f_e \right] = -\nu (f_e - f_M). \quad (1.6)$$

where ν is the effective electron collision frequency. The results obtained by [Rozmus et al., 1996], according to this method, are summarized in the following table where the mean effective collision frequency ν has been evaluated by ν_{ei} for simplicity.

	Conditions of validity	L_s	η_{abs}
CA	$L_s \gg \frac{v_{The}}{\nu_{ei}} \gg \frac{v_{The}}{\omega}$	$\frac{c}{\omega_{pe}}$	$\frac{2\nu_{ei}}{\omega_{pe}}$
NSE	$L_s \gg \frac{v_{Th,e}}{\omega} \gg \frac{v_{Th,e}}{\nu_{ei}}$	$\frac{c}{\omega_{pe}} \sqrt{\frac{2\nu_{ei}}{\omega}}$	$\frac{\omega}{\omega_{pe}} \sqrt{\frac{8\nu_{ei}}{\omega}}$
ASE	$L_s \ll \frac{v_{Th,e}}{\omega} \ll \frac{v_{Th,e}}{\nu_{ei}}$	$\left(\frac{2}{\pi}\right)^{1/6} \left(\frac{v_{Th,e}}{\omega}\right)^{1/3} \left(\frac{c}{\omega_{pe}}\right)^{2/3}$	$\frac{8}{3\sqrt{3}} \left(\frac{2}{\pi}\right)^{1/6} \left(\frac{v_{Th,e}}{c}\right)^{1/3} \left(\frac{\omega}{\omega_{pe}}\right)^{2/3}$
SIB	$\frac{v_{Th,e}}{\omega} \ll L_s \ll \frac{v_{Th,e}}{\nu_{ei}}$	$\frac{c}{\omega_{pe}}$	$8\sqrt{\frac{2}{\pi}} \left(\frac{v_{Th,e}}{c}\right)^3 \left(\frac{\omega_{pe}}{\omega}\right)^2$

The domains in the plane (ω_{pe}, ν_{ei}) , where each absorption mechanism occurs, are shown in the left panel of **Figure 1.2**. These absorption mechanisms lead to the target isochoric heating over the skin-depth L_s . In order to evaluate the absorption coefficient, one has first to relate the electron

temperature and the laser intensity according to Equation (1.2 c). At the LSI interface, the energy flux conservation $-\kappa_e(\partial T_e)/\partial x = \eta_{\text{abs}} I_L$ imposes the boundary condition and ensures a unique solution. By assuming a square temporal laser pulse shape and that the absorption coefficient η_{abs} depends on the electron temperature, one can find a self-similar solution of the heat equation (1.2 c) with the form $T_e(x, t) = T_0 \tau^{2/9} F(\zeta)$ [Zel'dovich and Raizer, 1966], where $\zeta = \xi/\tau^{7/9}$, $\xi = x/v_0 t_0$, $\tau = t/t_0$, $T_0 = m_e v_0^2/k_B$, $t_0 = (2\kappa_0/3n_e)(m_e/k_b)^{5/2} v_0^3$, $v_0 = (2\eta_{\text{abs}} I_L/3n_e m_e)^{1/3}$ and

$$\frac{d}{d\zeta} \left(F^{5/2} \frac{dF}{d\zeta} \right) - \frac{2F}{9} + \frac{7\zeta}{9} \frac{dF}{d\zeta} = 0. \quad (1.7)$$

This equation can be solved numerically, giving an expression for the temperature at the LSI interface [Gibbon, 2005]

$$T_I = T_e(x = 0, t) = 250 \left(\frac{n_i}{10^{23} \text{ cm}^{-3}} \right)^{-2/9} \left(\frac{\eta_{\text{abs}} I_L}{10^{15} \text{ W.cm}^{-2}} \right)^{4/9} \left(\frac{t}{100 \text{ fs}} \right)^{2/9} \text{ eV} \quad (1.8)$$

where n_i is the initial atomic density. This expression is implicit since the absorption coefficient depends on the temperature. However, by injecting this expression in the absorption coefficients, one can deduce the explicit expressions of the absorption coefficient for the CA, the NSE, the ASE and the SBI mechanisms assuming for simplicity $\ln \Lambda_{ei} = 4$. It reads respectively

$$\eta_{\text{abs}} = 2.64 \cdot 10^{-2} Z^{10} \left(\frac{n_i}{10^{23} \text{ cm}^{-3}} \right)^{-1} \left(\frac{I_L}{10^{15} \text{ W.cm}^{-2}} \right)^{-2/5} \left(\frac{t}{100 \text{ fs}} \right)^{-1/5}, \quad (1.9)$$

$$\eta_{\text{abs}} = 7.79 \cdot 10^{-2} \left(\frac{\lambda}{1 \mu\text{m}} \right)^{-3/8} Z^{3/8} \left(\frac{n_i}{10^{23} \text{ cm}^{-3}} \right)^{1/8} \left(\frac{I_L}{10^{15} \text{ W.cm}^{-2}} \right)^{-1/4} \left(\frac{t}{100 \text{ fs}} \right)^{-1/8}, \quad (1.10)$$

$$\eta_{\text{abs}} = 8.00 \cdot 10^{-2} \left(\frac{\lambda}{1 \mu\text{m}} \right)^{-18/25} Z^{-9/25} \left(\frac{n_i}{10^{23} \text{ cm}^{-3}} \right)^{-9/25} \left(\frac{I_L}{10^{15} \text{ W.cm}^{-2}} \right)^{2/25} \left(\frac{t}{100 \text{ fs}} \right)^{1/25} \quad (1.11)$$

$$\text{and } \eta_{\text{abs}} = 4.14 \cdot 10^{-2} \left(\frac{\lambda}{1 \mu\text{m}} \right)^{-6/5} Z^{3/5} \left(\frac{n_i}{10^{23} \text{ cm}^{-3}} \right)^{2/5} \left(\frac{I_L}{10^{15} \text{ W.cm}^{-2}} \right)^{2/5} \left(\frac{t}{100 \text{ fs}} \right)^{1/5}. \quad (1.12)$$

Even if the temperature dependence of the electron collision frequency $\nu_{ei} = \nu_0 T_e^{-3/2}$ and the thermal electron velocity $v_{th,e} = \sqrt{k_B T_e/m_e}$ has not been taken into account in Equation (1.8), these results are in good agreement with the more rigorous calculations of NSE and ASE absorption coefficients found by [Rozmus and Tikhonchuk, 1990]. It must be emphasized that collisions play an important role in the ASE and SBI mechanisms. The term "collisionless" comes from the fact that the electron collision frequency ν_{ei} does not appear explicitly in the absorption coefficient η_{abs} , but the electrons escaping the skin layer are thermalized in the bulk target.

1.1.2 Resonant Absorption

Let us consider now a laser pulse interacting with a large scale density gradient at an incidence angle θ with respect to the target normal direction \mathbf{e}_x (see **Figure 8**) such that the wave vector has the form $\mathbf{k} = |\mathbf{k}| (\cos \theta \mathbf{e}_x + \sin \theta \mathbf{e}_y)$. If the laser pulse is s-polarized i.e. if $\widehat{\widehat{\mathbf{E}}} = E_z(x) \exp(iky \sin \theta) \mathbf{e}_z$ where the double hat $\widehat{\widehat{}}$ means that we have also performed the y -Fourier transform of the electric field, one gets

$$\frac{d^2 \widehat{\widehat{E}}_z}{dx^2} + \left[\frac{\omega^2}{c^2} \epsilon(x, \omega) - \sin^2 \theta \right] \widehat{\widehat{E}}_z(x) = 0 \quad (1.13)$$

instead of Equation (1.3). According to the WKB approximation, the absorption coefficient can be estimated. It reads

$$\eta_{\text{abs}} = 1 - \exp\left(-\frac{8 L \nu_c \cos^3 \theta}{3 c}\right). \quad (1.14)$$

Thus, the turning point in the oblique incidence case, i.e., the position where the laser pulse is reflected is no longer at the critical surface x_c but at the position where the density $n_e = n_c \cos^2 \theta$. In the case where the laser pulse is p-polarized with the laser electric field in the plane (x, y) , it is more convenient to work with the magnetic field. One gets

$$\frac{d^2 \widehat{\widehat{B}}_z}{dx^2} - \frac{1}{\epsilon(x, \omega)} \frac{d\epsilon}{dx} \frac{d\widehat{\widehat{B}}_z}{dx} + \frac{\omega^2}{c^2} [\epsilon(x, \omega) - \sin^2 \theta] \widehat{\widehat{B}}_z(x) = 0 \quad (1.15)$$

while the electric field can be found from the Maxwell-Ampere law : $\widehat{\widehat{E}}_x = -c \sin \theta \widehat{\widehat{B}}_z / \epsilon$ and $\widehat{\widehat{E}}_y = -i(c^2 / \omega \epsilon) d\widehat{\widehat{B}}_z / dx$. Starting from Equation (1.15), it has been shown that the plasma resonance may cause a significant laser energy absorption [Freidberg et al., 1972]. In addition to the collisional absorption mechanism taken into account in Equation (1.15), it describes another absorption mechanism which does not depend on the collision frequency ν_c but only on the incidence angle θ , the laser frequency ω and the density gradient length L [Ginzburg, 1961]. The underlying physical process is the conversion of the incident laser wave into the resonant plasma wave near the critical density. [Ginzburg, 1961] provides the estimate of the absorption coefficient

$$\eta_{\text{abs}} \approx 2.65 \left(\frac{\omega L}{c}\right)^{2/3} \sin^2 \theta \exp\left(-\frac{4 \omega L \sin^3 \theta}{3 c}\right). \quad (1.16)$$

It means that, due to the presence of the longitudinal component of the electric field, electron plasma waves can be excited near the critical density. Indeed, at the turning point where the real part of the dielectric function vanishes, the magnetic field takes a finite value $\widehat{\widehat{B}}_{z0}$. It follows that $\widehat{\widehat{E}}_x = -c \sin \theta \widehat{\widehat{B}}_{z0} / \epsilon$ becomes very large, which means that the incident electromagnetic wave resonantly excites an electron plasma wave. A rigorous account for the collisional and/or thermal effects is needed to describe the plasma wave structure. Indeed, the excited electron plasma oscillations are

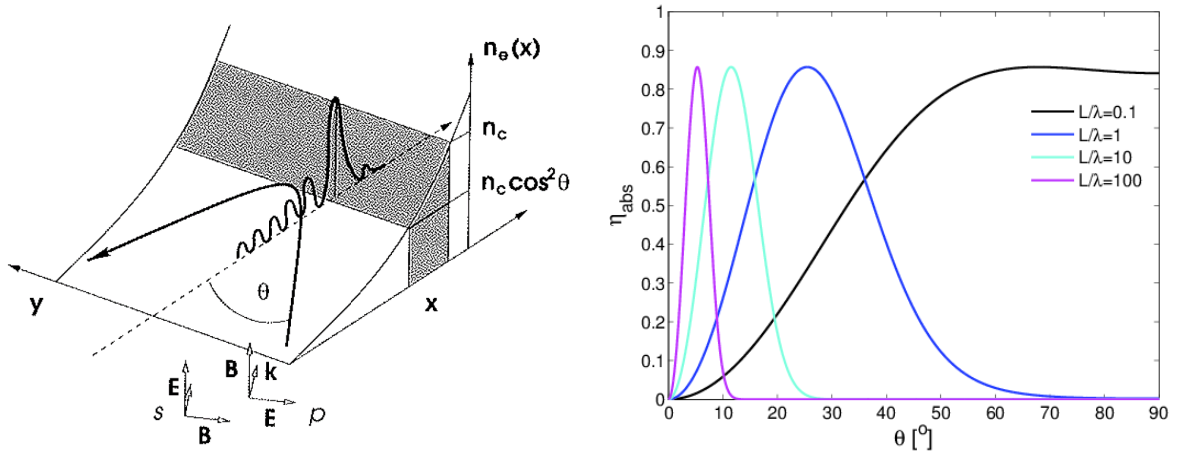


Figure 1.3: LSI resonant absorption scheme inspired by [Gibbon, 2005] (left) and resonant absorption coefficient of a p-polarized laser pulse η_{abs} as a function of the incidence angle θ (right)

convected by thermal effects from the critical density zone to a lower density zone. They are absorbed in the zone where the local wave vector $|\mathbf{k}| \approx 0.3\lambda_{\text{Debye}}^{-1}$ becomes comparable to the Debye screening length $\lambda_{\text{Debye}} = \sqrt{k_B T_e / 4\pi n_e e^2}$ [Forslund et al., 1975]. As the amplitude of electron plasma waves is sufficiently large, non-linear effects may become important leading to the density profile steepening near the critical density. At the same time, plasma oscillations excited at the critical density transfer their energy to energetic electrons. The resonant absorption may play an important role in the laser absorption of ICF pellet in the Conventional and Shock Ignition schemes due to the spherical symmetry of the capsule. It strongly depends on the angle between the capsule normal and the incident laser pulse as shown in **Figure 1.3**. Moreover, it can induce the density profile steepening and fast electrons acceleration. The energy of fast electrons scales with the intensity as [Forslund et al., 1977]

$$T_{\text{fast } e^-} \approx 14 \left[\left(\frac{T_e}{1 \text{ keV}} \right) \left(\frac{I_L}{10^{15} \text{ W.cm}^{-2}} \right) \left(\frac{\lambda}{1 \mu\text{m}} \right)^2 \right]^{1/3} \text{ keV}. \quad (1.17)$$

The resonant absorption can also occur in the case of a steep gradient density. In this case, the results obtained in this section can be generalized by taking the limit of $L \rightarrow 0$.

1.1.3 Ponderomotive Force and Parametric Instabilities

The 1st order response of the plasma electrons in the sub-critical zone in the cold plasma approximation (1.1) is given by

$$m_e \frac{\partial}{\partial t} (\delta \mathbf{v}_e^{(1)}) = -e \mathbf{E} \quad (1.18)$$

where $\mathbf{E} = \delta \mathbf{E}^{(1)}$ is the laser electric field assumed here to be a 1st order term in the perturbation expansion. The 1st order response consists in the plasma electron oscillations along the laser electric

field direction at the laser frequency ω , which are screening the laser field over a distance of the order of the skin depth L_s behind the critical surface. The 2nd order response of plasma electrons is given by

$$m_e \left[\frac{\partial}{\partial t} (\delta \mathbf{v}_e^{(2)}) + \left(\delta \mathbf{v}_e^{(1)} \cdot \frac{\partial}{\partial \mathbf{r}} \right) (\delta \mathbf{v}_e^{(1)}) \right] = -e \frac{\delta \mathbf{v}_e^{(1)}}{c} \times \mathbf{B}. \quad (1.19)$$

Thus, by noticing that the curl of Equation (1.18) provides $-(m_e/e)(\partial/\partial t) [(\partial/\partial \mathbf{r}) \times \delta \mathbf{v}_e^{(1)}] = (\partial/\partial \mathbf{r}) \times \mathbf{E} = -(1/c)(\partial \mathbf{B}/\partial t)$ and consequently $\mathbf{B} = (m_e c/e)(\partial/\partial \mathbf{r}) \times \delta \mathbf{v}_e^{(1)}$, one can write

$$\begin{aligned} m_e \frac{\partial}{\partial t} (\delta \mathbf{v}_e^{(2)}) &= -m_e (\delta \mathbf{v}_e^{(1)} \cdot \frac{\partial}{\partial \mathbf{r}}) (\delta \mathbf{v}_e^{(1)}) - m_e \delta \mathbf{v}_e^{(1)} \times \left(\frac{\partial}{\partial \mathbf{r}} \times \delta \mathbf{v}_e^{(1)} \right) \\ &= -\frac{\partial}{\partial \mathbf{r}} \left(\frac{1}{2} m_e \delta \mathbf{v}_e^{(1)2} \right). \end{aligned} \quad (1.20)$$

This non-linear force corresponds to the second order plasma response at the frequencies 0 and of 2ω . The **ponderomotive force** is the average of this quantity over a laser period. From a particle point of view, it can be seen as a pressure force exerted by the laser photons. For a monochromatic plane wave linearly polarized propagating in the x -direction with $\mathbf{E} = E_0(r, t) \sin(\omega t + kx) \mathbf{e}_y$ where $E_0(r, t)$ is the slowly varying laser electric field envelope, the laser intensity has the form $I_L(r, t) = cE_0(r, t)^2/8\pi$. In this case, the mean ponderomotive force over a laser period can be written

$$\mathbf{F}_{\text{pond}} = -\frac{\partial}{\partial \mathbf{r}} \left\langle \frac{1}{2} m_e \delta \mathbf{v}_e^{(1)2} \right\rangle = -\frac{\partial}{\partial \mathbf{r}} \left\langle \frac{e^2 \mathbf{E}^2}{2m_e \omega^2} \right\rangle = -\frac{2\pi e^2}{\omega^2 m_e c} \frac{\partial}{\partial \mathbf{r}} (I_L). \quad (1.21)$$

In the local plane, the laser intensity profile can be taken to be $I_L(r, t) = I_{\text{max}} \exp \left[-4 \ln 2 (r/\Delta r_{\text{FWHM}})^2 \right] f(t)$ where $r = \sqrt{y^2 + z^2}$ and Δr_{FWHM} is the spatial Full Width Half Maximum (FWHM) of the focal spot. Consequently, the ponderomotive force tends to eject plasma electrons from the focal spot center where the laser intensity is highest, leading to the ion density modification on the hydrodynamic time scale. Moreover, in the rising part of the laser pulse, the ponderomotive force is directed along the laser propagation axis and tends to push the plasma inward the target [Lee et al., 1977].

The three-wave parametric instabilities consist in a decomposition of the laser wave at ω into two daughter waves ω_1 and ω_2 where $\omega_1 > 0$ and $\omega_2 = \omega - \omega_1$ (Stokes configuration) or $\omega_1 < 0$ and $\omega_2 = \omega - \omega_1$ (anti-Stokes configuration). The Stokes decomposition is unstable and leads to an energy transfer from the laser pulse into the two daughter waves. According to the hydrodynamic equations (1.2), the laser electromagnetic waves scatters in the expanding corona (see **Figure 8**), off the density perturbations due to the excitation of Electron Plasma Waves (EPWs) or Ion Acoustic Waves (IAWs) at the frequency ω_1 . An electron current is generating the electromagnetic fields at the frequency ω_2 . It will be resonant if it corresponds to the electromagnetic dispersion relation. Then, as illustrated in **Figure 1.4**, this electromagnetic field perturbation coupled with the laser pulse electromagnetic field drives a ponderomotive force which resonantly amplifies the density perturbation if $\omega_1 = \omega - \omega_2$

corresponds to the dispersion relation of the longitudinal plasma waves (EPWs or IAWs). These non-linear processes are important because they can scatter the laser pulse and prevent it from reaching the absorption zone. In addition, part of the laser energy is transferred to EPWs, which can then transfer part of their energy into fast electrons. Also, the stimulated Brillouin scattering as well as the stimulated Raman scattering can lead to an energy transfer into the Daughter Electromagnetic Wave (DEW) propagating in the backward direction, which can destroy the laser optics.

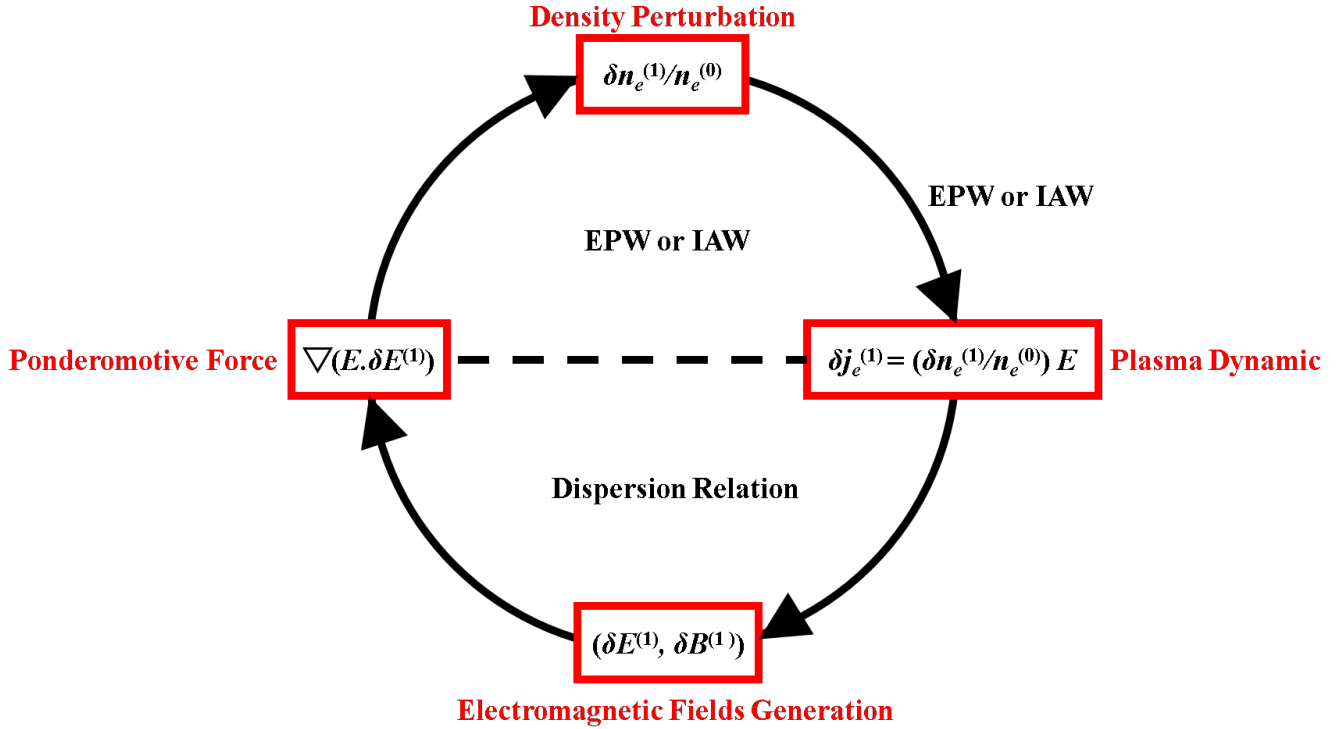


Figure 1.4: Parametric instabilities scheme

There are four distinct three-wave processes. They are summarized in the following table.

Instability type	Daughter 1	Daughter 2	Unstable zone
Acoustic Decay	EPW $\omega_1 \approx \omega$	IAW $\omega_2 \ll \omega$	$n_e \approx n_c$
Stimulated Brillouin Scattering	DEW $\omega_1 \approx \omega$	IAW $\omega_2 \ll \omega$	$n_e \in]0, n_c[$
Two-Plasmon-Decay	EPW $\omega_1 \approx \omega/2$	EPW $\omega_2 \approx \omega/2$	$n_e = n_c/4$
Stimulated Raman Scattering	DEW $\omega_1 \approx \omega/2$	EPW $\omega_2 \approx \omega/2$	$n_e \in]0, n_c/4[$

Experiments on indirect or direct drive ICF have shown that several tens of per cent of laser energy can be reflected due to stimulated Raman and Brillouin scatterings while part of the scattered light is absorbed in the corona thus modifying the absorption and accelerating fast electrons [Ebrahim et al., 1980] [Lindl, 1995]. It is expected in the Shock Ignition scheme that the stimulated Raman scattering plays an important role in the generation of energetic electrons [Klimo et al., 2010] [Klimo et al., 2014].

1.1.4 Simplified Scheme of Electron Acceleration by Landau Damping in strong Electron Plasma Waves

The resonant absorption of the laser pulse or parametric instabilities lead to the generation of strong Electron Plasma Waves (EPWs) in the corona. The Landau damping of such EPWs may lead to the acceleration of fast electrons. Instead of describing the Landau damping starting from classical kinetic theory (see **Appendix A**) as it is done by [Villani, 2014], let us just consider the trapping of one electron in one Fourier mode of such an electrostatic wave : $\mathbf{E} = E_0 \sin(\omega t - kx)\mathbf{e}_x$. The phase velocity reads $v_\varphi = \omega/k = v_{Th,e} \sqrt{3 + (1/k\lambda_{Debye})^2}$ according to the wave dispersion relation, where $v_{Th,e} = \sqrt{k_B T_e/m_e}$ is the electron thermal velocity. From the electron equation of motion in the wave frame moving at the velocity $v_\varphi \mathbf{e}_x$, we can derive the energy conservation equation

$$\frac{m_e}{2} \left(\frac{dX}{dt} \right)^2 - \frac{eE_0}{k} \cos(kX) = K \quad (1.22)$$

where X is the electron position in the wave frame and K is the total energy. The electron tra-

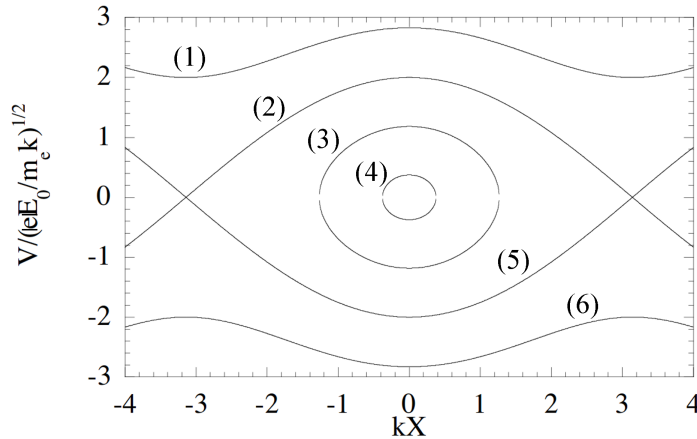


Figure 1.5: Solutions of (1.22) plotted in the phase-space ($V = dX/dt$ as a function of X) for $K = 3eE_0/k$ (1) and (6), $K = eE_0/m_e k$ (2) and (5), $K = eE_0/4m_e k$ (3), $K = -0.92eE_0/m_e k$ (4).

jectories are uni-directional only if $K > eE_0/k$ (see curves 1 and 6 in **Figure 1.5**). In the case where $eE_0/k > K > -eE_0/k$, the Equation (1.22) describes circling trajectories trapped in the wave (see trajectories (3) and (4) in **Figure 1.5**). The particular case $|K| = eE_0/k$ corresponds to the separatrix (see trajectories (2) and (5) in **Figure 1.5**) separating the passing and trapped particles. This simple analysis shows that a strong EPW can trap and accelerate electrons to energies up to $K \approx (\gamma_\varphi - 1) m_e c^2$ where $\gamma_\varphi = 1/\sqrt{1 - (v_\varphi/c)^2}$ written with the relativistic formalism here. In order to give an order of magnitude, let us assume that $k \approx 0.3\lambda_{Debye}^{-1}$ (value at which the Landau damping is optimal) and that the electron temperature scales as $T_e \propto (\eta_{abs} I_L \lambda^2)^{2/3}$, according to analysis presented in **section 1.1.1**. Then, one finds that the energy of accelerated electrons scales with the

absorption coefficient η_{abs} , the laser intensity I_L and the laser wavelength λ as

$$T_{\text{fast } e^-} \approx (\gamma_\varphi - 1) m_e c^2 \approx 12 k_B T_e \approx 33 \sqrt{\frac{A}{Z}} \left[\left(\frac{\eta_{\text{abs}}}{10\%} \right) \left(\frac{I_L}{10^{15} \text{ W.cm}^{-2}} \right) \left(\frac{\lambda}{1 \mu\text{m}} \right)^2 \right]^{2/3} \text{ keV}. \quad (1.23)$$

Concerning the Shock Ignition scheme ($I_L \approx 10^{15} \text{ W.cm}^{-2}$), fully kinetic large-scale two-dimensional simulations have been conducted recently [Klimo et al., 2010] [Klimo et al., 2014]. They show that a significant amount of the laser spike's energy is reflected and absorbed close to $n_c/4$ due to stimulated Raman scattering and that electrons are accelerated to energies up to several tens of keV in agreement with the previous estimate.

1.2 Laser solid interaction at Ultra-High Intensities

1.2.1 Single Electron Motion in an Ultra-High Intense Laser Pulse

Since the invention of CPA by [Strickland and Mourou, 1985], the laser pulse durations have come down from 1 ps to less than 5 fs, leading to an increase of laser pulse intensities by more than six orders of magnitude allowing to overpass the relativistic threshold of $I_L \lambda^2 \gtrsim 10^{18} \text{ W.cm}^{-2} \cdot \mu\text{m}^2$. In order to introduce this regime, we first consider the motion of a single electron in such a Ultra-High-Intense (UHI) laser pulse traveling in the positive x -direction. The wave vector potential is $\mathbf{A} = \left[0, \delta A_0 f(t) \cos \phi, \sqrt{1 - \delta^2} A_0 f(t) \sin \phi \right]^T$ where $\phi = 2\pi(ct - x)/\lambda$ is the wave phase, λ is the laser wavelength, $f(t)$ is a slowly varying laser pulse temporal envelope and δ is a polarization parameter such that $\delta \in \{-1, 0, 1\}$ corresponds to a linearly polarized wave and $\delta = \pm 1/\sqrt{2}$ corresponds to a circular wave. Using the relations $\mathbf{E} = -\partial\mathbf{A}/\partial t$ and $\mathbf{B} = c(\partial/\partial\mathbf{r}) \times \mathbf{A}$ as well as $\mathbf{v} \times [(\partial/\partial\mathbf{r}) \times \mathbf{A}] = [(\partial/\partial\mathbf{r}) \otimes \mathbf{A}] \cdot \mathbf{v} - [\mathbf{v} \cdot (\partial/\partial\mathbf{r})] (\mathbf{A})$, the motion of an electron in the presence of this electromagnetic field is given by the Lorentz equation

$$\frac{d\mathbf{p}}{dt} = -e \left(\mathbf{E} + \frac{\mathbf{v}}{c} \times \mathbf{B} \right) = e \left[\frac{\partial\mathbf{A}}{\partial t} + \left(\mathbf{v} \cdot \frac{\partial}{\partial\mathbf{r}} \right) (\mathbf{A}) \right] - e \frac{\partial}{\partial\mathbf{r}} \otimes \mathbf{A} \cdot \mathbf{v} \quad (1.24)$$

while the energy conservation equation reads

$$\frac{d}{dt} (\gamma m_e c^2) = -e \mathbf{v} \cdot \mathbf{E} = e \mathbf{v} \cdot \frac{\partial\mathbf{A}}{\partial t} \quad (1.25)$$

where $\mathbf{p} = \gamma m_e \mathbf{v}$ is the electron momentum, $\gamma = \sqrt{1 + (\mathbf{p}/m_e c)^2}$ its Lorentz factor and \mathbf{v} its velocity. The perpendicular component of Equation (1.24) reads

$$\frac{d\mathbf{p}_\perp}{dt} = e \left(\frac{\partial\mathbf{A}}{\partial t} + v_x \frac{\partial\mathbf{A}}{\partial x} \right) = e \frac{d\mathbf{A}}{dt}$$

which after integrating gives

$$\mathbf{p}_\perp = e\mathbf{A} \quad (1.26)$$

by assuming the electron is initially at rest. The longitudinal component of Equation (1.24) and Equation (1.25) gives

$$\frac{d}{dt}(p_x - \gamma m_e c) = -e \frac{v_y}{c} \left(\frac{\partial A_y}{\partial t} + c \frac{\partial A_y}{\partial x} \right) - e \frac{v_z}{c} \left(\frac{\partial A_z}{\partial t} + c \frac{\partial A_z}{\partial x} \right) = 0$$

because \mathbf{A} is a function of the phase ϕ , only. Thus, on one hand, $\gamma = 1 + (p_x/m_e c)$ while in the other hand, $\gamma = \sqrt{1 + (p_x/m_e c)^2 + (\mathbf{p}_\perp/m_e c)^2}$, by definition. These two relations give consequently

$$p_x = \frac{\mathbf{p}_\perp^2}{2m_e c} = \frac{m_e c}{2} \left(\frac{e\mathbf{A}}{m_e c} \right)^2 \quad \text{and} \quad \gamma = 1 + \frac{1}{2} \left(\frac{e\mathbf{A}}{m_e c} \right)^2. \quad (1.27)$$

By noticing that $d\phi/dt = (\partial\phi/\partial t) + v_x(\partial\phi/\partial x) = \omega/\gamma$ and by changing the variable $\mathbf{p} = \gamma m_e (d\mathbf{r}/dt) = \gamma m_e (d\phi/dt)(d\mathbf{r}/d\phi) = (2\pi m_e c/\lambda)(d\mathbf{r}/d\phi)$, the electron trajectory in the laboratory frame can be integrated starting from (1.26) and (1.27) assuming it is initially at the origin and neglecting the slowly varying terms. It reads

$$\begin{cases} t &= \frac{a_0^2}{4} \frac{T}{2\pi} \frac{2\delta^2 - 1}{2} \sin 2\phi + \left(1 + \frac{a_0^2}{4}\right) \frac{T}{2\pi} \phi \\ x &= \frac{a_0^2}{4} \frac{\lambda}{2\pi} \frac{2\delta^2 - 1}{2} \sin 2\phi + \frac{a_0^2}{4} \frac{\lambda}{2\pi} \phi \\ y &= a_0 \frac{\lambda}{2\pi} \delta \sin \phi \\ z &= -a_0 \frac{\lambda}{2\pi} \sqrt{1 - \delta^2} \cos \phi \end{cases} \quad (1.28)$$

Here, $T = \lambda/c$ and $a_0 = eA_0 f/m_e c = \sqrt{2e^2 I_L \lambda^2 / \pi m_e^2 c^5}$ where I_L is the laser intensity. Equation (1.28) shows that an electron interacting with a laser pulse starts to drift with an average momentum $\langle \mathbf{p} \rangle = (a_0^2/4)m_e c \mathbf{e}_x$, corresponding to a drift velocity

$$\mathbf{v}_D = \frac{\langle \mathbf{p} \rangle}{\langle \gamma \rangle m_e} = c \frac{a_0^2/4}{1 + a_0^2/4} \mathbf{e}_x. \quad (1.29)$$

Indeed, by performing the Lorentz transformation from the laboratory frame to the average rest frame moving at the velocity \mathbf{v}_D : $t_0 = \gamma_D (t - v_D x/c^2)$, $x_0 = \gamma_D (x - v_D t)$, $y_0 = y$ and $z_0 = z$ where

1.2. LASER SOLID INTERACTION AT ULTRA-HIGH INTENSITIES

$\gamma_D = 1/\sqrt{1 - (v_D/c)^2} = (1 + a_0^2/4)/\sqrt{1 + a_0^2/2}$, one gets

$$\begin{cases} t_0 = \frac{a_0^2/4}{1 + a_0^2/2} \frac{T_0}{2\pi} \frac{2\delta^2 - 1}{2} \sin 2\phi_0 + \frac{T_0}{2\pi} \phi_0 \\ x_0 = \frac{a_0^2/4}{1 + a_0^2/2} \frac{\lambda_0}{2\pi} \frac{2\delta^2 - 1}{2} \sin 2\phi_0 \\ y_0 = \frac{a_0}{\sqrt{1 + a_0^2/2}} \frac{\lambda_0}{2\pi} \delta \sin \phi_0 \\ z_0 = -\frac{a_0}{\sqrt{1 + a_0^2/2}} \frac{\lambda_0}{2\pi} \sqrt{1 - \delta^2} \cos \phi_0 \end{cases} \quad (1.30)$$

where the subscripts $_0$ denote the values in the average rest frame and for which the phase invariance $\phi_0 = \phi$ as well as the longitudinal Doppler-Fizeau relationship $T_0/T = \lambda_0/\lambda = \sqrt{(1 + v_D/c)/(1 - v_D/c)} = \sqrt{1 + a_0^2/2}$ have been used. In this frame, the drift component has disappeared and the electron trajectory consists only in oscillations at $2\omega_0$ in the x -direction and at ω_0 in the transverse direction. In the case of a linearly polarized laser pulse ($\delta = 1$), the electron trajectory describes a figure-of-eight as shown in **Figure 1.6**. If $I_L \lambda^2 \ll 10^{18} \text{ W.cm}^{-2} \cdot \mu\text{m}^2$, this longitudinal

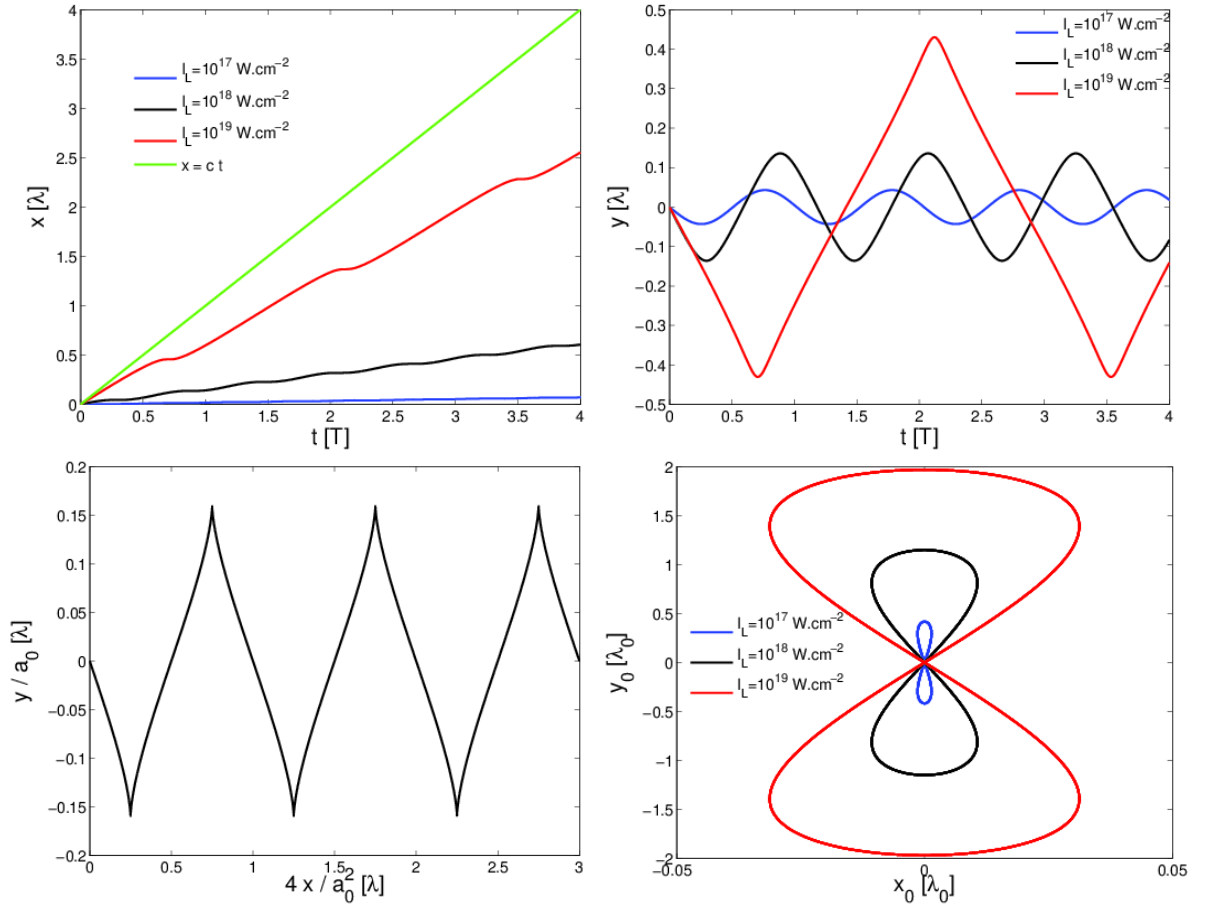


Figure 1.6: Plot of x vs t (top left), y vs t (top right), y vs x (down left) and y_0 vs x_0 (down right) for different values of the laser intensity with $f(t) = 1$ and $\delta = 1$ corresponding to $a_0 = 0.27, 0.85$ and 2.70 according to Equations (1.28) and (1.30).

drift is negligible ($a_0^2/4 \ll a_0$) and we find the transverse oscillations at the frequency ω considered in **sections 1.1**. In the opposite ultra-relativistic case where $I_L \lambda^2 \gg 10^{18} \text{ W.cm}^{-2} \cdot \mu\text{m}^2$ ($a_0^2/4 \gg a_0$), this longitudinal drift, accompanied with oscillations at 2ω is the main process. In the general case, the angle between the electron momentum and the laser pulse propagation direction is

$$\theta = \arctan\left(\frac{|\mathbf{p}_\perp|}{p_x}\right) = \arctan\left(\sqrt{\frac{2}{\gamma-1}}\right). \quad (1.31)$$

UHI laser experiments are usually conducted with short laser pulses interacting with a solid target with a steep density gradient. The analysis concerning the single electron response shows that electrons interacting with a UHI propagating laser plane wave stop moving immediately after the laser pulse ended. The electron motion is adiabatic and it cannot acquire energy directly from the laser pulse. Moreover, contrary to the non-relativistic case, the collisional friction force is negligible here due to a large amplitude of the laser electromagnetic fields and high temperatures in the skin-depth imposed by the laser absorption. Indeed, the surface temperature T_I at the solid-vacuum interface scales with the laser intensity as $I_L^{4/9}$ according to Equation (1.8). It can reach several keV for laser intensities $I_L \geq 10^{18} \text{ W.cm}^{-2}$. Consequently, in the relativistic regime, collisions cannot explain the break of this adiabaticity. The UHI Laser Solid Interaction has been therefore intensively studied for more than twenty years and a large number of collisionless processes can be found in the litterature to explain the experimentally observed accelerated electron.

1.2.2 Cold Plasma Approximation

In a fluid framework, the mechanisms of UHI laser electron acceleration can be described by replacing Equation (1.2) by the relativistic ones

$$\begin{aligned} \frac{\partial n_e}{\partial t} + \frac{\partial}{\partial \mathbf{r}} \cdot (n_e \mathbf{v}_e) &= 0 & (a) \\ \frac{\partial \mathbf{p}_e}{\partial t} + \left(\mathbf{v}_e \cdot \frac{\partial}{\partial \mathbf{r}} \right) (\mathbf{p}_e) &= -e \left(\mathbf{E} + \frac{\mathbf{v}_e}{m_e c} \times \mathbf{B} \right) & (b) \\ (\gamma_e - 1) m_e c^2 &= \sqrt{m_e^2 c^4 + \mathbf{p}_e^2 c^2} - m_e c^2 & (c) \end{aligned} \quad (1.32)$$

where $\mathbf{p}_e = \gamma_e m_e \mathbf{v}_e$ is the mean electron momentum, γ_e is the mean Lorentz factor and \mathbf{v}_e the mean velocity. It must be noted here that, in difference from the cold plasma approximation in the classical regime, the relativistic cold plasma approximation assumes that the electron distribution is monoenergetic and anisotropic. Indeed, due to the nonlinear relation between the single electron velocity and momentum $\mathbf{p} = \gamma m_e \mathbf{v}$, the relation $\mathbf{p}_e = \gamma_e m_e \mathbf{v}_e$ is valid only if all electrons have the same velocity \mathbf{v}_e and consequently the same mass $\gamma m_e = \gamma_e m_e$. This explains why Equation (1.2 c) for the electron temperature is replaced by Equation (1.32 c) with zero electron temperature. By working with the laser vector potential \mathbf{A} and the electrostatic potential Φ and by noticing that $2\gamma_e (m_e c)^2 (\partial/\partial \mathbf{r})(\gamma_e - 1) = (m_e c)^2 (\partial/\partial \mathbf{r})(\gamma_e^2) = (\partial/\partial \mathbf{r})(\mathbf{p}_e \cdot \mathbf{p}_e) = 2[\mathbf{p}_e \cdot (\partial/\partial \mathbf{r})](\mathbf{p}_e) + 2\mathbf{p}_e \times [\partial/\partial \mathbf{r}] \times$

$\mathbf{p}_e] \Rightarrow [\mathbf{v}_e \cdot (\partial/\partial \mathbf{r})](\mathbf{p}_e) = (\partial/\partial \mathbf{r})(\gamma_e - 1)m_e c^2 - \mathbf{v}_e \times [(\partial/\partial \mathbf{r}) \times \mathbf{p}_e]$, one can rewrite (1.32 b) as

$$\frac{\partial}{\partial t} (\mathbf{p}_e - e\mathbf{A}) = -\frac{\partial}{\partial \mathbf{r}} (\gamma_e - 1) m_e c^2 + \frac{\partial}{\partial \mathbf{r}} (e\Phi) + \mathbf{v}_e \times \left[\frac{\partial}{\partial \mathbf{r}} \times (\mathbf{p}_e - e\mathbf{A}) \right].$$

Thus, by taking the curl of this equation, one gets

$$\frac{d}{dt} \left[\frac{\partial}{\partial \mathbf{r}} \times (\mathbf{p}_e - e\mathbf{A}) \right] = \frac{\partial}{\partial t} \left[\frac{\partial}{\partial \mathbf{r}} \times (\mathbf{p}_e - e\mathbf{A}) \right] + \left(\mathbf{v}_e \cdot \frac{\partial}{\partial \mathbf{r}} \right) \left\{ \left[\frac{\partial}{\partial \mathbf{r}} \times (\mathbf{p}_e - e\mathbf{A}) \right] \right\} = 0$$

and assuming the electrons are initially at rest, one has necessarily

$$\left[\frac{\partial}{\partial \mathbf{r}} \times (\mathbf{p}_e - e\mathbf{A}) \right] = 0. \quad (1.33)$$

Finally, Equation (1.32) becomes so

$$\begin{aligned} \frac{\partial n_e}{\partial t} + \frac{\partial}{\partial \mathbf{r}} \cdot (n_e \mathbf{v}_e) &= 0 & (a) \\ \frac{\partial}{\partial t} (\mathbf{p}_e - e\mathbf{A}) &= \mathbf{F} + \frac{\partial}{\partial \mathbf{r}} (e\Phi) & (b) \\ (\gamma_e - 1)m_e c^2 &= \sqrt{m_e^2 c^4 + \mathbf{p}_e^2 c^2} - m_e c^2 & (c) \end{aligned} \quad (1.34)$$

where

$$\mathbf{F} = -\frac{\partial}{\partial \mathbf{r}} (\gamma_e - 1) m_e c^2 \quad (1.35)$$

is the non averaged **Relativistic Ponderomotive Force** which was extended from the classical theory [Stroschio et al., 1978]. This force leads to exotic effects compared to the non-relativistic regime and will be described more accurately in the next paragraph.

Let us consider a UHI elliptically polarized plane wave traveling in an underdense plasma $\omega_{pe} \leq \omega$ ($\omega_{pe} = \sqrt{4\pi Z n_i e^2 / m_e}$ is the classical plasma frequency) in the positive x -direction represented by its vector potential $\mathbf{A} = \left[0, \delta A_0 f(t) \cos \phi, \sqrt{1 - \delta^2} A_0 f(t) \sin \phi \right]^T$. In contrast with the single electron case, here, $\phi = 2\pi c(t - x/v_\phi)/\lambda$ where $v_\phi = \omega/k$ is the wave phase velocity. The system of equations (1.34) is coupled with the Maxwell equations (1.1) expressed for the vector potential \mathbf{A} and the electrostatic potential Φ in the Coulomb gauge ($(\partial/\partial \mathbf{r}) \cdot \mathbf{A} = 0$)

$$\begin{aligned} \left(\frac{\partial^2}{\partial \mathbf{r}^2} \right) (\Phi) &= 4\pi e (n_e - Z n_i) & (a) \\ \frac{\partial^2}{\partial t^2} (\mathbf{A}) - c^2 \left(\frac{\partial^2}{\partial \mathbf{r}^2} \right) (\mathbf{A}) &= 4\pi \mathbf{j}_e. & (b) \end{aligned} \quad (1.36)$$

Assuming plasma electrons are initially at rest and $f = 1$, the system of Equations {1.34, 1.36} reads

[Akhiezer and Polovin, 1956]

$$\begin{aligned}
 n_e &= \frac{\gamma_e m_e v_\phi}{\gamma_e m_e v_\phi - p_{e,x}} Z n_i \quad (\text{a}) \\
 \frac{d^2 \mathbf{p}_{e,\perp}}{d\phi^2} &= - \frac{1}{\gamma_e} \left(\frac{\omega_{pe}}{\omega} \right)^2 \frac{\gamma_e m_e v_\phi}{\gamma_e m_e v_\phi - p_{e,x}} \frac{v_\phi^2}{v_\phi^2 + c^2} \mathbf{p}_{e,\perp} \quad (\text{b}) \\
 \frac{d^2}{d\phi^2} (\gamma_e m_e c^2 - \mathbf{p}_{e,x} v_\phi) &= \frac{1}{\gamma_e} \left(\frac{\omega_{pe}}{\omega} \right)^2 \frac{\gamma_e m_e v_\phi}{\gamma_e m_e v_\phi - p_{e,x}} v_\phi p_{e,x}. \quad (\text{c})
 \end{aligned} \tag{1.37}$$

According to [Kaw and Dawson, 1970], Equations (1.37 b) and (1.37 c) in the limit $p_{e,x} \ll \gamma_e m_e v_\phi$ as well as $v_\phi^2/(v_\phi^2 + c^2) \approx 1$ and $\gamma_e m_e c^2 \ll p_{e,x} v_\phi$ take the non-relativistic form with $\omega_{pe}/\sqrt{\gamma_e}$ instead of ω_{pe} . This can be interpreted as a deeper penetration of electromagnetic waves in the target with an increased skin-depth $L_s \approx c\sqrt{\gamma_e}/\omega_{pe}$ instead of $L_s \approx c/\omega_{pe}$, due to the higher electron inertia $\gamma_e m_e$. This relativistic effect is called the **Self-Induced Transparency**. While this phenomenon has been observed in kinetic simulations [Lefebvre and Bonnaud, 1995] [Guérin et al., 1996], its experimental validation is still controversial [Gibbon, 2005]. Equations (1.37) provide the adequate theoretical formalism to extend some mechanisms to the relativistic regime as the **Relativistic Parametric Instabilities** [Guérin et al., 1995] and the **Relativistic Linear Resonant Absorption** [Yu et al., 1998]. These two mechanisms can be responsible for laser energy absorption by driving strong EPWs and accelerating fast electrons. Also, this formalism can be used to predict the **Direct Laser Acceleration** of fast electrons by Channeling the laser pulse [Pukhov et al., 1999] [Li et al., 2011]. However, these mechanisms take place in an underdense plasma ($n_e < n_c$) and they cannot explain the laser energy absorption reported in UHI laser-solid interaction experiments where the absorption may reach up to 70% [Sauerbrey et al., 1994]. Also, they cannot explain the fast electron energy spectrum reaching up to 10 MeV as measured experimentally by [Beg et al., 1997]. The following sections present the main absorption mechanisms operating in laser-solid interaction experiments in the relativistic regime.

1.2.3 Relativistic Ponderomotive Force and $\mathbf{j} \times \mathbf{B}$ heating

The ponderomotive force may push the plasma electrons inward the target at the center of the focal spot. Then, the plasma ions are accelerated due to the induced electrostatic fields. In the relativistic regime, the ponderomotive force (1.35) push the surface of a modestly overdense plasma over a distance of several laser wavelengths deep in a moderately overdense plasma on the sub-ps timescale [Wilks et al., 1992]. This so-called **Hole boring** process has been demonstrated experimentally at a laser intensity of $10^{18} \text{ W.cm}^{-2}$ by [Kalashnikov et al., 1994] by measuring the Doppler red-shifted reflected light. This effect was at the basis of the fast ignition scheme [Tabak et al., 1994]. One can derive the relativistic ponderomotive force expression (1.35) by projecting (1.34 b) on the parallel and

1.2. LASER SOLID INTERACTION AT ULTRA-HIGH INTENSITIES

perpendicular axes ($\mathbf{e}_\perp = \delta \cos \phi \mathbf{e}_y + \sqrt{1 - \delta^2} \sin \phi \mathbf{e}_x$) :

$$\begin{cases} \mathbf{p}_{e,\perp} &= e\mathbf{A} & \text{(a)} \\ \frac{\partial p_{e,x}}{\partial t} &= \frac{\partial}{\partial x} (e\Phi) + F & \text{(b)} \end{cases} \quad (1.38)$$

where

$$\mathbf{F} = -v_{e,x} \frac{\partial p_{e,x}}{\partial x} \mathbf{e}_x - \frac{1}{2\gamma_e m_e} \frac{\partial}{\partial x} (\mathbf{p}_{e,\perp}^2) \mathbf{e}_x. \quad (1.39)$$

Thus, if the laser pulse has a circular polarization, i.e., if $\delta = 1/\sqrt{2}$, the force reads

$$\mathbf{F} = -v_{e,x} \frac{\partial p_{e,x}}{\partial x} \mathbf{e}_x - \frac{e^2}{4\gamma_e m_e} \frac{\partial}{\partial x} (A_0^2) \mathbf{e}_x \quad (1.40)$$

while for a linear polarization i.e. for $\delta \in \{-1, 0, 1\}$, it reads

$$\mathbf{F} = -v_{e,x} \frac{\partial p_{e,x}}{\partial x} \mathbf{e}_x - \frac{e^2}{4\gamma_e m_e} \frac{\partial}{\partial x} \{A_0^2 [1 + \cos(2\omega t)]\} \mathbf{e}_x. \quad (1.41)$$

The ponderomotive force is usually defined by the average part of this force and it reads in both cases

$$\mathbf{F}_{\text{pond}} = \langle \mathbf{F} \rangle = -\frac{e^2}{4\gamma_e m_e} \frac{\partial}{\partial x} (A_0^2) \mathbf{e}_x. \quad (1.42)$$

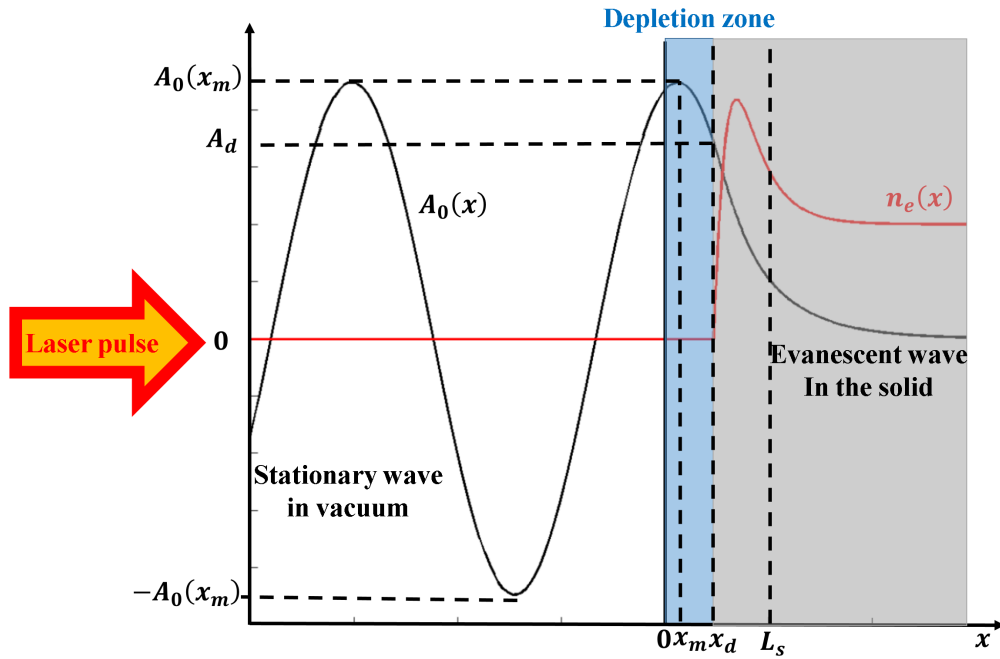


Figure 1.7: Schematic view of a UHI LSI in a step gradient density

Let us consider a UHI laser pulse of circular polarization normally incident on a steep density gradient. It is reflected, generating a stationary standing wave in vacuum while the electromagnetic field is evanescent inside the target over the skin-depth L_s . As explained above concerning the hole boring effect, there is an electron depletion zone $[0, x_d]$ where the plasma electrons have been pushed forward by the ponderomotive force. As the ponderomotive force is stationary, one can find an exact analytical solution of the system of Equations $\{(1.34), (1.36)\}$ assuming $\mathbf{A} = A_0(x)[\cos(\omega t)\mathbf{e}_y + \sin(\omega t)\mathbf{e}_z]/\sqrt{2}$ [Marburger and Tooper, 1975] [Siminos et al., 2012]. Neglecting the laser energy absorption, one finds

$$A_0(x) = \begin{cases} -2\frac{m_e c}{e} \sqrt{2\left(1 - \frac{\omega^2}{\omega_{pe}^2}\right)} \frac{\cosh\left[\omega \frac{x - x_m}{c} \sqrt{\frac{\omega_{pe}^2}{\omega^2} - 1}\right]}{\left(\frac{\omega_{pe}^2}{\omega^2} - 1\right) - \cosh^2\left[\omega \frac{x - x_m}{c} \sqrt{\frac{\omega_{pe}^2}{\omega^2} - 1}\right]} & \text{if } x \geq x_d \\ 2A_L \cos\left(2\pi \frac{x - x_d}{\lambda} + \varphi\right) = \frac{1}{4} \left[A_0(x)^2 + \frac{dA_0}{dx}\right]_{x=x_d}^{x=c/2\omega} \cos\left(2\pi \frac{x - x_d}{\lambda} + \varphi\right) & \text{if } x < x_d \end{cases} \quad (1.43)$$

and

$$n_e(x) = \begin{cases} Zn_i \left\{ 1 + \frac{\omega^2}{\omega_{pe}^2} \frac{e^2}{2\gamma_e m_e^2 \omega^2} \left[\left[\frac{1}{\gamma_e^2} \left(\frac{dA_0}{dx} \right)^2 + A_0 \frac{d^2 A_0}{dx^2} \right] \right\} & \text{if } x \geq x_d \\ 0 & \text{if } x < x_d \end{cases} \quad (1.44)$$

where

$$\gamma_e(x) = \sqrt{1 + \left(\frac{e\mathbf{A}}{m_e c}\right)^2} = \sqrt{1 + \left(\frac{eA_0}{m_e c}\right)^2}, \quad (1.45)$$

A_L is the initial normally incident laser pulse amplitude, φ is a constant phase delay, x_m is the position where the vector potential is maximum $A_0(x_m) = 2(m_e c/e) \sqrt{2(\omega_{pe}^2/\omega^2)[(\omega_{pe}^2/\omega^2) - 1]}$ and $x_d = -(1/2\pi en_i)A_0(x_d)(dA_0/dx)|_{x=x_d}/\gamma(x_d)$ is the target depth where the electrons have been displaced by the laser pulse ponderomotive force. These three parameters φ , x_m and x_d can be found by connecting the electron density n_e and the field A_0 at the depletion edge $x = x_d$ (see **Figure 1.7**). In the region $x < x_d$, the field behaves as in a vacuum. Assuming that the standing wave results from the superposition of two progressive waves of amplitude A_L (the laser energy absorption is neglected), one obtains the lower line of Equation (1.43). The upper line of Equation (1.43) comes from the resolution of the system of equations $\{(1.34), (1.36)\}$ in the region $x > x_d$. In the limit of a very dense solid $n_e \gg n_c$, this expression reduces to $A_0 \propto \exp[-(x - x_m)/L_s]$ with $L_s = c/\omega_{pe}$ being the skin-depth.

The linear polarization case $\mathbf{A} = A_L \cos(\omega t)\mathbf{e}_\perp$ is more complicated because one cannot find the analytical expression for γ_e as (1.45) obtained for the circular polarization case

[Bauer and Mulser, 2007]. However, in the limit $\omega_{p,e} \gg \omega$, an approximate solution reads

$$A_0(x) = \begin{cases} 2 \frac{\omega}{\omega_{p,e}} A_L \exp\left(-\frac{x-x_d}{L_s}\right) & \text{if } x \geq x_d \\ 2A_L \cos\left(2\pi \frac{x-x_d}{\lambda} + \varphi\right) & \text{if } x < x_d \end{cases} \quad (1.46)$$

where $L_s = c/\omega \sqrt{(\omega_{pe}^2/\omega^2) - 1} \approx c/\omega_{pe}$. The oscillating component of the ponderomotive force (1.41) in the linearly polarized case can lead to laser energy absorption [Kruer and Estabrook, 1985]. This mechanism is called **$\mathbf{j} \times \mathbf{B}$ heating** (and not ponderomotive heating!) due to the fact that it is induced by the oscillating component of (1.41), coming from the Lorentz force $(\mathbf{v}_e/c) \times \mathbf{B}$ term of (1.32). One can explain this mechanism as follows :

1. During a quarter of the laser cycle, between $t = -T/8$ and $t = T/8$, the cosine of (1.41) is positive and electrons from the plasma surface are ejected in vacuum by the Lorentz force.
2. A strong electrostatic field Φ is generated due to the induced charge separation according to Equation (1.36 a).
3. During the following quarter of the laser cycle, the cosine becomes negative and the electrons are consequently recalled by this ponderomotive force component but this time with an amplification due to the force $(\partial/\partial x)(e\Phi)$.
4. Thus, the electrons are reinjected in the overdense plasma where the local electromagnetic fields vanish behind the skin depth L_s .

Consequently, the adiabaticity of electron motion is broken at the moment when they are crossing the plasma skin layer and they acquire the kinetic energy gained from the electric force $(\partial/\partial x)(e\Phi)$. Thus, accelerated electrons escape from the laser solid interaction zone thanks to their residual energy. This acceleration mechanism has been confirmed by kinetic simulations [Wilks et al., 1992]. The authors find a good agreement between their numerical results and the estimate of the mean kinetic energy often called "temperature" of the accelerated electrons

$$T_e \approx \left(\sqrt{1 + \left\langle \left(\frac{e\mathbf{p}_{e,\perp}}{m_e c} \right)^2 \right\rangle} - 1 \right) m_e c^2 = \left(\sqrt{1 + \frac{a_0^2}{2}} - 1 \right) m_e c^2 \quad (1.47)$$

according to Equation (1.38 a) where $\langle \cdot \rangle$ means that the value has been averaged over a laser cycle and $a_0 = \sqrt{2e^2 I_L \lambda^2 / \pi m_e^2 c^5}$. This expression is commonly called the ponderomotive scaling due to the fact that it corresponds to the ponderomotive potential of a single electron [Bauer et al., 1995]. Besides, even if numerical simulations confirm that this process makes a significant contribution to the laser energy absorption, this temperature scaling differs from experimental results [Ping et al., 2008].

1.2.4 Brunel Effect and Vacuum heating

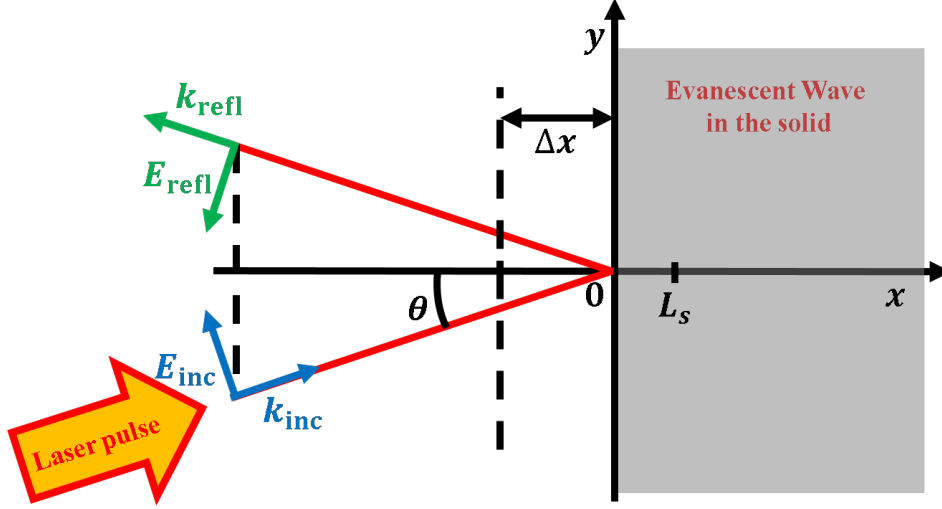


Figure 1.8: Schematic view of a UHI p-polarized laser pulse incident on a steep gradient density

Here, we consider an interaction of a linearly polarized UHI laser pulse with a steep density gradient at an oblique incidence with the angle θ as illustrated in **Figure 1.8**. The laser pulse vector potential reads $A_L \cos[\omega t - k(x \cos \theta + y \sin \theta)](-\sin \theta \mathbf{e}_x + \cos \theta \mathbf{e}_y)$. The role of collective electric fields in this configuration was demonstrated by [Brunel, 1987] thanks to kinetic simulations and a simplified analytical model. Thus, it would have been possible to place this subsection in the previous section. However, due to the fact that this mechanism plays an important role in UHI laser-plasma interaction, we have preferred to place it here. This mechanism can be understood in a one-dimensional approach, neglecting of the Lorentz force $(\mathbf{v}_e/c) \times \mathbf{B}$ in Equation (1.32). Thus, the system of Equations $\{(1.34), (1.36)\}$ reduces to

$$\mathbf{A} = \begin{cases} 2A_L \cos(\omega t + \varphi) \cos(kx \cos \theta) \sin \theta \mathbf{e}_x & \text{if } x \leq 0 \\ \propto \exp\left(-\frac{x - x_d}{L_s}\right) & \text{if } x > 0 \end{cases} \quad (\text{a})$$

$$\frac{\partial^2 \Phi}{\partial x^2} = 4\pi e (n_e - Zn_i) \quad (\text{b}) \quad (1.48)$$

$$\frac{\partial}{\partial t} + \frac{\partial}{\partial x} (n_e v_{e,x}) = 0 \quad (\text{c})$$

$$\frac{dp_{e,x}}{dt} = e \frac{\partial A}{\partial t} + e \frac{\partial \Phi}{\partial x} \quad (\text{d})$$

where $\varphi = ky \sin \theta$ is a constant phase parameter. The **Brunel heating** can be explained as follows

1. In the first half of the laser cycle, between $t = -(T/2) - \varphi/\omega$ and $t = -\varphi/\omega$, the cosine of (1.48 a) is negative. Thus, a sheath of electrons at the plasma interface ($x = 0^-$) is experiencing the longitudinal electric field (1.48 a) and is pulled out in vacuum up to a distance $\approx \Delta x$ according to Equations (1.48 c) and (1.48 d).

2. According to Equation (1.48 b), an electrostatic field is created in this zone $[-\Delta x, 0]$.
3. During the following half of the laser cycle, the cosine of (1.48 a) is positive and the electrons in this zone are consequently recalled back but this times with an amplification due to the electric force $(\partial/\partial x)(e\Phi)$, according to Equations (1.48 c) and (1.48 d).
4. The electrons are reinjected in the overdense plasma where the local electromagnetic fields vanish beyond the skin depth L_s according to Equation (1.48 a)

Consequently, the electron motion adiabaticity is broken and the electron gains a kinetic energy from the electrostatic field. Moreover, the accelerated electrons escape from the interaction zone thanks to this residual energy. Except for the time periodicity and the spatial configuration of the process, the Brunel heating mechanism is similar to the $\mathbf{j} \times \mathbf{B}$ one. By using the capacitor approximation for the step 2, approximating $v_{e,x} \approx 2eA_0/m_e$ for the step 3 and assuming that all electrons are lost in the solid for the step 4, one can estimate the laser energy absorption [Gibbon, 2005]

$$\eta_{\text{abs}} \approx \frac{1}{\pi a_0} f \left[\sqrt{1 + (f a_0 \sin \theta)^2} - 1 \right] \frac{\sin \theta}{\cos \theta}. \quad (1.49)$$

where $f = 1 + \sqrt{1 - (4a_0 \sin^3 \theta / \pi \cos \theta)}$ where the fast electrons "temperature" has been assumed

$$T_e \approx \left(\sqrt{1 + \frac{v_{e,x}^2}{c^2}} - 1 \right) m_e c^2 \approx \left(\sqrt{1 + 4a_0^2} - 1 \right) m_e c^2. \quad (1.50)$$

The maximum laser energy absorption is obtained with $\theta = 75^\circ$ according to Equation (1.49). Actually, it has been shown that not all electrons pushed out into vacuum return to the target each laser period [Brunel, 1988] [Gibbon and Bell, 1992]. Due to the presence in vacuum of non-stationary electromagnetic fields and a low density plasma, the electron orbits are more complex than those predicted in the capacitor approximation. According to kinetic simulation results, the maximum of laser absorption is obtained for $\theta \approx 45^\circ$ and the temperature scales with the laser intensity as $T_e \propto (I_L \lambda^2)^\alpha$ with α between 1/3 and 1/2. For these reasons, and notably because of recalling aspects of disorder, the term **Vacuum heating** is used to make the distinction. It is considered as one of the main absorption mechanisms.

1.2.5 Anharmonic Resonant Absorption

In the case of a linearly polarized incident laser pulse $A_L \cos[\omega t - k(x \cos \theta + y \sin \theta)] (-\sin \theta \mathbf{e}_x + \cos \theta \mathbf{e}_y)$ totally reflected by a steep density at normal or at oblique incidence, the Relativistic Harmonic Resonance Absorption mentioned in the introduction of this section may be mitigated due to the absence of any rarefaction wave. Moreover, the critical-surface oscillations driven by the laser ponderomotive force may lead to the broadening and the splitting of the harmonics [Ding et al., 2009] as well as an

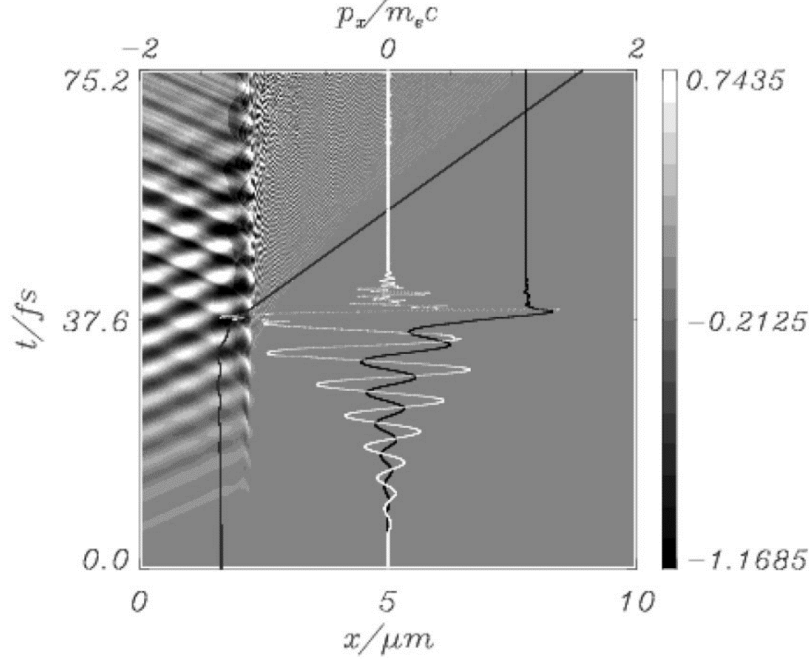


Figure 1.9: Test electron trajectory position $x(t)$ and momentum $p_x(t)/m_e c$ (black lines), total electric field E_x (white line) at position $x(t)$ plotted on the electric field (x, t) map from a kinetic simulation done with a constant laser pulse $a_0 = 0.3$ with an oblique incidence $\theta = 45^\circ$ focused on a steep gradient with fixed ions $Zn_i/n_c = 81$ [Mulser et al., 2008]

efficient laser energy absorption mechanism [Mulser et al., 2008]. Noticing that a break of adiabaticity under steady state conditions is obtained when $\langle \mathbf{j}_e \mathbf{E} \rangle \sim \langle \sin(\omega t + \varphi) \cos(\omega t) \rangle = (1/2) \sin \varphi \neq 0$ according to the Poynting theorem, the authors conclude that only an anharmonic resonance in the self-generated plasma potential may provide conditions for an efficient laser energy absorption as observed in UHI laser-solid interaction experiments. Indeed, by considering a constant density Zn_i , an electron layer of thickness d , oscillating with the amplitude ξ and by approximating the non-averaged ponderomotive force (1.41) by $\mathbf{F} \approx F_0 f(t) \sin(2\omega t) \mathbf{e}_x$, one can derive from Equation (1.36 a)

$$E_x(\xi) = -e \frac{\partial \Phi}{\partial x} = \begin{cases} 4\pi Zn_i e \left(1 - \frac{|\xi|}{2d}\right) \xi & \text{if } \xi \leq d \\ 4\pi Zn_i e \frac{\xi d}{2|\xi|} & \text{if } \xi > d \end{cases} \quad (1.51)$$

which along with Equation (1.38 b) gives the following equation of motion for the electron layer (in the non-relativistic approximation)

$$\frac{d^2 \xi}{dt^2} = F_0 f(t) \sin(2\omega t) - \begin{cases} \omega_{pe}^2 \left(1 - \frac{|\xi|}{2d}\right) \xi & \text{if } \xi \leq d \\ \frac{\omega_{pe}^2 d}{2|\xi|} \xi & \text{if } \xi > d \end{cases} \quad (1.52)$$

The anharmonic resonance heating can thus be understood as follows.

1. According to Equation (1.52), the electron layer oscillates at the frequency ω_{pe} inside the plasma where there is no driver ($F_0 = 0$).
2. With increasing oscillation amplitudes, the electron layer escapes from the plasma and experiences the non-averaged ponderomotive force $F_0 f(t) \sin(2\omega t)$.
3. According to Equation (1.52), the increasing oscillation amplitude $\xi_0 \geq d$ leads to a reduction of the oscillation frequency enabling a resonance condition at $2\omega_{pe}$.
4. Finally, due to the strong driver $F_0 f(t) \sin(2\omega t)$, the oscillation amplitudes may rise to $\xi_0 \rightarrow \infty$ with a pulsation $\approx \sqrt{\omega_{pe}^2 d / 2\xi_0} \rightarrow 0$

This means that between step 1 and step 3, there is a moment when the electron layer oscillation frequency is 2ω ($0 \leq 2\omega \leq \omega_{pe}$). At this moment, the electron layer oscillates in phase with the driver and enters the anharmonic resonance regime. This mechanism has been explained by considering the electron trajectories obtained in kinetic simulations as illustrated in **Figure 1.9**. According to the authors, this **Anharmonic Resonance Heating** in the self-generated plasma waves represents one of the leading electron acceleration mechanisms in UHI laser-solid interaction experiments and may explain energies of accelerated electrons many times the ponderomotive scaling observed in experiments [Cerchez et al., 2008].

1.2.6 Stochastic heating

While the motion of an electron in a single laser wave is deterministic, its motion in two counter-propagating electromagnetic waves can become chaotic if the frequencies of these two waves are different [Mendonça, 1983] [Forslund et al., 1985]. By "chaotic", one means that small differences in the initial conditions produce a large divergence in the electron trajectory with time. Thus, in other words, two counter-propagating electromagnetic waves with slightly different frequencies can break the adiabaticity of the electron motion. This happens in the case of large-scale density gradients and high laser intensities or a sufficiently long pulse 1 – 10 ps like in the Fast Ignition scenario. Let us consider a linearly polarized laser pulse $\mathbf{A}_1 = A_{1,0} \cos \phi_1 \mathbf{e}_y$ with $\phi_1 = \omega_1 t - k_1 x$ normally incident on a target with a large scale density gradient and a counterpropagating one $\mathbf{A}_2 = A_{2,0} \cos \phi_2 (\cos \alpha \mathbf{e}_y - \sin \alpha \mathbf{e}_x)$ with $\phi_2 = \omega_2 t - k_{2,\parallel} x - k_{2,\perp} y + \alpha_0$ which may originate from the reflection of the incident laser pulse or a Raman-backscattered wave as suggested by [Sheng et al., 2002]. The Hamiltonian of a single electron in such a configuration can be expressed in the extended space by [Jackson, 1975]

$$H = \gamma^2 m_e c^2 + (\mathbf{P} + e\mathbf{A}_1 + e\mathbf{A}_2)^2 c^2 - m_e c^2 \quad (1.53)$$

where $\mathbf{P} = \mathbf{p} - e\mathbf{A}_1 - e\mathbf{A}_2$. Indeed, in this case, $H = 0$ according to the momentum quadrivector invariance along directions of translational invariance only. According to [Rax, 1992], by assuming

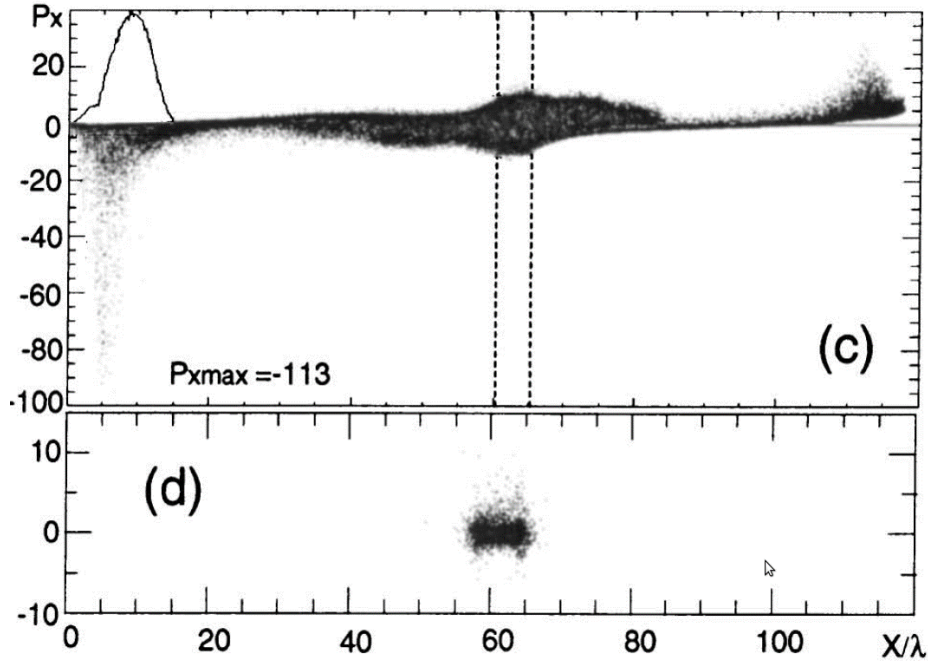


Figure 1.10: Distribution of longitudinal electron momenta normalized by $m_e c$ in space at $t = 110(2\pi c/\lambda)$ [Yu et al., 2000] obtained from a 1D relativistic kinetic simulation of a linearly polarized, Gaussian laser pulse with $a_1 = 7.5$, $\lambda_1 = 1 \mu\text{m}$, and width $L_1 = 15 \mu\text{m}$ normally incident on a foil of density $n_e = 10n_c$ (dashed lines) with (c) or without (d) the presence of a Deuterium preplasma of width $30 \mu\text{m}$ and density $n_e = 10^{-3}n_c$. The time averaged laser electric field normalized by $m_e c \lambda_1 / 2\pi c$ is also plotted in (c) (solid line).

$A_2 \ll A_1$, $\alpha = -\pi/2$ and by changing of variables from $(x, y, z, ct, p_x, p_y, p_z, \gamma m_e c)$ to the angle-action variables $(\theta, \varphi, \phi, E, P_{\parallel}, P_{\perp})$, it can be shown that H can be written as

$$H(x, y, z, ct, p_x, p_y, p_z, \gamma m_e c) = H^{(0)}(\theta, \varphi, \phi, E, P_{\parallel}, P_{\perp}) + \delta H^{(1)}(\theta, \varphi, \phi, E, P_{\parallel}, P_{\perp}) \quad (1.54)$$

where

$$\begin{aligned} H^{(0)} &= \gamma^2 m_e c^2 + (\mathbf{P} + e\mathbf{A}_1)^2 c^2 - m_e c^2 \\ &= E^2 - P_{\perp}^2 - P_{\parallel}^2 - M^2, \end{aligned} \quad (1.55)$$

with $M = \sqrt{1 + (a_1^2/2)}$ and $a_1 = eA_{1,0}/m_e c$, is the unperturbed Hamiltonian of the electron i.e. without the counterpropagating electromagnetic wave \mathbf{A}_2 and

$$\begin{aligned} \delta H^{(1)} &= 2 \left(\frac{\mathbf{P} + e\mathbf{A}_1}{m_e c} \right) \cdot \left(\frac{e\mathbf{A}_2}{m_e c} \right) m_e c^2 + O \left[\left(\frac{e\mathbf{A}_2}{m_e c} \right)^2 m_e c^2 \right] \\ &= a_2 m_e c^2 \sum_{N \in \mathbb{Z}} V_N(E, P_{\parallel}, P_{\perp}) \cos \left[\frac{k_{2,\parallel} c}{\omega_1} \varphi + \frac{k_{2,\perp} c}{\omega_1} \theta + \frac{\omega_2}{\omega_1} \phi + N(\varphi + \phi) \right] \end{aligned} \quad (1.56)$$

is the 1st order perturbation induced by the counterpropagating wave where $a_2 = eA_{2,0}/m_e c$,

$$V_N = \sum_{m \in \mathbb{Z}} \sum_{n \in \mathbb{Z}} \sum_{h=-2}^2 \delta_{h+m+2n}^N U_h J_m \left(\frac{a_1 m_e c P_{\perp} (\omega_2 - k_{2,\parallel} c)}{\omega_1 [P_{\parallel} - (E/c)]^2} + \frac{a_1 m_e c k_{2,\perp} c}{\omega_1 [P_{\parallel} - (E/c)]} \right) \\ \times J_n \left(\frac{k_{2,\parallel} c - \omega_2}{2\omega_1} \frac{(eA_{1,0})^2}{[P_{\parallel} - (E/c)]^2} \right),$$

and

$$U_h = 2 \left[\frac{P_{\perp}}{m_e c} \cos \alpha - \frac{P_{\parallel}}{m_e c} \sin \alpha \right] \delta_h^0 + a_1 \left(\cos \alpha + \frac{P_{\perp} \sin \alpha}{P_{\parallel} - (E/c)} \right) \delta_{|h|}^1 + \frac{a_1^2}{4} \frac{m_e c \sin \alpha}{[P_{\parallel} - (E/c)]} \delta_{|h|}^2$$

with J_m and J_n the Bessel functions. It is interesting to notice that according to the change of variable, $E = \langle \gamma \rangle m_e c^2$, $P_{\perp} = \langle p_y \rangle$ and $P_{\parallel} = \langle p_x \rangle$ where $\langle \cdot \rangle$ which means that the values are averaged over the laser pulse cycle $2\pi/\omega_1$. Indeed, in the case where $A_2 = 0$, the perturbation disappear and $H^{(0)} = 0$ can be integrated and one finds that the unperturbed electron motion consists in the figure-of-eight found in **section 1.2.1**

$$E(P_{\parallel}, P_{\perp}) = \sqrt{M^2 + P_{\parallel}^2 + P_{\perp}^2}. \quad (1.57)$$

Following standard perturbation techniques, one can solve the Hamilton equations by plugging the unperturbed motion ($\theta = (P_{\perp}/m_e c)\omega_1 \tau$, $\varphi = (P_{\parallel}/m_e c)\omega_1 \tau$ and $\phi = -(E/m_e c^2)\omega_1 \tau$ where τ is the proper time) in the argument of the perturbing cosines of the right hand side of Equation (1.56). According to the author, such a perturbation scheme fails to converge because of the occurrence of small resonant denominators when the cosine of the phase remains stationary which means that the system cannot be integrated whenever it exists one $N \in \mathbb{Z}$ such that

$$k_{2,\parallel} c \left(\frac{P_{\parallel}}{m_e c} \right) + k_{2,\perp} c \left(\frac{P_{\perp}}{m_e c} \right) - \omega_2 \left(\frac{E}{m_e c^2} \right) + N \omega_1 \left(\frac{P_{\parallel}}{m_e c} - \frac{E}{m_e c^2} \right) = 0. \quad (1.58)$$

It means that the electron motion is not anymore deterministic and becomes chaotic. The degree of chaoticity for each resonance N can be measured using the Chirikov criterion [Bourdier et al., 2005] but in the general case, kinetic simulations of the UHI laser-solid interaction are needed to find the stochastically accelerated electrons properties.

Efficient electron heating in two counter propagating electromagnetic waves was demonstrated in 1D relativistic kinetic simulations by [Yu et al., 2000]. A linearly polarized, Gaussian laser pulse with a peak amplitude $a_1 = 7.5$, a wavelength $\lambda_1 = 1 \mu\text{m}$, and a width $L_1 = 15 \mu\text{m}$ was normally incident and reflected from a foil of density $n_e = 10n_c$. The electron heating was observed in a Deuterium preplasma of a width $30 \mu\text{m}$ and a density $n_e = 10^{-3}n_c$. In **Figure 1.10**, one can clearly see the effect of the preplasma on the accelerated electrons momenta. Although the electron heating is probably due to stochastic effects, [Yu et al., 2000] do not mention it in their paper. Instead, they explain the electron heating up to several ponderomotive energies as follows. Firstly, the incident laser pulse carries

the accelerated electrons toward the target. As the preplasma behind the pulse maximum becomes positively charged, a relativistic electron return current is created. These counterpropagating electrons with negative momenta cover the entire preplasma and even extend beyond it into the vacuum area. In addition, the target electrons localized near the density jump are accelerated due to the $\mathbf{j} \times \mathbf{B}$ Heating. Highly accelerated electrons can be seen at the far right of the frame, showing that the forward accelerated electrons escaping from the incident laser pulse have passed through the foil target. As the reflected laser pulse propagates backwards in the preplasma, it accelerates a small number of electrons to energies several times those of the forward ones, as shown on the far left of **Figure 1.10 (c)**. For the authors, this strong backward acceleration is therefore attributed to the relativistic electrons return-current, which is missing in the case without preplasma.

As a conclusion, in a presence of a preplasma, laser-accelerated electrons may attain energies exceeding several times the ponderomotive energy, thus forming a hot tail in the energy spectrum, and have a significant angular divergence [Kemp et al., 2009]. This **Stochastic heating** dominates in the underdense plasma in the case of large-scale density gradients according to kinetic simulations and experiments. It largely prevails over the **Direct Laser Acceleration** as well as the **Linear Resonant Absorption** mechanisms [Kemp et al., 2014].

1.3 Particle-in-Cell method for Laser-Plasma Interaction simulations

Numerical simulations of kinetic processes in laser-plasma interactions are usually conducted with Particle-In-Cell codes. In **Part 3** of these manuscript, kinetic simulations will be used for characterization of the laser-generated fast electron transport. This section is dedicated to a brief description of the Particle-In-Cell modeling of Laser-Plasma Interaction.

1.3.1 Phase-Space Discretization for the Vlasov Equation

In order to simulate the interaction between an incident laser pulse and a plasma, one has to solve the Maxwell equations for the laser pulse propagation coupled with the Vlasov equation (see **Appendix A, section A.1.1**) for the kinetic plasma response to the electromagnetic fields. We use the relativistic formalism here and assume that the ions remain immobile. Let us note $f_e = f_e(\mathbf{r}, \mathbf{p}, t)$ the distribution function of plasma electrons. We do not consider the collisions here; they will be discussed in the next subsection. The Vlasov equation reads

$$\frac{\partial f_e}{\partial t} + \frac{\partial}{\partial \mathbf{r}} \cdot \left(\frac{\mathbf{p}}{\gamma m_e} f_e \right) - \frac{\partial}{\partial \mathbf{p}} \cdot \left[e \left(\mathbf{E} + \frac{\mathbf{v}}{c} \times \mathbf{B} \right) f_e \right] = 0 \quad (1.59)$$

1.3. PARTICLE-IN-CELL METHOD FOR LASER-PLASMA INTERACTION SIMULATIONS

where $\gamma = \sqrt{1 + (\mathbf{p}/m_e c)^2}$. Therefore, the distribution function $f_e(\mathbf{r}_l, \mathbf{p}_l, t)$ is constant at the electron trajectories defined by the equations of motion

$$\begin{aligned} \frac{d\mathbf{r}_l}{dt} &= \frac{\mathbf{p}_l}{\gamma_l m_e} \\ \frac{d\mathbf{p}_l}{dt} &= -e \left(\mathbf{E} + \frac{\mathbf{v}_l}{c} \times \mathbf{B} \right). \end{aligned} \quad (1.60)$$

From this observation, it comes naturally the idea to discretize the phase-space (\mathbf{r}, \mathbf{p}) into macroparticles $\{\mathbf{r}_l, \mathbf{p}_l\}$, $l \in [1..N_p]$ which are solutions of (1.60) depending only on their initial position $\mathbf{r}_l(t=0)$ and momentum $\mathbf{p}_l(t=0)$ in order to approach the solution of (2.1) [Birdsall and Fuss, 1969]. Of course, the number of macroparticles N_p is much less than the number N of electrons in the system. Indeed, $N = n_c \Delta x \Delta y \Delta z \approx 10^9 / \lambda [\mu\text{m}]^2$ at the critical density with numerical cells $\Delta x = \Delta y = \Delta z = 1 \mu\text{m}$; The best actual computer technology has allowed a maximum of $N_p \approx 10^{10}$ particles and calculation of 10^{10} time steps, requiring 10^4 hours of CPU. Besides, in the most cases, $N_p \ll N$ is sufficient to describe accurately the relevant long-range physical processes. The split explicit leapfrog scheme commonly called the Boris scheme is usually used to solve the electromagnetic macroparticle pusher (1.60) (see [Birdsall and Langdon, 1991] for other numerical methods). This numerical scheme reads :

$$\begin{aligned} 1^o) \quad \frac{\mathbf{p}_l^- - \mathbf{p}_l^{n-1/2}}{\Delta t/2} &= e\mathbf{E}^n \\ 2^o) \quad \mathbf{p}_l^* - \mathbf{p}_l^- &= T \mathbf{p}_l^- \times \frac{\mathbf{B}^n}{|\mathbf{B}^n|} \text{ where } T = \tan\left(\frac{-e|\mathbf{B}^n|}{2\gamma^- m_e}\right) \text{ with } \gamma^- = \sqrt{1 + \left(\frac{\mathbf{p}_l^-}{m_e c}\right)^2} \\ 3^o) \quad \mathbf{p}_l^+ - \mathbf{p}_l^* &= \frac{2T}{1+T^2} \mathbf{p}_l^* \times \frac{\mathbf{B}^n}{|\mathbf{B}^n|} \\ 4^o) \quad \frac{\mathbf{p}_l^{n+1/2} - \mathbf{p}_l^+}{\Delta t/2} &= e\mathbf{E}^n \\ 5^o) \quad \mathbf{v}_l^{n+1/2} &= \frac{\mathbf{p}_l^{n+1/2}}{\gamma_l^{n+1/2} m_e} \text{ where } \gamma_l^{n+1/2} = \sqrt{1 + \left(\frac{\mathbf{p}_l^{n+1/2}}{m_e c}\right)^2} \\ 5^o) \quad \mathbf{r}_l^{n+1} &= \mathbf{r}_l^n + \mathbf{v}_l^{n+1/2} \Delta t_n \end{aligned} \quad (1.61)$$

where n is the discrete time ($t_n = n\Delta t_n$). The complications come from the temporal and spatial variations of the electromagnetic fields in (1.60). These are the solutions of the Maxwell equations

$$\begin{aligned} \mathbf{E} &= -\frac{\partial \mathbf{A}}{\partial t} - \frac{\partial \Phi}{\partial \mathbf{r}} \\ \mathbf{B} &= c \frac{\partial}{\partial \mathbf{r}} \times \mathbf{A} \\ \frac{\partial^2}{\partial \mathbf{r}^2} (\Phi) &= 4\pi\rho \\ \frac{\partial^2 \mathbf{A}}{\partial t^2} - c^2 \frac{\partial^2}{\partial \mathbf{r}^2} (\mathbf{A}) &= 4\pi\mathbf{j}_e \end{aligned} \quad (1.62)$$

which depend on the electrical charge density ρ and the current density \mathbf{j}_e . These source terms must consequently be interpolated at each time t_n from knowing the N_p macroparticle positions and velocities. For example, the electrical charge is estimated as

$$\rho^{n,i,j,k} = \sum_{k=1}^{N_p} W \left[\mathbf{r}^{i,j,k} - \mathbf{r}_l^n \right] \quad (1.63)$$

where $\mathbf{r}^{i,j,k} = [x_i, y_j, z_k]^T$ with $x_i = x_{\min} + (i-1)\Delta x$, $y_j = y_{\min} + (j-1)\Delta y$ and $z_k = z_{\min} + (k-1)\Delta z$. The function

$$W \left[\mathbf{r}^{i,j,k} - \mathbf{r}_l^n \right] = \int_{x_i - \Delta x/2}^{x_i + \Delta x/2} dx \int_{y_j - \Delta y/2}^{y_j + \Delta y/2} dy \int_{z_k - \Delta z/2}^{z_k + \Delta z/2} dz \Pi(x_i - x_l^n, y_j - y_l^n, z_k - z_l^n) \quad (1.64)$$

is called the macroparticle weight. It depends on the interpolation function Π which can be a Dirac distribution $\delta^3[\mathbf{r}]$ (NGP method for Nearest-Grid-Point [Birdsall and Fuss, 1969]), a linear interpolating function (CIC method for Clouds in Clouds [Birdsall and Fuss, 1969]) and so on. Currently, third order (or more) interpolations are used in high performance PIC codes. The higher the interpolation order is, the higher the accuracy and the computational cost are. The electromagnetic fields are computed according to the well known finite difference schemes of the propagation equation for the vector potential and the Poisson equation for the scalar potential providing the electromagnetic fields. At the next time step, the fields are reinterpolated at the positions of the macroparticles to compute their trajectory at the following next time step.

$$(\mathbf{E}^n(\mathbf{r}_l), \mathbf{B}^n(\mathbf{r}_l)) = \sum_{i=1}^{N_x} \sum_{j=1}^{N_y} \sum_{k=1}^{N_z} W \left[\mathbf{r}^{i,j,k} - \mathbf{r}_l^n \right] \left(\mathbf{E}^n(\mathbf{r}^{i,j,k}), \mathbf{B}^n(\mathbf{r}^{i,j,k}) \right) \quad (1.65)$$

where N_x , N_y and N_z are the grid number respectively in the x , y and z directions. The interpolation function must be the same as for the particle weighting in order to limit the self-force induced by the macroparticles motion in the spatial mesh grid.

1.3.2 Binary Collision Modelling

Coulomb binary collisions are due to the mutual electromagnetic fields created by two interacting particles. The PIC method cannot take into account the binary collisions effects because the forces acting on the particles in a PIC scheme correspond to macroscopic fields, and because the collisional spatial scales are not resolved. As a result, inter-particle forces inside grid cells are underestimated. The binary collisions are described by introducing a Coulomb collision operator inside each cell. The usual method consists of a Monte-Carlo scheme simulating the interaction between each particle pair. Most of Coulomb collision operators used in today PIC codes are based on the binary collision model introduced by [Takizuka and Abe, 1977]. The main idea is based on the fact that, the plasma being

essentially collisionless, the binary Coulomb collisions occur only between particles separated by a distance of the order of the Debye length λ_{Debye} . Since a typical size of the PIC cell is close to λ_{Debye} , the interaction between particles in neighboring cells can be neglected. According to this method, all particles are firstly grouped to the cells (i, j, k) where they are located. Then, these particles are paired in a random way, so that one particle has at least one partner. Thus, selected pairs are collided according to the Monte-Carlo method based on the collision probability of collision proportional to the differential collision cross section. For example, the probability of a small angle and non-relativistic collision between an electron (1) and an electron or ion (2) is proportional to the Rutherford differential cross section (see **Appendix A, section A.2.1**). During the time step Δt_n , the scattering angle θ in the 2D collision plane follows the Gaussian stochastic process [Takizuka and Abe, 1977]

$$p(\theta) = \frac{\theta}{\langle \theta^2 \rangle_n} \exp\left(-\frac{\theta^2}{2\langle \theta^2 \rangle_n}\right) \text{ with } \langle \theta^2 \rangle_n = 4\pi \frac{n_\alpha Z_\alpha e^4}{(1/2)\mu^2 V^3} \ln \Lambda_{e\alpha} \Delta t_n \quad (1.66)$$

where Z_α is the charge of the particle (2), n_α is the density of particle (2), $\mu = m_e m_2 / (m_e + m_2)$ is the reduced mass in the center of mass frame and $\mathbf{V} = \mathbf{v}_1 - \mathbf{v}_2$ is the relative velocity. Inverting the relation (1.66) and randomly choosing a value p_R between 0 and 1 (uniform stochastic process) for the probability p , one obtains the scattering angle in the center of mass frame

$$\theta = \sqrt{-2\langle \theta^2 \rangle_{\Delta t_n} \ln p_R}. \quad (1.67)$$

Correspondingly, the azimuthal angle φ is chosen randomly between 0 and 2π according to the uniform statistic process. If plasma is nearly uniform, one can introduce a cumulative binary collision operator, as proposed by [Nanbu, 1997], which allows to increase the time step of the collision procedure.

1.3.3 Computational Constraints

The main time step restriction of PIC codes comes from the propagation equation for the vector potential \mathbf{A} . The time step must fulfill the Courant-Friedrichs-Lewy condition

$$\Delta t_n < \frac{1}{c} \left(\frac{1}{\Delta x^2} + \frac{1}{\Delta y^2} + \frac{1}{\Delta z^2} \right)^{-1/2}. \quad (1.68)$$

In addition, if the cumulative binary collision operator approximation cannot be introduced, the time step must be shorter than the characteristic collision time, $\nu_{ei} \Delta t_n < 1$. Moreover, the value of the laser frequency ω_0 limits the time step in the Boris scheme to $\omega_0 \Delta t_n < 2$. Concerning simulations of laser plasma interaction, the critical density zone where, typically $\omega_0 = \omega_{pe}$ needs to be considered with special attention because of strong laser-driven electron plasma waves. In that case, the spatial grid must satisfy the condition $\Delta x \approx \Delta y \approx \Delta z \approx c/\omega_{pe}$. In order to limit the non-conservative force associated with the particle-grid mapping, which leads to self-heating and numerical instabilities, the

space resolution has to be comparable to the plasma Debye length $\Delta x \approx \Delta y \approx \Delta z < v_{Th,e}/\omega_{pe} < c/\omega_{pe}$. This imposes a strong constraint in the case of dense and/or cold plasmas!

PIC codes represent one the most time consuming numerical tools used in Physics. To give an order of magnitude of a Laser Solid Interaction simulation in the context of fast ignition, a 100 μm size plasma needs 6250 spatial cells in 1D, $3.9 \cdot 10^7$ in 2D and $3.4 \cdot 10^{11}$ in 3D ($c/\omega_{pe} = 0.016 \mu\text{m}$) while the oscillation time is about $1/\omega_{pe} = 0.05$ fs. Correspondingly, about $4 \cdot 10^5$ time steps are needed for a 20 ps simulation [Kemp et al., 2014]. Still according to [Kemp et al., 2014], a number of macroparticles of 10^7 in 1D, $5 \cdot 10^9$ in 2D and $5 \cdot 10^{11}$ in 3D needs respectively 10^2 , $5.6 \cdot 10^4$ and $5.6 \cdot 10^6$ time steps. PIC codes are key tools to study the laser-plasma interaction in general, and the acceleration of fast electrons in particular in the context of the physics of fast and shock ignition.

1.4 Brief Summary of Laser Solid Interaction and Laser-Generated Relativistic Electron Beam Properties

High-Intensity Laser-Plasma Interaction (HILPI) has been studied for many years, motivated *inter alia* by the Inertial Confinement Fusion (ICF) concept. In the conventional ICF schemes, ns laser pulses interact with a sub-critical, long-scale length plasma (corona) and the dominant laser energy absorption mechanisms are inverse bremsstrahlung heating and the resonant absorption. Besides, parametric instabilities such as the acoustic decay, the stimulated Brillouin scattering, the two-plasmon-decay and the stimulated Raman scattering may be an origin of strong electrostatic fields. The Landau damping of such electrostatic plasma waves may be responsible for fast electron acceleration up to 100s of keV. For shorter laser pulses of several 10s or 100s of fs in the HILPI regime, the plasma has no time to expand so the laser pulse interacts with a solid steep gradient density. In this case, various absorption mechanisms may operate depending on the plasma temperature and density conditions : the collisional absorption, the normal skin effect, the sheath inverse bremsstrahlung and the anomalous skin effect. In the context of Shock Ignition, the laser spike has a duration of several 100s of ps and interacts with a hot and large-scale expanding corona. As a consequence, this changes considerably the conditions of excitation of parametric instabilities and a large amount of fast electrons is expected. This regime is still under investigation through extensive Particle-In-Cell simulations (briefly introduced in **section 1.3**) [Klimo et al., 2014]. Ultra-High Intensity Laser-Plasma interaction (UHILPI) has been studied since the 1990s, after the development of the chirped pulse amplification technique. It is an intense field of research with several unresolved questions. The details of absorption processes are still not well understood and new explanations for the break of adiabaticity in the laser-induced electron motion have been recently proposed [May et al., 2011] [Mulser et al., 2012] [Sanz et al., 2012]. The complexity of the laser-solid interaction due to strong nonlinearities and various competing processes (see **section 1.2**) require the use of numerical Particle-In-Cell kinetic simulations. One can briefly

summarize the obtained results as follows. While the particle acceleration is always due to the electric field work, what differentiates the main mechanisms at play is the source of the electric field. In the case of an obliquely incident laser pulse onto a steep gradient target, the standing wave structure consisting of the incident and reflected waves combined with the electrostatic field is the source of the vacuum heating. In the case of a normally incident laser pulse onto a steep gradient plasma, it is the longitudinal component of the Lorentz force, along with the electrostatic field, which is responsible for the $\mathbf{j} \times \mathbf{B}$ heating. In both cases, an electrostatic field induced by the plasma surface oscillation is responsible for the anharmonic resonant absorption of the laser energy. Actually, due to hole boring of the target, the vacuum heating operates also in the case of a normally incident UHI laser pulse. The electron acceleration depends also on the laser pulse contrast ($I_{L,\max}/I_{L,\min}$). A strong laser prepulse may ionize the surface, causing the plasma to expand. Then, the main laser pulse interacts with a large-scale expanding plasma. In this case, the Raman backward scattered laser light or the reflected laser pulse coupled with the incident laser pulse may lead to stochastic heating of the electrons. Due to a relatively long laser pulse duration (≈ 10 ps) in the Fast Ignition scheme, the fast electron acceleration mechanisms may change with time and extensive particle-in-cell simulations of the LPI are needed. The state of the art of UHILPI in the context of Fast Ignition can be found in [Kemp et al., 2014].

The physical processes described in **sections 1.2.3, 1.2.4, 1.2.5 and 1.2.6** allow us to make some conclusions concerning the properties of laser-generated relativistic electron beam Properties. Firstly, it can be shown, by using the electron momentum conservation in the plane perpendicular to the target normal that, in the case of a laser plane wave, obliquely incident on a steep gradient density profile, the angle between the propagation direction of a forward accelerated electron and the target normal reads [Sheng et al., 2000]

$$\theta_0 = \arctan \left\{ \left[\frac{2(\gamma - 1)(1 + \delta\Phi) - \delta\Phi^2}{(\gamma - 1 - \delta\Phi)^2} \sin^{-2} \theta + \tan^{-2} \theta \right]^{-1/2} \right\} \quad (1.69)$$

where $\delta\Phi = [e\Phi(z, t) - e\Phi_0]/m_e c^2$ is the variation of the electrostatic potential and θ is the laser incidence angle.

Concerning the time dependence of the forward accelerated electrons, one can assume that, at the target surface $z = 0$, the temporal envelope of the electron distribution follows the laser Gaussian shape of duration Δt FWHM:

$$f_z(z - v_0 t) = \frac{1}{\sqrt{2\pi \frac{(v_0 \Delta t)^2}{8 \ln 2}}} \exp \left[-4 \ln 2 \left(\frac{z - v_0 t}{v_0 \Delta t} \right)^2 \right]. \quad (1.70)$$

Here, the internal temporal structure of the electron bunches with the modulation at ω or 2ω has been omitted since it is usually not resolved in fast electron transport hybrid simulations (see **Chapter 5**).

v_0 is the mean velocity associated with the energy flux density of the forward accelerated electrons in the mean propagation z -direction such that the fast electron beam intensity $I_b = n_b \langle \varepsilon \rangle v_0 = \eta_{\text{abs}} I_L$ where η_{abs} is the laser-to-electrons conversion efficiency, I_L the laser pulse intensity, n_b the fast electron beam density and $\langle \varepsilon \rangle$ their mean kinetic energy. As explained in **Chapter 2**, the fast electron beam generates a counterpropagating **return current** in order to cancel the total electrical current. As explained in **Chapter 3**, this system of two counterpropagating currents may be unstable, leading to the generation of small-scale magnetic fields with amplitudes comparable to the laser magnetic field. Such self-generated magnetic fields can strongly deflect the electrons [Adam et al., 2006] [Pérez et al., 2013] thus producing a divergent beam. Another source of the electron beam divergence is the curvature of the electron acceleration region due to hole boring effects [Schmitz et al., 2012b]. The dependence of the electron beam divergence on the intensity can be described by the following empirical scaling law

$$\theta_{1/2} \approx 15^\circ + 30^\circ \log_{10} \left(\frac{I_L}{10^{18} \text{ W.cm}^{-2}} \right) \quad (1.71)$$

where $\theta_{1/2}$ is the cone apex angle. This scaling was deduced from experimental data by [Green et al., 2008]. Since the more energetic electrons are less deviated by these strong stochastic magnetic fields, the divergence angle $\theta_{1/2}$ depends also on the electron energy. Moreover, due to the laser transverse ponderomotive force and propagation effects in the preplasma, the divergence angle of the accelerated electrons increases with the radial distance [Debayle et al., 2010]. The resulting fast electron angular distribution can be approximated with the following form

$$f_\theta(\theta_e) = \frac{1}{\sqrt{2\pi} \frac{\Delta\theta_e^2}{8 \ln 2}} \exp \left[-4 \ln 2 \left(\frac{\theta_e - \theta_0}{\Delta\theta} \right)^{\alpha_0} \right] \quad (1.72)$$

where $\alpha_0 = 2$ or 4 , $\theta_0(r, \varepsilon, t)$ is the mean angle of electron emission which increases with the radial distance r from the beam axis and depends on the electron kinetic energy ε and the time t according to (1.69). $\Delta\theta(\varepsilon, t)$ is the dispersion angle which decreases with increasing electron kinetic energy. θ_e is the half apex angle of the cone oriented in the direction defined by θ_0 .

Experiments and simulations show that the laser-produced electron beam has approximately an axisymmetric Gaussian radial distribution of the form

$$f_r(r) = \frac{1}{2\pi \frac{\Delta r^2}{8 \ln 2}} \exp \left[-4 \ln 2 \left(\frac{r}{\Delta r} \right)^2 \right] \quad (1.73)$$

in the case of a normally incident laser pulse. here, $r = \sqrt{x^2 + y^2}$ is the distance from the beam axis and the beam radius FWHM Δr is two or three times the laser pulse radial FWHM. In the case of oblique incidence, in the (z, x) plane, the spatial distribution of the accelerated electrons can be

written as

$$f_x(x) = \frac{1}{\sqrt{2\pi} \frac{\Delta x^2}{8 \ln 2}} \exp \left[-4 \ln 2 \left(\frac{x - x_0}{\Delta x} \right)^2 \right] \quad (1.74)$$

where x_0 and Δx may depend on time. The distribution in the perpendicular direction f_y can be written similarly by replacing x by y and x_0 by y_0 in the previous Equation. Concerning the energy spectrum of the forward accelerated electrons, several interpolations have been proposed. There is a simple 1D exponential distribution :

$$f_\varepsilon(\varepsilon) = \frac{1}{k_B T_b} \exp \left(-\frac{\varepsilon}{k_B T_b} \right) \quad (1.75)$$

where T_b can be estimated according to (1.47), (1.50) or with other scalings. Other proposed interpolations such as a combination of two exponential functions

$$f_\varepsilon(\varepsilon) = \frac{\alpha_1}{k_B T_b} \exp \left(\frac{\varepsilon}{\alpha_2 k_B T_b} \right) + \frac{\alpha_3}{k_B T_b} \exp \left(\frac{\varepsilon}{\alpha_4 k_B T_b} \right), \quad (1.76)$$

a power law

$$f_\varepsilon(\varepsilon) = \alpha_5 \left(\frac{\varepsilon}{k_B T_b} \right)^{\alpha_6} \quad (1.77)$$

or

$$f_\varepsilon(\varepsilon) = \frac{\alpha_7}{k_B T_b} \exp \left(\frac{\varepsilon}{\alpha_8 k_B T_b} \right) + \frac{\alpha_9}{\varepsilon} \exp \left(\frac{\varepsilon}{\alpha_{10} k_B T_b} \right), \quad (1.78)$$

where $\{\alpha_i\}$ and T_b are parameters found from the fitting of experimental or simulation results. The total number of fast electrons can be written

$$N_0 = \frac{\eta_{\text{abs}} E_L}{\langle \varepsilon \rangle} \quad (1.79)$$

where $\langle \varepsilon \rangle$ is the mean electron kinetic energy and η_{abs} means the laser energy conversion into the forward accelerated fast electrons kinetic energy. By collecting available experimental and numerical results, two interpolations were proposed for the time integrated laser energy absorption coefficient [Davies, 2009]

$$\eta_{\text{abs}} = \left(\frac{I_L \lambda^2}{3.37 \cdot 10^{20} \text{ W.cm}^{-2} \cdot \mu\text{m}} \right)^{0.1958} \quad \text{or} \quad \eta_{\text{abs}} = \left(\frac{I_L \lambda^2}{4.30 \cdot 10^{21} \text{ W.cm}^{-2} \cdot \mu\text{m}} \right)^{0.2661}. \quad (1.80)$$

Note that the instantaneous laser energy absorption is expected to depend on time. The distribution function of the forward accelerated electron beam at the Laser-Solid Interface $z = 0$ can be written as follows

$$\Psi_b(x, y, z = 0, \varepsilon, \theta, \varphi, t) = N_0 f_x(x) f_y(y) f_z(-v_0 t) f_\varepsilon(\varepsilon) f_\theta(\theta, \varphi). \quad (1.81)$$

It is the number of fast electrons emitted from the Laser Plasma Interaction zone per unit of volume $d^3 \mathbf{r} = dx dy dz$, per unit of kinetic energy $d\varepsilon$ and per unit of steradian $d^2 \Omega = \sin \theta d\theta d\varphi$ at time t . It

can be used as an initial condition for electron transport studies.

1.4. BRIEF SUMMARY OF LASER SOLID INTERACTION AND LASER-GENERATED RELATIVISTIC ELECTRON BEAM PROPERTIES

Chapter 2

Electromagnetic Neutralization of a Laser-generated Relativistic Electron Beam

"The effects are always opposed to the causes that gave rise to them."

Heinrich Lenz

2.1. ELECTRIC FIELD GENERATED BY A MONOENERGETIC, COLLIMATED AND HOMOGENEOUS SEMI-INFINITE RELATIVISTIC ELECTRON BEAM PROPAGATING IN VACUUM

As described in the previous chapter, the interaction of (ultra) high-intensity short-pulse lasers with solid targets of density n_e generates large numbers of energetic electrons of density $n_b \ll n_e$. These fast electrons can only penetrate into the solid if the solid can supply an equivalent charge that electrically neutralize the fast electron beam. This electrical neutralization is done transversally to the beam propagation direction in the case of solid conductors and longitudinally in the case of solid insulators. While this electrostatically induced "return current" \mathbf{j}_e tends to compensate exactly the fast electron beam current \mathbf{j}_b for insulators, the magnetic neutralization of the fast electron beam occurs longitudinally for conductors. In the latter case, this is the magnetic neutralization of the beam that induces the generation of the return current \mathbf{j}_e which tends to exactly compensate the fast electron beam \mathbf{j}_b in agreement with the Lenz law. It allows the beam to propagate through the solid, overpassing the Alfvén-Lawson limit. This chapter is dedicated to describing these electromagnetic neutralization processes. Assuming a monoenergetic, collimated and homogeneous semi-infinite electron beam for simplicity, the self-consistent electromagnetic fields are derived in order to highlight the need of these electromagnetic neutralization processes allowing the beam to propagate. Assuming the beam to be rigid, its electric neutralization is derived in both cases highlighting the difference between the insulator and conductor cases. Then, the magnetic neutralization of the fast electron beams is derived in the case of laser-irradiated solid conductors.

2.1 Electric Field Generated by a Monoenergetic, Collimated and Homogeneous Semi-infinite Relativistic Electron Beam Propagating in Vacuum

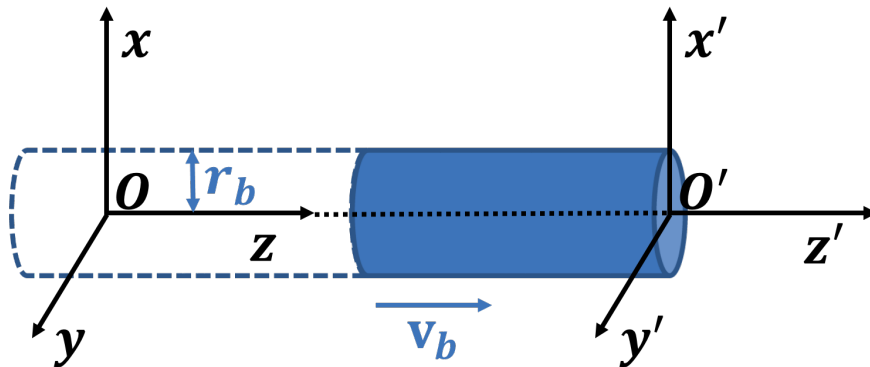


Figure 2.1: Schematic of a semi-infinite $]-\infty, O']$, axisymmetric, uniform, monoenergetic and collimated electron beam of radius r_b moving at the velocity $\mathbf{v}_b = v_b \mathbf{e}_z$ compared to the laboratory frame (O, x, y, z, t) and its associated beam rest frame (O', x', y', z', t') such that $O' \equiv O$ at $t = 0$.

Let us firstly consider the case of a semi-infinite $]-\infty, O']$, axisymmetric, uniform, monoenergetic

CHAPTER 2. ELECTROMAGNETIC NEUTRALIZATION OF A LASER-GENERATED RELATIVISTIC ELECTRON BEAM

and collimated relativistic electron beam propagating in vacuum along the z -axis with the velocity $\mathbf{v}_b = v_b \mathbf{e}_z$ compared to the laboratory frame (O, x, y, z, t) . One notes (O', x', y', z', t') the beam rest frame such that $O' \equiv O$ at $t = 0$ (see **Figure 2.1**). One notes r_b the beam radius and all values in the beam rest frame are denoted by a prime symbol '. There are no external electromagnetic fields and one works with the spatial cylindrical coordinates (r, θ, z) and the momentum cylindrical coordinates (p_r, p_θ, p_z) due to the geometry of the problem. According to the Einstein-Lorentz transformations, one has the relations for each event (\mathbf{r}, t) and for each beam electron of momentum \mathbf{p} and velocity \mathbf{v} .

$$\begin{cases} t' = \gamma_b \left(t - \frac{v_b z}{c^2} \right) \\ r' = r \\ \theta' = \theta \\ z' = \gamma_b (z - v_b t) \end{cases} \quad \text{and} \quad \begin{cases} \gamma' = \gamma_b \gamma \left(1 - \frac{v v_b}{c^2} \right) \\ p'_r = p_r \\ p'_\theta = p_\theta \\ p'_z = \gamma_b \gamma m_e (v_z - v_b) \end{cases}$$

where $\gamma_b = 1/\sqrt{1 - (v_b/c)^2}$ is the beam Lorentz factor, c is the velocity of light and m_e is the electron mass. In order to estimate the equilibrium (if it exists!) between the beam and the electric field it generates in the beam rest frame, one has to solve the Vlasov equation

$$\frac{\partial f'_b}{\partial t'} + \frac{\partial}{\partial \mathbf{r}'} \cdot (\mathbf{v}' f'_b) - \frac{\partial}{\partial \mathbf{p}'} \cdot \left[e \left(\mathbf{E}' + \frac{\mathbf{v}'}{c} \times \mathbf{B}' \right) f'_b \right] = 0 \quad (2.1)$$

coupled with the Maxwell equations

$$\frac{\partial^2 \Phi'}{\partial \mathbf{r}'^2} = 4\pi e n'_b \quad (2.2)$$

and

$$\frac{\partial^2 \mathbf{A}'}{\partial \mathbf{r}'^2} - \frac{1}{c^2} \frac{\partial^2 \mathbf{A}'}{\partial t'^2} = -\frac{4\pi}{c^2} \mathbf{j}'_b + \frac{1}{c^2} \frac{\partial}{\partial t'} \left(\frac{\partial \Phi'}{\partial \mathbf{r}'} \right) \quad (2.3)$$

where $f'_b(\mathbf{r}', \mathbf{p}', t') = f_b(\mathbf{r}', \mathbf{p}', t')$ is the electron beam distribution function in the beam rest frame (see **Appendix A, section A.1.1**). Also, it has been noted Φ' and \mathbf{A}' the electrostatic and vector potential ($\mathbf{B}' = c(\partial/\partial \mathbf{r}') \times \mathbf{A}'$ and $\mathbf{E}' = -(\partial\Phi'/\partial \mathbf{r}') - (\partial\mathbf{A}'/\partial t')$) with the Coulomb gauge ($(\partial/\partial \mathbf{r}') \cdot \mathbf{A}' = \mathbf{0}$), $n'_b = n_b/\gamma_b$ the beam charge density and $\mathbf{j}'_b = \mathbf{0}$ the beam current density. According to the least action principle, the constants of motion for an electron in the beam volume are the Hamiltonian H' , the canonical axial momentum P'_z and the angular momentum p'_θ which are given by

$$\begin{cases} H' = \gamma' m_e c^2 - e\Phi' \\ P'_z = p'_z - eA'_z \\ p'_\theta = \gamma' m_e (x'v'_y - y'v'_x). \end{cases} \quad (2.4)$$

Any function of these constants of motion is a solution of the Vlasov equation (2.1). Under our assumptions of a semi-infinite, homogeneous, axisymmetric, monoenergetic and collimated electron

2.1. ELECTRIC FIELD GENERATED BY A MONOENERGETIC, COLLIMATED AND HOMOGENEOUS SEMI-INFINITE RELATIVISTIC ELECTRON BEAM PROPAGATING IN VACUUM

beam, the distribution function reads consequently

$$f'_b(\mathbf{r}', \mathbf{p}', t') = n'_{b0} \Pi(r'_b - r') \Pi(-z') \frac{1}{2\pi m_e} \delta(H' - m_e c^2) \delta(p'_z - eA'_z) \quad (2.5)$$

where it has been noted Π the Heaviside distribution and δ the Dirac distribution. Starting from this distribution function, one can obtain the beam density in the beam rest frame by integrating it over the whole momentum space. It reads

$$\begin{aligned} n'_b(r', z', t') &= \int_{-\infty}^{\infty} p'_r dp'_r \int_{-\infty}^{\infty} dp'_z \int_0^{2\pi} d\theta f'_b(\mathbf{r}', \mathbf{p}', t') \\ &= n'_{b0} \Pi(r'_b - r') \Pi(-z') \frac{1}{m_e} \int_{-\infty}^{\infty} p'_r dp'_r \int_{-\infty}^{\infty} dp'_z \delta(H' - m_e c^2) \delta(p'_z - eA'_z) \\ &= n'_{b0} \Pi(r'_b - r') \Pi(-z') \frac{1}{m_e} \int_{-\infty}^{\infty} p'_r dp'_r \delta \left[m_e c^2 \left(\sqrt{1 + \left(\frac{p'_r}{m_e c} \right)^2 + \left(\frac{eA'_z}{m_e c} \right)^2} - 1 \right) - e\Phi' \right] \\ &= n'_{b0} \Pi(r'_b - r') \Pi(-z') m_e c^2 \int_1^{\infty} \gamma' d\gamma' \delta[(\gamma' - 1) m_e c^2 - e\Phi'] \\ &= n'_{b0} \Pi(r'_b - r') \Pi(-z') \left(1 + \frac{e\Phi'}{m_e c^2} \right) \end{aligned} \quad (2.6)$$

Injecting this expression in (2.2) using $\mathbf{E}' = -(\partial\Phi'/\partial\mathbf{r}')$ due to the fact $\mathbf{A}' = \mathbf{0}$ (because $\mathbf{j}'_b = \mathbf{0}$ and Φ' does not depend on the time t' in the beam rest frame), one gets the following equation for the electrostatic potential

$$\frac{\partial^2 \Phi'}{\partial r'^2} + \frac{1}{r'} \frac{\partial \Phi'}{\partial r'} + \frac{\partial^2 \Phi'}{\partial z'^2} - \frac{1}{\lambda'_b{}^2} \Pi(r'_b - r') \Pi(-z') \Phi' = 4\pi e n'_{b0} \Pi(r'_b - r') \Pi(-z') \quad (2.7)$$

where $\lambda'_b = c/\omega'_b = \sqrt{\gamma_b} \lambda_b$ is the beam skin depth in the beam rest frame and $\omega'_b = \sqrt{4\pi n'_{b0} e^2 / m_e} = \omega_b / \sqrt{\gamma_b}$ its natural plasma frequency. Even if one can find solutions of Equation (2.7) in each separated subspace ($z' > 0$), ($r' > r_b, z' \leq 0$) and ($r' \leq r_b, z' \leq 0$), it is impossible to find an analytical solution valid in the whole space by connecting continuously these electrostatic potentials and their spatial derivatives (the self-electric field) found in these three subspaces. Besides, one can estimate the longitudinal electric field by neglecting the radial spatial variation of the potential compared to the longitudinal one close to the z' -axis and the vacuum-beam interface at $z' = 0$. Equation (2.7) provides in this case

$$\Phi'(r' \rightarrow 0, z' \leq 0, t') = -\frac{m_e c^2}{e} \left[1 - \exp\left(\frac{z'}{\lambda'_b}\right) \right] \quad (2.8)$$

One deduces that the longitudinal self-electric field $E'_z = -(\partial\Phi'/\partial z')$ vanishes inside the beam front over approximately the beam skin depth λ'_b . According to the Lorentz transformation,

$$\begin{aligned} \mathbf{E}(r \rightarrow 0, z \leq v_b t, t) &= \mathbf{E}(r \rightarrow 0, z, t \geq z/v_b) \\ &= \mathbf{E}'(r' \rightarrow 0, z' > 0, t') \\ &= E_0 \exp\left[\frac{\gamma_b(z - v_b t)}{\lambda'_b}\right] \mathbf{e}_z \end{aligned} \quad (2.9)$$

CHAPTER 2. ELECTROMAGNETIC NEUTRALIZATION OF A LASER-GENERATED RELATIVISTIC ELECTRON BEAM

where $E_0 = -4\pi en'_{b0}\lambda'_b$. It means physically that each beam slice of thickness $\approx \lambda'_b$ generates a longitudinal electric field which is screened by the electromagnetic counter-reaction of its closest neighboring slices of same thickness so that the slices are screened one by one by each other except for the last slices close to the beam-front-vacuum interface at $z' = 0$. Thus, one can roughly estimate the longitudinal self-electric field generated at the beam front on the z' -axis by approximating the beam as a disk of density of effective charge per surface unit $\sigma'_b = -2n'_{b0}e\lambda'_b$ located at $z' = 0$. According to the Gauss theorem, one gets in this case

$$\mathbf{E}'(r' \rightarrow 0, z' > 0, t') \approx 2\pi\sigma'_b \left(1 - \frac{z'}{\sqrt{r_b'^2 + z'^2}} \right) \mathbf{e}_z \quad (2.10)$$

and consequently

$$\begin{aligned} \mathbf{E}(r \rightarrow 0, z > v_b t, t) &= \mathbf{E}(r \rightarrow 0, z, t < z/v_b) \\ &\approx E_0 \left(1 - \frac{\gamma_b(z - v_b t)}{\sqrt{r_b^2 + \gamma_b^2(z - v_b t)^2}} \right) \mathbf{e}_z. \end{aligned} \quad (2.11)$$

The factor 2 in the expression of the density of charge per surface unit σ'_b has been chosen in order to respect the continuity of the electric field at $z' = 0$ ($z = v_b t$). Also, far away from the beam front in the limit $z' \rightarrow -\infty$, one can neglect the longitudinal spatial variations of the electrostatic potential compared to the radial ones. The resulting equation has already been obtained and solved by [Hammer and Rostoker, 1970] while considering an infinite electron beam. This solution which respects the continuity conditions at $r = r_b$ and the boundary condition $\Phi'(r' = 0, z' \rightarrow -\infty, t') = 0$ is

$$\Phi'(r', z' \rightarrow -\infty, t') = \begin{cases} -\frac{m_e c^2}{e} \left[1 - I_0 \left(\frac{r'}{\lambda'_b} \right) \right] & \text{if } r' \leq r'_b \\ -\frac{m_e c^2}{e} \left[1 - I_0 \left(\frac{r'_b}{\lambda'_b} \right) \right] + \frac{m_e c^2}{e} \frac{r'_b}{\lambda'_b} I_1 \left(\frac{r'_b}{\lambda'_b} \right) \ln \left(\frac{r'}{r'_b} \right) & \text{if } r' > r'_b \end{cases} \quad (2.12)$$

where it has been noted I_ν the modified Bessel functions of the first kind. By applying the Lorentz transformation, one gets [Hammer and Rostoker, 1970]

$$\begin{aligned} \Phi(r, z \rightarrow -\infty, t) &= \Phi(r, z, t \rightarrow \infty) \\ &= \gamma_b [\Phi'(r', z' \rightarrow -\infty, t') - v_b A'_z(r', z' \rightarrow -\infty, t')] \\ &= \begin{cases} -\frac{\gamma_b m_e c^2}{e} \left[1 - I_0 \left(\frac{r}{\lambda'_b} \right) \right] & \text{if } r \leq r_b \\ -\frac{\gamma_b m_e c^2}{e} \left[1 - I_0 \left(\frac{r_b}{\lambda'_b} \right) \right] + \frac{\gamma_b m_e c^2}{e} \frac{r_b}{\lambda'_b} I_1 \left(\frac{r_b}{\lambda'_b} \right) \ln \left(\frac{r}{r_b} \right) & \text{if } r > r_b \end{cases} \end{aligned} \quad (2.13)$$

2.1. ELECTRIC FIELD GENERATED BY A MONOENERGETIC, COLLIMATED AND HOMOGENEOUS SEMI-INFINITE RELATIVISTIC ELECTRON BEAM PROPAGATING IN VACUUM

and consequently

$$\mathbf{E}(r, z \rightarrow -\infty, t) = \mathbf{E}(r, z, t \rightarrow \infty) = \begin{cases} \gamma_b E_0 I_1 \left(\frac{r}{\lambda'_b} \right) \mathbf{e}_r & \text{if } r \leq r_b \\ \gamma_b E_0 \frac{r_b}{r} I_1 \left(\frac{r_b}{\lambda'_b} \right) \mathbf{e}_r & \text{if } r > r_b \end{cases}. \quad (2.14)$$

In the case where $r_b \ll \lambda_b$, which implies $r_b \ll \lambda'_b$, one recovers the well known electric field generated by a homogeneous, infinite and cylindrical **rigid** electron beam which can be obtained according to the Gauss law :

$$\mathbf{E}_\infty = \begin{cases} -4\pi e n_{b0} \frac{r}{2} \mathbf{e}_r & \text{if } r \leq r_b \\ -4\pi e n_{b0} \frac{r_b^2}{2r} \mathbf{e}_r & \text{if } r > r_b \end{cases} \quad (2.15)$$

($I_1(x) \sim x/2$ when $x \rightarrow 0$). The term "rigid" means that it is assumed that the beam electrons are not affected by the electromagnetic fields they generate as well as by external electromagnetic fields.



Figure 2.2: Artist's view taken from [Macchi et al., 2013] showing a laser-generated electron beam trying to get out a solid target and the resulting electron cloud and accelerated ions.

We are more interested here in the opposite case where $r_b \gg \lambda_b$ since in relativistic laser-solid interaction experiments, the laser-generated electron beam has a radius $r_b \approx 10 \mu\text{m}$ while n_{b0} is necessarily less than the critical electron density $n_c \approx 10^{21} \text{ cm}^{-3}$ for a laser pulse of a $1 \mu\text{m}$ wavelength (cf. **Chapter 1**). Thus, λ_b is typically less than $\lambda_c \approx 0.2 \mu\text{m}$. Moreover, in such experiments, the Lorentz factor γ_b is typically less than 10 so that one can consider $r_b \gg \lambda'_b$. In this case, the solution (2.13) is not physical because the linear density of electric energy generated by the beam is greater than the linear density of the beam energy itself ($I_1(x) \sim \exp(x)/\sqrt{2\pi x}$ when $x \rightarrow \infty$). This is, of

course, physically impossible so that an electron beam cannot propagate in vacuum without being electrically neutralized by a background media or by an accompanying positively charged beam. In the case where there is no electric neutralization, the transport is necessarily inhibited. This is exactly what happens when a laser-generated electron beam tries to get out in vacuum from the solid target rear side (see **Figure 2.2**). When the beam electrons are escaping in vacuum, they create a spatial charge separation which prevents the electrons with energies smaller than the target potential from escaping the target. While the major part of beam electrons **reflux** inside the target, those with energies higher than the surface potential can escape, thus creating a net positive charge at the surface which is responsible for the generation of strong **Electromagnetic pulses** [Dubois et al., 2014]. Also, this strong electrostatic potential is responsible for the acceleration of light ions originated from impurities, i.e., thin layers of water or hydrocarbons which are ordinarily present on solid surfaces under standard experimental conditions. Such a positively charged ion beam accompanied by electrons is commonly detected in laser-solid interaction experiments. A large number of theoretical and experimental studies of accelerated ions have been published recently because of their interesting properties such as ultrashort duration, high brilliance and low emittance comparable with ion beams generated by a classical accelerator [Macchi et al., 2013].

2.2 Electric Neutralization of a Monoenergetic, Collimated and Homogeneous Rigid Relativistic Electron Beam Propagating in Solids or Dense Plasmas

2.2.1 Electric Neutralization of a Monoenergetic, Collimated and Homogeneous Rigid Relativistic Electron Beam Propagating in a Conductor

Let us consider the propagation in a conducting media of the semi-infinite electron beam studied in the previous subsection. Such a conducting media can be a plasma or a metal. Due to their huge inertia compared to the electrons and the time scale considered here, the ions (lattice) can be considered as immobile. For simplicity, one assumes that the plasma (metal) is infinite, homogeneous and one notes n_i the fixed ion density (or the density of atoms for metals), n_e the density, \mathbf{j}_e the current density and f_e the distribution function of the conducting electrons of the media where the electron beam is propagating through. For metals, these electrons are those of the conduction band ; $n_{e0} = Z_c n_{i0}$ with for example $Z_c = 3$ for Aluminum, $Z_c = 1$ for Copper, ... For plasmas, they are the ionized electrons: $n_{e0} = Z^* n_{i0}$ at $t = 0$ where Z^* is the plasma ionization state which depends on the plasma density and the plasma electron temperature T_e . As mentioned in the previous subsection, the electrical

2.2. ELECTRIC NEUTRALIZATION OF A MONOENERGETIC, COLLIMATED AND HOMOGENEOUS RIGID RELATIVISTIC ELECTRON BEAM PROPAGATING IN SOLIDS OR DENSE PLASMAS

equilibrium of the beam electrons with the self-generated electric field is physically impossible. One assumes so for simplicity that the electron beam is **rigid** in order to determine the electric response to the beam propagation in the conducting media. Also, one neglects the collisions of the beam electrons with the atoms, electrons or ions of the media which will be discussed in detail later on. Thus, instead of solving Equation (2.1) for the beam electrons, one has to determine the conducting electrons dynamics. This can be done by solving the Vlasov-Fokker-Planck equation in the BGK approximation for the conducting electrons (cf. **Appendix A, section A.3.1**)

$$\frac{\partial f'_e}{\partial t'} + \frac{\partial}{\partial \mathbf{r}'} \cdot (\mathbf{v}' f'_e) - \frac{\partial}{\partial \mathbf{p}'} \cdot \left[e \left(\mathbf{E}' + \frac{\mathbf{v}'}{c} \times \mathbf{B}' \right) f'_e \right] = -\nu' \left(f'_e - f'_M - \frac{\delta n'_e}{n'_{e0}} f'_M \right) \quad (2.16)$$

coupled to the Maxwell equations

$$\frac{\partial}{\partial \mathbf{r}'} \cdot \mathbf{E}' = -4\pi e (n'_b + n'_e - Z^* n'_i) \quad (2.17)$$

(for metals, Z^* must be replaced by Z_c),

$$\frac{\partial}{\partial \mathbf{r}'} \times \mathbf{E}' = -\frac{1}{c} \frac{\partial \mathbf{B}'}{\partial t'}, \quad (2.18)$$

and

$$\frac{\partial}{\partial \mathbf{r}'} \times \mathbf{B}' = \frac{4\pi}{c} (\mathbf{j}'_b + \mathbf{j}'_e + \mathbf{j}'_i) + \frac{1}{c} \frac{\partial \mathbf{E}'}{\partial t'} \quad (2.19)$$

where the term

$$\delta n'_e = \int_{\mathbb{R}^3} (f'_e - f'_M) d^3 \mathbf{p}'$$

is added to ensure the conservation of the number of conducting electrons. Assuming the latter are not relativistic in the laboratory frame, one has $\gamma' = \langle \gamma' \rangle_M = \gamma_b$. Consequently, $d^3 \mathbf{r}' d^3 \mathbf{p}' = (d^3 \mathbf{r} / \gamma_b)(d^3 \mathbf{p} / \gamma_b)$ and one has

$$f'_M(\mathbf{r}', \mathbf{p}', t') = \gamma_b^2 f_M(\mathbf{r}, \mathbf{p}, t) = \frac{\gamma_b^2 n_{e0}}{(2\pi m_e k_B T_e)^{3/2}} \exp \left[-\frac{p_x'^2 + p_y'^2}{2m_e k_B T_e} - \gamma_b^2 \frac{(p_z' + \gamma_b m_e v_b)^2}{2m_e k_B T_e} \right]$$

where $k_B T_e \ll m_e c^2$ is the conducting electron temperature in the laboratory frame. For simplicity, one assumes that ν' does not depend on the velocity of particles and that it is equal to the conducting electron-ion collision frequency in the beam rest frame ν'_{ei} . Also, in order to ensure the Lorentz-invariance of Equation (2.16), one has $\nu'_{ei} = \nu_{ei} / \gamma_b$ where ν_{ei} is the non-relativistic electron-ion collision frequency in the laboratory frame (see **Appendix A, section A.3.2**). By integrating (2.16) and (2.16) multiplied by \mathbf{p}' over the whole momentum space, one gets

$$\frac{\partial n'_e}{\partial t'} + \frac{\partial}{\partial \mathbf{r}'} \cdot (n'_e \mathbf{v}'_e) = 0 \quad (2.20)$$

and

$$\left[\frac{\partial}{\partial t'} + \left(\mathbf{v}'_e \cdot \frac{\partial}{\partial \mathbf{r}'} \right) \right] (\mathbf{p}'_e) = -e \left(\mathbf{E}' + \frac{\mathbf{v}'_e}{c} \times \mathbf{B}' \right) - \nu' (\mathbf{p}'_e - \mathbf{p}'_{e0}). \quad (2.21)$$

Here, the pressure tensor term has been neglected in (2.21) assuming the thermal velocity of the plasma electrons can be neglected in comparison with the beam velocity i.e. $\sqrt{k_B T_e / m_e} / \gamma_b \leq \sqrt{k_B T_e / m_e} \ll v_b$. Concerning laser-generated relativistic electron beams, the beam density n_b is necessarily less than the critical density $n_c \leq n_{e0}$ and one has $\gamma_b \approx 1 - 10$. Thus, one can linearize the non-linear set of equations $\{(2.17), (2.19), (2.18), (2.20), (2.21)\}$ with respect to the small parameter $n'_b / n'_e = n_b / \gamma_b^2 n_e$. One notes

$$\forall \xi \in \{n'_e, \mathbf{v}'_e, \mathbf{j}'_e, \mathbf{E}', \mathbf{B}'\}, \xi = \xi_0 + \delta \xi$$

where the ξ_0 are the values at $t = 0$ without the perturbation induced by the presence of the beam.

One has consequently $f'_{e0} = f'_M$,

$$n'_{e0} = \int_{\mathbb{R}^3} f'_M d^3 \mathbf{p}' = \gamma_b n_{e0}$$

in agreement with the Lorentz transformation of the charge/current density quadrivector,

$$\mathbf{p}'_{e0} = \frac{1}{n'_{e0}} \int_{\mathbb{R}^3} \mathbf{p}' f'_M d^3 \mathbf{p}' = -\gamma_b m_e \mathbf{v}_b \text{ which implies } \mathbf{v}'_{e0} = -\mathbf{v}_b \text{ and } \mathbf{j}'_{e0} = \gamma_b n_{e0} e \mathbf{v}_b.$$

The unperturbed plasma is initially quasineutral so that $Z^* n'_{i0} = n'_{e0}$, $\mathbf{j}'_{i0} = -\mathbf{j}'_{e0}$ and consequently $\mathbf{E}'_0 = \mathbf{B}'_0 = \mathbf{0}$. Assuming that the perturbed conducting electrons have a momentum $\delta p'_e \ll m_e c$, the linearized fluid equations are therefore

$$\delta \mathbf{v}'_e = \frac{\delta p'_{e,x} \mathbf{e}_x + \delta p'_{e,y} \mathbf{e}_y + \delta p'_{e,z} \mathbf{e}_z}{\gamma_b m_e}, \quad (2.22)$$

$$\frac{\partial \delta n'_e}{\partial t'} - v_b \frac{\partial \delta n'_e}{\partial \mathbf{r}'} + n'_{e0} \frac{\partial}{\partial \mathbf{r}'} \cdot (\delta \mathbf{v}'_e) = 0, \quad (2.23)$$

$$\left[\frac{\partial}{\partial t'} - v_b \frac{\partial}{\partial z'} \right] (\delta \mathbf{p}'_e) = -e \left(\delta \mathbf{E}' + \frac{\mathbf{v}_b}{c} \times \delta \mathbf{B}' \right) - \nu'_{ei} \delta \mathbf{p}'_e, \quad (2.24)$$

$$\frac{\partial}{\partial \mathbf{r}'} \cdot \delta \mathbf{E}' = -4\pi e (n'_b + \delta n'_e), \quad (2.25)$$

$$\frac{\partial}{\partial \mathbf{r}'} \times \delta \mathbf{E}' = -\frac{1}{c} \frac{\partial \delta \mathbf{B}'}{\partial t'}, \quad (2.26)$$

and

$$\frac{\partial}{\partial \mathbf{r}'} \times \delta \mathbf{B}' = \frac{4\pi}{c} \delta \mathbf{j}'_e + \frac{1}{c} \frac{\partial \delta \mathbf{E}'}{\partial t'} \quad (2.27)$$

where $\delta \mathbf{j}'_e = -n'_{e0} e \delta \mathbf{v}'_e + \delta n'_e e \mathbf{v}_b$. In the 1960's, advances in the production of high-current beams of relativistic electrons using a long coaxial capacitor [Graybill and Nablo, 1966], [Roberts and Bennett, 1968] stimulated experimental [Andrews et al., 1970] and theoretical [Cox and Bennett, 1970] research. In this context, [Hammer and Rostoker, 1970] and [Lee and Sudan, 1971] have solved the set of equations $\{(2.22), (2.23), (2.24)(2.25), (2.27), (2.26)\}$

2.2. ELECTRIC NEUTRALIZATION OF A MONOENERGETIC, COLLIMATED AND HOMOGENEOUS RIGID RELATIVISTIC ELECTRON BEAM PROPAGATING IN SOLIDS OR DENSE PLASMAS

under some assumptions we are going to explain. The authors used the Laplace-Fourier method (Laplace for t' and Fourier for \mathbf{r}') in order to replace all spatial and temporal derivatives by simple multiplications. Besides, interested in the behaviour of such beam-plasma system after the initial transients, i.e., far away from the beam front in the laboratory frame ($z \rightarrow -\infty$), they looked for solutions in the limit $t' \rightarrow \infty$ using the final-value theorem of Laplace transform theory:

$$\lim_{t' \rightarrow \infty} \widehat{\delta\xi}(\mathbf{k}, t') = \lim_{s \rightarrow 0} s \widehat{\delta\xi}(\mathbf{k}, s)$$

where $\widehat{\delta\xi}$ is the Fourier transform of $\delta\xi$ and $\widehat{\delta\xi}$ its Laplace-Fourier transform. Thus, due to the fact that the Fourier transform of the beam density is

$$\widehat{n}_b = 2\pi r'_b \frac{J_1(k_\perp)}{k_\perp} \int_{-\infty}^0 dz'_0 \exp(-ik_z z'_0),$$

where J_ν is the Bessel function of the first kind, they found that all these quantities $\delta\xi$ in the limit $t' \rightarrow \infty$ can be written

$$\begin{aligned} \delta\xi(\mathbf{r}', t' \rightarrow \infty) &= \frac{1}{(2\pi)^3} \int_0^\infty k_\perp dk_\perp \int_{-\infty}^\infty dk_z \lim_{s \rightarrow 0} s \widehat{\delta\xi}(\mathbf{k}, s) \\ &= \frac{1}{2\pi} \int_0^\infty k_\perp dk_\perp \int_{-\infty}^0 dz'_0 \int_{-\infty}^\infty dk_z \frac{P_\xi(k_\perp, k_z) J_1(k_\perp r'_b) J_{\nu_\xi}(k_\perp r')}{D_0(k_\perp, k_z)} \exp[ik_z (z' - z'_0)] \end{aligned} \quad (2.28)$$

where $P_\xi(k_\perp, k_z)$ are polynomials and $\nu_\xi = 1$ or 0 depending on ξ while

$$D_0(k_\perp, k_z) = \left[(k_z^2 + k_\perp^2) \left(k_z + i \frac{\nu'_{ei}}{v_b} \right) + \frac{k_z}{\lambda_e'^2} \right] \left[k_z \left(k_z + i \frac{\nu'_{ei}}{v_b} \right) - \left(\frac{c}{\gamma_b v_b \lambda_e'} \right)^2 \right]. \quad (2.29)$$

Here, $\lambda_e' = c/\omega_p' = \lambda_e/\sqrt{\gamma_b}$ is the plasma skin depth in the beam rest frame and $\omega_p' = \sqrt{\gamma_b} \omega_p$ is the Langmuir plasma frequency. In order to perform such k_z -integrations in the integrals (2.28) using the residue theorem, one has to determine the zeros k_ν for which $D_0(k_\perp, k_\nu) = 0$.

The second bracket term of (2.29) is easy to factorize and one finds the poles

$$k_1 = -i \frac{\nu'_{ei}}{2v_b} + \sqrt{\left(\frac{c}{\gamma_b v_b \lambda_e'} \right)^2 - \left(\frac{\nu'_{ei}}{2v_b} \right)^2} = -i \frac{\nu'_{ei}}{2v_b} + \frac{c}{\gamma_b v_b \lambda_e'} + o\left(\frac{\nu_{ei}}{\omega_p} \right) \quad (2.30)$$

and

$$k_2 = -i \frac{\nu'_{ei}}{2v_b} - \sqrt{\left(\frac{c}{\gamma_b v_b \lambda_e'} \right)^2 - \left(\frac{\nu'_{ei}}{2v_b} \right)^2} = -i \frac{\nu'_{ei}}{2v_b} - \frac{c}{\gamma_b v_b \lambda_e'} + o\left(\frac{\nu_{ei}}{\omega_p} \right). \quad (2.31)$$

The first one is more complicated and needs some approximations. [Hammer and Rostoker, 1970] have

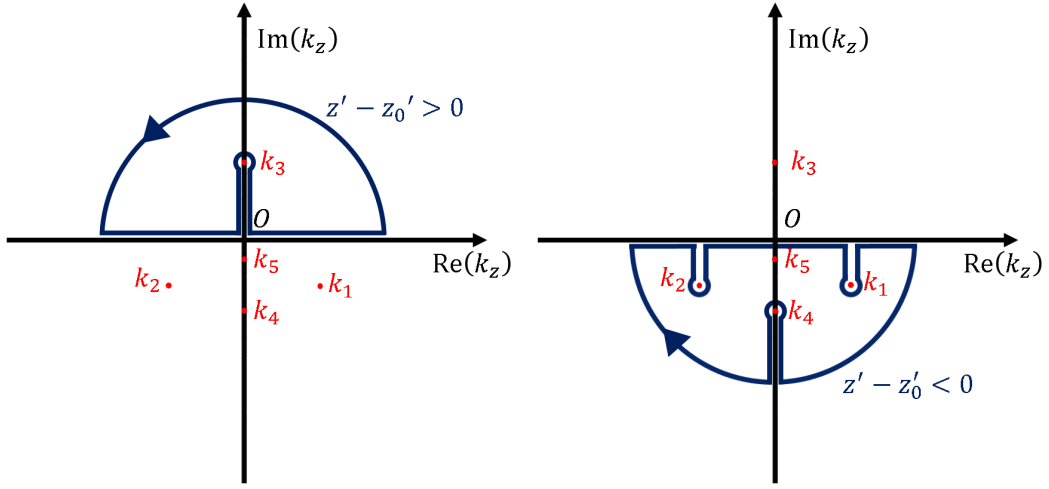


Figure 2.3: Integration contour used for the k_z -integration of (2.28) when $z' - z'_0 > 0$ (left) and when $z' - z'_0 < 0$ (right)

approximated

$$(k_z^2 + k_\perp^2) \left(k_z + i \frac{\nu'_{ei}}{v_b} \right) + \frac{k_z}{\lambda_e'^2} = k_z \left[(k_z^2 + k_\perp^2) + \frac{1}{\lambda_e'^2} \right] + o \left(\frac{\nu'_{ei}}{\omega'_p} \right)$$

by considering the weakly-collisional plasma case $\omega'_p/\nu'_{ei} \gg 1$. Thus, they found the poles

$$k_3 \approx i \frac{1}{\lambda_e'} \sqrt{1 + (\lambda_e' k_\perp)^2} \quad (2.32)$$

and

$$k_4 \approx -i \frac{1}{\lambda_e'} \sqrt{1 + (\lambda_e' k_\perp)^2}. \quad (2.33)$$

Actually, this is in the laboratory frame where the collisionless plasma condition must be verified so that it is the condition $\omega_p/\nu_{ei} \gg 1$ which must be considered and not $\omega'_p/\nu'_{ei} \gg 1$. Besides, in the original paper of [Hammer and Rostoker, 1970], the authors consider that $\omega_p = \omega'_p$ and not $\omega_p = \omega'_p/\sqrt{\gamma_b}$. However, this does not change the poles obtained by [Hammer and Rostoker, 1970] because $\omega_p/\nu_{ei} \gg 1$ still implies $\lambda_e' \nu'_{ei}/v_b \ll 1$. k_5 is then found by identification :

$$(k_z^2 + k_\perp^2) \left(k_z + i \frac{\nu'_{ei}}{v_b} \right) + \frac{k_z}{\lambda_e'^2} = (k_z - k_3)(k_z - k_4)(k_z - k_5)$$

which gives

$$k_5 \approx \begin{cases} -i \frac{\nu'_{ei}}{v_b} (\lambda_e' k_\perp)^2 & \text{if } \lambda_e' k_\perp \ll 1 \\ -i \frac{\nu'_{ei}}{v_b} & \text{if } \lambda_e' k_\perp \gg 1 \end{cases}$$

2.2. ELECTRIC NEUTRALIZATION OF A MONOENERGETIC, COLLIMATED AND HOMOGENEOUS RIGID RELATIVISTIC ELECTRON BEAM PROPAGATING IN SOLIDS OR DENSE PLASMAS

Thus, [Lee and Sudan, 1971] approximate

$$k_5 \approx -i \frac{\nu'_{ei}}{v_b} \frac{(\lambda'_e k_\perp)^2}{1 + (\lambda'_e k_\perp)^2} \quad (2.34)$$

which reproduces well both limits. One can notice that this expression (2.34) can also be obtained by assuming $k_z \ll k_\perp$ in the first bracket of (2.29). In the opposite case where $k_z \gg k_\perp$, one can also find the poles $\pm 2i/\lambda'_e$ but they correspond to vanishing solutions close to $z = v_b t$ over the plasma skin depth $\lambda_e/\gamma_b^{3/2}$ while we are interested here in the plasma response far away from the beam front, i.e., for $|z - v_b t| \gg \lambda_e/\gamma_b^{3/2}$. Like in the case studied by [Hammer and Rostoker, 1970], one can neglect the pole k_5 . Indeed, concerning laser-generated electron beams, the typical length scale we are interested in is in ranges from the collisional relaxation length $l_b = v_b/\nu_{ei} = l'_b/\gamma_b$ to the beam length $L_b \approx v_b \tau_L = L'_b/\gamma_b$ where τ_L is the laser pulse duration. In current experiments, τ_L is typically less than 1 – 10 ps and is consequently very small compared to the characteristic magnetic diffusion time

$$\tau_d = \frac{r_b^2}{\lambda_e^2 \nu_{ei}} = \frac{\tau'_d}{\gamma_b^3} \quad (2.35)$$

found by [Lee and Sudan, 1971]. Thus, for $z' - z'_0 > 0$, the k_z -integration can be performed according to the residue theorem along the contour defined by the real axis including the pole $k_z = k_3$ completed by a half-circle in the upper half k_z plane such as represented in the left panel of **Figure 2.3**. For $z' - z'_0 < 0$, it can be performed along the contour defined by the real axis including the pole $k_z = k_1, k_2$ and k_4 completed by a half-circle in the lower half k_z plane such as represented in the right panel of **Figure 2.3**. Finally, the z'_0 and k_\perp -integrations can be performed exactly in the limit $|z'| \gg \lambda'_e$ and gives [Hammer and Rostoker, 1970]

$$\left\{ \begin{array}{l} \delta E'_r(r', z' < 0, t' \rightarrow \infty) = 4\pi n'_b e r'_b \gamma_b^2 F_1(r') \left[\frac{v_b^2}{c^2} - g_c(z') \right] \\ \delta E'_\theta(r', z' < 0, t' \rightarrow \infty) = 0 \\ \delta E'_z(r', z' < 0, t' \rightarrow \infty) = -4\pi n'_b e r'_b \gamma_b \left[\frac{v_b}{\omega'_p r'_b} G_2(z') - g_s(z') F_2(r') \right] \\ \delta B'_r(r', z' < 0, t' \rightarrow \infty) = 0 \\ \delta B'_\theta(r', z' < 0, t' \rightarrow \infty) = -4\pi n'_b e r'_b \gamma_b^2 \frac{v_b}{c} F_1(r') [1 - g_c(z')] \\ \delta B'_z(r', z' < 0, t' \rightarrow \infty) = 0 \\ \delta n'_e(r', z' < 0, t' \rightarrow \infty) = -n'_b \left\{ G_1(z') + (\gamma_b^2 - 1) \frac{\omega'_p r'_b}{c} F_2(r') \left[1 - \frac{c}{v_b} g_c(z') \right] \right\} \\ \delta v'_{er}(r', z' < 0, t' \rightarrow \infty) = -\frac{n'_b}{n'_{e0}} \gamma_b \omega'_p r'_b g_s(z') F_1(r') \\ \delta v'_{ez}(r', z' < 0, t' \rightarrow \infty) = -\frac{n'_b}{n'_{e0}} v_b \left\{ G_1(z') - \frac{\omega'_p r'_b}{c} F_2(r') \left[1 - \frac{c}{v_b} g_c(z') \right] \right\} \end{array} \right. \quad (2.36)$$

where

$$\begin{aligned}
 g_c(z') &= \cos\left(\frac{\omega'_p z'}{\gamma_b v_b}\right) \exp\left(\frac{\nu'_{ei} z'}{2v_b}\right), \quad g_s(z') = \sin\left(\frac{\omega'_p z'}{\gamma_b v_b}\right) \exp\left(\frac{\nu'_{ei} z'}{2v_b}\right), \\
 G_1(z') &= \begin{cases} 1 - g_c(z') & \text{if } r' \leq r'_b \\ 0 & \text{if } r' > r'_b \end{cases}, \quad G_2(z') = \begin{cases} g_s(z') & \text{if } r' \leq r'_b \\ 0 & \text{if } r' > r'_b \end{cases}, \\
 F_1(r') &= \begin{cases} I_1\left(\frac{r'}{\lambda'_e}\right) K_1\left(\frac{r'_b}{\lambda'_e}\right) & \text{if } r' \leq r'_b \\ I_1\left(\frac{r'_b}{\lambda'_e}\right) K_1\left(\frac{r'}{\lambda'_e}\right) & \text{if } r' > r'_b \end{cases} \quad \text{and} \\
 F_2(r') &= \begin{cases} I_0\left(\frac{r'}{\lambda'_e}\right) K_1\left(\frac{r'_b}{\lambda'_e}\right) & \text{if } r' \leq r'_b \\ -I_1\left(\frac{r'_b}{\lambda'_e}\right) K_0\left(\frac{r'}{\lambda'_e}\right) & \text{if } r' > r'_b \end{cases}.
 \end{aligned}$$

Here, I_ν and K_ν are the modified Bessel functions respectively of the first and second kind (There is a mistake in [Hammer and Rostoker, 1970], Eq. (110) : it is " $+I_1(r'_b/\lambda'_e)K_1(r'/\lambda'_e)$ " and not " $-I_1(r'_b/\lambda'_e)K_1(r'/\lambda'_e)$ " in the lower line of the second bracket). The discontinuities at $r' = r'_b$ of the functions G_1 and G_2 are due to the discontinuous beam current profile and the cold plasma assumption. According to the Lorentz transformations, one can now deduce the electric response to the beam propagation of the conducting electrons far away from the beam front ($|z - v_b t| \gg \lambda_e/\gamma_b^{3/2}$) in the laboratory frame

$$\begin{cases} \delta n_e(r, z < v_b t, t \ll \tau_d) &= -n_b \begin{cases} 1 - \cos\left(\omega_p \sqrt{\gamma_b} \frac{z - v_b t}{v_b}\right) \exp\left[\frac{\nu_{ei}(z - v_b t)}{2v_b}\right] & \text{if } r' \leq r'_b \\ 0 & \text{if } r' > r'_b \end{cases} \\ \delta v_{er}(r, z < v_b t, t \ll \tau_d) &= -c \frac{n_b}{n_{e0}} \frac{r_b}{\lambda'_e} \sin\left(\omega_p \sqrt{\gamma_b} \frac{z - v_b t}{v_b}\right) \exp\left[\frac{\nu_{ei}(z - v_b t)}{2v_b}\right] F_1(r) \\ \delta E_r(r, z < v_b t, t \ll \tau_d) &= -4\pi n_b e r_b \cos\left(\omega_p \sqrt{\gamma_b} \frac{z - v_b t}{v_b}\right) \exp\left[\frac{\nu_{ei}(z - v_b t)}{2v_b}\right] F_1(r) \end{cases}. \quad (2.37)$$

Thus, the electric field generated by a relativistic electron beam far away from the beam front (2.15) expels radially a small fraction ($n_b/n_{e0} \ll 1$) of the conducting electrons out of the beam volume. This electron current generates a radial electric field which counteracts the electric field generated by the beam so that the full radial electric field $E_r = \delta E_r$ vanishes. This electric neutralization of the beam occurs within a time scale of few ν_{ei}^{-1} with oscillations at the plasma frequency $\omega'_p = \omega_p \sqrt{\gamma_b}$ evaluated in the beam rest frame. This frequency can become significant for very large values of γ_b . In the opposite case of a collisional plasma where $\nu_{ei} \gg \omega_{pe}$, k_1 becomes purely imaginary :

$$k_1 = -i \frac{1}{\gamma_b^2 \tau'_e v_b} + o\left[\left(\frac{\omega_p}{\nu_{ei}}\right)^3\right] \quad (2.38)$$

where $\tau'_e = \nu'_{ei}/\omega'_p{}^2 = \tau_e/\gamma_b^2$ is the Coulomb explosion time evaluated in the beam rest frame and k_2 coincides now with k_5 (in the limit $k_\perp \lambda'_e \gg 1$) while k_3 , k_4 and k_5 are unchanged. By repeating the

2.2. ELECTRIC NEUTRALIZATION OF A MONOENERGETIC, COLLIMATED AND HOMOGENEOUS RIGID RELATIVISTIC ELECTRON BEAM PROPAGATING IN SOLIDS OR DENSE PLASMAS

procedure described above, one obtains in this case for $|z - v_b t| \gg \lambda_e / \gamma_b^{3/2}$:

$$\left\{ \begin{array}{l} \delta n_e(r, z < v_b t, t \ll \tau_d) = - n_b \begin{cases} 1 - \exp\left(\gamma_b \frac{z - v_b t}{\tau_e}\right) & \text{if } r' \leq r'_b \\ 0 & \text{if } r' > r'_b \end{cases} \\ \delta v_{er}(r, z < v_b t, t \ll \tau_d) = \frac{c}{n_{e0}} \frac{n_b}{\lambda'_e} \frac{r_b}{\nu_{ei} \sqrt{\gamma_b}} \exp\left(\gamma_b \frac{z - v_b t}{\tau_e}\right) F_1(r) \\ \delta E_r(r, z < v_b t, t \ll \tau_d) = - 4\pi n_b e r_b \exp\left(\gamma_b \frac{z - v_b t}{\tau_e}\right) F_1(r) \end{array} \right. \quad (2.39)$$

Thus, the electron beam is electrically neutralized in a time scale of τ_e / γ_b . In agreement with [Cox and Bennett, 1970], the oscillations at the plasma frequency ω'_p have disappeared and the magnitude of the radial velocity is lower because of a greater influence of the electron-ion collisions.

2.2.2 Electric Neutralization of a Monoenergetic, Collimated and Homogeneous Rigid Relativistic Electron Beam Propagating in a Dielectric

The propagation of a semi-infinite electron beam in a non-conducting media is more complicated. The experiments show that the laser-generated electron beam can propagate deeply in the target while there is no free electrons in dielectrics ($Z^* = 0$) to electrically neutralize the beam. This paradox is solved by noticing that the atoms in a dielectric can be ionized in collisions with the beam electrons (or with the newborn electrons released by ionization), by the self-consistent electric field at the beam front (2.11) or by the electrostatic field induced by the space-charge separation. Let us consider that the electron beam is generated in the laser-solid interaction zone at $z \lesssim 0$ over a small thickness λ_s (cf. **Chapter 1**) and is propagating in a semi-infinite dielectric ($z > 0$). [Tikhonchuk, 2002] has shown that the ionization of dielectric atoms by the self-consistent electric field at the beam front (2.11) is much more important than their collisional ionization by the impact of beam electrons. Indeed, according to our estimate (2.11) and assuming the typical values of laser-generated electron beam parameters $n_b \approx n_c$ and $\gamma_b \approx 1 - 10$, the typical value of the self-consistent electric field at the beam front is $E_0 = -4\pi e n'_b \lambda'_b \approx -10^{12} \text{ V.m}^{-1}$ which represents $\approx 10\%$ of the atomic electric field $E_{\text{Bohr},n} = -Z^3 e / n^2 r_{\text{Bohr}}^2 \approx -5(Z^3 / n^2) 10^{11} \text{ V.m}^{-1}$ in the Bohr hydrogenoid approximation (for example for Carbon, $Z = 6$ and $n = 2$). Thus, the field is sufficiently high to induce a tunnelling ionization with the characteristic rate of $\approx 1 \text{ fs}^{-1}$ according to [Keldysh, 1965] while the collisional ionization probability does not exceed $\approx 100 \text{ ns}^{-1}$ according to [Tikhonchuk, 2002]. Besides, still according to the author, the self-consistent electric field is not sufficient to fully explain a deep penetration of laser-generated electron beam in dielectrics as observed in experiments due to the screening of the self-consistent electric field by newborn electrons. The space-charge-separation electric field must so be taken into account. [Debayle and Tikhonchuk, 2007] have developed a quasi-

stationary 1D model of the laser-generated electron beam transport through a dielectric material that we are going to present here. In this model, the atoms and new born ions are assumed to be at rest due to their huge inertia compared to the electrons and the small time scale considered here. The new born free electrons dynamics is resolved according to the hydrodynamic equation for the conduction electron density (see **Appendix B, section B.1.2**)

$$\frac{\partial n_e}{\partial t} + \frac{\partial}{\partial z} (n_e v_{ez}) = \frac{\partial n_i}{\partial t} = -\frac{\partial n_n}{\partial t} = \nu_E (n_n - n_i) + \nu_{en} (n_n - n_i) - \nu_{rec} n_i \quad (2.40)$$

where $\nu_E = \nu_E(E_z)$ is the electric field ionization rate, $\nu_{en} = \nu_{en}(n_e, T_e)$ is the collisional ionization rate depending on the conducting electrons density n_e and their temperature T_e and ν_{rec} is the three-body recombination rate, the hydrodynamic equation for the conduction electron momentum

$$\frac{\partial j_{e,z}}{\partial t} = \frac{e^2}{m_e} n_e E_z - \nu_{ei} j_{e,z} \quad (2.41)$$

where the left hand side takes into account the temporal part of the electron inertia and the hydrodynamic equation for the conduction electron internal energy

$$\frac{3}{2} \frac{\partial}{\partial t} (n_e k_B T_e) = j_{e,z} E_z - 2I_p \frac{\partial n_i}{\partial t} \quad (2.42)$$

where the second term in the right hand side, depending on the mean ionization potential I_p , accounts for the energy losses due to the ionization and finally the Saha's equation

$$\frac{n_i}{n_n - n_i} = \frac{\nu_{en}}{\nu_{rec}}, \quad (2.43)$$

based on the detailed equilibrium between the collisional ionization process and the three body recombination. In a 1D model, the magnetic field is neglected while the electric field is estimated according to the Maxwell-Gauss equation

$$\frac{\partial E_z}{\partial z} = -4\pi e (n_e + n_b - n_i) - 4\pi \frac{I_p}{E_z} \frac{\partial n_i}{\partial z} \quad (2.44)$$

where the last term in the right hand side accounts for the dielectric polarization P_z induced by the field ionization process such that $(\partial P_z / \partial z) = (I_p / E_z) (\partial n_i / \partial z)$ [Debayle and Tikhonchuk, 2007]. Also, for simplicity, only the first ionization of atoms is taken into account, leading to an ionization state $Z^* = 1$. One can notice that direct collisional ionization of atoms by the beam electrons is neglected here as the pressure of the new born electrons, because their thermal velocity is small compared to their mean velocity. The beam is assumed to be rigid since the ionization losses are relatively small for present day laser-generated electron beam currents. The 1D approximation consists in considering only the beam transport close to the z-axis rejecting the beam radius r_b to the infinity. Consequently, the self-consistent electric field at the beam front cancels. One can roughly estimate the space-charge-

2.3. MAGNETIC NEUTRALIZATION OF A MONOENERGETIC, COLLIMATED AND HOMOGENEOUS RIGID RELATIVISTIC ELECTRON BEAM PROPAGATING IN A CONDUCTOR

separation electric field on the time scale $t \ll \nu_E^{-1}$ by solving (2.44) assuming

$$\begin{cases} n_e(z, t \ll \nu_E^{-1}) &= (n_{e0} - n_b)(\Pi[z + \lambda_s] - \Pi[z]) \\ n_i(z, t \ll \nu_E^{-1}) &= n_{i0}(\Pi[z + \lambda_s] - \Pi[z]) \\ n_b(z, t) &= n_{b0}(\Pi[z] - \Pi[z - v_b t]) \end{cases}$$

where $n_{e0} = n_{i0}$ is the free electron/ion density of the laser-dielectric interaction zone. This condition accounts for the lack of the forward accelerated electrons in this zone as well as their propagation inside the target. The resulting space-charge separation electric field reads

$$E_z(0 < z < v_b t, t \ll \nu_E^{-1}) \approx 4\pi e(2n_{b0})(v_b t - z). \quad (2.45)$$

Contrary to the self-consistent electric field (2.11), this electric field (2.45) is positive. Its maximal value is close to $4\pi e n_{b0} v_b / \nu_E$ which has the same order of magnitude as E_0 and can consequently lead to the tunnel ionization of the neutral atoms. Moreover, by coupling the Maxwell-Gauss equation (2.44) with the charge conservation equation $-e(\partial/\partial t)(n_e + n_b - n_i) = (\partial/\partial z)(j_{e,z} + j_b)$, one gets

$$\frac{\partial E_z}{\partial t} = -4\pi(j_b + j_{ez}) - \frac{\partial P_z}{\partial t}. \quad (2.46)$$

This Ampère-like equation (2.46) shows that the charge-space-separation electric field induces electrostatically a "return current" in the dielectric which tends to cancel the total current. This return current generates an Ohmic electric field according to Equation (2.41). The new born electrons are strongly heated by Joule effect according to Equation (2.42) and participate in the collisional ionization of the dielectric according to Equation (2.40). Finally, the beam current is electrically neutralized in agreement with the the charge conservation equation except close to the beam front where the "return current" induces a lack of free electrons. These time-dependent processes are leading to an additional beam energy loss compared to laser-metal interaction as shown experimentally by [Pisani et al., 2000].

2.3 Magnetic Neutralization of a Monoenergetic, Collimated and Homogeneous Rigid Relativistic Electron Beam Propagating in a Conductor

Let us consider here a monoenergetic cylindrical and semi-infinite electron beam propagating in a medium assuming that it is already electrically neutralized. In a plasma or a conducting metal, the beam is neutralized electrically by the radial expulsion of background electrons out of the beam volume while in a dielectric material, this is the electrostatically induced "return current" which longitudinally neutralizes the beam. However, we show in this subsection that, even electrically neutralized, a

CHAPTER 2. ELECTROMAGNETIC NEUTRALIZATION OF A LASER-GENERATED RELATIVISTIC ELECTRON BEAM

high current of electron beam cannot propagate without its magnetic neutralization. We start from Equations (2.1), (2.3) and the Maxwell-Gauss equation

$$\frac{\partial^2 \Phi'}{\partial \mathbf{r}'^2} = 0 \quad (2.47)$$

which accounts for the electric beam neutralization. By performing an analysis similar to that of **Section 2.1**, one can show that, far away from the beam front i.e. for $|z| \gg \lambda'_b$, the beam remains homogeneous $n'_b = n'_{b0} \Pi(r_b - r)$, the electrostatic potential $\Phi' = 0$ and the vector potential

$$A'_z(r', z' \rightarrow -\infty, t') = \begin{cases} A_0 \left[1 - I_0 \left(\frac{r'}{\lambda'_b} \right) \right] & \text{if } r' \leq r_b \\ A_0 \left[1 - I_0 \left(\frac{r_b}{\lambda'_b} \right) \right] - A_0 \frac{r'_b}{\lambda'_b} I_1 \left(\frac{r'_b}{\lambda'_b} \right) \ln \left(\frac{r'}{\lambda'_b} \right) & \text{if } r > r_b \end{cases} \quad (2.48)$$

where $A_0 = -\gamma_b \beta_b m_e c / e$. Consequently, according to the Lorentz transformation of the fields, the magnetic field in the laboratory frame reads

$$\mathbf{B}(r, z \rightarrow -\infty, t) = \begin{cases} \frac{A_0}{\lambda'_b} I_1 \left(\frac{r}{\lambda'_b} \right) \mathbf{e}_\theta & \text{if } r \leq r_b \\ \frac{A_0}{\lambda'_b} I_1 \left(\frac{r_b}{\lambda'_b} \right) \frac{r_b}{r} \mathbf{e}_\theta & \text{if } r > r_b. \end{cases} \quad (2.49)$$

In the case where $r_b \ll \lambda'_b$, one retrieves the well known magnetic field generated by a homogeneous, infinite and cylindrical **rigid** electron beam, which can be obtained according to the Ampère law :

$$\mathbf{B}_\infty = \begin{cases} \frac{4\pi}{c} j_b \frac{r}{2} \mathbf{e}_\theta & \text{if } r \leq r_b \\ \frac{4\pi}{c} j_b \frac{r_b^2}{2r} \mathbf{e}_\theta & \text{if } r > r_b \end{cases} \quad (2.50)$$

($I_1(x) \sim x/2$ when $x \rightarrow 0$). In order to explain observations concerning cosmic rays, [Alfvén, 1939] has studied the trajectories of beam electrons in this self-consistent magnetic fields (2.50). Indeed, thanks to the electrical neutralization and to the fact that n_b is constant inside the beam, the beam electron kinetic energy is constant. By integrating the beam electrons equation of motion, [Alfvén, 1939] showed that if the beam current $I_b = j_b \pi r_b^2$ is sufficiently small, their motion is approximatively sinusoidal as illustrated by the trajectory a in **Figure 2.4**. As the current I_b increases, the trajectory passes through the beam axis at a greater angle (trajectory b) until $I_b = I_A$ for which the particle passes through the axis perpendicular to it (trajectory c). If I_b is increased still further, the net particle motion is backward, as shown by orbit e and the extreme case of orbit f. It means that the electron beam propagation is stopped due to the action of the self-generated magnetic field on the beam electrons. According to [Lawson, 1959], the threshold value I_A can be defined as the current for which the beam electron Larmor radius R_L in the maximum self-magnetic field, is equal to the half of the beam radius.

2.3. MAGNETIC NEUTRALIZATION OF A MONOENERGETIC, COLLIMATED AND HOMOGENEOUS RIGID RELATIVISTIC ELECTRON BEAM PROPAGATING IN A CONDUCTOR

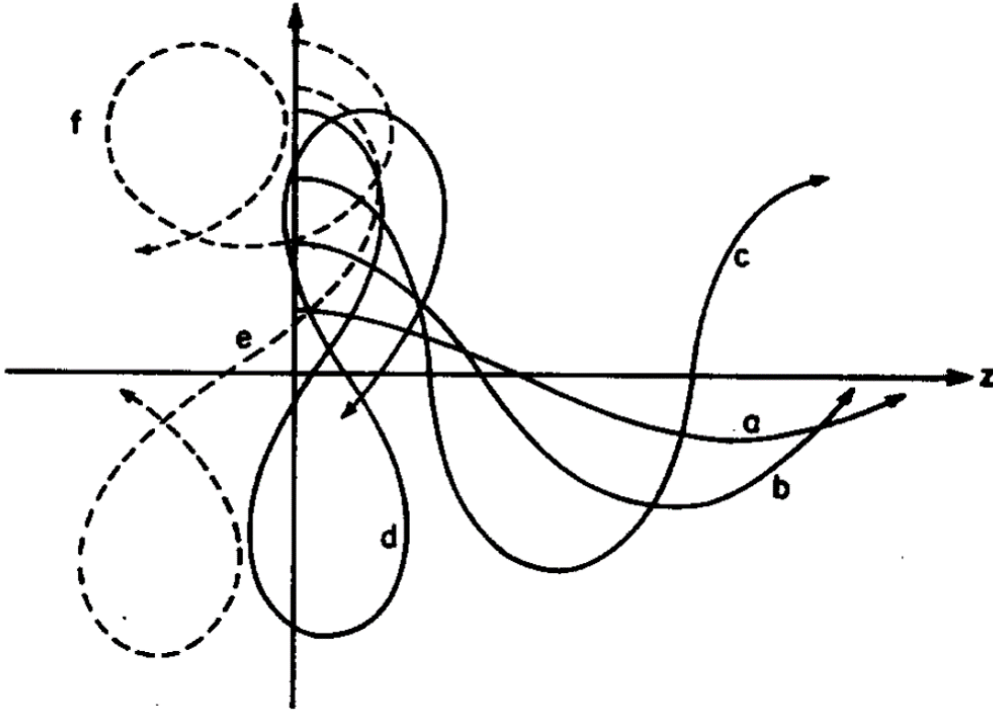


Figure 2.4: Trajectories of beam electrons starting in the z -direction at various distance from the axis of a uniform and electrically neutralized relativistic electron beam. Solid (dashed) curves represent particle trajectories with net motion forward (inward) taken from [Alfvén, 1939]

One obtains according to this criterion the well-known Alfvén-Lawson limit

$$I_A = -\gamma_b \beta_b \frac{m_e c^3}{e} \approx -17 \gamma_b \beta_b \text{ kA.} \quad (2.51)$$

Concerning laser-generated electron beams, the typical current is greater than I_A by many orders of magnitude while experiments show clearly the signature of the beam propagation deep inside the irradiated target. Moreover, for laser-generated electron beam, we have typically $r_b \gg \lambda_b$, which is the opposite to the condition for which the solution (2.50) was obtained. In the case where $r_b \gg \lambda_b$, (2.49) is not physical because we obtain that the linear density of magnetic energy generated by the beam is greater than the linear density of the beam energy ($I_1(x) \sim \exp(x)/\sqrt{2\pi x}$ when $x \rightarrow \infty$). This is of course physically impossible. In order to break this paradox, we will show here that, in addition to the electrical neutralization, an electron beam cannot propagate without being also magnetically neutralized.

Let us consider so a rigid relativistic electron beam propagating through a conducting medium (plasma or metal) and let us calculate the magnetic response of the medium to the beam propagation. The system of equations to be solved $\{(2.16), (2.17), (2.18), (2.19)\}$ was already introduced in the previous **section 2.2.1**. According to [Hammer and Rostoker, 1970], assuming $n_b \ll n_e$, a weakly

CHAPTER 2. ELECTROMAGNETIC NEUTRALIZATION OF A LASER-GENERATED RELATIVISTIC ELECTRON BEAM

collisional ($\nu_{ei} \ll \omega_p$) and cold plasma (neglecting the pressure effects) and considering the time scales small compared to the diffusion time τ_d , one obtains the solutions (2.36). Then performing the Lorentz-transformations, one finds

$$\left\{ \begin{array}{l}
 \delta E_z(r, z < v_b t, t \ll \tau_d) = -4\pi n_b e r_b \sin\left(\omega_p \sqrt{\gamma_b} \frac{z - v_b t}{v_b}\right) \exp\left[\frac{\nu_{ei}(z - v_b t)}{2v_b}\right] \\
 \quad \times \begin{cases} \frac{v_b \lambda'_e}{c r_b} - I_0\left(\frac{r}{\lambda'_e}\right) K_1\left(\frac{r_b}{\lambda'_e}\right) & \text{if } r \leq r_b \\ I_1\left(\frac{r_b}{\lambda'_e}\right) K_0\left(\frac{r}{\lambda'_e}\right) & \text{if } r > r_b \end{cases} \\
 \delta j_{e,z}(r, z < v_b t, t \ll \tau_d) = -j_b \begin{cases} 1 - \frac{r_b}{\lambda'_e} I_0\left(\frac{r}{\lambda'_e}\right) K_1\left(\frac{r_b}{\lambda'_e}\right) & \text{if } r \leq r_b \\ \frac{r_b}{\lambda'_e} I_1\left(\frac{r_b}{\lambda'_e}\right) K_0\left(\frac{r}{\lambda'_e}\right) & \text{if } r > r_b \end{cases} \\
 \quad + \frac{j_b}{\sqrt{\gamma_b}} \cos\left(\omega_p \sqrt{\gamma_b} \frac{z - v_b t}{v_b}\right) \exp\left[\frac{\nu_{ei}(z - v_b t)}{2v_b}\right] \\
 \quad \times \begin{cases} 1 - \frac{c r_b}{v_b \lambda'_b} I_0\left(\frac{r}{\lambda'_e}\right) K_1\left(\frac{r_b}{\lambda'_e}\right) & \text{if } r \leq r_b \\ \frac{c r_b}{v_b \lambda'_b} I_1\left(\frac{r_b}{\lambda'_e}\right) K_0\left(\frac{r}{\lambda'_e}\right) & \text{if } r > r_b \end{cases} \\
 \delta B_\theta(r, z < v_b t, t \ll \tau_d) = \frac{4\pi}{c} j_b r_b \begin{cases} I_1\left(\frac{r}{\lambda'_e}\right) K_1\left(\frac{r_b}{\lambda'_e}\right) & \text{if } r \leq r_b \\ I_1\left(\frac{r_b}{\lambda'_e}\right) K_1\left(\frac{r}{\lambda'_e}\right) & \text{if } r > r_b \end{cases}
 \end{array} \right. \quad (2.52)$$

That solution shows that, within the time scale of the beam electrical neutralization (few ν_{ei}^{-1}), a temporal variation of the magnetic field generated by the beam induces a longitudinal electric field. This electric field accelerates a return current of plasma electrons $\delta j_{e,z}$ which tends to cancel the total net current ($j_b + j_{e,z} = 0$) over the time scale ν_{ei}^{-1} except in the narrow zone at the beam edge $r_b \pm \lambda'_e$. This is in agreement with the Lenz law which stipulates that the effects of the magnetic field generated by the beam counteract its cause, that is the total net current here. The longitudinal electric field δE_z vanishes over the time scale ν_{ei}^{-1} . Besides, as the two counterpropagating currents do not cancel each other exactly, the magnetic field generated by the return current does not completely cancel the magnetic field generated by the beam. There is a residual magnetic field δB_θ localized at the beam edge $r_b \pm \lambda'_e$. The difference between expressions (2.52) and the original results of [Hammer and Rostoker, 1970] comes from the fact that here, the relationship $\omega'_p = \sqrt{\gamma_b} \omega_p$ has been taken into account (and not $\omega'_p = \omega_p$ like [Hammer and Rostoker, 1970]). Also, as pointed out by [Lee and Sudan, 1971], the magnetically induced return current and consequently the residual magnetic field diffuse over the time scale τ_d estimated by Equation (2.35) (see also **Chapter 3**). According to [Cox and Bennett, 1970], in the case of a collisional plasma ($\nu_{ei} \gg \omega_{pe}$), the time scale of the magnetic neutralization is defined by the Coulomb explosion time τ_e/γ_b . In this case, the resolution of the system of Equations {(2.16), (2.17), (2.18), (2.19)} using the same methodology as

2.3. MAGNETIC NEUTRALIZATION OF A MONOENERGETIC, COLLIMATED AND HOMOGENEOUS RIGID RELATIVISTIC ELECTRON BEAM PROPAGATING IN A CONDUCTOR

[Hammer and Rostoker, 1970] gives

$$\left\{ \begin{array}{l}
 \delta E_z(r, z < v_b t, t \ll \tau_d) = -4\pi n_b e r_b \exp \left[\frac{\gamma_b (z - v_b t)}{\tau_e} \right] \\
 \quad \times \begin{cases} \frac{v_b \lambda'_e}{c r_b} - I_0 \left(\frac{r}{\lambda'_e} \right) K_1 \left(\frac{r_b}{\lambda'_e} \right) & \text{if } r \leq r_b \\ I_1 \left(\frac{r_b}{\lambda'_e} \right) K_0 \left(\frac{r}{\lambda'_e} \right) & \text{if } r > r_b. \end{cases} \\
 \delta j_{e,z}(r, z < v_b t, t \ll \tau_d) = -j_b \begin{cases} 1 - \frac{r_b}{\lambda'_e} I_0 \left(\frac{r}{\lambda'_e} \right) K_1 \left(\frac{r_b}{\lambda'_e} \right) & \text{if } r \leq r_b \\ \frac{r_b}{\lambda'_e} I_1 \left(\frac{r_b}{\lambda'_e} \right) K_0 \left(\frac{r}{\lambda'_e} \right) & \text{if } r > r_b \end{cases} \\
 \quad + j_b \frac{\omega_p}{\nu_{ei}} \exp \left[\frac{\gamma_b (z - v_b t)}{\tau_e} \right] \\
 \quad \times \begin{cases} 1 - \frac{c r_b}{v_b \lambda'_e} I_0 \left(\frac{r}{\lambda'_e} \right) K_1 \left(\frac{r_b}{\lambda'_e} \right) & \text{if } r \leq r_b \\ \frac{c r_b}{v_b \lambda'_e} I_1 \left(\frac{r_b}{\lambda'_e} \right) K_0 \left(\frac{r}{\lambda'_e} \right) & \text{if } r > r_b \end{cases} \\
 \delta B_\theta(r, z < v_b t, t \ll \tau_d) = \frac{4\pi}{c} j_b r_b \begin{cases} I_1 \left(\frac{r}{\lambda'_e} \right) K_1 \left(\frac{r_b}{\lambda'_e} \right) & \text{if } r \leq r_b \\ I_1 \left(\frac{r_b}{\lambda'_e} \right) K_1 \left(\frac{r}{\lambda'_e} \right) & \text{if } r > r_b \end{cases}
 \end{array} \right. \quad (2.53)$$

In contrast to the collisionless case treated by [Hammer and Rostoker, 1970], the oscillatory component of the return current and the longitudinal electric field have disappeared here. Also, the magnitude of the time-dependent component of the return current is smaller than in the collisionless case because of greater influence of collisions.

Magnetic neutralization proceeds differently through an insulator. In this case, the "return current" is already generated due to the induced charge-space-electric field. Thus, one cannot separate the electric and magnetic neutralization of the beam but the resulting beam-"return current" system is actually very similar : there is also a residual magnetic field at the beam edge. Thus, in both cases (insulator or conductor), at the end of the beam electromagnetic neutralization, the beam-plasma system consists in a relativistic electron beam, a quasi-opposite counterpropagating return current and immobile ions. Such a system can be extremely unstable. The state of the art of the instability theory is presented in the next **Chapter 3**.

Chapter 3

Collective Effects of Relativistic Electron Beam Transport in Solids and Dense Plasmas

"In relativity, movement is continuous, causally determinate and well defined, while in quantum mechanics it is discontinuous, not causally determinate and not well defined."

David Bohm

When propagating through a material, laser-generated fast electron beams are electromagnetically neutralized over a time scale of the background electron-ion collision time ν_{ei}^{-1} or the background Coulomb explosion time τ_e/γ_b depending on the temperature and density conditions. In solids and dense plasmas, these time scales are typically of the order of a few fs. The electric field generated by the electron beam expels radially a small part of the background electrons $\sim n_b \ll n_e$ out of the beam volume in case of metals or plasmas. In case of insulators, the longitudinal electric field generated by the fast electrons at the beam front initiates the field ionization of the material and accelerates the newborn free electrons. The field ionization is followed by the collisional ionization by these accelerated free electrons in the zone where the space-charge electrostatic field is screened. This electrostatically induced "return current" \mathbf{j}_e tends to exactly compensate the beam current density $\mathbf{j}_e \approx -\mathbf{j}_b$. In both cases (insulators or conductors), the resulting electric field cancels at the end of the neutralization process. Concerning metals or plasmas, the temporal variation of the magnetic field generated by the beam induces a longitudinal electric field that accelerates a return current of background free electrons. This magnetically induced return current \mathbf{j}_e tends also to exactly compensate the beam current density $\mathbf{j}_e \approx -\mathbf{j}_b$ in agreement with the Lenz law. However, in both cases (insulator or conductor), the magnetic neutralization is not perfect. A fine surface around the beam edge of the order of the background skin depth λ'_e remains non neutralized and a residual magnetic field remains locally. However, this residual magnetic field must be mitigated in case of smoother radial gradients of the beam where $[(1/n_b)(\partial n_b/\partial r)]^{-1} \gg \lambda'_e$. This chapter presents the collective effects, taking place at time scales larger than the beam neutralization time. Indeed, in this PhD studies, we are interested in a time scale ranging from a few fs to a few hundreds of ps since the studied laser-pulse durations τ_L are typically of about 10 fs – 100 ps.

3.1 Quasi-static Approximation

3.1.1 Background Electrons Dynamics after the Beam Electromagnetic Neutralization

In dense background media such as solids or dense plasmas, the background electrons can be assumed sufficiently collisional and close to equilibrium (Maxwell-Boltzmann or Fermi-Dirac distribution functions) so that they may be modelled by a non-relativistic fluid approach. Such a fluid model for the background requires that departures from collisional equilibrium are small. For example, fluid models break down when electric fields are greater than $m_e \nu_{ei} v_{Te}/e$ because they may be responsible for the acceleration of runaway electrons that are not taken into account by the hydrodynamic theory. The non-relativistic assumption comes from the fact that the beam density n_b is small compared to the background conducting electrons density n_e . Thus, the background response to the beam propagation can be considered as a small perturbation and the induced background electron velocities are small

compared to $v_b \leq c$. Also, over the time scale considered here, ions/atoms can be considered immobile because of their huge inertia compared to the electron mass. Thus, the background response to the beam propagation can be described by the hydrodynamic equations

$$\frac{\partial n_e}{\partial t} + \frac{\partial}{\partial \mathbf{r}} \cdot (n_e \mathbf{v}_e) = 0 \quad (3.1)$$

and

$$\begin{aligned} & m_e n_e \left[\frac{\partial}{\partial t} + \left(\mathbf{v}_e \cdot \frac{\partial}{\partial \mathbf{r}} \right) \right] (\mathbf{v}_e) \\ &= -n_e e \left[\mathbf{E} + \frac{\mathbf{v}_e}{c} \times \mathbf{B} \right] - \frac{\partial}{\partial \mathbf{r}} \cdot (P_e \mathbf{I} - \boldsymbol{\tau}_e) + \mathbf{R}_{ei} \end{aligned} \quad (3.2)$$

for the background free electrons, only (see **Appendix B, section B.1.2**). The relativistic electron beam and the background electrons interact via the macroscopic electromagnetic fields \mathbf{E} and \mathbf{B} . Direct collisions of background electrons with beam electrons do not appear in Equations (3.1) and (3.2). This is due to the fact that, since $n_b \ll n_e$, they are negligible compared to collisions with background ions/atoms or background electrons. Here, we focus on the electromagnetic fields; the collisional effects of relativistic electron beam transport are considered in the next **Chapter 4**. In the time scale considered here, the beam has already been neutralized electrically so that the charge neutrality equation

$$n_e + n_b = \sum_i Z_i n_i. \quad (3.3)$$

replaces the Maxwell-Gauss Equation. The ion charge state Z_i depends on the local temperature and properties of the material. n_b being small compared to n_e , the latter equation is valid on length scales much longer than the Debye length like in the usual hydrodynamic approach. Also, over time scales larger than the Langmuir wave time scale ω_p^{-1} , one can neglect the electron inertia (left hand side term in Equation (3.2)). In this case, oscillations of the laser-generated electron beam at the laser frequency ω_L or $2\omega_L$ cannot be resolved properly and are not taken into account. Also, the fluid viscosity is neglected and the Braginskii or the Lee-More transport coefficients $\mathbf{R}_{ei} = en_e \boldsymbol{\eta} \cdot \mathbf{j} - k_B \boldsymbol{\beta} \cdot \frac{\partial T_e}{\partial \mathbf{r}}$ are usually used (see **Appendix B, sections B.2.3 and B.2.4**). As a result, Equation (3.2) is usually replaced by the more simple equation

$$\mathbf{E} = \boldsymbol{\eta} \cdot \mathbf{j}_e - \frac{1}{n_e e} \frac{\partial}{\partial \mathbf{r}} (n_e k_B T_e) \quad (3.4)$$

commonly called the Ohm's law. Assuming that the cyclotron frequency $\omega_c = |eB|/m_e c$ is small compared to ν_{ei} , the magnetization of the background electrons is neglected and the resistivity tensor is usually taken to be isotropic $\boldsymbol{\eta} = \eta \mathbf{I}$. Also, the thermal force is neglected since, in general, it is small compared to the friction force. The electromagnetic fields are defined by the Maxwell-Faraday equation

$$\frac{\partial \mathbf{B}}{\partial t} = -c \frac{\partial}{\partial \mathbf{r}} \times \mathbf{E} \quad (3.5)$$

3.1. QUASI-STATIC APPROXIMATION

and the Maxwell-Ampère equation

$$\frac{\partial \mathbf{E}}{\partial t} = c \frac{\partial}{\partial \mathbf{r}} \times \mathbf{B} - 4\pi (\mathbf{j}_e + \mathbf{j}_b) = 0 \quad (3.6)$$

with the initial conditions of zero field divergences $(\partial/\partial \mathbf{r}) \cdot \mathbf{B} = 0$ and $(\partial/\partial \mathbf{r}) \cdot \mathbf{E} = 0$. The **quasi-static approximation** consists in neglecting the displacement current $(\partial \mathbf{E}/\partial t)$ in the Maxwell-Ampere equation (3.6). This is fully justified as the background electron inertia is neglected, as one considers time scales larger than ω_p^{-1} and space scales larger than the plasma skin depth λ_e . Sometimes, due to the fact that $\mathbf{j}_e \approx -\mathbf{j}_b$ on spatial scales larger than λ_e , the Maxwell-Ampère Equation (3.6) is not resolved and \mathbf{j}_e is directly replaced by $-\mathbf{j}_b$ in (3.4). The system of Equations (3.6), (3.4) and (3.5) describes the self-generated electromagnetic field

$$\mathbf{E} = -\eta \mathbf{j}_b + \frac{\eta c}{4\pi} \frac{\partial}{\partial \mathbf{r}} \times \mathbf{B} - \frac{1}{n_e e} \frac{\partial}{\partial \mathbf{r}} (n_e k_B T_e) \quad (3.7)$$

and

$$\frac{1}{c} \frac{\partial \mathbf{B}}{\partial t} + \frac{\partial}{\partial \mathbf{r}} \times \left(\frac{\eta c}{4\pi} \frac{\partial}{\partial \mathbf{r}} \times \mathbf{B} \right) = \eta \frac{\partial}{\partial \mathbf{r}} \times \mathbf{j}_b + \frac{\partial \eta}{\partial \mathbf{r}} \times \mathbf{j}_b - \frac{k_B}{n_e e} \frac{\partial n_e}{\partial \mathbf{r}} \times \frac{\partial T_e}{\partial \mathbf{r}}. \quad (3.8)$$

The second term in the left hand side of Equation (3.8) describes the magnetic field diffusion. One can understand easily now the characteristic time scale (2.35) proposed by [Lee and Sudan, 1971]. Indeed, considering space scale of the order of the beam radius r_b , the diffusion operator gives the time scale

$$\tau_d = \frac{4\pi r_b^2}{\eta c^2} = \frac{r_b^2}{\lambda_e^2 \nu_{ei}}$$

because $\eta = 4\pi \nu_{ei} / \omega_p^2$, by definition. There are three source terms for magnetic field generation in Equation (3.8), depending on the beam current density, the electrical resistivity and the background electron temperature and density gradients, while the self-generated electric field \mathbf{E} is mainly given by $-\eta \mathbf{j}_b$ as already explained. These self-generated electromagnetic fields play an important role in the relativistic electron beam transport. The magnetic field due to the curl of the beam current density tends to pinch the relativistic electron beam, the magnetic field due to the resistivity gradients tends to move the relativistic electrons from low electrical resistivity zones to higher ones, while the resistive electric field slows down the relativistic electrons [Davies et al., 1997]. The magnetic field generated by the temperature-density crossed gradients in (3.8) may modify the beam transport on a time scale of a few picoseconds [Nicolai et al., 2011] but on shorter time scales, it can be neglected. Using the same assumptions and methodology as [Hammer and Rostoker, 1970], [Lee and Sudan, 1971] derived the electron background response to the propagation of a semi-infinite, monoenergetic, cylindrical, collimated and rigid relativistic homogenous electron beam on a time scale large compared to ν_{ei}^{-1} or τ_e / γ_b . Following the notations introduced in **Chapter 2**, [Lee and Sudan, 1971] considered only the

pole k_5 . Their solution reads in the limit $|z - v_b t| \gg \lambda_e$

$$n_e(r, z < v_b t, t \gg \nu_{ei}^{-1} \text{ or } \tau_e) = -n_b \begin{cases} 1 & \text{if } r \leq r_b \\ 0 & \text{if } r > r_b \end{cases} \quad (3.9)$$

for the background electron density and

$$\begin{aligned} j_{e,z}(r, z < v_b t, t \gg \nu_{ei}^{-1} \text{ or } \tau_e) &= -j_b r_b \int_0^\infty dk_\perp \frac{J_0(k_\perp r) J_1(k_\perp r_b)}{1 + (k_\perp \lambda'_e)^2} \exp\left[\frac{\nu_{ei}(z - v_b t)}{v_b} \frac{(k_\perp \lambda'_e)^2}{1 + (k_\perp \lambda'_e)^2}\right] \\ &\approx -j_b \left[1 - \exp\left(\gamma_b^2 \frac{v_b \tau_d}{4(z - v_b t)}\right)\right] \text{ when } r \ll \lambda'_e. \end{aligned} \quad (3.10)$$

for the diffused background return current. This last expression shows that the return current starts from the perfect neutralization $j_{e,z} = -j_b$ and then decreases in the time scale of τ_d and in a spatial scale of $\tau_d v_b$.

3.1.2 Electric and Magnetic Fields Radial Profiles

Since laser-generated electron beam lengths are small compared to the diffusion length $v_b \tau_L \ll v_b \tau_d$, let us consider here time scales shorter than the diffusion time (2.35). Due to the fact that there are many orders of magnitude between ν_{ei}^{-1} or τ_e/γ_b and τ_d , one has to solve accurately Equations (3.7) and (3.8). In order to estimate the radial profiles of the electric and magnetic field induced by a laser-generated electron beam, [Fill, 2001] assumed a homogenous conducting background with a constant resistivity η_0 , an axisymmetric rigid electron beam of the form

$$j_b = \begin{cases} j_{b0} \sin^2\left(\pi \frac{t - z/v_b}{2\tau_L}\right) \exp\left(-\frac{r^2}{2r_b^2}\right) & \text{if } z \leq v_b t < z + 2v_b \tau_L \\ 0 & \text{else} \end{cases}$$

and the scaling

$$\frac{\tau_d}{\tau_L} \gg \left(\frac{r_b}{\tau_L c}\right)^2, \quad \frac{\tau_d}{\tau_L} \gg \left(\frac{r_b}{\delta r_b}\right)^2, \quad (3.11)$$

where $\delta r_b^{-1} \sim \partial/\partial r$. Starting from (3.8), he thus obtained for the magnetic field

$$\begin{aligned} B_\theta(r, z, t) &= \eta_0 c \int_0^t \frac{\partial j_b}{\partial r} dt \\ &= j_{b0} \frac{2\pi r}{c} \frac{\tau_L}{\tau_d} \exp\left(-\frac{r^2}{2r_b^2}\right) \text{ at } t = \tau_L. \end{aligned} \quad (3.12)$$

Indeed, under the assumption (3.11), the diffusion term can be neglected, while the homogenous background assumption cancels all the source terms except the one due to the curl of the beam

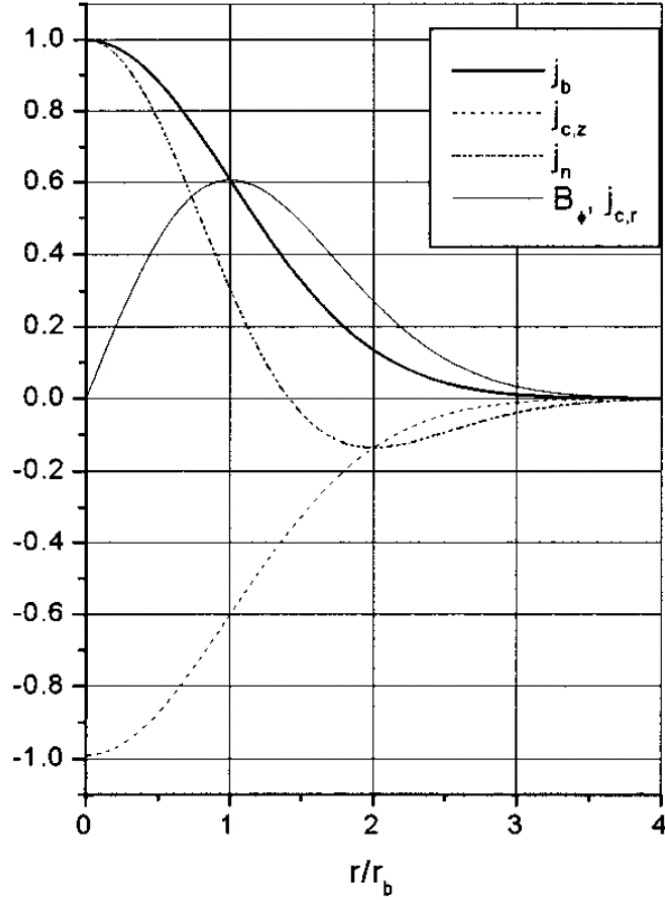


Figure 3.1: Radial profile of beam current density j_b , return current density $j_{e,z}$ ($j_{c,z}$ with the Fills notations), net current density $j_{n,z}$ (j_n), azimuthal magnetic field B_θ (B_φ), and radial current density $j_{e,r} = j_{n,r}$ ($j_{c,r}$) at peak of a pulse $t = \tau_L$. The beam current is assumed to have a Gaussian radial profile. The various quantities are normalized with respect to the beam current density amplitude j_{b0} . In addition, the following scaling factors are used: τ_L/τ_d for $j_{n,z}$, $2\pi r_b \tau_L/\tau_d c$ for B_θ . The radial current has the same spatial profile as the B-field. Its scaling factor is $r_b/\tau_d c$. The return current is drawn for a ratio $\tau_d/\tau_L = 100$ [Fill, 2001]

current density. The background current density is deduced by using the Maxwell-Ampere law (3.6) knowing the magnetic field (3.12). It reads

$$j_{e,r} = j_{n,r} \text{ and } j_{e,z} = -j_b + j_{n,z} \quad (3.13)$$

where the net total current density

$$\mathbf{j}_n = \frac{c}{4\pi} \frac{\partial}{\partial \mathbf{r}} \times \mathbf{B} \quad (3.14)$$

and consequently

$$\left\{ \begin{array}{l} j_{n,r} = -\frac{c}{4\pi} \frac{\partial B_\theta}{\partial z} \approx -\frac{1}{4\pi} \frac{\partial B_\theta}{\partial t} \approx -\frac{\eta_0 c}{4\pi} \frac{\partial j_b}{\partial r} \\ \approx j_{b0} \left(\frac{r}{c\tau_d} \right) \exp\left(-\frac{r^2}{2r_b^2}\right) \text{ at } t = \tau_L \\ j_{n,z} = \frac{c}{4\pi} \frac{1}{r} \frac{\partial}{\partial r} (rB_\theta) = \frac{\eta_0 c^2}{4\pi} \int_0^t \frac{1}{r} \frac{\partial j_b}{\partial r} + \frac{\partial^2 j_b}{\partial r^2} dt \\ = j_{b0} \frac{\tau_L}{\tau_d} \left(1 - \frac{r^2}{2r_b^2} \right) \exp\left(-\frac{r^2}{2r_b^2}\right) \text{ at } t = \tau_L \end{array} \right. \quad (3.15)$$

assuming $v_b \approx c$. Finally, by using Ohm's law (3.7) and by neglecting the pressure term, the electric field can be deduced knowing the return current \mathbf{j}_e . The profiles of the current and the magnetic field are shown in **Figure 3.1**. The small factor τ_L/τ_d in (3.15) explains why the magnetic curl in the Maxwell-Ampere equation (3.6) is usually neglected and why the return current density is usually considered as the exact opposite to the beam current density $\mathbf{j}_e = -\mathbf{j}_b$. However, such an "initial situation" $j_{e,z} = -j_b$ is extremely unstable. One has to solve self-consistently Equation (3.7) for the background electrons and the relativistic kinetic equation for the fast electron beam to model correctly the laser-generated electron beam transport.

3.2 Beam-Plasma Instabilities

3.2.1 Linear Theory of Collisionless Instabilities

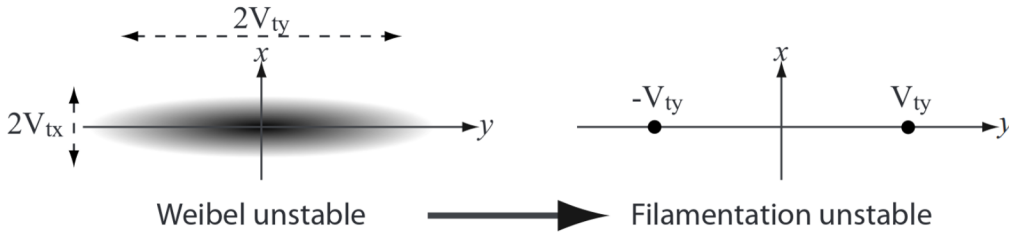


Figure 3.2: Typical distribution functions subject to the Weibel and the Filamentation instabilities [Bret et al., 2010b].

Since the 1950's with the discovery of the longitudinal electrostatic "two-stream instability" by [Bohm and Gross, 1949], it is known that such a system of two counterpropagating electron beam is unstable. Later, in order to determine the physical mechanism responsible for the purely transverse instability growth found by [Weibel, 1959] and associated with an anisotropic two-temperature Maxwellian plasma, [Fried, 1959] found a second class of instabilities by modelling the Weibel-unstable distribution function by two cold counterpropagating electron beams as illustrated in **Figure 3.2**. This purely transverse instability is called the "filamentation instability". However, these two designations are often used interchangeably in the literature (Weibel or filamentation) even if this equivalence

3.2. BEAM-PLASMA INSTABILITIES

holds only for symmetric beams. The longitudinal and transverse instabilities are two limits of a more general instability called the "oblique instability" [Bludman et al., 1960]. Let us consider here the propagation in the z -direction of an axisymmetric relativistic electron beam in a dense plasma on the time scale $t \approx \tau_L$ such that ν_{ei}^{-1} or $\tau_e/\gamma_b \ll \tau_L \ll \tau_d$. In this case, while plasma ions can still be assumed immobile, the electrical and the magnetical neutralization of the beam has already occurred and one has

$$n_e^{(0)} + n_b^{(0)} - Z^* n_i = 0 \text{ and } \mathbf{j}_e^{(0)} + \mathbf{j}_b^{(0)} = 0 \text{ with } n_b^{(0)} \ll n_e^{(0)}. \quad (3.16)$$

The superscript " (0) " denotes here the initial equilibrium in charge and in current between the electron beam denoted by the subscript " b " and the background conducting electrons denoted by the subscript " e ". Contrary to the previous **Chapter 2**, the beam is not considered here as a perturbation but as a part of the equilibrium (0) . One notes $n_j(\mathbf{r}, t)f_j(\mathbf{p}, \mathbf{t})$, $j \in \{e, b\}$ the distribution functions in the laboratory frame of both populations. We neglect the collisional effects so that $n_j f_j$ are solutions of the Vlasov equation with the electromagnetic fields given by the Maxwell equations (see **Appendix A, section A.1.1**). Also, we neglect the boundary conditions assuming that the perturbation space scale in the z -direction is much smaller than the characteristic size of the system. In order to address relativistic thermal spreads $k_B T_j$, we model the initial distribution functions by drifting Maxwell-Jüttner distribution functions [Jüttner, 1911]

$$f_j^{(0)}(\mathbf{p}) = \frac{k_B T_j / m_e c^2}{4\pi \gamma_j (m_e c)^3 K_2\left(\frac{m_e c^2}{\gamma_j k_B T_j}\right)} \exp\left[-\frac{m_e c^2}{k_B T_j} \left(\gamma - \beta_j \frac{p_z}{m_e c}\right)\right] \quad (3.17)$$

where $\gamma = \sqrt{1 + \mathbf{p}^2 / (m_e c)^2}$, $v_{j0} = \beta_j c$ the initial drift velocity in the z -directions of species j , $\gamma_j = 1/\sqrt{1 - \beta_j^2}$ the corresponding Lorentz factors and K_2 the modified Bessel function of the second kind. The standard method for studying instabilities consists in working in the Fourier's space

$$\forall \xi \in \{n_e, n_b, \mathbf{j}_e, \mathbf{j}_b, \mathbf{E}, \mathbf{B}\}, \hat{\xi}(\mathbf{k}, \omega) = \int_{\mathbb{R}^3} d^3\mathbf{r} \int_{-\infty}^{\infty} dt \xi(\mathbf{r}, t) \exp(i\mathbf{k} \cdot \mathbf{r} - i\omega t)$$

and consider a small perturbation $\delta\hat{\xi} \ll \hat{\xi}^{(0)}$ of the initial equilibrium $\hat{\xi}^{(0)}$ such that $\hat{\xi} = \hat{\xi}^{(0)} + \delta\hat{\xi}$ in order to determine eventual temporally exponentially increasing terms $\exp(\delta t)$. Here, $\delta = \text{Im}\{\omega(\mathbf{k})\}$ and depends on the excitation mode \mathbf{k} . Applying this method to our considered equilibrium (0) , one can look for unstable modes, characterized by their linear growth rate δ , by determining a solution of the dispersion relation in the form $\omega = \omega_r + i\delta$ where $\omega_r = \text{Re}\{\omega\}$ for which $\delta > 0$. According to [Bret et al., 2010b], without specifying any favored direction for \mathbf{k} , the linearized system of equations consisting in the two Vlasov equations for the two distribution functions $n_j f_j$ coupled with the Maxwell

CHAPTER 3. COLLECTIVE EFFECTS OF RELATIVISTIC ELECTRON BEAM TRANSPORT IN SOLIDS AND DENSE PLASMAS

equations for the electromagnetic fields (\mathbf{E} , \mathbf{B}) gives the dispersion relation

$$\left\{ \begin{array}{l} \epsilon_{xx}\omega^2 - \mathbf{k}^2 c^2 = 0 \quad (\text{a}) \\ \text{or} \\ (\omega^2 \epsilon_{zz} - k_y^2 c^2) (\epsilon_{yy}\omega^2 - k_z^2 c^2) - (\epsilon_{yz}\omega^2 - k_y k_z c^2)^2 = 0 \quad (\text{b}) \end{array} \right. \quad (3.18)$$

where

$$\forall(\alpha, \beta) \in \{x, y, z\}^2, \epsilon_{\alpha\beta}(\mathbf{k}, \omega) = \delta_{\alpha\beta} + \sum_i \frac{\omega_j^2}{\omega^2} \int_{\mathbb{R}^3} d^3\mathbf{p} \frac{p_\alpha}{\gamma} \frac{\partial f_j^{(0)}}{\partial p_\beta} + \sum_i \frac{\omega_j^2}{\omega^2} \int_{\mathbb{R}^3} d^3\mathbf{p} \frac{p_\alpha p_\beta}{\gamma^2} \frac{\mathbf{k} \cdot \left(\frac{\partial f_j^{(0)}}{\partial \mathbf{p}} \right)}{m_e \omega - \frac{\mathbf{k} \cdot \mathbf{p}}{\gamma}}$$

is the dielectric tensor, $\omega_j = \sqrt{4\pi n_j e^2 / m_e}$ is the electron plasma frequency of species j and $\delta_{\alpha\beta}$ is the Kronecker symbol. This dispersion equation has two main branches. The first one, defined by Equation (3.18 a), pertains to modes with an electric field along the x -axis. Such modes are therefore purely transverse for any \mathbf{k} such that $\mathbf{k} \cdot \mathbf{e}_x = 0$. The second branch (3.18 b) defines modes with an electric field lying within the (y, z) plane, which contains longitudinal and transverse components. When considering wave-vectors \mathbf{k} in the flow direction such that $k_y = 0$, the off-diagonal term ϵ_{yz} vanishes and (3.18 b) reduces to

$$(\epsilon_{yy}\omega^2 - k_z^2 c^2) \epsilon_{zz} = 0. \quad (3.19)$$

Whereas the first factor may yield unstable modes, the remaining dispersion equation $\epsilon_{zz} = 0$ defines modes with an electric field aligned with the flow. These are the two-stream modes, which are therefore purely longitudinal. If we now consider wave vectors normal to the flow, with $k_z = 0$, we recover the dispersion equation for the filamentation instability

$$\epsilon_{yy} \left(\epsilon_{zz}\omega^2 - \frac{k_y^2 c^2}{\omega^2} \right) = \epsilon_{yz}. \quad (3.20)$$

Thus, contrary to a common assumption, the filamentation instability is generally not purely transverse. It is purely transverse only in the case where $\epsilon_{yz} = 0$ and consequently

$$\epsilon_{zz} - \frac{k_y^2 c^2}{\omega^2} = 0, \quad (3.21)$$

which corresponds to two perfectly symmetric counterpropagating electron beams which is not our case since $n_b/n_e \ll 1$ (and therefore $v_b \gg v_e$). The domain of preponderance of each instability class has been numerically computed in the (n_b, n_e, T_b) parameters space by [Bret et al., 2010b] for a fixed plasma hot temperature $k_B T_e = 5$ keV. The surfaces that delimit regions governed by different instability classes are displayed in **Figure 3.3** and coloured according to the local maximum growth rate in the \mathbf{k} -space. The two-stream instability prevails for non relativistic beam drift energies ($\gamma_b - 1 \ll$

3.2. BEAM-PLASMA INSTABILITIES

1) as well as in the weakly relativistic systems with hot enough beams. Filamentation modes govern systems where the beam and plasma densities are similar. Oblique modes are dominant for our case of laser-generated electron beam propagation in a dense plasma. Also, oblique modes dominate for hot enough relativistic beams. These results are illustrated by the lower panels of **Figure 3.3** showing the plasma density observed in 2D PIC simulations each ruled by a distinct instability class.

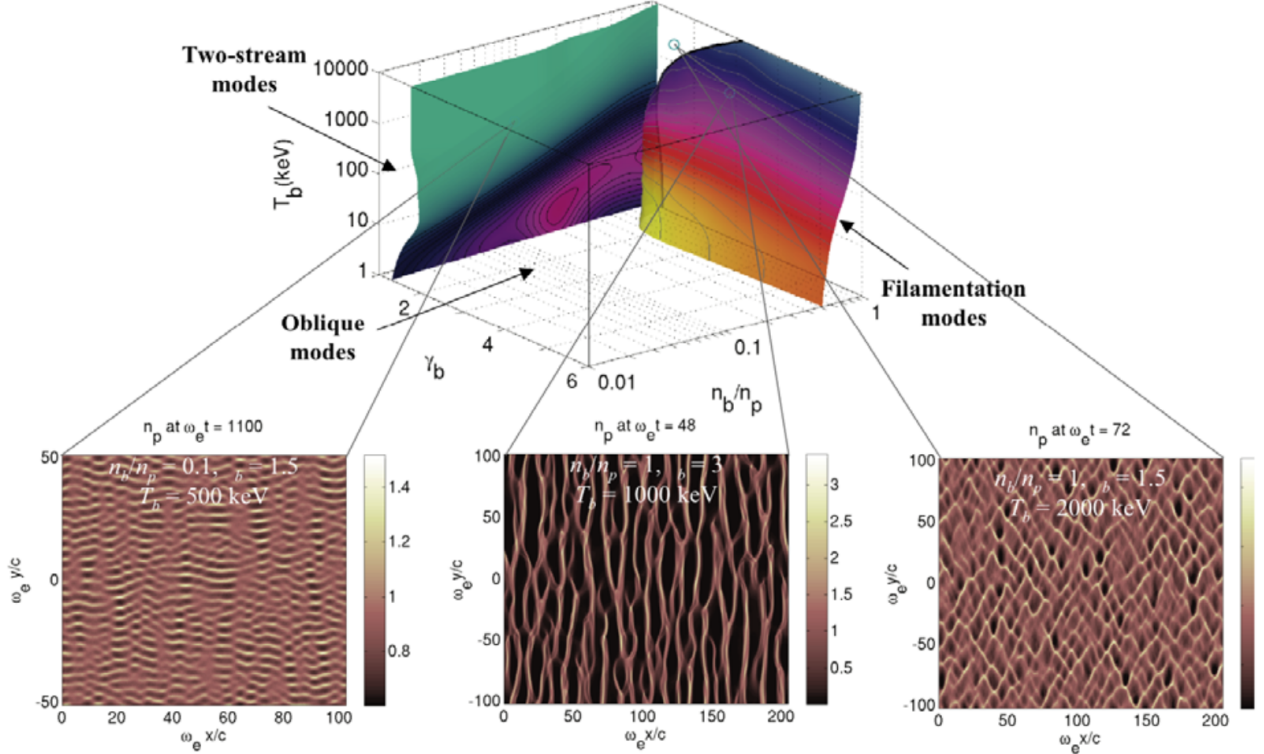


Figure 3.3: (top) Hierarchy of the two-stream, oblique and filamentation modes in the (n_b, n_e, T_b) parameter space for Maxwell-Jüttner distribution functions. (bottom) Plasma density profiles at the end of the linear phase as predicted by 2D PIC simulations, each ruled by a specific instability class. Here, the plasma temperature is $T_e = 5$ keV and the beam flows in the y -axis [Robinson et al., 2014]

Finding analytical expressions for the different growth rates δ is difficult due to the presence of the Lorentz factor γ in the integrals defining the dielectric tensor components. However, these triple integrals can be reduced to much more tractable one-dimensional quadratures using a change of variables mentioned in [Wright and Hadley, 1975]. It allows to find scaling laws for the maximum of each instability in the case of high γ_b and high T_b . It reads still according to [Bret et al., 2010b]

$$\begin{aligned}
 \delta_F^{\max} &\propto \left(\frac{n_b}{n_e} \right)^{3/2} \gamma_b^{-1/2} T_b^{-3/2}, \\
 \delta_O^{\max} &\propto \left(\frac{n_b}{n_e} \right) \gamma_b^{-1/3} T_b^{-1} \text{ and} \\
 \delta_{TS}^{\max} &\propto \left(\frac{n_b}{n_e} \right) \gamma_b T_b^{-1},
 \end{aligned} \tag{3.22}$$

respectively for the filamentation instability, the oblique instability and the two-stream instability. In the case where the fast electron beam temperature is sufficiently small

$$\frac{k_B T_b}{m_e c^2} < \frac{3}{2^{10/3}} \left(\frac{n_b}{n_e} \right)^{2/3} \gamma_b^{1/3} \frac{(1 + \gamma_b^{-2})^{2/3}}{(1 + \gamma_b^{-1})^2}, \quad (3.23)$$

the background electrons and the beam electrons can be considered as cold fluids according to [Bret et al., 2010a]. In this particular case, starting from the hydrodynamic equations with the cold approximation for both populations, coupled with the Maxwell-Gauss equation, one obtains the system of equations

$$\begin{cases} ik_z \delta \widehat{E}_z & = -4\pi e (\delta \widehat{n}_b + \delta \widehat{n}_e) \\ (\omega - k_z v_{e0}) \delta \widehat{n}_e & = k_z n_e^{(0)} \delta \widehat{v}_{e,z} \\ (\omega - k_z v_{b0}) \delta \widehat{n}_b & = k_z n_b^{(0)} \delta \widehat{v}_{b,z} \\ im_e (\omega - k_z v_{e0}) \delta \widehat{v}_{e,z} & = e \delta \widehat{E}_z \\ i\gamma_b^3 m_e (\omega - k_z v_{b0}) \delta \widehat{v}_{b,z} & = e \delta \widehat{E}_z \end{cases} \quad (3.24)$$

for the two-stream instability, assuming that the problem is one-dimensional ($k_x = k_y = 0$ and thus, neglecting the magnetic field). The combination of the previous equations provides the dispersion relation

$$1 - \frac{\omega_e^2}{(\omega - k_z v_{e0})^2} - \frac{\omega_b^2}{\gamma_b^3 (\omega - k_z v_{b0})^2} = 0. \quad (3.25)$$

The imaginary part of unstable mode $\delta = \text{Im}\{\omega\} > 0$ presents a maximum at the wave number $k_z = \omega_e/v_{b0}$ and it is cut off at higher wave numbers. This maximum can be approximated by

$$\delta_{TS}^{\max}(T_b \rightarrow 0) \approx \frac{\sqrt{3}\omega_e}{2\gamma_b} \left(\frac{n_b^{(0)}}{2n_e^{(0)}} \right)^{1/3}. \quad (3.26)$$

For the filamentation instability, assuming $k_z = k_y = 0$, the hydrodynamic equations in the cold approximation for both populations, coupled with the Maxwell equations gives

$$\begin{cases} ik_x \delta \widehat{E}_x & = -4\pi e (\delta \widehat{n}_b + \delta \widehat{n}_e) \\ \omega \delta \widehat{B}_y & = -\frac{k_x}{\omega} \delta \widehat{E}_z \\ ik_x \delta \widehat{B}_y & = -\frac{4\pi}{c} e \left(n_e^{(0)} \delta \widehat{v}_{e,z} - v_{e0} \delta \widehat{n}_e + n_b^{(0)} \delta \widehat{v}_{b,z} + v_{b0} \delta \widehat{n}_b \right) - i\frac{\omega}{c} \delta \widehat{E}_z \\ \omega \delta \widehat{n}_e & = k_x n_e^{(0)} \delta \widehat{v}_{e,x} \\ \omega \delta \widehat{n}_b & = k_x n_b^{(0)} \delta \widehat{v}_{b,x} \\ im_e \omega \delta \widehat{v}_{e,z} & = e \delta \widehat{E}_z \\ im_e \omega \delta \widehat{v}_{e,x} & = e \left(\delta \widehat{E}_x - \frac{v_{e0}}{c} \delta \widehat{B}_y \right) \\ i\gamma_b^3 m_e \omega \delta \widehat{v}_{b,z} & = e \delta \widehat{E}_z \\ i\gamma_b m_e \omega \delta \widehat{v}_{b,x} & = e \left(\delta \widehat{E}_x + \frac{v_{b0}}{c} \delta \widehat{B}_y \right) \end{cases} \quad (3.27)$$

3.2. BEAM-PLASMA INSTABILITIES

In the limit $n_b^{(0)} \ll n_e^{(0)}$, the determinant of this system provides the following dispersion relation

$$(\omega^2 - \omega_e^2) [\omega^4 - (k_x^2 c^2 + \omega_e^2) \omega^2 - \omega_e^2 (1 + \gamma_b^{-1}) v_{e0}^2 k_x^2] - \omega_e^4 (1 - \gamma_b^{-1})^2 v_{e0}^2 k_x^2 = 0. \quad (3.28)$$

According to the equation, the unstable solution $\delta = \text{Im}\{\omega\} > 0$ saturates at high wave numbers

$$\omega_{\max} = \omega_e \beta_b \sqrt{\frac{n_b^{(0)}}{n_e^{(0)}} \frac{\sqrt{3\gamma_b - 1}}{\gamma_b}}. \quad (3.29)$$

In the limit $\omega \ll \omega_e$, the unstable solution can be written

$$\delta_F^{\max}(T_b \rightarrow 0) \approx \omega_{\max} \frac{k_x v_{e0}}{\sqrt{k_x^2 c^2 + \omega_e^2}}. \quad (3.30)$$

3.2.2 Non-linear Evolution and Saturation Effects

The instability enters a nonlinear phase when the perturbations $\delta\hat{\xi}$ become of the same order of magnitude as $\hat{\xi}^{(0)}$. In this case, the linearization of the equations is no longer valid and some saturation effects occur. The non-linear behaviour of these instabilities can be studied with PIC codes. However, some key aspects of saturation effects can be understood from physical considerations. The two-stream instability may give rise to a periodic chain of holes in the electron phase space. This coherent structuring implies that a single mode eventually dominates the unstable spectrum. Oppositely, a broad perturbation spectrum, like for laser-generated electron beam, may cause a quasilinear relaxation of the beam. Scattering in the velocity space of primary unstable waves outside the beam-resonant region limits their growth and the related beam energy loss. The instability saturation comes from the growing waves that are trapping electrons which oscillate and form a vortex in the phase-space. A simplified description of such electron trapping by Landau damping in strong electron plasma waves has already been presented in **Chapter 1, section 2.1.4**.

The nonlinear development of the filamentation instability can be understood as follows. Electrons of both beams interact through their microscopic currents. Electrons moving in opposite directions repel each other. Thus, the initial charge and current neutral equilibrium is unstable. The magnetic fields grow due to the rearrangement of beam electrons into spatially separated current filaments, until it becomes sufficiently strong to confine the particles within a filament. The laser-generated beam electrons are therefore strongly compressed while the electrons of the denser return current are expelled. The tenuous beam electrons are channeled into filaments, which are immersed in an almost uniform background return current. Such currents filaments can be remarkably stable according to PIC simulations [Bret et al., 2010b]. This magnetic trapping was identified as the main mechanism responsible for quenching the initial filamentation growth.

The main collisionless instability concerning laser-generated relativistic electron beam transport

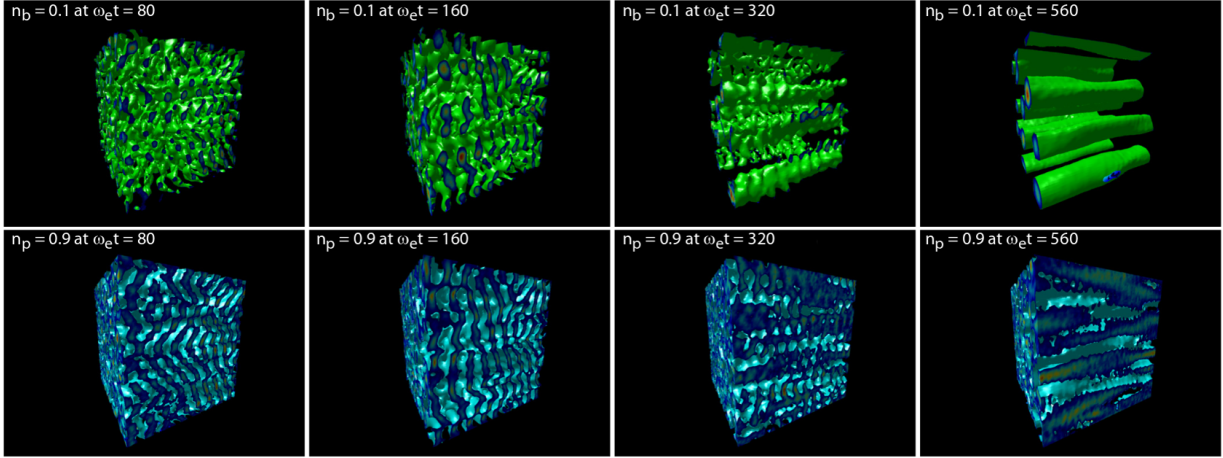


Figure 3.4: 3D PIC simulation of a Maxwell-Jüttner beam-plasma system with $n_b/n_e = 0.1$, $\gamma_b = 3$, $T_b = 50$ keV and $T_e = 5$ keV. Isosurfaces of the beam (upper plots) and plasma (lower plots) density profiles at successive times. The beam flows rightward [Bret et al., 2010b]

in solids or dense plasmas is the oblique instability which is mixture of the filamentation and two-stream instabilities. The nonlinear stage of this instability is illustrated in **Figure 3.4**. Numerical simulations of electron beam transport in plasmas have also confirmed that the oblique instability is an important heating mechanism of background electrons and may also induce the background ion heating due to decay of ion acoustic waves generated in the parametric decay of Langmuir waves.

3.2.3 Resistive Filamentation Instability

Collisions of the return current electrons are expected to influence the development of the instabilities in high density, low temperature regions due to the scaling of the background electron-ion collision frequency $\nu_{ei} \propto n_i/T_e^{3/2}$ (see **Appendix A, section A.3.2**). As a consequence, the previous results concerning the different instabilities inherent to the transport of laser-generated relativistic electron beam transport through heated solids or dense plasmas may be affected by these collisions. An analysis of the collisional two-stream instability for Maxwell-Jüttner electron distribution functions and using the electron-ion Landau operator (see **Appendix A, section A.2.2**) has been recently carried out, as illustrated in the left panel of **Figure 3.5**, according to [Robinson et al., 2014]. In the presence of collisions, the peak growth rate drops from $\delta_{TS} = 5.3 \times 10^{-3}$ to 1.1×10^{-3} , while the dominant wave number remains approximately the same. If strong enough, collisions may completely stabilize the two-stream mode. The oblique modes are affected by collisions in a similar fashion, exhibiting complete stabilization in the strongly collisional limit [Hao et al., 2012]. As first demonstrated by [Molvig, 1975], an opposite phenomenon occurs for the filamentation modes. For a dilute and energetic enough relativistic electron beam, collisions keep it unstable regardless of the transverse temperature. The right panel of **Figure 3.5**, which is extracted from [FIORE et al., 2010] by [Robinson et al., 2014], illustrates this tendency by comparing the wave number dependence of the

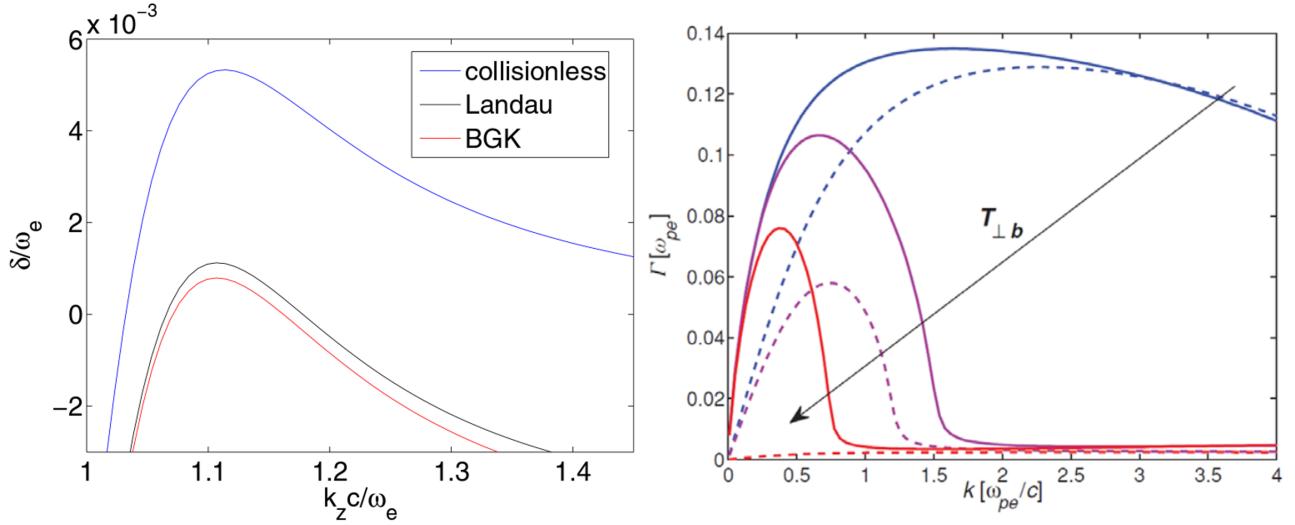


Figure 3.5: (Left panel) Growth rate of the two-stream instability (Maxwell-Juttner initial distribution function) normalized by ω_e versus k_z normalized by the plasma skin depth $\lambda_e = c/\omega_e$ with (red, black) and without (blue) electron-ion collisions for $n_e = 10^{23}$ cm^{-3} , $n_b/n_e = 0.01$, $T_b = 100$ keV, $\gamma_b = 3$, $T_e = 1$ keV, $Z^* = Z = 10$ and a Coulomb logarithm (see **Appendix A, section A.2.3**) $\ln \Lambda_{ei} = 2$; (Right panel) Filamentation growth rate (Maxwell-Juttner initial distribution function) normalized by ω_e versus k_z normalized by the plasma skin depth $\lambda_e = c/\omega_e$ in collisionless (dashed lines) and collisional (solid lines) configurations for $\gamma_b = 5$, $T_e = 10$ keV, $n_b/n_e = 0.1$, $\nu_{ei} = 0.5\omega_p$ and increasing transverse temperature $T_{b\perp} = 0.5$ keV (blue), $T_{b\perp} = 0.5$ keV (magenta) and $T_{b\perp} = 0.5$ keV (red). Both plots are taken from [Robinson et al., 2014]

collisionless and collisional filamentation growth rates for waterbag distributions (squared distribution functions in the momentum space fitting roughly Maxwell-Juttner distributions but allowing to separate the longitudinal temperature $T_{j,z}$ and the transverse one $T_{j,\perp}$). A BGK collision model (see **Appendix A, section A.3.1**) is employed with $\nu = 0.5\omega_p$. While the instability is weakened and confined to smaller wave numbers as the beam transverse temperature is increasing, it is also enhanced in the presence of collisions, especially in the large temperature limit. PIC simulations also confirmed the predicted robustness of the collisional filamentation and the generation of filamentary structures [Karmakar et al., 2008]. In this collisional regime, the filamentation instability is called the **resistive filamentation instability**. Let us derive a simple dispersion relation for this instability. We still assume $n_e \gg n_b$ and we still neglect collisions of beam electrons with plasma particles so that f_b still satisfies the Vlasov equation. Also, we still consider the quasi-neutrality $n_e - Z^*n_i = 0$ and we neglect the displacement current in the Maxwell-Ampere equation so that the Maxwell equations reduce to

$$\frac{\partial}{\partial \mathbf{r}} \times \mathbf{B} = \frac{4\pi}{c} \left(\mathbf{j}_e - e \int_{\mathbb{R}^3} \frac{\mathbf{p}}{\gamma m_e} f_b d^3 \mathbf{p} \right) \quad (3.31)$$

and

$$\frac{\partial}{\partial \mathbf{r}} \times \mathbf{E} = -\frac{1}{c} \frac{\partial \mathbf{B}}{\partial t}. \quad (3.32)$$

The background ions are still assumed immobile and the background electron dynamic is described by the Ohm's law (3.4)

$$\mathbf{E} = \eta \mathbf{j}_e \quad (3.33)$$

for which we retain only the main term. Also, we consider a constant resistivity $\eta = \eta_0$ in space and time. Finally, we still consider that the initial beam distribution function is a drifted Maxwell-Juttner distribution function. The set of equations for the self-generated electromagnetic fields gives

$$\frac{\partial \mathbf{B}}{\partial t} + \frac{\partial}{\partial \mathbf{r}} \times \left(\frac{\eta_0 c^2}{4\pi} \frac{\partial}{\partial \mathbf{r}} \times \mathbf{B} \right) = \eta_0 c \frac{\partial}{\partial \mathbf{r}} \times \mathbf{j}_b, \quad (3.34)$$

$$\frac{\partial \mathbf{E}}{\partial t} + \frac{\partial}{\partial \mathbf{r}} \times \left(\frac{\eta_0 c^2}{4\pi} \frac{\partial}{\partial \mathbf{r}} \times \mathbf{E} \right) = -\eta_0 \frac{\partial \mathbf{j}_b}{\partial t} \quad (3.35)$$

and consequently

$$\begin{cases} \widehat{\delta E}_z = \frac{i \frac{4\pi\omega}{c^2}}{k_x^2 - i \frac{4\pi\omega}{\eta_0 c^2}} \widehat{\delta j}_{b,z} & \text{(a)} \\ \widehat{\delta E}_x = -\eta_0 \widehat{\delta j}_{b,x} & \text{(b)} \end{cases} \quad (3.36)$$

The linearized Vlasov equation reads

$$\widehat{\delta f}_b = \frac{ie n_b^{(0)}}{\omega} \left[\widehat{\delta \mathbf{E}} + \frac{\mathbf{p} \cdot \widehat{\delta \mathbf{E}}}{1 - \frac{k_x p_x}{\gamma m_e \omega}} \frac{k_x}{\gamma m_e \omega} \mathbf{e}_x \right] \cdot \frac{\partial f_b^{(0)}}{\partial \mathbf{p}} \quad (3.37)$$

and gives consequently

$$\begin{aligned} \widehat{\delta j}_{b,z} &= - \frac{in_b^{(0)} e^2}{m_e \omega} \int_{\mathbb{R}^3} \frac{p_z}{\gamma} \left(\widehat{\delta E}_x \frac{\partial f_b^{(0)}}{\partial p_x} + \widehat{\delta E}_z \frac{\partial f_b^{(0)}}{\partial p_z} + \frac{k_x}{\gamma m_e \omega} \frac{p_x \widehat{\delta E}_x + p_z \widehat{\delta E}_z}{1 - \frac{k_x p_x}{\gamma m_e \omega}} \frac{\partial f_b^{(0)}}{\partial p_x} \right) d^3 \mathbf{p} \\ &= - \left[\frac{in_b^{(0)} e^2}{m_e \omega} \int_{\mathbb{R}^3} \frac{p_z}{\gamma} \frac{1}{1 - \frac{k_x p_x}{\gamma m_e \omega}} \frac{\partial f_b^{(0)}}{\partial p_x} d^3 \mathbf{p} \right] \widehat{\delta E}_x \\ &\quad - \left[\frac{in_b^{(0)} e^2}{m_e \omega} \int_{\mathbb{R}^3} \frac{p_z}{\gamma} \left(\frac{\partial f_b^{(0)}}{\partial p_z} + \frac{\frac{k_x p_z}{\gamma m_e \omega}}{1 - \frac{k_x p_x}{\gamma m_e \omega}} \frac{\partial f_b^{(0)}}{\partial p_x} \right) d^3 \mathbf{p} \right] \widehat{\delta E}_z \end{aligned} \quad (3.38)$$

By neglecting $\widehat{\delta E}_x$ compared to $\widehat{\delta E}_z$ in (3.38), due to the fact that in general the longitudinal beam current density j_{bz} is greater than the transverse component j_{bx} , and injecting (3.38) in (3.36 a), one

3.2. BEAM-PLASMA INSTABILITIES

finally finds the dispersion relation for the resistive filamentation instability

$$1 - \frac{\frac{\omega_b^2}{k_x^2 c^2}}{1 - i \frac{4\pi\omega}{k_x^2 \eta_0 c^2}} \left[\int_{\mathbb{R}^3} \frac{p_z}{\gamma} \frac{\partial f_b^{(0)}}{\partial p_z} d^3 \mathbf{p} + \int_{\mathbb{R}^3} \frac{p_z}{\gamma} \frac{\frac{k_x p_z}{\gamma m_e \omega}}{1 - \frac{k_x p_x}{\gamma m_e \omega}} \frac{\partial f_b^{(0)}}{\partial p_x} d^3 \mathbf{p} \right] = 0. \quad (3.39)$$

By performing the integrals for a low-temperature Maxwell-Juttner distribution function, the dispersion relation can finally be written with the form [Gremillet et al., 2002]

$$-i \frac{4\pi\omega}{\eta_0 \omega_b^2} + \left(\frac{k_x c}{\omega_b} \right)^2 + \frac{1}{\gamma_b^3} + \frac{1}{\gamma_b} \left(\frac{\beta_b}{\beta_{Th,b}} \right)^2 F' \left(\frac{1}{\beta_{Th,b}} \frac{\omega}{k_x c} \right) = 0 \quad (3.40)$$

where

$$F'(\xi) = \frac{1}{\sqrt{\pi}} \int \frac{1}{(u - \xi)^2} \exp(-u^2) du$$

is the derivative of the Fried–Compte function F and $\beta_{Th,b} = \sqrt{2k_B T_b / \gamma_b m_e c^2}$ is the thermal beam velocity normalized by c . The growth rate δ of the resistive filamentation instability can be deduced by looking for the solution of the dispersion relation (3.40) in the form $\omega = i\delta$. It is plotted in the left panel of **Figure 3.6**. The growth rate δ increases when increasing the plasma resistivity η_0 . For

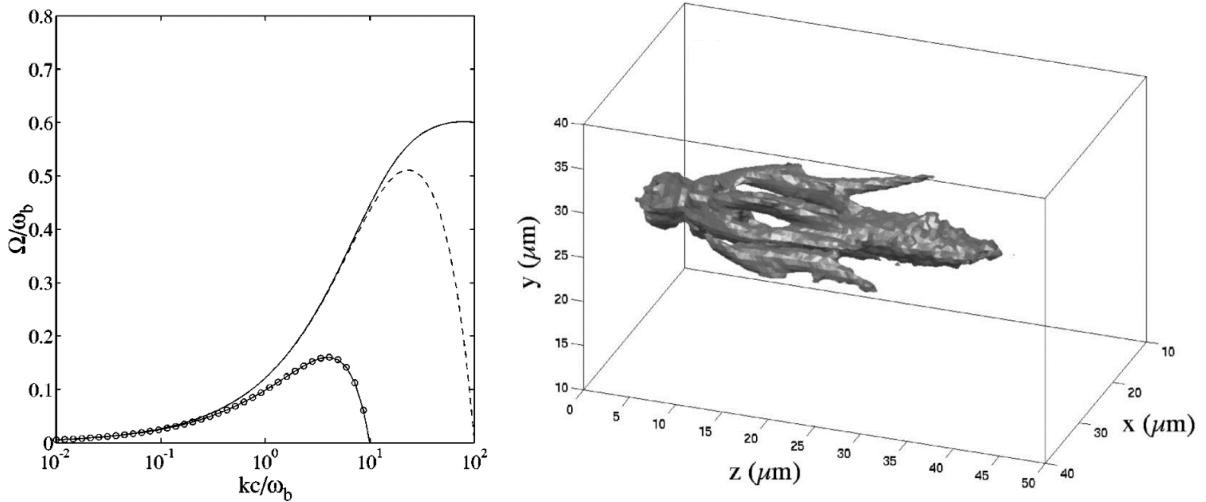


Figure 3.6: (Left panel) Growth rate of the resistive filamentation instability Ω normalized by the beam plasma frequency as a function of the wave vector in the transverse direction k normalized by the beam skin depth c/ω_b for $\beta_{Th,b}/\beta_b = 0.001$ (solid), 0.01 (dotted) and 0.1 (circles). The beam density is $n_b = 10^{20} \text{ cm}^{-3}$, the beam Lorentz factor is $\gamma_b = 2$, and the target resistivity is $\eta_0 = 10^{-6} \Omega \cdot \text{m}$; (Right panel) 3D Isosurface associated to $\mathbf{j}_b = 4.8 \cdot 10^{11} \text{ A} \cdot \text{cm}^{-2}$ of a Gaussian-shaped beam of monoenergetic 0.5 MeV electron beam penetrating a 0.5-eV silica solid at normal incidence. The beam current density is plotted at time $t = 405 \text{ fs}$ from a 3D PaRIS hybrid PIC simulation. Both plots are taken from [Gremillet et al., 2002].

$\beta_{Th,b}/\beta_b = 0.01$ and $\eta_0 = 10^{-8} \Omega \cdot \text{m}$, the growth rate maximizes at a value three times lower than

observed in the left panel of **Figure 3.6**. For a cold beam $T_b = 0$, the asymptotic approximation of F' can be used ($F'(\xi) \sim \xi^{-2}$ when $\xi \gg 1$), which leads to [Gremillet et al., 2002]

$$\frac{4\pi}{\eta_0\omega_b} \left(\frac{\delta}{\omega_b}\right)^3 + \left[\left(\frac{k_x c}{\omega_b}\right)^2 + \frac{1}{\gamma_b^3} \right] \left(\frac{\delta}{\omega_b}\right)^2 - \frac{1}{\gamma_b} \left(\frac{\beta_b k_x c}{\omega_b}\right)^2 = 0 \quad (3.41)$$

In the high- k_x limit $k_x c/\omega_b \gg \sqrt{4\pi\beta_b/\eta_0\omega_b\sqrt{\gamma_b}}$, when the magnetic diffusion is faster than the pinching of the perturbation, the instability growth rate is saturated at $\delta = \omega_b\beta_b/\sqrt{\gamma_b}$.

3.3 Temperature Dependence of Fast Electrons Transport

3.3.1 Temperature Dependence of the Background Electrical Resistivity and Ionization State

The key ingredient for fast electron transport models are the transport coefficients and the ionization states of the material through which the fast electrons propagate. An ideal (fully ionized, weakly coupled, non degenerate) plasma model is insufficient. At high density, it is important to account for the Fermi-Dirac electron statistics. The exclusion principle causes the electrons to have random momentum even at zero temperature. These quantum effects become significant when the electrons temperature is below the Fermi energy

$$k_B T_e < E_F = \frac{\hbar^2}{2m_e} (3\pi^2 n_e)^{2/3}. \quad (3.42)$$

Ionization state

The ionization state Z^* of the material defines the ratio of free and bound electrons in the material. Based on the Thomas-Fermi model, [More, 1985] has proposed a useful formula for the ionization state as a function of the density $\rho = n_i m_i$ and electron temperature T_e of the material. It reads

$$Z^* = Z_{TF}^* \left(\frac{T_e}{Z^{4/3}}, \frac{n_i m_u}{Z} \right) = Z \frac{X_Z}{1 + X_Z + \sqrt{1 + 2X_Z}} \quad (3.43)$$

3.3. TEMPERATURE DEPENDENCE OF FAST ELECTRONS TRANSPORT

where Z is the atomic number of the material, m_u is the atomic mass unit and

$$\begin{aligned}
 T_0 &= T_e[eV]/Z^{4/3}, \\
 R &= n_i m_u / Z, \\
 T_f &= \frac{T_0}{1 + T_0}, \\
 A_Z &= 0.003323 T_0^{0.9718} + 9.26148 \cdot 10^{-5} T_0^{3.10165}, \\
 B_Z &= -\exp -1.763 + 1.43175 T_f + 0.31546 T_f^7, \\
 C_Z &= -0.366667 T_f + 0.983333, \\
 Q_1 &= A_Z R^{B_Z}, \\
 Q &= \left(R^{C_Z} + Q_1^{C_Z} \right)^{1/C_Z} \text{ and} \\
 X_Z &= 14.3139 Q^{0.6624}.
 \end{aligned}$$

This formula is accurate for $Z \gtrsim 10$ and it badly estimates the ionization state at a low temperature. Indeed, the Thomas-Fermi model is inadequate for capturing the metal-insulator transition since it neglects any atomic structure effects on the ionization equilibrium and thus gives a too high ionization level at low temperatures. Therefore, [Desjarlais, 2001] proposed a weighted blend of Thomas-Fermi and a single ionization Saha model with a pressure ionization correction. This model provides smooth transitions between the Thomas-Fermi model and the non-ideal Saha limit. The Saha contribution is determined from

$$f_e = \frac{1}{2} \left(\sqrt{K^2 + 4K} - K \right)$$

where

$$K = 2 \frac{g_1}{g_0} \frac{1}{n_i} \left(\frac{2\pi m_e k_B T_e}{\hbar^2} \right)^{3/2} \exp \left\{ -\frac{I}{k_B T_e} \left[1 - \left(\frac{1.5e^2}{I(3/4\pi n_i)^{1/3}} \right)^{3/2} \right] \right\}.$$

The statistical weights g_0 and g_1 correspond to the ground state of the neutral atom and singly ionized ion respectively, I is the first ionization energy, n_i is the total neutral plus ion number density. For both Cu and Al, $g_0 = 2$ and $g_1 = 1$, but in general the level degeneracy $g = 2J + 1$ is used. The second term in parentheses in the exponential gives a semi-empirical pressure ionization correction. The ionization state is finally given by

$$Z^* = f_e^{2/Z_{TF}^*} Z_{TF}^* + \left(1 - f_e^{2/Z_{TF}^*} Z_{TF}^* \right) f_e, \quad (3.44)$$

according to [Desjarlais, 2001].

Electrical resistivity

The electrical resistivity is a key parameter for relativistic electron beam transport. According to the Drude model, it can be written as

$$\eta = \frac{m_e \nu_e}{n_e e^2} \quad (3.45)$$

where ν_e is the background electron relaxation rate. The Lee-More model [Lee and More, 1984] is usually used to estimate the relaxation rate. It takes into account the electron degeneracy by using the Fermi-Dirac distribution (see **Appendix B, section B.2.4**) that covers the domain of temperatures from $k_B T \approx E_F$ to the hot Spitzer regime [Cohen et al., 1950] [Spitzer and Härm, 1953]. For lower temperatures in the solid and liquid phase, a different electron collision time is used. It is evaluated according to

$$\tau = \frac{1}{\nu_e} = \max \{ \tau_{ec}, \tau_{\text{melt}}, \tau_{\text{min}} \} \quad (3.46)$$

where the electron collision frequency $\tau_{ec}^{-1} = \tau_{ei}^{-1} + \tau_{en}^{-1}$ accounts for the collisions on ions τ_{ei}^{-1} with the Lee-More degeneracy corrections and on atoms τ_{en}^{-1} improved by [Desjarlais, 2001] while τ_{melt} and τ_{min} stem from a Bloch-Gruneisen melting model [Ziman, 1961] and a minimum time based on inter-atom spacing $\tau_{\text{min}} = (3/4\pi n_i)^{1/3} / \sqrt{(k_B T_e + E_F)/m_e}$. The melt model gives $\tau_{\text{melt}} = 50(T_{\text{melt}}/T)\tau_{\text{min}}$ with the material dependant constant 50 decreasing somewhat for $T > T_{\text{melt}}$. In the left panel of **Figure 3.7**, the electrical resistivity of Beryllium with $\rho = 1.84 \text{ g.cm}^{-3}$ taken from [Robinson et al., 2014] is plotted versus the temperature and is also compared with numerical results allowing to determine the free parameters of the Lee-More model. Also, the hot Spitzer resistivity with and without the electron-electron collisions correction factor (see **Appendix B, section B.2.2**) is plotted with the cold melting model. For Hydrogen plasmas, as suggested by [Lambert et al., 2011], comparing it with ab initio molecular dynamic computations, the electrical resistivity can be evaluated as $\eta^{-2} = \eta_{\text{Hubbard}}^{-2} + \eta_{\text{Spitzer}}^{-2}$ where η_{Spitzer} is the hot temperature Spitzer plasma transport coefficient and η_{Hubbard} is the low temperature transport coefficient found by [Hubbard, 1966]. Comparisons between such expression for Hydrogen plasmas with different densities are plotted in the right panel of **Figure 3.7**.

The main disadvantage of such models (Lee-More and Hubbard-Spitzer) is that they assume $T_i = T_e = T$ and they do not account for a different ion/lattice temperature T_i than the conducting electron temperature T_e . A two-temperature model for the electrical resistivity of Copper and Aluminum has been proposed by [Eidmann et al., 2000] and later improved by [Chimier et al., 2007]. In this model, the collision frequency of the electrons ν_e is evaluated by taking the weighted average of the electron relaxation rate in different temperature regimes

$$\nu_e^{-2} = (\nu_{e-ph} + \nu_{e-e})^{-2} + \nu_c^{-2} + \nu_{\text{Spitzer}}^{-2}. \quad (3.47)$$

In the low temperature regime, the mean free path is evaluated by $v_e / (\nu_{e-ph} + \nu_{e-e})$ where ν_{e-ph} is the electron-phonon collision rate, ν_{e-e} is the electron-electron collision rate and $v_e = \sqrt{(2E_F + T_e)/m_e}$ is the electron velocity. In the high temperature regime, the mean free path is evaluated by $v_e / \nu_{\text{Spitzer}}$. In the intermediate range of temperatures, the mean free path is written as v_e / ν_c where $\nu_c = v_e / (3/4\pi n_i)^{1/3}$. However, for other materials than Copper and Aluminum, experimental or numerical data are needed to fix the free parameters of the model. The electrical resistivities η from

3.3. TEMPERATURE DEPENDENCE OF FAST ELECTRONS TRANSPORT

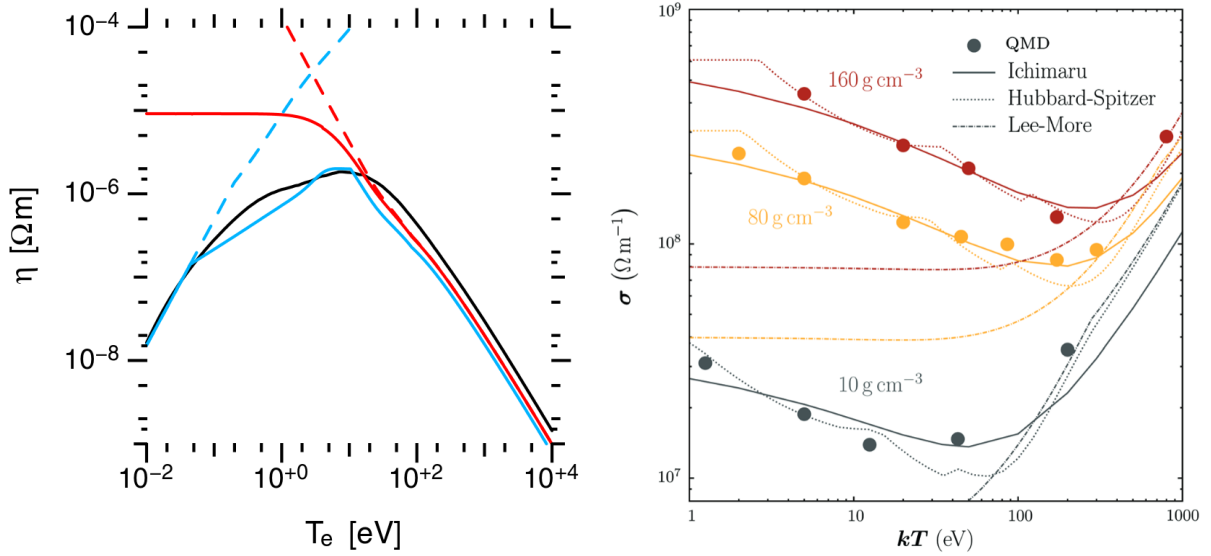


Figure 3.7: (Left panel) Electrical resistivity of Beryllium with $\rho = 1.84 \text{ g.cm}^{-3}$ taken from [Robinson et al., 2014] versus the temperature (cyan solid curve) compared with numerical results (black solid curve). The hot Spitzer resistivity (red) with (solid line) and without (dashed line) the electron-electron collisions correction factor (see **Appendix B, section B.2.2**) is also plotted with the cold melting model (dashed cyan line). (Right panel) Electrical conductivity ($\sigma = 1/\eta$) taken from [Lambert et al., 2011] obtained numerically for Hydrogen plasmas with different densities as a function of temperature compared with Hubbard-Spitzer, Lee-More, and Ichimaru models.

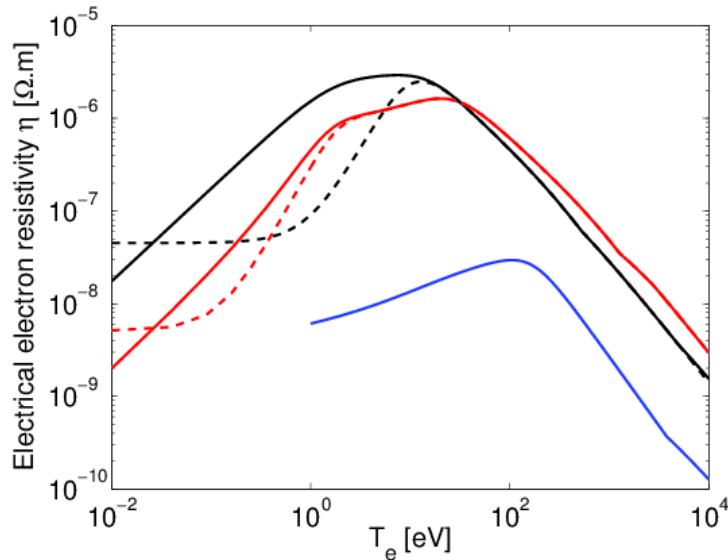


Figure 3.8: Electrical resistivity η for Aluminum (black) and Copper (red) as a function of the electron temperature plotted in two particular cases : $T_i = 300K$ (dashed curves) and $T_i = T_e$ (solid curves) and for Hydrogen ($\rho = 50 \text{ g.cm}^{-3}$) with $T_i = T_e$ (solid blue curve).

the Eidmann-Chimier model are plotted for Aluminum, Copper as well as the Hubbard-Spitzer electrical resistivity of a highly compressed Hydrogen in **Figure 3.8**. Concerning the Hubbard electrical

resistivity, a least square fit from the ion-ion coupling parameter Γ table of [Hubbard, 1966] is used to avoid discontinuities. For dielectric materials (insulators), the situation is much more complicated and one usually needs extensive quantum molecular dynamic computations. For example, the left panel of **Figure 3.9** shows huge differences between the electrical resistivity given by the Lee-More model and such a computation, solving the the Kubo-Greenwood equation [MacLellan et al., 2013]. For a same material, [McKenna et al., 2011] found strong differences between the electrical resistivity of amorphous and diamond Carbon, as illustrated in the right panel of **Figure 3.9**.

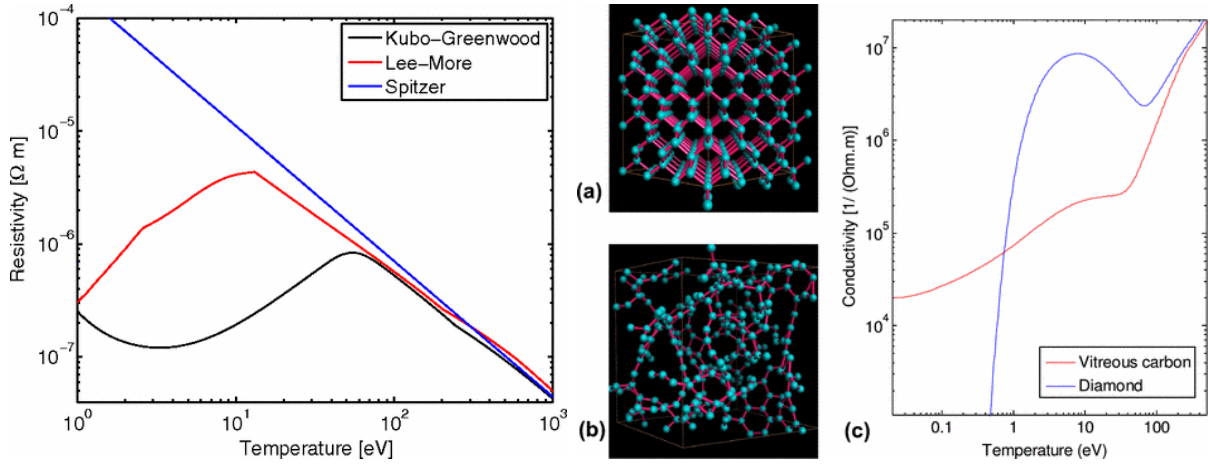


Figure 3.9: (Left panel) Theoretical calculations of the resistivity of silicon as a function of temperature: The black line represents ab initio quantum molecular dynamic calculations coupled with the Kubo-Greenwood equation, the red line the Lee-More model, and the blue line the Spitzer model [MacLellan et al., 2013]. (Right panel) Structure of (a) diamond and (b) vitreous carbon. (c) Electrical conductivity as a function of temperature for both carbon allotropes computed with a quantum molecular dynamic code [McKenna et al., 2011].

3.3.2 Heat Equations

The electrical resistivity of background electrons may change significantly due to the heating induced by the beam energy deposition, the Ohmic heating by the return current and the resistive filamentation instability. This heating needs to be accounted for in fast electron transport models. Under the assumption $T_e = T_i = T$, the energy conservation equation reads (see **Appendix B, section B.3.1**)

$$C_V \left[\frac{\partial}{\partial t} + \left(\mathbf{u} \cdot \frac{\partial}{\partial \mathbf{r}} \right) \right] (T) + \frac{\partial}{\partial \mathbf{r}} \cdot \mathbf{q} = -P \frac{\partial}{\partial \mathbf{r}} \cdot \mathbf{u} + \boldsymbol{\tau} \odot \left(\frac{\partial}{\partial \mathbf{r}} \otimes \mathbf{u} \right) + \mathbf{j} \cdot \mathbf{E} + W \quad (3.48)$$

where

$$C_V = \frac{3}{2} k_B (Z^* + 1) n_i$$

is the plasma thermal capacity (electrons + ions). According to the assumptions presented in the **section 3.1.1** of this chapter, the magnetization and the ion conduction are neglected so that the

3.3. TEMPERATURE DEPENDENCE OF FAST ELECTRONS TRANSPORT

thermal flux reduces to

$$\mathbf{q} = \mathbf{q}_e = -\kappa_e \frac{\partial T_e}{\partial \mathbf{r}} \quad (3.49)$$

where κ_e is the background electron thermal conduction evaluated within the same models as presented in the previous subsection for the electrical resistivity η . These two transport coefficients are indeed related by the Lorenz relation

$$\frac{\kappa_e}{\sigma T_e} = \gamma_L \quad (3.50)$$

where γ_L is the Lorenz factor (see **Appendix B, section B.2.4**). The background fluid is assumed to be incompressible ($\partial/\partial \mathbf{r} \cdot \mathbf{u} = 0$), the viscosity is neglected and the ions are assumed immobile. Thus, the fluid current density reduces to the background electron return current $\mathbf{j} = \mathbf{j}_e$ and the electric field is given by the system of equations $\{(3.7), (3.8)\}$ presented in **section 3.1.1**. The direct collisional heating of the background electrons by the beam electrons is taken into account via the heating source term

$$W = - \int_{\mathbb{R}^3} \varepsilon \left(\frac{\partial f_b}{\partial t} \right)_{\text{coll}} d^3 \mathbf{p} \quad (3.51)$$

which is nothing else than the energy lost by the beam electrons due to collisions with the background electrons (cf. **Chapter 4**).

In the two-temperature model, which is notably the case for relativistic electron transport in solids, the background electrons are firstly heated due to the beam energy deposition. Then, they transfer their energy to ions. Therefore, Equation (3.48) must be replaced by the two energy conservation equations

$$C_{V,e} \left[\frac{\partial}{\partial t} + \left(\mathbf{u}_e \cdot \frac{\partial}{\partial \mathbf{r}} \right) \right] (T_e) + \frac{\partial}{\partial \mathbf{r}} \cdot \mathbf{q}_e = W + Q_{ei}. \quad (3.52)$$

and

$$C_{V,i} \left[\frac{\partial}{\partial t} + \left(\mathbf{u}_i \cdot \frac{\partial}{\partial \mathbf{r}} \right) \right] (T_i) = Q_{ie} \quad (3.53)$$

where

$$Q_{ie} = -Q_{ei} + \eta \mathbf{j}_e^2 = 2 \frac{m_e}{m_i} C_{V,e} \bar{v}_{ei} (T_e - T_i). \quad (3.54)$$

For plasmas, \bar{v}_{ei} may be expressed by the [Lee and More, 1984] formula accounting for the electrons degeneracy at $T_e \approx E_f$ (see **Appendix B, section B.2.4**) while

$$C_{V,e} = \frac{3}{2} k_B Z^* n_i \quad \text{and} \quad C_{V,i} = \frac{3}{2} k_B n_i \quad (3.55)$$

are the plasma electron and ion thermal capacities. However, these last expressions need to be improved for low temperature materials in the solid/liquid phase.

3.3.3 Plasma Heating by an Electron Beam

A simple model have been proposed by [Bell and Kingham, 2003] and [Davies, 2003] in order to account for the effects of the background electron heating. These are the self-collimation of the beam and the beam hollowing, respectively. The model assumes that the return current equals the beam current as explained in **section 3.1.1**

$$\mathbf{j}_b + \mathbf{j}_e = 0. \quad (3.56)$$

The background electron dynamic is modelled according to the Ohm's law retaining only the main term

$$\mathbf{E} = \eta \mathbf{j}_e = -\eta \mathbf{j}_b \quad (3.57)$$

with a resistivity of the form

$$\eta = \eta_0 \left(\frac{T}{T_0} \right)^\alpha \quad (3.58)$$

where T_0 is a characteristic temperature. The background electron heating is taken into account according to Equation (3.52), neglecting the ion heating and the thermal conduction. In addition, [Bell and Kingham, 2003] assumes the plasma is fully ionized and thus estimates the electron thermal capacity according to $C_{V,e} = (3/2)k_B Z n_i$. Contrary to [Bell and Kingham, 2003], [Davies, 2003] just assumes a constant thermal capacity $C_{V,e}$. The heat equation (3.52) thus reduces to

$$C_{V,e} \frac{\partial T_e}{\partial t} = \eta \mathbf{j}_b^2. \quad (3.59)$$

This equation can be generalized to the case of a metallic target with the solid Sommerfeld thermal capacity $C_{V,e} = C_{V,e0}(T_e/T_0)$, replacing in the expressions below the parameter α by $\alpha + 1$ and $C_{V,e}$ by $C_{V,e0}$. The magnetic field is given by the Maxwell-Faraday equation

$$\frac{\partial \mathbf{B}}{\partial t} = -c \frac{\partial}{\partial \mathbf{r}} \times \mathbf{E} = \eta c \frac{\partial}{\partial \mathbf{r}} \times \mathbf{j}_b + c \frac{\partial \eta}{\partial \mathbf{r}} \times \mathbf{j}_b. \quad (3.60)$$

The beam is assumed to be rigid, collimated and axisymmetric of the form

$$\mathbf{j}_b = j_{b0}(r) \left[\Pi \left(t - \frac{z}{v_b} \right) - \Pi(t) \right] \mathbf{e}_z \text{ with } j_{b0} = -j_0 \exp \left(-\frac{r^2}{r_b^2} \right) \quad (3.61)$$

where $j_0 > 0$ and Π is the Heaviside function. It is emitted from $z = 0$ and moves with the constant velocity $\mathbf{v}_b = v_b \mathbf{e}_z$. The Gaussian radial shape corresponds to the shape of the laser pulse. Therefore, the magnetic field is azimuthal $\mathbf{B} = B_\theta \mathbf{e}_\theta$ and the electric field is longitudinal $\mathbf{E} = E_z \mathbf{e}_z$. The beam transport strongly depends on the parameter α . In the case where $\alpha > 1$ which corresponds to cold solid/liquid temperatures ($0 < \alpha < 2$ for $k_B T_e < E_F$ according to the resistivity models presented in **section 3.3.1**), one finds diverging solutions for the temperature ($T_e \rightarrow \infty$) at very short times $t - (z/v_b) = C_{V,e} T_0 / (\alpha - 1) \eta_0 j_{b0}^2$. However, this unphysical behaviour must be mitigated because the

3.3. TEMPERATURE DEPENDENCE OF FAST ELECTRONS TRANSPORT

temperature growth for α is actually limited by the Fermi temperature $k_B T_e \approx E_F$ since that, at this temperature, the parameter α becomes negative and then reach the value $\alpha = -3/2$ of the hot temperature plasma regime. Thus, according to [Davies, 2003], (3.59) gives

$$T = \begin{cases} T_0 \exp\left(\frac{\eta_0 j_{b0}^2 \tau}{C_{V,e} T_0}\right) & \text{if } \alpha = 1 \\ T_0 \left[1 + (1 - \alpha) \frac{\eta_0 j_{b0}^2 \tau}{C_{V,e} T_0}\right]^{1/(1-\alpha)} & \text{if } \alpha < 1 \end{cases} \quad (3.62)$$

where it has been noted $\tau = t - (z/v_b)$. Knowing the temperature, one can express the electric field according to Ohm's law

$$E_z = \begin{cases} -\eta_0 j_{b0} \exp\left(\frac{\eta_0 j_{b0}^2 \tau}{C_{V,e} T_0}\right) & \text{if } \alpha = 1 \\ -\eta_0 j_{b0} \left[1 + (1 - \alpha) \frac{\eta_0 j_{b0}^2 \tau}{C_{V,e} T_0}\right]^{\alpha/(1-\alpha)} & \text{if } \alpha < 1 \end{cases} \quad (3.63)$$

And, the magnetic field follows from the Maxwell-Faraday equation by making the change of variables $t \rightarrow \tau$

$$B_\theta = \begin{cases} -c \frac{dj_{b0}}{dr} \frac{C_{V,e} T_0}{j_{b0}^2} \left[1 + \left(\frac{2\eta_0 j_{b0}^2 \tau}{C_{V,e} T_0} - 1\right) \frac{T}{T_0}\right] & \text{if } \alpha = 1 \\ -c \frac{dj_{b0}}{dr} \frac{C_{V,e} T_0}{j_{b0}^2} \left[1 + \frac{1 + \alpha T}{1 - \alpha T_0} - \frac{2}{1 - \alpha} \frac{\eta}{\eta_0}\right] & \text{if } \alpha < 1 \end{cases} \quad (3.64)$$

Self-collimation of the beam

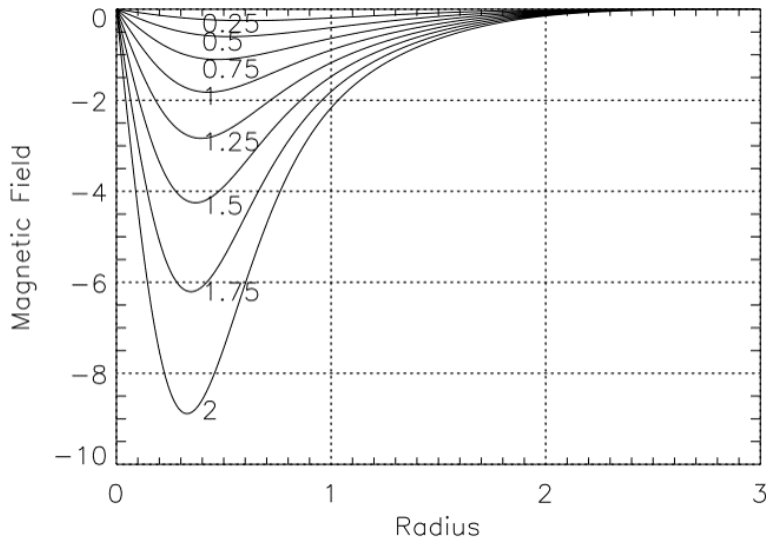


Figure 3.10: Magnetic field B_θ normalized by $j_0 \tau_0 / c$ versus the radius r normalized by r_b at different times τ / τ_0 taken from [Davies, 2003]

In the limit of weak heating $\tau/\tau_0 \ll 1$ where

$$\tau_0 = \frac{C_{V,e}T_0}{\eta_0 j_{b0}^2}, \quad (3.65)$$

one obtains from (3.63) and (3.64) to first order in τ/τ_0

$$E_z = -\eta_0 j_{b0} \left(1 + \alpha \frac{\tau}{\tau_0} \right) \quad (3.66)$$

and

$$B_\theta = -\eta_0 c \frac{dj_{b0}}{dr} \tau \quad (3.67)$$

for $\alpha \leq 1$. This results is similar to the one obtained by [Fill, 2001], presented in **section 3.1.2**. The magnetic field is negative and it reaches a minimum value at $r = r_b/\sqrt{2}$, as illustrated in **Figure 3.10**. This magnetic field may be responsible for the beam pinching. [Bell and Kingham, 2003] estimated the angle θ that a fast electron will be deflected while propagating over the distance $r_b/\tan\theta_{1/2}$ by

$$\theta = \frac{|eB_\theta|r_b}{\gamma m_e c \tan\theta_{1/2}} \quad (3.68)$$

where the unperturbed beam doubles its radius. here, $\theta_{1/2}$ is the divergence half-angle of the beam (which has not been taken into account in the previous derivations). The collimation condition can be estimated as $\theta = \theta_{1/2}$. For example, [Bell and Kingham, 2003] considered the Spitzer resistivity ($\alpha = -3/2$) and a fast electron beam with a mean kinetic energy $k_B T_b$ and a current I_b , that is related to the laser intensity I_L as $I_b = |e|\eta_{L \rightarrow e} I_L$ where $\eta_{L \rightarrow e}$ is the laser-to-electrons conversion efficiency. Approximating $dj_{b0}/dr \approx -j_0/r_b$ where $j_0 = I_b/k_B T_b$, they conclude that the beam collimation occurs if

$$\theta_{1/2} \tan\theta_{1/2} = \frac{3|e|n_e k_B T_b}{\gamma m_e c \beta \eta_{L \rightarrow e} I_L} \left[\frac{2\eta_0 j_0^2}{3|e|n_e} + T_0^{5/2} \right]^{2/5}. \quad (3.69)$$

Consequently, considering the experimental scaling (1.71) for the divergence half-angle $\theta_{1/2}$, we deduce that $\theta_{1/2}$ is in general too high for allowing the self-collimation of the beam.

Beam hollowing

According to [Davies, 2003], in the opposite limit of a strong heating $\tau \gg \tau_0$, one obtains

$$E_z = \begin{cases} -\eta_0 j_{b0} \exp\left(\frac{\eta_0 j_{b0}^2 \tau}{C_{V,e} T_0}\right) & \text{if } \alpha = 1 \\ -\eta_0^{1/(1-\alpha)} j_{b0}^{(1+\alpha)/(1-\alpha)} \left[\frac{(1-\alpha)\tau}{C_{V,e} T_0}\right]^{\alpha/(1-\alpha)} & \text{if } \alpha < 1 \end{cases} \quad (3.70)$$

and

$$B_\theta \approx -(1+\alpha)\eta c \frac{dj_{b0}}{dr} \tau \quad (3.71)$$

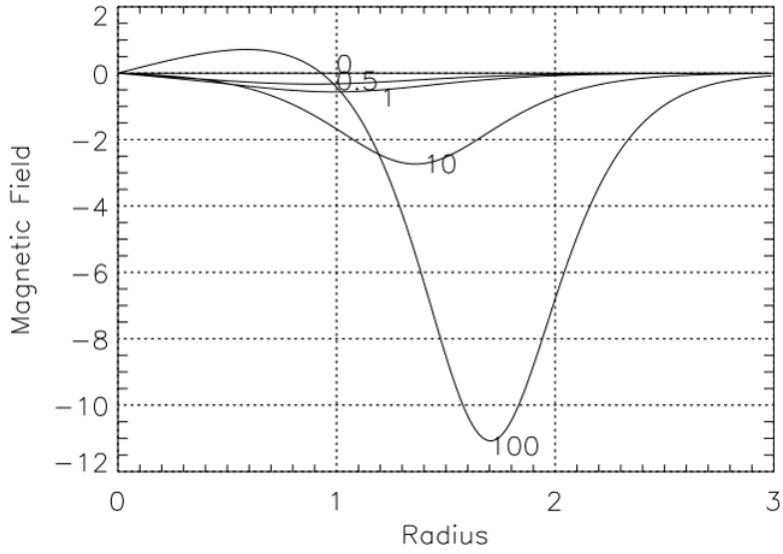


Figure 3.11: Magnetic field B_θ normalized by $j_0\tau_0/c$ versus the radius r normalized by r_b at different times τ/τ_0 taken from [Davies, 2003]

for $\alpha \leq 1$. It is striking to notice that for $\alpha < -1$ typical of the Spitzer regime, the electric field decreases with the current beam density and the magnetic field changes sign as illustrated in **Figure 3.11**. This positive value of B_θ deviates the beam electrons from the propagation axis and tends to hollow the beam. This effect has been later observed experimentally and numerically [Davies et al., 2006] [McKenna et al., 2011].

Chapter 4

Collisional Effects in Relativistic Electron Transport through Solids and Dense Plasmas

"If quantum mechanics hasn't profoundly shocked you, you haven't understood it yet."

Niels Bohr

4.1. BINARY COLLISIONS OF A RELATIVISTIC ELECTRON WITH BACKGROUND PARTICLES

This chapter review the theory of collisions of laser-generated relativistic electrons with particles of the material they are propagating through, such as free electrons, bound electrons, screened free electrons or ions. Due to the fact that the beam electrons travel at a relativistic velocity much greater than background electron or ion velocities, the principal effects of collisions are the beam electrons energy losses and their angular scattering. As the beam electron density is much less than the background electron density $n_b \ll n_e$, a single fast particle model provides an adequate description of these drag and scattering processes. After describing the differential cross section for collisions of a relativistic electron with a background particule at rest, the following subsections are devoted to the slowing down and angular scattering theories of a relativistic electron. The last subsection presents the relativistic Vlasov-Fokker-Planck equation for the laser-generated electron beam that describes these effects.

4.1 Binary Collisions of a Relativistic Electron with Background Particles

4.1.1 Electron-Electron Binary Collisions

Let us consider firstly a collision of a relativistic electron with a momentum \mathbf{p} with a target electron $\alpha \in \{\text{free } e^-, \text{ bound } e^- \text{ or free screened } e^-\}$ with a momentum \mathbf{p}_α such that

$$|\mathbf{p}_\alpha| \ll |\mathbf{p}|. \quad (4.1)$$

Thus, the target electron can be assumed to be initially at rest and one has the following relations between the center of mass frame and the laboratory frame :

$$\left\{ \begin{array}{l} \varepsilon^* = \gamma^* m_e c^2 = \sqrt{\frac{\gamma+1}{2}} m_e c^2 \quad (a) \\ \mathbf{p}^* = \sqrt{\frac{\gamma+1}{2}} \mathbf{p} \quad (b) \\ \sin \theta^* = \frac{\sqrt{\frac{\gamma+1}{2}} \sin 2\theta}{1 + \left(\frac{\gamma+1}{2} - 1\right) \sin^2 \theta} \quad (c) \end{array} \right. \quad (4.2)$$

where * means that the values are taken in the center of mass frame, γ is the Lorentz factor of the relativistic electron projectile and θ is the scattering angle. Consequently, one can obtain a relation between the normalized energy loss in one binary collision $w = \frac{\Delta\gamma}{\gamma-1}$ and the scattering angle θ^*

$$w = \frac{1 - \cos \theta^*}{2}, \quad (4.3)$$

starting from the momentum 4-vector invariance and using the momentum and energy conservation relations. It implies that

$$dw = \frac{d\Omega^*}{4\pi}. \quad (4.4)$$

and one can interchangeably use the differential cross sections

$$\left(\frac{d\sigma_\alpha}{dw}\right) = 4\pi \left(\frac{d\sigma_\alpha}{d\Omega^*}\right) \quad (4.5)$$

and $(d\sigma_\alpha/d\Omega^*)$. By using the fundamental principle of Einstein's mechanics for the effective particle motion in the Coulomb central force, one can relate the collision impact parameter \mathbf{b} and the normalized energy loss w by the following formula

$$w = \frac{2e^4}{m_e v^2} \frac{1}{(\gamma - 1)m_e c^2} \frac{1}{b^2} \quad (4.6)$$

As a consequence, similarly to the non relativistic case (see **Appendix A, section A.2.1 and A.2.3**), one has to distinguish between collisions

- with an impact parameter $b_{e,\min} < b < b_{e,\max}$ for collisions with a small momentum transfer from the relativistic electron to a free plasma electron target where

$$b_{e,\min} = \frac{\hbar}{2p^*} \quad (4.7)$$

is the De Broglie wavelength of electrons in the center of mass frame and

$$b_{e,\max} = \max \left\{ \lambda_{\text{Debye}}, \left(\frac{3}{4\pi n_i} \right)^{1/3} \right\} \quad (4.8)$$

is the plasma screening length as explained for the non-relativistic case in **Appendix A, section A.2.2**. Besides, $b_{e,\min}$ is directly chosen to be the De Broglie wavelength here. Indeed, in the case of a relativistic electron projectile, the De Broglie wavelength is always much larger than the Landau length. In the relativistic approach considered here, it is more convenient to deal with w instead of b . The equivalent boundaries are therefore $w_{\min} < w < w_{\max}$. $w_{\max} = 1/2$ must be taken due to the indiscernability of the electrons. That means that it is the more energetic electron outgoing from the collision which is considered as the primary electron (projectile). $w_{\min} = w_c$ is a cut-off used to distinguish the binary collisions from the collective interaction. It is assumed that $w_{\min} = w_c$ is much less than the beam electron energy and much greater than the energy of any electron in the material. One may estimate it by $(b_{e,\min}/b_{e,\max})^2$.

- with an impact parameter $b > b_{e,\max}$ for collisions with a small momentum transfer from the relativistic electron to a bound or screened free plasma electron target, which are affected by a collective contribution of the surrounding electrons. The equivalent boundary is $w < w_c$ and

4.1. BINARY COLLISIONS OF A RELATIVISTIC ELECTRON WITH BACKGROUND PARTICLES

this collective part will be treated in the next subsection devoted to the fast electron slowing down.

- with an impact parameter $b < b_{e,\min}$ for collisions of beam electrons with a large momentum transfer. Due to the fact that the probability of such a collision is small compared to the two previous ones, we neglect this contribution.

For the binary part, one can use the Möller scattering formula [Möller, 1932]. It consists in an approximate solution to the Dirac equation to order $\alpha v/c$ (the first Born approximation) where α is the fine structure constant. Indeed, [Möller, 1932] considered two interacting electrons, described by the two component Dirac wave-functions; He ignored the two components referring to negative energy states. He expressed the charge and current densities corresponding to the transition of the electron 1 from the initial state to the final state thanks to the obtained Dirac matrix tensor. In accordance with a procedure proposed by Klein in 1927, he then expressed the corresponding retarded potentials he obtained thanks to the Maxwell equations with the deduced charge and current densities of the particle 1 as sources. Finally, he solved the Dirac equation for the particle 2 with the presence of these fields and he identified the transition probability for the corresponding two-body system. Although the method was controversial because of its unsymmetrical approach and the lack of electromagnetic fields quantization, the result was readily confirmed in experiments [Champion, 1932] and a few years later by more rigorous quantum electrodynamic treatments [Bhabha, 1936], as well explained in [Beretstetskii et al., 1982]. The Moller differential cross section reads

$$\left(\frac{d\sigma}{d\Omega^*}\right)_{e,f} = \frac{e^4(\mathbf{p}^{*2}c^2 + \varepsilon^{*2})^2}{4\mathbf{p}^{*4}\varepsilon^{*2}} \left[\frac{4}{\sin^4\theta^*} - \frac{3}{\sin^2\theta^*} + \left(\frac{\mathbf{p}^{*2}c^2 + \varepsilon^{*2}}{\mathbf{p}^{*2}}\right)^2 \left(1 + \frac{4}{\sin^2\theta^*}\right) \right]. \quad (4.9)$$

The first term in the square brackets correspond to the relativistic generalization of the Rutherford differential cross section formula (see **Appendix A, section A.2.1**) while the other terms account for the quantum spin and exchange effects. Usually, as already mentioned, one may use the equivalent and simpler form

$$\left(\frac{d\sigma}{dw}\right)_{e,f} = \frac{2\pi e^4}{(\gamma-1)\beta^2 m_e^2 c^4} \left[\frac{1}{w^2} + \frac{1}{(1-w)^2} + \left(\frac{\gamma-1}{\gamma}\right)^2 - \frac{2\gamma-1}{\gamma^2 w(1-w)} \right]. \quad (4.10)$$

4.1.2 Electron-Ion Binary Collisions

Let us consider now a collision of a relativistic electron with a momentum \mathbf{p} with a target ion with a charge $Z^*|e|$ and a momentum \mathbf{p}_i satisfying (4.1) with $\alpha = i$. One can assume that the ion is initially at rest. Here, one consider only the “the binary part” where $b_{i,\min} < b < b_{i,\max}$. In this case, the

laboratory frame coincides with the center of mass frame, since $m_e/m_i \ll 1$. One has consequently

$$b_{i,\min} = \frac{\hbar}{2p} \quad (4.11)$$

which is much larger than $b_{e,\min}$ for ultra relativistic electron projectiles while

$$b_{i,\max} = b_{e,\max}. \quad (4.12)$$

The quantum relativistic differential cross section of such a binary collision has been obtained by [Mott, 1932]. It reads

$$\left(\frac{d\sigma}{d\Omega} \right)_i = \frac{(Z^* e^2)^2 \varepsilon^2}{4\mathbf{p}^4 \sin^4 \frac{\theta}{2}} \left(1 - \frac{\mathbf{v}^2}{c^2} \sin^2 \frac{\theta}{2} \right). \quad (4.13)$$

The first term in the parenthesis is the relativistic generalization of the Rutherford differential cross section and the second term is the quantum spin effect correction. In the first order in the small parameter m_e/m_i , the electron conserves the energy in a collision with a target ion. It can be compared with a collision of a tennis ball with a rigid wall. The tennis ball does not lose its energy but it is strongly deflected. Instead of working with the maximum impact parameter $b_{\alpha,\max}$ when integrating the differential cross section over all impact parameters b , some authors prefer to add a screening factor in the expression of the differential cross sections (4.9) and (4.13) and integrate from $b = b_{\alpha,\min}$ to $b \rightarrow \infty$ (see for example [Atzeni et al., 2009b]).

4.2 Slowing Down of a Relativistic Electron in Solids and Dense Plasmas

4.2.1 Stopping Powers of relativistic Electrons

The stopping power of an electron is the electron energy loss $d\varepsilon$ per unit path length ds due to collisions with the particles of the medium. It is defined as

$$\left(\frac{d\varepsilon}{ds} \right) = (\gamma - 1) m_e c^2 n_i \int_0^{1/2} w \frac{d\sigma}{dw} dw. \quad (4.14)$$

Collisions with ions do not contribute to the slowing down of electrons due to their large mass compared to the electron mass. One may separate in this integral the contributions of the binary collisions with free electrons ($w > w_c$) from those of the bound electrons and/or with the screened free electrons ($w < w_c$).

Concerning the binary part, one can use the Moller differential cross section (4.10). The integration

4.2. SLOWING DOWN OF A RELATIVISTIC ELECTRON IN SOLIDS AND DENSE PLASMAS

gives for cold solids

$$\begin{aligned} \left(\frac{d\varepsilon}{ds}\right)_{e,\text{binary}} &= (\gamma - 1) m_e c^2 n_i \int_{w_c}^{1/2} w \left(\frac{d\sigma}{dw}\right)_{e,f} dw \\ &= -\frac{2\pi n_i Z e^4}{m_e v^2} \left[\ln\left(\frac{1}{4w_c}\right) + 1 - \frac{2\gamma - 1}{\gamma^2} \ln 2 + \frac{1}{8} \left(\frac{\gamma - 1}{\gamma}\right)^2 \right] \end{aligned} \quad (4.15)$$

In case of plasmas, the contribution of collisions with background free electrons can be obtained by replacing Z by Z^* in the previous Equation (4.15) :

$$\left(\frac{d\varepsilon}{ds}\right)_{e,f} = -\frac{2\pi n_i Z^* e^4}{m_e v^2} \left[\ln\left(\frac{1}{4w_c}\right) + 1 - \frac{2\gamma - 1}{\gamma^2} \ln 2 + \frac{1}{8} \left(\frac{\gamma - 1}{\gamma}\right)^2 \right]. \quad (4.16)$$

The first term in the square brackets corresponds to the well known Coulomb logarithm from the non-relativistic theory (see **Appendix A, section A.2.3**). That is why the term w_c may thus be estimated by $(b_{e,\text{min}}/b_{e,\text{max}})^2$. This corresponds to the non relativistic stopping power Coulomb logarithm, in the limit $\gamma \rightarrow 1$ [Jackson, 1975]. The other terms account for the quantum relativistic effects.

For a combination of historical and mathematical reasons, the energy loss due to the collective response of the material is artificially divided into two parts

- The “Bethe part” for collisions with bound electrons (accounting for the mean excitation energy per atom I_{ex}) for a impact parameters b smaller than the interatomic/interionic distance. This corresponds to the beam electrons interacting with one atom/ion.
- The ”density effect” or ”plasmon part” for impact parameters b greater than the interatomic/interionic distance for which the relativistic electron projectile interacts with many electrons at the same time.

The contribution of collisions with bound electrons in a cold solid has been determined by [Bethe, 1932], considering the energy transferred to the excitation of an atom by the electric field of a charged electron moving at constant velocity. It reads

$$\begin{aligned} \left(\frac{d\varepsilon}{ds}\right)_{e,\text{Bethe}} &= (\gamma - 1) m_e c^2 n_i \int_0^{w_c} w \left(\frac{d\sigma}{dw}\right)_{e,b} dw \\ &= -\frac{2\pi n_i Z e^4}{m_e v^2} \left\{ \ln \left[\frac{2w_c (\gamma^2 - 1) (\gamma - 1)}{(I_{\text{ex}}/m_e c^2)^2} \right] - \beta^2 \right\}. \end{aligned} \quad (4.17)$$

A striking results is that the cut-off w_c at which the two models are patched together cancel out for

cold solids when adding the two integral contributions (4.15) and (4.17) [Rohrlich and Carlson, 1954]

$$\left(\frac{d\varepsilon}{ds}\right)_{e,\text{binary}} + \left(\frac{d\varepsilon}{ds}\right)_{e,\text{Bethe}} = -\frac{4\pi n_i Z e^4}{m_e v^2} \left\{ \begin{aligned} & \ln \left[\sqrt{\gamma+1} \frac{(\gamma-1)m_e c^2}{I_{\text{ex}}} \right] - \frac{\ln 2}{2} + \frac{1}{16} \\ & - \frac{\ln 2 + (1/8)}{\gamma} + \frac{(1/2)\ln 2 + (9/16)}{\gamma^2} \end{aligned} \right\}. \quad (4.18)$$

It gives confidence in these expressions, even though neither model is valid for intermediate energy losses, where no analytical model is available. In the case of ionized solids, one can thus extend (4.18) for the stopping power of a relativistic electron by colliding with bound electrons, by replacing Z by $(Z - Z^*)$:

$$\left(\frac{d\varepsilon}{ds}\right)_{e,b} = -\frac{4\pi n_i (Z - Z^*) e^4}{m_e v^2} \left\{ \begin{aligned} & \ln \left[\sqrt{\gamma+1} \frac{(\gamma-1)m_e c^2}{I_{\text{ex}}} \right] - \frac{\ln 2}{2} + \frac{1}{16} \\ & - \frac{\ln 2 + (1/8)}{\gamma} + \frac{(1/2)\ln 2 + (9/16)}{\gamma^2} \end{aligned} \right\}. \quad (4.19)$$

The complexities of dealing with coupled, quantized oscillations of multiple bound electrons are hidden in the mean excitation potential I_{ex} . In very general terms, it can be written as the logarithm mean of all possible transitions of bound electrons between the energy levels E_i and E_j , weighted by the transition probability f_{ij}

$$\ln I_{\text{ex}} = \sum_{i,j} f_{ij} \ln (E_i - E_j). \quad (4.20)$$

In the simple case of a single, undamped, harmonic oscillator at frequency ω , one has $I_{\text{ex}} = \hbar\omega$. This is a good approximation for a plasma, giving the mean excitation $I_{\text{ex}} = \hbar\omega_p$. An approximate model for the mean excitation potential of bound electrons in an ion was proposed by [More, 1985]. In this simplified theoretical model known as the local plasma approximation,

$$\ln I_{\text{ex}} = \int_{\mathbb{R}^3} f_e(\mathbf{r}) \ln(\hbar\omega_p) d^3\mathbf{r}, \quad (4.21)$$

where f_e is the bound electron probability density function. In order to obtain the electron distribution around an ion, [More, 1985] used the Thomas-Fermi model and found that the result could be described by

$$I_{\text{ex}}(Z^*) = I_{\text{ex}}(0) \frac{\exp \left[1.29(Z^*/Z)^{0.72-1.18(Z^*/Z)} \right]}{\sqrt{1 - (Z^*/Z)}} \quad (4.22)$$

where $I_{\text{ex}}(0) = ZE_0$ with $E_0 = 10$ eV empirically chosen to fit the quantum calculus made by [McGuire, 1982] for Aluminum, Krypton and Gold.

The second part of the collective contribution to the stopping power is the density effect correction δ . It has been firstly derived by [Fermi, 1940], using a purely classical calculation representing the plasma electrons response to the electron projectile perturbation by a single harmonic oscillator. It gives a reduction in the energy loss due to the electric field generated by the fast electron, shielded by

4.2. SLOWING DOWN OF A RELATIVISTIC ELECTRON IN SOLIDS AND DENSE PLASMAS

the collective response of electrons in the material. It is called the density effect correction because it increases with the electron density. According to [Fermi, 1940], it can be obtained analytically in the limit of ultrarelativistic electron projectile and reads in this case

$$\delta = 2 \ln \left(\frac{\gamma \hbar \omega_p}{I_{\text{ex}}} \right) - \beta^2. \quad (4.23)$$

For a plasma, where $I_{\text{ex}} = \hbar \omega_p$, this expression is valid for all cases of interest. For solids and consequently bound electrons, where typically $I_{\text{ex}} \gg \hbar \omega_p$, the expression obtained by [Pines and Bohm, 1952]

$$\left(\frac{d\varepsilon}{ds} \right)_p = \frac{2\pi n_i Z^* e^4}{m_e v^2} \delta = -\frac{4\pi n_i Z^* e^4}{m_e v^2} \ln \left(\frac{c\sqrt{\gamma^2 - 1}/\gamma}{\omega_p b_{e,\text{max}}} \right) \quad (4.24)$$

may be used. This formula was originally derived for a non-relativistic electron projectile. However, it is valid in the limit $\gamma \rightarrow \infty$ and for intermediate γ as well.

A relativistic electron can also lose energy by emitting bremsstrahlung radiations. It is a small correction to the total collisional energy losses in the range of beam electron energies considered in this manuscript. However, the radiative stopping power

$$\left(\frac{d\varepsilon}{ds} \right)_b = -\frac{4\pi(Z - Z^*)(Z - Z^* + 1)n_i e^4 \alpha}{m_e c^2 \gamma} \frac{1}{\pi} \left[\ln(2\gamma) - \frac{1}{3} \right], \quad (4.25)$$

obtained by [Heitler and Sauter, 1933] is taken into account. This formula is valid in the case where $1 \ll \gamma \ll 1/\alpha Z^{1/3}$ according to [Bethe and Heitler, 1934] and it is sufficient for our needs. Indeed, according to [Berger and Seltzer, 1964], radiative losses become predominant for relativistic electrons with energies greater than

$$E_c \approx \frac{800 \text{ MeV}}{Z + 1.2} \quad (4.26)$$

while we consider in this manuscript laser generated electrons in the range 10 keV - 10 MeV and low or intermediate Z -material. The resulting total stopping power reads

$$\left(\frac{d\varepsilon}{ds} \right) = \left(\frac{d\varepsilon}{ds} \right)_{e,f} + \left(\frac{d\varepsilon}{ds} \right)_{e,b} + \left(\frac{d\varepsilon}{ds} \right)_p + \left(\frac{d\varepsilon}{ds} \right)_b. \quad (4.27)$$

This expression is valid in the first Born approximation i.e. for low or intermediate Z -materials. Also, there is an uncertainty at low energies due to the lack of shell corrections which are required when the velocity of the incident electron is comparable to the velocities of the atomic electrons, especially those in the inner shells. As a consequence, the formula (4.27) is valid for laser-generated relativistic electrons of kinetic energies greater than $\approx 1 - 10$ keV.

As illustrated in **Figure 4.1**, it is worth noticing that, even if the contributions of the bound electrons and the free electrons depend strongly on the temperature via their densities depending on the

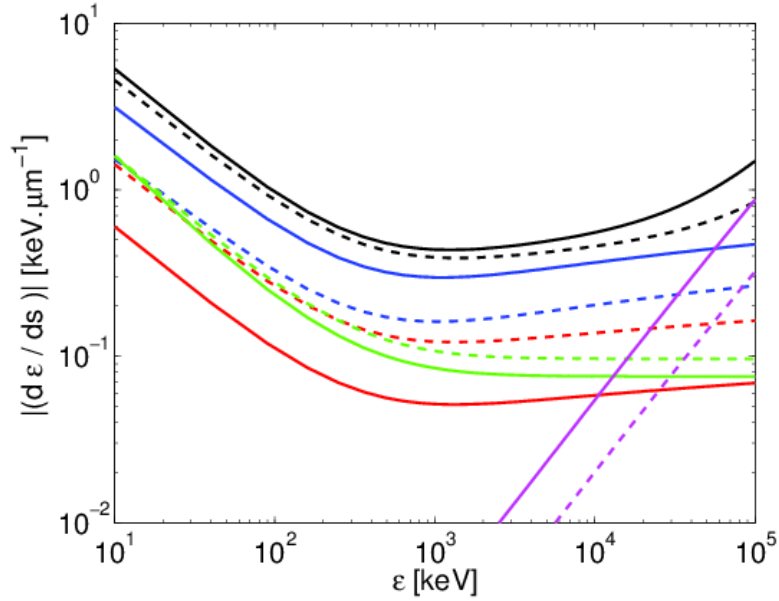


Figure 4.1: Total stopping power of a relativistic electron in Aluminum ($\rho = 2.7 \text{ g.cm}^{-3}$) versus its kinetic energy according to formula (4.27) (black) and the different contributions due to free electrons (red), bound electrons (blue), screened free electrons/plasmons (green) and bremsstrahlung losses (magenta) at ambient temperature $T_e = T_i = 300 \text{ K}$ (solid lines) and $T_e = T_i = 100 \text{ eV}$ (dashed lines).

ionization state Z^* , the total stopping power weakly depends on the temperature (logarithmically). The contribution of the bound electrons at a low temperature is essentially balanced by the contribution of the free electrons at a higher temperature. It can be understood qualitatively because, in both cases, the amount of electrons encountered by the electron projectile is the same. The total stopping power (4.27) is plotted in **Figure 4.2** versus the electron kinetic energy $(\gamma - 1)m_e c^2$ for materials that will be studied in this manuscript. One can see a change of slope around $\varepsilon = m_e c^2 \approx 511 \text{ keV}$. In the non-relativistic side, the stopping power decreases with the non-relativistic kinetic energy $(1/2)m_e v^2$. This is a consequence of the Rutherford cross section which decreases with the transferred momentum. In the relativistic domain, an opposite behavior appears; the stopping power increases with the electron kinetic energy. This is due to the fact that the velocity has reached its maximum value of $\lesssim c$ and does not change anymore while the electron inertia γm_e in the relativistic Coulomb logarithm is increasing so that the kinetic energy exchanged during each collision increases with the kinetic energy. Moreover, for more energetic electrons, the radiation loss becomes predominant compared to the collisional ones. It is well known that the more energetic the electron is, the more the electron radiates. In **Figure 4.2**, the formula (4.27) is also compared with the total stopping power provided by the online database ESTAR (<http://physics.nist.gov/PhysRefData/Star/Text/ESTAR.html>) based on the ICRU report 37 [Brice, 1985]. Discrepancies between Formula (4.27) and ESTAR appear for relativistic electrons with kinetic energies greater than 10 MeV mainly due to the simple expression for the radiation stopping power (4.25). In the ESTAR database, the total collision stopping power is also calculated from the theory by [Bethe, 1932] but with a more accurate density-effect correction evaluated accord-

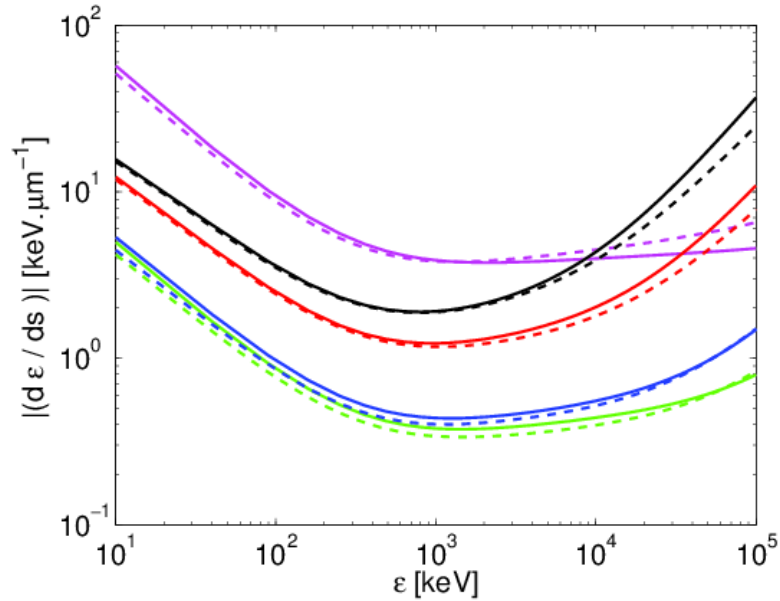


Figure 4.2: Total stopping power of a relativistic electron versus its kinetic energy according to formula (4.27) (solid line) compared to the ESTAR database (dashed lines) plotted for different materials : dense Hydrogen plasma ($Z=1$) with $\rho = 10 \text{ g.cm}^{-3}$ (magenta), amorphous solid Carbon ($Z=6$) with $\rho = 2.1 \text{ g.cm}^{-3}$ (green), solid Aluminum ($Z=13$) with $\rho = 2.7 \text{ g.cm}^{-3}$ (blue), solid Copper ($Z=29$) with $\rho = 8.96 \text{ g.cm}^{-3}$ (red) and solid Tantalum ($Z=73$) with $\rho = 16.69 \text{ g.cm}^{-3}$ (black).

ing to [Sternheimer, 1952] [Sternheimer et al., 1982] and the mean excitation potential I_{ex} adopted in the ICRU Report 37 [Brice, 1985]. The uncertainties of the calculated collision stopping powers for electrons are estimated [Brice, 1985] to be 1 % to 2 % above 100 keV, 2 % to 3 % (in low- Z materials) and 5 % to 10 % (in high- Z materials) in the range between 10 keV and 100 keV. The radiative stopping powers are evaluated in ESTAR with a combination of theoretical bremsstrahlung cross sections described by [Seltzer and Berger, 1985]. Analytical formulas (using a high-energy approximation) are used above 50 MeV, and accurate numerical results of [Pratt et al., 1977] below 2 MeV. Cross sections in the intermediate energy region from 2 MeV to 50 MeV are obtained by interpolation, a procedure whose accuracy was confirmed by more detailed calculations for a few cases. The uncertainties of the radiative stopping powers are estimated to be 2 % above 50 MeV, 2 % to 5 % between 50 MeV and 2 MeV, and 5 % below 2 MeV.

4.2.2 Range of a Relativistic Electron Propagating in a Dense Plasma

By neglecting the bremsstrahlung losses (4.25) and using the relation (4.23) for the density effect, the total stopping power of a relativistic electron propagating in a fully ionized plasma with the atomic

number Z can be estimated as

$$\left(\frac{d\varepsilon}{ds}\right) = -4\pi \frac{Zn_i e^4}{m_e v^2} \ln \Lambda_{ee}^{\text{rel}} \quad (4.28)$$

with the relativistic electron-electron Coulomb logarithm, usually called drag number,

$$\begin{aligned} \ln \Lambda_{ee}^{\text{rel}} &= \ln \left[\sqrt{\gamma+1} \frac{(\gamma-1)m_e c^2}{I_{\text{ex}}} \right] - \frac{\ln 2}{2} + \frac{1}{16} - \frac{\ln 2 + (1/8)}{\gamma} + \frac{(1/2) \ln 2 + (9/16)}{\gamma^2} - \frac{\delta}{2} \\ &= \ln \left[\frac{m_e c^2}{\hbar \omega_p} \right] - \frac{\ln 2}{2} + \frac{1}{16} + f(\gamma) \end{aligned} \quad (4.29)$$

with

$$f(\gamma) = \ln \left[\sqrt{\gamma+1} \frac{(\gamma-1)}{\gamma} \right] - \frac{\ln 2 + (1/8)}{\gamma} + \frac{(1/2) \ln 2 + (9/16)}{\gamma^2}. \quad (4.30)$$

The (undeflected) range of an electron with the initial kinetic energy $\varepsilon_0 = (\gamma_0 - 1)m_e c^2$ is given by

$$R = m_e c^2 \int_{\gamma_0}^1 \left(\frac{d\varepsilon}{ds}\right)^{-1} d\gamma. \quad (4.31)$$

One can estimate it by replacing $f(\gamma)$ by a constant value f^* in the integral. It reads, by noting $(\ln \Lambda_{ee}^{\text{rel}})^* = \ln(m_e c^2 / \hbar \omega_p) - (\ln 2/2) + (1/16) + f^*$, according to [Atzeni et al., 2009b]

$$R = \frac{(\gamma_0 - 1)^2}{\gamma_0} \frac{(m_e c^2)^2}{4\pi Z n_i e^4 (\ln \Lambda_{ee}^{\text{rel}})^*}. \quad (4.32)$$

For an equimolar DT plasma ($Z = 1$), still according to [Atzeni et al., 2009b], one gets by expanding the logarithm of $(\ln \Lambda_{ee}^{\text{rel}})^*$ around $\rho = 300 \text{ g.cm}^{-3}$ and by assuming $f^* = 0$

$$R [\mu\text{m}] \approx 23.7 \frac{\varepsilon_0 [\text{MeV}]^2}{0.34 + 0.66\varepsilon_0 [\text{MeV}]} \left(\frac{300 \text{ g.cm}^{-3}}{\rho} \right)^{1.066}. \quad (4.33)$$

However, this formula assumes that the beam electron trajectory is a straight line and consequently overestimates the effective penetration length (along the initial electron velocity) of a relativistic electron into a plasma owing to its angular scattering by colliding the background ions and electrons.

4.3 Angular Scattering of a Relativistic Electron in Solids and Dense Plasmas

In materials with $Z \gg 1$, the fast electron scattering is dominated by elastic collisions with ions and impact parameters b much greater than the De Broglie wavelength. For low Z materials such as Hydrogen plasmas, angular scattering on target electrons also plays an important role. We may describe the angular scattering of a relativistic electron colliding with target electrons, by following the method used for the estimate of the total stopping power of relativistic electrons, as presented in the

4.3. ANGULAR SCATTERING OF A RELATIVISTIC ELECTRON IN SOLIDS AND DENSE PLASMAS

previous **section 4.2.1**. Collisions on target electrons with the scattering angle above θ_c (respectively below w_c) need a statistical treatment of the electric field due to random thermal fluctuations and will not be described in this section. Here, we will only describe the angular scattering of a relativistic electron by colliding with target electrons with a scattering angle below θ_c (respectively above w_c), i.e., we will only consider the electrons angular scattering due to binary collisions. The binary collisions with target ions are described by the Mott scattering formula (4.13) which can be written with the simpler form

$$\left(\frac{d\sigma}{d\Omega}\right)_i = \frac{(Z^*e^2)^2}{4(pv)^2 \sin^4 \theta/2} (1 - \beta^2 \sin^2 \theta/2). \quad (4.34)$$

Concerning binary collisions of a relativistic electron with free electrons of the material, one can use the Möller scattering formula (4.9) expressed in the laboratory frame according to the relation (4.2 c). It reads

$$\left(\frac{d\sigma}{d\Omega}\right)_e = \frac{4e^4 \cos \theta}{(pv)^2} \left\{ \frac{1}{\sin^4 \theta} + \frac{(\gamma + 1)^2}{4 \cos^4 \theta} + \frac{[(\gamma^2 - 1)/\gamma]^2}{[(\gamma - 1) \sin^2 \theta + 2]^2} - \frac{(2\gamma - 1)(\gamma + 1)}{2\gamma^2 \sin^2 \theta \cos^2 \theta} \right\}. \quad (4.35)$$

According to [Atzeni et al., 2009b], although one can retain all terms, it suffices to consider the leading term at small θ corresponding to the relativistic generalization of the Rutherford differential cross section (see **Appendix A, section A.2.1**)

$$\left(\frac{d\sigma}{d\Omega}\right)_e = \frac{4e^4 \cos \theta}{(pv)^2 \sin^4 \theta}. \quad (4.36)$$

Indeed, the scattering at small angle θ gives the dominant contribution to the mean scattering angle $\sqrt{\langle \theta^2 \rangle}$, as described in the next **sections 4.3.1** and **4.3.2**. This approximation does not lead to significant errors in the resulting range of laser-generated electron's energies.

4.3.1 Multiple Scattering Theory by Lewis

We start here from the simpler multiple scattering theory by [Lewis, 1950] and we restrict this subsection to fully ionized plasmas as done by [Solodov and Betti, 2008] and [Atzeni et al., 2009b] avoiding collisions with $\theta < \theta_c$. In the Lewis theory, the mean scattering angle can be evaluated according to

$$\langle \cos \theta \rangle = \exp(-k_1 s) \quad (4.37)$$

where s is the relativistic electron path length and k_1^{-1} is the relativistic electron mean free path. Expanding both sides of equation (4.37) for small values of the arguments ($\theta \ll 1$ and $k_1 s \ll 1$) considering only small angle collisions, one gets

$$\langle \theta^2 \rangle = 2k_1 s. \quad (4.38)$$

The mean free path of the relativistic electron -which is the key parameter of such a model- has two contributions : its angular scattering due to binary collisions with electrons and its angular scattering due to binary collisions on ions

$$k_1 = k_{1,e} + k_{1,i} \quad (4.39)$$

where

$$k_{1,\alpha} = 2\pi n_\alpha \int_{\theta_{\alpha,\min}}^{\theta_{\alpha,\max}} (1 - \cos \theta) \left(\frac{d\sigma}{d\Omega} \right)_\alpha \sin \theta d\theta. \quad (4.40)$$

According to the quantum theory of diffraction, $\theta_{\alpha,\min}$ (which corresponds to the cut-off θ_c) can be estimated by

$$\theta_{\alpha,\min} = 4\pi \frac{b_{\alpha,\max}}{b_{\alpha,\min}}, \quad (4.41)$$

where $b_{\alpha,\min}$ and $b_{\alpha,\max}$ are the limiting impact parameters defined by (4.7), (4.8), (4.11) and (4.12). For scattering on electrons, $\theta_{e,\max}$ is the deflection angle corresponding to the maximum energy loss $w_{\max} = 1/2$ and reads consequently

$$\theta_{e,\max} = \arcsin \sqrt{\frac{2}{\gamma + 3}} \quad (4.42)$$

according to (4.2). For the scattering on target ions, due to their greater inertia, the maximum angular deflection is

$$\theta_{i,\max} = \pi. \quad (4.43)$$

According to [Atzeni et al., 2009b], one gets consequently for the scattering on target electrons

$$k_{1,e} = 4\pi \frac{Z n_i e^4}{(pv)^2} \left\{ \ln \left(\frac{b_{e,\max}}{b_{e,\min}} \right) - \frac{1 + \ln [2(\gamma + 3)]}{2} \right\}, \quad (4.44)$$

retaining only the leading terms. Following the same procedure, one gets for target ions

$$k_{1,i} = 4\pi \frac{Z^2 n_i e^4}{(pv)^2} \left[\ln \left(\frac{b_{i,\max}}{b_{i,\min}} \right) - \frac{1 + \beta^2}{2} \right]. \quad (4.45)$$

One can see from (4.44) and (4.45) that the contribution of binary collisions with ions is Z times greater than the contribution of binary collisions with electrons.

4.3.2 Multiple Scattering Theory by Moliere

The multiple scattering theory by [Moliere, 1948], later improved by [Bethe, 1953] and [Nardi and Zinamon, 1978], provides a more accurate description for the angular distribution function of a relativistic electron beam. It consists in solving the transport equation for the angular

4.3. ANGULAR SCATTERING OF A RELATIVISTIC ELECTRON IN SOLIDS AND DENSE PLASMAS

distribution function $f(\boldsymbol{\Omega}, s)$ of the electron beam

$$\frac{\partial f}{\partial s} = \sum_{\alpha=e,i} n_{\alpha} \int [f(\boldsymbol{\Omega} - \boldsymbol{\Omega}', s) - f(\boldsymbol{\Omega}, s)] \left(\frac{d\sigma}{d\boldsymbol{\Omega}'} \right)_{\alpha} d\boldsymbol{\Omega}' \quad (4.46)$$

where $\boldsymbol{\Omega} - \boldsymbol{\Omega}'$ is the direction of electron velocity before the last scattering event, s is the electron path length and the differential cross sections are given by (4.34) and (4.36). For simplicity, we will only consider here the binary collisions of beam electrons with target ions. The equation (4.46) is solved by expanding the distribution function on the spherical harmonic functions $Y_{lm}(\theta, \varphi)$ depending on the unassociated Legendre polynomials $P_l(\cos \theta)$. In the small angle approximation, the Legendre polynomials can be approximated by the 0th order Bessel function of the first kind $P_l(\theta) \approx J_0(l\theta)$, and the sum over l can be replaced by a continuous integral. Thus, one obtains

$$f(\theta, s) = \int_0^{\infty} l J_0(l\theta) \exp \left[2\pi n_i s \int_{\theta_{i,\min}}^{\theta_{i,\max}} \left(\frac{d\sigma}{d\boldsymbol{\Omega}'} \right)_i (J_0(l\theta') - 1) \theta' d\theta' \right] dl \quad (4.47)$$

where $\theta_{i,\min}$ is given by (4.41) and $\theta_{i,\max}$ by (4.43). By expanding the exponential and performing the integrals, one obtains

$$f(\theta, s) = \sum_{n=0}^{\infty} f^{(n)}(\theta, s) = \sum_{n=0}^{\infty} \frac{1}{n! B^n} \int_{\mathbb{R}} u J_0 \left(\frac{\theta u}{\chi_c \sqrt{B}} \right) \exp \left(-\frac{u^2}{4} \right) \left[\frac{u^2}{4} \ln \left(\frac{u^2}{4} \right) \right]^n du \quad (4.48)$$

where

$$B = W \left(-1, -\left(\frac{\theta_{i,\min}}{\chi_c} \right)^2 \right)$$

with $W(-1, x)$ the Lambert W-function (the inverse function of $x = y \exp y$ on the intervals $y \in [-\infty, -1]$, $x \in [-1, 0]$) and

$$\chi_c^2 = 4\pi n_i s \left(\frac{Z r_e}{\gamma \beta^2} \right)^2.$$

In the limit of small angle scattering θ , the 0th order function

$$f^{(0)}(\theta, s) = 2 \exp \left(-\frac{\theta^2}{\chi_c^2 B} \right). \quad (4.49)$$

is sufficient to describe the angular distribution of the relativistic electrons. Indeed, as all collisions are independant, one would have deduced, according to the central limit theorem, that the deflection probability $f(\theta, s)$ can be described by such a normal law. Thus, the quadratic mean angle can be deduced. It reads

$$\sqrt{\langle \theta^2 \rangle} = \chi_c \sqrt{2 \ln \left(\frac{\chi_c}{\theta_{i,\min}} \right)}. \quad (4.50)$$

4.4 Belyaev-Budker Collision Integral

A more general framework for description of the relativistic electron beam transport is the relativistic kinetic equation. The collision integral of this equation has been obtained by [Belyaev and Budker, 1956] generalizing the Landau collision integral (see **Appendix A, section A.2.3**) to the relativistic regime. Here, we present the phenomenological approach from [Landau and Lifshitz, 1981], used to derive the equation. The general form of the electron kinetic equation reads

$$\frac{\partial f_b}{\partial t} + \frac{\partial}{\partial \mathbf{r}} (\mathbf{v} f_b) - \frac{\partial}{\partial \mathbf{p}} \left[e \left(\mathbf{E} + \frac{\mathbf{v}}{c} \times \mathbf{B} \right) f_b \right] = \left(\frac{\partial f_b}{\partial t} \right)_{\text{coll}}. \quad (4.51)$$

Conservation of the number of particles implies that the collision integral has the form

$$\left(\frac{\partial f_b}{\partial t} \right)_{\text{coll}} = - \frac{\partial}{\partial \mathbf{p}} \cdot \mathbf{F}_{\text{coll}} \quad (4.52)$$

where \mathbf{F}_{coll} is the particle flux in momentum space due to binary collisions. Let us consider a small area near a point \mathbf{p} in momentum space, perpendicular to the p_μ -axis where $\mu \in \{x, y, z\}$. The flux component $F_{\text{coll},\mu}$ is a difference between the number of electrons crossing this area from left to right per time unit and those crossing it from right to left due to binary collisions. If a particle $\alpha \in \{i, e\}$ receives in a collision a μ -component of momentum equal to $\Delta p_\mu > 0$, it will cross the small area from left to right, thus increasing the value of its momentum from $p_\mu - \Delta p_\mu$ to p_μ . Hence, the total number of particles crossing the area from left to right is

$$\sum_{\alpha=i,e} \int_{\Delta p_\mu > 0} d^3 \Delta \mathbf{p} \int_{\mathbb{R}^3} d^3 \mathbf{p}_\alpha \int_{p_\mu - \Delta p_\mu}^{p_\mu} P(\mathbf{p}, \mathbf{p}_\alpha, \Delta \mathbf{p}) f_b(\mathbf{r}, \mathbf{p}, t) f_\alpha(\mathbf{r}, \mathbf{p}_\alpha, t) dp_\mu$$

where

$$P(\mathbf{p}, \mathbf{p}_\alpha, \Delta \mathbf{p}) f_b(\mathbf{r}, \mathbf{p}, t) f_\alpha(\mathbf{r}, \mathbf{p}_\alpha, t) d^3 \mathbf{p}_\alpha d^3 \Delta \mathbf{p}$$

is the number of collisions occurring per time unit between an electron with momentum \mathbf{p} and a particle α with momentum \mathbf{p}_α in the range $d^3 \mathbf{p}_\alpha$. After the collision, the particles acquire the momenta $\mathbf{p} + \Delta \mathbf{p}$ and $\mathbf{p}_\alpha - \Delta \mathbf{p}$, respectively. Similarly, the number of particles crossing that area from right to left may be written as

$$\sum_{\alpha=i,e} \int_{\Delta p_\mu > 0} d^3 \Delta \mathbf{p} \int_{\mathbb{R}^3} d^3 \mathbf{p}_\alpha \int_{p_\mu - \Delta p_\mu}^{p_\mu} P(\mathbf{p}, \mathbf{p}_\alpha, -\Delta \mathbf{p}) f_b(\mathbf{r}, \mathbf{p} + \Delta \mathbf{p}, t) f_\alpha(\mathbf{r}, \mathbf{p}_\alpha - \Delta \mathbf{p}, t) dp_\mu.$$

From now, we omit the variables \mathbf{r} and t for brevity in the equations since the collisions take place locally in space and time. By virtue of the principle of detailed balance, the probability density of such a momentum exchanged is necessarily a symmetrical function with regard to the interchange of

4.4. BELYAEV-BUDKER COLLISION INTEGRAL

the initial and final particles states :

$$P(\mathbf{p}, \mathbf{p}_\alpha, \Delta\mathbf{p}) = P(\mathbf{p}, \mathbf{p}_\alpha, -\Delta\mathbf{p}).$$

Thus, after adding these two contributions and replacing the integration over $d\mathbf{p}_\mu$ by a multiplication by Δp_μ , one obtains the Boltzmann result (see **Appendix A, section A.1.4**)

$$F_{\text{coll},\mu} = \sum_{\alpha=i,e} \int_{\Delta p_\mu > 0} d^3\Delta\mathbf{p} \int_{\mathbb{R}^3} d^3\mathbf{p}_\alpha P(\mathbf{p}, \mathbf{p}_\alpha, \Delta\mathbf{p}) [f_b(\mathbf{p})f_\alpha(\mathbf{p}_\alpha) - f_b(\mathbf{p} + \Delta\mathbf{p})f_\alpha(\mathbf{p}_\alpha - \Delta\mathbf{p})] \Delta p_\mu. \quad (4.53)$$

One can express the probability density P in terms of the differential collision-cross-section as

$$P d^3\Delta\mathbf{p} = v_{r,\alpha} d^2\sigma_\alpha \quad (4.54)$$

where $v_{r,\alpha} = c\sqrt{\tilde{\gamma}_\alpha^2 - 1}/\tilde{\gamma}_\alpha$ is the relative velocity of one particle in the rest frame of the other during their collision, $\tilde{\gamma}_\alpha = \gamma\gamma_\alpha/\gamma_*^2$ and $\gamma_* = 1/\sqrt{(1 - \mathbf{v}\cdot\mathbf{v}_\alpha/c^2)}$. This expression tends to $|\mathbf{v} - \mathbf{v}_\alpha|$ in the non-relativistic limit. Under the assumption of a small momentum transfer $\Delta\mathbf{p}$ compared to \mathbf{p} and \mathbf{p}_α (also called the small angle assumption, see **Appendix A, section A.2.2**), one can expand the difference in the square brackets of (4.53) to give

$$F_{\text{coll},\mu} = \sum_{\alpha=i,e} \sum_{\nu=x,y,z} \int_{\mathbb{R}^3} d^3\mathbf{p}_\alpha U_{\mu\nu}^\alpha \left[f_b(\mathbf{p}) \frac{\partial f_\alpha}{\partial p_{\alpha,\nu}} - f_\alpha(\mathbf{p}_\alpha) \frac{\partial f_b}{\partial p_\nu} \right] \quad (4.55)$$

where

$$U_{\mu\nu}^\alpha = \frac{1}{2} \int \Delta p_\mu \Delta p_\nu v_{r,\alpha} d^2\sigma_\alpha. \quad (4.56)$$

For a small angle deviation, the exchanged momentum $\Delta\mathbf{p}'$ is perpendicular to the velocity \mathbf{v}' (\mathbf{v}'_α) in the electron projectile rest frame (in the α particle rest frame, respectively). The tensor $U_{\mu\nu}^\alpha$ is therefore transverse to these vectors. According to [Belyaev and Budker, 1956], the only one possible particle-symmetric tensor leading to a Lorentz-invariant collision integral and satisfying

$$\mathbf{U}^\alpha \cdot \mathbf{v}' = \mathbf{U}^\alpha \cdot \mathbf{v}'_\alpha = 0 \quad (4.57)$$

where

$$\mathbf{v}' = \frac{\gamma_*^2}{\gamma_\alpha} \left[\mathbf{v} + \left(\frac{\gamma_\alpha - 1}{v_\alpha^2} \mathbf{v} \cdot \mathbf{v}_\alpha - \gamma_\alpha \right) \cdot \mathbf{v}_\alpha \right]$$

and

$$\mathbf{v}'_\alpha = \frac{\gamma_*^2}{\gamma} \left[\mathbf{v}_\alpha + \left(\frac{\gamma - 1}{v^2} \mathbf{v} \cdot \mathbf{v}_\alpha - \gamma \right) \cdot \mathbf{v} \right]$$

are the relative velocities of one particle expressed in the rest frame of the another (and having the same norm $v_{r,\alpha}$) is

$$U_{\mu\nu}^{\alpha} = \frac{1}{2} U_0^{\alpha} \left\{ \delta_{\mu\nu} - \frac{1}{(\tilde{\gamma}_{\alpha}^2 - 1)} \left[\frac{p_{\mu} p_{\nu}}{(m_e c)^2} - \frac{p_{\alpha,\mu} p_{\alpha,\nu}}{(m_{\alpha} c)^2} + \tilde{\gamma}_{\alpha} \left(\frac{p_{\mu} p_{\alpha,\nu}}{m_e m_{\alpha} c^2} + \frac{p_{\alpha,\mu} p_{\nu}}{m_e m_{\alpha} c^2} \right) \right] \right\}. \quad (4.58)$$

The scattering potential coming from the diagonal terms reads

$$U_0^{\alpha} = \frac{1}{2} \int \Delta \mathbf{p}^2 v_{r,\alpha} d^2 \sigma_{\alpha}. \quad (4.59)$$

However, in the litterature, one can find the Belyaev-Budker scattering potential expressed with the relativistic generalization of the Rutherford differential cross-section (A.49), mentioned in the introduction for both ions and electrons :

$$U_0^{\alpha} = 4\pi \frac{q_{\alpha}^2 e^2 \ln \Lambda_{e\alpha}}{v_{r,\alpha}}$$

where $\ln \Lambda_{e\alpha} = \ln (b_{\alpha,\max}/b_{\alpha,\min})$ and $q_{\alpha} = e$ for $\alpha = e$ and $q_{\alpha} = Ze$ for $\alpha = i$ (see for example [Braams and Karney, 1987]). Obviously, the Belyaev-Budker collision tensor tends to the Landau collision tensor (see **Appendix A, section A.2.2**) in the non-relativistic limit.

Chapter 5

Existing Simulation Methods for Fast Electron Transport

"If people do not believe that mathematics is simple, it is only because they do not realize how complicated life is."

John Von Neumann

The numerical computation of the Vlasov-Fokker-Planck equation (4.51) is crucial for understanding the physics of laser-generated relativistic electron beam transport. The relativistic kinetic equation takes into account both collective and collisional effects and it is coupled with Maxwell's equations. The numerical computation of this system of equations is extremely challenging because of the large number of variables of the distribution function and the extremely small time and spatial numerical steps compared to the several ps and hundreds of μm needed for fast electron transport studies in the context of inertial confinement fusion. Compared with a hydrodynamic fluid model, a kinetic model is computationally expensive, as such a model not only contains spatial information but also momentum coordinates, and is therefore of high dimensionality and rich in information. In this chapter, we review the existing numerical tools. We start from the Particle-in-Cell (PIC) methods and then proceed to describe the Eulerian methods commonly called "Vlasov-Fokker-Planck methods". Actually, there is no Vlasov-Fokker-Planck codes which solve the Vlasov-Belyaev-Budker equation (4.51) but, as we will demonstrate in **Chapter 6**, applied to laser-generated relativistic electron beam transport, the Belyaev-Budker collision tensor can be simplified into a Landau-like collision tensor. Finally, we describe the less expensive "Vlasov-Fokker-Planck methods" based on expansions of the distribution function.

5.1 Particle-In-Cell methods

5.1.1 Full Particle-in-Cell methods

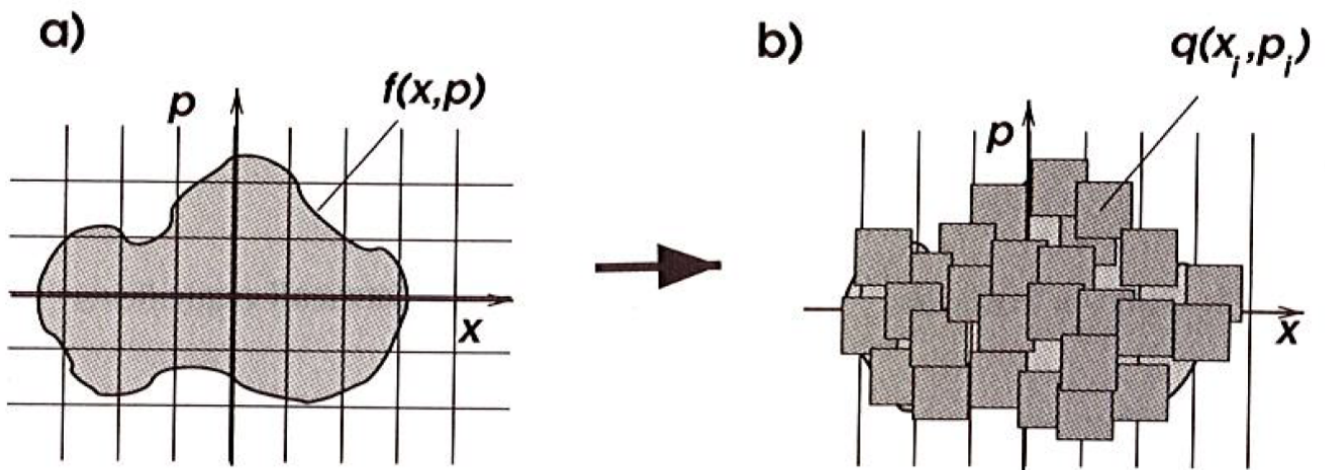


Figure 5.1: Schematic view of the discretization in the 6D phase-space of the full distribution function $f = f_b + f_e$ (a) in a series of discrete charge clouds with eventually different weights q_i (b) according to the PIC method [Gibbon, 2005].

The Particle-In-Cell (PIC) method, introduced in **Chapter 1** for laser-plasma interaction sim-

ulations, approximates the Vlasov equation by a series of discrete charge clouds, which evolve in a 6-dimensional phase-space similarly to the original Liouville N -body problem of classical point-like particles (cf **Appendix A, section A.1.2**). The principal difference between the PIC method and another particle method, like a molecular dynamics model, is that the interactions between particles are mediated by the electromagnetic fields calculated on a finite-difference grid, while the particles are allowed to occupy an arbitrary location in the phase-space. This approach circumvents the necessity to compute a huge number of binary interactions between individual particles while retaining N -body particle dynamics. However, by representing the whole electron population by N_p macroelectrons q_i , $i \in [1, N_p]$, weighted by the number of electrons each macroelectron represents, the PIC method does not account for the binary collisions. The collisions must be taken into account separately using a Monte-Carlo collision operator. Indeed, if $N_p = N$, the self-consistent electromagnetic fields computed from the Maxwell equations would account naturally for the binary collisions. But, the fact that $N_p \ll N$ because of computational restrictions and that binary collision space scales, much smaller than the Debye length, are usually not resolved, only collective effects are taken into account. Therefore, a Monte-Carlo method for modelling collisions is crucial. As already explained in **Chapter 1**, [Takizuka and Abe, 1977] developed a robust algorithm for dealing with binary collisions. The key computational step is to pair particles within a cell randomly and perform a rotation in the center-of-mass frame. This method has been extended for relativistic particles by [Sentoku and Kemp, 2008] [Pérez et al., 2012] and their model can be generalized to arbitrary particle weights as proposed by [Nanbu, 1997]. However, the momentum and energy are not always conserved in each individual collision, and it has been shown that this method does not relax to the Maxwell-Jüttner equilibrium distribution function [Peano et al., 2009]. In addition, the non-conservative force associated with the particle-grid mapping leads to self-heating and in some cases to a numerical instability, thus modifying the plasma properties. Nevertheless, if the resolution is high enough, such that the numerical space step $\Delta x \leq \lambda_{\text{Debye}}$, the effects associated with the aliasing terms are unimportant. The PIC codes which resolve λ_{Debye} are the best tools for studying Laser-Plasma Interaction, turbulences in tokamaks, plasma-based accelerators, relativistic shocks, ion propulsion, and many other problems. However, concerning the problem of fast electron transport in solids or dense plasmas, the Debye length is very small compared to the characteristic scale of the problem, and the simulations become too expensive. Moreover, by focusing on small-scale collisional effects, one loses precision in resolving large scale collective effects such as introduced in **Chapter 3**. It has been early proposed to use so implicit PIC methods without resolving λ_{Debye} by relating the fields at the new time to the particle positions and momenta at the new time [Cohen et al., 1982] or by using only the moments of the distribution function needed in the Maxwell equations (ρ and \mathbf{j}) at the new time [Mason, 1981]. More recently, [Welch et al., 2004] have implemented an implicit electromagnetic field solver in the commercialized 3-Dimensional PIC code *LSP*.

5.1.2 Hybrid Particle-in-Cell methods

Even if PIC codes are perfect tools for studying hot and relatively low density plasmas, they do not incorporate all the Physics needed for describing the fast electron transport in solids and dense plasmas such as the background electrons degeneracy, the presence of bound electrons and in general atomic or molecular structure of materials and their equation of states. Therefore, it has been proposed more recently by [Davies et al., 1997] [Davies, 2002] and [Gremillet et al., 2002] to use the PIC method only for the laser-generated fast electron component f_b of the full electrons distribution function by using a cut-off in the kinetic energy $\varepsilon_{\min} = 1 - 20$ keV separating the fast electrons $> \varepsilon_{\min}$ and the background electrons $< \varepsilon_{\min}$. In this "hybrid" method, the background electron dynamics are resolved according to hydrodynamic equations or simplified ones, such as introduced in **Chapter 3**, allowing to account for the response of background electrons via their transport coefficients η and κ_e , their thermal capacities $C_{V,e}$, the electron-ion equilibration Q_{ie} which may vary from the solid state to the plasma state as well as eventual equation of states $P_e = P_e(\rho, T_e)$ different from the ideal gas. This natural separation of the electrons into two interlinked populations assumes that the background plasma responds instantaneously to the fast electron beam transport in order to ensure the electromagnetic beam neutralization, introduced in **Chapter 2**, without modifying the beam. Thus, splitting of the populations is only valid when $n_b \ll n_e$ and when the fast electrons' mean kinetic energy $k_B T_b$ is much greater than the mean thermal energy of the background electrons $k_B T_e$. The Ohmic approximation (approximating the hydrodynamic momentum conservation equation by Ohm's law) is usually accompanied by the neglect of the displacement current in the Maxwell-Ampère equation. Therefore, it does not allow for modeling of Langmuir plasma waves and/or perturbations of the quasineutrality. Binary collisions of beam electrons with background particles are taken into account in the electromagnetic particle pusher by adding a continuous slowing down term $-\nu_d \mathbf{p}$ and a Langevin term \mathbf{R} representing a random rotation of \mathbf{p} due to the angular scattering. The equation of motion of a macroelectron $k \in [1, N_p]$ can therefore be written

$$\frac{d\mathbf{p}_k}{dt} = q_k \left(\mathbf{E} + \frac{\mathbf{v}_k}{c} \times \mathbf{B} \right) - \nu_d \mathbf{p}_k + \mathbf{R} \quad (5.1)$$

where ν_d is chosen such that the total stopping power of the electrons contained by the macroelectron k reads

$$\begin{aligned} \left(\frac{d\varepsilon}{ds} \right) (\gamma_k) &= \frac{1}{v_k} \frac{d\gamma_k}{dt} m_e c^2 = \frac{1}{v_k} \frac{\mathbf{p}_k}{\gamma_k (m_e c)^2} \left(\frac{d\mathbf{p}_k}{dt} \right)_{\text{coll}} = -\nu_d p_k \\ &\Rightarrow \nu_d = -\frac{1}{p} \left(\frac{d\varepsilon}{ds} \right) \end{aligned} \quad (5.2)$$

and the Langevin term \mathbf{R} is treated by a Monte-Carlo method constructed in such a way that the mean angular scattering value $\langle \theta^2 \rangle$ is defined by the multiple scattering theory of Moliere or Lewis. This equation is implemented in the PaRIS [Gremillet et al., 2002] and ZUMA [Strozzi et al., 2012] hybrid PIC codes. For example, in the case of a fully ionized plasma, the multiple scattering theory

of Lewis (4.38) reads

$$\frac{\langle \theta^2 \rangle}{s} = 2k_1 \quad (5.3)$$

where k_1 is given (4.39), according to [Solodov and Betti, 2008] or [Atzeni et al., 2009b].

There are some cases where the "hybrid assumption" is not fully justified. For example, it is not possible to distinguish between the fast and slow electrons in thin laser-irradiated targets where fast electrons are crossing the laser-plasma interaction zone many times. In addition, even if the "hybrid assumption" is justified, as in the case of thick targets, one needs to extract from the full PIC simulation the properties of the fast electrons in order to initialize the hybrid simulation. More recently, an improved model, named the two-region PIC, was proposed by [Cohen et al., 2010]. In this model, the simulation box is separated into a low plasma density region of the laser-plasma interaction and a high density region where the laser-generated fast electrons are propagating through. The position of the boundary between these two regions is taken at the density $100n_c$. In the low density region, the plasma is described by a full PIC algorithm with collisions taken into account. In the high density region, the Maxwell's equations are reduced to Ohm's law for the electric fields and the Ampère's law for the magnetic field. This reduced field solver is similar to the one used in the hybrid PIC models, whereas the background plasma comprises macroparticles as in a traditional PIC model. However, the difficulty of this model arises from the continuity of electromagnetic fields near the boundary between the two regions which can be violated due to the noise of the full Maxwell solver. This noise is usually several orders of magnitude higher than the one of the reduced field solver, which may mask the real value of the field given to the reduced field solver after a long period of simulation. This issue may be partially solved by increasing the spatial resolution and using a large number of macroparticles per cell.

5.2 Vlasov-Fokker-Planck methods

5.2.1 Full Vlasov-Fokker-Planck methods

Another approach consists in solving the Vlasov-Fokker-Planck equation (4.51) with finite-difference schemes for the spatial advection, advection in the momentum space due to the electromagnetic fields and the collisional friction and diffusion. This is a fundamentally different approach for the description of a system of particles compared to the PIC method. It considers a continuous distribution function and solves the kinetic equation on a Eulerian grid. These methods are very expensive in terms of numerical cost due to a huge number of variables that have to be resolved (3 in space and 3 in momentum). Therefore, hybrid versions have also been proposed for the same reasons as for PIC codes. Besides, due to the robustness and the long history of PIC codes (see for example [Birdsall and Langdon, 1991]), the finite-difference techniques have only been developed recently after

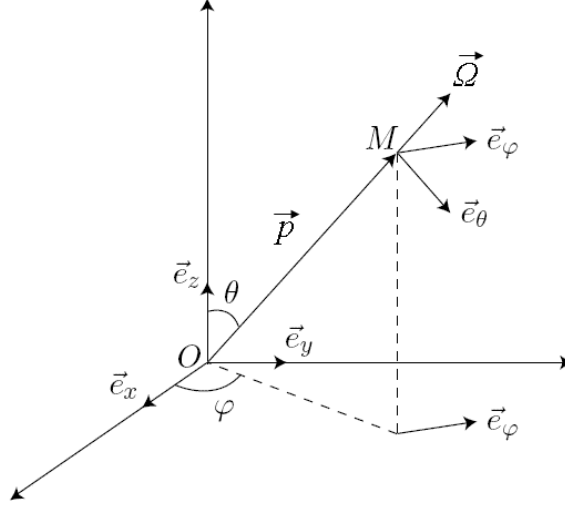


Figure 5.2: Spherical coordinates corresponding to Equation (5.4). $\boldsymbol{\Omega} = \mathbf{p}/p = [\sin \theta \cos \varphi, \sin \theta \sin \varphi, \cos \theta]^T$, $\mathbf{e}_\theta = [\cos \theta \cos \varphi, \cos \theta \sin \varphi, -\sin \theta]^T$ and $\mathbf{e}_\varphi = [-\sin \varphi, \cos \varphi, 0]^T$.

the pioneering work by [Bell et al., 1981]. Besides, I did not find in the literature codes that solve the full Vlasov-Belyaev-Budker equation (4.51), using, for example, the Rosenbluth potentials proposed by [Braams and Karney, 1987]. The published codes solve the Vlasov equation with the Landau collisional operator, which is only valid for relativistic electrons colliding with non-relativistic background particles. Indeed, in the case of a "hybrid model", as it will be demonstrated in the next **Chapter 6**, the Belyaev-Budker collision tensor can be simplified into a Landau-like collision operator. Considering the spherical coordinates (p, θ, φ) for the momentum space (see **Figure 5.2**) and assuming a fully ionized plasma, the kinetic equation reads, following the notations used by [Yokota et al., 2006]

$$\begin{aligned}
 \frac{\partial f_b}{\partial t} &+ \frac{\partial}{\partial x} [v \sin \theta \cos \varphi f_b] + \frac{\partial}{\partial y} [v \sin \theta \sin \varphi f_b] + \frac{\partial}{\partial z} [v \cos \theta f_b] \\
 &+ \frac{1}{p^2} \frac{\partial}{\partial p} \{ p^2 [F_x \sin \theta \cos \varphi + F_y \sin \theta \sin \varphi + F_z \cos \theta] f_b \} \\
 &+ \frac{1}{p \sin \theta} \frac{\partial}{\partial \theta} \{ \sin \theta [F_x \cos \theta \cos \varphi + F_y \cos \theta \sin \varphi - F_z \sin \theta] f_b \} \\
 &+ \frac{1}{p \sin \theta} \frac{\partial}{\partial \varphi} \{ [-F_x \sin \varphi + F_y \cos \varphi] f_b \} \\
 &= \frac{m_e^2}{p^2} \frac{\partial}{\partial p} \left[\gamma^2 \left(\frac{Y_{ee} n_e}{m_e} + \frac{Y_{ei} n_i}{m_i} \right) f_b \right] \\
 &+ \frac{1}{2} (Y_{ee} n_e + Y_{ei} n_i) \frac{\gamma m_e}{p^3} \left\{ \frac{1}{\sin \theta} \frac{\partial}{\partial \theta} \left(\sin \theta \frac{\partial f_b}{\partial \theta} \right) + \frac{1}{\sin^2 \theta} \frac{\partial^2 f_b}{\partial \varphi^2} \right\}.
 \end{aligned} \tag{5.4}$$

where

$$F_x = -e[E_x - (v/c) \cos \theta B_y + (v/c) \sin \theta \sin \varphi B_z],$$

$$F_y = -e[E_y + (v/c) \cos \theta B_x - (v/c) \sin \theta \cos \varphi B_z],$$

$$F_z = -e[E_z + (v/c) \sin \theta \cos \varphi B_y - (v/c) \sin \theta \sin \varphi B_x]$$

are the components of the force depending on the self-generated electromagnetic fields (\mathbf{E} , \mathbf{B}) while

$$Y_{ee} = 4\pi e^4 \ln \Lambda_{ee}^{\text{rel}}$$

and

$$Y_{ei} = 4\pi Z^2 e^4 \ln \Lambda_{ei}^{\text{rel}}$$

are the coefficients coming from the stopping power/angular scattering formulas of the relativistic electrons respectively by colliding electrons and ions. Besides, except for the code developed by [Yokota et al., 2006], the Vlasov-Landau codes developed for fast electron transport do not take into account the γ -dependence in the relativistic Coulomb logarithms $\ln \Lambda_{ee}^{\text{rel}}$ and $\ln \Lambda_{ei}^{\text{rel}}$ in Y_{ee} and Y_{ei} [Sherlock, 2009] [Duclous et al., 2009]. While this approximation is fully justified for non-relativistic electrons, this γ -dependence defines the energy loss compartment of relativistic electrons, as explained in **Chapter 4, section 4.2.1**. Thus, by fixing numerical values for $\ln \Lambda_{ee}^{\text{rel}}$ and $\ln \Lambda_{ei}^{\text{rel}}$, one underestimates the relativistic electron energy loss and the material heating. Even in the original paper by [Yokota et al., 2006], the factor $[(Y_{ee}n_e/m_e) + (Y_i n_i/m_i)]$ of the collisional friction term appears outside the p -derivative which means that the factors $\ln \Lambda_{ee}^{\text{rel}}$ and $\ln \Lambda_{ei}^{\text{rel}}$ are supposed to be independent of p . An excellent review dedicated to Vlasov-Fokker-Planck numerical modeling is given by [Thomas et al., 2012].

5.2.2 Distribution Function Expansion methods

Spherical Harmonic Expansion method

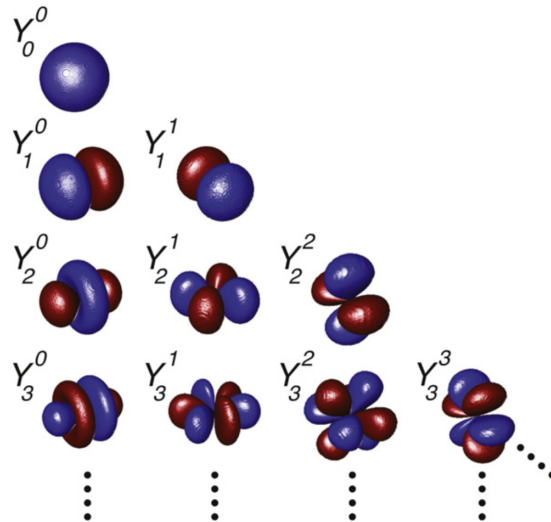


Figure 5.3: Iso-surfaces of the first 10 spherical harmonics Y_l^m , $0 \leq m \leq l \leq 3$ multiplied by $\exp(-p^2)$ [Tzoufras et al., 2011]

The computational cost of solving (5.4) can be prohibitive. Indeed, even if one considers mod-

5.2. VLASOV-FOKKER-PLANCK METHODS

estly 10^2 cells for each dimension, one needs to memorize $10^{6 \times 2} = 10^{12}$ values of the distribution function f_b at each time step which represents 8 To in double-precision. Depending on the Courant–Friedrichs–Lewy condition which defines the time step Δt and the simulation time $t_f = N_f \Delta t$, Vlasov-Fokker-Planck simulations can become extremely expensive in terms of computer memory and/or time computation. In practice, the full Vlasov-Fokker-Planck equation is resolved in 1D-1V, 1D-2V, 1D-3V or at maximum 2D-3V. Another approach consists in expanding the distribution function f_b in spherical harmonics in the momentum-space, as initially proposed by [Bell et al., 2006]. This expansion reads

$$f_b(\mathbf{r}, \mathbf{p}, t) = \sum_{l=0}^{N_l} \sum_{m=-l}^l f_l^m(\mathbf{r}, |\mathbf{p}|, t) P_l^{|m|}(\cos \theta) \exp(im\varphi) \quad (5.5)$$

where f_l^{-m} equals the complex conjugate of f_l^m and $P_l^{|m|}(\cos \theta)$ are the associated Legendre polynomials (including the Condon-Shortley phase $(-1)^m$)

$$P_l^m(x) = (-1)^m (1-x^2)^{m/2} \frac{d^m P_l}{dx^m}$$

with

$$P_l(x) = \frac{1}{2^l l!} \frac{d^l}{dx^l} (x^2 - 1)^l$$

the unassociated Legendre polynomials. For example, the first associated Legendre polynomials read

$$\begin{aligned} P_0^0(x) &= 1, \\ P_1^0(x) &= x, \\ P_1^1(x) &= -(1-x^2)^{1/2}, \\ P_2^0(x) &= \frac{1}{2}(3x^2-1), \\ P_2^1(x) &= -3x(1-x^2)^{1/2} \text{ and} \\ P_2^2(x) &= 3(1-x^2). \end{aligned}$$

The spherical harmonic expansion (5.5) is exact for $N_l \rightarrow \infty$ but, in practice, N_l is chosen, depending on the degree of anisotropy of a given physical problem. The larger the indices (l, m) are, the more directional/anisotropic the harmonics are. Recently, [Tzoufras et al., 2011] developed a relativistic Fokker-Planck code, called OSHUN, following this approach initially proposed for non-relativistic electrons (KALOS code by [Bell et al., 2006]). [Tzoufras et al., 2011] shown that $N_l \geq 13$ (≈ 100 harmonics f_l^m) are sufficient to study the relativistic collisionless two-stream and filamentation instabilities presented in **Chapter 3**. However, it is expected that collisional effects reduce the needed degree of anisotropy N_l . In addition to reducing the number of variables from 6 (x, y, z, p_x, p_y, p_z) to only 4 ($x, y, z, |p|$), the advantage of the spherical harmonic decomposition is that the Y_l^m are the

eigenfunction of the Laplace-Beltrami operator

$$\Delta_{\theta,\varphi}(f_b) = \frac{1}{\sin\theta} \frac{\partial}{\partial\theta} \left(\sin\theta \frac{\partial f_b}{\partial\theta} \right) + \frac{1}{\sin^2\theta} \frac{\partial^2 f_b}{\partial\varphi^2}$$

of the Vlasov-Fokker-Planck diffusion term in (5.4). Indeed, by noting

$$Y_l^m(\theta, \varphi) = \sqrt{\frac{2l+1}{4\pi} \frac{(l-m)!}{(l+m)!}} P_l^m(\cos\theta) \exp(im\varphi), \quad -l \leq m \leq l \quad (5.6)$$

the spherical harmonics, one has

$$\Delta_{\theta,\varphi}(Y_l^m) = -l(l+1)Y_l^m. \quad (5.7)$$

This method gives rise to a set of coupled differential equations for the coefficients f_l^m , obtained starting from the Vlasov-Landau equation (5.4). They read

$$\begin{aligned} \frac{\partial f_l^m}{\partial t} &- \mathfrak{A}_{x,l}^m - \mathfrak{A}_{y,l}^m - \mathfrak{A}_{z,l}^m - \mathfrak{E}_{x,l}^m - \mathfrak{E}_{y,l}^m - \mathfrak{E}_{z,l}^m - \mathfrak{B}_l^m \\ &= \frac{\partial}{\partial p} \left[\frac{1}{v^2} \left(\frac{Y_{ee} n_e}{m_e} + \frac{Y_{ei} n_i}{m_i} \right) f_l^m \right] - \frac{l(l+1)}{2} (Y_{ee} n_e + Y_{ei} n_i) \frac{\gamma m_e}{p^3} f_l^m. \end{aligned} \quad (5.8)$$

The advection terms in space are given for $m \neq 0$ by

$$\mathfrak{A}_{z,l}^m = -v \frac{\partial}{\partial z} \left[\left(\frac{l-m}{2l-1} \right) f_{l-1}^m + \left(\frac{l+m+1}{2l+3} \right) f_{l+1}^m \right],$$

$$\begin{aligned} \mathfrak{A}_{x,l}^m + \mathfrak{A}_{y,l}^m &= \frac{v}{2} \left[\left(\frac{\partial}{\partial x} - i \frac{\partial}{\partial y} \right) \frac{f_{l-1}^{m-1}}{2l-1} - \left(\frac{\partial}{\partial x} + i \frac{\partial}{\partial y} \right) (l-m)(l-m-1) \frac{f_{l-1}^{m+1}}{2l-1} \right. \\ &\quad \left. - \left(\frac{\partial}{\partial x} - i \frac{\partial}{\partial y} \right) \frac{f_{l+1}^{m-1}}{2l+3} + \left(\frac{\partial}{\partial x} + i \frac{\partial}{\partial y} \right) (l+m+1)(l+m+2) \frac{f_{l+1}^{m+1}}{2l+3} \right] \end{aligned}$$

and for $m = 0$ by

$$\mathfrak{A}_{x,l}^0 + \mathfrak{A}_{y,l}^0 = \text{Re} \left\{ -v \left(\frac{\partial}{\partial x} + i \frac{\partial}{\partial y} \right) \left[-\frac{l(l-1)}{2l-1} f_{l-1}^1 + \frac{(l+1)(l+2)}{2l+3} f_{l+1}^1 \right] \right\}.$$

The advection terms in the momentum space due to the electric field are given by

$$\mathfrak{E}_{z,l}^m = eE_z \left[\frac{l-m}{2l-1} p^{l-1} \frac{\partial}{\partial p} \left(p^{-(l-1)} f_{l-1}^m \right) + \frac{l+m+1}{2l+3} p^{-(l+2)} \frac{\partial}{\partial p} \left(p^{l+2} f_{l+1}^m \right) \right]$$

and, for $m \neq 0$ by

$$\begin{aligned} \mathfrak{E}_{x,l}^m + \mathfrak{E}_{y,l}^m &= \frac{e}{2} \left[\begin{aligned} &\frac{E_x - iE_y}{2l-1} p^{l-1} \frac{\partial}{\partial p} \left(p^{-(l-1)} f_{l-1}^{m-1} \right) \\ &- \frac{E_x + iE_y}{2l-1} (l-m)(l-m-1) p^{l-1} \frac{\partial}{\partial p} \left(p^{-(l-1)} f_{l-1}^{m+1} \right) \\ &- \frac{E_x - iE_y}{2l+3} p^{-(l+2)} \frac{\partial}{\partial p} \left(p^{l+2} f_{l+1}^{m-1} \right) \\ &+ \frac{E_x + iE_y}{2l+3} (l+m+1)(l+m+2) p^{-(l+2)} \frac{\partial}{\partial p} \left(p^{l+2} f_{l+1}^{m+1} \right) \end{aligned} \right] \end{aligned}$$

and for $m = 0$ by

$$\begin{aligned} \mathfrak{E}_{x,l}^0 + \mathfrak{E}_{y,l}^0 &= \text{Re} \left\{ e (E_x + iE_y) \left[\begin{aligned} &-\frac{l(l-1)}{2l-1} p^{l-1} \frac{\partial}{\partial p} \left(p^{-(l-1)} f_{l-1}^1 \right) \\ &+ \frac{(l+1)(l+2)}{2l+3} p^{-(l+2)} \frac{\partial}{\partial p} \left(p^{l+2} f_{l+1}^1 \right) \end{aligned} \right] \right\}. \end{aligned}$$

Finally, the rotational term in the momentum space due to the magnetic field is given for $m \neq 0$ by

$$\mathfrak{B}_l^m = -i \frac{eB_z}{\gamma m_e c} m f_l^m + \frac{e}{2\gamma m_e c} \left[(l-m)(l+m+1) (B_y - iB_x) f_l^{m+1} - (B_y + iB_x) f_l^{m-1} \right]$$

and for $m = 0$ by

$$\mathfrak{B}_l^0 = l(l+1) \frac{e}{\gamma m_e c} \text{Re} \left\{ (B_y - iB_x) f_l^1 \right\}.$$

The electron-electron collision operator in OSHUN [Tzoufras et al., 2011] [Tzoufras et al., 2013] is based on the non-relativistic Rosenbluth potentials [Rosenbluth et al., 1957]

$$\left(\frac{\partial f_b}{\partial t} \right)_{\text{coll,ee}} = -\frac{4\pi e^4 \ln \Lambda_{ee}}{m_e^2} \left\{ \frac{\partial}{\partial \mathbf{v}} \cdot \left(f_b \frac{\partial h[f_b]}{\partial \mathbf{v}} \right) - \frac{1}{2} \left(\frac{\partial}{\partial \mathbf{v}} \otimes \frac{\partial}{\partial \mathbf{v}} \right) : \left[f_b \left(\frac{\partial}{\partial \mathbf{v}} \otimes \frac{\partial g[f_b]}{\partial \mathbf{v}} \right) \right] \right\} \quad (5.9)$$

$$\text{where } \frac{\partial^4 g}{\partial \mathbf{v}^4} [f_b] = \frac{\partial^2 h}{\partial \mathbf{v}^2} [f_b] = -8\pi f_b$$

while the electron-ion collision operator is based on the non-relativistic Lorentzian approximation (see **Appendix A, section A.3.2**)

$$\left(\frac{\partial f_b}{\partial t} \right)_{\text{coll,ei}} = -\frac{4\pi n_i Z^2 e^4 \ln \Lambda_{ei}}{m_e^2 v^3} f_b = -\frac{\nu_{ei}}{2} f_b. \quad (5.10)$$

In order to account for this electron-ion collision operator, one just has to replace Y_{ei} by 0 in the collisional friction term of (5.8) (first term in the right hand side) and replace $\ln \Lambda_{ei}^{\text{rel}}$ by the classical Coulomb logarithm $\ln \Lambda_{ei}$ (see **Appendix A, section A.2.3**) in Y_{ei} of the angular diffusion term (second term in the right hand side). The electron-electron collision operator (5.9) is more difficult to solve numerically. In OSHUN, in order to break the interdependence between the amplitudes f_l^m and allow for rapid numerical calculations, it is linearized assuming that f_b is weakly anisotropic

$f_b = f_0^0 + \delta f_b$. According to [Tzoufras et al., 2011], it gives

$$\begin{aligned} \left(\frac{\partial f_0^0}{\partial t} \right)_{\text{coll},ee} &= \frac{4\pi e^4 \ln \Lambda_{ee}}{m_e^2} 4\pi (f_0^0)^2 + \frac{4\pi e^4 \ln \Lambda_{ee}}{m_e^2} \frac{1}{2} \left(\frac{\partial}{\partial \mathbf{v}} \otimes \frac{\partial g[f_0^0]}{\partial \mathbf{v}} \right) : \left(\frac{\partial}{\partial \mathbf{v}} \otimes \frac{\partial f_0^0}{\partial \mathbf{v}} \right) \\ &= \frac{(4\pi)^2 e^4 \ln \Lambda_{ee}}{3m_e^2} \frac{1}{v^2} \frac{\partial}{\partial v} \left[\frac{1}{v} \frac{\partial W[f_0^0]}{\partial v} \right] \end{aligned} \quad (5.11)$$

for the isotropic part where

$$W[f_0^0] = f_0^0 \int_0^v f_0^0 v^4 dv + v^3 f_0^0 \int_v^\infty f_0^0 v dv - 3 \int_v^\infty f_0^0 v dv \int_0^v f_0^0 v^2 dv$$

according to [Bobylev and Chuyanov, 1976] and

$$\begin{aligned} \left(\frac{\partial \delta f_b}{\partial t} \right)_{\text{coll},ee} &= 8\pi \frac{4\pi e^4 \ln \Lambda_{ee}}{m_e^2} f_0^0 \delta f_b + \frac{1}{2} \left(\frac{\partial}{\partial \mathbf{v}} \otimes \frac{\partial g[f_0^0]}{\partial \mathbf{v}} \right) : \left(\frac{\partial}{\partial \mathbf{v}} \otimes \frac{\partial \delta f_b}{\partial \mathbf{v}} \right) \\ &+ \frac{1}{2} \left(\frac{\partial}{\partial \mathbf{v}} \otimes \frac{\partial f_0^0}{\partial \mathbf{v}} \right) : \left(\frac{\partial}{\partial \mathbf{v}} \otimes \frac{\partial g[\delta f_b]}{\partial \mathbf{v}} \right) \end{aligned} \quad (5.12)$$

for the anisotropic perturbation. In order to account for this electron-electron collision operator, one just has to replace Y_{ee} by 0 in (5.8) and add (5.11) in the right hand side of Equation (5.8) with $m = l = 0$ and $(\partial f_l^m / \partial t)_{\text{coll},ee}$ coming from the decomposition in spherical harmonics of (5.12) (see [Tzoufras et al., 2011]) in the right hand side of the other equations (5.8) with $l \neq 0$. These collision operators are out of the scope of laser-generated relativistic electron beam transport presented in this manuscript. The details of numerical methods used to discretize these collision operators can be found in [Tzoufras et al., 2011]. The authors point out that for certain problems it would be extremely expensive to apply an explicit scheme for the collisions of the anisotropic part of the distribution function. Concerning the Vlasov part, i.e. the left hand side of equation (5.8), all advection terms in the phase-space are differentiated by using the central difference scheme of the second order. While periodic and reflecting boundaries in space have been implemented, the behavior of the harmonics at $p = 0$ has been chosen such that $f_{l \geq 1}^m(p) = f_l^m(p_1)(p/p_1)^l$ and that the isotropic part of the distribution has an extremum at $p = 0$ in order to get the p -derivatives at $p = p_0$ where $p_k = p_0 + k\Delta p$ with $p_0 = \Delta p/2$ and Δp the numerical momentum step. An iteration loop involving a list of successive operations on each harmonic is performed such that each operator in the (l, m) -equation (5.8) depends only on f_l^m . These operations are found by starting from (5.8) to find the effect that each f_l^m has on its neighboring amplitudes in (l, m) space. Thus, (5.8) can finally be written with the form

$$\frac{\partial f_l^m}{\partial t} = F(f_l^m, t) \quad (5.13)$$

and be therefore numerically solved by using the Runge-Kutta methods up to the 4th order.

Cartesian Tensor Scalar Product Expansion method

Another expansion of the distribution function has been proposed by [Johnston, 1960] and [Shkarofsky, 1963] for plasmas. This tensor scalar product expansion reads

$$f_b(\mathbf{r}, \mathbf{p}, t) = \frac{1}{4\pi} f_0(\mathbf{r}, |\mathbf{p}|, t) + \frac{3}{4\pi} \mathbf{f}_1(\mathbf{r}, |\mathbf{p}|, t) \cdot \boldsymbol{\Omega} + \sum_{l \geq 2}^{N_l} \frac{C_l}{4\pi} \mathbf{f}_l(\mathbf{r}, |\mathbf{p}|, t) \odot_l \boldsymbol{\Omega}^{(l)} \quad (5.14)$$

where

$$C_l = \frac{(2l+1)!}{2l!},$$

$\boldsymbol{\Omega} = \mathbf{p}/p = [\sin \theta \cos \varphi, \sin \theta \sin \varphi, \cos \theta]^T$ (see **Figure 5.2**), $\boldsymbol{\Omega}^{(l)}$ is the $(l-1)$ tensor products of $\boldsymbol{\Omega}$ with itself

$$\boldsymbol{\Omega}^{(l)} = \boldsymbol{\Omega} \otimes \dots \otimes \boldsymbol{\Omega} = (\Omega_{i_1} \Omega_{i_2} \dots \Omega_{i_l})_{(i_1, i_2, \dots, i_l) \in \{x, y, z\}^l}$$

and \odot_l is the l times contracted product which means that

$$\mathbf{A} \odot_l \mathbf{B} = \sum_{i_1=x, y, z} \sum_{i_2=x, y, z} \dots \sum_{i_l=x, y, z} A_{i_1, i_2, \dots, i_l} B_{i_1, i_2, \dots, i_l}$$

where \mathbf{A} and \mathbf{B} are l th order tensors. Thus, f_0 is a scalar (1 term f_0), \mathbf{f}_1 is a vector (3 terms $f_{1,x}$, $f_{1,y}$ and $f_{1,z}$), \mathbf{f}_2 is a second order tensor (9 terms $f_{2,xx}$, $f_{2,xy}$, $f_{2,xz}$, $f_{2,yx}$, $f_{2,yy}$, $f_{2,yz}$, $f_{2,zx}$, $f_{2,zy}$ and $f_{2,zz}$), \mathbf{f}_3 is a third order tensor (27 terms $f_{3,i_1 i_2 i_3}$, $(i_1, i_2, i_3) \in \{x, y, z\}^3$) and so on... The expansion (5.14) is exact in the limit $N_l \rightarrow \infty$ and it is equivalent to the spherical harmonics expansion (5.5) cut at the same order N_l . Indeed, by writing the spherical harmonic decomposition (5.5) with the form [Tzoufras et al., 2011]

$$f_b(\mathbf{r}, \mathbf{p}, t) = \sum_{l=0}^{N_l} \sum_{m=0}^l \sum_0^1 f_{lms}(\mathbf{r}, |\mathbf{p}|, t) Y_{lms}(\theta, \varphi) \quad (5.15)$$

where

$$Y_{lms}(\theta, \varphi) = \sqrt{\frac{2l+1}{4\pi} \frac{(l-m)!}{(l+m)!}} P_l^m(\cos \theta) \begin{cases} \frac{\delta_{0s} \cos(m\phi) + \delta_{1s} \sin(m\phi)}{\sqrt{2}} & \text{if } m > 0 \\ \delta_{0s} & \text{if } m = 0 \end{cases},$$

one has [Johnston, 1960]

$$\sum_{l=1}^{N_l} \frac{C_l}{4\pi} \mathbf{f}_l(\mathbf{r}, |\mathbf{p}|, t) \odot_l \boldsymbol{\Omega}^{(l)} = \sum_{l=1}^{N_l} \sum_{m=0}^l \sum_0^1 f_{lms}(\mathbf{r}, |\mathbf{p}|, t) Y_{lms}(\theta, \varphi). \quad (5.16)$$

For example, we have

$$\frac{1}{4\pi} f_0 = \frac{f_{000}}{\sqrt{4\pi}},$$

and

$$\begin{aligned} \frac{3}{4\pi} \mathbf{f}_1 \cdot \boldsymbol{\Omega} &= \frac{3}{4\pi} (f_{1,x} \sin \theta \cos \varphi + f_{1,y} \sin \theta \sin \varphi + f_{1,z} \cos \theta) \\ &= \sqrt{\frac{3}{4\pi}} \left(f_{100} \cos \theta - \frac{f_{110}}{2} \sin \theta \cos \varphi - \frac{f_{111}}{2} \sin \theta \sin \varphi \right). \end{aligned}$$

According to these two first examples, one can clearly see, that the dependences in $\cos^{a_l} \theta \sin^{b_l} \theta \cos^{c_l} \varphi \sin^{d_l} \varphi$ are strictly the same where a_l , b_l , c_l , and d_l are constants depending on l . However, it is not true for the second order term

$$\frac{C_2}{4\pi} \mathbf{f}_2 : \boldsymbol{\Omega} \otimes \boldsymbol{\Omega} \neq \sum_{m=0}^2 \sum_0^1 f_{2ms}(\mathbf{r}, |\mathbf{p}|, t) Y_{lms}(\theta, \varphi)$$

because 1 , $\boldsymbol{\Omega}$ and $\boldsymbol{\Omega} \otimes \boldsymbol{\Omega}$ are not orthogonal (with the definition of the scalar product \odot_l) contrary to the spherical harmonics. Actually, this is 1 , $\boldsymbol{\Omega}$ and $\boldsymbol{\Omega} \otimes \boldsymbol{\Omega} - (1/3)\mathbf{I}$ that are orthogonal. Indeed, according to (5.15), the relation between the Y_{lms} and the Y_l^m are straightforward and reads

$$\begin{pmatrix} Y_{lm0} \\ Y_{lm1} \end{pmatrix} = \frac{1}{\sqrt{2}} \begin{pmatrix} 1 & (-1)^m \\ -i & i(-1)^m \end{pmatrix} \cdot \begin{pmatrix} Y_l^{|m|} \\ Y_l^{-|m|} \end{pmatrix}$$

while the relation between the f_{lms} and the f_l^m are

$$f_l^m = \sqrt{\frac{2l+1}{4\pi} \frac{(l-m)!}{(l+m)!}} \frac{f_{lm0} - i f_{lm1}}{\sqrt{2}}.$$

Thus, one gets the relations for the three first components

$$f_0 = 4\pi f_0^0, \tag{5.17}$$

$$\mathbf{f}_1 = \frac{4\pi}{3} \begin{pmatrix} 2\text{Re}\{f_1^1\} \\ -2\text{Im}\{f_1^1\} \\ f_1^0 \end{pmatrix}, \tag{5.18}$$

and

$$\mathbf{f}_2 - \frac{1}{3} f_0 \mathbf{I} = \frac{4\pi}{15} \begin{pmatrix} 12\text{Re}\{f_2^2\} - f_2^0 & -12\text{Im}\{f_2^2\} & 6\text{Re}\{f_2^1\} \\ -12\text{Im}\{f_2^2\} & 12\text{Re}\{f_2^2\} - f_2^0 & -6\text{Im}\{f_2^1\} \\ 6\text{Re}\{f_2^1\} & -6\text{Im}\{f_2^1\} & 2f_2^0 \end{pmatrix} \tag{5.19}$$

where \mathbf{I} is the 2nd order unit tensor.

In the case where the Cartesian tensor scalar product expansion is cut at the first order $N_l = 1$, each \mathbf{f}_l corresponds to the l th order angular moment of the distribution function f_b :

$$\mathbf{f}_l(\mathbf{r}, |\mathbf{p}|, t) = p^2 \int_{S_2} f(\mathbf{r}, \mathbf{p}, t) \boldsymbol{\Omega}^{(\ell)} d^2 \boldsymbol{\Omega} \tag{5.20}$$

5.2. VLASOV-FOKKER-PLANCK METHODS

where it has been noted S_2 the unity sphere in the momentum space, defined by $\{(\theta, \varphi), \theta \in [0, \pi], \varphi \in [0, 2\pi[\}$ (see **Figure 5.2**). Thus, while it is strictly equivalent to the spherical harmonic expansion, the Cartesian tensor scalar product expansion cut at the 1st order has the advantage to directly relate the physical quantities and the expansion terms \mathbf{f}_l . In our case of relativistic electron beam transport, f_0 yields directly to the beam number density

$$n_b = \int_{\mathbb{R}^3} f_b d^3 \mathbf{p} = \int_0^\infty f_0 dp \quad (5.21)$$

and the beam kinetic energy density

$$K_b = n_b (\gamma_b - 1) m_e c^2 = \int_{\mathbb{R}^3} (\gamma - 1) m_e c^2 f_b d^3 \mathbf{p} = \int_0^\infty (\gamma - 1) m_e c^2 f_0 dp \quad (5.22)$$

while \mathbf{f}_1 yields directly to the beam current density

$$\mathbf{j}_b = -n_b e \mathbf{v}_b = e \int_{\mathbb{R}^3} \mathbf{v} f_b d^3 \mathbf{p} = -e \int_0^\infty v \mathbf{f}_1 dp \quad (5.23)$$

where \mathbf{v}_b is the mean beam electrons velocity, the mean beam electrons momentum

$$\mathbf{p}_b = \frac{1}{n_b} \int_{\mathbb{R}^3} \mathbf{p} f_b d^3 \mathbf{p} = \frac{1}{n_b} \int_0^\infty p \mathbf{f}_1 dp \quad (5.24)$$

and the beam kinetic energy flux

$$\mathbf{F}_b = \int_{\mathbb{R}^3} (\gamma - 1) m_e c^2 \mathbf{v} f_b d^3 \mathbf{p} = \int_0^\infty (\gamma - 1) m_e c^2 v \mathbf{f}_1 dp. \quad (5.25)$$

In this cartesian tensor scalar product approach cut at the 1st order, the l th order equation that have to be solved in order to get the expansion term \mathbf{f}_l can be obtained by integrating over the unity sphere S_2 the Vlasov-Fokker-Planck equation (5.4) multiplied by $\Omega^{(l)}$. According to (5.20), these two first equations of the hierarchy read

$$\frac{\partial f_0}{\partial t} + \frac{\partial}{\partial \mathbf{r}} \cdot (v \mathbf{f}_1) - \frac{\partial}{\partial p} (e \mathbf{f}_1 \cdot \mathbf{E}) = \frac{\partial}{\partial p} \left[\frac{1}{v^2} \left(\frac{Y_{ee} n_e}{m_e} + \frac{Y_{ei} n_i}{m_i} \right) f_0 \right] \quad (5.26)$$

and

$$\begin{aligned} & \frac{\partial \mathbf{f}_1}{\partial t} + \frac{\partial}{\partial \mathbf{r}} \cdot (v \mathbf{f}_2) - \frac{\partial}{\partial p} (e \mathbf{f}_2 \cdot \mathbf{E}) + \frac{e}{p} (f_0 \mathbf{I} - \mathbf{f}_2) \cdot \mathbf{E} + \frac{e}{\gamma m_e c} \mathbf{f}_1 \times \mathbf{B} \\ &= \frac{\partial}{\partial p} \left[\frac{1}{v^2} \left(\frac{Y_{ee} n_e}{m_e} + \frac{Y_{ei} n_i}{m_i} \right) \mathbf{f}_1 \right] - (Y_{ee} n_e + Y_{ei} n_i) \frac{\gamma m_e}{p^3} \mathbf{f}_1. \end{aligned} \quad (5.27)$$

In addition to the increasing complexity of the obtained equations with increasing l , one can notice that each l th order equation for \mathbf{f}_l makes appearing the $(l+1)$ th order component \mathbf{f}_{l+1} . Consequently, the (N_l+1) th order component appearing in the N_l th order equation has to be approximated to close

the set of equations. This is done by imposing the PN closure relation

$$\mathbf{f}_{N_i+1} = \int_{S_2} f_b \boldsymbol{\Omega}^{(N_i+1)} d^2 \boldsymbol{\Omega} \approx \int_{S_2} \left[\sum_{l=0}^{N_i} \frac{C_l}{4\pi} \mathbf{f}_l \odot_l \boldsymbol{\Omega}^{(l)} \right] \boldsymbol{\Omega}^{(N_i+1)} d^2 \boldsymbol{\Omega}.$$

In practice, assuming a small perturbation of the isotropy, the Cartesian models are often limited to the 1st order approximation (P1) in order to make fast computations. This was for example usually done in studies of the non local thermal flux carried out by suprathermal electrons [Matte et al., 1984] [Schurtz et al., 2000] [Nicolai et al., 2006] [Schurtz et al., 2007]. In this case, the second order angular moment expression reduces to the isotropic part of (5.19)

$$\mathbf{f}_2 = \frac{1}{3} f_0 \mathbf{I}. \quad (5.28)$$

Injecting it in the 1st order equation, one gets the so-called diffusive approximation characterized by the two equations

$$\frac{\partial f_0}{\partial t} + \frac{\partial}{\partial \mathbf{r}} \cdot (v \mathbf{f}_1) - \frac{\partial}{\partial p} (e \mathbf{f}_1 \cdot \mathbf{E}) = \frac{\partial}{\partial p} \left[\frac{1}{v^2} \left(\frac{Y_{ee} n_e}{m_e} + \frac{Y_{ei} n_i}{m_i} \right) f_0 \right]$$

and

$$\begin{aligned} & \frac{\partial \mathbf{f}_1}{\partial t} + \frac{v}{3} \frac{\partial f_0}{\partial \mathbf{r}} - \frac{\partial}{\partial p} \left(\frac{e}{3} f_0 \mathbf{E} \right) + \frac{e}{p} \frac{2}{3} f_0 \cdot \mathbf{E} + \frac{e}{\gamma m_e c} \mathbf{f}_1 \times \mathbf{B} \\ & = \frac{\partial}{\partial p} \left[\frac{1}{v^2} \left(\frac{Y_{ee} n_e}{m_e} + \frac{Y_{ei} n_i}{m_i} \right) \mathbf{f}_1 \right] - (Y_{ee} n_e + Y_{ei} n_i) \frac{\gamma m_e}{p^3} \mathbf{f}_1. \end{aligned}$$

5.3 Conclusion

Aspect	PIC (collisionless)	PIC (binary collisions)	PIC (hybrid)	VFP (full)	VFP (hybrid)	VFP (expanded)
Efficiency	High	High	High	Low	Reasonable	Reasonable
Time/space constraint	Restrictive (fs, 10 μm)	Restrictive (fs, 10 μm)	Somewhat restrictive (ps, 100 μm)	Restrictive (fs, μm)	Somewhat restrictive (ps, 100 μm)	Reasonable (ps, 100 μm – ns, mm)
Noise/finesse	Poor	Poor	Fair	Good	Good	Good
Treatment of collisionless phenomena	Good	Good	Good	Good	Good	Good–Poor (depends on no. expansion terms)
Treatment of semi-collisional phenomena ($\ln A_{ei} \gg 1$)	None	Good	None	Good	Good	Good
Treatment of highly-collisional phenomena ($\ln A_{ei} \leq 1$)	None	None	Reasonable	None	Reasonable	None

Figure 5.4: Qualitative summary of the benefits and drawbacks of different approaches [Thomas et al., 2012]

The pros and cons of each technique, finite difference Vlasov-Fokker-Planck and finite particle methods are summarized in the **Figure 5.4**, taken from [Thomas et al., 2012]. Particle-in-cell (PIC)

5.3. CONCLUSION

methods are listed with the headings Collisionless, Binary collisions, and Hybrid methods; Vlasov-Fokker-Planck (VFP) methods are listed as Full, Hybrid and Expanded, with Full being the full finite-differenced phase-space, Hybrid having the same basic fluid model as the PIC Hybrid model, and Expanded meaning using the spherical harmonic or Cartesian tensor expansion. The first three aspects of the codes, "Efficiency", "Time/space constraint" and "Noise/finesse" are rather qualitative. Efficiency is how the information is stored, it relates to how fast the code is expected to be, and is the most subjective rating. PIC methods store information in a minimal way, and are therefore both listed as "High". Full Vlasov-Fokker-Planck would typically contain the most redundancy of information storage, as the full phase-space needs to be stored. Hybrid and Expanded Vlasov-Fokker-Planck are listed as "Reasonable" as they store momentum phase-space information in a more efficient way than Full Vlasov-Fokker-Planck. Time/space constraint is also somewhat subjective, and is based on running a "typical" code on a "typical" cluster of ≈ 100 processors in terms of what are the maximum length and timescales that could be "reasonably simulated" for a hot solid target interaction, based on the timescales in published results. Noise/finesse entries are more quantitative, in that Vlasov-Fokker-Planck codes are naturally smoothed, whereas PIC methods are subject to noise due to the finite number of discrete particles, with the Hybrid PIC therefore naturally being less subject to noise. It is worth pointing out that while PIC codes tend to be noisy, which in some cases may provide an unreasonably large seed perturbation for instabilities to grow from, Vlasov-Fokker-Planck codes may be unrealistically smoothed [Thomas et al., 2012]. It is possible that numerical diffusion in Vlasov-Fokker-Planck codes damps real physical instabilities. The last three aspects describe the relative treatment of phenomena in different regimes of $\ln \Lambda_{ei}$ and the relative evaluations are therefore related to the physical equations involved. The most important difference between PIC codes and Vlasov type codes is the issue of graininess, with PIC codes exhibiting artificially high levels of it and Vlasov codes completely lacking it. The presence of granularity in PIC codes is not fundamentally an issue of inadequate statistics, because no matter how high the number of simulation particles is, graininess will never completely disappear from a PIC code (as it is also true for an actual physical system) [Thomas et al., 2012]. This allows PIC codes to model instabilities from noise and to incorporate physics associated with complex particle trajectories. For inertial confinement fusion plasmas however, the lack of statistical smoothness can obscure and modify the physics [Thomas et al., 2012]. Furthermore, numerical effects associated with finite size simulation particles can severely compromise the reliability of the results. Vlasov and Vlasov-Fokker-Planck codes produce results without noise, which allow for clear physical pictures to emerge since Vlasov-Fokker-Planck codes represent the plasma using distribution functions, lack of statistics is never an issue [Thomas et al., 2012]. However, if the distribution function is not described with sufficient details, the physics cannot be modelled accurately, and as a result Vlasov-Fokker-Planck codes are also prone to numerical artifacts.

As a conclusion, both hybrid PIC codes and hybrid Vlasov-Fokker-Planck codes are the best and complementary numerical tools for solving the Vlasov-Belyaev-Budker equation applied to laser-

generated relativistic electron beam transport. Moreover, expanded Vlasov-Fokker-Planck hybrid method are able to limit the numerical cost imposed by the kinetic description of the relativistic electron beam transport. Besides, cutting the expansion of the distribution function N_l may lead to unphysical results since the resulting distribution function may become negative if N_l is not taken sufficiently large for resolving strong anisotropy [Dubroca et al., 2010]. Starting from the V-F-P equation for a Lorentzian gaz of non relativistic electrons, the authors proposed therefore to close the set of equation by using a special closure relation based on the principle of the Minerbo maximum angular entropy approximation [Minerbo, 1977] [Minerbo, 1978], from radiative transfer theory. It allows to close the set of equations by evaluating the 2nd order angular moment \mathbf{f}_2 of the distribution function needed in the 1st order angular moment equation. Contrary to the largely used approximation of the distribution function with the two first Legendre polynomial P1, this M1 model allows to describe the distribution function with an arbitrary local anisotropy.

5.3. CONCLUSION

Part II

Development, Implementation and Validation of a New Reduced Model for Fast Electron Transport in Solids and Dense Plasmas

Chapter 6

Development of a Reduced Model for Laser-generated Relativistic Electron Beam Transport in Solids and Dense Plasmas

” My original decision to devote myself to science was a direct result of the discovery which has never ceased to fill me with enthusiasm since my early youth—the comprehension of the far from obvious fact that the laws of human reasoning coincide with the laws governing the sequences of the impressions we receive from the world about us; that, therefore, pure reasoning can enable man to gain an insight into the mechanism of the latter. In this connection, it is of paramount importance that the outside world is something independent from man, something absolute, and the quest for the laws which apply to this absolute appeared to me as the most sublime scientific pursuit in life. ”

Max Planck

In this chapter, the Landau-like relativistic collision tensor, mentioned in the previous **Chapter 5** and allowing to obtain the Vlasov-Fokker-Planck (V-F-P) equation (5.4), is derived from the Belyaev-Budker collision tensor and applied to relativistic electron beam transport in solids and dense plasmas. It allows us to introduce the relativistic Coulomb logarithms, coming from the relativistic electron stopping powers, in the V-F-P equation. Moreover, it allows us to naturally relate the fast electrons angular scattering mean free path by colliding free, bound and screened free background electrons and background ions with the corresponding stopping powers. It has been shown in **Chapter 5** that the best compromise between the accuracy and the numerical cost of a fast electron transport model can be obtained with a hybrid and expanded relativistic V-F-P method. Such a new reduced kinetic model, developed in this PhD, is presented. It consists in computing the two first angular moments of the distribution function, according to Equations (5.27) and (5.28) in order to make computations as fast as possible. However, in order to preserve the accuracy of calculations in case of strong anisotropy, a special closure relation based on the Minerbo maximum angular entropy approximation [Minerbo, 1977] [Minerbo, 1978], from radiative transfer theory, has been adapted. It allows to close the set of equations by evaluating the anisotropic part of the 2nd order angular moment \mathbf{f}_2 of the distribution function needed in the 1st order angular moment equation (5.28). Contrary to the largely used approximation of the distribution function expanded on the two first Legendre polynomials, often called P1, this M1 model allows to describe the distribution function with an arbitrary local anisotropy. It is shown that the model is exact for fully isotropic and fully anisotropic local angular distribution functions. Furthermore, it relates both of these extrema in the expression of \mathbf{f}_2 . The equation of the local angular entropy of fast electron beam is derived and the limitations of the model are discussed. Developments of new plasma transport coefficients necessary to model the self-generated electromagnetic fields are also proposed.

6.1 Kinetic Description of Relativistic Electron Beam Transport in Solids and Dense Plasmas

6.1.1 The Relativistic Vlasov-Belyaev-Budker Equation Applied to Relativistic Electron Beam Transport

We note $f_b(\mathbf{r}, \mathbf{p}, t)$ the distribution function of the relativistic electron beam in the laboratory frame. It is the solution of the relativistic Vlasov-Belyaev-Budker equation

$$\frac{\partial f_b}{\partial t} + \frac{\partial}{\partial \mathbf{r}} \cdot \left(\frac{\mathbf{p}}{\gamma m_e} f_b \right) - \frac{\partial}{\partial \mathbf{p}} \cdot \left[e \left(\mathbf{E} + \frac{\mathbf{p}}{\gamma m_e c} \times \mathbf{B} \right) f_b \right] = \sum_{\alpha} C_{\alpha}[f_b] \quad (6.1)$$

where

$$C_\alpha[f_b] = -\frac{\partial}{\partial \mathbf{p}} \cdot \int_{\mathbb{R}^3} \mathbf{U}_\alpha \cdot \left[f_b \frac{\partial f_\alpha}{\partial \mathbf{p}_\alpha} - \frac{\partial f_b}{\partial \mathbf{p}} f_\alpha \right] d^3 \mathbf{p}_\alpha \quad (6.2)$$

with \mathbf{U}_α the Belyaev-Budker collision operator (see **Chapter 4, section 4.4**). The collision operator $C_\alpha[f_b]$ comes from a 2nd order expansion of the Boltzmann collision integral in the small angle scattering limit:

$$\Delta \mathbf{p} = \Delta p_\parallel \frac{\mathbf{p}}{p} + \Delta p_\perp \frac{\mathbf{b}}{b} \quad \text{with } p \gg \Delta p_\perp \gg \Delta p_\parallel, \quad (6.3)$$

where \mathbf{b} is the impact parameter vector and $\Delta \mathbf{p}$ is the momentum transfer in a collision of a relativistic beam electron with momentum \mathbf{p} with a particle α having a momentum \mathbf{p}_α (cf. **Annexe A, section A.2.2**). Here, α particles can be ions, bound electrons, free electrons or screened free electrons of the medium where the relativistic electron beam is propagating through. We neglect the binary collisions of the beam electrons with themselves since $n_b \ll n_e$. (6.3) means that each binary collision occurs in the 2D plane $(\mathbf{p}, \mathbf{p}_\alpha)$ and leads to an exchange of momentum mostly in the perpendicular direction to \mathbf{p} . Indeed, even if large angle collisions lead to a large change in momentum after each collision, the probability that they occur is small compared to the probability of small angle collisions. The Belyaev-Budker collision tensor reads

$$\begin{aligned} \mathbf{U}_\alpha = & \frac{1}{2} U_{\alpha,0} \left\{ \mathbf{I} - \frac{1}{(\tilde{\gamma}_\alpha^2 - 1)} \left[\frac{\mathbf{p}}{m_e c} \otimes \frac{\mathbf{p}}{m_e c} - \frac{\mathbf{p}_\alpha}{m_\alpha c} \otimes \frac{\mathbf{p}_\alpha}{m_\alpha c} \right. \right. \\ & \left. \left. + \tilde{\gamma}_\alpha \left(\frac{\mathbf{p}}{m_e c} \otimes \frac{\mathbf{p}_\alpha}{m_\alpha c} + \frac{\mathbf{p}_\alpha}{m_\alpha c} \otimes \frac{\mathbf{p}}{m_e c} \right) \right] \right\}. \end{aligned} \quad (6.4)$$

It is often expressed with the scattering potential $U_{\alpha,0} = 4\pi Z_\alpha^2 e^4 \ln \Lambda_{e\alpha} / v_{r,\alpha}$ expanded within the classical Rutherford cross section $(d\sigma_\alpha/d\Omega)^{\text{Ruth}}$ [Belyaev and Budker, 1956] [Landau and Lifshitz, 1981] [Braams and Karney, 1987]. But, in a more general case i.e. without integrating it within a given cross section, the scattering potential reads

$$U_{\alpha,0} = \frac{1}{2} \int \Delta \mathbf{p}^2 v_{r,\alpha} d\sigma_\alpha. \quad (6.5)$$

$v_{r,\alpha} = c\sqrt{\tilde{\gamma}_\alpha^2 - 1}/\tilde{\gamma}_\alpha$ is the relative velocity of one particle in the rest frame of the another, $\tilde{\gamma}_\alpha = \gamma\gamma_\alpha/\gamma_*^2$ and $\gamma_* = 1/\sqrt{(1 - \mathbf{v} \cdot \mathbf{v}_\alpha/c^2)}$ (cf. **Chapter 4, section 4.4**). In addition to the small angle scattering assumption (6.3), we make the assumption that the target particles α remain non relativistic after each binary collision with a relativistic beam electron. That is to say, we neglect high energy secondary electrons

$$|\mathbf{p}_\alpha| \ll |\Delta \mathbf{p}| \ll m_\alpha c. \quad (6.6)$$

Under the assumption (6.3), the 2D binary collision problem consists in solving 6 unknown variables (the momenta and energy of each particle after the collision) while having 7 equations (1 energy conservation equation, 4 momenta conservation equations and the 2 Einstein relationships between energies and momenta). Consequently, there is 1 relation between 2 chosen free parameters which

6.1. KINETIC DESCRIPTION OF RELATIVISTIC ELECTRON BEAM TRANSPORT IN SOLIDS AND DENSE PLASMAS

are for example the scattering angle θ and the relative energy loss of the relativistic electron $w = \Delta\gamma/(\gamma - 1)$ in the laboratory frame. So, one is free to work with $d\sigma_\alpha/dw$ instead of $d\sigma_\alpha/d\Omega$. Moreover, under the assumption (6.6), the energy conservation equation for one collision, $\Delta\gamma_\alpha m_\alpha c^2 + \Delta\gamma m_e c^2 = 0$, provides

$$\Delta p_\perp^2 = -2m_\alpha \Delta\gamma m_e c^2. \quad (6.7)$$

This naturally leads to a relation between the stopping power of relativistic electrons due to collisions with the α particles and the scattering potential $U_{\alpha,0}$. Knowing the differential cross section $d\sigma_\alpha/dw$, one can define the loss of electron kinetic energy $\varepsilon = (\gamma - 1)m_e c^2$ per unit path length ds as follows (cf. **Chapter 4, section 4.2.1**)

$$\left(\frac{d\varepsilon}{ds}\right)_\alpha = \varepsilon n_\alpha \int_{w_{\alpha,\min}}^{w_{\alpha,\max}} w \left(\frac{d\sigma_\alpha}{dw}\right) dw \quad (6.8)$$

with n_α the density of the α particles. The integration limits $w_{\alpha,\min}$ and $w_{\alpha,\max}$ in (6.8) depend on the nature of collisions. For collisions on free electrons, $w_{\text{free,max}} = 1/2$ due to the indiscernibility of electrons and a cut-off w_c is used to distinguish between binary collisions and collisions where collective effects take place. That is to say, for collisions on bound and screened free electrons. These latter collisions can be understood respectively in terms of energy transfer to the excitation of bound electrons by the beam electron electric field and in terms of energy transfer to plasma waves in quanta of $\hbar\omega_{pe}$ (plasmons). For collisions on plasma ions, $w_{i,\min}$ and $w_{i,\max}$ correspond to the commonly used impact parameters. All details are given in **Chapter 4, sections 4.2.1** and **4.2.2** and are summarized in **Figure 6.1**.

Injecting the expression (6.7) in (6.5) and noticing that $v_{r,\alpha} \sim v$ under the assumptions (6.3) and (6.6), one finds the following relation between the scattering potential $U_{\alpha,0}$ and the electron stopping power $(d\varepsilon/ds)_\alpha$

$$U_{\alpha,0} = -\frac{m_\alpha v}{n_\alpha} \left(\frac{d\varepsilon}{ds}\right)_\alpha. \quad (6.9)$$

Moreover, according to assumptions (6.3) and (6.6), one has $\gamma_\alpha \sim 1$, $\tilde{\gamma}_\alpha \sim \gamma$ and the Belyaev-Budker tensor (6.4) can thus be simplified to

$$\mathbf{U}_\alpha = \frac{U_{\alpha,0}}{2} \left[\mathbf{I} - \frac{\mathbf{p} \otimes \mathbf{p}}{p^2} \right] \quad (6.10)$$

and its divergence to

$$\frac{\partial}{\partial \mathbf{p}_\alpha} \cdot \mathbf{U}_\alpha = -\frac{U_{\alpha,0}}{m_\alpha v} \frac{\mathbf{p}}{p}. \quad (6.11)$$

Instead of momentum, it is more convenient to work with the kinetic energy ε of the relativistic electrons. Besides, the structure of the collision tensor motivates to use spherical coordinates $(\Omega, \mathbf{e}_\theta, \mathbf{e}_\phi)$ where $\Omega = \mathbf{p}/p$. Instead of f_b , we make use of the distribution function Ψ depending on the kinetic

energy ε and the propagation direction $\boldsymbol{\Omega}$

$$\Psi(\mathbf{r}, \varepsilon, \boldsymbol{\Omega}, t) = (p^2/v) f_b(\mathbf{r}, \mathbf{p}, t), \quad (6.12)$$

where p^2/v comes from the Jacobian of the change of variables from \mathbf{p} to $(\varepsilon, \boldsymbol{\Omega})$. By defining

$$S(\mathbf{r}, \varepsilon, t) = - \sum_{\alpha} \left(\frac{d\varepsilon}{ds} \right)_{\alpha} \quad (6.13)$$

the total stopping power (> 0) and

$$\nu(\mathbf{r}, \varepsilon, t) = - \sum_{\alpha} \frac{m_{\alpha} v}{p^2} \left(\frac{d\varepsilon}{ds} \right)_{\alpha} \quad (6.14)$$

the total angular isotropization rate, one may integrate the collision integral (6.2) by parts and express the Vlasov-Belyaev-Budker equation in the laboratory frame (6.1) as

$$\begin{aligned} \frac{\partial \Psi}{\partial t} + \frac{\partial}{\partial \mathbf{r}} \cdot (v \boldsymbol{\Omega} \Psi) - \frac{\partial}{\partial \varepsilon} [v (e \mathbf{E} \cdot \boldsymbol{\Omega} + S) \Psi] \\ - \frac{\partial}{\partial \boldsymbol{\Omega}} \cdot \left\{ (\mathbf{I} - \boldsymbol{\Omega} \otimes \boldsymbol{\Omega}) \cdot \left[\frac{e}{p} \left(\mathbf{E} + \frac{v \boldsymbol{\Omega}}{c} \times \mathbf{B} \right) \Psi + \frac{\partial}{\partial \boldsymbol{\Omega}} \left(\frac{\nu}{2} \Psi \right) \right] \right\} = 0 \end{aligned} \quad (6.15)$$

where

$$\frac{\partial}{\partial \boldsymbol{\Omega}} \cdot [(\mathbf{I} - \boldsymbol{\Omega} \otimes \boldsymbol{\Omega}) \cdot \mathbf{A}] = \frac{1}{\sin \theta} \frac{\partial}{\partial \theta} (\sin \theta A_{\theta}) + \frac{1}{\sin \theta} \frac{\partial A_{\varphi}}{\partial \varphi}$$

and

$$\frac{\partial}{\partial \boldsymbol{\Omega}} \cdot [(\mathbf{I} - \boldsymbol{\Omega} \otimes \boldsymbol{\Omega}) \cdot \frac{\partial f}{\partial \boldsymbol{\Omega}}] = \frac{1}{\sin \theta} \frac{\partial}{\partial \theta} \left(\sin \theta \frac{\partial f}{\partial \theta} \right) + \frac{1}{\sin^2 \theta} \frac{\partial^2 f}{\partial \varphi^2}$$

is the Laplace-Beltrami operator. It is the same equation as Equation (5.4), but written for $\Psi(\mathbf{r}, \varepsilon, \boldsymbol{\Omega}, t)$ instead of $f_b(\mathbf{r}, p, \theta, \varphi, t)$.

6.1.2 Collisional Effects of Relativistic Electron Transport in Solids and Dense Plasmas

The analysis presented above in the section 6.1.1 shows that the V-F-P equation (6.15) usually derived for free electrons can be extended to a more general case by replacing the Coulomb scattering potential $U_{\alpha,0}$ by the realistic stopping power according to Equation (6.9). We use the general expression for the stopping powers in solids and dense plasmas

$$\left(\frac{d\varepsilon}{ds} \right)_{\alpha} = -4\pi \frac{n_{\alpha} Z_{\alpha}^2 e^4}{m_{\alpha} v^2} \ln \Lambda_{e\alpha}^{\text{rel}}. \quad (6.16)$$

Z_{α} equals 1 for electrons and equals the nuclear charge Z for ions. As detailed in **Chapter 4 section 4.2.1**, the Coulomb logarithm $\ln \Lambda_{e\alpha}^{\text{rel}}$ is calculated using the Möller cross section [Möller, 1932] for col-

6.1. KINETIC DESCRIPTION OF RELATIVISTIC ELECTRON BEAM TRANSPORT IN SOLIDS AND DENSE PLASMAS

α	n_α	$\ln \Lambda_{e\alpha}^{\text{rel}}$
ions	n_i	$\ln \Lambda_{ei}^{\text{clas}} - \frac{2\gamma^2 - 1}{2\gamma^2}$
free e ⁻	$Z^* n_i$	$\ln \Lambda_{ee}^{\text{clas}} - \ln 2 + \frac{1}{2} - \frac{2\gamma - 1}{2\gamma^2} \ln 2 + \frac{1}{16} \left(\frac{\gamma - 1}{\gamma} \right)^2$
bound e ⁻	$(Z - Z^*) n_i$	$\ln \left(\frac{(\gamma - 1) m_e c^2}{I_{\text{ex}}} \sqrt{\frac{\gamma + 1}{2}} \right) + \frac{1}{2\gamma^2} - \frac{2\gamma - 1}{2\gamma^2} \ln 2 + \frac{1}{16} \left(\frac{\gamma - 1}{\gamma} \right)^2$
plasmons	$Z^* n_i$	$\ln \left(\frac{c\sqrt{\gamma^2 - 1}/\gamma}{\omega_{p,e} \max \{ \lambda_{\text{Debye}}, (3/4\pi n_i)^{1/3} \}} \right)$

Figure 6.1: Expressions for the Coulomb Logarithms $\ln \Lambda_{e\alpha}^{\text{rel}}$ and the densities n_α of the stopping powers (6.16). Z^* is the ionization state and $\ln \Lambda_{e\alpha}^{\text{clas}} = \max \{2, \ln (b_{\text{max}}/b_{\text{min},\alpha})\}$ is the “classical” Coulomb logarithm where $b_{\text{max}} = \max \{ \lambda_{\text{Debye}}, (3/4\pi n_i)^{1/3} \}$ is the upper impact parameter and $b_{\text{min},\alpha} = \hbar/(2m_e c \sqrt{\gamma^2 - 1})$ if $\alpha = \text{ions}$ ($b_{\text{min},\alpha} = \hbar/(2m_e c \sqrt{(\gamma - 1)/2})$ if $\alpha = \text{free electrons}$) is the lower impact parameter.

lisions with free plasma electrons. The cut-off used to distinguish between the binary part (collision with plasma free electrons) and the collective one (collisions with plasma bound and screened electrons) is evaluated by $w_c = \lambda_{\text{De Broglie}}^2 / \max \{ \lambda_{\text{Debye}}^2, (3/4\pi n_i)^{2/3} \}$. The Mott cross section [Mott, 1932] is used for collisions with ions. An extension of the Bethe formula [Bethe, 1932] is used with a mean excitation potential I_{ex} provided by [More, 1985] to take into account collisions with plasma bound electrons. The Fermi density effect correction [Fermi, 1940] is taken into account according to the Pines and Bohm cross section [Pines and Bohm, 1952] for collisions with screened free electrons (plasmons). These expressions for stopping powers are derived in the first Born approximation for low and intermediate Z plasmas and for electrons with kinetic energies greater than approximately 10 keV. The expressions for the densities n_α and the Coulomb logarithms $\ln \Lambda_{e\alpha}^{\text{rel}}$ of (6.16) are summarized in **Figure 6.1**. Even if Bremsstrahlung losses of the relativistic electrons can be neglected in the considered range of energies (10 keV - 10 MeV), a radiative stopping power from [Heitler and Sauter, 1933]

$$\left(\frac{d\varepsilon}{ds} \right)_{\text{rad}} = -4\pi \frac{(Z - Z^*)(Z - Z^* + 1)n_i e^4}{m_e c^2 \gamma} \frac{\alpha}{\pi} \left[\ln(2\gamma) - \frac{1}{3} \right]$$

is added into S . Due to a very small mass ratio $m_e/m_i \ll 1$, the contribution of the stopping power on ions $(d\varepsilon/ds)_i$ is negligible compared to those on electrons.

Concerning the angular diffusion of the beam electrons, it is worth noting that the isotropization rate

$$\nu = \sum_{\alpha} \nu_{\alpha} \text{ with } \nu_{\alpha} = 4\pi \frac{n_{\alpha} Z_{\alpha}^2 e^4}{\gamma^2 m_e^2 v^3} \ln \Lambda_{e\alpha}^{\text{rel}} \quad (6.17)$$

deduced from (6.14) and (6.16) does not depend on the α particles mass. It is plotted in the left panel of **Figure 6.2** for Aluminum ($\rho = 2.7 \text{ g.cm}^{-3}$) versus the electron kinetic energy with the separate

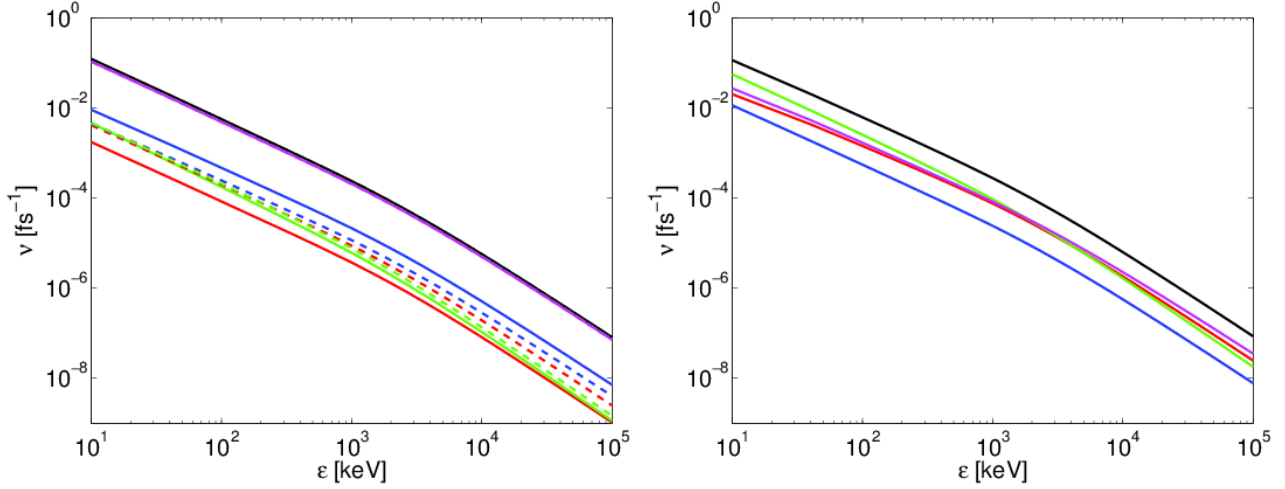


Figure 6.2: (Left panel) Total isotropization rate ν in Aluminum ($\rho = 2.7 \text{ g.cm}^{-3}$) versus its kinetic energy according to formula (6.17) (black) and the different contributions due to free electrons (red), bound electrons (blue), screened free electrons/plasmons (green) and ions (magenta) at ambient temperature $T_e = T_i = 300 \text{ K}$ (solid lines) and $T_e = T_i = 100 \text{ eV}$ (dashed lines). (Right panel) Total isotropization rate ν in Hydrogen ($\rho = 10 \text{ g.cm}^{-3}$ and $T = 100 \text{ eV}$) versus its kinetic energy according to formula (6.17) (black) and the separate contributions due to free electrons (red), bound electrons (blue), screened free electrons/plasmons (green) and ions (magenta).

ν_α of collisions with background free electrons, bound electrons, screened free electrons/plasmons and ions at ambient temperature ($T_e = T_i = 300 \text{ K}$) and $T_e = T_i = 100 \text{ eV}$. It shows that, for intermediate and high Z plasmas, the electron beam scattering on ions is dominant compared to their scattering on electrons by a factor Z . One can also notice that, as for the total stopping power (see **Chapter 4, section 4.2.1**), the isotropization rate ν weakly depends on the background temperature (logarithmically). The isotropization rate (6.17) is also plotted for Hydrogen ($\rho = 10 \text{ g.cm}^{-3}$ and $T = 100 \text{ eV}$) versus the electron kinetic energy in the right panel of **Figure 6.2** with the separate contributions of collisions with background free electrons, bound electrons, screened free electrons/plasmons and ions. It shows that for the Hydrogen plasmas, the scattering on both plasma ions and electrons provides comparable contributions. One also sees that, in the case of beam electrons with kinetic energies less than $\approx 100 \text{ keV}$, propagating in a degenerate Hydrogen plasma, collisions on screened free electrons/plasmons provide the main contribution to the beam electrons angular scattering. The linearization of the Belyaev-Budker collision tensor has allowed us to determine a relation between the stopping power on α particles $(d\varepsilon/ds)_\alpha$ and the corresponding isotropization rate $\nu_\alpha = v/\lambda_{\alpha,\text{lpm}}$ where $\lambda_{\alpha,\text{lpm}} = 1/k_{1,\alpha}$ is the angular scattering mean free path. This relation reads

$$\nu_\alpha = \frac{m_\alpha}{\gamma m_e} \frac{1}{p} \left(\frac{d\varepsilon}{ds} \right)_\alpha. \quad (6.18)$$

One deduces consequently that the total slowing down rate $\nu_d = (1/p)(d\varepsilon/ds)$ introduced in Equation

6.1. KINETIC DESCRIPTION OF RELATIVISTIC ELECTRON BEAM TRANSPORT IN SOLIDS AND DENSE PLASMAS

(5.2) is approximately γ times greater than the total isotropization rate ν of the beam electrons :

$$\nu_d = \gamma(\nu - \nu_i) + \frac{1}{p} \left(\frac{d\varepsilon}{ds} \right)_{\text{rad}} \quad (6.19)$$

in the limit $m_e/m_i \ll 1$.

6.1.3 Background Electrons Dynamics in the "Hybrid" Assumption

As detailed in **Chapter 3, section 3.1.1**, we consider that the beam is already electromagnetically neutralized. That is to say, $n_e = Z^*n_i - n_b \approx Z^*n_i$ ($n_b \ll n_e$), and we neglect the displacement current in the Maxwell-Ampere equation

$$\frac{\partial}{\partial \mathbf{r}} \times \mathbf{B} = \frac{4\pi}{c} (\mathbf{j}_e + \mathbf{j}_b), \quad (6.20)$$

considering times greater than the beam electromagnetic neutralization time (see **Chapter 2**). The plasma dynamics is taken into account by the generalized Ohm equation (3.4)

$$\mathbf{E} = \eta \mathbf{j}_e - \frac{1}{n_e e} \frac{\partial}{\partial \mathbf{r}} (n_e k_B T_e). \quad (6.21)$$

Considering a space scale larger than the plasma skin depth $\lambda_e = c/\omega_{pe}$, which is typically less than a fraction of microns, the electron inertia has been neglected in (6.21). It has been assumed an isotropic resistivity tensor $\boldsymbol{\eta} = \eta \mathbf{I}$ (no magnetization effects) and the ideal gas expression for the electron pressure $P_e = n_e k_B T_e$. As also discussed in **Chapter 3, section 3.1.1**, the electron viscosity, the thermal force, the magnetic force and the friction force due to collisions with beam electrons have been neglected compared to the friction force by colliding with background particles. In order to account for the induced electric field, one has to add the Maxwell-Faraday equation (3.5)

$$\frac{\partial}{\partial \mathbf{r}} \times \mathbf{E} = -\frac{1}{c} \frac{\partial \mathbf{B}}{\partial t}. \quad (6.22)$$

Thus, the system of equations (6.20), (6.21) and (6.22) provides the self-generated electromagnetic field equations (3.7) and (3.8)

$$\mathbf{E} = -\eta \mathbf{j}_b + \frac{\eta c}{4\pi} \frac{\partial}{\partial \mathbf{r}} \times \mathbf{B} - \frac{1}{n_e e} \frac{\partial}{\partial \mathbf{r}} (n_e k_B T_e) \quad (6.23)$$

and

$$\frac{1}{c} \frac{\partial \mathbf{B}}{\partial t} + \frac{\partial}{\partial \mathbf{r}} \times \left(\frac{\eta c}{4\pi} \frac{\partial}{\partial \mathbf{r}} \times \mathbf{B} \right) = \eta \frac{\partial}{\partial \mathbf{r}} \times \mathbf{j}_b + \frac{\partial \eta}{\partial \mathbf{r}} \times \mathbf{j}_b - \frac{k_B}{n_e e} \frac{\partial n_e}{\partial \mathbf{r}} \times \frac{\partial T_e}{\partial \mathbf{r}}. \quad (6.24)$$

The role of each term in these equations is discussed in **Chapter 3, section 3.1.1**.

As detailed in **Chapter 3, section 3.3.2**, the energy deposition by the electron beam produces

a heating and a hydrodynamic motion of the plasma. On the picosecond time scale, the dominant effect is the electron heating while the ion motion is much less important. So, in our model, the ions are assumed to be immobile. Both collisional and collective effects contribute to the plasma heating. The electron temperature T_e of the plasma is calculated in our model according to Equation (3.52)

$$C_{V,e} \frac{\partial T_e}{\partial t} - \frac{\partial}{\partial \mathbf{r}} \cdot \left(\kappa_e \frac{\partial T_e}{\partial \mathbf{r}} \right) = W_e - G(T_e - T_i) \quad (6.25)$$

where the the hydrodynamic velocity divergence, the electron viscosity effects and the thermal force have been neglected. Also, the thermal electron conductivity tensor has been assumed to be scalar $\kappa_e = \kappa_e \mathbf{I}$ (no magnetization effects) and it has been noted $C_{V,e}$ the background electron heat capacity. The heating source term (3.51)

$$W_e = \int d\varepsilon \int_{S_2} d^2\Omega (v S_{\text{col}} \Psi) + \eta \mathbf{j}_e^2 \quad (6.26)$$

is evaluated by calculating the direct energy loss of the beam electrons in collisions with the background electrons according to (6.15) and the friction of background electrons on background particles $-\mathbf{R}_{ei} \cdot \mathbf{v}_e = \eta \mathbf{j}_e^2$. Thus, S_{col} reads

$$S_{\text{col}} = - \left(\frac{d\varepsilon}{ds} \right)_{\text{free } e^-} - \left(\frac{d\varepsilon}{ds} \right)_{\text{bound } e^-} - \left(\frac{d\varepsilon}{ds} \right)_{\text{plasmons}}. \quad (6.27)$$

Finally, G is the electron-ion equilibration coupling factor. The ion temperature is evaluated from Equation (3.53)

$$C_{V,i} \frac{\partial T_i}{\partial t} = W_i = G(T_e - T_i). \quad (6.28)$$

Here, $C_{V,i}$ is the background ion thermal capacity. The thermal ion conductivity has been neglected since it is negligible in the considered time scale. Also, the energy loss of the relativistic electron beam from collisions with the ions has been neglected compared to $G(T_e - T_i)$.

The energy conservation equation of the full system consisting of the beam electrons, the background electrons, the background ions, the bremsstrahlung photons and the electromagnetic fields can be obtained starting from the Poynting theorem. It reads

$$W_i + (W_e - W_i) + W_{\text{brem}} + W_{\text{em}} + \frac{\partial}{\partial \mathbf{r}} \cdot \mathbf{\Pi} = -W_b = \int d\varepsilon \int_{S_2} d^2\Omega (v S \Psi) - \mathbf{j}_b \cdot \mathbf{E}. \quad (6.29)$$

Here, due to the fact that it is usually small, the pressure force has been neglected compared to the friction force in the Ohm's law (6.21) to write $\eta \mathbf{j}_e^2 = \mathbf{j}_e \cdot \mathbf{E}$. The part of the beam power density converted into the electromagnetic power density

$$W_{\text{em}} = \frac{\partial}{\partial t} \left(\frac{\mathbf{E}^2 + \mathbf{B}^2}{8\pi} \right) \quad (6.30)$$

is negligible compared to W_e as well as the divergence of the Poynting vector $\mathbf{\Pi} = \mathbf{E} \times \mathbf{B}/4\pi c$. The term

$$W_{\text{brem}} = - \int d\varepsilon \int_{S_2} d^2\Omega \left[v \left(\frac{d\varepsilon}{ds} \right)_{\text{brem}} \Psi \right] \quad (6.31)$$

comes from the bremsstrahlung power losses of beam electrons and W_b is the full power lost by the fast electron beam. For low Z material, we have shown in **Chapter 4, section 4.2.1** that bremsstrahlung losses of beam electrons are negligible compared to their collisional losses. As the transport of bremsstrahlung photons is not taken into account in our model, we make an implicit assumption that photons deposit directly their energy in the material and therefore include W_{brem} in W_e . However, for intermediate Z materials and/or depending on the material opacity, this assumption could not be sufficient and W_{brem} is considered separately.

6.2 M1 Model for Relativistic Electron Beam Transport

6.2.1 Spherical Harmonic and Cartesian Tensor Scalar Product Expansions

A standard method of resolution of the V-F-P equation (6.15) consists in using a spherical harmonic decomposition (see **Chapter 5, section 5.2.2**). This approach takes advantage of the fact that the spherical harmonics constitute a full set of orthogonal functions on the unity sphere S_2 and they are the eigen functions of the Laplace-Beltrami operator [Tzoufras et al., 2011]. Another approach consists in using a Cartesian tensor scalar product expansion (5.14)

$$\Psi = \sum_{l=0}^{\infty} \frac{C_l}{4\pi} \Psi_l \odot_l \Omega^{(\ell)} \quad (6.32)$$

where $C_l = (2l+1)!/2^l l!$, $\Omega^{(\ell)}$ equals the $(l-1)$ tensor products of Ω with itself $\Omega \otimes \dots \otimes \Omega$ and \odot_l is the l times contracted product. The N th order Lagrange polynomial approximation (Cartesian tensor scalar product expansion with $\ell_{\text{max}} = N$) is strictly equivalent to the spherical harmonic expansion approximation with $\ell_{\text{max}} = N$ [Johnston, 1960]. This method gives rise to a set of differential equations where each equation, describing the l th order component Ψ_l , involves the $(l+1)$ th order component Ψ_{l+1} . Consequently, the $(N+1)$ th order component has to be approximated to close the set of equations. This is done by imposing the PN closure relation

$$\Psi_{N+1}(\mathbf{r}, \varepsilon, t) = \int_{S_2} \Psi \Omega^{(N+1)} d^2\Omega \approx \int_{S_2} \left[\sum_{l=0}^N \frac{C_l}{4\pi} \Psi_l \odot_l \Omega^{(\ell)} \right] \Omega^{(N+1)} d^2\Omega.$$

In practice, the models are limited to the 1st order approximation (P1) in order to make fast computations. In this approach, the decomposition components Ψ_l correspond to the l th order angular

moments of the distribution function Ψ

$$\Psi_\ell(\mathbf{r}, \varepsilon, t) = \int_{S_2} \Psi \Omega^{(\ell)} d^2\Omega, \quad (6.33)$$

and the first two equations can be obtained by integrating (6.15) multiplied by $\Omega^{(\ell)}$ over the unity sphere S_2 . They read

$$\frac{\partial \Psi_0}{\partial t} + \frac{\partial}{\partial \mathbf{r}} \cdot (v \Psi_1) - \frac{\partial}{\partial \varepsilon} [v (e \Psi_1 \cdot \mathbf{E} + S \Psi_0)] = 0 \quad (6.34)$$

and

$$\frac{\partial \Psi_1}{\partial t} + \frac{\partial}{\partial \mathbf{r}} \cdot (v \Psi_2) - \frac{\partial}{\partial \varepsilon} [v (e \Psi_2 \cdot \mathbf{E} + S \Psi_1)] = -\frac{e}{p} (\Psi_0 - \Psi_2) \cdot \mathbf{E} - \frac{e}{\gamma m_e c} \Psi_1 \times \mathbf{B} - \nu \Psi_1. \quad (6.35)$$

The second order angular moment Ψ_2 is evaluated by using the P1 approximation $\Psi \approx \Psi_{P1} = \Psi_0/4\pi + 3\Psi_1 \cdot \Omega/4\pi$ of (6.32)

$$\Psi_2 = \int \Psi \Omega \otimes \Omega d^2\Omega \approx \int \Psi_{P1} \Omega \otimes \Omega d^2\Omega = \frac{1}{3} \Psi_0 \mathbf{I} \quad (6.36)$$

which is the second order angular moment of an isotropic angular distribution function. Consequently, the P1 approximation (6.36) is limited to weakly anisotropic distributions and it does not allow to evaluate the anisotropic part of Ψ_2 . Moreover, Ψ_{P1} may become negative if the anisotropic part $3\Psi_1 \cdot \Omega/4\pi < 0$ is greater than the isotropic part $\Psi_0/4\pi$ [Dubroca et al., 2010].

6.2.2 M1 closure

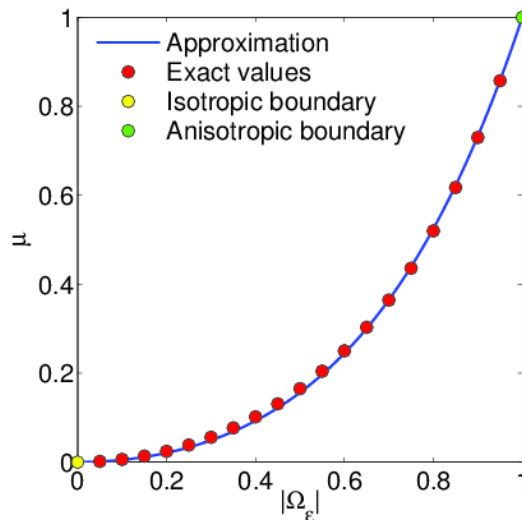


Figure 6.3: Closure parameter μ as a function of the anisotropic parameter $|\Omega_\varepsilon| = |\Psi_1|/\Psi_0$ (solid blue curve) plotted within the approximation (6.59). The dots are the exact values of μ for some values of $|\Omega_\varepsilon|$.

6.2. M1 MODEL FOR RELATIVISTIC ELECTRON BEAM TRANSPORT

Another approach consists in solving the set of equations (6.34) and (6.35) with a more general closure relation. A general expression for a 2nd order tensor in a system with one preferential direction given by the vector $\Psi_1/|\Psi_1|$ reads

$$\Psi_2 = \frac{1}{3}\Psi_0\mathbf{I} + \mu\Psi_0\left(\frac{\Psi_1 \otimes \Psi_1}{|\Psi_1|^2} - \frac{1}{3}\mathbf{I}\right) \quad (6.37)$$

where $\mu = \mu(\Psi_0, \Psi_1)$ is a closure parameter depending on the two first angular moments [Eddington, 1926]. Indeed, let us define the eigenvalues χ_1 , χ_2 and χ_3 of the tensor Ψ_2/Ψ_0 , associated with the eigenvectors \mathbf{u}_1 , \mathbf{u}_2 and \mathbf{u}_3 , respectively. According to the definitions (6.33) of the angular moments of the distribution function Ψ , we deduce that

$$\text{Tr}\left(\frac{\Psi_2}{\Psi_0}\right) = \chi_1 + \chi_2 + \chi_3 = \frac{1}{\Psi_0} \int_{S_2} \text{Tr}(\Omega \otimes \Omega) \Psi d^2\Omega = 1. \quad (6.38)$$

Due to the fact that we truncate the Cartesian tensor scalar product expansion at the 1st order, there is only one preferential direction $\mathbf{n} = \Psi_1/|\Psi_1|$ for beam electrons at the space location \mathbf{r} and having the kinetic energy ε at time t . As a consequence, the vector $(\Psi_2/\Psi_0) \cdot \mathbf{n}$ must be invariant under a rotation around the \mathbf{n} -axis and so \mathbf{n} must be an eigenvector of Ψ_2/Ψ_0 [Levermore, C.D., 1984]. Let us choose $\mathbf{u}_1 = \mathbf{n}$. By symmetry, the plane perpendicular to \mathbf{u}_1 must also be a sub-eigenspace of Ψ_2/Ψ_0 so that the eigenspace $(\mathbf{u}_1, \mathbf{u}_2, \mathbf{u}_3)$ is an orthonormal basis of \mathbb{R}^3 . It implies that the corresponding eigenvalues read

$$\chi_2 = \chi_3 = \frac{1 - \chi_1}{2}, \quad (6.39)$$

according to the trace identity relation (6.38). Let us note $\{\alpha_{ij}, (i, j) \in \{1, 2, 3\}^2\}$ the components of the tensor Ψ_2/Ψ_0 in this orthonormal basis $(\mathbf{u}_1, \mathbf{u}_2, \mathbf{u}_3)$:

$$\frac{\Psi_2}{\Psi_0} = \sum_{i=1}^3 \sum_{j=1}^3 \alpha_{ij} \mathbf{u}_i \otimes \mathbf{u}_j. \quad (6.40)$$

By definition of eigenvectors, we have

$$\forall k \in \{1, 2, 3\}, \frac{\Psi_2}{\Psi_0} \cdot \mathbf{u}_k = \chi_k \mathbf{u}_k. \quad (6.41)$$

Injecting (6.40) in (6.41), we obtain

$$\begin{aligned} \forall k \in \{1, 2, 3\}, \quad & \sum_{i=1}^3 \sum_{j=1}^3 \alpha_{ij} \mathbf{u}_i \otimes \mathbf{u}_j \cdot \mathbf{u}_k = \chi_k \mathbf{u}_k \\ \Rightarrow \quad & \sum_{i=1}^3 \sum_{j=1}^3 \alpha_{ij} (\mathbf{u}_i \cdot \mathbf{u}_k) \mathbf{u}_j = \chi_k \mathbf{u}_k \\ \Rightarrow \quad & \sum_{j=1}^3 \alpha_{kj} \mathbf{u}_j = \chi_k \mathbf{u}_k \end{aligned} \quad (6.42)$$

and we deduce the components of Ψ_2/Ψ_0 :

$$\forall(k, j) \in \{1, 2, 3\}^2, \alpha_{kj} = \delta_{kj}\chi_k. \quad (6.43)$$

Accounting for (6.43) and the axisymmetry relation (6.39) in (6.40), we finally obtain the closure relation (6.37) with

$$\mu = \frac{3\chi_1 - 1}{2}. \quad (6.44)$$

In radiation transfer theory, χ_1 is called the Eddington factor [Minerbo, 1977] [Levermore, 1979] [Pomeranin, 1981] [Dubroca and Feugeas, 1999]. Finally, according to the definition (6.33) of Ψ_2 , the tensor Ψ_2/Ψ_0 is symmetric and positive-definite since it is the second order angular moment of a positive unit density of probability on the unit sphere S_2 . Thus,

$$\forall k \in \{1, 2, 3\}, 0 \leq \chi_k \leq 1. \quad (6.45)$$

The closure relation (6.37) is exact for both totally isotropic angular distributions ($\mu = 0$ or $\chi_1 = 1/3$) and totally anisotropic angular distributions ($\mu = 1$ or $\chi_1 = 1$).

According to the method derived by [Minerbo, 1977] [Minerbo, 1978] in the context of radiation transport and extended to electron transport by [Dubroca et al., 2010], the underlying parameter μ can be estimated by maximizing the local angular entropy of beam electrons with a given kinetic energy under the constraints of the definition of the angular moments Ψ_0 and Ψ_1 . Let us demonstrate so the closure relation (6.37) following this approach. The maximum local angular entropy principle is discussed in detail in the next **section 6.2.3**. The local angular entropy per unit energy of the beam is defined by

$$H_\varepsilon[\Psi] = - \int_{S_2} \Psi (\ln \Psi - 1) d^2\Omega. \quad (6.46)$$

The distribution function Ψ_{M1} , maximizing the local angular entropy $H_\varepsilon[\Psi]$, is obtained by the method of Lagrange multipliers. This is a strategy for finding the local maxima and minima of a function subject to equality constraints. For instance, we want to maximize the local angular entropy (6.46) subject to the definition (6.33) of the two first angular moments Ψ_0 and Ψ_1 . We introduce the 4-dimensional vector $\alpha = (\alpha_0, \alpha_1)^T$ where α_0 and α_1 , called Lagrange multipliers, are living in the same space than the angular moments Ψ_0 and Ψ_1 , respectively. To incorporate these constraints, we introduce the functional of this maximization problem, called Lagrangian, defined by

$$L_\varepsilon[\Psi, \alpha] = H_\varepsilon[\Psi] - \alpha_0 \left(\Psi_0 - \int_{S_2} \Psi d^2\Omega \right) - \alpha_1 \cdot \left(\Psi_1 - \int_{S_2} \Psi \Omega d^2\Omega \right). \quad (6.47)$$

The critical points of the Lagrangian (6.47) occur at saddle points. Note that

$$\frac{\partial L_\varepsilon}{\partial \alpha} [\Psi = \Psi_{M1}, \alpha] = 0 \quad (6.48)$$

6.2. M1 MODEL FOR RELATIVISTIC ELECTRON BEAM TRANSPORT

implies the constraints of the definition (6.33) of the two first angular moments with $\Psi = \Psi_{M1}$, $\ell = 0$ and $\ell = 1$. The maximizing distribution function Ψ_{M1} is defined by the Equation

$$\frac{\partial L_\varepsilon}{\partial \Psi} [\Psi = \Psi_{M1}, \boldsymbol{\alpha}] = 0 \quad (6.49)$$

where $\partial/\partial\Psi$ is the functional derivative. It is defined by

$$\int_{S_2} \frac{\partial L_\varepsilon}{\partial \Psi} [\Psi, \boldsymbol{\alpha}] \delta \Psi d^2 \boldsymbol{\Omega} = \lim_{\epsilon \rightarrow 0} \frac{L_\varepsilon[\Psi + \epsilon \delta \Psi, \boldsymbol{\alpha}] - L_\varepsilon[\Psi, \boldsymbol{\alpha}]}{\epsilon} \quad (6.50)$$

where $\delta\Phi$ is an arbitrary function of $\boldsymbol{\Omega}$ and $\epsilon\delta\Psi$ is the variation of Ψ . According to the definition (6.46) of the beam local angular entropy and the Lagrangian (6.47) of this maximization problem, we find

$$L_\varepsilon[\Psi + \epsilon\delta\Psi, \boldsymbol{\alpha}] - L_\varepsilon[\Psi, \boldsymbol{\alpha}] = \int_{S_2} \epsilon\delta\Psi (-\ln \Psi + \alpha_0 + \alpha_1 \cdot \boldsymbol{\Omega}) d^2 \boldsymbol{\Omega} + O(\epsilon^2) \quad (6.51)$$

which gives

$$\int_{S_2} \frac{\partial L_\varepsilon}{\partial \Psi} [\Psi, \boldsymbol{\alpha}] \delta \Psi d^2 \boldsymbol{\Omega} = \int_{S_2} \delta \Psi (-\ln \Psi + \alpha_0 + \alpha_1 \cdot \boldsymbol{\Omega}) d^2 \boldsymbol{\Omega}. \quad (6.52)$$

Therefore, according to the definition (6.49) of the maximizing distribution function Ψ_{M1} , we deduce that, whatever the function $\delta\Psi$,

$$\int_{S_2} \delta \Psi (-\ln \Psi_{M1} + \alpha_0 + \alpha_1 \cdot \boldsymbol{\Omega}) d^2 \boldsymbol{\Omega} = 0. \quad (6.53)$$

The only possible solution of the previous equation is

$$\Psi_{M1} = \exp(\alpha_0 + \boldsymbol{\alpha}_1 \cdot \boldsymbol{\Omega}). \quad (6.54)$$

Then, the Lagrange multipliers α_0 and $\boldsymbol{\alpha}_1$ have to be evaluated in terms of physical quantities by using the constraints given by Equation (6.48). One has

$$\Psi_0 = \int_{S_2} \Psi_{M1} d^2 \boldsymbol{\Omega} = \exp(\alpha_0) \frac{4\pi \sinh |\boldsymbol{\alpha}_1|}{|\boldsymbol{\alpha}_1|} \quad (6.55)$$

and

$$\boldsymbol{\Psi}_1 = \int_{S_2} \Psi_{M1} \boldsymbol{\Omega} d^2 \boldsymbol{\Omega} = \exp(\alpha_0) \frac{4\pi \sinh |\boldsymbol{\alpha}_1|}{|\boldsymbol{\alpha}_1|} \left(\coth |\boldsymbol{\alpha}_1| - \frac{1}{|\boldsymbol{\alpha}_1|} \right) \frac{\boldsymbol{\alpha}_1}{|\boldsymbol{\alpha}_1|}. \quad (6.56)$$

The detailed calculation of these two integrals can be found in [Wright and Hadley, 1975]. From (6.55) and (6.56), one deduces an expression for the anisotropy vector

$$\boldsymbol{\Omega}_\varepsilon = \frac{\boldsymbol{\Psi}_1}{\Psi_0} = \left(\coth |\boldsymbol{\alpha}_1| - \frac{1}{|\boldsymbol{\alpha}_1|} \right) \frac{\boldsymbol{\alpha}_1}{|\boldsymbol{\alpha}_1|}. \quad (6.57)$$

It is defined as the mean propagation direction of the electrons having the energy ε at the position \mathbf{r}

at the time t . Due to the triangular inequality applied to (6.33) with $\ell = 1$, one has

$$0 \leq |\boldsymbol{\Omega}_\varepsilon| \leq 1. \quad (6.58)$$

Although the bijective relation (6.57) cannot be inverted analytically, one can fit the real values of $\boldsymbol{\alpha}_1$ by

$$\boldsymbol{\alpha}_1 \approx \frac{3\boldsymbol{\Omega}_\varepsilon}{1 - \frac{|\boldsymbol{\Omega}_\varepsilon|^2}{2} (1 + |\boldsymbol{\Omega}_\varepsilon|^2)}. \quad (6.59)$$

It is compared with the real value of $\boldsymbol{\alpha}_1$ for some values of $|\boldsymbol{\Omega}_\varepsilon|$ in **Figure 6.3**, where the dependence of the anisotropy vector $\boldsymbol{\Omega}_\varepsilon$ on the closure parameter μ is plotted. Consequently, one deduces an explicit expression for the approximate beam distribution function

$$\Psi_{M1} = \Psi_0 \frac{|\boldsymbol{\alpha}_1|}{4\pi \sinh |\boldsymbol{\alpha}_1|} \exp(\boldsymbol{\alpha}_1 \cdot \boldsymbol{\Omega}). \quad (6.60)$$

In the isotropic case where $|\boldsymbol{\alpha}_1| \ll 1$ ($|\boldsymbol{\Omega}_\varepsilon| \ll 1$), the M1 model reduces to the one-polynomial approximation P1. But, in the opposite case of a strong anisotropy $|\boldsymbol{\alpha}_1| \rightarrow \infty$ ($|\boldsymbol{\Omega}_\varepsilon| \rightarrow 1$), the function $\Psi_{M1} \rightarrow \Psi_0 \delta[\boldsymbol{\Omega} - \boldsymbol{\Omega}_\varepsilon]$ where δ is the Dirac distribution. By substituting (6.60) in the definition (6.33) of Ψ_2 , one obtains the closure relation

$$\Psi_2 \approx \int_{S_2} \Psi_{M1} \boldsymbol{\Omega} \otimes \boldsymbol{\Omega} d^2\boldsymbol{\Omega} = \frac{1}{3} \Psi_0 \mathbf{I} + \mu \Psi_0 \left(\frac{\boldsymbol{\Psi}_1 \otimes \boldsymbol{\Psi}_1}{|\boldsymbol{\Psi}_1|^2} - \frac{1}{3} \mathbf{I} \right) \quad (6.61)$$

with the closure parameter

$$\mu = 1 - 3 \left(\frac{\coth |\boldsymbol{\alpha}_1|}{|\boldsymbol{\alpha}_1|} - \frac{1}{|\boldsymbol{\alpha}_1|^2} \right) \approx \frac{|\boldsymbol{\Omega}_\varepsilon|^2}{2} (1 + |\boldsymbol{\Omega}_\varepsilon|^2). \quad (6.62)$$

Here, we refer again to [Wright and Hadley, 1975] for the detailed calculation of this integral. This M1 closure relation (6.61) provides an interpolation between the local beam-like case where all electrons at the position \mathbf{r} with the energy ε move in the same direction $\boldsymbol{\Omega}_\varepsilon = \mathbf{e}_z$ and the local isotropic case where all electrons at the position \mathbf{r} with the energy ε move in all directions with the same probability ($\boldsymbol{\Omega}_\varepsilon = \mathbf{0}$). It preserves consequently the advantage of the P1 model in fast computing while angular distributions are described with a much better precision.

6.2.3 Properties of the M1 closure

Introduction

While the M1 closure shows a very good performance in the studies of radiation transfer, it is not evident that the local angular entropy maximization under the constraints of the definition of the

angular moments Ψ_0 and Ψ_1 provides the best possible closure relation for electrons, which are charged particles evolving under the action of the Lorentz force. We refer here to Minerbo who justified this closure concerning photons by saying : “In communication theory, it is shown that the information content is the negative of the entropy of the distribution. Thus, by using the maximum entropy criterion, one avoids introducing information that is not available. This approach is conceptually superior to the use of an ad hoc model for the intensity” (i.e. Ψ_1). Concerning the relativistic electrons considered here, even if their angular scattering tends to isotropize their angular distribution and increase their angular entropy, self-generated electromagnetic fields may not follow the same trend. One can deduce the local angular entropy dissipation rate $(\partial H_\varepsilon/\partial t)_{\text{col}}$ starting from the V-F-P equation (6.15) and by integrating it over the unity sphere in the momentum space S_2 . Here, we define the local angular entropy as

$$H_\varepsilon[\Psi](\mathbf{r}, \varepsilon, t) = - \int_{S_2} \Psi \left[\ln \Psi - 1 + \ln \left(\frac{v}{p^2} \right) \right] d^2\Omega. \quad (6.63)$$

It is different from (6.46) by a constant term and therefore does not modify the results obtained in the previous section **6.2.2**. This definition allows us to relate the local angular entropy with the Boltzmann entropy $H[f_b]$ (see **Appendix A, section A.1.5**) by the simple relation

$$H[f_b](\mathbf{r}, t) = - \int_{\mathbb{R}^3} f_b (\ln f_b - 1) d^3\mathbf{p} = \int_0^\infty H_\varepsilon[\Psi] d\varepsilon. \quad (6.64)$$

By noting $\phi = \Psi[1 - \ln(v/p^2)] - \Psi \ln \Psi$, the equation for the time derivative of the local angular entropy reads

$$\frac{dH_\varepsilon}{dt} = \frac{\partial H_\varepsilon}{\partial t} + \frac{\partial}{\partial \mathbf{r}} \cdot \int_{S_2} v \boldsymbol{\Omega} \phi d^2\Omega - \frac{\partial}{\partial \varepsilon} \left[\int_{S_2} v (e\mathbf{E} \cdot \boldsymbol{\Omega} + S) \phi d^2\Omega \right] = \left(\frac{\partial H_\varepsilon}{\partial t} \right)_{\text{col}} \quad (6.65)$$

with

$$\left(\frac{\partial H_\varepsilon}{\partial t} \right)_{\text{col}} = \frac{\nu}{2} \int_{S_2} \frac{1}{\phi} \left[\left(\frac{\partial \phi}{\partial \theta} \right)^2 + \left(\frac{\partial \phi}{\partial \varphi} \right)^2 \right] d^2\Omega - \Psi_0 \frac{v}{p^2} \frac{\partial}{\partial \varepsilon} (p^2 S). \quad (6.66)$$

M1 Closure and Collisional Effects of Fast Electron Transport

The local angular entropy dissipation rate $(\partial H_\varepsilon/\partial t)_{\text{col}}$, which is the angular entropy time evolution of a M1 mesoscopic particle following its trajectory in the $(\mathbf{r}, \varepsilon)$ -space, contains two terms according to the previous equation (6.53). The term depending on the isotropization rate ν is positive and consequently increases the angular entropy H_ε with time. But, the sign of $(\partial H_\varepsilon/\partial t)_{\text{col}}$ depending also on the total stopping power S is not defined. Let us estimate so the contribution of each term assuming that

$$\int_{S_2} \frac{1}{\phi} \left[\left(\frac{\partial \phi}{\partial \theta} \right)^2 + \left(\frac{\partial \phi}{\partial \varphi} \right)^2 \right] d^2\Omega \sim \Psi_0$$

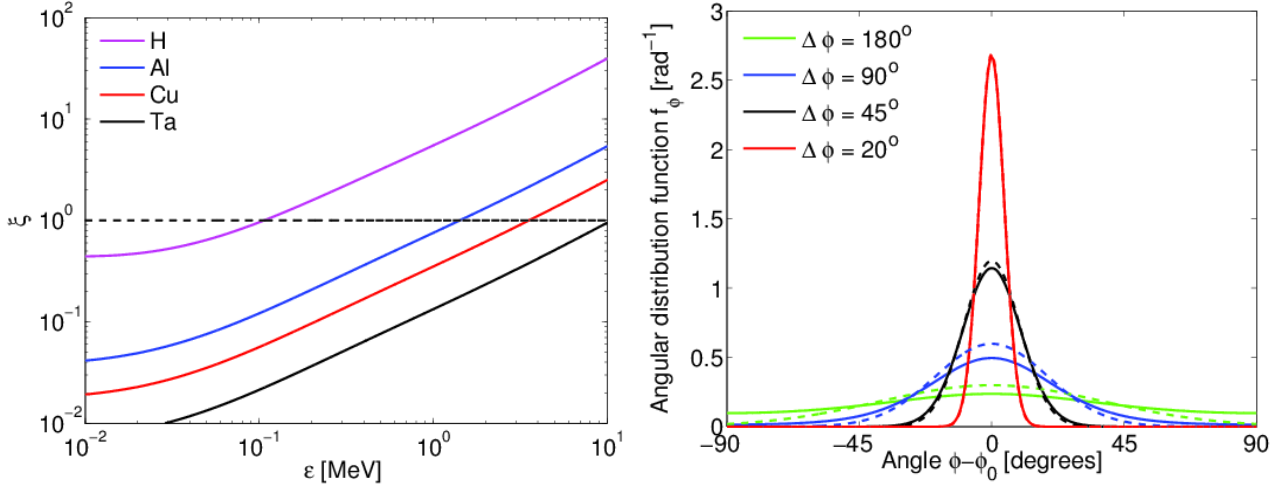


Figure 6.4: (Left panel) Ratio ξ versus the kinetic energy of electrons according to Equation (6.67) for dense Hydrogen ($\rho = 10 \text{ g.cm}^{-3}$, $Z = 1$), Aluminum ($\rho = 2.7 \text{ g.cm}^{-3}$, $Z = 13$), Copper ($\rho = 8.96 \text{ g.cm}^{-3}$, $Z = 29$) and Tantalum ($\rho = 16.65 \text{ g.cm}^{-3}$, $Z = 73$) at $T = 100 \text{ eV}$. (Right panel) Comparison between the M1 approximation (8.23) (full curves) and the statistic normal law (dashed curves) for $\Delta\varphi = 180^\circ$ (green), $\Delta\varphi = 90^\circ$ (blue), 45° (black) and 20° (red).

have the same order of magnitude. In this case, one may evaluate each term by comparing the ratio

$$\xi = \frac{2}{\nu} \frac{v}{p^2} \frac{\partial}{\partial \varepsilon} (p^2 S)$$

with 1. By neglecting the electron bremsstrahlung losses, one obtains

$$\xi = \frac{2\gamma\beta^2}{1 + Z \frac{\ln \Lambda_{ei}^{\text{rel}}}{\ln \Lambda_{ee}^{\text{rel}}}} \left[2 + \frac{\gamma}{\ln \Lambda_{ee}^{\text{rel}}} \frac{\partial}{\partial \gamma} (\ln \Lambda_{ee}^{\text{rel}}) \right] \quad (6.67)$$

where $\ln \Lambda_{ee}^{\text{rel}} = (Z^*/Z)(\ln \Lambda_{e,\text{free } e^-}^{\text{rel}} + \ln \Lambda_{e,\text{plasmons}}^{\text{rel}}) + (1 - Z^*/Z) \ln \Lambda_{e,\text{bound } e^-}^{\text{rel}}$ and $\ln \Lambda_{ea}^{\text{rel}}$ the Coulomb logarithms given in **Figure 6.1**. It is plotted in the left panel of **Figure 6.4** for Hydrogen, Aluminum, Copper and Tantalum assuming $Z^* = 0$ to simplify the calculation of the relativistic electron-electron Coulomb logarithm derivative. This assumption does not modify the value of ξ since the total stopping power and the isotropization rate do not depend on Z^* (see **Chapter 4, section 4.2.1**). One can notice that ξ strongly depends on the atomic number of the material Z and that the M1 closure seems to be fully justified for the electrons with kinetic energies $\varepsilon \leq 100 \text{ keV}$ for Hydrogen ($Z = 1$), $\varepsilon \leq 1 \text{ MeV}$ for Aluminum ($Z = 13$), $\varepsilon \leq 3 \text{ MeV}$ for Copper ($Z = 29$) and $\varepsilon \leq 10 \text{ MeV}$ for Tantalum ($Z = 73$). It means that, above these values, the energy exchange between energy groups of beam electrons, due to their slowing down, does not allow to consider each group as a closed system and thus does not allow to justify the maximum angular entropy criterion. This is due to the fact that the slowing down rate is γ times greater than the angular diffusion rate (see Equation (6.19)). This limitation is compatible with the characteristics of laser-generated electrons. The number of electrons with kinetic

6.2. M1 MODEL FOR RELATIVISTIC ELECTRON BEAM TRANSPORT

energies above these material-dependant threshold values represent only a small part of the whole beam electron population (see **Chapter 1, section 1.2.7**). Moreover, being more energetic, these electrons propagate faster in the target compared to others so that their local angular distribution is quasi-anisotropic and therefore, is well described by the M1 model. Thus, one can conclude that the collisional effects of laser-generated electron fully justify the M1 closure for their transport in solids and dense plasmas. Indeed, by orienting the Cartesian coordinates such that

$$\boldsymbol{\alpha}_1 = \frac{8 \ln 2}{\Delta \varphi^2} \begin{pmatrix} \sin \varphi_0 \\ 0 \\ \cos \varphi_0 \end{pmatrix} \Leftrightarrow \boldsymbol{\Omega}_\varepsilon = \left| \coth \left(\frac{8 \ln 2}{\Delta \varphi^2} \right) - \frac{\Delta \varphi^2}{8 \ln 2} \right| \begin{pmatrix} \sin \varphi_0 \\ 0 \\ \cos \varphi_0 \end{pmatrix}, \quad (6.68)$$

we obtain the angular distribution function averaged over the polar angle θ

$$\begin{aligned} \int_0^\pi \Psi_{\text{M1}} \sin \theta d\theta &= \Psi_0 \frac{|\boldsymbol{\alpha}_1|}{4 \sinh |\boldsymbol{\alpha}_1|} (\{I_1 [|\boldsymbol{\alpha}_1| \cos (\varphi - \varphi_0)] + L_{-1} [|\boldsymbol{\alpha}_1| \cos (\varphi - \varphi_0)]\}) \\ &\approx \frac{\Psi_0}{\sqrt{2\pi \frac{\Delta \varphi^2}{8 \ln 2}}} \exp \left[-4 \ln 2 \frac{(\varphi - \varphi_0)^2}{\Delta \varphi^2} \right] \end{aligned} \quad (6.69)$$

which is nothing else than the 0th order statistical normal law obtained in the multiple scattering theory by Moliere (see **Chapter 4, section 4.3.2**). They are strictly similar in the anisotropic limit and diverge slightly in the isotropic limit, as illustrated in the right panel of **Figure 6.4**. The integration has been carried out in the same way as for (6.55), (6.56) and (6.61) that is to say, by expanding the exponential in power series, by performing the integration of the different sinus power according to the formula 3.621 from [Gradshteyn and Ryzhik, 1965] and by applying the doubling formula for Gamma functions 8.335.1 from [Gradshteyn and Ryzhik, 1965]. Then, the sum was split in odd and even terms which were compared with the definitions 9.6.10 and 12.2.1 from [Abramowitz and Stegun, 1965] of the modified Bessel function of the first kind I_ν and the modified Struve function L_ν .

However, even if the collisional effects can justify the M1 closure in the problem of fast electron transport, the third term in the left hand side of (6.65) shows that the self-generated electric field affects the local angular entropy time evolution (i.e. the angular entropy obtained without following the trajectory of a M1 mesoparticle in the $(\mathbf{r}, \varepsilon)$ -space). This is not the case for the Boltzmann entropy, since by integrating over all kinetic energies (6.65), this term vanishes to give

$$\frac{dH}{dt} = \frac{\partial H}{\partial t} + \frac{\partial}{\partial \mathbf{r}} \cdot \int_0^\infty \int_{S_2} v \boldsymbol{\Omega} \phi d^2 \boldsymbol{\Omega} d\varepsilon = \int_0^\infty \left(\frac{\partial H_\varepsilon}{\partial t} \right)_{\text{col}} d\varepsilon. \quad (6.70)$$

It must be emphasized here that, similarly to the maximum local angular entropy criterion, the Boltzmann H-theorem does not apply here. Indeed, contrary to the Boltzmann H-theorem demonstration presented in **Appendix A, section A.1.5**, the right hand side term of (6.70) is not necessarily

positive. It would have been positive if the whole electron population (beam electrons + background electrons) were taken into account in Ψ , which is not the case in our "hybrid" assumption. Energy exchanges between the beam and background electrons do not allow to consider the beam electrons as a closed system.

M1 Closure and Collective Effects of Fast Electron Transport

In order to illustrate the M1 closure in a collisionless case, let us evaluate the dispersion relation (3.39) for the resistive filamentation instability with the M1 model. As in **Chapter 3, section 3.2.3**, we neglect the pressure force in (6.21), consider $k_y = k_z = 0$ and assume $|E_z| \gg |E_x|$. While the system of equations $\{(6.20), (6.22), (6.21)\}$ provides the same relations as (3.36), for the electric field, the linearization of the M1 equations (6.34), (6.35) and (6.61) is different. The distribution function at the equilibrium is the Maxwell-Juttner distribution function (3.17) expressed as a function of $(\varepsilon, \boldsymbol{\Omega})$:

$$\Psi^{(0)} = \Psi_{\text{M-J}} = n_b^{(0)} \frac{\gamma^2 \beta k_B T_b / m_e c^2}{4\pi \gamma_b (m_e c^2) K_2 \left(\frac{m_e c^2}{\gamma_b k_B T_b} \right)} \exp \left[-\frac{m_e c^2}{k_B T_b} \left(\gamma - \beta_b \frac{p_z}{m_e c} \right) \right]. \quad (6.71)$$

Being a particular case of distribution functions of the kind (6.60), one can deduce easily the angular moments of the distribution function at the equilibrium. They read

$$\Psi_0^{(0)} = \frac{4\pi \sinh |\boldsymbol{\alpha}_1|}{|\boldsymbol{\alpha}_1|} n_b^{(0)} \frac{\gamma^2 \beta k_B T_b / m_e c^2}{4\pi \gamma_b (m_e c^2) K_2 \left(\frac{m_e c^2}{\gamma_b k_B T_b} \right)} \exp \left(-\frac{\gamma m_e c^2}{k_B T_b} \right), \quad (6.72)$$

$$\boldsymbol{\Psi}_1^{(0)} = \Psi_0^{(0)} \left(\coth |\boldsymbol{\alpha}_1| - \frac{1}{|\boldsymbol{\alpha}_1|} \right) \frac{\boldsymbol{\alpha}_1}{|\boldsymbol{\alpha}_1|} \quad (6.73)$$

and

$$\boldsymbol{\Psi}_2^{(0)} = \frac{1}{3} \Psi_0^{(0)} \mathbf{I} + \mu^{(0)} \Psi_0^{(0)} \left(\frac{\boldsymbol{\Psi}_1^{(0)} \otimes \boldsymbol{\Psi}_1^{(0)}}{|\boldsymbol{\Psi}_1^{(0)}|^2} - \frac{1}{3} \mathbf{I} \right) \quad (6.74)$$

where

$$\mu^{(0)} = 1 - 3 \left(\frac{\coth |\boldsymbol{\alpha}_1|}{|\boldsymbol{\alpha}_1|} - \frac{1}{|\boldsymbol{\alpha}_1|^2} \right) \text{ and } \boldsymbol{\alpha}_1 = \frac{m_e c^2}{k_B T_b} \beta_b \frac{p}{m_e c} \mathbf{e}_z.$$

The linearized M1 equations (6.34), (6.35) and (6.61) read

$$\frac{\partial \delta \Psi_0}{\partial t} + \frac{\partial}{\partial \mathbf{r}} \cdot (v \delta \boldsymbol{\Psi}_1) - e \frac{\partial}{\partial \varepsilon} \left(v \boldsymbol{\Psi}_1^{(0)} \right) \cdot \delta \mathbf{E} = 0, \quad (6.75)$$

$$\frac{\partial \delta \boldsymbol{\Psi}_1}{\partial t} + \frac{\partial}{\partial \mathbf{r}} \cdot (v \delta \boldsymbol{\Psi}_2) - e \frac{\partial}{\partial \varepsilon} \left(v \boldsymbol{\Psi}_2^{(0)} \right) \cdot \delta \mathbf{E} = -\frac{e}{p} \left(\Psi_0^{(0)} - \boldsymbol{\Psi}_2^{(0)} \right) \cdot \delta \mathbf{E} - \frac{e}{\gamma m_e c} \boldsymbol{\Psi}_1^{(0)} \times \delta \mathbf{B} \quad (6.76)$$

and

$$\delta \boldsymbol{\Psi}_2 = \frac{\partial \boldsymbol{\Psi}_2}{\partial \Psi_0} \left(\Psi_0^{(0)}, \boldsymbol{\Psi}_1^{(0)} \right) \delta \Psi_0 + \frac{\partial \boldsymbol{\Psi}_2}{\partial \boldsymbol{\Psi}_1} \left(\Psi_0^{(0)}, \boldsymbol{\Psi}_1^{(0)} \right) \cdot \delta \boldsymbol{\Psi}_1. \quad (6.77)$$

6.2. M1 MODEL FOR RELATIVISTIC ELECTRON BEAM TRANSPORT

Let us note the tensors

$$\mathbf{T}_0 = \frac{\partial \Psi_2}{\partial \Psi_0} \left(\Psi_0^{(0)}, \Psi_1^{(0)} \right) \text{ and } \forall i \in \{x, y, z\}, \mathbf{T}_{1,i} = \frac{\partial \Psi_2}{\partial \Psi_{1,i}} \left(\Psi_0^{(0)}, \Psi_1^{(0)} \right)$$

such that

$$\delta \Psi_2 = \mathbf{T}_0 \delta \Psi_0 + \mathbf{T}_{1,x} \delta \Psi_{1,x} + \mathbf{T}_{1,y} \delta \Psi_{1,y} + \mathbf{T}_{1,z} \delta \Psi_{1,z}. \quad (6.78)$$

Their general expressions are

$$\begin{aligned} \forall (i, j) \in \{x, y, z\}^2, (T_0)_{ij} &= \frac{1}{3} \delta_{ij} - \left(\frac{\Psi_1^{(0)}}{\Psi_0^{(0)}} \right)^2 \left[1 + 2 \left(\frac{\Psi_1^{(0)}}{\Psi_0^{(0)}} \right)^2 \right] \left(\frac{\Psi_{1,i}^{(0)} \Psi_{1,j}^{(0)}}{\Psi_1^{(0)2}} - \frac{1}{3} \delta_{ij} \right) \\ &+ \mu^{(0)} \left(\frac{\Psi_{1,i}^{(0)} \Psi_{1,j}^{(0)}}{\Psi_1^{(0)2}} - \frac{1}{3} \delta_{ij} \right) \end{aligned} \quad (6.79)$$

and

$$\begin{aligned} \forall (i, j) \in \{x, y, z\}^2, (T_{1,i})_{xj} &= \frac{\Psi_{1,i}^{(0)}}{\Psi_0^{(0)}} \left[1 + 2 \left(\frac{\Psi_1^{(0)}}{\Psi_0^{(0)}} \right)^2 \right] \left(\frac{\Psi_{1,x}^{(0)} \Psi_{1,j}^{(0)}}{\Psi_1^{(0)2}} - \frac{1}{3} \delta_{xj} \right) \\ &+ \mu^{(0)} \frac{\Psi_0^{(0)}}{\Psi_1^{(0)4}} \left[\Psi_1^{(0)2} \left(\delta_{ix} \Psi_{1,j}^{(0)} + \delta_{ij} \Psi_{1,x}^{(0)} \right) - 2 \Psi_{1,x}^{(0)} \Psi_{1,i}^{(0)} \Psi_{1,j}^{(0)} \right]. \end{aligned} \quad (6.80)$$

Performing the Fourier transform of Equations (6.75), (6.76) and (6.78), neglecting $\delta \widehat{E}_x$ and using the Maxwell-Faraday equation for the magnetic field ($\delta \widehat{\mathbf{B}} = -(k_x c / \omega) \delta \widehat{E}_z \mathbf{e}_y$), we obtain the matrix relation

$$\mathbf{A} \cdot \delta \widehat{\mathbf{X}} = -ie \mathbf{Y}^{(0)} \delta \widehat{E}_z \quad (6.81)$$

where

$$\delta \widehat{\mathbf{X}} = \begin{pmatrix} \delta \widehat{\Psi}_0 \\ \delta \widehat{\Psi}_{1,x} \\ \delta \widehat{\Psi}_{1,y} \\ \delta \widehat{\Psi}_{1,z} \end{pmatrix}, \mathbf{Y}^{(0)} = \begin{pmatrix} (d/d\varepsilon) \left(v \Psi_{1,z}^{(0)} \right) \\ -k_x \Psi_{1,z}^{(0)} / \gamma m_e \omega \\ 0 \\ 0 \end{pmatrix}$$

and

$$A = \begin{pmatrix} -\omega & k_x v & 0 & 0 \\ k_x v (T_0)_{xx} & k_x v (T_{1,x})_{xx} - \omega & k_x v (T_{1,y})_{xx} & k_x v (T_{1,z})_{xx} \\ k_x v (T_0)_{xy} & k_x v (T_{1,x})_{xy} & k_x v (T_{1,y})_{xy} - \omega & k_x v (T_{1,z})_{xy} \\ k_x v (T_0)_{xz} & k_x v (T_{1,x})_{xz} & k_x v (T_{1,y})_{xz} & k_x v (T_{1,z})_{xz} - \omega \end{pmatrix}.$$

Let us consider here the limit $T_b \rightarrow 0$ for simplicity. In this case, the Lagrange multiplier $|\alpha_1| \rightarrow \infty$ and the equilibrium distribution function (6.71) becomes purely anisotropic and monoenergetic, giving

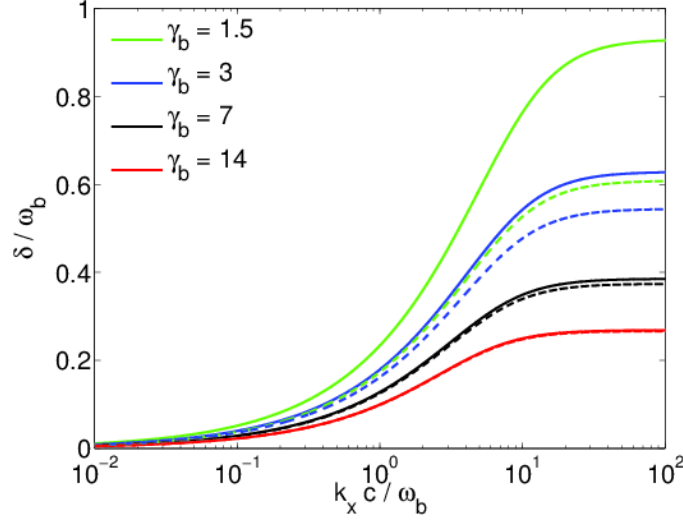


Figure 6.5: Comparison between the resistive filamentation growth rate in the M1 approximation (full curves) and the resistive filamentation growth rate (3.41) (dashed curves) for $\eta_0 = 10^{-6} \Omega.m$, $T_b \rightarrow 0$, $n_b^{(0)} = 10^{21} \text{ cm}^{-3}$ ($\omega_b = 1.78 \text{ fs}^{-1}$) and different values of $\gamma_b = 1.5$ (green), 3 (blue), 7 (black) and 14 (red).

consequently

$$\Psi_0^{(0)} = \frac{n_b^{(0)}}{m_e c^2} \delta[\gamma - \gamma_b], \Psi_1^{(0)} = \Psi_0^{(0)} \mathbf{e}_z \text{ and } \Psi_2^{(0)} = \Psi_0^{(0)} \mathbf{e}_z \otimes \mathbf{e}_z. \quad (6.82)$$

In this case, we obtain $(T_0)_{xx} = (T_{1,x})_{xz} = -(T_{1,z})_{xx} = 1$ and $(T_0)_{xy} = (T_0)_{xz} = (T_{1,x})_{xx} = (T_{1,x})_{xy} = (T_{1,y})_{xx} = (T_{1,y})_{xy} = (T_{1,y})_{xz} = (T_{1,z})_{xy} = (T_{1,z})_{xz} = 0$ and the matrix A reduces to the simpler form

$$A = \begin{pmatrix} -\omega & k_x v & 0 & 0 \\ k_x v & -\omega & 0 & -k_x v \\ 0 & 0 & -\omega & 0 \\ 0 & k_x v & 0 & -\omega \end{pmatrix}. \quad (6.83)$$

Then, the solution of equation (6.81) reads

$$\delta \hat{\mathbf{X}} = -ie \mathbf{A}^{-1} \cdot \mathbf{Y}^{(0)} \delta \hat{E}_z = i \frac{e}{\omega^3} \begin{pmatrix} (d/d\varepsilon) (v \Psi_0^{(0)}) (k_x^2 c^2 \beta^2 + \omega^2) - k_x^2 c^2 \beta (\Psi_0^{(0)} / \gamma m_e c) \\ k_x \omega [v(d/d\varepsilon) (v \Psi_0^{(0)}) - c(\Psi_0^{(0)} / \gamma m_e c)] \\ 0 \\ k_x^2 v [v(d/d\varepsilon) (v \Psi_0^{(0)}) - c(\Psi_0^{(0)} / \gamma m_e c)] \end{pmatrix} \delta \hat{E}_z. \quad (6.84)$$

This provides us with the expression for the beam current density perturbation

$$\delta \hat{\mathbf{j}}_b = -e \int_0^\infty \delta \hat{\Psi}_{1,z} v d\varepsilon \mathbf{e}_z = i \left(\frac{k_x c}{\omega} \right)^2 \frac{\omega_b^2 \beta_b^2}{4\pi \omega \gamma_b} \left(1 + \frac{3}{\gamma_b^2} \right) \delta \hat{E}_z \mathbf{e}_z \quad (6.85)$$

where $\omega_b = \sqrt{4\pi n_b^{(0)} e^2 / m_e}$ is the electron beam plasma frequency. Injecting (6.85) in (3.36 a), we

obtain the dispersion relation for the unstable mode $\omega = i\delta$

$$\frac{4\pi}{\eta_0\omega_b} \left(\frac{\delta}{\omega_b}\right)^3 + \left(\frac{k_x c}{\omega_b}\right)^2 \left(\frac{\delta}{\omega_b}\right)^2 - \frac{1}{\gamma_b} \left(\frac{\beta_b k_x c}{\omega_b}\right)^2 \left(1 + \frac{3}{\gamma_b^2}\right) = 0. \quad (6.86)$$

It has to be compared with the dispersion relation (3.41) obtained starting from the Vlasov equation

$$\frac{4\pi}{\eta_0\omega_b} \left(\frac{\delta}{\omega_b}\right)^3 + \left[\left(\frac{k_x c}{\omega_b}\right)^2 + \frac{1}{\gamma_b^3}\right] \left(\frac{\delta}{\omega_b}\right)^2 - \frac{1}{\gamma_b} \left(\frac{\beta_b k_x c}{\omega_b}\right)^2 = 0.$$

A term $\propto 1/\gamma_b^3$ has disappeared in the second term, while another term $\propto 3/\gamma_b^2$ has appeared in the third term. This is due to the fact that the Maxwell equations depend on the hydrodynamic moments n_b and \mathbf{j}_b of the beam distribution function $\Psi^{(0)}$ and not directly on its angular moments Ψ_0 and Ψ_1 . Indeed, contrary to the reference case of the Vlasov equation (3.37) where the currents in (3.36) are calculated with p_x , p_y and p_z -integrals, in the M1 approximation there appear only ε -integrals since the integration over angles $\boldsymbol{\Omega} = \mathbf{p}/p$ has already been performed before the coupling of the equations. Therefore, the integration of $Y_0^{(0)}$ and $Y_{1,x}^{(0)}$ over ε leads to a different result. The instability growth rates $\delta > 0$, solutions of (6.86) and (3.41), are plotted in **Figure 6.5** for $\eta_0 = 10^{-6} \Omega\cdot\text{m}$, $n_b^{(0)} = 10^{21} \text{ cm}^{-3}$ ($\omega_b = 1.78 \text{ fs}^{-1}$) and different values of γ_b . The M1 approximation largely overestimates the filamentation resistivity growth rate in the short wavelength region $k_x c/\omega_b \gg 1$ for low mean electron energies $\gamma_b \gtrsim 1$. Indeed, according to (6.86), the growth rate obtained in the M1 approximation attains the value

$$\delta_{\text{M1}}^{\text{max}} = \delta_{\text{Vlasov}}^{\text{max}} \sqrt{1 + \frac{3}{\gamma_b^2}} \quad \text{where} \quad \delta_{\text{Vlasov}}^{\text{max}} = \frac{\omega_b \beta_b}{\sqrt{\gamma_b}}. \quad (6.87)$$

However, for larger electron energies, above $\gamma_b \approx 3$ ($\langle\varepsilon\rangle \approx 1 \text{ MeV}$), the M1 model provides the solution with an error less than $\approx 15\%$. For $\gamma_b \gtrsim 7$ ($\langle\varepsilon\rangle \approx 3 \text{ MeV}$), the M1 model makes an error less than $\approx 3\%$. This example partially confirms the argument given by Minerbo, and quoted in the introduction of this section, concerning the justification of the M1 closure (6.61) when neglecting collisions of beam electrons with background particles.

Conclusion

Since the development of thermodynamics, physicists have discovered two main principles that govern physical processes. The first one is the least action principle. A particle evolves from a state A , at the space location \mathbf{r}_A and time t_A , to a state B at the space location \mathbf{r}_B and time t_B , by following the trajectory from \mathbf{r}_A to \mathbf{r}_B that minimizes its action. The action of the particle being its kinetic energy, minus its potential energy, integrated over time between t_A and t_B , it means that particles will always move following the trajectory that minimizes its kinetic energy compared to its potential energy, imposed by the surrounding force fields (there is a similar law concerning photons called the

Fermat's principle). This "energy minimization principle" is at the origin of many theories in Physics from optical geometry and Newton's mechanics to quantum electrodynamics [Feynman et al., 1963]. However, another tendency arises when studying a system consisting of a lot of particles. In principle, one may think that all the physical properties of such a system can be determined by its microscopic state, i.e. by the description of the positions and momenta of all particles. Actually, because the number of particles is so large, the details of the motion of individual particles is mostly irrelevant to the behavior of the system as a whole. Indeed, according to thermodynamics and statistical physics, the macroscopic state of a system is defined by a distribution on the microstates that are accessible to the system in the course of its thermal fluctuations. In order to describe this discrete set (continuous set) of microscopic states of a system, J.W. Gibbs introduced the statistical entropy

$$H = -k_B \sum_i p_i \ln p_i \left(H = -k_B \int f \ln f, \text{ respectively} \right) \quad (6.88)$$

where E_i is the energy of the microscopic state i , and p_i is the probability that it occurs during the system's fluctuations (f is the particles distribution function, respectively). The difference between this last expression, the Boltzmann entropy (6.64) and the local angular entropy (6.46) or (6.63) simply comes from an additive constant. The above expression of the statistical entropy is also used in communication theory and it is called the Shannon Entropy. It is the opposite of the information content of signals, consisting in a succession of binary numbers. L. Boltzmann showed that the statistical entropy of an isolated system of particles can only rise with time

$$\frac{dH}{dt} \geq 0 \quad (6.89)$$

(see **Appendix A, section A.1.5**) and that the thermodynamic equilibrium is obtained when all the accessible microscopic states of the system are equally likely. Thus, the thermodynamic equilibrium is the configuration corresponding to the maximum of a system's entropy for a given set of accessible microscopic states. In other words, the thermodynamic equilibrium is the macroscopic configuration in which the lack of information is maximal. This is the second main principle mentioned previously. The difficulties happen due to the fact that both principles ("Energy minimization" and "Entropy maximization") are mutually exclusive. For example, according to the least action principle, the particle can move from \mathbf{r}_B to \mathbf{r}_A by the same trajectory as he moved from \mathbf{r}_A to \mathbf{r}_B . Indeed, the time is reversible in the equations describing the particle dynamics (Newton's fundamental principle of mechanics, Einstein's fundamental principle of mechanics or Schrödinger's fundamental principle of quantum mechanics). It is not the case for a system of many particles. The increase of entropy can proceed in an irreversible way, since the second law of Thermodynamics (6.89) is not time-reversible.

Concerning fast electron transport in solids or dense plasmas, these two principles are in competition. Collective effects are described by the particles dynamics in the self-generated electromagnetic fields and therefore follows the "Energy Minimization Principle". Oppositely, the collisional effects

tend to homogenize the particles momentum distribution and are therefore better described by the "Entropy Maximization Principle". In this section, it has been shown that collisional effects ensure that the local angular entropy

$$\frac{dH_\varepsilon}{dt} \geq 0 \quad (6.90)$$

for fast electrons with kinetic energies less than a threshold value ε_{th} , depending on the atomic number Z of the material. Concerning laser-generated fast electron beams, this threshold ε_{th} is sufficiently large compared to their typical kinetic energies. Moreover, laser-generated fast electrons with energies greater than ε_{th} propagate deeper in the laser-irradiated target and have consequently a local angular distribution close to the anisotropic limit for which the M1 closure is exact. In order to check the M1 closure in a collisionless case, where there is more arguments in favor of "minimizing the action" instead of "maximizing the angular entropy", we have derived the dispersion relation of the resistive filamentation instability, obtained with the M1 model, in the limit $T_b \rightarrow 0$, and we have compared it to the reference Vlasov case presented in **Chapter 3, section 3.2.3**. An advantage of the M1 closure in this derivation is that the angular moments of the Maxwell-Juttner distribution function of the beam $\Psi^{(0)}$ are easy to obtain since the Maxwell-Juttner distribution is a particular case of the more general distribution function Ψ_{M1} . That can be explained by the following mathematical relation

$$\begin{aligned} H[\Psi_{\text{M-J}}] &= \max_{\Psi} \{H[\Psi]\} \\ &= \max_{\Psi} \left\{ \int_0^\infty H_\varepsilon[\Psi] d\varepsilon \right\} \\ &\leq \int_0^\infty \max_{\Psi} \{H_\varepsilon[\Psi]\} d\varepsilon \\ &\leq \int_0^\infty H_\varepsilon[\Psi_{\text{M1}}] d\varepsilon. \end{aligned} \quad (6.91)$$

This relation shows that the M1 approximation overestimates the Boltzmann entropy of the beam and that the maximum angular entropy distribution function (6.61) can be obtained by multiplying the maximum entropy Maxwell-Juttner distribution function (6.71) with a Dirac distribution in energy

$$\Psi_{\text{M1}}(\mathbf{r}, \varepsilon_0, \boldsymbol{\Omega}, t) = \delta[\varepsilon - \varepsilon_0] \Psi_{\text{MJ}}(\mathbf{r}, \varepsilon, \boldsymbol{\Omega}, t), \quad (6.92)$$

as explained by [Wright and Hadley, 1975]. Besides, this study has shown that the M1 model overestimates the instability growth rate for $\gamma_b \gtrsim 1$. However, the resistive filamentation instability is reproduced with an error of less than 15 % for $\gamma_b \geq 3$. This result is surprising since there is no reason to maximize the angular entropy in such a collisionless case. It can be explained by the argument given by Minerbo, saying that "by using the maximum entropy criterion, one avoids introducing information that is not available." Nevertheless, it will be shown in **Chapter 8** that the closure relation (6.61) allows for a sufficiently accurate and fast computation of the V-F-P equation (6.15) with an arbitrary degree of anisotropy. Moreover, contrary to P1, it continuously relates the anisotropic and isotropic regimes while satisfying the physical constraints $\Psi_0 \geq 0$ and $0 \leq |\boldsymbol{\Omega}_\varepsilon| \leq 1$ thanks to the exponential form of the

underlying distribution function (6.60). Several numerical experiments in the non-relativistic regime, carried out for the comparison of the M1 model with the full V-F-P code [Duclous et al., 2009], have shown good agreements with a much reduced computation time [Mallet et al., 2014].

6.3 Physics of the Background Material

The response of the background particles to the beam propagation is described by the diffusion equation of the magnetic field (6.24), the Ohm's law (6.23) and the heat equations (6.25) and (6.28). These equations depend on the electrical resistivity η , thermal electron conductivity κ_e , thermal capacities $C_{V,e}$ and $C_{V,i}$ and the electron-ion coupling factor G . All these parameters depend on the density and temperatures of the target material. In the case of laser-irradiated solid targets, the solid is initially cold and these different parameters are given by the solid state physics theory. One talks about the lattice thermal capacity and electron-lattice coupling factor instead of the ion thermal capacity and electron-ion coupling factor, in a plasma. However, the collisional and collective losses of the fast electron beam rapidly induce the ionization of the material and the heating of the background free electrons, which in turn heat the lattice. The material enters consequently the liquid and then the plasma state. While the plasma parameters are known, there is no theory predicting the material parameters in the transient domain between these states. In the case of insulators or Warm Dense Matter (WDM), quantum molecular dynamics computations allow to evaluate these parameters. This section is dedicated to the description of these parameters in metals.

6.3.1 Ionization State Z^* and Thermal Capacities $C_{V,\alpha}$

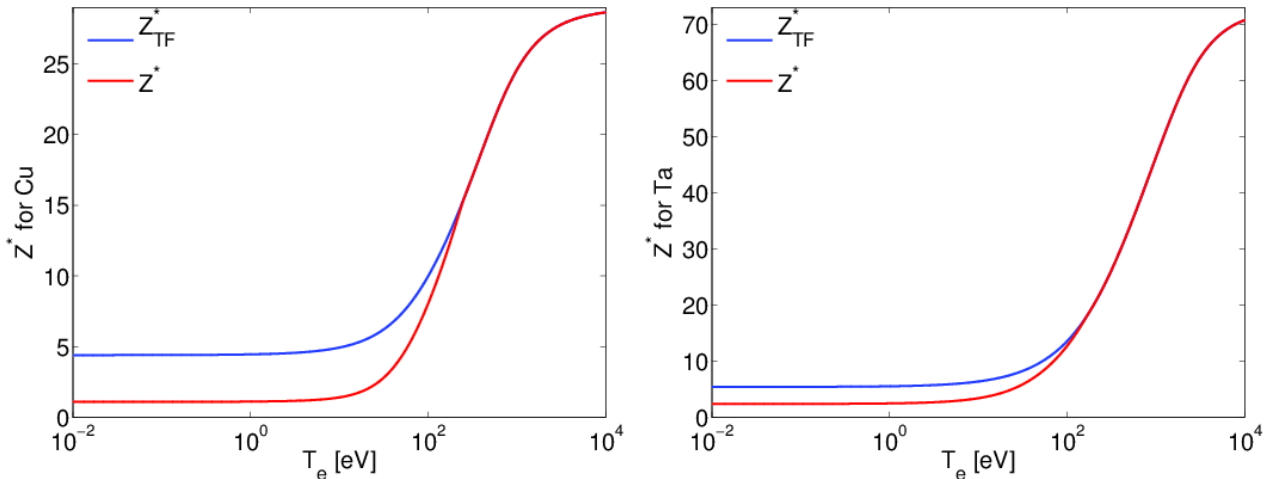


Figure 6.6: Ionization state given by (6.93) (red) compared to the More formula (3.43) (blue) for Copper (Left panel) and Tantalum (Right panel).

6.3. PHYSICS OF THE BACKGROUND MATERIAL

The ionization state Z^* is an important parameter, which allows us to determine the density of free electrons $n_{e,f} = Z^*n_i$ and bound electrons $n_{e,b} = (Z - Z^*)n_i$ in the solid. As explained in **Chapter 3, section 3.3.1**, Z^* can be estimated by the More Formula (3.43) based on the Thomas-Fermi model. However, the Thomas-Fermi model is inadequate for capturing the metal-insulator transition since it neglects any atomic structure effects on the ionization equilibrium. Contrary to the treatment proposed by [Desjarlais, 2001], which consists in imposing a smooth transition from Thomas-Fermi to non-ideal Saha at low temperature, we impose phenomenologically the adequate value of the ionization state $Z^* = Z_c$ at a low temperature, where Z_c is the number of electrons per atom in the conduction band (s-band), as

$$Z^* = \{[(1 - f_e) Z_c]^{a_1} + [f Z_{TF}^*]^{a_1}\}^{1/a_1} \quad (6.93)$$

where Z_{TF}^* is the ionization state given by (3.43) and

$$f = K^{1/Z_{TF}^*} \text{ with } K = \frac{1}{2} \left[1 + \tanh \left(\frac{k_B T_e - a_2 E_F}{a_3 E_F} \right) \right].$$

Here, E_F is the Fermi energy given by Equation (3.42) with $n_e = Z_c n_i$, a_1 and a_2 are parameters that allow for adjusting a smooth transition from Z_c to Z_{TF}^* while a_2 determines the temperature at which the transition occurs. For example, $Z_c = 3$, $a_1 = a_2 = 1$ and $a_3 = 0.05$ for Aluminum, $Z_c = 1$, $a_1 = 2$, $a_2 = 35$ and $a_3 = 1.925$ for Copper and $Z_c = 2$, $a_1 = 2$, $a_2 = 20$ and $a_3 = 1.25$ for Tantalum provide good estimates for the charge state, as illustrated in **Figure 6.6**. By taking $Z^* = Z_c$ at the solid temperature instead of $Z^* \approx 0$ as [Desjarlais, 2001], we empirically account for the collisions between free electrons and neutral atoms in the calculation of transport coefficients η and κ_e by taking into account collisions between free electrons and phonons (see the next **section 6.3.2**).

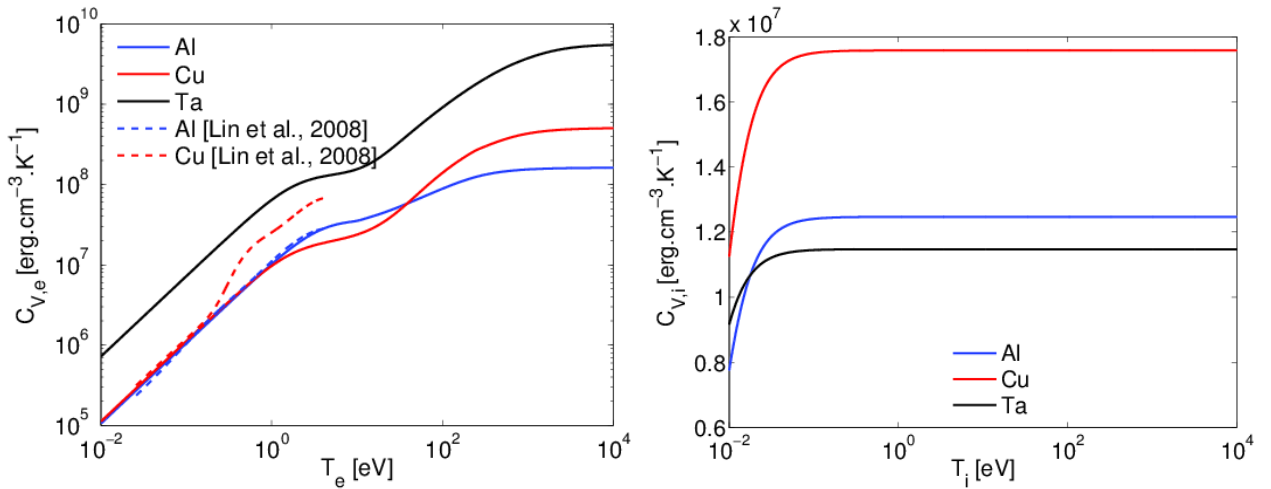


Figure 6.7: (Left panel) Electron thermal capacity (6.100) for Tantalum (solid black curve) and comparison between the electron thermal capacity (6.100) (full curve) and the results by [Lin et al., 2008] (dashed curves) for Aluminum (blue) and Copper (red). (Right panel) Ion thermal capacity (6.105) for Tantalum (black), Copper (red) and Aluminum (blue)

CHAPTER 6. DEVELOPMENT OF A REDUCED MODEL FOR LASER-GENERATED RELATIVISTIC ELECTRON BEAM TRANSPORT IN SOLIDS AND DENSE PLASMAS

Knowing the ionization state, one can deduce the electron thermal capacity in the hot plasma temperatures. It follows from the perfect electron gas expression (see **Annexe B, section B.1.1**)

$$C_{V,e}^{\text{hot}} = \frac{3}{2} Z^* n_i k_B. \quad (6.94)$$

However, we need to model it in the whole range of electron temperatures starting from the ambient temperature $T_e \approx 300\text{K}$ to $k_B T_e \approx 10\text{keV}$. It is known from experiments that, at temperatures below the Fermi temperature (3.42), the electron heat capacity of metals can be written

$$C_{V,e}^{\text{cold}} = \gamma_{\text{exp}} T_e \quad (6.95)$$

where γ_{exp} is the Sommerfeld parameter. From a theoretical point of view, the thermal capacity of degenerate electrons at low temperatures is defined as

$$C_{V,e}^{\text{cold}} = \frac{dU_e}{dT_e} = \int_0^\infty (\varepsilon - E_F) \frac{\partial f_{FD}}{\partial T_e} g(\varepsilon) d\varepsilon \quad (6.96)$$

where U_e is the total electron thermal energy, ε is the electron kinetic energy,

$$f_{FD}(\varepsilon, \mu, T_e) = \frac{1}{1 + \exp\left(\frac{\varepsilon - \mu}{k_B T_e}\right)} \quad (6.97)$$

is the Fermi-Dirac distribution function depending on the chemical potential μ and the Fermi energy E_F (3.42), expressed with the electron density $n_e = Z^* n_i$ and $g(\varepsilon)$ is the electron Density of States (DOS). By assuming that $g(\varepsilon) \approx g(E_F)$ and by approximating the DOS g by the free electron gas expression

$$g(\varepsilon) = \frac{1}{2\pi^2} \left(\frac{2m_e}{\hbar^2}\right)^{3/2} \sqrt{\varepsilon}, \quad (6.98)$$

one finds

$$C_{V,e}^{\text{cold}} = \gamma_{\text{th}} T_e \quad \text{with} \quad \gamma_{\text{th}} = \frac{\pi^2 n_e k_B}{2 E_F}. \quad (6.99)$$

However, γ_{th} is usually of the expected magnitude, but often does not agree very closely with the measured value γ_{exp} . Moreover, computational analysis based on first-principles electronic structure calculations of the electron DOS have recently shown large deviations from the commonly used linear approximations (6.95) [Lin et al., 2008] [Bévilion et al., 2014]. An interpolation formula presents a good compromise, allowing to describe the electron thermal capacity in the whole range of considered temperatures :

$$C_{V,e} = \left[(\gamma T_e)^{-2} + \left(\frac{3}{2} Z^* n_i k_B \right)^{-2} \right]^{-1/2} \quad (6.100)$$

where $\gamma = 912\text{erg.cm}^{-3}.\text{K}^{-2}$ for Aluminum, $968\text{erg.cm}^{-3}.\text{K}^{-2}$ for Copper and $5428.8\text{erg.cm}^{-3}.\text{K}^{-2}$ for Tantalum. The temperature dependence of the electron heat capacity is illustrated in the left panel

6.3. PHYSICS OF THE BACKGROUND MATERIAL

of **Figure 6.7**.

At the plasma state, the ion thermal capacity is given by the ideal gas expression (see **Annexe B, section B.1.1**)

$$C_{V,i}^{\text{hot}} = \frac{3}{2}n_i k_B. \quad (6.101)$$

In the cold solid phase, the lattice thermal capacity is due to phonons. According to experiments, it can be written

$$C_{V,i}^{\text{cold}} = A_{\text{exp}} T_i^3. \quad (6.102)$$

According to the Debye theory of phonons, the expression for this constant below the Debye temperature T_D reads

$$A_{\text{th}} = \frac{12\pi^4 n_i k_B}{5T_D^3}. \quad (6.103)$$

However, above $T_e = 300$ K, the Einstein model is sufficient to describe the lattice heat capacity. It is calculated by using the Bose-Einstein distribution function for the phonons

$$f_{BE}(\omega, T_i) = \frac{1}{\exp\left(\frac{\hbar\omega}{k_B T_i}\right) - 1} \quad (6.104)$$

where ω is the phonon frequency and by assuming the Einstein phonon DOS $g(\omega) = \delta(\omega - \omega_E)$. Then, the lattice heat capacity reads

$$C_{V,i}^{\text{cold}} = \frac{dU_i}{dT_i} = \int_0^\infty \hbar\omega \frac{\partial f_{BE}}{\partial T_i} g(\omega) d\omega = k_B n_i \left(\frac{\hbar\omega_E}{k_B T_i}\right)^2 \frac{\exp\left(\frac{\hbar\omega_E}{k_B T_i}\right)}{\left[\exp\left(\frac{\hbar\omega_E}{k_B T_i}\right) - 1\right]^2} \quad (6.105)$$

where $\hbar\omega_E$ is the Einstein temperature. For example, $\hbar\omega_E = 284$ K for Aluminum, 278 K for Copper and 193 K for Tantalum. Contrary to the Debye temperature, the Einstein temperature is difficult to find in the literature for some metals. In this case, one can use the empirical relation $\hbar\omega_E/k_B T_D \approx (\pi/6)^{1/3}$. However, the Einstein heat capacity tends to $k_B n_i$ instead of $(3/2)k_B n_i$ when $T_i \gg \hbar\omega_E$. Consequently, a good compromise, allowing to describe the ion thermal capacity in the whole range of considered temperatures, can be obtained by estimating it as

$$C_{V,i} = \frac{3}{2}k_B n_i \left(\frac{\hbar\omega_E}{k_B T_i}\right)^2 \frac{\exp\left(\frac{\hbar\omega_E}{k_B T_i}\right)}{\left[\exp\left(\frac{\hbar\omega_E}{k_B T_i}\right) - 1\right]^2}. \quad (6.106)$$

It is plotted in the right panel of **Figure 6.7** for Aluminum, Copper and Tantalum.

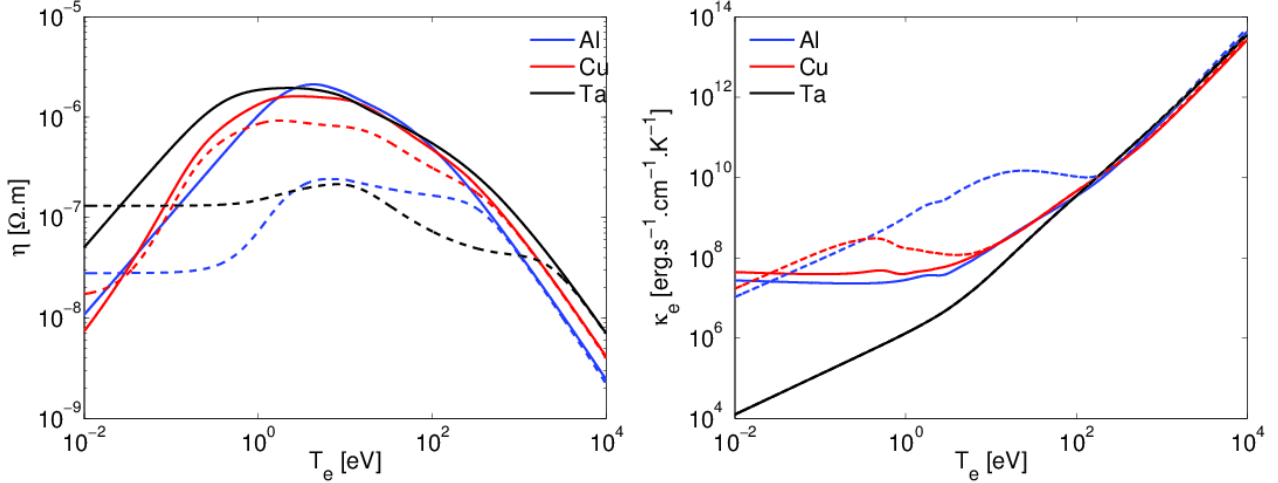
6.3.2 Two-Temperature Electron Transport Coefficients η and κ_e


Figure 6.8: Electrical resistivity (6.107) (Left panel) and thermal electron conductivity (6.108) (Right panel) for Aluminum (blue), Copper (red) and Tantalum (black) at $T_i = 300$ K (dashed curves) and at $T_i = T_e$ (full curves).

As explained in **Chapter 3, section 3.3.1**, the Lee-More model [Lee and More, 1984] assumes equal electron and ion temperatures. Another model that takes into account $T_i \neq T_e$ was proposed by [Chimier et al., 2007]. Here, we propose to merge these two models. In our approach, the electrical resistivity reads

$$\eta = \frac{m_e \nu_e}{n_e e^2} \frac{1}{A^\alpha \left(\frac{\mu}{k_B T_e} \right)} \quad (6.107)$$

and the thermal electron conductivity reads

$$\kappa_e = \gamma_L \frac{T_e}{\eta} = \frac{n_e k_b^2 T_e}{m_e \nu_e} A^\beta \left(\frac{\mu}{k_B T_e} \right) \quad \text{with} \quad \gamma_L = \frac{A^\beta \left(\frac{\mu}{k_B T_e} \right)}{A^\alpha \left(\frac{\mu}{k_B T_e} \right)} \left(\frac{k_B}{e} \right)^2. \quad (6.108)$$

They are plotted in **Figure 6.8** for Aluminum, Copper and Tantalum. Here, the free electron density is given by $n_e = Z^* n_i$ where Z^* is computed according to (6.93) so that at low temperatures $n_e = Z_c n_i$ is the density of s-band electrons. The Lorenz factor γ_L is computed according to the functions A^α and A^β provided by [Lee and More, 1984] (see **Appendix B, section B.2.4**) allowing to reproduce the Wiedemann-Franz law at solid temperatures

$$\gamma_L^{\text{cold}} = \frac{\pi^2}{3} \left(\frac{k_B}{e} \right)^2 \quad (6.109)$$

6.3. PHYSICS OF THE BACKGROUND MATERIAL

and the Spitzer result at plasma temperatures

$$\gamma_L^{\text{hot}} = 4 \left(\frac{k_B}{e} \right)^2. \quad (6.110)$$

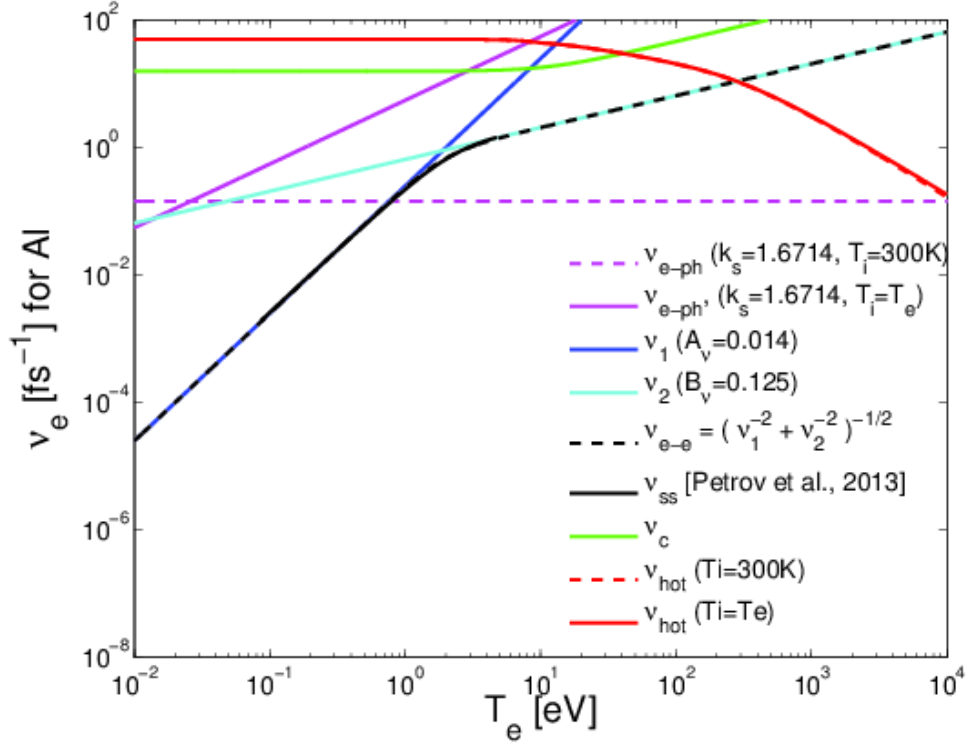


Figure 6.9: Contributions of the different electron collision frequencies in the electrical resistivity of Aluminum (6.107) with (6.111) ($Z_s = 3$, $Z_d = 0$). The electron frequency contributions are indicated in the Figure.

The electron collision frequency is computed according to the harmonic mean

$$\nu_e = \left[(\nu_{e-ph} + \nu_{e-e})^{-2} + \nu_c^{-2} + \nu_{\text{hot}}^{-2} \right]^{-1/2}. \quad (6.111)$$

At hot plasma temperatures, ν_e is therefore given by

$$\nu_{\text{hot}} = \frac{\bar{\nu}_{ei}}{\gamma_E} \text{ for } \eta \text{ and } \nu_{\text{hot}} = \frac{\bar{\nu}_{ei}}{\epsilon \delta T} \text{ for } \kappa_e \quad (6.112)$$

where γ_E and $\epsilon \delta T$ are the electron-electron collision correction factors following the notation from [Spitzer and Härm, 1953]. They can be fit as a function of Z^* according to the table given by [Spitzer and Härm, 1953] (see the fits given in **Annexe B, section B.2.2**). For $\bar{\nu}_{ei}$, we use the Lee-More electron-ion collision frequency

$$\bar{\nu}_{ei} = \frac{2\sqrt{2}\pi(Z^*)^2 n_i e^4 \ln \Lambda_{ei}}{3\sqrt{m_e}(k_B T_e)^{3/2} \left[1 + \exp\left(-\frac{\mu}{k_B T_e}\right) \right] F_{1/2}\left(\frac{\mu}{k_B T_e}\right)} \quad (6.113)$$

CHAPTER 6. DEVELOPMENT OF A REDUCED MODEL FOR LASER-GENERATED RELATIVISTIC ELECTRON BEAM TRANSPORT IN SOLIDS AND DENSE PLASMAS

where the Coulomb logarithm $\ln \Lambda_{ei}$ is given in **Appendix A, section A.2.3**, allowing to account for the electron degeneracy close to the Fermi temperature (see **Appendix B, section B.2.4**). At a low temperature, ν_e is given by a sum of the electron-phonon collision frequency and the electron-electron collision frequency

$$\nu_e^{\text{cold}} = \nu_{e-ph} + \nu_{e-e}. \quad (6.114)$$

According to [Lee and More, 1984] and [Chimier et al., 2007], we impose that the mean free path v_e/ν_e of the electrons cannot exceed the mean interionic distance v_e/ν_e in the intermediate range of temperatures where $\nu_c = v_e/(3/4\pi n_i)^{1/3}$, $v_e = \sqrt{3k_B(T_F + T_e)/m_e}$ and $T_F = E_F/k_B$. In the model proposed by [Chimier et al., 2007], the electron-electron collision frequency is

$$\nu_{e-e} = A_\nu \frac{k_B}{\hbar T_F} T_e^2 \quad (6.115)$$

and the electron-phonon collision frequency is

$$\nu_{e-ph} = k_s \frac{2e^2 k_B}{\hbar^2 \sqrt{\frac{2k_B T_F}{m_e}}} T_i \quad (6.116)$$

where k_s and A_ν are parameters depending on the material. At the ambient temperature, the electron-phonon collision frequency ν_{e-ph} is the main contribution in the electron momentum dumping. Therefore, while the parameter k_s can be obtained by imposing the measured value of the electrical resistivity $m_e \nu_{e-ph}/n_e e^2$ at the ambient temperature, the parameter A_ν of the electron-electron collision frequency ν_{e-e} is usually unknown. Moreover, it has been recently shown experimentally [Fourment et al., 2014] that collisions of s-band with d-band electrons make an important contribution to the electron collision frequency ν_e for transition and noble metals while the expression (6.115) corresponds to the low one-temperature asymptotics accounting for the collisions between s-band electrons only (Fermi liquid model).

[Inogamov and Petrov, 2010] and [Petrov et al., 2013] have developed a semi-analytical model by using the electron kinetic equation, the matrix element for the scattering probability and a screened Coulomb potential describing the interaction between s-band electrons and s or d-band electrons. In their approach, the electron-electron collision frequency is given by

$$\nu_{e-e} = \bar{\nu}_{s-s} + \bar{\nu}_{s-d}. \quad (6.117)$$

According to [Inogamov and Petrov, 2010], the s-s electrons collision frequency reads

$$\bar{\nu}_{s-s} = \frac{\int_0^\infty -\frac{\partial f_{FD}}{\partial \varepsilon}(\varepsilon_1) \nu_{s-s}(\varepsilon_1) d\varepsilon_1}{\int_0^\infty -\frac{\partial f_{FD}}{\partial \varepsilon}(\varepsilon_1) d\varepsilon_1} \quad (6.118)$$

6.3. PHYSICS OF THE BACKGROUND MATERIAL

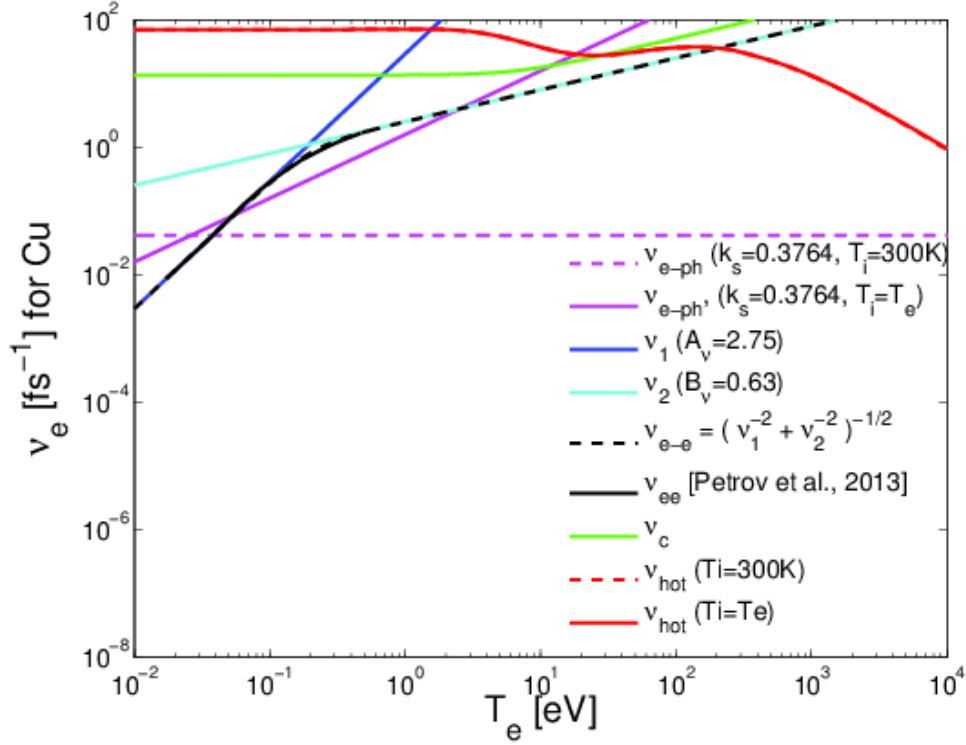


Figure 6.10: Contributions of the different electron collision frequencies in the electrical resistivity of Copper (6.107) with (6.111) ($Z_s = 1$, $Z_d = 10$). The electron frequency contributions are indicated in the Figure.

where f_{FD} the Fermi-Dirac electron distribution function (6.97), ε_1 is the energy of electrons 1 and $\nu_{s-s}(\varepsilon_1)$ is the collision frequency for an electron 1 colliding electrons 2 having the energies ε_2 given by

$$\nu_{ss}(k_1) = \frac{2m_e^2}{(2\pi)^3 \hbar^5 k_1} \int dq \int dk_2 \int d\alpha \int d\beta k_2 U(q)^2 S(k_1, k_2, \alpha, \beta) \delta[\alpha - \beta]. \quad (6.119)$$

$$U(q) = \frac{4\pi e^2}{q^2 + k_{\text{screen}}^2}$$

is the screened Coulomb repulsion of electrons with the screening reciprocal length, estimated by the Lindhard screening length $k_{\text{screen}} = \sqrt{4\pi e^2 / (\partial\mu / \partial n_e)}$.

$$\begin{aligned} S(k_1, k_2, \alpha, \beta) &= f_{FD}(\varepsilon_2) [1 - f_{FD}(\varepsilon_1 - \alpha)] [1 - f_{FD}(\varepsilon_2 + \beta)] \\ &+ f_{FD}(\varepsilon_1 - \alpha) f_{FD}(\varepsilon_2 + \beta) [1 - f_{FD}(\varepsilon_2)] \end{aligned}$$

is the statistical factor describing the admissible energy states for the electrons 1 and 2 before and after their binary collision, α is the energy loss of the electron 1 and β is the energy gain of the electron 2 during the collision. The Dirac distribution $\delta[\alpha - \beta]$ describes the energy conservation in the collision. First, the authors consider the one-band metal for all s band electrons with the simple

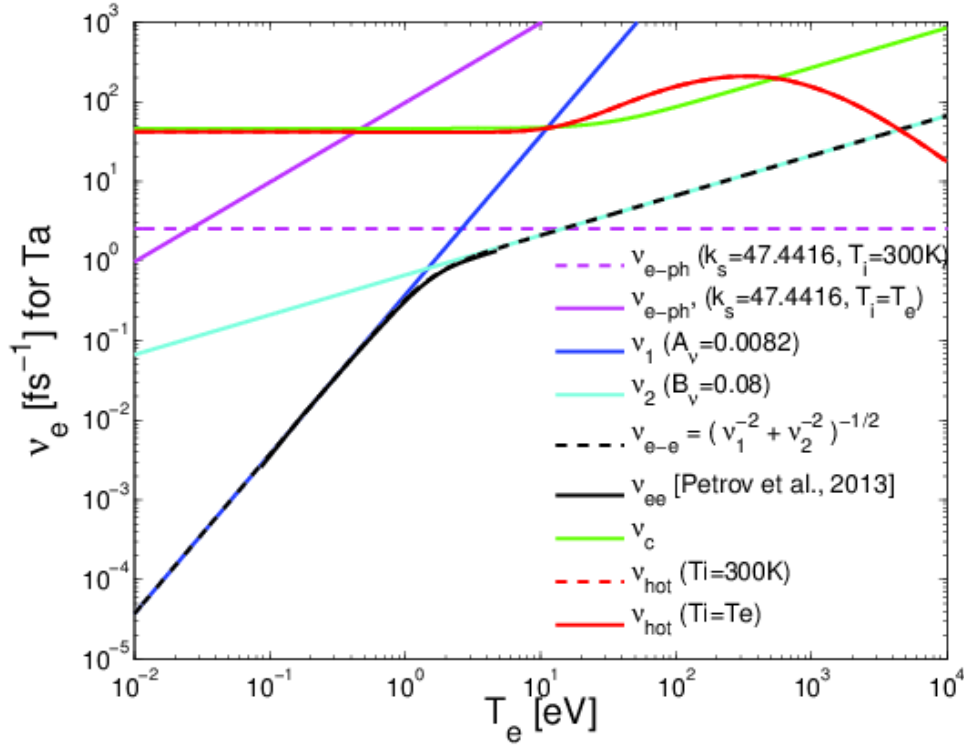


Figure 6.11: Contributions of the different electron collision frequencies in the electrical resistivity of Tantalum (6.107) with (6.111) ($Z_s = 2$, $Z_d = 3$). The electron frequency contributions are indicated in the Figure.

parabolic dispersion law $\varepsilon(k) = \hbar^2 k^2 / 2m_e$. The (α, β) -integration is straightforward and gives

$$\begin{aligned}
 s(\alpha) = \int d\alpha \int d\beta S(k_1, k_2, \alpha, \beta) \delta[\alpha - \beta] &= k_B T_e \frac{1 + \exp\left(\frac{\varepsilon_1 - \mu}{k_B T_e}\right)}{1 + \exp\left(\frac{\varepsilon_2 - \mu}{k_B T_e}\right)} \frac{\exp\left(\frac{\varepsilon_2 - \mu}{k_B T_e}\right)}{1 - \exp\left(\frac{\varepsilon_1 + \varepsilon_2 - 2\mu}{k_B T_e}\right)} \\
 &\times \ln \left[\frac{\exp\left(\frac{\varepsilon_1 - \mu}{k_B T_e}\right) + \exp\left(\frac{\alpha}{k_B T_e}\right)}{1 + \exp\left(\frac{\alpha + \varepsilon_2 - \mu}{k_B T_e}\right)} \right].
 \end{aligned} \tag{6.120}$$

Then, the authors split the domain of integration as illustrated in the left panel of **Figure 6.12** to finally obtain

$$\nu_{s-s}(k_1) = \frac{2m_e^2}{(2\pi)^3 \hbar^5 k_1} (I_{a1} + I_{a2} + I_b + I_c + I_d) \tag{6.121}$$

6.3. PHYSICS OF THE BACKGROUND MATERIAL

where

$$\begin{aligned}
 I_{a1} &= \int_0^{k_1} dq \int_{k_1-q}^{k_1+q} dk_2 k_2 U(q)^2 [s(\alpha'') - s(\beta')], \\
 I_{a2} &= \int_{k_1}^{\infty} dq \int_{-k_1+q}^{k_1+q} dk_2 k_2 U(q)^2 [s(\alpha'') - s(\beta')], \\
 I_b &= \int_0^{k_1} dq \int_{k_1+q}^{\infty} dk_2 k_2 U(q)^2 [s(\alpha'') - s(\alpha')], \\
 I_c &= 0 \\
 I_d &= \int_0^{k_1} dq \int_0^{k_1-q} dk_2 k_2 U(q)^2 [s(\beta'') - s(\beta')]
 \end{aligned}$$

with $\beta' = (\hbar^2/2m_e)(q^2 - 2k_2q)$, $\beta'' = (\hbar^2/2m_e)(q^2 + 2k_2q)$, $\alpha' = -(\hbar^2/2m_e)(q^2 + 2k_1q)$ and $\alpha'' = -(\hbar^2/2m_e)(q^2 - 2k_1q)$. The dependence of $\nu_{ss}(k_1)$ on the density is implicitly taken into account via the chemical potential μ according to the relation

$$n_e = Z^* n_i = \int_0^{\infty} f_{FD}(\varepsilon) g(\varepsilon) d\varepsilon \quad (6.122)$$

where $g(\varepsilon)$ is the free electron gas DOS (6.98). In the limit $T_e \rightarrow 0$ in (6.121), which implies $I_{a1} + I_{a2} + I_b + I_d \rightarrow I_{a1} + I_{a2}$ and by approximating the s-band electron collision frequency by its value in the vicinity of the Fermi surface $k_F = 2m_e E_F / \hbar^2$, i.e. by approximating $\bar{\nu}_{s-s} \approx \nu_{s_s}(k_F)$, the authors finally estimate

$$A_\nu = \frac{\pi E_F m_e^3 e^4}{8 \hbar^6 k_F^4} \left[\frac{(2k_F/k_{\text{screen}})^4}{1 + (2k_F/k_{\text{screen}})^2} + \left(\frac{2k_F}{k_{\text{screen}}} \right)^3 + \arctan \left(\frac{2k_F}{k_{\text{screen}}} \right) \right]. \quad (6.123)$$

According to [Petrov et al., 2013], the s-d electron collision frequency is estimated with the same method but, with two terms in the electron DOS as

$$g(\varepsilon) = g_s(\varepsilon) + g_d(\varepsilon) \quad (6.124)$$

where, for s-band electrons, the authors use

$$\varepsilon = \varepsilon_s + \frac{\hbar^2 k^2}{2m_s} \quad (6.125)$$

and

$$g_s(\varepsilon) = \begin{cases} \frac{1}{2\pi^2} \left(\frac{2m_s}{\hbar^2} \right)^{3/2} \sqrt{\varepsilon - \varepsilon_s} & \text{if } \varepsilon \geq \varepsilon_s \\ 0 & \text{else} \end{cases} \quad (6.126)$$

while for the d-band electrons, they use

$$\varepsilon' = \varepsilon'_1 + \frac{\hbar^2 k'^2}{2m_s} \quad (6.127)$$

and

$$g_d(\varepsilon') = \begin{cases} \frac{1}{2\pi^2} \left(\frac{2m_d}{\hbar^2} \right)^{3/2} \sqrt{\varepsilon' - \varepsilon'_1} & \text{if } \varepsilon'_1 \leq \varepsilon' \leq \varepsilon'_2 \\ 0 & \text{else} \end{cases} . \quad (6.128)$$

Here, ε_s , ε'_1 , ε'_2 are parameters determined by fitting the best as possible the real electron DOS of the metal while m_s and m_d are the effective mass of s-band and d-band electrons, respectively. Such effective mass approximation is common in Solid States Physics in order to model the interaction of electrons with the periodic lattice potential, the interaction of electrons with phonons or the interaction of electrons with themselves. [Petrov et al., 2013] model these effective masses according to

$$m_s = (3\pi^2 n_s)^{2/3} \frac{\hbar^2}{2(E_F - \varepsilon_s)} \quad (6.129)$$

and

$$m_d = (3\pi^2 n_d)^{2/3} \frac{\hbar^2}{2(E_F - \varepsilon'_1)} \quad (6.130)$$

where n_s and n_d are the densities of s-band electrons ($n_s = Z^* n_i$) and d-band electrons. An example is given for Tungsten in the right panel of **Figure 6.12**.

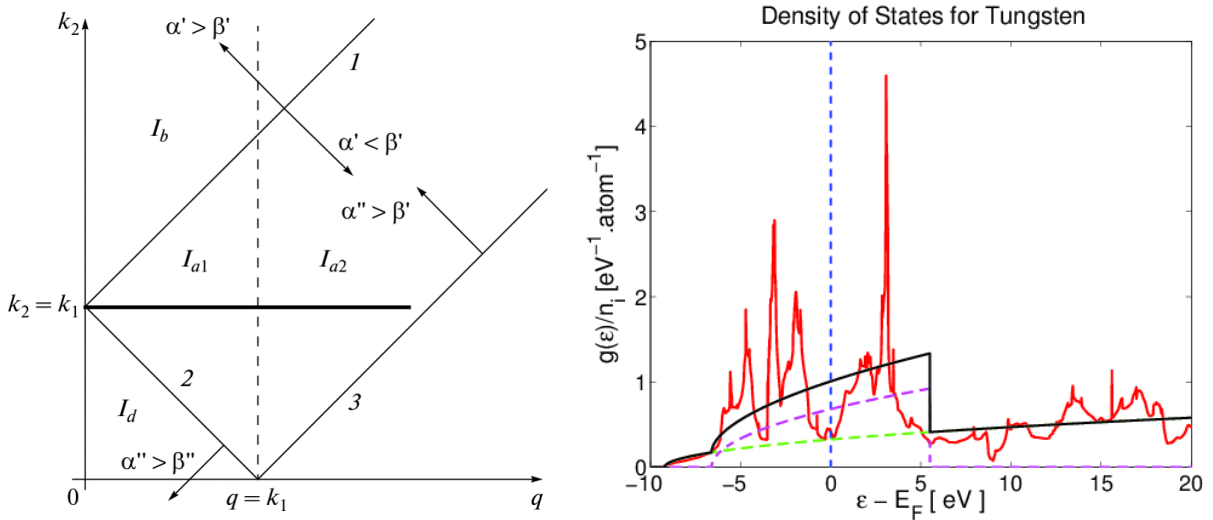


Figure 6.12: (Left panel) Regions in plane qk_2 over which integrals I_{a1} , I_{a2} , I_b and I_d of (6.119) are taken. The heavy segment indicates the image of the Fermi surface at $T_e \rightarrow 0$ and $k_1 = k_F$ (Fermi wave number) [Inogamov and Petrov, 2010]. (Right panel) Example of fit (6.124) for Tungsten (solid black curve) compared to ab initio calculation done by [Lin et al., 2008] (solid red curve); the s-band electrons contribution g_s in (6.124) (dashed green curve) is plotted with $m_s = 0.9m_e$ ($E_F - \varepsilon_s = -9.2$ eV) and the d-band electrons contribution g_d in (6.124) (dashed magenta curve) is plotted with $m_d = 1.7m_e$ ($E_F - \varepsilon_1 = -6.6$ eV and $\varepsilon_2 = E_F + 5.5$ eV); the Fermi energy value is $E_F = 17.969$ eV (dashed blue curve).

The upper limit ε'_2 in (6.128) complicates the calculation of the multiple integrals I_μ in Equation (6.121). The electron-electron collision frequency (6.117) is therefore computed numerically for any

6.3. PHYSICS OF THE BACKGROUND MATERIAL

electron temperature $T_e \ll T_F$. they can be found for some metals at <http://laser.itp.ac.ru>. For other metals, one can directly compute the electron collision frequency at a low temperature according to the algorithm proposed in the Appendix of the original paper by [Inogamov and Petrov, 2010]. It is very useful for determining the parameter A_ν . However, we have noticed that the electron-electron collision frequency (6.117) can be fit with a sufficient accuracy according to

$$\nu_{e-e} = (\nu_1^{-2} + \nu_2^{-2})^{-1/2} \quad (6.131)$$

with

$$\nu_1 = A_\nu \frac{k_B T_e^2}{\hbar T_F} \text{ and } \nu_2 = B_\nu \frac{k_B}{\hbar} \sqrt{T_e T_F} \quad (6.132)$$

where A_ν and B_ν are parameters to be determined, depending on the material as illustrated in **Figure 6.9** for Aluminum, in **Figure 6.10** for Copper and in **Figure 6.11** for Tantalum. We have obtained a sufficiently accurate fit with $k_s = 1.6714$, $A_\nu = 0.014$ and $B_\nu = 0.125$ for Aluminum, $k_s = 0.3764$, $A_\nu = 2.75$ and $B_\nu = 0.63$ for Copper and $k_s = 47.4416$, $A_\nu = 0.0082$ and $B_\nu = 0.08$ for Tantalum. They can be compared with the electrical resistivity of Aluminum and Copper from the Eidmann-Chimer model illustrated in **Figure 3.8** of **Chapter 3, section 3.3.1**.

6.3.3 Electron-Ion/Lattice Coupling Term G

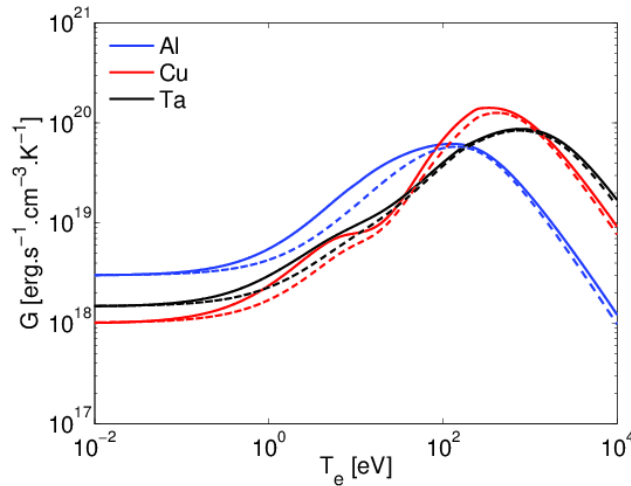


Figure 6.13: Electron-ion coupling factor (6.137) for Aluminum (blue), Copper (red) and Tantalum (black) at $T_i = 300$ K (dashed curves) and at $T_i = T_e$ (full curves).

Last but not least, the electron-ion/lattice energy exchange is described by the parameter G in Equations (6.25) and (6.28). Its value varies considerably in the range from the ambient temperature $T_e \approx 300$ K to the hot plasma $T_e \approx 10$ keV. Concerning the high temperature regime, we use the

plasma expression [Brysk et al., 1975] (see **Appendix B, section B.2.4**)

$$G_{\text{hot}} = 2 \frac{m_e}{m_i} C_{V,e} \bar{\nu}_{ei} \quad (6.133)$$

where $\bar{\nu}_{ei}$ is given by (6.113) allowing to account for electrons degeneracy close to the Fermi temperature. In the limit of low temperatures $T_e, T_i < T_F$, but $T_e, T_i \gg T_D$, the rate of energy transfer per unit volume from the electrons to the lattice in a metal can be written according to [Kaganov et al., 1957]

$$G_{\text{cold}}(T_e - T_i) = \frac{\pi^2}{6} n_i m_e c_s^2 \left(\frac{1}{\tau_e(T_e, T_e)} - \frac{1}{\tau_e(T_i, T_i)} \right). \quad (6.134)$$

This expression was obtained by assuming a Fermi-Dirac distribution for electrons, a Bose-Einstein distribution for phonons, and by accounting for one-phonon emission and absorption processes. Here, c_s is the speed of sound in the solid and $\tau_e = 1/\nu_e^{\text{cold}}$ is the electron relaxation time. By neglecting ν_2^{-2} compared to ν_1^{-2} in the electron-electron collision frequency (6.131) at low temperatures (see **Figure 6.9, Figure 6.10** and **Figure 6.11**), one can write

$$\tau_e(T_e, T_i) = \frac{1}{A_e T_e^2 + B_i T_i} \quad (6.135)$$

where $A_e = A_\nu k_B / \hbar T_F$ and $B_i = 2k_s e^2 k_B / \hbar^2 \sqrt{2k_B T_F / m_e}$. Injecting this relation in (6.134), one finally obtains according to [Chen et al., 2005]

$$G_{\text{cold}} = G_{\text{RT}} \left[1 + \frac{T_e + T_i}{\aleph T_F} \right] \quad (6.136)$$

where $G_{\text{RT}} = \pi^2 B_i n_i m_e c_s^2 / 6$ is the room temperature electron-lattice coupling factor and $\aleph = B_i / A_e T_F$ is a parameter chosen from comparison with experimental or theoretical data such as those proposed by [Lin et al., 2008] or [Petrov et al., 2013]. The cold and hot regime are related according to

$$G = [G_{\text{cold}}^{-2} + G_{\text{hot}}^{-2}]^{-1/2}. \quad (6.137)$$

The value of \aleph calculated with A_ν and k_s given in the previous subsection, does not allow for patching the two regimes around the Fermi temperature. A better interpolation can be obtained with $\aleph = 0.2$. The room temperature value can be found in the literature : $G_{\text{RT}} = 1.10^{18} \text{ erg.s}^{-1}.\text{cm}^{-3}.\text{K}^{-1}$ for Aluminum, $G_{\text{RT}} = 3.10^{18} \text{ erg.s}^{-1}.\text{cm}^{-3}.\text{K}^{-1}$ for Copper and $G_{\text{RT}} = 1.5.10^{18} \text{ erg.s}^{-1}.\text{cm}^{-3}.\text{K}^{-1}$ for Tantalum. The electron-ion coupling factors are plotted in **Figure 6.13**.

6.4 Conclusion

We have linearized the Belyaev-Budker collision tensor by applying it to the study of laser-generated fast electron beam transport in solids or dense plasmas, assuming a small momentum transfer in

6.4. CONCLUSION

a collision. The production of secondary electrons is neglected, assuming the residual energy of background electrons after a collision with a beam electron is smaller than the exchanged momentum $\Delta \mathbf{p}$ of a consecutive collision with another beam electron. These assumptions allowed us to obtain a more simple Landau-like collision tensor. Moreover, it allows us to relate the angular scattering collision frequency by colliding background particles (free electrons, bound electrons, screened free electrons/plasmons or ion nuclei) with the corresponding stopping powers according to an Einstein-like relation, similar to the one obtained for Brownian motion of particles. This allows us to obtain more accurate expressions compared to the angular scattering theories presented in **Chapter 4**, by retaining all terms in the Moller relativistic Coulomb logarithm instead of the relativistic generalization of Rutherford term, only. However, our model is limited to low density beams $n_b \ll n_e$ since the collisions of beam electrons with themselves and the production of secondary electrons are neglected.

The analysis, presented in **Chapter 5**, of existing numerical methods for solving the obtained Vlasov-Fokker-Planck (V-F-P) equation (6.15)

$$\begin{aligned} \frac{\partial \Psi}{\partial t} + \frac{\partial}{\partial \mathbf{r}} \cdot (v \boldsymbol{\Omega} \Psi) - \frac{\partial}{\partial \varepsilon} [v (e \mathbf{E} \cdot \boldsymbol{\Omega} + S) \Psi] \\ - \frac{\partial}{\partial \boldsymbol{\Omega}} \cdot \left\{ (\mathbf{I} - \boldsymbol{\Omega} \otimes \boldsymbol{\Omega}) \cdot \left[\frac{e}{p} \left(\mathbf{E} + \frac{v \boldsymbol{\Omega}}{c} \times \mathbf{B} \right) \Psi + \frac{\partial}{\partial \boldsymbol{\Omega}} \left(\frac{\nu}{2} \Psi \right) \right] \right\} = 0 \end{aligned}$$

oriented our choice towards a hybrid and expanded "Vlasov-Fokker-Planck" method. In order to make numerical computations as fast as possible, we limit the angular order of expansion to the 1st order. We derived the equations (6.34) and (6.35) by integrating over the unity sphere in the momentum space the V-F-P equation (6.15) multiplied by 1 and $\boldsymbol{\Omega}$, respectively :

$$\frac{\partial \Psi_0}{\partial t} + \frac{\partial}{\partial \mathbf{r}} \cdot (v \boldsymbol{\Psi}_1) - \frac{\partial}{\partial \varepsilon} [v (e \boldsymbol{\Psi}_1 \cdot \mathbf{E} + S \Psi_0)] = 0$$

and

$$\frac{\partial \boldsymbol{\Psi}_1}{\partial t} + \frac{\partial}{\partial \mathbf{r}} \cdot (v \boldsymbol{\Psi}_2) - \frac{\partial}{\partial \varepsilon} [v (e \boldsymbol{\Psi}_2 \cdot \mathbf{E} + S \boldsymbol{\Psi}_1)] = -\frac{e}{p} (\Psi_0 - \boldsymbol{\Psi}_2) \cdot \mathbf{E} - \frac{e}{\gamma m_e c} \boldsymbol{\Psi}_1 \times \mathbf{B} - \nu \boldsymbol{\Psi}_1$$

where the $\boldsymbol{\Psi}_\ell$ are the angular moments of the distribution function Ψ , S is the total stopping power of the beam electrons introduced in **Chapter 4** and ν is their total angular isotropization rate. Contrary to an equivalent spherical harmonic decomposition, the beam density and current are directly related to the angular moments :

$$n_b = \int_{\varepsilon_{\min}}^{\infty} \Psi_0 d\varepsilon$$

and

$$\mathbf{j}_b = -e \int_{\varepsilon_{\min}}^{\infty} v \boldsymbol{\Psi}_1 d\varepsilon.$$

Here, the parameter ε_{\min} comes from the "hybrid" assumption, which consists in separating the beam electrons population $\varepsilon > \varepsilon_{\min}$ and the background electrons population $\varepsilon < \varepsilon_{\min}$. Contrary to the

widely used P1 approximation, also usually called the "diffusion approximation", which consists in the closure relation $\Psi_2 = (1/3)\Psi_0\mathbf{I}$, our M1 model accounts for an arbitrary degree of anisotropy by using the closure

$$\Psi_2 = \frac{1}{3}\Psi_0\mathbf{I} + \mu\Psi_0 \left(\frac{\Psi_1 \otimes \Psi_1}{|\Psi_1|^2} - \frac{1}{3}\mathbf{I} \right).$$

$$\mu \approx \frac{|\Omega_\varepsilon|^2}{2} \left(1 + |\Omega_\varepsilon|^2 \right)$$

is estimated according to the Minerbo maximum angular entropy criterion depending on the anisotropy vector $\Omega_\varepsilon = \Psi_1/\Psi_0$. Such a closure is exact for local (in space and kinetic energy) angular distribution functions either fully isotropic or fully anisotropic, while the parameter μ allows us to relate these limits. Obviously, the first order expansion reduces the information concerning the beam electrons local angular distribution function. However, the maximum angular entropy criterion analysis shows that it allows for a sufficient accuracy for laser-generated fast electron beam transport. Indeed, we showed that collisional effects of laser-generated electron beam transport in solids or dense plasma fully justified such a closure. Besides, comparison of the full kinetic and the M1 approach for the analysis of the collisionless resistive filamentation instability for which there is no reason to maximize the local angular entropy, shows that our model describes the instability growth rate with an error of few 10s of % in the particular case of a monoenergetic electron beam.

This chapter terminates with a discussion of the self-consistent hydrodynamic response of the laser-irradiated target material to the beam propagation as well as the self-generated electromagnetic fields. We consider the time scale greater than the electromagnetic neutralization time of the beam ν_{ei}^{-1} or τ_e/γ_e , presented in **Chapter 2**. Similarly to other hybrid models, our model assumes that the beam is not modified during its electromagnetic neutralization. This is a strong assumption in case of propagation through insulators since the ionization processes occur in this time scale, implying additional energy losses of the electron beam that are omitted here. In our hybrid model, the self-generated magnetic field verifies the diffusion equation (6.24)

$$\frac{1}{c} \frac{\partial \mathbf{B}}{\partial t} + \frac{\partial}{\partial \mathbf{r}} \times \left(\frac{\eta c}{4\pi} \frac{\partial}{\partial \mathbf{r}} \times \mathbf{B} \right) = \eta \frac{\partial}{\partial \mathbf{r}} \times \mathbf{j}_b + \frac{\partial \eta}{\partial \mathbf{r}} \times \mathbf{j}_b - \frac{k_B}{n_e e} \frac{\partial n_e}{\partial \mathbf{r}} \times \frac{\partial T_e}{\partial \mathbf{r}}$$

with the source terms introduced in **Chapter 3** and the self-generated electric field is given by the Ohm's law (6.23)

$$\mathbf{E} = -\eta \mathbf{j}_b + \frac{\eta c}{4\pi} \frac{\partial}{\partial \mathbf{r}} \times \mathbf{B} - \frac{1}{n_e e} \frac{\partial}{\partial \mathbf{r}} (n_e k_B T_e)$$

also discussed with details in **Chapter 3**. Thus, we have neglected the magnetization effects, the background electrons viscosity, the collisional friction of the background electrons due to collisions with beam electrons, the displacement current in the Maxwell-Ampère equation (quasi-static approximation), the background electrons inertia and we have considered the ideal gas expression for the equation of state $P_e = P_e(n_e, T_e)$ of background electrons. These assumptions are justified in the case of laser-generated electron beam transport in dense targets as it was explained in **Chapter 3**.

6.4. CONCLUSION

However, the effect of electron inertia and the quasi-static approximation may be responsible for an additional time-dependent heating of the background electrons, as it was demonstrated recently by [Sherlock et al., 2014], and eventual angular deviations of the fast electrons due to strong local magnetic fields. Nevertheless, the self-generated electromagnetic fields described by Equations (6.23) and (6.24) account for the main processes of laser-generated relativistic electron beam transport in solids or dense plasmas. They depend on the electrical resistivity η of the material and its spatial gradients, which depend on the electron and ion temperatures of the material. Thus, the electron temperature evolution needs to be described self-consistently according to the electron heat equation (6.25)

$$C_{V,e} \frac{\partial T_e}{\partial t} - \frac{\partial}{\partial \mathbf{r}} \cdot \left(\kappa_e \frac{\partial T_e}{\partial \mathbf{r}} \right) = W_e - G (T_e - T_i)$$

where

$$W_e = \int_{\varepsilon_{\min}}^{\infty} v S_{\text{col}} \Psi_0 d\varepsilon + \eta \mathbf{j}_e^2.$$

The background ion heating is described self-consistently according to the heat equation (6.28)

$$C_{V,i} \frac{\partial T_i}{\partial t} = G (T_e - T_i).$$

In our model, we neglect the ion motion and the ion thermal conductivity, considering times scales smaller than 10th of ps. These heat equations are in agreement with the assumptions made with respect to the self-consistent electromagnetic fields (no viscosities, no magnetization effects, no inertiae and no collisional friction by colliding the beam electrons in η) except for the temporal derivatives of the temperatures that have not been neglected here. We also proposed new expressions for the heat capacities $C_{V,e}$ and $C_{V,i}$, the electrical resistivity η , the electron thermal conductivity κ_e and the electron-ion coupling factor G , allowing to describe metals from the solid state at the room temperature ≈ 300 K through the liquid and Warm and Dense Matter (WDM) states to the hot plasma state with temperatures ≈ 10 keV. The collisions of background free electrons with d-band bound electrons are taken into account according to recent studies showing the importance of this relaxation process.

Chapter 7

Numerical Implementation of the Model

"I have tried to read philosophers of all ages and have found many illuminating ideas but no steady progress toward deeper knowledge and understanding. Science, however, gives me the feeling of steady progress: I am convinced that theoretical physics is actual philosophy. It has revolutionized fundamental concepts, e.g., about space and time (relativity), about causality (quantum theory), and about substance and matter (atomistics), and it has taught us new methods of thinking (complementarity) which are applicable far beyond physics."

Max Born

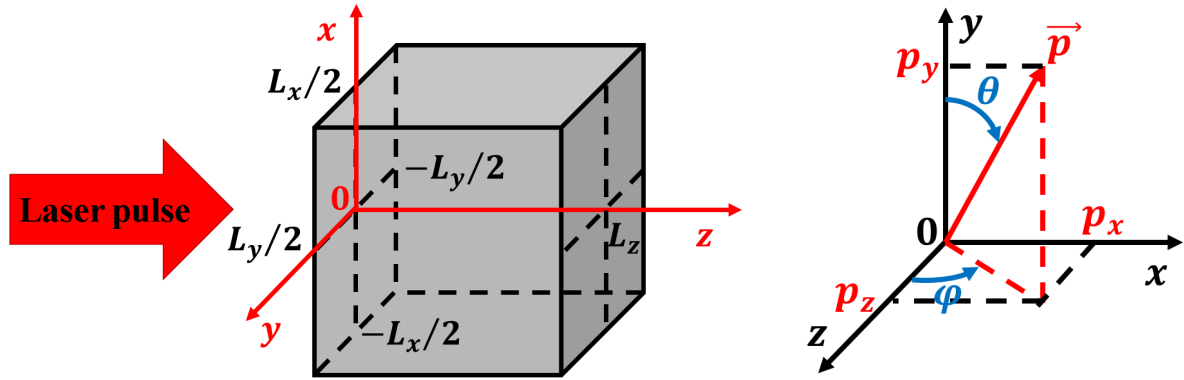


Figure 7.1: Spatial simulation box (Left panel) and Momentum Simulation box (Right panel)

This chapter is dedicated to the numerical implementation with *Fortran F90* of the new reduced model for fast electron transport in solids or dense plasmas presented in **Chapter 6**. The equations that have to be solved are summarized in the conclusion of **Chapter 6**. The code contains four main packages as illustrated in **Figure 7.2**, depending on 16 *Fortran* files ".f90". The file *accuracy.f90* allows to define the accuracy of reals numbers computed with the code. The double-precision floating-point format is used. The physical constants are defined in the file *physical_constants.f90*. The initialization parameters of the simulation, defined in *data.f90*, describe the laser-irradiated target properties. It include also some options concerning the desired numerical methods and the desired diagnostics for the simulation as well as the simulation box sizes (L_x , L_y and L_z) and parameters of the laser-generated fast electron distribution function injected at $z = 0$, as illustrated in the left panel of **Figure 7.1**. Relations between the fast electron kinetic energy, its momentum and its velocity are computed in the file *special_relativity.f90*. The non-relativistic Coulomb logarithms needed for the transport coefficients as well as the logarithmic term of the relativistic Coulomb logarithms and plasma parameters such as the plasma frequency, Fermi temperatures, Debye length, etc... are computed in the file *coulomb_logarithms.f90*. The Fermi integrals F_j and the chemical potential μ , needed for the transport coefficients are computed in the file *Fermi_integrales.f90* according to accurate fits provided by [Aymerich-Humet et al., 1983] and [ANTIA, 1993]. The file *collisional_terms.f90* allows for the computations of the fast electron stopping powers and the fast electron isotropization rates. The file *resistivity.f90* allows for the computations of the transport coefficients.

The first package deals with the computation of the M1 equations. It is based on three *Fortran* files. The file *M1.f90* defines subroutines needed for the numerical scheme. The file *initialization.f90* describes the fast electrons injection at $z = 0$. And the file *boundaries_conditions.f90* defines the boundary conditions. The fast electron beam distribution function at $z = 0$ can be taken from a Particle-In-Cell (PIC) simulation of the laser-target interaction. In this case, the parameters that has been described in **Chapter 1, section 1.4** and depending on this preliminary simulation are computed in the file *initialization.f90*. The angular moments of the initial distribution function are deduced from the PIC simulation according to the geometry presented in the right panel of **Figure**

7.1. The second package concerns the computation of the electromagnetic fields. It is based on two *Fortran* files : the file *MHD.f90* which allows for computing the electromagnetic fields and the file *conjugated_gradients.f90* allows for solving the magnetic field diffusion operator. The third package deals with the computation of the two heat equations. It is based on the *Fortran* file *temperatures.f90*. The last package deals with the diagnostics that have been implemented in the code. It is based on the *Fortran* file *diagnostics.f90*. It allows for storing the numerical simulation results in text files ".dat". Finally, the main *Fortran* file *scheme.f90* provides the coupling between the packages. Parallelization and vectorization of the different loops have been implemented with the *open mp* library and the code is compiled with *ifort* which can be freely obtained at <https://software.intel.com/>. For example, on a *Linux terminal*, the instruction "`ifort -prec-div -prec-sqrt -openmp -openmp-report2 -r8 -o exec acuracy.f90 physical_constants.f90 data.f90 special_relativity.f90 coulomb_logarithms.f90 Fermi_integrales.f90 collisional_terms.f90 resistivity.f90 M1.f90 diagnostics.f90 initialization.f90 conjugated_gradients.f90 MHD.f90 temperatures.f90 boundaries_conditions.f90 scheme.f90`" allows for the compilation of the code and the instruction "`time OMP_NUM_THREADS=8 ./exec`" allows for its execution on 8 CPU. In the code, the space variables are normalized by $L = 1 \mu\text{m}$, the time is normalized by $\tau = 1 \text{ fs}$ and the masses are normalized by $M = \text{keV}/c^2$, except for the distribution function which is normalized by its maximum value. The chosen units correspond to the typical values in laser-generated fast electron transport. For example, the velocity of light is $\approx 0.3 \mu\text{m}/\text{fs}$ and the fast electrons may have energies from a few keV to several MeV. In the following, the variables are discretized as follows.

$$\forall l \in [1, N_\varepsilon], \varepsilon_l[\text{keV}] = \varepsilon_{\min} + \frac{\Delta\varepsilon}{2} + (l-1)\Delta\varepsilon \text{ where } N_\varepsilon = \mathbb{E} \left\{ \frac{L_\varepsilon}{\Delta\varepsilon} \right\} \quad (7.1)$$

where the index l , is used for the kinetic energy variable ε of the fast electrons, ε_{\min} may vary from a few keV to 20 keV and L_ε may vary from a few MeV to 10th of MeV depending on the simulation. Concerning the discretization of space, we use

$$\forall i \in [1, N_x], x_i[\mu\text{m}] = -\frac{L_x}{2} + \frac{\Delta x}{2} + (i-1)\Delta x \text{ where } N_x = \mathbb{E} \left\{ \frac{L_x}{\Delta x} \right\} + 1, \quad (7.2)$$

indexed by i for the position in the x -direction,

$$\forall j \in [1, N_y], x_j[\mu\text{m}] = -\frac{L_y}{2} + \frac{\Delta y}{2} + (j-1)\Delta y \text{ where } N_y = \mathbb{E} \left\{ \frac{L_y}{\Delta y} \right\} + 1, \quad (7.3)$$

indexed by j for the position in the y -direction and

$$\forall k \in [1, N_z], z_k[\mu\text{m}] = \frac{\Delta z}{2} + (k-1)\Delta z \text{ where } N_z = \mathbb{E} \left\{ \frac{L_z}{\Delta z} \right\}, \quad (7.4)$$

indexed by k for the position in the z -direction according to **Figure 7.1**. Finally, we discretize the

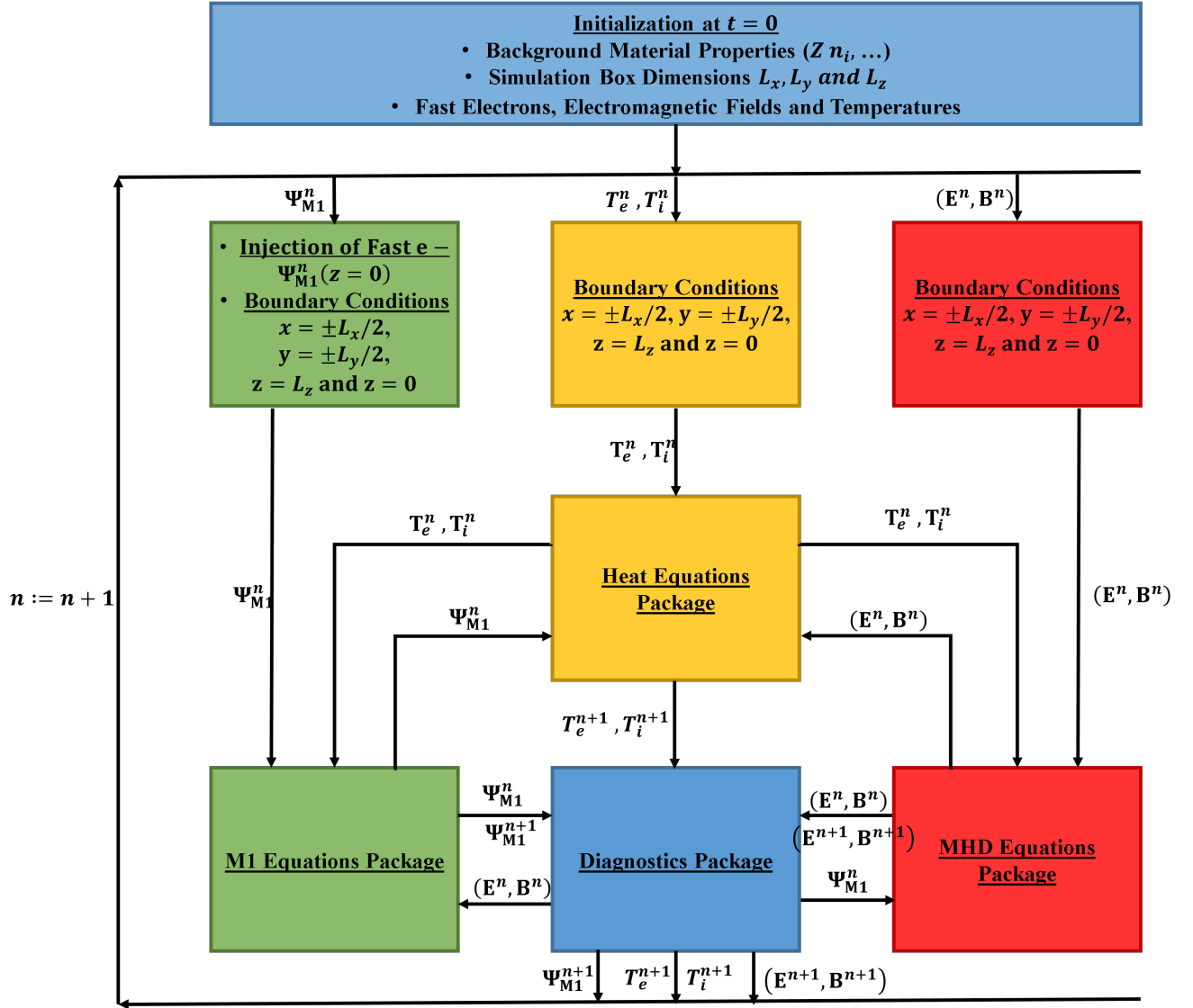


Figure 7.2: Synoptic Diagram describing the code.

time and we index it by n according to

$$\forall n \in \mathbb{N}^*, t_n[\text{fs}] = (n - 1)\Delta t_n \quad (7.5)$$

where the time step Δt_n depends on the Courant–Friedrichs–Lewy (CFL) condition for the resolution of M1 equations.

The first section of this chapter is dedicated to the numerical schemes used for the resolution of the M1 equations. The second section deals with the numerical schemes used to compute self-consistently the electromagnetic fields. The third section is dedicated to the numerical schemes used to solve self-consistently the heat equations.

7.1 M1 equations

According to **Chapter 6, section 6.2.1 and 6.2.2**, the M1 equations that have to solved are

$$\begin{aligned} \frac{\partial \Psi_0}{\partial t} &+ \frac{\partial}{\partial x} [v(\varepsilon)\Psi_{1,x}] + \frac{\partial}{\partial y} [v(\varepsilon)\Psi_{1,y}] + \frac{\partial}{\partial z} [v(\varepsilon)\Psi_{1,z}] \\ &- \frac{\partial}{\partial \varepsilon} \left[S(x, y, z, \varepsilon, t)v(\varepsilon)\Psi_0 \right. \\ &\quad \left. + eE_x(x, y, z, t)v(\varepsilon)\Psi_{1,x} + eE_y(x, y, z, t)v(\varepsilon)\Psi_{1,y} + eE_z(x, y, z, t)v(\varepsilon)\Psi_{1,z} \right], \\ &= 0 \end{aligned} \quad (7.6)$$

$$\begin{aligned} \frac{\partial \Psi_{1,x}}{\partial t} &+ \frac{\partial}{\partial x} [v(\varepsilon)\Psi_{2,xx}] + \frac{\partial}{\partial y} [v(\varepsilon)\Psi_{2,xy}] + \frac{\partial}{\partial z} [v(\varepsilon)\Psi_{2,xz}] \\ &- \frac{\partial}{\partial \varepsilon} \left[S(x, y, z, \varepsilon, t)v(\varepsilon)\Psi_{1,x} \right. \\ &\quad \left. + eE_x(x, y, z, t)v(\varepsilon)\Psi_{2,xx} + eE_y(x, y, z, t)v(\varepsilon)\Psi_{2,xy} + eE_z(x, y, z, t)v(\varepsilon)\Psi_{2,xz} \right] \\ &= -\frac{e}{p(\varepsilon)} \left[(\Psi_0 - \Psi_{2,xx})E_x(x, y, z, t) - \Psi_{2,xy}E_y(x, y, z, t) - \Psi_{2,xz}E_z(x, y, z, t) \right] \\ &- \frac{e}{\gamma(\varepsilon)m_e c} \left[\Psi_{1,y}B_z(x, y, z, t) - \Psi_{1,z}B_y(x, y, z, t) \right] - \nu(x, y, z, \varepsilon, t)\Psi_{1,x} \end{aligned} \quad (7.7)$$

$$\begin{aligned} \frac{\partial \Psi_{1,y}}{\partial t} &+ \frac{\partial}{\partial x} [v(\varepsilon)\Psi_{2,yx}] + \frac{\partial}{\partial y} [v(\varepsilon)\Psi_{2,yy}] + \frac{\partial}{\partial z} [v(\varepsilon)\Psi_{2,yz}] \\ &- \frac{\partial}{\partial \varepsilon} \left[S(x, y, z, \varepsilon, t)v(\varepsilon)\Psi_{1,y} \right. \\ &\quad \left. + eE_x(x, y, z, t)v(\varepsilon)\Psi_{2,yx} + eE_y(x, y, z, t)v(\varepsilon)\Psi_{2,yy} + eE_z(x, y, z, t)v(\varepsilon)\Psi_{2,yz} \right] \\ &= -\frac{e}{p(\varepsilon)} \left[-\Psi_{2,yx}E_x(x, y, z, t) + (\Psi_0 - \Psi_{2,yy})E_y(x, y, z, t) - \Psi_{2,yz}E_z(x, y, z, t) \right] \\ &- \frac{e}{\gamma(\varepsilon)m_e c} \left[\Psi_{1,z}B_x(x, y, z, t) - \Psi_{1,x}B_z(x, y, z, t) \right] - \nu(x, y, z, \varepsilon, t)\Psi_{1,y} \end{aligned} \quad (7.8)$$

and

$$\begin{aligned} \frac{\partial \Psi_{1,z}}{\partial t} &+ \frac{\partial}{\partial x} [v(\varepsilon)\Psi_{2,zx}] + \frac{\partial}{\partial y} [v(\varepsilon)\Psi_{2,zy}] + \frac{\partial}{\partial z} [v(\varepsilon)\Psi_{2,zz}] \\ &- \frac{\partial}{\partial \varepsilon} \left[S(x, y, z, \varepsilon, t)v(\varepsilon)\Psi_{1,z} \right. \\ &\quad \left. + eE_x(x, y, z, t)v(\varepsilon)\Psi_{2,zx} + eE_y(x, y, z, t)v(\varepsilon)\Psi_{2,zy} + eE_z(x, y, z, t)v(\varepsilon)\Psi_{2,zz} \right] \\ &= -\frac{e}{p(\varepsilon)} \left[-\Psi_{2,zx}E_x(x, y, z, t) - \Psi_{2,zy}E_y(x, y, z, t) + (\Psi_0 - \Psi_{2,zz})E_z(x, y, z, t) \right] \\ &- \frac{e}{\gamma(\varepsilon)m_e c} \left[\Psi_{1,x}B_y(x, y, z, t) - \Psi_{1,y}B_x(x, y, z, t) \right] - \nu(x, y, z, \varepsilon, t)\Psi_{1,z} \end{aligned} \quad (7.9)$$

where $\Psi_0 = \Psi_0(x, y, z, \varepsilon, t)$ is the 0th order angular moment and $\Psi_1 = \Psi_1(x, y, z, \varepsilon, t)$ is the 1st order angular moment of the distribution function while $\Psi_2 = \Psi_2(x, y, z, \varepsilon, t)$ is the 2nd order angular moment given by the M1 closure :

$$\forall (i, j) \in \{x, y, z\}^2, \Psi_{2,ij} = \frac{1}{3}\delta_{ij}\Psi_0 + \mu\Psi_0 \left[\frac{\Psi_{1,i}\Psi_{1,j}}{\Psi_{1,x}^2 + \Psi_{1,y}^2 + \Psi_{1,z}^2} - \frac{1}{3}\delta_{ij} \right] \quad (7.10)$$

with

$$\mu(x, y, z, \varepsilon, t) = \frac{1}{2\Psi_0^2} \left(\Psi_{1,x}^2 + \Psi_{1,y}^2 + \Psi_{1,z}^2 \right) \left[1 + \frac{1}{\Psi_0^2} \left(\Psi_{1,x}^2 + \Psi_{1,y}^2 + \Psi_{1,z}^2 \right) \right].$$

7.1.1 Second Order Explicit HLL Scheme for the Fast Electron Advection in Space and Fast Electron Slowing Down due to the Self-Generated Electric field

First order HLL scheme

Let us consider firstly the 1D-3V case, in order to point out the major features of the numerical scheme that is used to solve the fast electrons advection in space and in kinetic energy space (due to their collective energy losses). In this 1D case, the equations that have to be solved are (7.6) and (7.7) with $\Psi_{1,y} = \Psi_{1,z} = 0$. The 3D-3V case will be further generalized in the section. Therefore, we are here interested in the numerical resolution of two 1D coupled equations

$$\begin{aligned} \frac{\partial \Psi_0}{\partial t} + \frac{\partial}{\partial \xi} (u_\xi \Psi_{1,x}) &= 0 \\ \frac{\partial \Psi_{1,x}}{\partial t} + \frac{\partial}{\partial \xi} (u_\xi \Psi_{2,xx}) &= 0 \end{aligned} \quad (7.11)$$

with

$$\Psi_{2,xx} = \frac{1 + 2\mu}{3} \Psi_0 \text{ and } \mu = \frac{1}{2} \left(\frac{\Psi_{1,x}}{\Psi_0} \right)^2 \left[1 + \left(\frac{\Psi_{1,x}}{\Psi_0} \right)^2 \right]$$

describing the fast electrons advection in the x -direction in space ($\xi = x$ and $u_x = v(\varepsilon)$) or the fast electrons advection in the ε -direction in the kinetic energy space due to their collective energy losses ($\xi = \varepsilon$ and $u_\varepsilon = -eE_x(x, t)v(\varepsilon)$), appearing in (7.6) and (7.7).

This hyperbolic system (7.11) can be solved numerically with respect to the realizability domain

$$\mathcal{A} = \{ (\Psi_0, \Psi_{1,x}) / \Psi_0 \geq 0 \text{ and } |\Psi_{1,x}| \leq \Psi_0 \} \quad (7.12)$$

by using the HLL scheme (from the name of its founders A. Harten, P. Lax and B. Van Leer) developed for the radiative transfer equations [Harten et al., 1983] [Dubroca and Feugeas, 1999] [Berthon et al., 2010]. According to the finite volume method, we define the mean values in each cell :

$$\Psi_0^{n,i,l} = \frac{1}{\Delta x \Delta \varepsilon} \int_{x_i - \Delta x/2}^{x_i + \Delta x/2} \int_{\varepsilon_l - \Delta \varepsilon/2}^{\varepsilon_l + \Delta \varepsilon/2} \Psi_0(x, \varepsilon, t_n) dx d\varepsilon, \quad (7.13)$$

$$\Psi_{1,x}^{n,i,l} = \frac{1}{\Delta x \Delta \varepsilon} \int_{x_i - \Delta x/2}^{x_i + \Delta x/2} \int_{\varepsilon_l - \Delta \varepsilon/2}^{\varepsilon_l + \Delta \varepsilon/2} \Psi_{1,x}(x, \varepsilon, t_n) dx d\varepsilon \quad (7.14)$$

and

$$\Psi_{2,xx}^{n,i,l} = \frac{1}{\Delta x \Delta \varepsilon} \int_{x_i - \Delta x/2}^{x_i + \Delta x/2} \int_{\varepsilon_l - \Delta \varepsilon/2}^{\varepsilon_l + \Delta \varepsilon/2} \Psi_{2,xx}(x, \varepsilon, t_n) dx d\varepsilon. \quad (7.15)$$

Let us note Φ the vector $\Phi = (\Psi_0, \Psi_{1,x})^T$, i_ξ the index i (if $\xi = x$) or l (if $\xi = \varepsilon$) depending on ξ and $F = F(\Phi)$ the vector $F = (\Psi_{1,x}, \Psi_{2,xx})^T$ depending on Φ . According to the HLL scheme, one can update at each time step the new value Φ^{n+1,i_ξ} at time t_{n+1} in the cell i_ξ , knowing the previous values Φ^{n,i_ξ} at time t_n according to

$$\Phi^{n+1,i_\xi} = \Phi^{n,i_\xi} - \frac{\Delta t_n}{\Delta \xi} \left[F_{\text{HLL}}^{n,i_\xi+1/2} - F_{\text{HLL}}^{n,i_\xi-1/2} \right] \quad (7.16)$$

where the HLL fluxes are given by

$$F_{\text{HLL}}^{n,i_\xi+1/2} = u_\xi^{n,i_\xi} \frac{(u_\xi^{n,i_\xi+1}/u_\xi^{n,i_\xi})F^{n,i_\xi+1} + F^{n,i_\xi}}{2} - \left| u_\xi^{n,i_\xi} \right| \frac{(u_\xi^{n,i_\xi+1}/u_\xi^{n,i_\xi})\Phi^{n,i_\xi+1} - \Phi^{n,i_\xi}}{2} \quad (7.17)$$

and

$$F_{\text{HLL}}^{n,i_\xi-1/2} = u_\xi^{n,i_\xi} \frac{F^{n,i_\xi} + (u_\xi^{n,i_\xi-1}/u_\xi^{n,i_\xi})F^{n,i_\xi-1}}{2} - \left| u_\xi^{n,i_\xi} \right| \frac{\Phi^{n,i_\xi} - (u_\xi^{n,i_\xi-1}/u_\xi^{n,i_\xi})\Phi^{n,i_\xi-1}}{2}. \quad (7.18)$$

In the case where $\xi = x$ for which $u_\xi = v(\varepsilon)$ does not depend on ξ , the ratios $(u_\xi^{n,i_\xi \pm 1}/u_\xi^{n,i_\xi})$ appearing in the the HLL fluxes (7.17) and (7.18) are equal to 1. In the case where $\xi = \varepsilon$ for which $u_\xi = -eE_x(x, t)v(\varepsilon)$ depends on ξ , the ratios reduce to v_{l+1}/v_l and v_{l-1}/v_l where $\forall l \in [1, N_\varepsilon]$, $v_l = v(\varepsilon_l)$. This has been deduced from the case where u_ξ does not depend on ξ . Indeed, let us define $\widehat{\Phi} = v\Phi$ and $\widehat{F} = vF$. In this case, the realizability domain is still the same :

$$\widehat{\mathcal{A}} = \left\{ \left(\widehat{\Psi}_0, \widehat{\Psi}_{1,x} \right) / \widehat{\Psi}_0 \geq 0 \text{ and } \left| \widehat{\Psi}_{1,x} \right| \leq \widehat{\Psi}_0 \right\} \quad (7.19)$$

while the equation (7.11) for $\xi = \varepsilon$ can be written

$$\frac{\partial \widehat{\Phi}}{\partial t} - \frac{\partial}{\partial p} \left(eE_x(x, t)\widehat{F} \right) = 0 \quad (7.20)$$

as $(d\varepsilon/dp) = v$. Therefore, the velocity u_ε depending on ε in (7.11) has disappeared and, since $u_p = -eE_x$ does not depend on p , we can compute this equation with the same way as (7.11) for which u_ξ does not depend on ξ . We obtain consequently (7.16) with the ratios $(u_\xi^{n,i_\xi \pm 1}/u_\xi^{n,i_\xi})$ which are equal to 1. By coming back to Φ and F instead of $\widehat{\Phi}$ and \widehat{F} , we finally obtain (7.11) with the ratios $(u_\xi^{n,i_\xi \pm 1}/u_\xi^{n,i_\xi})$.

The 1st order HLL scheme is stable and the numerical solutions are in the realizability domain

7.1. M1 EQUATIONS

(7.12) if the Courant-Friedrich-Lewy (CFL) condition

$$\Delta t_n < \frac{\Delta \xi}{\max_{i_\xi \in [1, N_\xi]} \{u_\xi^{n, i_\xi}\}} \quad (7.21)$$

is verified. However, according to numerical experiments that I have performed during this thesis, the consistency error of this 1st order explicit HLL scheme

$$\begin{aligned} \epsilon_{\text{HLL}, 1\text{D}}^{n, i_\xi} &= \frac{\Phi^{n+1, i_\xi} - \Phi^{n, i_\xi}}{\Delta t_n} + \frac{F_{\text{HLL}}^{n, i_\xi+1/2} - F_{\text{HLL}}^{n, i_\xi-1/2}}{\Delta \xi} - \left[\frac{\partial \Phi}{\partial t} \Big|^{n, i_\xi} + \frac{\partial}{\partial \xi} (u_\xi F) \Big|^{n, i_\xi} \right] \\ &= \frac{\Delta t_n}{2} \frac{\partial^2 \Phi}{\partial t^2} \Big|^{n, i_\xi} - \frac{\Delta \xi}{2} \frac{\partial^2}{\partial \xi^2} (|u_\xi| \Phi) \Big|^{n, i_\xi} + O(\Delta t^2 + \Delta \xi^2) \end{aligned} \quad (7.22)$$

is not sufficiently small for values $\Delta \xi$ about a fraction of microns (if $\xi = x$) or about a keV (if $\xi = \varepsilon$) typical of laser-generated fast electron transport studies. We used therefore the 2nd order explicit HLL scheme.

2nd order HLL scheme

The second order explicit HLL scheme can be obtained by replacing the HLL fluxes (7.17) and (7.18) by

$$F_{\text{HLL}}^{n, i_\xi+1/2} = u_\xi^{n, i_\xi} \frac{(u_\xi^{n, i_\xi+1}/u_\xi^{n, i_\xi})F^{n, i_\xi+1, -} + F^{n, i_\xi, +}}{2} - |u_\xi^{n, i_\xi}| \frac{(u_\xi^{n, i_\xi+1}/u_\xi^{n, i_\xi})\Phi^{n, i_\xi+1, -} - \Phi^{n, i_\xi, +}}{2} \quad (7.23)$$

and

$$F_{\text{HLL}}^{n, i_\xi-1/2} = u_\xi^{n, i_\xi} \frac{F^{n, i_\xi, -} + (u_\xi^{n, i_\xi-1}/u_\xi^{n, i_\xi})F^{n, i_\xi-1, +}}{2} - |u_\xi^{n, i_\xi}| \frac{\Phi^{n, i_\xi, -} - (u_\xi^{n, i_\xi-1}/u_\xi^{n, i_\xi})\Phi^{n, i_\xi-1, +}}{2}, \quad (7.24)$$

respectively [Dubroca, 2012]. Here, the sign + indicates

$$\forall i_\xi \in [1, N_\xi], \Phi^{n, i_\xi, +} = \Phi^{n, i_\xi} + P^{n, i_\xi} \frac{\Delta \xi}{2} \text{ and } F^{n, i_\xi, +} = F(\Phi^{n, i_\xi, +}) \quad (7.25)$$

while the sign - indicates

$$\forall i_\xi \in [1, N_\xi], \Phi^{n, i_\xi, -} = \Phi^{n, i_\xi} - P^{n, i_\xi} \frac{\Delta \xi}{2} \text{ and } F^{n, i_\xi, -} = F(\Phi^{n, i_\xi, -}). \quad (7.26)$$

P^{n, i_ξ} is the vector defined by

$$\begin{aligned} P^{n, i_\xi} &= \min \left(0, \max \left(\frac{\Phi^{n, i_\xi+1} - \Phi^{n, i_\xi}}{\Delta \xi}, \frac{\Phi^{n, i_\xi} - \Phi^{n, i_\xi-1}}{\Delta \xi} \right) \right) \\ &\quad + \max \left(0, \min \left(\frac{\Phi^{n, i_\xi+1} - \Phi^{n, i_\xi}}{\Delta \xi}, \frac{\Phi^{n, i_\xi} - \Phi^{n, i_\xi-1}}{\Delta \xi} \right) \right). \end{aligned} \quad (7.27)$$

However, these 2nd order HLL fluxes (7.23) and (7.24) may lead to numerical solutions outside the realizability domain (7.12); while $\Psi_0 \geq 0$ is respected, it is not necessarily the case for the condition $|\Psi_{1,x}| \leq \Psi_0$. Consequently, we introduce a value Θ at each time step and in each cell i_ξ defined by

$$\Phi^{n,i_\xi,+} = \Phi^{n,i_\xi} + P^{n,\xi} \Theta \frac{\Delta\xi}{2} \text{ and } \Phi^{n,i_\xi,-} = \Phi^{n,i_\xi} - P^{n,\xi} \Theta \frac{\Delta\xi}{2} \quad (7.28)$$

such that $|\Psi_{1,x}| \leq \Psi_0$ [Dubroca, 2012]. Thus, by injecting (7.28) in the conditions $(\Psi_{1,x}^{n,i_\xi,+})^2 \leq (\Psi_0^{n,i_\xi,+})^2$ or $(\Psi_{1,x}^{n,i_\xi,-})^2 \leq (\Psi_0^{n,i_\xi,-})^2$, we obtain the following condition

$$(\Psi_0^{n,i_\xi})^2 - (\Psi_{1,x}^{n,i_\xi})^2 \pm 2\Theta' \left(P_0^{n,i_\xi} \Psi_0^{n,i_\xi} - P_{1,x}^{n,i_\xi} \Psi_{1,x}^{n,i_\xi} \right) \frac{\Delta\xi}{2} + \Theta'^2 \left((P_0^{n,i_\xi})^2 - (P_{1,x}^{n,i_\xi})^2 \right) \frac{\Delta\xi^2}{4} \geq 0. \quad (7.29)$$

Consequently, if $\Psi_0^{n,i_\xi} = \Psi_{1,x}^{n,i_\xi}$ or if the discriminant of the trinomial left hand side is negative, we can impose $\Theta = 1$ without problems. But, if we find solution $\Theta' \in [0, 1]$ cancelling the trinomial left hand side, allowing to obtain $(\Psi_0^{n,i_\xi,\pm})^2 \geq (\Psi_{1,x}^{n,i_\xi,\pm})^2$, we impose $\Theta = \min \Theta'$. In other exotic cases, we come back to the 1st order HLL scheme by imposing $\Theta = 0$. The 2nd order HLL scheme allows for a much smaller consistency error $O(\Delta t + \Delta\xi^2)$ compared to the 1st order consistency error (7.22) $O(\Delta t + \Delta\xi)$ while the CFL condition (7.21) remains the same.

Generalization to the 3D-3V case

We note $\forall \zeta \in \{x, y, z\}$, $E_\zeta(x_i, y_j, z_k, t_n) = E_\zeta^{n,i,j,k}$

$$\Psi_0^{n,i,j,k,l} = \frac{1}{\Delta x \Delta y \Delta z \Delta \varepsilon} \int_{x_i - \Delta x/2}^{x_i + \Delta x/2} \int_{y_j - \Delta y/2}^{y_j + \Delta y/2} \int_{z_k - \Delta z/2}^{z_k + \Delta z/2} \int_{\varepsilon_l - \Delta \varepsilon/2}^{\varepsilon_l + \Delta \varepsilon/2} \Psi_0(x, y, z, \varepsilon, t_n) dx dy dz d\varepsilon \quad (7.30)$$

and

$$\Psi_{1,\zeta}^{n,i,j,k,l} = \frac{1}{\Delta x \Delta y \Delta z \Delta \varepsilon} \int_{x_i - \Delta x/2}^{x_i + \Delta x/2} \int_{y_j - \Delta y/2}^{y_j + \Delta y/2} \int_{z_k - \Delta z/2}^{z_k + \Delta z/2} \int_{\varepsilon_l - \Delta \varepsilon/2}^{\varepsilon_l + \Delta \varepsilon/2} \Psi_{1,\zeta}(x, y, z, \varepsilon, t_n) dx dy dz d\varepsilon. \quad (7.31)$$

Also, we define the vector $\Phi = (\Psi_0, \Psi_{1,x}, \Psi_{1,y}, \Psi_{1,z})^T$ and $\forall \zeta \in \{x, y, z\}$ and the vectors $F_\zeta = F_\zeta(\Phi) = (\Psi_{1,\zeta}, \Psi_{2,\zeta x}, \Psi_{2,\zeta y}, \Psi_{2,\zeta z})^T$ depending on Φ . This subsection is dedicated to the generalization of the numerical resolution of the two 1D coupled equations (7.11) to the numerical resolution of the four "4D" (3D-1 ε) coupled equations

$$\frac{\partial \Phi}{\partial t} + \sum_{\xi=x,y,z,\varepsilon} \left[\sum_{\zeta=x,y,z} \frac{\partial}{\partial \xi} (u_{\xi\zeta} F_\zeta) \right] = 0 \quad (7.32)$$

where the $u_{\xi\zeta}$ are recapitulated in **Figure 7.3**. The 2nd order explicit HLL scheme applied to these

7.1. M1 EQUATIONS

$\xi \setminus \zeta$	x	y	z
x	$v(\varepsilon)$	0	0
y	0	$v(\varepsilon)$	0
z	0	0	$v(\varepsilon)$
ε	$-eE_x(x, y, z, t)$	$-eE_y(x, y, z, t)$	$-eE_z(x, y, z, t)$

Figure 7.3: Expression of $u_{\xi, \zeta}$ in (7.32) depending on ξ and ζ .

four "4D" coupled equations reads

$$\begin{aligned}
 \Phi^{n+1, i, j, k, l} = \Phi^{n, i, j, k, l} & - (\Delta t_n / \Delta x) \left[F_{x, \text{HLL}}^{n, i+1/2, j, k, l} - F_{x, \text{HLL}}^{n, i-1/2, j, k, l} \right] \\
 & - (\Delta t_n / \Delta y) \left[F_{y, \text{HLL}}^{n, i, j+1/2, k, l} - F_{y, \text{HLL}}^{n, i, j-1/2, k, l} \right] \\
 & - (\Delta t_n / \Delta z) \left[F_{z, \text{HLL}}^{n, i, j, k+1/2, l} - F_{z, \text{HLL}}^{n, i, j, k-1/2, l} \right] \\
 & - (\Delta t_n / \Delta \varepsilon) \left[F_{\varepsilon, \text{HLL}}^{n, i, j, k, l+1/2} - F_{\varepsilon, \text{HLL}}^{n, i, j, k, l-1/2} \right]
 \end{aligned} \tag{7.33}$$

where the HLL fluxes are given by

$$\begin{aligned}
 F_{x, \text{HLL}}^{n, i+1/2, j, k, l} &= v_l \left[\frac{F_x^{i+1, -} + F_x^{i, +}}{2} \right]^{n, j, k, l} - |v_l| \left[\frac{\Phi^{i+1, -} - \Phi^{i, +}}{2} \right]^{n, j, k, l}, \\
 F_{x, \text{HLL}}^{n, i-1/2, j, k, l} &= v_l \left[\frac{F_x^{i, -} + F_x^{i-1, +}}{2} \right]^{n, j, k, l} - |v_l| \left[\frac{\Phi^{i, -} - \Phi^{i-1, +}}{2} \right]^{n, j, k, l}, \\
 F_{y, \text{HLL}}^{n, i, j+1/2, k, l} &= v_l \left[\frac{F_y^{j+1, -} + F_y^{j, +}}{2} \right]^{n, i, k, l} - |v_l| \left[\frac{\Phi^{j+1, -} - \Phi^{j, +}}{2} \right]^{n, i, k, l}, \\
 F_{y, \text{HLL}}^{n, i, j-1/2, k, l} &= v_l \left[\frac{F_y^{j, -} + F_y^{j-1, +}}{2} \right]^{n, i, k, l} - |v_l| \left[\frac{\Phi^{j, -} - \Phi^{j-1, +}}{2} \right]^{n, i, k, l}, \\
 F_{z, \text{HLL}}^{n, i, j, k+1/2, l} &= v_l \left[\frac{F_z^{k+1, -} + F_z^{k, +}}{2} \right]^{n, i, j, l} - |v_l| \left[\frac{\Phi^{k+1, -} - \Phi^{k, +}}{2} \right]^{n, i, j, l}, \\
 F_{z, \text{HLL}}^{n, i, j, k-1/2, l} &= v_l \left[\frac{F_z^{k, -} + F_z^{k-1, +}}{2} \right]^{n, i, j, l} - |v_l| \left[\frac{\Phi^{k, -} - \Phi^{k-1, +}}{2} \right]^{n, i, j, l}, \\
 F_{\varepsilon, \text{HLL}}^{n, i, j, k, l+1/2} &= -eE_x^{n, i, j, k} v_l \left[\frac{(v_{l+1}/v_l) F_x^{l+1, -} + F_x^{l, +}}{2} \right]^{n, i, j, k} - |eE_x^{n, i, j, k} v_l| \left[\frac{(v_{l+1}/v_l) \Phi^{l+1, -} - \Phi^{l, +}}{2} \right]^{n, i, j, k} \\
 &+ -eE_y^{n, i, j, k} v_l \left[\frac{(v_{l+1}/v_l) F_y^{l+1, -} + F_y^{l, +}}{2} \right]^{n, i, j, k} - |eE_y^{n, i, j, k} v_l| \left[\frac{(v_{l+1}/v_l) \Phi^{l+1, -} - \Phi^{l, +}}{2} \right]^{n, i, j, k} \\
 &+ -eE_z^{n, i, j, k} v_l \left[\frac{(v_{l+1}/v_l) F_z^{l+1, -} + F_z^{l, +}}{2} \right]^{n, i, j, k} - |eE_z^{n, i, j, k} v_l| \left[\frac{(v_{l+1}/v_l) \Phi^{l+1, -} - \Phi^{l, +}}{2} \right]^{n, i, j, k}
 \end{aligned}$$

and

$$\begin{aligned}
 F_{\varepsilon, \text{HLL}}^{n,i,j,k,l-1/2} &= -eE_x^{n,i,j,k} v_l \left[\frac{F_x^{l,-} + (v_{l-1}/v_l)F_x^{l-1,+}}{2} \right]^{n,i,j,k} - |eE_x^{n,i,j,k} v_l| \left[\frac{\Phi^{l,-} - (v_{l-1}/v_l)\Phi^{l-1,+}}{2} \right]^{n,i,j,k} \\
 &+ -eE_y^{n,i,j,k} v_l \left[\frac{F_y^{l,-} + (v_{l-1}/v_l)F_y^{l-1,+}}{2} \right]^{n,i,j,k} - |eE_y^{n,i,j,k} v_l| \left[\frac{\Phi^{l,-} - (v_{l-1}/v_l)\Phi^{l-1,+}}{2} \right]^{n,i,j,k} \\
 &+ -eE_z^{n,i,j,k} v_l \left[\frac{F_z^{l,-} + (v_{l-1}/v_l)F_z^{l-1,+}}{2} \right]^{n,i,j,k} - |eE_z^{n,i,j,k} v_l| \left[\frac{\Phi^{l,-} - (v_{l-1}/v_l)\Phi^{l-1,+}}{2} \right]^{n,i,j,k}.
 \end{aligned}$$

Here, for all indexes $i_\xi \in \{i, j, k, l\}$ corresponding respectively to the random variable $\xi \in \{x, y, z, \varepsilon\}$,

$$\Phi^{n,i_\xi,+} = \Phi^{n,i_\xi} + \Theta P^{n,i_\xi} \frac{\Delta\xi}{2} \quad \text{and} \quad \Phi^{n,i_\xi,-} = \Phi^{n,i_\xi} - \Theta P^{n,i_\xi} \frac{\Delta\xi}{2} \quad (7.34)$$

where

$$\begin{aligned}
 P^{n,i_\xi} &= \min \left(0, \max \left(\frac{\Phi^{n,i_\xi+1} - \Phi^{n,i_\xi}}{\Delta\xi}, \frac{\Phi^{n,i_\xi} - \Phi^{n,i_\xi-1}}{\Delta\xi} \right) \right) \\
 &+ \max \left(0, \min \left(\frac{\Phi^{n,i_\xi+1} - \Phi^{n,i_\xi}}{\Delta\xi}, \frac{\Phi^{n,i_\xi} - \Phi^{n,i_\xi-1}}{\Delta\xi} \right) \right)
 \end{aligned}$$

and

$$\begin{aligned}
 \text{if} \quad \exists \Theta' \in [0, 1] / & \quad (\Psi_0^{n,i_\xi})^2 - (\Psi_{1,x}^{n,i_\xi})^2 - (\Psi_{1,y}^{n,i_\xi})^2 - (\Psi_{1,z}^{n,i_\xi})^2 \\
 & \pm 2\Theta' \left(P_0^{n,i_\xi} \Psi_0^{n,i_\xi} - P_{1,x}^{n,i_\xi} \Psi_{1,x}^{n,i_\xi} - P_{1,y}^{n,i_\xi} \Psi_{1,y}^{n,i_\xi} - P_{1,z}^{n,i_\xi} \Psi_{1,z}^{n,i_\xi} \right) \frac{\Delta\xi}{2} \\
 & + \Theta'^2 \left((P_0^{n,i_\xi})^2 - (P_{1,x}^{n,i_\xi})^2 - (P_{1,y}^{n,i_\xi})^2 - (P_{1,z}^{n,i_\xi})^2 \right) \frac{\Delta\xi^2}{4} = 0
 \end{aligned}$$

then $\Theta = \min \Theta'$

else $\Theta = 1$.

This "4D" explicit 2nd order HLL scheme is stable and the numerical solutions are in the realizability domain

$$\mathcal{A} = \{(\Psi_0, \Psi_1) / \Psi_0 \geq 0 \text{ and } |\Psi_1| \leq \Psi_0\} \quad (7.35)$$

if the CFL condition

$$\Delta t_n < \frac{1}{v_{\max} \left(\frac{1}{\Delta x} + \frac{1}{\Delta y} + \frac{1}{\Delta z} \right) + \frac{ev_{\max}}{\Delta\varepsilon} \sqrt{(E_{x,\max}^n)^2 + (E_{y,\max}^n)^2 + (E_{z,\max}^n)^2}}. \quad (7.36)$$

7.1. M1 EQUATIONS

is verified. Also, we can estimate the consistency error in the worst case (i.e. in the 1st order case) :

$$\begin{aligned}
\epsilon_{\text{HLL}}^{n,i,j,k,l} &= \frac{\Delta t_n}{2} \frac{\partial^2 \Phi}{\partial t^2} \Big|^{n,i,j,k,l} - \frac{\Delta \varepsilon}{2} \left[\left(|eE_x^{n,i,k,k}| + |eE_y^{n,i,k,k}| + |eE_z^{n,i,k,k}| \right) \frac{\partial^2}{\partial \varepsilon^2} (v\Phi) \Big|^{n,i,k,k,l} \right] \\
&- \frac{\Delta x}{2} \frac{\partial^2}{\partial x^2} (v\Phi) \Big|^{n,i,k,k,l} - \frac{\Delta y}{2} \frac{\partial^2}{\partial y^2} (v\Phi) \Big|^{n,i,k,k,l} - \frac{\Delta z}{2} \frac{\partial^2}{\partial z^2} (v\Phi) \Big|^{n,i,k,k,l} \\
&+ O\left(\Delta t^2 + \Delta x^2 + \Delta y^2 + \Delta z^2 + \Delta \varepsilon^2\right)
\end{aligned} \tag{7.37}$$

7.1.2 Downwind Explicit Scheme for the Fast Electron Collisional Slowing Down

Concerning the slowing down due to collisional effects, we have to solve the equation

$$\frac{\partial \Phi}{\partial t} - \frac{\partial}{\partial \varepsilon} \left[S(x, y, z, \varepsilon, t) v(\varepsilon) \Phi \right] = 0. \tag{7.38}$$

Since the total stopping power S is always positive, we can use the simple downwind scheme

$$\Phi^{n+1,i,j,k,l} = \Phi^{n,i,j,k,l} + \frac{\Delta t_n}{\Delta \varepsilon} \left[S^{n,i,j,k,l+1} v_{l+1} \Phi^{n,i,j,k,l+1} - S^{n,i,j,k,l} v_l \Phi^{n,i,j,k,l} \right] \tag{7.39}$$

where it has been noted $S^{n,i,j,k,l} = S(x_i, y_j, z_k, \varepsilon_l, t_n)$ the opposite of the total discretized stopping power of the fast electrons. This 1st order downwind scheme is stable if the CFL condition

$$\Delta t_n < \frac{\Delta \varepsilon}{2 S_{\max} v_{\max}} \tag{7.40}$$

is verified and the consistency error is

$$\epsilon_{\text{S}}^{n,i,j,k,l} = \frac{\Delta t_n}{2} \frac{\partial^2 \Phi}{\partial t^2} \Big|^{n,i,j,k,l} - \frac{\Delta \varepsilon}{2} \frac{\partial^2}{\partial \varepsilon^2} (Sv\Phi) \Big|^{n,i,j,k,l} + O\left(\Delta t^2 + \Delta \varepsilon^2\right). \tag{7.41}$$

7.1.3 Explicit Scheme for the Fast Electron Angular Deviations

The fast electron angular deviations are due to the self-generated electric and magnetic fields and the angular scattering. Let us note $\gamma_l = \gamma(\varepsilon_l)$ the discretized Lorentz factor, $p_l = p(\varepsilon_l)$ the discretized momenta and $\forall \zeta \in \{x, y, z\}$, $B_\zeta(x_i, y_j, z_k, t_n) = B_\zeta^{n,i,j,k}$ the components of the self-generated magnetic field. This subsection is dedicated to the numerical resolution of the equation

$$\frac{\partial \Phi}{\partial t} = \Gamma_E + \Gamma_B + \Gamma_\nu. \tag{7.42}$$

where

$$\Gamma_E^{n,i,j,k,l} = -\frac{e}{pl} \begin{pmatrix} 0 \\ \left(\Psi_0^{n,i,j,k,l} - \Psi_{2,xx}^{n,i,j,k,l} \right) E_x^{n,i,j,k} - \Psi_{2,xy}^{n,i,j,k,l} E_y^{n,i,j,k} - \Psi_{2,xz}^{n,i,j,k,l} E_z^{n,i,j,k} \\ - \Psi_{2,yx}^{n,i,j,k,l} E_x^{n,i,j,k} + \left(\Psi_0^{n,i,j,k,l} - \Psi_{2,yy}^{n,i,j,k,l} \right) E_y^{n,i,j,k} - \Psi_{2,yz}^{n,i,j,k,l} E_z^{n,i,j,k} \\ - \Psi_{2,zx}^{n,i,j,k,l} E_x^{n,i,j,k} - \Psi_{2,zy}^{n,i,j,k,l} E_y^{n,i,j,k} - \left(\Psi_0^{n,i,j,k,l} - \Psi_{2,zz}^{n,i,j,k,l} \right) E_z^{n,i,j,k} \end{pmatrix} \quad (7.43)$$

is the angular deviation term due to the self-generated electric field,

$$\Gamma_B^{n,i,j,k,l} = -\frac{e}{\gamma m_e c} \begin{pmatrix} 0 \\ \Psi_{1,y}^{n,i,j,k,l} B_z^{n,i,j,k} - \Psi_{1,z}^{n,i,j,k,l} B_y^{n,i,j,k} \\ \Psi_{1,z}^{n,i,j,k,l} B_x^{n,i,j,k} - \Psi_{1,x}^{n,i,j,k,l} B_z^{n,i,j,k} \\ \Psi_{1,x}^{n,i,j,k,l} B_y^{n,i,j,k} - \Psi_{1,y}^{n,i,j,k,l} B_x^{n,i,j,k} \end{pmatrix} \quad (7.44)$$

is the angular deviation term due to the self-generated magnetic field and

$$\Gamma_\nu^{n,i,j,k,l} = -\nu_{n,i,j,k,l} \begin{pmatrix} 0 \\ \Psi_{1,x}^{n,i,j,k,l} \\ \Psi_{1,y}^{n,i,j,k,l} \\ \Psi_{1,z}^{n,i,j,k,l} \end{pmatrix} \quad (7.45)$$

is the angular deviation term due to the fast electron collisional angular scattering. We use the explicit numerical scheme

$$\Phi^{n+1,i,j,k,l} = \Phi^{n,i,j,k,l} + \Delta t_n \left(\Gamma_E^{n,i,j,k,l} + \Gamma_B^{n,i,j,k,l} + \Gamma_\nu^{n,i,j,k,l} \right). \quad (7.46)$$

It is stable if the approximated CFL condition

$$\Delta t_n < \frac{1}{\omega_{c,\max} + \nu_{\max} + \frac{e}{p_{\min}} \sqrt{(E_{x,\max}^n)^2 + (E_{y,\max}^n)^2 + (E_{z,\max}^n)^2}} \quad (7.47)$$

is verified where $\omega_{c,\max} = e\sqrt{(B_{x,\max}^n)^2 + (B_{y,\max}^n)^2 + (B_{z,\max}^n)^2}/m_e c$ is the most restrictive fast electron cyclotron frequency and ν_{\max} is the most restrictive fast electron isotropization rate ν . The consistency error of this scheme is directly given by

$$\epsilon_A^{n,i,j,k,l} = \frac{\Delta t_n}{2} \frac{\partial^2 \Phi}{\partial t^2} \Big|^{n,i,j,k,l} + O(\Delta t^2). \quad (7.48)$$

7.1.4 Summary of the Full Explicit Scheme

As a conclusion, we use the numerical scheme

$$\begin{aligned}
\Phi^{n+1,i,j,k,l} = \Phi^{n,i,j,k,l} & - (\Delta t_n / \Delta x) \left[F_{x,\text{HLL}}^{n,i+1/2,j,k,l} - F_{x,\text{HLL}}^{n,i-1/2,j,k,l} \right] \\
& - (\Delta t_n / \Delta y) \left[F_{y,\text{HLL}}^{n,i+1/2,j,k,l} - F_{y,\text{HLL}}^{n,i-1/2,j,k,l} \right] \\
& - (\Delta t_n / \Delta z) \left[F_{z,\text{HLL}}^{n,i,j,k+1/2,l} - F_{z,\text{HLL}}^{n,i,j,k-1/2,l} \right] \\
& - (\Delta t_n / \Delta \varepsilon) \left[(-S^{n,i,j,k,l+1})v_{l+1}\Phi^{n,i,j,k,l+1} - (-S^{n,i,j,k,l})v_l\Phi^{n,i,j,k,l} \right] \\
& - (\Delta t_n / \Delta \varepsilon) \left[F_{\varepsilon,\text{HLL}}^{n,i,j,k,l+1/2} - F_{\varepsilon,\text{HLL}}^{n,i,j,k,l-1/2} \right] \\
& + \Delta t_n \left(\Gamma_E^{n,i,j,k,l} + \Gamma_B^{n,i,j,k,l} + \Gamma_\nu^{n,i,j,k,l} \right).
\end{aligned} \tag{7.49}$$

It is stable with the respect of the approximate CFL condition

$$\begin{aligned}
\frac{1}{\Delta t_n} & > v_{\max} \left(\frac{1}{\Delta x} + \frac{1}{\Delta y} + \frac{1}{\Delta z} \right) + \frac{2S_{\max}^n v_{\max}}{\Delta \varepsilon} + \frac{e v_{\max} \sqrt{E_{x,\max}^n{}^2 + E_{y,\max}^n{}^2 + E_{z,\max}^n{}^2}}{\Delta \varepsilon} \\
& + v_{\max}^n + \omega_{c,\max}^n + \frac{e \sqrt{E_{x,\max}^n{}^2 + E_{y,\max}^n{}^2 + E_{z,\max}^n{}^2}}{p_{\min}}.
\end{aligned} \tag{7.50}$$

In practice, the CFL condition is mainly constrained by the resolution of the spatial derivatives and leads to time step Δt_n of a fraction of fs. The resolution of the kinetic energy derivative due to collective energy losses constrains the CFL condition only near the peak of the laser pulse which corresponds to the peak of the self-generated electric field. The consistency error can be estimated by

$$\begin{aligned}
\epsilon^{n,i,j,k,l} & = \frac{\Delta t_n}{2} \frac{\partial^2 \Phi}{\partial t^2} \Big|^{n,i,j,k,l} - \frac{\Delta \varepsilon}{2} \left[\left(|eE_x^{n,i,k,k}| + |eE_y^{n,i,k,k}| + |eE_z^{n,i,k,k}| \right) \frac{\partial^2}{\partial \varepsilon^2} (v\Phi) \Big|^{n,i,k,k,l} \right] \\
& - \frac{\Delta x}{2} \frac{\partial^2}{\partial x^2} (v\Phi) \Big|^{n,i,k,k,l} - \frac{\Delta y}{2} \frac{\partial^2}{\partial y^2} (v\Phi) \Big|^{n,i,k,k,l} - \frac{\Delta z}{2} \frac{\partial^2}{\partial z^2} (v\Phi) \Big|^{n,i,k,k,l} \\
& - \frac{\Delta \varepsilon}{2} \frac{\partial^2}{\partial \varepsilon^2} (Sv\Phi) \Big|^{n,i,j,k,l} + O\left(\Delta t^2 + \Delta x^2 + \Delta y^2 + \Delta z^2 + \Delta \varepsilon^2\right).
\end{aligned} \tag{7.51}$$

However, in practice, the consistency error of the simulation results is measured by computing the percentage of error in the time-and-space-integrated energy conservation equation (6.29).

7.1.5 First order Implicit Scheme for the Collisional Terms in the case of Very Dense Plasmas

In the case of laser-generated fast electron transport in a very dense plasma like in the Fast Ignition or the Shock Ignition Scheme for Inertial Confinement Fusion, the total stopping power S and the angular isotropization rate ν may severely restrict the CFL criterion (7.21). Therefore, I also introduce implicit

numerical schemes for these two terms in order to relax the CFL condition to the less restrictive one :

$$\begin{aligned} \frac{1}{\Delta t_n} &> v_{\max} \left(\frac{1}{\Delta x} + \frac{1}{\Delta y} + \frac{1}{\Delta z} \right) + \frac{e v_{\max} \sqrt{E_{x,\max}^n{}^2 + E_{y,\max}^n{}^2 + E_{z,\max}^n{}^2}}{\Delta \varepsilon} \\ &+ \omega_{c,\max}^n + \frac{e \sqrt{E_{x,\max}^n{}^2 + E_{y,\max}^n{}^2 + E_{z,\max}^n{}^2}}{p_{\min}}. \end{aligned} \quad (7.52)$$

In this case, we firstly compute all the other terms :

$$\begin{aligned} \Phi^{*,i,j,k,l} = \Phi^{n,i,j,k,l} &- (\Delta t_n / \Delta x) \left[F_{x,\text{HLL}}^{n,i+1/2,j,k,l} - F_{x,\text{HLL}}^{n,i-1/2,j,k,l} \right] \\ &- (\Delta t_n / \Delta y) \left[F_{y,\text{HLL}}^{n,i+1/2,j,k,l} - F_{y,\text{HLL}}^{n,i-1/2,j,k,l} \right] \\ &- (\Delta t_n / \Delta z) \left[F_{z,\text{HLL}}^{n,i,j,k+1/2,l} - F_{z,\text{HLL}}^{n,i,j,k-1/2,l} \right] \\ &- (\Delta t_n / \Delta \varepsilon) \left[F_{\varepsilon,\text{HLL}}^{n,i,j,k,l+1/2} - F_{\varepsilon,\text{HLL}}^{n,i,j,k,l-1/2} \right] \\ &+ \Delta t_n \left(\Gamma_E^{n,i,j,k,l} + \Gamma_B^{n,i,j,k,l} \right). \end{aligned} \quad (7.53)$$

Then, the collisional effects are taken into account implicitly :

$$\Psi_0^{n+1,i,j,k,l} = \frac{\Phi_0^{*,i,j,k,l} + \frac{S_{n,i,j,k,l+1} v_{l+1} \Delta t_n}{\Delta \varepsilon} \Phi_0^{*,i,j,k,l+1}}{1 + \frac{S_{n,i,j,k,l} v_l \Delta t_n}{\Delta \varepsilon}} \quad (7.54)$$

and $\forall \zeta \in \{x, y, z\}$,

$$\Psi_{1,\zeta}^{n+1,i,j,k,l} = \frac{\Phi_{1,\zeta}^{*,i,j,k,l} + \frac{S_{n,i,j,k,l+1} v_{l+1} \Delta t_n}{\Delta \varepsilon} \Phi_{1,\zeta}^{*,i,j,k,l+1}}{1 + \frac{S_{n,i,j,k,l} v_l \Delta t_n}{\Delta \varepsilon} + \nu_{n,i,j,k,l} \Delta t_n}. \quad (7.55)$$

In order to improve the consistency error of the numerical scheme for the collisional slowing down of the fast electrons, I have also tested the centered implicit scheme. However, it led to solutions outside the realizability domain (7.35). That is why, we have finally chosen the simpler implicit and explicit downwind schemes.

7.1.6 Fast Electron Injection and Escaping Boundary Conditions

The fast electron injection in the simulation box is performed by defining the angular moments Φ_{ini} of the distribution function $\Psi_{\text{M1}}(x_i, y_j, z_1, \varepsilon_l, \theta, \varphi, t_n)$ in the first cells in the z -direction $z = z_1$ at each time step t_n (see **Figure 7.1**). The distribution function may depend on parameters introduced in **Chapter 1, section 1.4** that are deduced from a Particle-In-Cell simulation of the laser-target interaction. It may happen that fast electrons are still propagating in the simulation box while the laser pulse is off. In this case, we define the laser pulse duration t_{source} such that for times $t_n \geq t_{\text{source}}$, we stop injecting fast electrons by imposing $\Phi_{\text{ini}} = \mathbf{0}$. This section is dedicated to the boundary conditions at the simulation box boundaries $x = \pm L_x/2$, $y = \pm L_y/2$, $z = 0$ and $z = L_z$ as well as the

7.1. M1 EQUATIONS

kinetic energy space boundaries $\varepsilon = \varepsilon_{\min}$ and $\varepsilon = L_\varepsilon$.

In a first attempt, we decided to let the fast electrons escape the target at the target spatial boundaries (see **Chapter 9** for the fast electrons refluxing). One may therefore naively think that it would be sufficient to impose for example $\Phi^{n,i,j,N_z+1,l} = \Phi^{n,i,j,N_z+2,l} = 0$, which means that there are no fast electrons in vacuum at the target rear side, so that all fast electrons with a positive momentum $p_l \Psi_{1,z}^{n,i,j,N_z,l}$ will escape from the target boundary $k = N_z$. Actually, it is not so easy. Indeed, what really matters is the fast electron fluxes at $z = L_z$ which are computed according to the HLL scheme. Thus, concerning this example, this is the HLL flux $F_{z,HLL}^{n,i,j,N_z,l}$ that must be taken equal to $F_z^{n,i,j,N_z,l}$ and not directly $F_z^{n,i,j,N_z,l}$. Consequently, for this example, we have to impose the following boundary condition at the target rear side :

$$\begin{aligned} \text{If } \Psi_{1,z}^{n,i,j,N_z,l} > 0 \quad \text{then} \quad & \Phi^{n,i,j,N_z+2,l} = \Phi^{n,i,j,N_z+1,l} = \Phi^{n,i,j,N_z,l} \\ \text{else} \quad & \Phi^{n,i,N_z+2,l} = \Phi^{n,i,N_z+1,l} = \mathbf{0}. \end{aligned} \tag{7.56}$$

If the fast electrons have a positive momentum $p_l \Psi_{1,z}^{n,i,j,N_z,l}$ in the z -direction at the target rear side $k = N_z$, it means that they are going to escape from the target so that we have to impose $\Phi^{n,i,j,N_z+2,l} = \Phi^{n,i,j,N_z+1,l} = \Phi^{n,i,j,N_z,l}$ such that the HLL flux in the z -direction at the rear side reads

$$F_{z,HLL}^{n,i,j,N_z+1/2,l} = v_l \left[\frac{F_z^{N_z+1,-} + F_z^{N_z,+}}{2} \right]^{n,i,j,l} - |v_l| \left[\frac{\Phi^{N_z+1,-} - \Phi^{N_z,+}}{2} \right]^{n,i,j,l} = F_z^{n,i,j,N_z,l}.$$

In the opposite case where the fast electrons have a negative momentum $p_l \Psi_{1,z}^{n,i,j,N_z,l}$ at the target rear side $k = N_z$, we impose no fast electrons in vacuum $k = N_z + 1$ and $k = N_z + 2$ so that we do not inject fast electrons according to the HLL flux expression. By generalizing to other target boundaries,

we impose the following boundary conditions :

$$\begin{aligned}
 & \text{If } t < t_{\text{source}} && \text{then } \Phi^{n,i,j,0,l} = \Phi^{n,i,j,1,l} = \Phi_{\text{ini}}^{n,i,j,1,l} \\
 \text{else if } & \Psi_{1,z}^{n,i,j,2,l} < 0 \text{ and } t > t_{\text{source}} && \text{then } \Phi^{n,i,j,0,l} = \Phi^{n,i,j,1,l} = \Phi^{n,i,j,2,l} \\
 \text{else} & && \Phi^{n,i,j,0,l} = \Phi^{n,i,j,1,l} = \mathbf{0}, \\
 \\
 & \text{If } \Psi_{1,y}^{n,i,1,k,l} < 0 && \text{then } \Phi^{n,i,-1,k,l} = \Phi^{n,i,0,k,l} = \Phi^{n,i,1,k,l} \\
 \text{else} & && \Phi^{n,i,-1,k,l} = \Phi^{n,i,0,k,l} = \mathbf{0}, \\
 \\
 & \text{If } \Psi_{1,y}^{n,i,N_y,k,l} > 0 && \text{then } \Phi^{n,i,N_y+1,k,l} = \Phi^{n,i,N_y+2,j,k,l} = \Phi^{n,i,N_y,k,l} \quad (7.57) \\
 \text{else} & && \Phi^{n,i,N_y+1,k,l} = \Phi^{n,i,N_y+2,k,l} = \mathbf{0}, \\
 \\
 & \text{If } \Psi_{1,x}^{n,1,j,k,l} < 0 && \text{then } \Phi^{n,-1,j,k,l} = \Phi^{n,0,j,k,l} = \Phi^{n,1,j,k,l} \\
 \text{else} & && \Phi^{n,-1,j,k,l} = \Phi^{n,0,j,k,l} = \mathbf{0} \text{ and} \\
 \\
 & \text{If } \Psi_{1,x}^{n,N_x,j,k,l} > 0 && \text{then } \Phi^{n,N_x+1,j,k,l} = \Phi^{n,N_x+2,j,k,l} = \Phi^{n,N_x,j,k,l} \\
 \text{else} & && \Phi^{n,N_x+1,j,k,l} = \Phi^{n,N_x+2,j,k,l} = \mathbf{0}.
 \end{aligned}$$

Concerning the target corners, the priority is given to the z -axis fluxes, assuming that L_x and L_y have been chosen sufficiently large.

The boundary conditions concerning the HLL fluxes in the kinetic energy space are simpler since in our laser-generated fast electron transport model, fast electrons only lose their kinetic energy. Consequently, we impose

$$\Phi^{n,i,j,k,-1} = \Phi^{n,i,j,k,0} = \Phi^{n,i,j,k,1} \quad (7.58)$$

in order to let the fast electrons lose all their energy according to the HLL fluxes at the low energy boundary $\varepsilon = \varepsilon_{\text{min}}$. Since $n_b \ll n_e$, these electrons with energies less than ε_{min} are not injected in the background electrons population and are just removed from the system. In the opposite boundary, we impose

$$\Phi^{n,i,j,k,N_\varepsilon+1} = \Phi^{n,i,j,k,N_\varepsilon+2} = \mathbf{0} \quad (7.59)$$

in order to avoid injection of fast electrons at the high energy boundary $\varepsilon = L_\varepsilon$.

7.2 Self-Generated Electromagnetic Fields

According to the previous section, we know exactly the fast electron distribution function Ψ_{M1}^n at each time step n in the whole simulation box. Therefore, we can compute the laser-generated fast electron

7.2. SELF-GENERATED ELECTROMAGNETIC FIELDS

beam density according to

$$n_b^{n,i,j,k} = n_b(x_i, y_j, z_k, t_n) = \sum_{l=1}^{N_\varepsilon} \Psi_0^{n,i,j,k,l} \Delta\varepsilon \quad (7.60)$$

and the beam current density according to

$$\mathbf{j}_b^{n,i,j,k} = \mathbf{j}_b(x_i, y_j, z_k, t_n) = -e \sum_{l=1}^{N_\varepsilon} \Psi_1^{n,i,j,k,l} v_l \Delta\varepsilon. \quad (7.61)$$

Also, as illustrated in **Figure 7.2**, the background electron and ion temperatures at time t_n , T_e^n and T_i^n , are known in each cell, allowing to compute the electrical resistivity $\eta^{n,i,j,k}$ and the background electron density $n_e^{n,i,j,k} = (Z^*)^{n,i,j,k} n_i^{n,i,j,k,l}$ in each cell at time t_n . This section is dedicated to the resolution of the self-generated electromagnetic fields at each time step t_n . The equations that have to be solved self-consistently in 3 dimensions for the self-generated magnetic fields are

$$\begin{aligned} & \frac{\partial B_x}{\partial t} - \frac{\partial}{\partial y} \left(\frac{\eta(x, y, z, t) c^2}{4\pi} \frac{\partial B_x}{\partial y} \right) - \frac{\partial}{\partial z} \left(\frac{\eta(x, y, z, t) c^2}{4\pi} \frac{\partial B_x}{\partial z} \right) \\ = & - \frac{\partial}{\partial y} \left(\frac{\eta(x, y, z, t) c^2}{4\pi} \frac{\partial B_y}{\partial x} \right) - \frac{\partial}{\partial z} \left(\frac{\eta(x, y, z, t) c^2}{4\pi} \frac{\partial B_z}{\partial x} \right) \\ + & \eta(x, y, z, t) c \left(\frac{\partial j_{b,z}}{\partial y} - \frac{\partial j_{b,y}}{\partial z} \right) \\ + & j_{b,z} c \frac{\partial \eta}{\partial y} - j_{b,y} c \frac{\partial \eta}{\partial z} \\ + & \frac{k_{BC}}{n_e e} \left(\frac{\partial n_e}{\partial z} \frac{\partial T_e}{\partial y} - \frac{\partial n_e}{\partial y} \frac{\partial T_e}{\partial z} \right), \end{aligned} \quad (7.62)$$

$$\begin{aligned} & \frac{\partial B_y}{\partial t} - \frac{\partial}{\partial z} \left(\frac{\eta(x, y, z, t) c^2}{4\pi} \frac{\partial B_y}{\partial z} \right) - \frac{\partial}{\partial x} \left(\frac{\eta(x, y, z, t) c^2}{4\pi} \frac{\partial B_y}{\partial x} \right) \\ = & - \frac{\partial}{\partial z} \left(\frac{\eta(x, y, z, t) c^2}{4\pi} \frac{\partial B_z}{\partial y} \right) - \frac{\partial}{\partial x} \left(\frac{\eta(x, y, z, t) c^2}{4\pi} \frac{\partial B_x}{\partial y} \right) \\ + & \eta(x, y, z, t) c \left(\frac{\partial j_{b,x}}{\partial z} - \frac{\partial j_{b,z}}{\partial x} \right) \\ + & j_{b,x} c \frac{\partial \eta}{\partial z} - j_{b,z} c \frac{\partial \eta}{\partial x} \\ + & \frac{k_{BC}}{n_e e} \left(\frac{\partial n_e}{\partial x} \frac{\partial T_e}{\partial z} - \frac{\partial n_e}{\partial z} \frac{\partial T_e}{\partial x} \right) \end{aligned} \quad (7.63)$$

and

$$\begin{aligned} & \frac{\partial B_z}{\partial t} - \frac{\partial}{\partial x} \left(\frac{\eta(x, y, z, t) c^2}{4\pi} \frac{\partial B_z}{\partial x} \right) - \frac{\partial}{\partial y} \left(\frac{\eta(x, y, z, t) c^2}{4\pi} \frac{\partial B_z}{\partial y} \right) \\ = & - \frac{\partial}{\partial x} \left(\frac{\eta(x, y, z, t) c^2}{4\pi} \frac{\partial B_x}{\partial z} \right) - \frac{\partial}{\partial y} \left(\frac{\eta(x, y, z, t) c^2}{4\pi} \frac{\partial B_y}{\partial z} \right) \\ + & \eta(x, y, z, t) c \left(\frac{\partial j_{b,y}}{\partial x} - \frac{\partial j_{b,x}}{\partial y} \right) \\ + & j_{b,y} c \frac{\partial \eta}{\partial x} - j_{b,x} c \frac{\partial \eta}{\partial y} \\ + & \frac{k_{BC}}{n_e e} \left(\frac{\partial n_e}{\partial y} \frac{\partial T_e}{\partial x} - \frac{\partial n_e}{\partial x} \frac{\partial T_e}{\partial y} \right) \end{aligned} \quad (7.64)$$

while the self-generated electric fields can be deduced knowing the self-generated magnetic field according to

$$E_x = -\eta(x, y, z, t)j_{b,x} + \frac{\eta(x, y, z, t)c}{4\pi} \left(\frac{\partial B_z}{\partial y} - \frac{\partial B_y}{\partial z} \right) - \frac{k_B}{n_e(x, y, z, t)e} \frac{\partial}{\partial x} (n_e T_e), \quad (7.65)$$

$$E_y = -\eta(x, y, z, t)j_{b,y} + \frac{\eta(x, y, z, t)c}{4\pi} \left(\frac{\partial B_x}{\partial z} - \frac{\partial B_z}{\partial x} \right) - \frac{k_B}{n_e(x, y, z, t)e} \frac{\partial}{\partial y} (n_e T_e) \quad (7.66)$$

and

$$E_z = -\eta(x, y, z, t)j_{b,z} + \frac{\eta(x, y, z, t)c}{4\pi} \left(\frac{\partial B_y}{\partial x} - \frac{\partial B_x}{\partial y} \right) - \frac{k_B}{n_e(x, y, z, t)e} \frac{\partial}{\partial z} (n_e T_e). \quad (7.67)$$

The first line of the B-field equations (7.62), (7.63) and (7.64) describes the diffusion of the B-field component B_ξ , $\xi \in \{x, y, z\}$ in the plane perpendicular to the ξ -axis. The second line describes the coupling between the different B-field components, which cancels in two dimensions. The third line describes the B-field source term due to the curl of the beam density current while the fourth line describes the B-field source due to resistivity gradients. Finally, the fifth line describes the B-field source term due to the background electron temperature-density crossed gradients. The first term in the left hand side of the E-field equations (7.65), (7.66) and (7.67) provides the main contribution due to the beam density component \mathbf{j}_b in the return current expression $\mathbf{j}_e = \mathbf{j}_t - \mathbf{j}_b$. The second term comes from the total net current $\mathbf{j}_t = (c/4\pi)(\partial/\partial\mathbf{r}) \times \mathbf{B}$ according to the Maxwell-Ampere equation with the quasi-static approximation. Finally, the last term comes from the pressure force. This latter is usually very small compared to other terms.

7.2.1 Second Order Implicit Scheme describing the Self-Generated Magnetic Fields Diffusion and Second Order Explicit Schemes describing the Self-Generated Magnetic Fields Sources

Here, we describe the numerical methods used to solve the magnetic fields equations (7.62), (7.63) and (7.64). For simplicity, we present the resolution of the y -component of the B-field (7.63) in each slice $y = y_{j_0}$, indexed by j_0 . This numerical scheme can be generalized to the x -component of the B-field (7.62) by permuting $x \rightarrow z$, $y \rightarrow x$ and $z \rightarrow y$ ($j_0 \rightarrow i_0$, $i \rightarrow k$ and $k \rightarrow j$) and to the z -component of the B-field (7.64) by permuting $x \rightarrow y$, $y \rightarrow z$ and $z \rightarrow x$ ($j_0 \rightarrow k_0$, $i \rightarrow j$ and $k \rightarrow i$). Thus, let us note

$$B_{y,\text{cour}}^{n,i,j_0,k} = \eta^{n,i,j_0,k} c \Delta t_n \left(\frac{j_{b,x}^{n,i,j_0,k+1} - j_{b,x}^{n,i,j_0,k-1}}{2\Delta z} - \frac{j_{b,z}^{n,i+1,j_0,k} - j_{b,z}^{n,i-1,j_0,k}}{2\Delta x} \right) \quad (7.68)$$

7.2. SELF-GENERATED ELECTROMAGNETIC FIELDS

the discretized B_y -field generated at the time interval between t_n and $t_n + \Delta t_n$ due to the curl of the beam current density,

$$B_{y,\text{res}}^{n,i,j_0,k} = j_{b,x}^{n,i,j_0,k} c \Delta t_n \frac{\eta^{n,i,j_0,k+1} - \eta^{n,i,j_0,k-1}}{2\Delta z} - j_{b,z}^{n,i,j_0,k} c \Delta t_n \frac{\eta^{n,i+1,j_0,k} - \eta^{n,i-1,j_0,k}}{2\Delta x} \quad (7.69)$$

the discretized B_y -field generated at the time interval between t_n and $t_n + \Delta t_n$ due to the resistivity gradients,

$$B_{y,\text{cross}}^{n,i,j_0,k} = \frac{k_{BC}}{en_e} \Delta t_n \left(\frac{n_e^{n,i+1,j_0,k} - n_e^{n,i-1,j_0,k}}{2\Delta x} \frac{T_e^{n,i,j_0,k+1} - T_e^{n,i,j_0,k-1}}{2\Delta z} - \frac{n_e^{n,i,j_0,k+1} - n_e^{n,i,j_0,k-1}}{2\Delta z} \frac{T_e^{n,i+1,j_0,k} - T_e^{n,i-1,j_0,k}}{2\Delta x} \right) \quad (7.70)$$

the discretized B_y -field generated at the time interval between t_n and $t_n + \Delta t_n$ due to the background electrons temperature-density crossed gradients and

$$B_{y,3D}^{n,i,j_0,k} = -\Delta t_n \left[\frac{1}{2\Delta z} \left(\frac{\eta^{n,i,j_0,k+1} c^2 B_z^{n,i,j_0+1,k+1} - B_z^{n,i,j_0-1,k+1}}{4\pi} \frac{2\Delta y}{\eta^{n,i,j_0,k-1} c^2 B_z^{n,i,j_0+1,k-1} - B_z^{n,i,j_0-1,k-1}} \right) + \frac{1}{2\Delta x} \left(\frac{\eta^{n,i+1,j_0,k} c^2 B_x^{n,i+1,j_0+1,k} - B_x^{n,i+1,j_0-1,k}}{4\pi} \frac{2\Delta y}{\eta^{n,i-1,j_0,k} c^2 B_x^{n,i-1,j_0+1,k} - B_x^{n,i-1,j_0-1,k}} \right) \right] \quad (7.71)$$

the discretized B_y -field generated between t_n and $t_n + \Delta t_n$ due to 3D effects, all expressed fully explicitly with second order schemes. The diffusion of the y -component of the B-field B_y in the plane (x, z) is computed semi-implicitly according to the numerical scheme :

$$\begin{aligned} \frac{B_y^{n+1,i,j_0,k} - B_y^{n,i,j_0,k}}{\Delta t_n} &= \frac{\eta^{n,i+1/2,j_0,k} c^2 B_y^{n+1,i+1,j_0,k} - B_y^{n+1,i,j_0,k}}{4\pi \Delta x} \frac{\Delta x}{\eta^{n,i-1/2,j_0,k} c^2 B_y^{n+1,i,j_0,k} - B_y^{n+1,i-1,j_0,k}} \\ &+ \frac{4\pi \Delta x}{\eta^{n,i,j_0,k+1/2} c^2} \frac{\Delta x}{B_y^{n+1,i,j_0,k+1} - B_y^{n+1,i,j_0,k}} \\ &- \frac{4\pi \Delta z}{\eta^{n,i,j_0,k-1/2} c^2} \frac{\Delta z}{B_y^{n+1,i,j_0,k} - B_y^{n+1,i,j_0,k-1}} \\ &+ \frac{4\pi \Delta z}{\Delta t_n} \frac{\Delta z}{\left(B_{y,\text{cour}}^{n,i,j_0,k} + B_{y,\text{res}}^{n,i,j_0,k} + B_{y,\text{cross}}^{n,i,j_0,k} + B_{y,3D}^{n,i,j_0,k} \right)} \end{aligned} \quad (7.72)$$

where it has been noted

$$\forall i_\xi \in \{i, k\} \text{ corresponding to } \xi \in \{x, z\}, \eta^{i_\xi+1/2} = \frac{2\eta^{i_\xi+1}\eta^{i_\xi}}{\eta^{i_\xi} + \eta^{i_\xi+1}} \text{ and } \eta^{i_\xi-1/2} = \frac{2\eta^{i_\xi}\eta^{i_\xi-1}}{\eta^{i_\xi} + \eta^{i_\xi-1}}. \quad (7.73)$$

CHAPTER 7. NUMERICAL IMPLEMENTATION OF THE MODEL

\mathbf{x}_{n+1} can be approached with the wanted error ϵ by using the following conjugated gradients algorithm :

$$\begin{aligned}
 & m := 0 \\
 & \mathbf{x}_{n+1}^{(m)} := \mathbf{y}_n \\
 & \mathbf{r}_m := \mathbf{y}_n - \mathbb{A} \cdot \mathbf{x}_{n+1}^{(m)} \\
 & \mathbf{p}_m := \mathbf{r}_m \\
 & \text{While } |\mathbf{r}_m| > \epsilon |\mathbf{y}_n| \quad \text{do} \quad \alpha_m := \frac{\mathbf{r}_m^T \cdot \mathbf{r}_m}{\mathbf{p}_m^T \cdot \mathbb{A}_n \cdot \mathbf{p}_m} \\
 & \quad \quad \quad \mathbf{x}_{n+1}^{(m+1)} := \mathbf{x}_{n+1}^{(m)} + \alpha_m \mathbf{p}_m \\
 & \quad \quad \quad \mathbf{r}_{m+1} := \mathbf{r}_m - \alpha_m \mathbb{A}_n \cdot \mathbf{p}_m \\
 & \quad \quad \quad \beta_m := \frac{\mathbf{r}_{m+1}^T \cdot \mathbf{r}_{m+1}}{\mathbf{r}_m^T \cdot \mathbf{r}_m} \\
 & \quad \quad \quad \mathbf{p}_{m+1} := \mathbf{r}_{m+1} + \beta_m \mathbf{p}_m \\
 & \quad \quad \quad m := m + 1 \\
 & \text{end do.}
 \end{aligned}$$

Also, a Jacobi preconditionner is used so that it is $\mathbb{A}'_n \cdot \mathbf{x}_{n+1} = \mathbf{y}'_n$ that is actually solved instead of $\mathbb{A}_n \cdot \mathbf{x}_{n+1} = \mathbf{y}_n$ where $\mathbb{A}'_n = \mathbb{P}_n^{-1} \cdot \mathbb{A}$ and $\mathbf{y}'_n = \mathbb{P}_n^{-1} \cdot \mathbf{y}_n$ with

$$\mathbb{P}_n = \begin{bmatrix}
 d_1^{N_x, N_z} & & & & & & & & \\
 & \ddots & & & & & & & \\
 & & d_1^{1, N_z} & & & & & & \\
 & & & \ddots & & & & & \\
 & & & & d_1^{i, k} & & & & \\
 & & & & & \ddots & & & \\
 & & & & & & d_1^{N_x, 1} & & \\
 & & & & & & & \ddots & \\
 & & & & & & & & d_1^{1, 1}
 \end{bmatrix} \quad (0)$$

in order to work with a better conditioned matrix. Usually, tens of m -iterations are needed to obtain \mathbf{x}_{n+1} with an error of $\epsilon = 10^{-14}$. The consistency error in the discretization of \mathbf{y}_n is $O(\Delta t_n + \Delta x^2 + \Delta y^2 + \Delta z^2)$. An option in the *Fortran* file *data.f90* allows for deciding to compute or not the magnetic field diffusion. In the case where the magnetic diffusion is not computed, the magnetic field B_y^{n+1} is directly given by (7.80) with the $N_x N_z$ -dimensional unity matrix \mathbb{I} instead of \mathbb{A}_n i.e. $\mathbf{x}_{n+1} = \mathbf{y}_n$. In the 3D-3V case where the fast electrons are injected parallel to the z -axis (without an angle of incidence), the z -component of the B-field B_z is small compared to the other transverse components B_x and B_y . In this particular case, the conjugated gradients algorithm does not work since the residues \mathbf{r}_m are

very small. We may deduce the z -component of the B-field B_z^n by knowing the transverse components (B_x^n, B_y^n) and by imposing the Maxwell-Thomson equation $(\partial/\partial\mathbf{r})\cdot\mathbf{B} = 0$. However, for simplicity, this method has not been implemented in the code and an option in the *Fortran* file *data.f90* allows for deciding or not the computation of the diffusion of this z -component B_z^n of the magnetic field.

7.2.2 Deduction of the Self-Generated Electric Field from the Magnetic Fields

Instead of solving similar equations than (7.62), (7.63) and (7.64) for the self-generated electric field, we can compute directly the electric field at each time step t_n by knowing the self generated magnetic field at the same time step t_n according to

$$E_x^{n,i,j,k} = -\eta^{n,i,j,k} j_{b,x}^{n,i,j,k} + \frac{\eta^{n,i,j,k} c}{4\pi} \left(\frac{B_z^{n,i,j+1,k} - B_z^{n,i,j-1,k}}{2\Delta y} - \frac{B_y^{n,i,j,k+1} - B_y^{n,i,j,k-1}}{2\Delta z} \right) - \frac{k_B}{en_e^{n,i,j,k}} \frac{n_e^{n,i+1,j,k} T_e^{n,i+1,j,k} - T_e^{n,i-1,j,k} n_e^{n,i-1,j,k}}{2\Delta x}, \quad (7.82)$$

$$E_y^{n,i,j,k} = -\eta^{n,i,j,k} j_{b,y}^{n,i,j,k} + \frac{\eta^{n,i,j,k} c}{4\pi} \left(\frac{B_x^{n,i,j,k+1} - B_x^{n,i,j,k-1}}{2\Delta z} - \frac{B_z^{n,i+1,j,k} - B_z^{n,i-1,j,k}}{2\Delta x} \right) - \frac{k_B}{en_e^{n,i,j,k}} \frac{n_e^{n,i,j+1,k} T_e^{n,i,j+1,k} - T_e^{n,i,j-1,k} n_e^{n,i,j-1,k}}{2\Delta y} \quad (7.83)$$

and

$$E_z^{n,i,j,k} = -\eta^{n,i,j,k} j_{b,z}^{n,i,j,k} + \frac{\eta^{n,i,j,k} c}{4\pi} \left(\frac{B_y^{n,i+1,j,k} - B_y^{n,i-1,j,k}}{2\Delta x} - \frac{B_x^{n,i,j+1,k} - B_x^{n,i,j-1,k}}{2\Delta y} \right) - \frac{k_B}{en_e^{n,i,j,k}} \frac{n_e^{n,i,j,k+1} T_e^{n,i,j,k+1} - T_e^{n,i,j,k-1} n_e^{n,i,j,k-1}}{2\Delta z}. \quad (7.84)$$

The second term in the right hand side of each equation (7.82), (7.83) and (7.84) represents the discretized components of the total net current

$$\mathbf{j}_t = \mathbf{j}_b + \mathbf{j}_e = \frac{c}{4\pi} \frac{\partial}{\partial\mathbf{r}} \times \mathbf{B}, \quad (7.85)$$

multiplied by $\eta^{n,i,j,k}$.

7.2.3 Boundary Conditions

We suppose that the lateral dimensions of the simulation box L_x and L_y have been chosen sufficiently large to impose vanishing magnetic fields at the transverse boundaries :

$$\mathbf{B}^{n,-1,j,k} = \mathbf{B}^{n,0,j,k} = \mathbf{B}^{n,N_x+1,j,k} = \mathbf{B}^{n,N_x+2,j,k} = \mathbf{0} \quad (7.86)$$

and

$$\mathbf{B}^{n,i,-1,k} = \mathbf{B}^{n,i,0,k} = \mathbf{B}^{n,i,N_y+1,k} = \mathbf{B}^{n,i,N_y+2,k} = \mathbf{0}. \quad (7.87)$$

Concerning the target rear side ($z = L_z$), we impose the same boundary condition assuming the target is sufficiently deep (see **Chapter 9** for the fast electrons refluxing) :

$$\mathbf{B}^{n,i,j,N_z+1} = \mathbf{B}^{n,i,j,N_z+2} = \mathbf{0}. \quad (7.88)$$

At the laser-irradiated side of the target, we assume that the magnetic field is the same as in the first cells $z = z_1$ ($k = 1$) where it is usually maximal :

$$\mathbf{B}^{n,i,j,-1} = \mathbf{B}^{n,i,j,0} = \mathbf{B}^{n,i,j,1}. \quad (7.89)$$

Concerning the self-generated electric fields, the same boundary conditions are used i.e. :

$$\mathbf{E}^{n,-1,j,k} = \mathbf{E}^{n,0,j,k} = \mathbf{E}^{n,N_x+1,j,k} = \mathbf{E}^{n,N_x+2,j,k} = \mathbf{0}, \quad (7.90)$$

$$\mathbf{E}^{n,i,-1,k} = \mathbf{E}^{n,i,0,k} = \mathbf{E}^{n,i,N_y+1,k} = \mathbf{E}^{n,i,N_y+2,k} = \mathbf{0}. \quad (7.91)$$

$$\mathbf{E}^{n,i,j,N_z+1} = \mathbf{E}^{n,i,j,N_z+2} = \mathbf{0} \quad (7.92)$$

and

$$\mathbf{E}^{n,i,j,-1} = \mathbf{E}^{n,i,j,0} = \mathbf{E}^{n,i,j,1}. \quad (7.93)$$

Finally, the priority is given to the boundary conditions in the z -direction at the simulation box corners.

7.3 Second order Explicit Schemes for the Heat Equations

According to the two previous sections, we know exactly the distribution function Ψ_{M1}^n as well as the electric field \mathbf{E}^n at the time step t_n in the whole simulation box. These data are needed for the

7.3. SECOND ORDER EXPLICIT SCHEMES FOR THE HEAT EQUATIONS

numerical resolution of the background electron and ion Heat equations

$$\begin{aligned} C_{V,e}(x, y, z, t) \frac{\partial T_e}{\partial t} - \frac{\partial}{\partial x} \left(\kappa_e(x, y, z, t) \frac{\partial T_e}{\partial x} \right) - \frac{\partial}{\partial y} \left(\kappa_e(x, y, z, t) \frac{\partial T_e}{\partial y} \right) - \frac{\partial}{\partial z} \left(\kappa_e(x, y, z, t) \frac{\partial T_e}{\partial z} \right) \\ = W_e(x, y, z, t) - G(x, y, z, t) (T_e - T_i) \end{aligned} \quad (7.94)$$

and

$$C_{V,i}(x, y, z, t) \frac{\partial T_i}{\partial t} = G(x, y, z, t) (T_e - T_i). \quad (7.95)$$

The energy deposition due to the direct collisional energy losses of fast electrons and the Ohmic heating by the return current is deduced from the MHD and M1 packages as illustrated in **Figure 7.2** according to

$$W_e^{n,i,j,k} = \sum_{l=1}^{N_\varepsilon} \left(S_{\text{col}}^{n,i,j,k,l} v_l \Psi_0^{n,i,j,k,l} \Delta\varepsilon \right) + \eta^{n,i,j,k} \left[(j_{e,x}^{n,i,j,k})^2 + (j_{e,y}^{n,i,j,k})^2 + (j_{e,z}^{n,i,j,k})^2 \right] \quad (7.96)$$

where it has been noted $S_{\text{col}}^{n,i,j,k,l} = S_{\text{col}}(x_i, y_j, z_k, \varepsilon_l, t_n)$ the discretized stopping power of fast electrons due to collisions with background electrons (free, bound and screened free) and $\mathbf{j}_e^n = \mathbf{j}_t^n - \mathbf{j}_b^n$ the return current deduced from the beam current density \mathbf{j}_b^n (7.61) and the total current density \mathbf{j}_t^n depending on the curl of the magnetic field \mathbf{B}^n . According to the previous **section 7.2.2**, its discretized values are

$$j_{t,x}^{n,i,j,k} = \frac{c}{4\pi} \left(\frac{B_z^{n,i,j+1,k} - B_z^{n,i,j-1,k}}{2\Delta y} - \frac{B_y^{n,i,j,k+1} - B_y^{n,i,j,k-1}}{2\Delta z} \right), \quad (7.97)$$

$$j_{t,y}^{n,i,j,k} = \frac{c}{4\pi} \left(\frac{B_x^{n,i,j,k+1} - B_x^{n,i,j,k-1}}{2\Delta z} - \frac{B_z^{n,i+1,j,k} - B_z^{n,i-1,j,k}}{2\Delta x} \right) \quad (7.98)$$

and

$$j_{t,z}^{n,i,j,k} = \frac{c}{4\pi} \left(\frac{B_y^{n,i+1,j,k} - B_y^{n,i-1,j,k}}{2\Delta x} - \frac{B_x^{n,i,j+1,k} - B_x^{n,i,j-1,k}}{2\Delta y} \right). \quad (7.99)$$

Also, the discretized values of the electron-ion/lattice coupling factor $G^{n,i,j,k}$ and the thermal capacities $C_{V,e}^{n,i,j,k}$ and $C_{V,i}^{n,i,j,k}$ are calculated from the known temperatures T_e^n and T_i^n at the time step t_n . In what follows, we explain how the electron temperature T_e^{n+1} and the ion temperature T_i^{n+1} at t_{n+1} are computed.

Let us begin with the equation for the ion temperature. It is computed according to

$$T_i^{n+1,i,j,k} = T_i^{n,i,j,k} + \Delta t_n \frac{G^{n,i,j,k}}{C_{V,i}^{n,i,j,k}} \left(T_e^{n,i,j,k} - T_i^{n,i,j,k} \right). \quad (7.100)$$

This numerical scheme is stable with the respect of the approximated CFL condition

$$\Delta t_n < \left(\frac{C_{V,i}}{G} \right)_{\max} \quad (7.101)$$

and present a consistency error $O(\Delta t_n)$. The worst case is the Spitzer regime for Tantalum where $C_{V,i} \approx 10^7 \text{ erg.cm}^{-3}.\text{s}^{-1}.\text{K}^{-1}$ and $G \approx 10^{20} \text{ erg.cm}^{-3}.\text{s}^{-1}.\text{K}^{-1}$ that gives $\Delta t_n \lesssim 100 \text{ fs}$, which is much less restrictive than the CFL criterion for solving the M1 equations (7.50) or (7.52). The heat equation for the background electron temperature is computed according to the 2nd order explicit scheme

$$\begin{aligned}
 T_e^{n+1,i,j,k} &= T_e^{n,i,k} + \Delta t_n \frac{W_e^{n,i,j,k}}{C_{V,e}^{n,i,j,k}} - \Delta t_n \frac{G^{n,i,j,k}}{C_{V,e}^{n,i,j,k}} \left(T_e^{n,i,j,k} - T_i^{n,i,j,k} \right) \\
 &+ \frac{\Delta t_n}{C_{V,e}^{n,i,j,k} \Delta x} \left(\kappa_e^{n,i+1/2,j,k} \frac{T_e^{n,i+1,j,k} - T_e^{n,i,j,k}}{\Delta x} - \kappa_e^{n,i-1/2,j,k} \frac{T_e^{n,i,j,k} - T_e^{n,i-1,j,k}}{\Delta x} \right) \\
 &+ \frac{\Delta t_n}{C_{V,e}^{n,i,j,k} \Delta y} \left(\kappa_e^{n,i,j+1/2,k} \frac{T_e^{n,i,j+1,k} - T_e^{n,i,j,k}}{\Delta y} - \kappa_e^{n,i,j-1/2,k} \frac{T_e^{n,i,j,k} - T_e^{n,i,j-1,k}}{\Delta y} \right) \\
 &+ \frac{\Delta t_n}{C_{V,e}^{n,i,j,k} \Delta z} \left(\kappa_e^{n,i,j,k+1/2} \frac{T_e^{n,i,j,k+1} - T_e^{n,i,j,k}}{\Delta z} - \kappa_e^{n,i,j,k-1/2} \frac{T_e^{n,i,j,k} - T_e^{n,i,j,k-1}}{\Delta z} \right)
 \end{aligned} \tag{7.102}$$

where it has been noted

$$\forall i_\xi \in \{i, j, k\} \text{ corresponding to } \{x, y, z\}, \quad \kappa_e^{i_\xi+1/2} = \frac{2\kappa_e^{i_\xi+1} \kappa_e^{i_\xi}}{\kappa_e^{i_\xi} + \kappa_e^{i_\xi+1}} \text{ and } \kappa_e^{i_\xi-1/2} = \frac{2\kappa_e^{i_\xi} \kappa_e^{i_\xi-1}}{\kappa_e^{i_\xi} + \kappa_e^{i_\xi-1}}. \tag{7.103}$$

This scheme is stable with the respect of the approximated CFL condition

$$\Delta t_n < \frac{1}{2 \left(\frac{\kappa_e}{C_{V,e}} \right)_{\max} \left(\frac{1}{\Delta x^2} + \frac{1}{\Delta y^2} + \frac{1}{\Delta z^2} \right) + \left(\frac{G}{C_{V,e}} \right)_{\max}} \tag{7.104}$$

and presents a consistency error $O(\Delta t + \Delta x^2 + \Delta y^2 + \Delta z^2)$. In practice, as for the ion temperature equation, this CFL condition is much less restrictive than the CFL for the M1 equations (7.50) or (7.52). In the worst case, in the hot Spitzer regime for Tantalum with a coupling factor $G \approx 10^{20} \text{ erg.cm}^{-3}.\text{s}^{-1}.\text{K}^{-1}$, a thermal capacity $C_{V,e} \approx 10^9 \text{ erg.cm}^{-3}.\text{s}^{-1}.\text{K}^{-1}$ and a thermal conduction $\kappa_e \approx 10^{13} \text{ erg.cm}^{-1}.\text{s}^{-1}.\text{K}^{-1}$, we obtain that Δt_n must be less than several fs, which is larger than a fraction of fs imposed by the CFL condition for the M1 equations. Concerning the boundary conditions, we impose the same temperatures at the target boundaries with a priority for the z -axis at the simulation box corners :

$$T_\alpha^{n,-1,j,k} = T_\alpha^{n,0,j,k} = T_\alpha^{n,1,j,k} \text{ and } T_\alpha^{n,N_x+1,j,k} = T_\alpha^{n,N_x+2,j,k} = T_\alpha^{n,N_x,j,k}, \tag{7.105}$$

$$T_\alpha^{n,i,-1,k} = T_\alpha^{n,i,0,k} = T_\alpha^{n,i,1,k} \text{ and } T_\alpha^{n,i,N_y+1,k} = T_\alpha^{n,i,N_y+2,k} = T_\alpha^{n,i,N_y,k} \tag{7.106}$$

and

$$T_\alpha^{n,i,j,-1} = T_\alpha^{n,i,j,0} = T_\alpha^{n,i,j,1} \text{ and } T_\alpha^{n,i,j,N_z+1} = T_\alpha^{n,i,j,N_z+2} = T_\alpha^{n,i,j,N_z} \tag{7.107}$$

for both electrons temperature ($\alpha = e$) and ions temperature ($\alpha = i$). Sometimes, for short laser pulses with a duration less than 100 fs, the fast electron transport simulation takes only several hundreds

of fs, and one can neglect the electron thermal conductivity. Therefore, an option in the *Fortran* file *data.f90* allows for deciding to compute or not the thermal electron diffusion. In the case where the thermal electron diffusion is not computed, the background electron temperature T_e^{n+1} is directly given by (7.102) with $\kappa_e = 0$ in each cell. Also, sometimes, we only know the transport coefficients η and κ depending on $T_e = T_i = T$ and not $T_i \neq T_e$. In this case, T^{n+1} is directly given by (7.102) with $G = 0$ while the background ion heat equation is not computed. An option in the *Fortran* file *data.f90* also allows for deciding to compute or not the temperatures T_e and T_i or only $T = T_e = T_i$.

7.4 Summary

We have implemented with *Fortran 90* the reduced model for fast electron transport in solids or dense plasmas presented in **Chapter 6**. The numerical resolution of the M1 equations is performed according to the 2nd order explicit HLL scheme for the advection of the fast electrons in space and in the kinetic energy space due to the collective effects. It allows to respect the physical constraints $\Psi_0 \geq 0$ and $|\Psi_1| \leq \Psi_0$ that define the realizability domain. The angular deviations of the fast electrons due to the self-generated electromagnetic field are also computed explicitly. Concerning the collisional effects, they can be computed explicitly or implicitly depending on the density of the target material. In the implicit case, the advection in the kinetic energy space due to the collisional slowing down is computed according to the implicit downwind scheme. The implicit centered scheme does not allow for respecting the realizability domain. Therefore, in order to make comparisons between implicit and fully explicit computations, we also use the explicit downwind scheme.

The self-generated electromagnetic fields as well as the background temperature(s) are computed self-consistently according to second order explicit schemes except for the magnetic field diffusion, which is computed implicitly according to the conjugated gradients algorithm. The numerical model is constrained by the CFL condition of the resolution of the M1 equations. The package diagnostics (see **Figure 7.2**) allows to write the computational results at each time step (Ψ_{M1} , (\mathbf{E}, \mathbf{B}) , T_e , T_i , ...) in 86 text files ".dat" with one text file per quantity. For example, the contribution of each source term to the B_y -field is written in a separate file. That is the contribution of the the curl of the beam current density :

$$\frac{\partial B_{y,\text{cour}}}{\partial t} - \frac{\partial}{\partial z} \left(\frac{\eta c^2}{4\pi} \frac{\partial B_{y,\text{cour}}}{\partial z} \right) - \frac{\partial}{\partial x} \left(\frac{\eta c^2}{4\pi} \frac{\partial B_{y,\text{cour}}}{\partial x} \right) = \eta c \left(\frac{\partial j_{b,x}}{\partial z} - \frac{\partial j_{b,z}}{\partial x} \right)$$

the contribution due to the resistivity gradients :

$$\frac{\partial B_{y,\text{res}}}{\partial t} - \frac{\partial}{\partial z} \left(\frac{\eta c^2}{4\pi} \frac{\partial B_{y,\text{res}}}{\partial z} \right) - \frac{\partial}{\partial x} \left(\frac{\eta c^2}{4\pi} \frac{\partial B_{y,\text{res}}}{\partial x} \right) = j_{b,x} c \frac{\partial \eta}{\partial z} - j_{b,z} c \frac{\partial \eta}{\partial x}$$

the contribution due to the temperature-density crossed gradients

$$\frac{\partial B_{y,\text{cross}}}{\partial t} - \frac{\partial}{\partial z} \left(\frac{\eta c^2}{4\pi} \frac{\partial B_{y,\text{cross}}}{\partial z} \right) - \frac{\partial}{\partial x} \left(\frac{\eta c^2}{4\pi} \frac{\partial B_{y,\text{cross}}}{\partial x} \right) = \frac{k_B c}{n_e e} \left(\frac{\partial n_e}{\partial x} \frac{\partial T_e}{\partial z} - \frac{\partial n_e}{\partial z} \frac{\partial T_e}{\partial x} \right)$$

and the contribution due to 3D effects

$$\frac{\partial B_{y,3D}}{\partial t} - \frac{\partial}{\partial z} \left(\frac{\eta c^2}{4\pi} \frac{\partial B_{y,3D}}{\partial z} \right) - \frac{\partial}{\partial x} \left(\frac{\eta c^2}{4\pi} \frac{\partial B_{y,3D}}{\partial x} \right) = -\frac{\partial}{\partial z} \left(\frac{\eta c^2}{4\pi} \frac{\partial B_z}{\partial y} \right) - \frac{\partial}{\partial x} \left(\frac{\eta c^2}{4\pi} \frac{\partial B_x}{\partial y} \right)$$

are computed and written separately. It is also performed for the other components B_x and B_z , etc... In the case where the CFL condition strongly constrains the time step, it is possible to chose the intervals Δt_{diag} between the two consecutive time steps at which the simulation results are saved in the text files in order to limit the memory needed to stock the information.

The consistency error of the full numerical model is estimated by measuring the percentage error in the discretized energy conservation equation (6.29) integrated in space and time at $t = t_{N_t}$:

$$U_{\text{inj}} = U_{\text{brem}} + U_E + U_B + U_{\text{col}} + U_{\text{res}} + U_b + U_{\text{out}} \quad (7.108)$$

where

$$U_{\text{inj}} = \sum_{n=1}^{N_t} \sum_{i=1}^{N_x} \sum_{j=1}^{N_y} \sum_{l=1}^{N_\varepsilon} \Psi_{1,z}^{n,i,j,1,l} \varepsilon_l v_l \Delta t_n \Delta x \Delta y \Delta \varepsilon \quad (7.109)$$

is the total fast electrons' kinetic energy injected in the simulation box from $t = 0$ to $t = t_{N_t}$ (it also accounts for eventual escaping electrons at the irradiated side of the target $z = 0$),

$$\begin{aligned} U_{\text{out}} &= \sum_{n=1}^{N_t} \sum_{i=1}^{N_x} \sum_{j=1}^{N_y} \sum_{l=1}^{N_\varepsilon} \Psi_{1,z}^{n,i,j,N_z,l} \varepsilon_l v_l \Delta t_n \Delta x \Delta y \Delta \varepsilon \\ &- \sum_{n=1}^{N_t} \sum_{i=1}^{N_x} \sum_{k=1}^{N_z} \sum_{l=1}^{N_\varepsilon} \Psi_{1,y}^{n,i,1,k,l} \varepsilon_l v_l \Delta t_n \Delta x \Delta z \Delta \varepsilon \\ &+ \sum_{n=1}^{N_t} \sum_{i=1}^{N_x} \sum_{k=1}^{N_z} \sum_{l=1}^{N_\varepsilon} \Psi_{1,y}^{n,i,N_y,k,l} \varepsilon_l v_l \Delta t_n \Delta x \Delta z \Delta \varepsilon \\ &- \sum_{n=1}^{N_t} \sum_{j=1}^{N_y} \sum_{k=1}^{N_z} \sum_{l=1}^{N_\varepsilon} \Psi_{1,x}^{n,1,j,k,l} \varepsilon_l v_l \Delta t_n \Delta y \Delta z \Delta \varepsilon \\ &+ \sum_{n=1}^{N_t} \sum_{j=1}^{N_y} \sum_{k=1}^{N_z} \sum_{l=1}^{N_\varepsilon} \Psi_{1,x}^{n,N_x,j,k,l} \varepsilon_l v_l \Delta t_n \Delta y \Delta z \Delta \varepsilon \end{aligned} \quad (7.110)$$

is the total fast electrons' kinetic energy escaped from the simulation box from $t = 0$ to $t = t_{N_t}$ at $z = L_z$ (first line), $x = -L_y/2$ (second line), $y = L_y/2$ (third line), $x = -L_x/2$ (fourth line) and $x = L_x/2$ (fifth line),

$$U_b = \sum_{i=1}^{N_x} \sum_{j=1}^{N_y} \sum_{k=1}^{N_z} \sum_{l=1}^{N_\varepsilon} \Psi_0^{N_t,i,j,k,l} \varepsilon_l \Delta x \Delta y \Delta z \Delta \varepsilon \quad (7.111)$$

7.4. SUMMARY

is the instantaneous beam kinetic energy at $t = t_{N_t}$,

$$U_E = \sum_{i=1}^{N_x} \sum_{j=1}^{N_y} \sum_{k=1}^{N_z} \frac{(E_x^{N_t,i,j,k})^2 + (E_y^{N_t,i,j,k})^2 + (E_z^{N_t,i,j,k})^2}{2} \Delta x \Delta y \Delta z \quad (7.112)$$

is the instantaneous electric energy in the simulation box at $t = t_{N_t}$,

$$U_B = \sum_{i=1}^{N_x} \sum_{j=1}^{N_y} \sum_{k=1}^{N_z} \frac{(B_x^{N_t,i,j,k})^2 + (B_y^{N_t,i,j,k})^2 + (B_z^{N_t,i,j,k})^2}{2} \Delta x \Delta y \Delta z \quad (7.113)$$

is the instantaneous magnetic energy in the simulation box at $t = t_{N_t}$,

$$\begin{aligned} U_{\text{col}} &= \sum_{n=1}^{N_t} \sum_{i=1}^{N_x} \sum_{j=1}^{N_y} \sum_{k=1}^{N_z} W_{e,\text{col}}^{n,i,j,k} \Delta t_n \Delta x \Delta y \Delta z \\ &= \sum_{n=1}^{N_t} \sum_{i=1}^{N_x} \sum_{j=1}^{N_y} \sum_{k=1}^{N_z} \sum_{l=1}^{N_\varepsilon} \Psi_0^{n,i,j,k,l} S_{\text{col}}^{n,i,j,k,l} v_l \Delta t_n \Delta x \Delta y \Delta z \Delta \varepsilon \end{aligned} \quad (7.114)$$

is the total kinetic energy lost (gain) by the fast electrons (background electrons) by colliding the background electrons (by being collided by fast electrons),

$$U_{\text{brem}} = - \sum_{n=1}^{N_t} \sum_{i=1}^{N_x} \sum_{j=1}^{N_y} \sum_{k=1}^{N_z} \sum_{l=1}^{N_\varepsilon} \Psi_0^{n,i,j,k,l} \left(\frac{d\varepsilon}{ds} \right)_{\text{brem}}^{n,i,j,k,l} v_l \Delta t_n \Delta x \Delta y \Delta z \Delta \varepsilon \quad (7.115)$$

is the total kinetic energy lost (gained) by the fast electrons (bremsstrahlung photons) by radiating bremsstrahlung photons (emitted by the fast electrons) and finally

$$\begin{aligned} U_{\text{res}} &= \sum_{n=1}^{N_t} \sum_{i=1}^{N_x} \sum_{j=1}^{N_y} \sum_{k=1}^{N_z} W_{e,\text{res}}^{n,i,j,k} \Delta t_n \Delta x \Delta y \Delta z \\ &= \sum_{n=1}^{N_t} \sum_{i=1}^{N_x} \sum_{j=1}^{N_y} \sum_{k=1}^{N_z} \sum_{l=1}^{N_\varepsilon} \left(\begin{aligned} &e E_x^{n,i,j,k} \Psi_{1,x}^{n,i,j,k,l} \\ &+ e E_y^{n,i,j,k} \Psi_{1,y}^{n,i,j,k,l} \\ &+ e E_z^{n,i,j,k} \Psi_{1,z}^{n,i,j,k,l} \end{aligned} \right) v_l \Delta t_n \Delta x \Delta y \Delta z \Delta \varepsilon \end{aligned} \quad (7.116)$$

is the total kinetic energy lost by the fast electrons due to the electric field induced by the magnetic neutralization of the beam. As already mentioned, except for intermediate Z materials like Tantalum, we include the bremsstrahlung losses directly in $W_{e,\text{col}}$ and U_{col} even if it is a rough approximation since the bremsstrahlung photons do not deposit their energy locally but propagate in the material depending on its opacity. Also, since $\mathbf{j}_t = (c/4\pi)(\partial/\partial\mathbf{r}) \times \mathbf{B} \approx \mathbf{0}$ and $-(k_B/n_e e)(\partial/\partial\mathbf{r})(n_e T_e)$ is small compared to $\eta \mathbf{j}_b$, we can consider that the total kinetic energy lost by the fast electrons U_{res} , due to their slowing down by the electric field induced by the magnetic neutralization of the beam, is also

the total kinetic energy gained by the background electrons due to their acceleration by this electric field.

7.4. SUMMARY

Chapter 8

Validation of the Model

”There are two possible outcomes: if the result confirms the hypothesis, then you’ve made a measurement. If the result is contrary to the hypothesis, then you’ve made a discovery.”

Enrico Fermi

This chapter is dedicated to the validation of the model. In a first time, a 2D-3V academic case of a monoenergetic and collimated fast electron beam propagating in a warm and dense hydrogen plasma is presented. It allows us to demonstrate the major features of the M1 approximation and to derive analytical expressions for the various quantities computed by the code. Therefore, it serves to check the simulation results and to validate the numerical methods described in **Chapter 7**. Secondly, a more realistic simulation of a laser-generated fast electron beam transport in a thin Aluminum target is presented. The laser-generated fast electron beam distribution function is obtained from a 2D-2V Particle-In-Cell (PIC) simulation of the laser plasma simulation, conducted by [Gremillet, 2012] with the PIC code CALDER [Lefebvre et al., 2003]. The resulting 2D-3V M1 simulation of the laser-generated fast electron transport is compared with a 3D-3V fast electron transport simulation conducted by [Gremillet, 2012] with the hybrid PIC code PaRIS [Gremillet et al., 2002] [Martinolli et al., 2006]. It shows that the M1 approximation is sufficiently accurate to reproduce the hybrid PIC simulation results.

8.1 2D-3V Academic Case

8.1.1 Introduction

As a first illustration of the M1 model, we consider the simple case of a quasi-monoenergetic and monodirectional ($\mathbf{\Omega}_\varepsilon(z=0) = \mathbf{e}_z$) relativistic electron beam injected at $z = 0$ in a 2D box ($100 \mu\text{m} \times 100 \mu\text{m}$) of a Hydrogen plasma with a density $\rho = 50 \text{ g.cm}^{-3}$ and an initial temperature $T_0 = 1 \text{ eV}$. A Gaussian distribution centered at $\varepsilon_0 = (\gamma_0 - 1)m_e c^2 = 1 \text{ MeV}$ with a 50 keV standard deviation is used for the beam energy spectrum. A Gaussian temporal shape centered at $t_0 = 1750 \text{ fs}$ with a standard deviation of $\sigma_t = 500 \text{ fs}$ and a Gaussian spatial shape with a standard deviation of $\sigma_x = 10 \mu\text{m}$ have also been used. The electron beam has a total energy of $U = 10 \text{ J}$. As already mentioned in **Chapter 6**, we neglect the electron-ion energy exchange, assume $Z^* = 1$, $T_i = T_e = T$ and $C_V = (3/2)k_B n_i$ in the heat equation. Even if the background electron thermal conduction can be neglected in this simulation due to the small considered time scale ($\approx \text{ps}$), it is computed according to the Hubbard-Spitzer model (for the electrical resistivity η and the thermal electron conduction κ_e ; see **Chapter 3, section 3.3.1**) in order to check the numerical method for solving the thermal diffusion. The spatial resolution has been chosen $\Delta x = \Delta z = 1 \mu\text{m}$ while the energy resolution has been chosen $\Delta\varepsilon = 5 \text{ keV}$ with $\varepsilon_{\min} = 20 \text{ keV}$ and the maximum electron energy $L_\varepsilon = 1.2 \text{ MeV}$, so that the computation time needed is about 5 hours on 20 CPU with the full explicit numerical scheme. In this academic case, due to the high Hydrogen density, which implies strongly collisional beam transport, and a low plasma electrical resistivity because of plasma electrons degeneracy, for the value of the initial beam

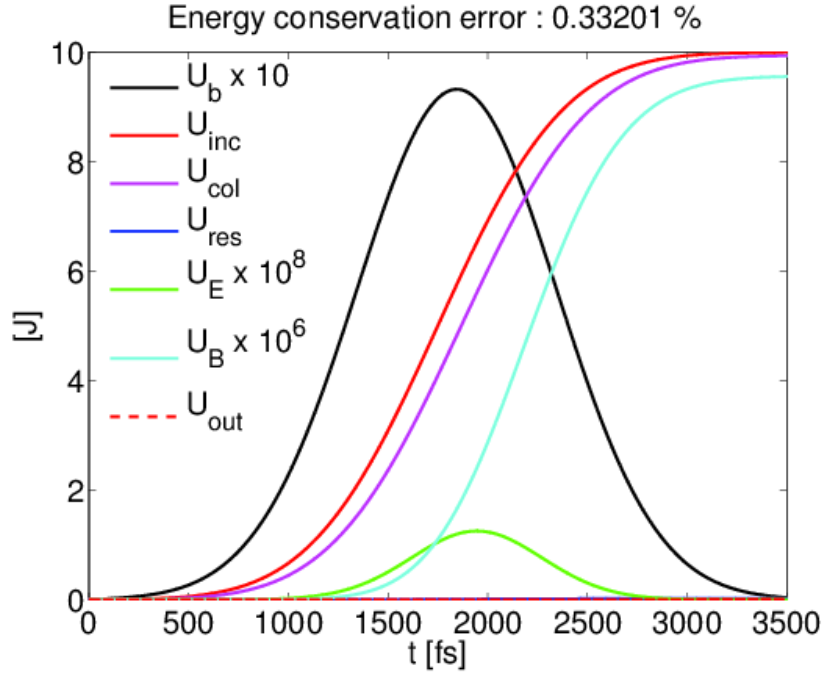


Figure 8.1: Instantaneous beam energy $U_b \times 10$ (solid black), integrated beam energy balanced between injected and escaping electrons at $z = 0$ U_{inc} (solid red), escaped energy U_{out} from the simulation box (dashed red), total collisional energy loss U_{col} (solid magenta), total “collective” U_{res} energy loss (solid blue), instantaneous electric energy $U_E \times 10^8$ (solid green) and instantaneous magnetic energy $U_B \times 10^6$ (solid cyan) from the M1 simulation according to the formula given in **Chapter 7, section 7.4.1**.

current density

$$j_b(x, z, t) = j_{b0} \exp \left\{ -\frac{x^2}{2\sigma_x^2} - \frac{[z - v_0(t - t_0)]^2}{2(v_0\sigma_t)^2} \right\} \quad (8.1)$$

with $j_{b0} = Ue/(2\pi)^{3/2}\epsilon_0\sigma_x^2\sigma_t = -1.27 \cdot 10^{12}$ A.cm⁻² and $v_0 = c(1 - 1/\gamma_0^2)^{1/2}$, the collisional effects are predominant compared to the collective ones. In **Figure 8.1**, various contributions to the total energy integrated in space and time, as defined in **Chapter 7, section 7.4**, are plotted versus time. It shows that the numerical simulation have been sufficiently converged with an error in the energy conservation of $\approx 0.3\%$.

8.1.2 Plasma Heating and Self-generated Electromagnetic Fields

By assuming a Dirac distribution in energy centered at ϵ_0 for Ψ_0 and by neglecting the Ohmic heating by the return current as well as the electron thermal conduction, we can evaluate from the heat equation (6.25) the plasma temperature distribution due to collisional losses of the beam close to $z = 0$ (to ensure the rigid beam approximation):

$$T(x, z, t) \approx T_0 + T_1 \exp \left(-\frac{x^2}{2\sigma_x^2} \right) F(z, t) \quad (8.2)$$

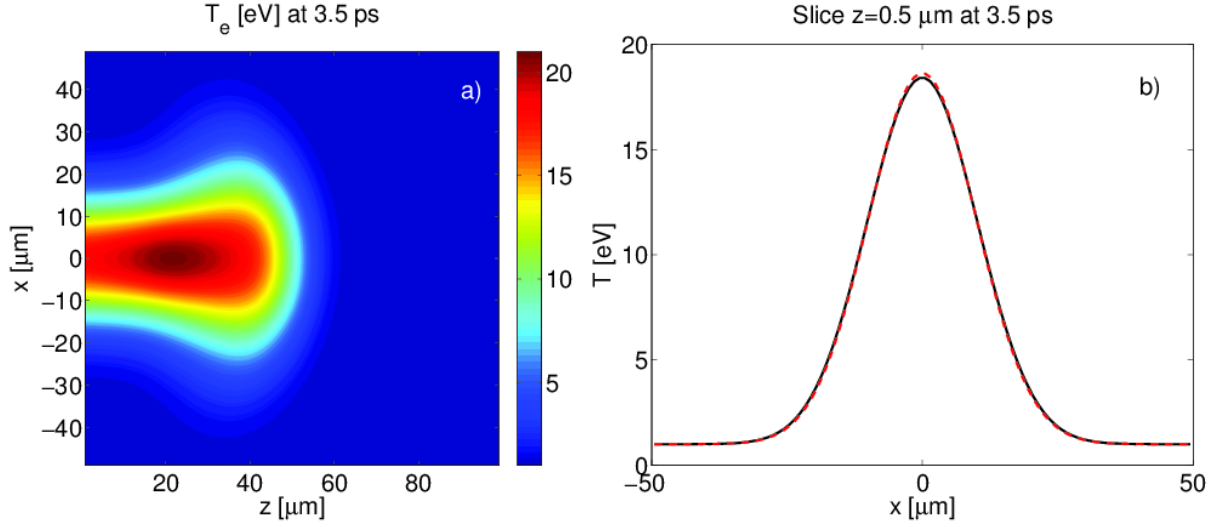


Figure 8.2: Hydrogen temperature T [eV] at $t = 3.5$ ps from the simulation (a) and a comparison of the temperature T profiles at $z = 0.5 \mu\text{m}$ from the simulation (solid black) and the estimate (8.2) (dashed red) at $t = 3.5$ ps (b).

where $F(z, t) = 1 - \text{erf}[(t_0 + z/v_0 - t)/\sigma_t\sqrt{2}]$, erf is the error function and $T_1 = S(\varepsilon_0)U/4\pi^2C_V\varepsilon_0\sigma_x^2 \approx 17.6$ eV. A comparison of the simulation profile at $z = 0.5 \mu\text{m}$ and $t = 3.5$ ps with the estimate (8.2) shows a good agreement, as illustrated in **Figure 8.2 b**). That confirms that neglecting the temperature diffusion as well as the indirect electron beam energy deposition via Ohmic heating $W_{e,\text{res}}$ is a good approximation. Indeed, the diffusion time of the temperature is about $C_V\sigma_x^2/\kappa_e \approx 100 - 1000$ ns, which is large compared to the few ps time interval considered here. Along the z -axis, the temperature rises from $z = 0$ to $z \approx 30 \mu\text{m}$ reaching a maximum value of $T = 21$ eV and then it decreases to the initial value T_0 due to the beam's energy losses discussed in the next section.

By neglecting the resistive diffusion of the magnetic field ($\eta c^2(t - z/v_0 - t_0)/2\pi\sigma_x^2 \ll 1$ at the considered times of a few ps) and by approximating the temperature dependence of the resistivity in the self-generated magnetic diffusion equation (6.24) as $\eta \approx \eta_0(T/T_0)^\alpha$ where $\eta_0 = 9.10^{-9} \Omega\cdot\text{m}$ and $\alpha = 0.25$ according to the Hubbard theory in this regime (see **Chapter 3, section 3.3.1, Figure 3.8**), the estimate (8.2) of the temperature allows us to evaluate the self-generated magnetic field close to $z = 0$:

$$B_y = B_{y,j} + B_{y,\eta} \quad (8.3)$$

where

$$B_{y,j} \approx B_0 \frac{T_0 (x/\sigma_x)}{T_1 \alpha + 1} \left[\left(\frac{T}{T_0} \right)^{\alpha+1} - 1 \right] \quad (8.4)$$

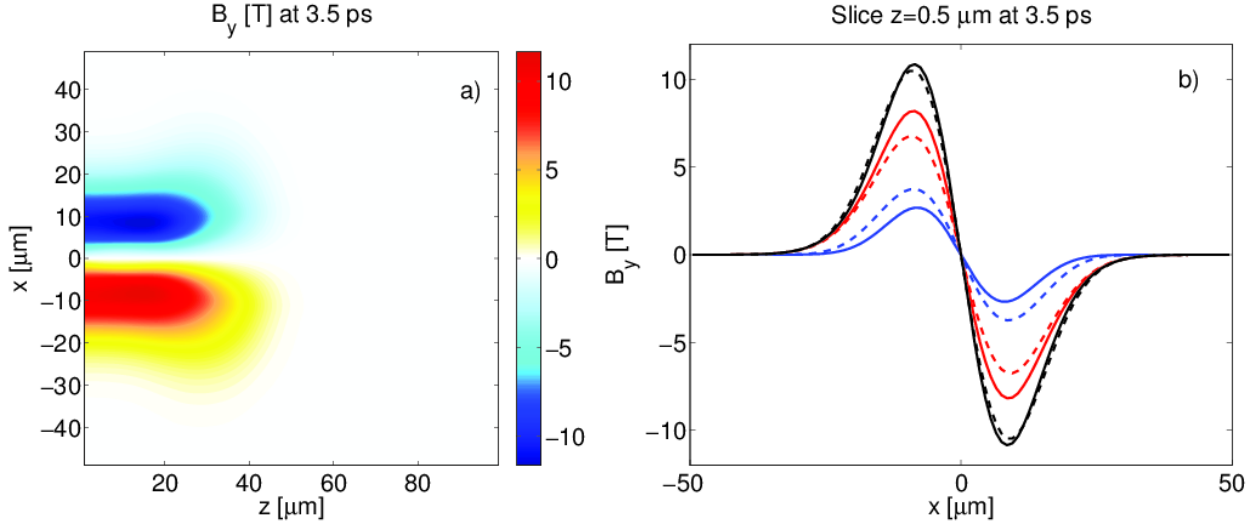


Figure 8.3: Magnetic field B_y [T] at 3.5 ps from the simulation (a) and comparison between the magnetic field $B_y = B_{j,y} + B_{\eta,y}$ profile at $z = 0.5 \mu\text{m}$ and $t = 3.5 \text{ ps}$ (solid black) where $B_{j,y}$ is the contribution due to the beam current density gradients (solid red) and $B_{\eta,y}$ the contribution due to the resistivity gradient (solid blue) from the simulation and their respective estimates (8.3) (dashed black), (8.4) (dashed red) and (8.5) (dashed blue) (b).

is the contribution due to the beam current density and

$$B_{y,\eta} \approx B_0 \frac{T_1}{T_0} \frac{\alpha(x/\sigma_x) \exp\left(-\frac{x^2}{\sigma_x^2}\right)}{\left[1 + \frac{T_1}{T_0} \exp\left(-\frac{x^2}{2\sigma_x^2}\right)\right]^{1-\alpha}} F(z, t) \quad (8.5)$$

is the contribution due to the resistivity gradients. Here, $B_0 = j_{b0}(\eta c/\sigma_x)\sigma_t\sqrt{\pi/2} \approx -7.95 \text{ T}$ and $F(z, t)$ of (8.2) has been approximated by the Heaviside function $H(t - z/v_0 - t_0)$ to get these results. These analytic estimates are plotted and compared with the simulation results in **Figure 8.3 b)**. It confirms that the resistivity gradient makes a significant contribution to the self-generated magnetic field even for Hydrogen temperatures below 20 eV. The temperature-density crossed gradients do not contribute to the magnetic field generation because the plasma electron density is constant.

By neglecting the plasma pressure gradients and the self-generated magnetic field in (6.23), we can also evaluate the self-generated electric field

$$E_z \approx -\eta j_{b0} \exp\left\{-\frac{x^2}{2\sigma_x^2} - \frac{[z - v_0(t - t_0)]^2}{2(v_0\sigma_t)^2}\right\}. \quad (8.6)$$

The maximum value of the slowing down electric force $-e\mathbf{E}\cdot\boldsymbol{\Omega}_e$ is $e\eta j_{b0} \approx 0.1 \text{ keV}\cdot\mu\text{m}^{-1}$. It is very small compared to S (see **Chapter 4, section 4.2.1, Figure 4.1**). This confirms again that the resistive heating $W_{e,\text{res}}$ in the heat equation is negligible. According to the estimates (8.4) and (8.5), the maximum of the beam cyclotron frequency $\omega_c = eB_y/\gamma m_e c$ is about $eB_0/m_e c \approx 1 \text{ ps}^{-1}$ at $x = \sigma_x$,

$z = 0$ and $t = 3.5$ ps. Consequently, the inequality $\omega_c \ll \nu$ is verified in this particular case (see **Chapter 6, section 6.1.2, Figure 6.2**). Thus, the effects of the self-generated electromagnetic fields are negligible and the evolution of the electron beam is essentially collisional.

8.1.3 Kinetic evolution of the electron beam

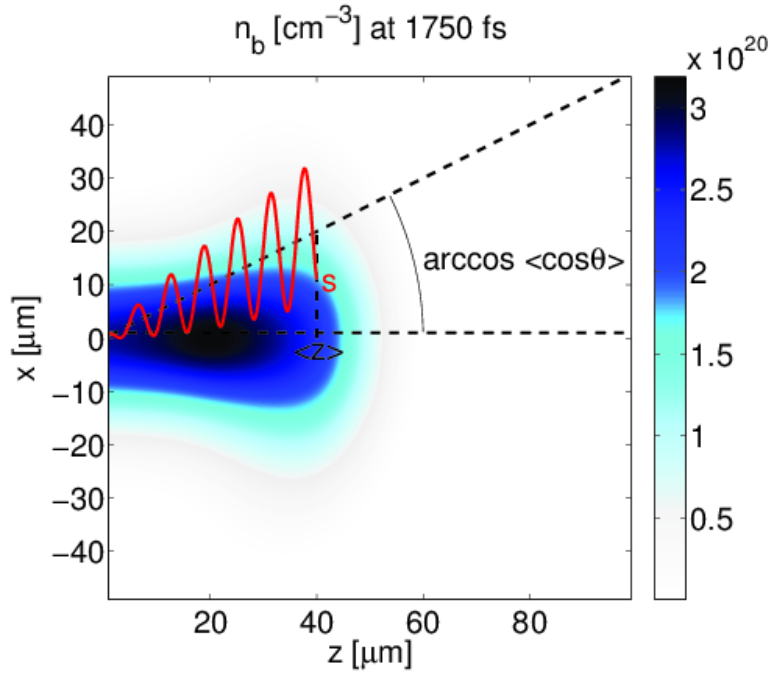


Figure 8.4: Electron beam density n_b [cm^{-3}] at $t = 1750$ fs from the simulation. The electron trajectory (oscillating red curve) is arbitrary and is presented here to illustrate the definitions of the mean cosine of the angle between the z -axis and the position of the beam electron $\langle \cos \theta \rangle$ and the path length following the electron trajectory in the $(\mathbf{r}, \varepsilon)$ space s .

We can evaluate the mean position on the z -axis of a beam electron with an initial energy ε_0 and an initial velocity $\mathbf{v}_0 = v_0 \mathbf{e}_z$ at $z = 0$ by

$$\langle z \rangle(\varepsilon) = \int_0^s \langle \cos \theta \rangle(s) ds = \int_{\varepsilon_0}^{\varepsilon} \langle \cos \theta \rangle(\varepsilon) \left(\frac{d\varepsilon}{ds} \right)^{-1} d\varepsilon. \quad (8.7)$$

Notations are illustrated in **Figure 8.4** : $\langle \cos \theta \rangle$ is the mean cosine of the angle between the z -axis and the position of the beam electron and s is the path length following the electron trajectory in the $(\mathbf{r}, \varepsilon)$ space. In this academic case, the total stopping power can be written

$$\frac{d\varepsilon}{ds} = -S = -4\pi \frac{n_e r_e^2 m_e c^2}{\beta^2} \ln \Lambda_e \quad (8.8)$$

where $\ln \Lambda_e$ is the sum of the Coulomb logarithms $\ln \Lambda_{e\alpha}^{\text{rel}}$ of beam electrons scattering on the bound,

free and screened plasma electrons (6.16), r_e is the classical electron radius and the stopping power on plasma ions has been neglected since $m_e/m_i \ll 1$. For the case of a plasma with degenerate electrons ($T = 1 - 20$ eV $\ll T_F = 351$ eV for $\rho = 50$ g.cm $^{-3}$), the drag number $\ln \Lambda_e$ can be evaluated in the limit $\beta \rightarrow 1$ as

$$\ln \Lambda_e = \ln \frac{m_e c^2}{\hbar \omega_{pe}} + \frac{9}{16} - \frac{\ln 2}{2} + f(\gamma) \quad (8.9)$$

where $f(\gamma) = \ln(\beta\sqrt{\gamma-1}) - [(1/8) + \ln 2]/\gamma + [(1/16) + (1/2)\ln 2]/\gamma^2$ (see **Chapter 4, section 4.2.2**).

The mean cosine $\langle \cos \theta \rangle$ can be evaluated in the M1 model (6.34), (6.35) and (6.61) by noticing that $\langle \cos \theta \rangle = \mathbf{\Omega}_\varepsilon \cdot \mathbf{e}_z$. Then, neglecting the self-generated electromagnetic field \mathbf{E} and \mathbf{B} , we find

$$\frac{d}{ds} \langle \cos \theta \rangle = -k_1 \langle \cos \theta \rangle - \frac{1}{\Psi_0} \frac{\partial}{\partial \mathbf{r}} \cdot (\mathbf{\Pi}_\varepsilon \cdot \mathbf{e}_z) \quad (8.10)$$

where $\mathbf{\Pi}_\varepsilon = \frac{1-\mu}{3} \Psi_0 \mathbf{I} + \Psi_0 \left(\mu - |\mathbf{\Omega}_\varepsilon|^2 \right) \frac{\mathbf{\Psi}_1 \otimes \mathbf{\Psi}_1}{|\mathbf{\Psi}_1|^2}$ and $\frac{d}{ds} = \frac{1}{v} \left[\frac{\partial}{\partial t} + v \mathbf{\Omega}_\varepsilon \cdot \frac{\partial}{\partial \mathbf{r}} - Sv \frac{\partial}{\partial \varepsilon} \right]$.

It has also been noted

$$k_1 = \frac{\nu}{v} = 4\pi \frac{n_e r_e^2}{\gamma^2 \beta^4} \left(\ln \Lambda_e + \ln \Lambda_{ei}^{\text{rel}} \right) \quad (8.11)$$

the inverse of the beam electrons mean free path where $\ln \Lambda_{ei}^{\text{rel}} = \ln [2(3/4\pi n_i)^{1/3}/(\hbar/m_e c)] - 1 + \ln(\sqrt{\gamma^2 - 1}) + 1/\gamma^2$ is the Coulomb logarithm from the stopping power of the beam electrons on ions. Assuming that $|\mathbf{\Omega}_\varepsilon| \approx 1$ which implies $\mathbf{\Pi}_\varepsilon \approx \mathbf{0}$, we may neglect the second term in the right hand side of (8.10) and obtain, in agreement with the multiple scattering theory of Lewis (see **Chapter 4, section 4.3.1**), that

$$\langle \cos \theta \rangle(\varepsilon) \approx \exp \left(- \int_0^s k_1(s) ds \right) = \exp \left(- \int_{\varepsilon_0}^\varepsilon k_1(\varepsilon) \left(\frac{d\varepsilon}{ds} \right)^{-1} d\varepsilon \right). \quad (8.12)$$

As it was suggested in [Solodov and Betti, 2008] and [Robiche et al., 2010], the ratio $\ln \Lambda_{ei}^{\text{rel}} / \ln \Lambda_e$ can be considered as a constant (the ratio $\ln \Lambda_{ei}^{\text{rel}} / \ln \Lambda_e$ attains its minimum when $\gamma = 1$ with the value 0.50 and it is maximum when $\gamma \approx 3$ with the value 0.64) and we obtain

$$\langle \cos \theta \rangle \approx \left[\frac{(\gamma - 1)/(\gamma + 1)}{(\gamma_0 - 1)/(\gamma_0 + 1)} \right] \frac{\ln \Lambda_e + \ln \Lambda_{ei}^{\text{rel}}}{2 \ln \Lambda_e}. \quad (8.13)$$

Following the arguments by [Atzeni et al., 2009b] (see **Chapter 4, section 4.2.2**), we neglect the γ -dependance of $f(\gamma)$ in $(d\varepsilon/ds)^{-1}$ of (8.9) and we note $\ln \Lambda_e^* = \ln(m_e c^2 / \hbar \omega_{pe}) + (9/16) - (\ln 2/2) \approx 7.98$ for $\rho = 50$ g.cm $^{-3}$. Moreover, by considering $(\ln \Lambda_e + \ln \Lambda_{ei}^{\text{rel}}) / 2 \ln \Lambda_e \approx 1$ in $\langle \cos \theta \rangle$ of (8.7), the mean electron propagation distance can be estimated as

$$\langle z \rangle \approx \frac{1}{4\pi n_e r_e^2 \ln \Lambda_e^*} \frac{\gamma_0 + 1}{\gamma_0 - 1} \left[\frac{\gamma_0^2 - 1}{\gamma_0} - \frac{\gamma^2 - 1}{\gamma} - 2 \ln \left(\frac{\gamma_0}{\gamma} \right) \right]. \quad (8.14)$$

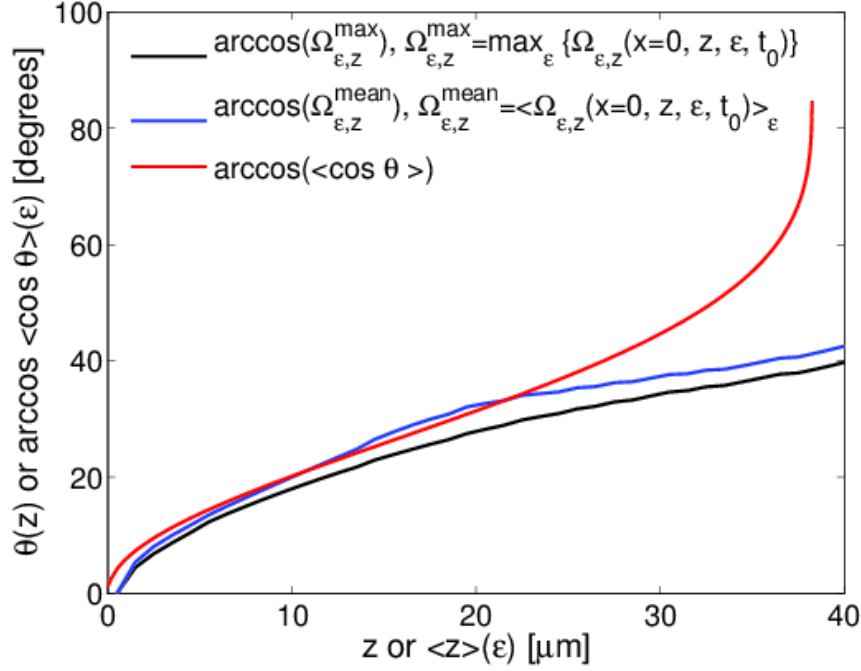


Figure 8.5: Comparison between the simulation results at $t = t_0$: $\arccos(\Omega_{\varepsilon,z}^{\max})$ versus z where $\Omega_{\varepsilon,z}^{\max} = \Omega_{\varepsilon,z}(x=0, z, \varepsilon_m, t_0) = \max_{\varepsilon} \{\Omega_{\varepsilon,z}(x=0, z, \varepsilon, t_0)\}$ (black curve), $\arccos(\Omega_{\varepsilon,z}^{\text{mean}})$ versus z where $\Omega_{\varepsilon,z}^{\text{mean}} = \langle \Omega_{\varepsilon,z}(x=0, z, \varepsilon, t_0) \rangle_{\varepsilon}$ over $|\varepsilon_m - \varepsilon| < 200$ keV (blue curve) and the analytical estimates $\arccos \langle \cos \theta \rangle(\varepsilon)$ (from (8.13)) versus $\langle z \rangle(\varepsilon)$ (from (8.14)) (red curve).

Actually, $(\ln \Lambda_e + \ln \Lambda_{ei}^{\text{rel}}) / 2 \ln \Lambda_e$ is minimum when $\gamma = 1$ with the value 0.75 and it is maximum when $\gamma \approx 3$ with the value 0.82. Then, the penetration depth of the beam electrons with an initial kinetic energy ε_0 and an initial velocity $\mathbf{v}_0 = v_0 \mathbf{e}_z$ at $z = 0$ can be written as

$$L_p = \langle z \rangle(\varepsilon \rightarrow 0) = \xi R \quad (8.15)$$

where

$$R = \int_{\varepsilon_0}^0 \left(\frac{d\varepsilon}{ds} \right)^{-1} d\varepsilon = \frac{1}{4\pi n_e r_e^2 \ln \Lambda_e^*} \frac{(\varepsilon_0/m_e c^2)^2}{1 + \varepsilon_0/m_e c^2} \quad (8.16)$$

is the range of the beam electrons with an initial kinetic energy ε_0 (see **Chapter 4, section 4.2.2**) and

$$\xi = \left(\frac{\gamma_0 + 1}{\gamma_0 - 1} \right)^2 \frac{1}{\beta_0^2} \left(\beta_0^2 - 2 \frac{\ln \gamma_0}{\gamma_0} \right) \quad (8.17)$$

is the correction due to angular scattering. It is equal to 2/3 when $\gamma_0 \rightarrow 1$ and it increases to 1 when $\gamma_0 \rightarrow \infty$. These values are in agreement with the approximation of the penetration depth (30) in [Atzeni et al., 2009b], which assumes a factor $\xi \approx 0.8$ to recover the Monte Carlo simulation. For $\rho = 50 \text{ g.cm}^{-3}$ and $\varepsilon_0 = 1 \text{ MeV}$, we find $R \approx 54 \mu\text{m}$ and $\xi \approx 0.7$, which corresponds to $L_p \approx 38 \mu\text{m}$. This is in agreement with our simulation results shown in **Figure 8.2 a)** and **Figure 8.4**. The estimates (8.13) and (8.14) predict the mean position $\langle z \rangle$ and the mean diffusion angle $\arccos \langle \cos \theta \rangle$

of $\approx 10 \mu\text{m}$ and $\approx 20^\circ$ respectively for $p_z/m_e c = 2.5$, $\approx 20 \mu\text{m}$ and $\approx 30^\circ$ for $p_z/m_e c = 2$ and $\approx 30 \mu\text{m}$ and $\approx 45^\circ$ for $p_z/m_e c = 1.7$. This is in agreement with the numerical results obtained for the electron beam distribution function in the M1 approximation (6.60) as illustrated in **Figure 8.6, panels b), c) and d)**, respectively. Close to $z = L_p$, the analytic estimates $\langle z \rangle$ and $\langle \cos \theta \rangle$ differ from the numerical results as shown in **Figure 8.5**. This is due to the singularity at the penetration depth L_p in this particular case of monoenergetic electron beam in (8.13) and (8.14) and to the fact that the last term in the right hand side of (8.10) cannot be neglected anymore when the local angular distribution is close to be isotropic.

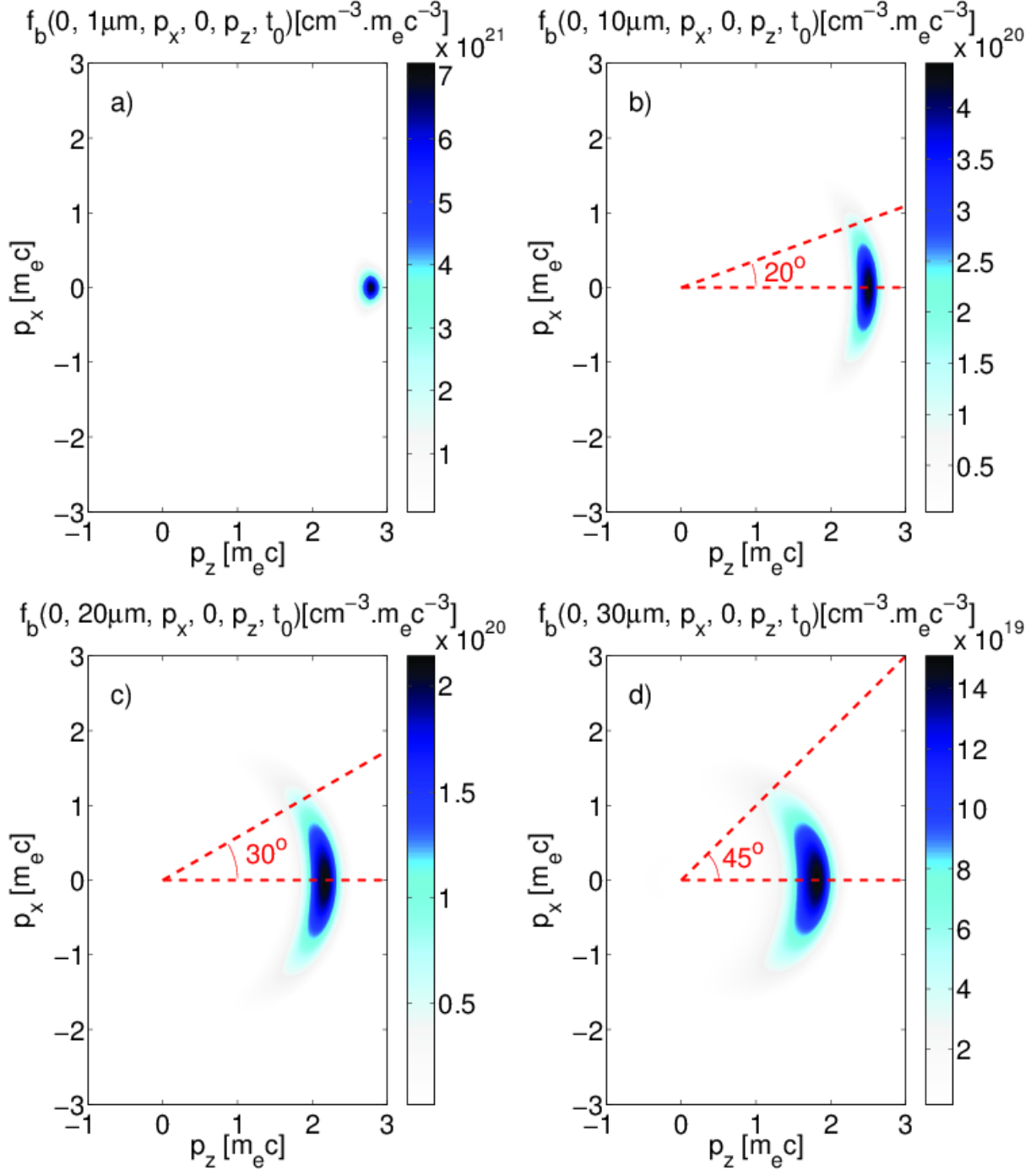


Figure 8.6: Electron beam distribution function f_b [$\text{cm}^{-3} \cdot m_e c^{-3}$] from the simulation on the z -axis at $t = 1750$ fs, $p_y = 0$ and at different depth $z = 1 \mu\text{m}$ (a), $z = 10 \mu\text{m}$ (b), $z = 20 \mu\text{m}$ (c) and $z = 30 \mu\text{m}$ (d). The **dashed red curves** represent the analytical estimates of $\arccos(\cos\theta)(\varepsilon)$ evaluated at the kinetic energies ε corresponding to $\langle z \rangle(\varepsilon) = 10 \mu\text{m}$ (b), $20 \mu\text{m}$ (c) and $30 \mu\text{m}$ (d).

8.1.4 Summary

We have derived an analytical estimate of the temperature of a Hydrogen plasma heated through the direct collisional losses of a monoenergetic and collimated fast electron beam. It is in good agreement with the numerical result close to the fast electron injection zone. That fact validates the numerical scheme used to solve the Heat Equations presented in **Chapter 7, section 7.3**. Moreover, the analytical estimates of the self-generated magnetic fields generated due to the curl of the beam current density and the resistivity gradients, assuming that the Hubbard electrical resistivity follows roughly $\eta = \eta_0(T/T_0)^\alpha$ with $\eta_0 = 9.10^{-9} \Omega.m$ and $\alpha = 0.25$ in the considered range of temperatures. These estimates are in agreement with the magnetic fields calculated numerically close to the fast electron injection zone. The agreement between analytical estimates and numerical solutions concerning the self-generated electromagnetic fields validates the numerical schemes presented in **Chapter 7, section 7.2**. In addition, by neglecting the collective effects in this academic case, we obtained estimates of the mean propagation angle $\langle \cos \theta \rangle$ and the fast electron penetration depth L_p due to collisional effects. An analytical expression of the correction factor

$$\xi = \left(\frac{\gamma_0 + 1}{\gamma_0 - 1} \right)^2 \frac{1}{\beta_0^2} \left(\beta_0^2 - 2 \frac{\ln \gamma_0}{\gamma_0} \right)$$

due to the fast electrons angular scattering have been derived in the expression of the penetration depth L_p in agreement with the empirical value given by [Atzeni et al., 2009b]. The estimates for $\langle \cos \theta \rangle$ and L_p are also in good agreement with the M1 simulation results, thus validating the numerical schemes used to solve the M1 equations presented in **Chapter 7, section 7.1**.

8.2 2D-3V Realistic Simulation of Laser-generated Relativistic Electron Beam Transport

8.2.1 Introduction

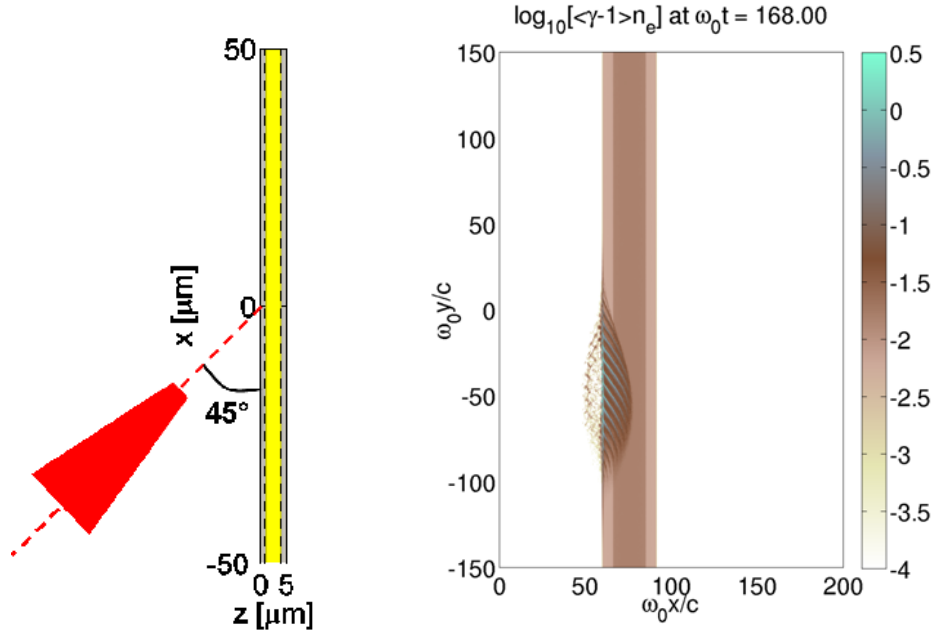


Figure 8.7: (Left panel) Scheme of the thin solid target irradiated by the ultra-high intense laser pulse. (Right panel) 2D spatial map of the mean kinetic energy of the laser-generated fast electrons normalized by $n_e m_e c^2$, at $t = 168 \omega_0^{-1}$ where ω_0 is the laser frequency, according to the Particle-In-Cell (PIC) simulation of the laser plasma simulation conducted by [Gremillet, 2012]. The z -axis in all the following section (like in the Left Panel) corresponds to the x -axis of the PIC simulation picture (Right panel) and the x -axis correspond to the y -axis, respectively

In this section, the M1 model is compared to a hybrid PIC simulation of a relativistic electron beam propagation in a thin solid target, motivated by an experimental campaign [SANTOS et al., 2013]. The target is composed of three successive layers of 1 μm of Aluminum, 3 μm of Copper and 1 μm of Aluminum as illustrated in the left panel of **Figure 8.7**. A linearly polarized laser pulse with a wavelength $\lambda = 800$ nm, a total energy $E_L = 0.7$ J and a 26 fs Full Width at Half Maximum (FWHM) time duration is focused with a peak intensity of $I_L = 3.10^{19}$ W.cm $^{-2}$ at a 45° incident angle. Plasma mirrors have been used in this experiment to avoid prepulse/preplasma so that the main electron acceleration mechanism during the laser-target interaction is the $\mathbf{j} \times \mathbf{B}$ heating (see **Chapter 1, section 1.2**) and the accelerated electrons propagate mainly in the laser pulse propagation direction. The laser-generated fast electron beam's initial properties are obtained from a 2D-2V fully PIC simulation of the laser-plasma interaction [Gremillet, 2012] using the code CALDER [Lefebvre et al., 2003] as illustrated in the right panel of **Figure 8.7**. The energy distribution of the laser-generated electron

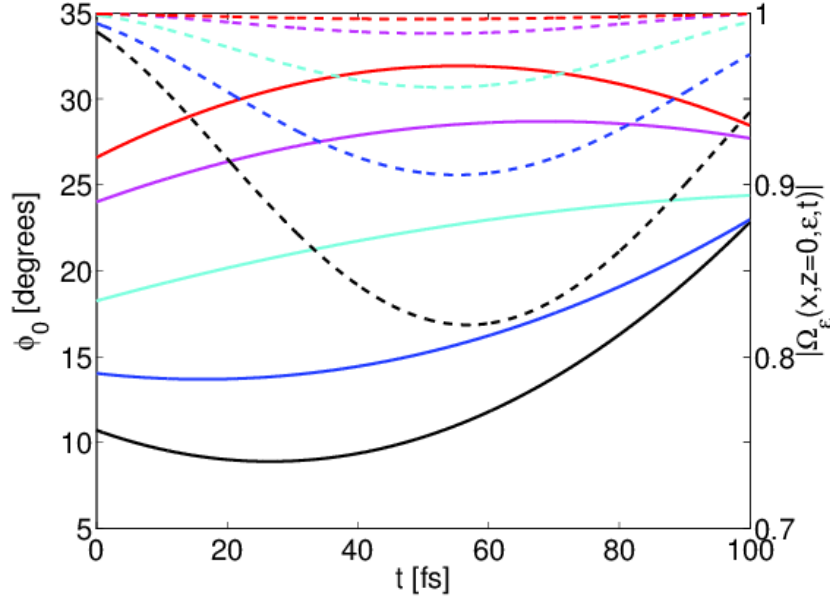


Figure 8.8: Propagation direction angle $\varphi_0(\varepsilon, t)$ (full curves) from PIC simulation and anisotropic parameter $|\Omega_\varepsilon(\varepsilon, t)|$ (dashed curves) deduced from $\Delta\varphi(\varepsilon, t)$ for the different considered energy ranges 20-50 keV (black), 50-100 keV (blue), 100-500 keV (cyan), 500-1000 keV (magenta) and 1000-5000 keV (red).

beam $F_\varepsilon(\varepsilon, t)$, its angular $F_\varphi(\varepsilon, \varphi, t)$ and spatial $F_x(x, t)$ distribution as well as the instantaneous conversion efficiency $\eta_{L \rightarrow e}(t)$ from the laser to the beam have been interpolated by [Gremillet, 2012]. Here, we present how they are adapted to initializing the angular moments Ψ_0 and Ψ_1 at $z = 0$. Firstly, the cut-off $\varepsilon_{\min} = 20$ keV is used to distinguish between the beam electrons and the bulk electrons. Secondly, the initial beam distribution is parameterized according to the PIC simulation:

$$F_\varepsilon(\varepsilon, t) = \begin{cases} 0 & \text{if } \varepsilon > \varepsilon_{\max} \\ \exp \left[\frac{c_1}{(\gamma(\varepsilon) + c_2)^{c_3}} - c_4\gamma(\varepsilon) - c_5 \right] & \text{else} \end{cases}, \quad (8.18)$$

$$F_\varphi(\varepsilon, \varphi, t) = \exp \left[-4 \ln 2 \left(\frac{\varphi - \varphi_0}{\Delta\varphi} \right)^2 \right] \quad (8.19)$$

and

$$F_x(x, t) = \exp \left[-4 \ln 2 \left(\frac{x - x_0}{\Delta x} \right)^2 \right] \quad (8.20)$$

where $c_1(t)$, $c_2(t)$, $c_3(t)$, $c_4(t)$, $c_5(t)$, $\varepsilon_{\max}(t)$, $x_0(t)$, $\Delta x(t)$, $\nu_{L \rightarrow e}(t)$ have a polynomial time dependence and $\Delta\varphi(\varepsilon, t)$ and $\varphi_0(\varepsilon, t)$ have a polynomial time dependence depending on the energy range ($\varepsilon[\text{keV}] \in [20, 50]$, $[50, 100]$, $[100, 500]$, $[500, 1000]$ or $[1000, 5000]$) as illustrated in **Figure 8.8**. In order to

8.2. 2D-3V REALISTIC SIMULATION OF LASER-GENERATED RELATIVISTIC ELECTRON BEAM TRANSPORT

relate these fits with the angular moments Ψ_0 and Ψ_1 of the M1 model, we assume

$$\boldsymbol{\alpha}_1(\boldsymbol{\Omega}_\varepsilon(x, z=0, \varepsilon, t)) = \frac{8 \ln 2}{\Delta\varphi(\varepsilon, t)^2} \begin{pmatrix} \sin \varphi_0(\varepsilon, t) \\ 0 \\ \cos \varphi_0(\varepsilon, t) \end{pmatrix}, \quad (8.21)$$

which is equivalent to

$$\boldsymbol{\Omega}_\varepsilon(x, z=0, \varepsilon, t) = \left| \coth \left(\frac{8 \ln 2}{\Delta\varphi(\varepsilon, t)^2} \right) - \frac{\Delta\varphi(\varepsilon, t)^2}{8 \ln 2} \right| \begin{pmatrix} \sin \varphi_0(\varepsilon, t) \\ 0 \\ \cos \varphi_0(\varepsilon, t) \end{pmatrix} \quad (8.22)$$

in such a way that, in agreement with the angular notations introduced in **Chapter 7, Figure 7.1**,

$$\begin{aligned} & \int_0^\pi \Psi_{\text{M1}}(x, z=0, \varepsilon, \theta, \varphi, t) \sin \theta d\theta \\ = & \Psi_0(x, z=0, \varepsilon, t) \frac{|\boldsymbol{\alpha}_1(\varepsilon, t)|}{4 \sinh |\boldsymbol{\alpha}_1(\varepsilon, t)|} \left\{ \begin{aligned} & I_1 \left[|\boldsymbol{\alpha}_1(\varepsilon, t)| \cos(\varphi - \varphi_0(\varepsilon, t)) \right] \\ & + L_{-1} \left[|\boldsymbol{\alpha}_1(\varepsilon, t)| \cos(\varphi - \varphi_0(\varepsilon, t)) \right] \end{aligned} \right\} \\ \approx & \frac{\Psi_0(x, z=0, \varepsilon, t)}{\sqrt{2\pi} \frac{\Delta\varphi(\varepsilon, t)^2}{8 \ln 2}} \exp \left[-4 \ln 2 \frac{(\varphi - \varphi_0(\varepsilon, t))^2}{\Delta\varphi^2} \right]. \end{aligned} \quad (8.23)$$

as already discussed in **Chapter 6, section 6.2.3**. The first angular moment has been initialized as follows:

$$\Psi_0(x, z=0, \varepsilon, t) = N_0(t) f_x(x, t) f_z(z=0, t) f_\varepsilon(\varepsilon, t) \quad (8.24)$$

where

$$N_0(t) = \nu_{L \rightarrow e}(t) \frac{E_L}{k_B T_{b0}(t) \sqrt{2\pi} \frac{\Delta y^2}{8 \ln 2}} \quad (8.25)$$

is the number of electrons per unit length in the third y -dimension (not taken into account in this simulation) with $\Delta y = 8.6 \mu\text{m}$,

$$f_x(x, t) = \frac{F_x(x, t)}{\sqrt{2\pi} \frac{\Delta x(t)^2}{8 \ln 2}} \quad (8.26)$$

is the normalized transverse spatial distribution function,

$$f_z(z=0, t) = \frac{1}{V_b(t) \sqrt{2\pi} \frac{\Delta t^2}{8 \ln 2}} \exp \left[-4 \ln 2 \left(\frac{t - t_c}{\Delta t} \right)^2 \right] \quad (8.27)$$

is the normalized longitudinal spatial distribution at $z = 0$ and

$$f_\varepsilon(\varepsilon, t) = \frac{F_\varepsilon(\varepsilon, t)}{\int_{\varepsilon_{\min}}^{\infty} F_\varepsilon(\varepsilon, t) d\varepsilon} \quad (8.28)$$

is the normalized energy spectrum of the fast electrons. Here, $t_c = 40$ fs,

$$k_B T_{b0}(t) = \langle \varepsilon \rangle(t) = \int_{\varepsilon_{\min}}^{\infty} \varepsilon f_\varepsilon(\varepsilon, t) d\varepsilon \quad (8.29)$$

is the initial "beam temperature" and

$$V_b(t) = \frac{\langle \varepsilon \mathbf{v} \rangle(t)}{\langle \varepsilon \rangle(t)} \cdot \mathbf{e}_z = \int_{\varepsilon_{\min}}^{\infty} \frac{\varepsilon v(\varepsilon)}{k_B T_{b0}(t)} |\boldsymbol{\Omega}_\varepsilon(x, z = 0, \varepsilon, t)| \cos(\varphi_0(\varepsilon, t)) f_\varepsilon(\varepsilon, t) d\varepsilon \quad (8.30)$$

is the velocity at which the beam kinetic energy is injected in the simulation box at $z = 0$ in the z -direction. Finally, the first order angular momentum is initialized according to (8.21) :

$$\boldsymbol{\Psi}_1(x, z = 0, \varepsilon, t) = \Psi_0(x, z = 0, \varepsilon, t) \boldsymbol{\Omega}_\varepsilon(x, z = 0, \varepsilon, t). \quad (8.31)$$

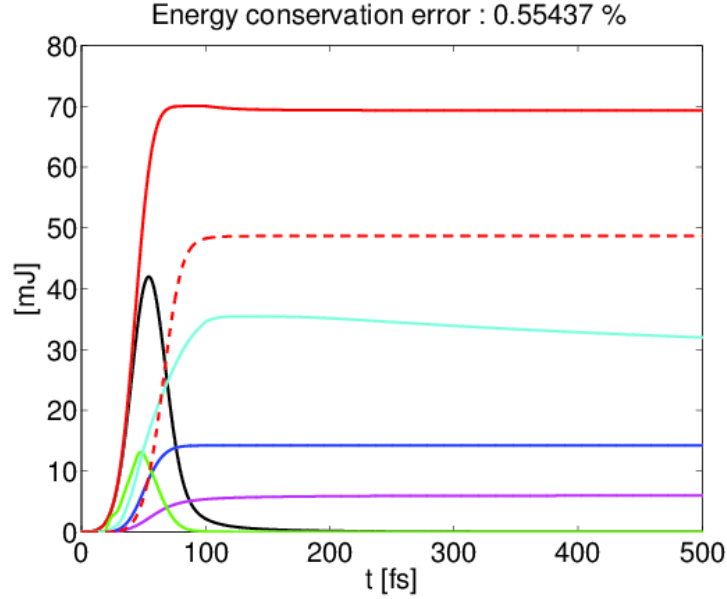


Figure 8.9: Instantaneous beam energy $U_b \times 10$ (solid black), integrated beam energy balanced between injected and escaping electrons at $z = 0$ U_{inc} (solid red), escaped energy U_{out} at $z = 5 \mu\text{m}$ (dashed red), total collisional energy loss U_{col} (solid magenta), total “collective” U_{res} energy loss (solid blue), instantaneous electric energy $U_E \times 10^3$ (solid green) and instantaneous magnetic energy $U_B \times 10^3$ (solid cyan) from the M1 simulation according to the formula given in **Chapter 7, section 7.4.1**.

For this transport simulation, the Eidmann-Chimer model for the electrical resistivity and the thermal conductivity, introduced in **Chapter 3, section 3.3.1**, have been used (see **Figure 3.8**). The More formula for the ionization state Z^* has been used without the corrections introduced in **Chapter 6, section 6.3.1**. Both background electron and ion heat equations have been computed with the plasma expression for the thermal capacities and the electron-ion coupling factor. The spatial resolution has been chosen $\Delta x = \Delta z = 0.25 \mu\text{m}$ while the energy resolution has been chosen $\Delta \varepsilon = 10$ keV, in the range from $\varepsilon_{\text{min}} = 20$ keV to 3 MeV so that the computation time needed is about 4 hours and 40 minutes on 20 CPU. Absorbing conditions at the target boundaries have been used so that the refluxing of the beam electrons at both the rear and irradiated sides of the target was suppressed. As illustrated in **Figure 8.9**, the percentage of error in the energy conservation equation is about 0.5%. The total injected energy at $z = 0$ is ≈ 70 mJ, which represents a conversion efficiency from the laser to the electron beam of $\approx 10\%$. The electromagnetic energy is negligible compared to the beam energy by a factor ≈ 1000 . The heating of the target due to the return current (≈ 10 mJ) exceeds by roughly two times the direct collisional heating by the beam electrons. Thus, contrary to the previous academic case, collective effects are here predominant. Indeed, while the maximum initial beam density is close to the critical density $n_{b,\text{max}} \approx 10^{21} \text{ cm}^{-3}$, the maximum value of the initial beam current density $\mathbf{j}_{b,\text{max}}$ is above $10^{12} \text{ A.cm}^{-2}$ and the Aluminum and Copper electrical resistivity is much higher than that of Hydrogen (see **Figure 3.8**).

8.2.2 Comparison with the Hybrid PIC Simulation

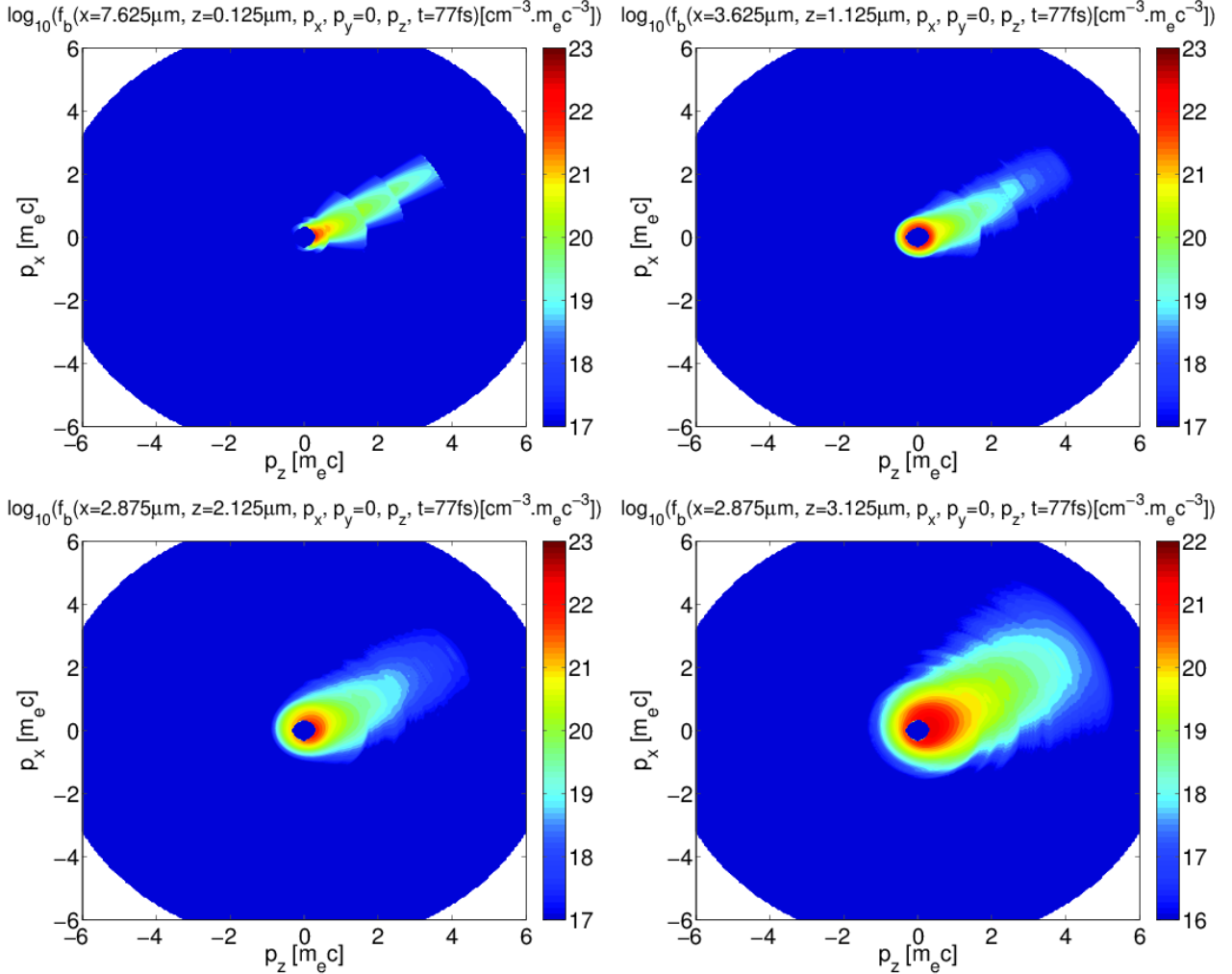


Figure 8.10: Distribution function $f_b(p_x, p_z)$ from the M1 simulation at $t = 77$ fs and different target depth : $z = 0.125 \mu\text{m}$ (Up Left), $z = 1.125 \mu\text{m}$ (Up Right), $z = 2.125 \mu\text{m}$ (Down Left) and $z = 3.125 \mu\text{m}$ (Down Right). Each plot corresponds to the transverse position x where the beam density n_b is maximum at the given depth z .

Figure 8.10 shows the evolution of the fast electron distribution function f_b with the target depth. It is plotted in the plane (p_x, p_y) since the M1 distribution function is locally axisymmetric around the mean propagation direction Ω_ε . At $z = 0.125 \mu\text{m}$, we can distinguish between the different initial angular distributions, depending on the energy range ($\varepsilon[\text{keV}] \in [20, 50]$, $[50, 100]$, $[100, 500]$, $[500, 1000]$ or $[1000, 5000]$), as explained above. In the first cells of Copper located at $z = 1.125 \mu\text{m}$, the lower energy electrons are already almost fully isotropized while the more energetic ones retain their initial anisotropy. The angular spread rises with increasing depth z while the mean energy steadily decreases.

8.2. 2D-3V REALISTIC SIMULATION OF LASER-GENERATED RELATIVISTIC ELECTRON BEAM TRANSPORT

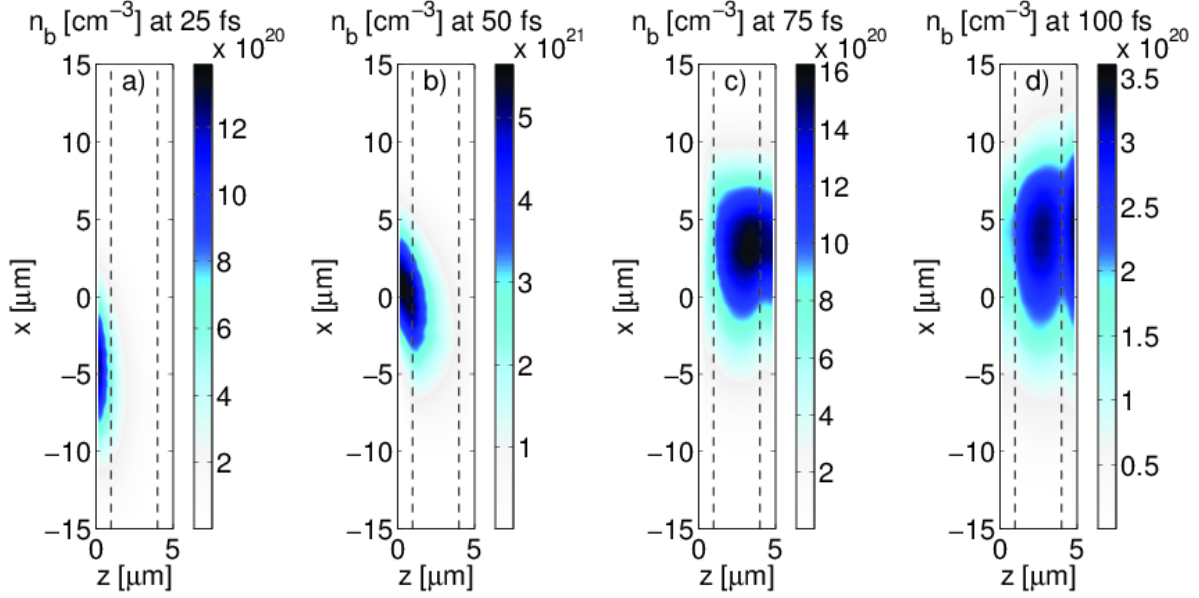


Figure 8.11: Electron beam density n_b [cm^{-3}] from the M1 simulation at $t = 25$ fs (a), $t = 50$ fs (b), $t = 75$ fs (c), and $t = 100$ fs (d),

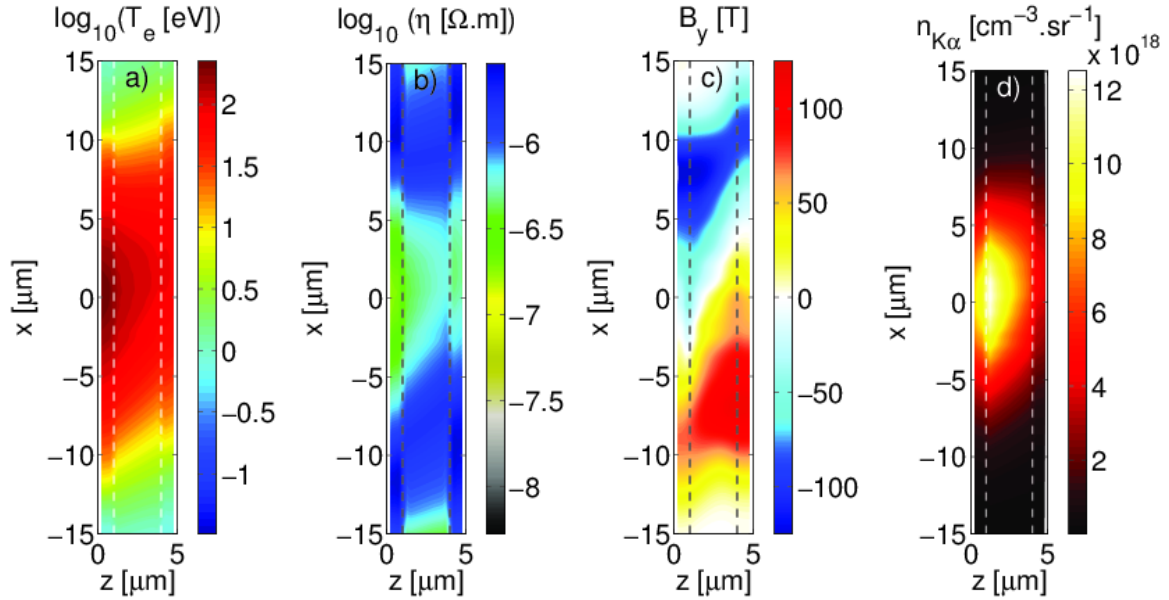


Figure 8.12: Plasma electron temperature T_e [eV] in a logarithmic scale (a), plasma electrical resistivity η [$\Omega\cdot\text{m}$] in a logarithmic scale (b), self-generated magnetic field B_y [T] (c) and time integrated density of K α photons emitted per steradian $n_{K\alpha}$ [$\text{cm}^{-3}\cdot\text{sr}^{-1}$] (d) from the M1 simulation at $t = 500$ fs.

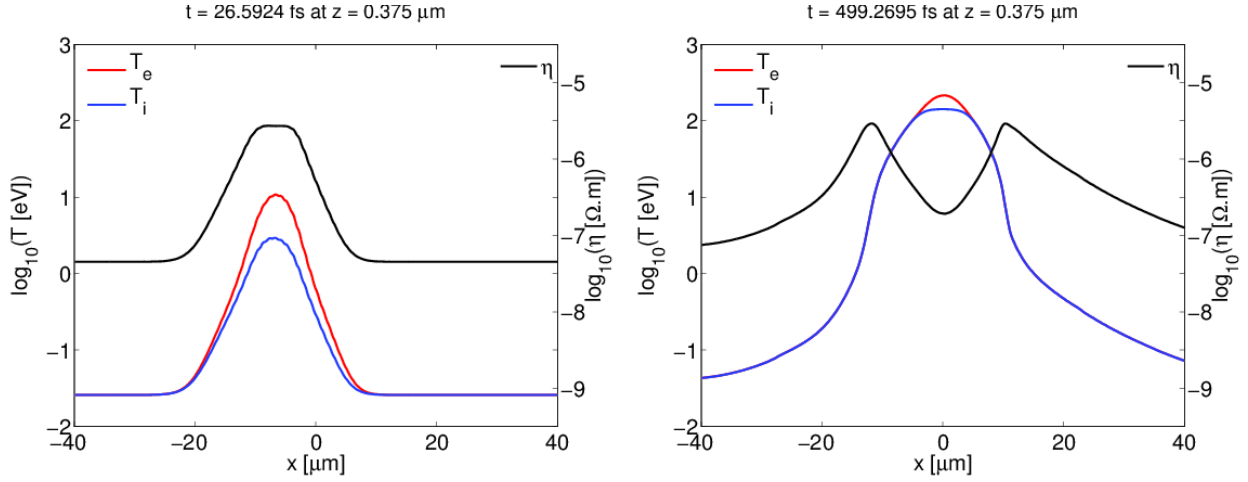


Figure 8.13: Slices at $z = 0.375$ μm of the resistivity (black curve), the electron temperature (red curve) and the ion temperature (blue curve) at $t = 26.6$ fs (Left panel) and $t = 499.3$ fs (Right panel).

According to **Figures 8.9** and **8.11**, almost all beam electrons reach the rear side of the target after approximately 100 fs. The self-generated magnetic field reaches its maximum value of approximately 200 T in the first Aluminum layer at the end of the beam propagation and then decreases down to 100 T at 500 fs (see **Figure 8.12 c**). The main contribution to the magnetic field is due to the curl of the beam current density but the electrical resistivity gradients play also an important role: at 27 fs, the plasma electrons have been heated up to the Fermi temperature (≈ 10 eV) in the first Aluminum layer as illustrated in the left panel of **Figure 8.13**. Consequently, the electrical resistivity in this area goes from the solid-liquid phase to the hot plasma phase and decreases with the temperature. The same scenario appears in the Copper layer at 40 fs and later in the rear Aluminum layer. The consequence is that the electrical resistivity gradients tend to hollow the beam as illustrated in the right panel of **Figure 8.13** and explained in **Chapter 3, section 3.3.3**. In spite of the relative complexity of this laser-generated electron beam transport, the results of the M1 simulation are close to those of the 3D-3V hybrid PIC simulation performed with distinct (although similar) models for the thermodynamic parameters (Z^* , η , κ_e , $C_{V,e}$, $C_{V,i}$ and G). The same behaviour is recovered for the temperature profile of the target as shown in **Figure 8.14**. We can observe the signature of a dominant Ohmic heating in the Copper layer ($z = 1 \rightarrow 4$ μm) where the temperature profile is lower. Indeed, Copper is less resistive but denser than Aluminum; if direct collisional losses were dominant, the Copper temperature would be higher than in Aluminum, which is not the case here.

8.2.3 Conclusion

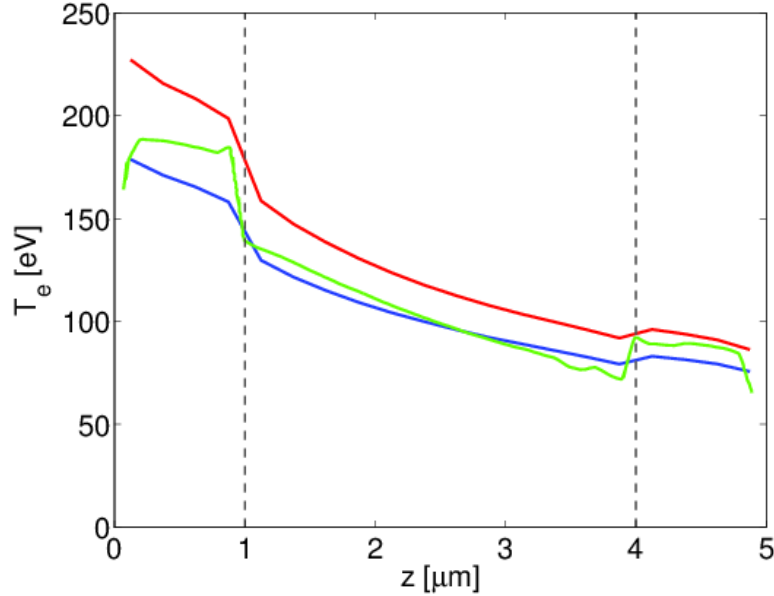


Figure 8.14: Comparison at $t = 500$ fs between the mean electron temperature $\langle T_e \rangle$ over $|x_{\max} - x| < 5 \mu\text{m}$ profile obtained with M1 (blue) and the one obtained with the hybrid PIC code Paris (green) [Gremillet, 2012]. x_{\max} is defined as the position where $T_e(x_{\max}, z)$ is the maximum electron temperature at a given depth z (red).

The test simulation performed in this section shows that the M1 model reproduces well the results obtained with a hybrid PIC simulation concerning a realistic laser-generated electron beam transport, inspired by an experimental campaign conducted on the UHI100 laser facility. The initial beam distribution is deduced from a 2D PIC simulation of the laser-plasma interaction. The electron beam density and current temporal evolution as well as the self-generated electromagnetic fields are in agreement with the hybrid PIC simulation. The final temperature in the target agrees with the hybrid PIC results, showing the dominance of the collective effects. The time integrated emission of $K\alpha$ photons has been computed by using the empirical expression for K-shell ionization cross section by electron impact [Hombourger, 1998] and the K-shell fluorescence yield probability provided by [Bambynek, 1984]. It is plotted in **Figure 8.12 d)** at $t = 500$ fs. There is an important discrepancy between the simulation result and the experimental data concerning the $K\alpha$ spot size. This can be explained by the refluxing of beam electrons from the target boundaries, which enhances their lateral expansion and consequently increases the $K\alpha$ emission spot size. Note, however, that, at this stage, collisions between the background free electrons and the d-band electrons in Copper are not taken into account. These two effects will be considered in **Part III**.

Part III

Applications to the Study of Laser-Generated Fast Electron Beam Transport in the Context of ICF

Chapter 9

Application to the $K\alpha$ emission during Fast Electron Transport in Solid Targets

"God made solids, but surfaces were the work of the devil."

Wolfgang Pauli

From an experimental point of view, many methods may be used to diagnose the properties of electrons produced by intense laser pulses, including vacuum electron spectrometry [Wei et al., 2004] [Yabuuchi et al., 2010], nuclear activation [Hatchett et al., 2000] [Ledingham et al., 2000], optical emission from foams [Jung et al., 2005], optical probing [Norreys et al., 2006] [Ping et al., 2012], x-rays bremsstrahlung spectrometry [Chen et al., 2009] [Westover et al., 2011], Incoherent Transition Radiation (ITR) or Coherent Transition Radiation (CTR) spectrometry and imagery [Santos et al., 2002] [Storm et al., 2009] and $K\alpha$ fluorescence measurements [Stephens et al., 2004] [Baton et al., 2008]. Each technique has advantages and disadvantages for measuring aspects of the electron beam. The vacuum electron spectroscopy measures the properties of electrons escaping the target, which may differ from those of the electrons in the bulk of the material [Yabuuchi et al., 2010]. The nuclear activation is likewise sensitive to very energetic (> 10 MeV) x-rays, which are produced by high-energy electrons outside the spectral region with the best coupling to the dense core in Fast Ignition [Kodama R. et al., 2002]. The x-ray bremsstrahlung spectrometers, that measure the light emitted by the fast electrons thanks to a set of compact filter-stack based x-ray detectors, are sensitive to x-rays in the 10-700 keV range corresponding to energetic electrons (> 1 MeV) [Westover et al., 2011]. The CTR and ITR techniques are operating in the visible domain by detecting the emission produced by fast electrons crossing the rear target. [Santos et al., 2002] showed that by imaging this transition radiation, the spatial distribution of electrons emerging from the target can be accurately measured. When the emerging hot electron flux is modulated at the laser frequency and/or its harmonics, the emitted CTR can be much brighter than the ITR that results from un-bunched electrons. The coherent addition of the transition radiation from periodically bunched hot electrons also yields information on the acceleration mechanism, as the spectrum of the CTR is intimately related to the period of the bunches [Baton et al., 2003] [Zheng et al., 2003] [Schroeder et al., 2004] [Bellei et al., 2012].

The most commonly used diagnostic is the imaging of X-rays that are produced in the cold target material as the electrons propagate through the target. The $K\alpha$ radiation is due to the atomic electron transitions to K-shell holes produced in a collision of a hot electron with an atom of the target material; see **Figure 9.1**. When an outer shell electron fills the vacancy, the energy is released in a form of Auger electron or an emission of a photon. The cross section for this K-shell electron impact ionization peaks at the electron energy roughly two to three times the ionization energy and decays slowly at higher energies. Since most materials used in experiments have K-shell transitions in the tens of keV range, this X-ray imaging technique is, in principle, sensitive to electrons with energies as low as tens of keV. However, with an electron energy distribution extending to much higher energies, the signal of the lowest energy electrons will be diminished and masked. Imaging this K-shell X-ray emission with a spherically bent diffraction crystal has become so a powerful diagnostic of hot electron beams. However, it has been shown that a $K\alpha$ image is not solely determined by the initial population of forward directed hot electrons, but also depends upon “delayed” hot electrons, and in fact continues to evolve long after the end of the laser interaction [Ovchinnikov et al., 2011]. Firstly, there is a population of hot electrons created in the laser-plasma interaction that acquire

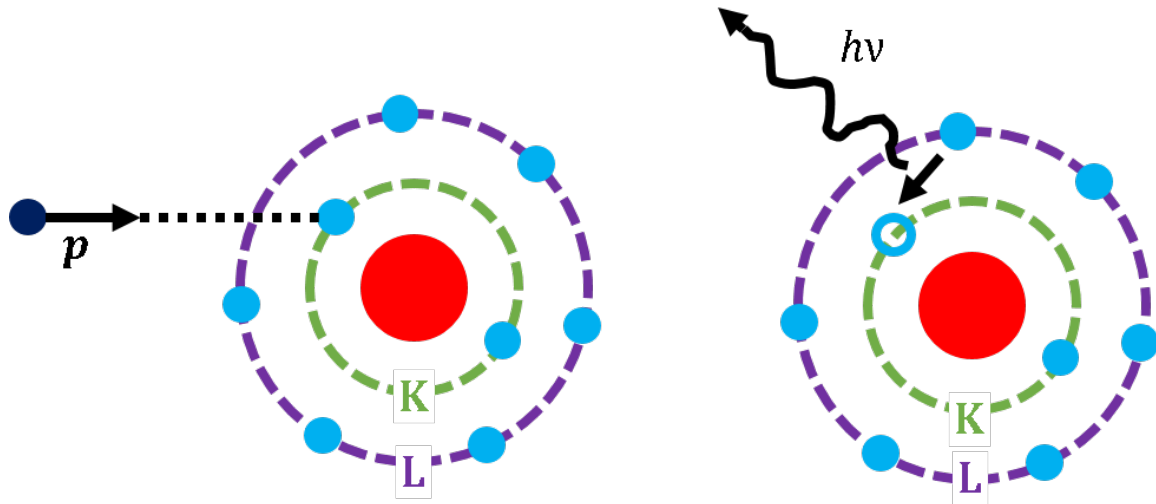


Figure 9.1: Scheme illustrating the collisional ionization of a K-shell electron of a cold atom by a laser-generated fast electron (Left panel) and the recombination of the electron-generated hole by a L-shell electron of the cold atom, which results in the emission of a $K\alpha$ photon (Right panel).

a velocity direction opposite that of the laser and subsequently reflux off the front surface of the target, deflect when they encounter magnetic fields and then spread far from the laser focal spot [Pérez et al., 2013]. These delayed fast electrons create significant features in the $K\alpha$ time-integrated images. Secondly, the electrons refluxing from the sides and the rear of the target also contribute to the final $K\alpha$ image [Ovchinnikov et al., 2011]. Indeed, shortly after the beginning of the laser-plasma interaction, the hot electrons leave the target, making it positively charged. This gives rise to strong electric fields that cause most of the escaping electrons return to the target. In some experiments the refluxing is minimized by increasing the target dimensions and/or by using materials with short stopping distances.

More recently, a novel technique of shadowgraphy coupled to phase contrast imaging has been proposed. The Linac Coherent Light Source (LCLS) at the SLAC National Accelerator Laboratory in Stanford (United States of America) is one of few available sources of high peak brightness photons suitable for studies of transient behaviour of hot electrons. They can provide a sub-ps temporal resolution and a spatial resolution of the order of several $10\ \mu\text{m}$ (inaccessible for conventional sources). The basic principle of this novel technique relies on the shift of the K-edge of the target atoms after the hot electrons have created a K-shell vacancy. This shift is sufficiently large (about 400 eV for an electron in the K-shell of Copper according to Atomic Physic numerical computations) to be used as a femtosecond X-ray switch. This technique will allow to observe traces of hot electron transport, depending on whether electrons have created K-shell hole(s) or not in the atoms, thus leading to a transparent or opaque material for the LCLS photons. The vacancies created by a collisional ionization of cold atoms are also those responsible for the emission of $K\alpha$ photons. Tuned to a photon energy just above the K-edge, these photons, primarily absorbed before the hot electrons propagate, will be

transmitted after their propagation. However, this technique, directly related to the $K\alpha$ emission, can be biased because of refluxing of hot electrons at boundaries. Cross-correlation of this $K\alpha$ emission with direct observations of the hot electrons inside the sample may remove this ambiguity.

This chapter is dedicated to the implementation of the commonly used $K\alpha$ photons diagnostic in the M1 model for the fast electron transport in solids or dense plasmas, presented in **Part II**. Indeed, thanks to the fast computations allowed by the M1 model, sufficiently long times (several tens of ps) and large spatial dimensions (several hundreds of μm) can be computed with a relatively small computational cost. We will study the recirculation of the fast electrons due to their reflection at the target borders, the K-shell hole dynamics and 3-dimensional effects on photon emission. It will be also possible to apply these developments to the novel technique of shadowgraphy based on the LCLS X-ray source. In a first time, the model for the computation of the emission of $K\alpha$ photons is presented. Secondly, the model is applied to the interpretation of experiments conducted by [SANTOS et al., 2013] on the UHI100 laser facility of the CEA (Saclay) introduced in the previous section **Chapter 8, section 2**. The source of fast electrons was calculated by [Gremillet, 2012] with a fully Particle-In-Cell (PIC) simulation. The electron transport is described with the M1 model by taking into account the reflexing effect. The emission of $K\alpha$ photons emitted by the Copper tracer layer located at different depths is calculated and compared with the experimental results.

9.1 Computational Methods for Estimating the Emission of $K\alpha$ Photons

9.1.1 Fast Electron Recirculation and M1 Model for Fast Electron Transport

Fast Electron Recirculation in the M1 Model

The $K\alpha$ images obtained in the laser plasma interaction experiments are contaminated by the electrons refluxing off the target sides. Indeed, the propagation of fast electrons in vacuum is limited by the Alfvén-Lawson limit $I_{\text{max}} \approx -17\gamma_b\beta_b$ kA and the space charge electric field. Most of the beam electrons are thus strongly decelerated and then accelerated in the opposite direction by the space charge electric field at the target boundary in the beam Debye sheath $\lambda_{D,b} = \sqrt{k_B T_b / 4\pi\Gamma_b n_b e^2} \approx 7.43 \cdot 10^{-3} \mu\text{m} \sqrt{T_b[\text{keV}] / \Gamma_b n_b [10^{21} \text{cm}^{-3}]}$, which is less than one micron. Here, $k_B T_b$ is the beam electrons temperature (and not their mean kinetic energy!) and $\Gamma_b = \Gamma(\mathbf{p}_b)$ is the bulk Lorentz factor where \mathbf{p}_b is the mean momentum of beam electrons. In a first attempt, electron refluxing can be described as specular reflections off the target boundaries.

However, one issue of the M1 model is that, by working with the angular averaged values, it

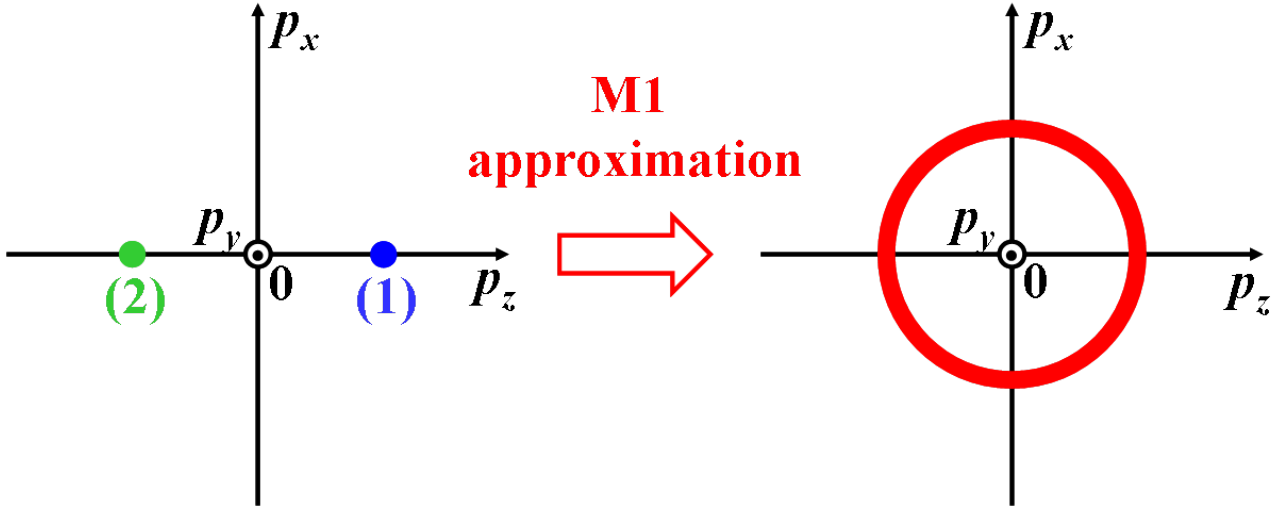


Figure 9.2: Schematic illustrating the M1 limitation in the case of two counterpropagating anisotropic and monoenergetic electron beam having the same energy.

cannot make a distinction between an isotropic angular distribution function and two monoenergetic, collimated and counterpropagating electron beams, as illustrated in **Figure 9.2**. It might be possible to extend the model to the second order of the hierarchy M2. In this approach, the three first angular moments are computed according to

$$\frac{\partial \Psi_0}{\partial t} + \frac{\partial}{\partial \mathbf{r}} \cdot (v \Psi_1) - \frac{\partial}{\partial \varepsilon} (v S \Psi_0 + e v \Psi_1 \cdot \mathbf{E}) = 0, \quad (9.1)$$

$$\frac{\partial \Psi_1}{\partial t} + \frac{\partial}{\partial \mathbf{r}} \cdot (v \Psi_2) - \frac{\partial}{\partial \varepsilon} (v S \Psi_1 + e v \Psi_2 \cdot \mathbf{E}) = -\frac{e}{p} (\Psi_0 \mathbf{I} - \Psi_2) \cdot \mathbf{E} - \frac{e}{\gamma m_e c} \Psi_1 \times \mathbf{B} - \nu \Psi_1 \quad (9.2)$$

and

$$\begin{aligned} & \frac{\partial \Psi_2}{\partial t} + \frac{\partial}{\partial \mathbf{r}} \cdot (v \Psi_3) - \frac{\partial}{\partial \varepsilon} (v S \Psi_2 + e v \Psi_3 \cdot \mathbf{E}) \\ &= -\frac{e}{p} (\Psi_1 \otimes \mathbf{E} + \mathbf{E} \otimes \Psi_1 - 2 \Psi_3 \cdot \mathbf{E}) - \frac{2e}{\gamma m_e c} [\Psi_2 \cdot \mathbf{T}(\mathbf{B}) - \mathbf{T}(\mathbf{B}) \cdot \Psi_2] - 3\nu \left(\Psi_2 - \frac{1}{3} \Psi_0 \mathbf{I} \right) \end{aligned} \quad (9.3)$$

where it has been noted $\mathbf{T}(\mathbf{B})$ the tensor

$$\mathbf{T}(B_x, B_y, B_z) = \begin{pmatrix} 0 & B_z & -B_y \\ -B_z & 0 & B_x \\ B_y & -B_x & 0 \end{pmatrix} \text{ such that } \forall \mathbf{V} \in \mathbb{R}^3, \mathbf{T}(\mathbf{B}) \cdot \mathbf{V} = \mathbf{V} \times \mathbf{B}.$$

The third order angular moment Ψ_3 (third order tensor \rightarrow 27 terms) must be computed according to the Minerbo maximum entropy criterion in order to close the system. However, this option is outside the scope of this thesis.

Two Sets of M1 Equations as a Solution for the M1 Limitation

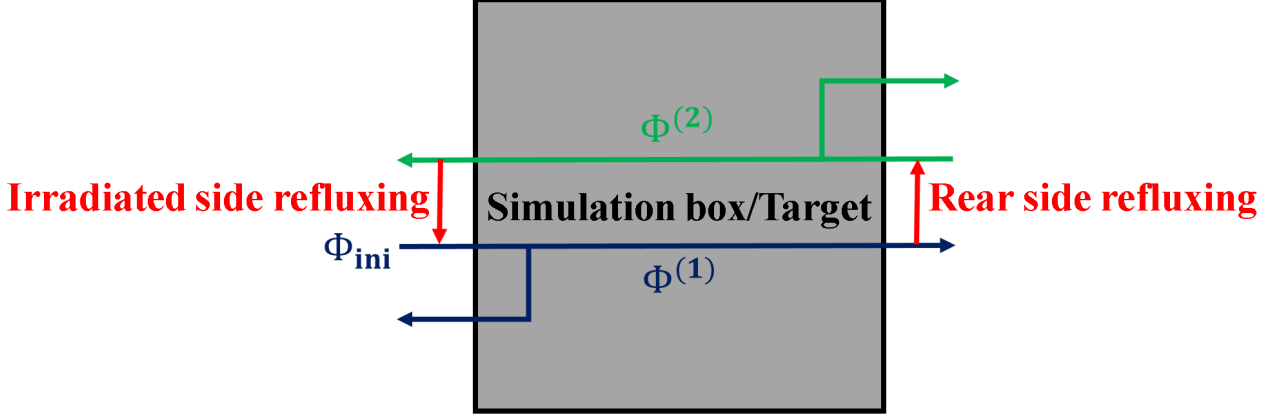


Figure 9.3: Schematic of the method used to account for the fast electrons refluxing at the laser-irradiated side and/or the rear side of the target by solving two sets of M1 equations for two counterpropagating fast electron beams.

Instead, we choose another possibility that consists in solving two sets of M1 equations for each counterpropagating electron beam in order to account for the fast electrons refluxing : one set of M1 equations (see **Chapter 6, section 6.2**), for the angular moments $\Psi_0^{(1)}$ and $\Psi_1^{(1)}$, is computed for the fast electrons population propagating in the laser pulse propagation direction and another one, for the angular moments $\Psi_0^{(2)}$ and $\Psi_1^{(2)}$, is computed for the refluxed electrons population that propagate in the opposite direction. While the absorbing boundary conditions, detailed in **Chapter 7, section 7.1.6**, are not modified, we initialize the electron beam ⁽²⁾ propagating in the backward direction upon assuming specular reflections off the target rear side of the forward-propagating beam ⁽¹⁾. It is expected that we do not lose much of physics since $\lambda_{D,b}$ is small compared to the considered space scales Δz and since only a small part of fast electrons is escaping from the target (few percents). From a numerical point of view, it reads, according to the HLL scheme for the fast electrons spatial advection (see **Chapter 7** for the notations) :

$$\text{If } \Psi_{1,z}^{(1),n,i,j,N_z,l} > 0 \text{ then } \begin{cases} \Psi_0^{(2),n,i,j,N_z+2,l} = \Psi_0^{(2),n,i,j,N_z+1,l} = \Psi_0^{(1),n,i,j,N_z,l} \\ \Psi_{1,x}^{(2),n,i,j,N_z+2,l} = \Psi_{1,x}^{(2),n,i,j,N_z+1,l} = \Psi_{1,x}^{(1),n,i,j,N_z,l} \\ \Psi_{1,y}^{(2),n,i,j,N_z+2,l} = \Psi_{1,y}^{(2),n,i,j,N_z+1,l} = \Psi_{1,y}^{(1),n,i,j,N_z,l} \\ \Psi_{1,z}^{(2),n,i,j,N_z+2,l} = \Psi_{1,z}^{(2),n,i,j,N_z+1,l} = -\Psi_{1,z}^{(1),n,i,j,N_z,l} \end{cases} \quad (9.4)$$

else $\phi^{(2),n,i,j,N_z+2} = \phi^{(2),n,i,j,N_z+1} = \mathbf{0}$

and

$$\text{If } \Psi_{1,z}^{(2),n,i,j,2,l} < 0 \text{ then } \phi^{(2),n,i,j,0,l} = \phi^{(2),n,i,j,1,l} = \phi^{(2),n,i,j,2,l} \quad (9.5)$$

else $\phi^{(2),n,i,j,0,l} = \phi^{(2),n,i,j,1,l} = \mathbf{0}$.

Concerning the other boundary conditions at $x = \pm L_x/2$, $y = \pm L_y/2$, $\varepsilon = \varepsilon_{\min}$ and $\varepsilon = L_\varepsilon$, we use

the boundary conditions explained in **Chapter 7, section 7.1.6**, assuming L_x and L_z are taken sufficiently large (several hundreds of μm) to avoid fast electrons refluxing at the target lateral boundaries as it is usually the case in experiments.

Also, the use of large transverse dimensions L_x and L_y allows us to neglect the electromagnetic fields at the transverse simulation box boundaries $\pm L_x/2$ and $\pm L_y/2$, as explained in **Chapter 7, section 7.2.3**. However, contrary to **Chapter 7, section 7.2.3**, we cannot impose the same boundary condition at the target rear side $z = L_z$. Instead of Equations (7.88) and (7.92), we impose the same boundary conditions as at the irradiated side of the target (7.89) and (7.93). It reads respectively :

$$\mathbf{B}^{n,i,j,N_z+2} = \mathbf{B}^{n,i,j,N_z+1} = \mathbf{B}^{n,i,j,N_z} \quad (9.6)$$

and

$$\mathbf{E}^{n,i,j,N_z+2} = \mathbf{E}^{n,i,j,N_z+1} = \mathbf{E}^{n,i,j,N_z} . \quad (9.7)$$

In the case of a normally incident laser pulse on a solid target, the electrons coming back to the laser-plasma interaction zone may be strongly deviated due to the presence of local magnetic fields or they may enter in the underdense preplasma. In all cases, we assume that these electrons are taken into account by the Particle-In-Cell (PIC) simulation of the laser plasma interaction Φ_{ini} and we consequently let all fast electrons ⁽¹⁾ and ⁽²⁾ escape from the target in the laser-irradiated side. However, in the case of a high contrast, short pulse obliquely incident on the target, the laser-generated fast electrons ⁽¹⁾ propagate mainly in the laser pulse propagation direction. The refluxed fast electrons ⁽²⁾, coming from the target rear side arrive at an abrupt solid-vacuum interface at the laser irradiated side of the target away from the laser plasma interaction zone. Therefore, in this case, we also account for the refluxing of the fast electrons ⁽²⁾ at the front side. Thus, after initializing the laser-generated fast electron ⁽¹⁾ as

$$\begin{array}{ll} \text{If } t < t_{\text{source}} & \text{then } \phi^{(1),n,i,j,0,l} = \phi^{(1),n,i,j,1,l} = \phi_{\text{ini}}^{n,i,j,1,l} \\ \text{else if } \Psi_{1,z}^{(1),n,i,j,2,l} < 0 \text{ and } t > t_{\text{source}} & \text{then } \phi^{(1),n,i,j,0,l} = \phi^{(1),n,i,j,1,l} = \phi^{(1),n,i,j,2,l} \\ \text{else} & \phi^{(1),n,i,j,0,l} = \phi^{(1),n,i,j,1,l} = \mathbf{0} \end{array} \quad (9.8)$$

by knowing the fast electron distribution ϕ_{ini} according to the PIC simulation of the laser plasma interaction, we add the fast electrons component due to the refluxing of the fast electrons population propagating backward ⁽²⁾ as follows.

$$\text{If } \Psi_{1,z}^{(2),n,i,j,2,l} < 0 \quad \text{then} \quad \left\{ \begin{array}{l} \Psi_0^{(1),n,i,j,0,l} = \Psi_0^{(1),n,i,j,1,l} = \Psi_0^{(1),n,i,j,1,l} + \Psi_0^{(2),n,i,j,2,l} \\ \Psi_{1,x}^{(1),n,i,j,0,l} = \Psi_{1,x}^{(1),n,i,j,1,l} = \Psi_{1,x}^{(1),n,i,j,1,l} + \Psi_{1,x}^{(2),n,i,j,2,l} \\ \Psi_{1,y}^{(1),n,i,j,0,l} = \Psi_{1,y}^{(1),n,i,j,1,l} = \Psi_{1,y}^{(1),n,i,j,1,l} + \Psi_{1,y}^{(2),n,i,j,2,l} \\ \Psi_{1,z}^{(1),n,i,j,0,l} = \Psi_{1,z}^{(1),n,i,j,1,l} = \Psi_{1,z}^{(1),n,i,j,1,l} - \Psi_{1,z}^{(2),n,i,j,2,l} \end{array} \right. \quad (9.9)$$

An option in the *Fortran 90* file *data.f90* allows for enabling or not the refluxing of fast electrons at

9.1. COMPUTATIONAL METHODS FOR ESTIMATING THE EMISSION OF $K\alpha$ PHOTONS

the target rear side and another one for enabling or not the refluxing of fast electrons at the target irradiated side. This is illustrated in **Figure 9.3**. Obviously, solving two sets of M1 equations doubles the computational cost. Also, the beam density reads now

$$n_b = \int_{\varepsilon_{\min}}^{L\varepsilon} \left(\Psi_0^{(1)} + \Psi_0^{(2)} \right) d\varepsilon \rightarrow n_b^{n,i,j,k} = \sum_{l=1}^{N_\varepsilon} \left(\Psi_0^{(1),n,i,j,k,l} + \Psi_0^{(2),n,i,j,k,l} \right) \Delta\varepsilon \quad (9.10)$$

while the beam current density needed to compute the self-generated electromagnetic fields reads now

$$\mathbf{j}_b = -e \int_{\varepsilon_{\min}}^{L\varepsilon} v \left(\Psi_1^{(1)} + \Psi_1^{(2)} \right) d\varepsilon \rightarrow \mathbf{j}_b^{n,i,j,k} = -e \sum_{l=1}^{N_\varepsilon} v_l \left(\Psi_1^{(1),n,i,j,k,l} + \Psi_1^{(2),n,i,j,k,l} \right) \Delta\varepsilon. \quad (9.11)$$

In the following, we note $\Psi_0 = \Psi_0^{(1)} + \Psi_0^{(2)}$ and $\Psi_1 = \Psi_1^{(1)} + \Psi_1^{(2)}$.

9.1.2 Emission of $K\alpha$ Photons in Hybrid Models due to Laser-generated Fast Electron Beam

K-shell emission is produced when a fast electron knocks out a K-shell electron from an atom in the solid target is then replaced by an electron from an outer shell - a transition that leads to the emission of a photon with a characteristic energy in the x-ray band (see **Figure 9.1**). If the outer electron comes from the L-shell, the emission is called $K\alpha$; if it comes from the M-shell, it is called $K\beta$. Depending on the orbital moment of the L-shell electron, one can distinguish between a more energetic $K\alpha_1$ photon and a less energetic $K\alpha_2$ photon. According to the Dipole Transition Criterion, $K\alpha$ emission is more probable than $K\beta$ emission while $K\alpha_1$ emission is more probable than $K\alpha_2$ emission. Therefore, the majority of K-shell diagnostics used in laser solid experiments rely on the detection of $K\alpha_1$ photons. A fundamental parameter is the collisional K-shell electron ionization cross section. According to [Davies et al., 2013] for Copper tracer layer, the empirical formula provided by [Hombourger, 1998]

$$\sigma_K(\varepsilon) = 2\pi r_{\text{Bohr}}^2 G_r(\varepsilon) D(\varepsilon) \left(\frac{E_0}{E_K} \right)^{C(\varepsilon)} \quad (9.12)$$

is the most accurate expression found by the authors in the literature for the K-shell electron ionization cross section induced by a collision with a laser-generated fast electron with a kinetic energy ε . Here, $r_{\text{Bohr}} = 5.2918 \cdot 10^{-9}$ cm is the Bohr radius, $E_0 = 13.61$ eV is the fundamental Hydrogen state energy, E_K is the ionization energy of the K-shell electron depending on the atomic number Z of the material,

$$D(\varepsilon) = \left(3.125 - \frac{4.172}{U} + \frac{1.877}{U^2} \right) \frac{\ln U}{U}, \quad (9.13)$$

$$C(\varepsilon) = 2.0305 - \frac{0.3160}{U} + \frac{0.1545}{U^2} \quad (9.14)$$

CHAPTER 9. APPLICATION TO THE $K\alpha$ EMISSION DURING FAST ELECTRON TRANSPORT IN SOLID TARGETS

Material	Z	E_K [eV]	$h\nu_{K\alpha_1}$ [eV]	$h\nu_{K\alpha_2}$ [eV]	$I_{K\alpha_2}/I_{K\alpha_1}$	$h\nu_{K\beta}$ [eV]	$I_{K\beta}/I_{K\alpha}$
Al	13	1559.6	1486.70	1486.27	0.5	1557.45	0.02
Cu	29	8979	8047.78	8027.83	0.51	8905.29	0.12
Ta	73	67416	57532.	56277	0.57	65223	0.22

Figure 9.4: Values of a K-shell electron ionization energy E_K , energy of a $K\alpha_1$, $K\alpha_2$ and $K\beta$ photon $h\nu_{K\alpha_1}$, $h\nu_{K\alpha_2}$ and $h\nu_{K\beta}$, and ratios $I_{K\alpha_2}/I_{K\alpha_1}$ and $I_{K\beta}/I_{K\alpha}$ of the K-lines intensities depending on the atomic number Z of the material.

where $U = \varepsilon/E_K$ is the normalized kinetic energy of the fast electron and

$$G_r(\varepsilon) = \frac{(1+2J)(U+J)^2 \left[(1+U)(U+2J)(1+J)^2 \right]^{3/2}}{(U+2J)(1+J)^2 [J^2(1+2J) + U(U+2J)(1+J^2)]^{3/2}} \quad (9.15)$$

is the Gryzinski coefficient where $J = m_e c^2/E_K$ is the normalized electron mass energy. Actually, there is a mistake in the original paper by [Hombourger, 1998]. It is $2J$ and not only 2 as colored in red in (9.15) [Gryziński, 1965a] [Gryziński, 1965b].

According to [Davies et al., 2013], **it is usually assumed that the fraction of atoms with empty K-shells, as a result of collisions with fast electrons, is negligible. Under this assumption**, by knowing the K-shell fluorescence yield ω_K depending on the atomic number Z of the material, one may directly deduce the number of $K\alpha$ and $K\beta$ photons emitted per unit of time, volume and steradian according to

$$\begin{aligned} \left(\frac{dn_{\alpha_1}}{dt} \right)_{\text{Emitted}} &= \frac{1}{4\pi} F_{K\alpha_1} F_{K\alpha} \omega_K \frac{2n_i}{\tau_b} \text{ with } F_{K\alpha_1} = \frac{1}{1 + \frac{I_{K\alpha_2}}{I_{K\alpha_1}}} \text{ and } F_{K\alpha} = \frac{1}{1 + \frac{I_{K\beta}}{I_{K\alpha}}}, \\ \left(\frac{dn_{\alpha_2}}{dt} \right)_{\text{Emitted}} &= \frac{1}{4\pi} F_{K\alpha_2} F_{K\alpha} \omega_K \frac{2n_i}{\tau_b} \text{ with } F_{K\alpha_2} = \frac{1}{1 + \frac{I_{K\alpha_1}}{I_{K\alpha_2}}} = 1 - F_{K\alpha_1} \\ \text{and } \left(\frac{dn_{\beta}}{dt} \right)_{\text{Emitted}} &= \frac{1}{4\pi} F_{K\beta} \omega_K \frac{2n_i}{\tau_b} \text{ with } F_{K\beta} = \frac{1}{1 + \frac{I_{K\alpha}}{I_{K\beta}}} = 1 - F_{K\alpha} \end{aligned} \quad (9.16)$$

where

$$\tau_b = \left(\int_{\varepsilon_{\min}}^{\infty} \Psi_0 \sigma_K v d\varepsilon \right)^{-1}. \quad (9.17)$$

Here, n_i is the ion density, $I_{K\alpha_1}$, $I_{K\alpha_2}$, $I_{K\alpha}$ and $I_{K\beta}$ are the intensities of a single $K\alpha$ or $K\beta$ photon signal, respectively. Their values, depending on the atomic number Z , are given in **Figure 9.4** according to [Thomson et al., 2009]. The factor $1/4\pi$ comes from the fact that the photons emission is assumed to be isotropic. $F_{K\alpha_i} F_{K\alpha} \omega_K$ and $F_{K\beta} \omega_K$ are the probabilities that a photon $K\alpha_i$ or $K\beta$, respectively, is emitted when a K-shell hole is recombined by a L-shell electron or a M-shell electron, respectively. $2n_i$ is the density of holes induced by the ionization of K-shell electrons (there are **two** electrons in the K-shell of atoms used in experiments). τ_b is the characteristic ionization

9.1. COMPUTATIONAL METHODS FOR ESTIMATING THE EMISSION OF $K\alpha$ PHOTONS

time or the inverse of the ionization frequency. It accounts for the fast electron energy distribution $\Psi_0(\mathbf{r}, \varepsilon, t)$ at the space location \mathbf{r} and time t and the ionization probability $\sigma_K(\varepsilon)v(\varepsilon)$ that a fast electron with a kinetic energy ε ionize one K-shell electron. According to [Kahoul A. et al., 2011], the K-shell fluorescence yield can be estimated as

$$\omega_K = 0.985 \frac{(Z/30.896)^{3.847}}{1 + (Z/30.896)^{3.847}}. \quad (9.18)$$

This formula fits the experimental results compiled by [BAMBYNEK et al., 1972] and [Krause and Oliver, 1979] with an error less than 5 % except Aluminum with a deviation of 14 % compared to [Krause and Oliver, 1979]. The time integrated number of $K\alpha_1$ photons emitted per unit of volume and steradian

$$n_{\alpha_1}(\mathbf{r}, t) = \int_0^t \left(\frac{dn_{\alpha_1}}{dt} \right)_{\text{Emitted}} dt \quad (9.19)$$

is computed self-consistently with the fast electron beam transport hybrid model, as illustrated in **Figure 8.12 d)** of **Chapter 8, section 8.2**. It can be directly compared with the experimental time-integrated $K\alpha_1$ signal.

9.1.3 K-shell Hole Density Dynamics

As explained in the previous subsection, the method of computing the emission of $K\alpha$ photons (9.19) is based on five assumptions :

1. The hole lifetime τ_K due to K-shell fluorescence, Auger and Coster-Kronig effects is small compared to the ionization time τ_b .
2. The numerical time step of the fast electron transport hybrid model Δt_n is large compared to the hole lifetime τ_K so that the density of holes $n_H(\mathbf{r}, t_{n+1})$ attains its maximum value $2n_i(\mathbf{r}, t_n)\tau_K/\tau_b(\mathbf{r}, t_n)$.
3. The target is fully transparent for the $K\alpha$ photons.
4. The K-shell photoionization by the X-rays emitted by the fast electrons or other laser-plasma processes is negligible compared to the collisional ionization by the fast electrons.
5. The K-shell fluorescence yield ω_K and the collisional ionization cross section σ_K do not depend on the target temperature.

A more detailed analysis of $K\alpha$ emission was proposed by [Thomas et al., 2013]. It allows us to demonstrate that, while the assumption 1 is fully justified, one must be careful with the assumption 2, which is depending on the tracer material.

Let us note n_{H1} the density of atoms with one hole in the K-shell. According to [Thomas et al., 2013], its temporal evolution can be described by the following kinetic equation

$$\frac{\partial n_{H1}}{\partial t} = R_{K1} - \frac{n_{H1}}{\tau_K} \text{ where } R_{K1} = 2 \frac{n_i - n_{H1}}{\tau_b} \quad (9.20)$$

is the ionization rate depending on the density of available K-shell holes $2(n_i - n_{H1})$. $\tau_K = \hbar/\Gamma_K$ is the hole life time deduced from the K-shell natural level width Γ_K (\ll Heisenberg incertitude principle). The factor 2 in R_{K1} comes from the assumption that the K-shell is initially full, as it is the case in the laser-solid experiments. Let us note n_{H2} the density of atoms in the solid target with two holes in the K-shell. According to [Thomas et al., 2013], its temporal evolution can be described by the following kinetic equation

$$\frac{\partial n_{H2}}{\partial t} = R_{K2} - \frac{n_{H2}}{\tau_K} \text{ where } R_{K2} = \frac{n_{H1} - n_{H2}}{\tau_b} \quad (9.21)$$

is the ionization rate of the second K-shell electron and $(n_{H1} - n_{H2})$ is the density of available atoms with only one K-shell hole. Then, the total number of atoms with one or two holes in the K-shell $n_H = n_{H1} + n_{H2}$ evolves according to the following kinetic equation

$$\frac{\partial n_H}{\partial t} + \left(\frac{1}{\tau_b} + \frac{1}{\tau_K} \right) n_H = \frac{2n_i}{\tau_b}. \quad (9.22)$$

9.1. COMPUTATIONAL METHODS FOR ESTIMATING THE EMISSION OF $K\alpha$ PHOTONS

According to [Thomas et al., 2013], the K-shell natural level width can be estimated by

$$\Gamma_K = \exp(-0.0002725Z^2 + 0.09932Z - 2.160) \text{ eV}, \quad (9.23)$$

which agrees with the results compiled by [Krause, 1979] with an error less than $\approx 10\%$ for $Z \geq 10$. The hole lifetime $\tau_K = \hbar/\Gamma_K$ is plotted in the right panel of **Figure 9.5**. As proposed by [Thomas et al., 2013], one can solve analytically Equation (9.22) to determine in each numerical spatial cell (i, j, k) the hole density $n_H^{n+1,i,j,k}$ at $t_n + \Delta t_n$ as a function of the ionization time

$$\tau_b^{n,i,j,k} = \frac{1}{\sum_{l=1}^{N_\varepsilon} \Psi_0^{n,i,j,k,l} \sigma_K(\varepsilon_l) v_l \Delta \varepsilon} \quad (9.24)$$

and the hole density $n_H^{n,i,j,k}$ at time t_n . It reads [Thomas et al., 2013]

$$\begin{aligned} n_H^{n+1,i,j,k} &= n_H^{n,i,j,k} + \left(n_H^{n,i,j,k} - \frac{2n_i^{n,i,j,k}}{\Gamma^{n,i,j,k} \tau_b^{n,i,j,k}} \right) \left[\exp(-\Gamma^{n,i,j,k} \Delta t_n) - 1 \right] \\ &= \left(1 - \Gamma^{n,i,j,k} \Delta t_n \right) n_H^{n,i,j,k} + \frac{2n_i^{n,i,j,k} \Delta t_n}{\tau_b^{n,i,j,k}} + O \left[\left(\Gamma^{n,i,j,k} \Delta t_n \right)^2 \right] && \text{if } \Gamma^{n,i,j,k} \Delta t_n \ll 1 \\ &= \frac{2n_i^{n,i,j,k}}{\Gamma^{n,i,j,k} \tau_b^{n,i,j,k}} && \text{if } \Gamma^{n,i,j,k} \Delta t_n \gg 1 \end{aligned} \quad (9.25)$$

where it has been noted $\Gamma^{n,i,j,k} = (1/\tau_K) + (1/\tau_b^{n,i,j,k})$.

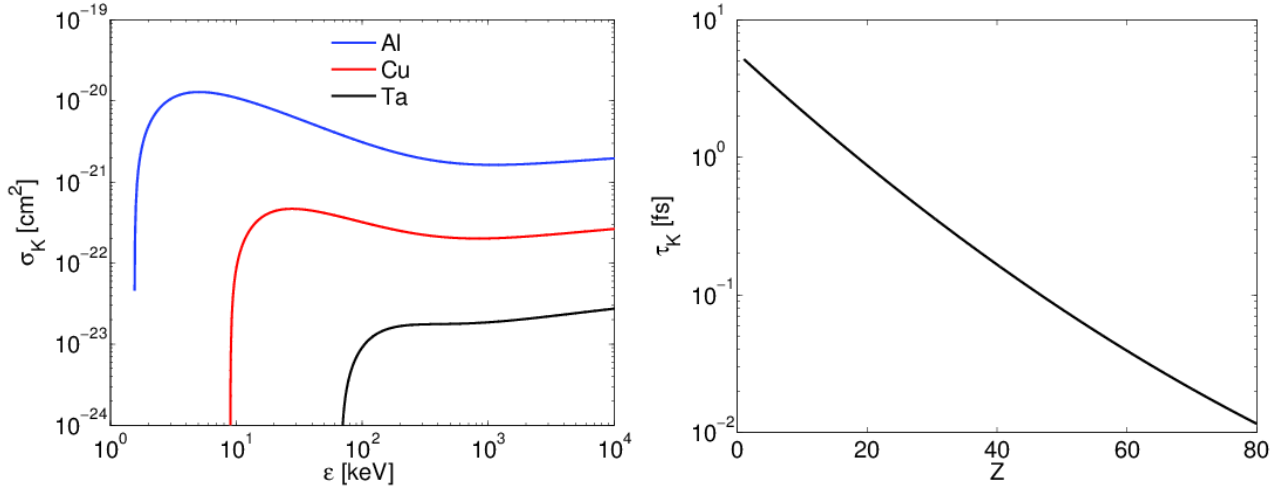


Figure 9.5: (Left panel) Collisional K-shell electron ionization cross section σ_K on the electron kinetic energy ϵ for Aluminum (blue curve), Copper (red curve) and Tantalum (black curve) according to Equation (9.12); (Right panel) Dependence of the hole lifetime $\tau_K = \hbar/\Gamma_K$ on the atomic number Z according to Equation (9.23).

Let us compare the typical values of τ_b and τ_K . Assuming the electron distribution function in the form $\Psi_0 \approx (n_{b0}/k_B T_b) \exp(-\epsilon/k_B T_b)$ with the mean kinetic energy $k_B T_b \gg E_K$ and approximating the collisional K-shell electron ionization cross section σ_K by the Heaviside function $\sigma_K(\epsilon) \approx \sigma_0 \Pi[\epsilon - E_K]$ (see the left panel of **Figure 9.5**), one obtains

$$\tau_b \approx \frac{3 \cdot 10^7 \text{ fs}}{n_{b0} [10^{21} \text{ cm}^{-3}] \sigma_0 [\text{barns}]} \quad (9.26)$$

It gives $\tau_b/\tau_K \approx 4 \cdot 10^3$ for Aluminum ($n_{b0} = 10^{21} \text{ cm}^{-3}$, $\tau_K = 1.628 \text{ fs}$, $\sigma_0 \approx 5 \cdot 10^{-21} \text{ cm}^2$ and $E_K = 1559.6 \text{ eV}$), $\tau_b/\tau_K \approx 2 \cdot 10^5$ for Copper ($n_{b0} = 10^{21} \text{ cm}^{-3}$, $\tau_K = 0.4028 \text{ fs}$, $\sigma_0 \approx 4 \cdot 10^{-22} \text{ cm}^2$ and $E_K = 8979 \text{ eV}$) and $\tau_b/\tau_K \approx 6 \cdot 10^7$ for Tantalum ($n_{b0} = 10^{21} \text{ cm}^{-3}$, $\tau_K = 0.01731 \text{ fs}$, $\sigma_0 \approx 3 \cdot 10^{-23} \text{ cm}^2$ and $E_K = 67416 \text{ eV}$). We deduce consequently that the assumption 1 is fully justified and that we can consider $\Gamma^{n,i,j,k} = 1/\tau_K$. However, depending on the material and on the numerical time step Δt_n , the assumption 2 is not necessarily verified as the hole lifetime can be comparable with the numerical time step $\Delta t_n \approx 0.5 \text{ fs}$ (see the CFL condition (7.50) of **Chapter 7, section 7.1.4** or (7.52) of **Chapter 7, section 7.1.5**). Besides, for intermediate Z materials like Tantalum $\Delta t_n \gg \tau_K = 0.01731 \text{ fs}$, we obtain $n_H^{n+1,i,j,k} \rightarrow 2n_i^{n,i,j,k} \tau_K/\tau_b^{n,i,j,k}$ by making $\Gamma \rightarrow 1/\tau_K \gg 1/\Delta t_n$ in (9.25). According to [Thomas et al., 2013], the $K\alpha_1$ emission rate reads per unit of time, volume and steradian reads

$$\left(\frac{dn_{\alpha_1}}{dt} \right)_{\text{Emitted}} = \frac{1}{4\pi} F_{K\alpha_1} F_{K\alpha} \omega_K \frac{n_H}{\tau_K} \quad (9.27)$$

Therefore, in the particular case where $\Gamma^{n,i,j,k} \Delta t_n = \Delta t_n/\tau_K + o(\tau_K/\tau_b) \gg 1$ as for Tantalum, (9.25) and (9.27) lead to the standard expression (9.19) of the time integrated density of $K\alpha$ photons emitted per steradian. It is not the case for Copper and Aluminum. Consequently, we decide to take into

9.1. COMPUTATIONAL METHODS FOR ESTIMATING THE EMISSION OF $K\alpha$ PHOTONS

account the hole density dynamics in our model. It will be also useful for studies of the temporal dynamics of the hole density in the context of the X-ray shadowgraphy.

The analytical solution of (9.22) for $t \in [t_n, t_n + \Delta t_n]$ is

$$n_H^{i,j,k}(t) = \left(n_H^{i,j,k,n} - \frac{2n_i^{n,i,j,k}}{\Gamma^{n,i,j,k}\tau_b^{n,i,j,k}} \right) \exp\left(-\Gamma^{n,i,j,k}(t-t_n)\right) + \frac{2n_i^{n,i,j,k}}{\Gamma^{n,i,j,k}\tau_b^{n,i,j,k}} \quad (9.28)$$

by assuming that $\tau_b^{n,i,j,k}$ and $n_i^{n,i,j,k}$ are constants during the numerical time step. Correspondingly, we compute the $K\alpha_1$, $K\alpha_2$ and $K\beta$ photons number emitted per unit of time, volume and steradian according to

$$\begin{aligned} \left(\frac{dn_{\alpha 1}}{dt}\right)_{\text{Emitted}}^{n,i,j,k} &= \frac{1}{4\pi} F_{K\alpha 1} F_{K\alpha}\omega_K \frac{\langle n_H^{i,j,k} \rangle_n}{\tau_K}, \\ \left(\frac{dn_{\alpha 2}}{dt}\right)_{\text{Emitted}}^{n,i,j,k} &= \frac{1}{4\pi} F_{K\alpha 2} F_{K\alpha}\omega_K \frac{\langle n_H^{i,j,k} \rangle_n}{\tau_K}, \\ \text{and } \left(\frac{dn_{\beta}}{dt}\right)_{\text{Emitted}}^{n,i,j,k} &= \frac{1}{4\pi} F_{K\beta}\omega_K \frac{\langle n_H^{i,j,k} \rangle_n}{\tau_K} \end{aligned} \quad (9.29)$$

where

$$\begin{aligned} \langle n_H^{i,j,k} \rangle_n &= \frac{1}{\Delta t_n} \int_{t_n}^{t_n+\Delta t_n} n_H^{i,j,k}(t) dt \\ &= \frac{n_H^{n,i,j,k} - n_H^{n+1,i,j,k} + 2n_i^{n,i,j,k}(\Delta t_n/\tau_b^{n,i,j,k})}{\Gamma^{n,i,j,k}\Delta t_n} \end{aligned} \quad (9.30)$$

according to the analytical solution (9.28), with $n_H^{n+1,i,j,k}$ given by Equation (9.25). The time integrated number of photons emitted from the cell (i, j, k) per unit of volume and steradian at time t_{N_t} is then given by

$$n_{\alpha 1}^{N_t,i,j,k} = \sum_{n=1}^{N_t} \left(\frac{dn_{\alpha 1}}{dt}\right)_{\text{Emitted}}^{n,i,j,k} \Delta t_n. \quad (9.31)$$

9.2 Application to the Saclay UHI100 Experiment

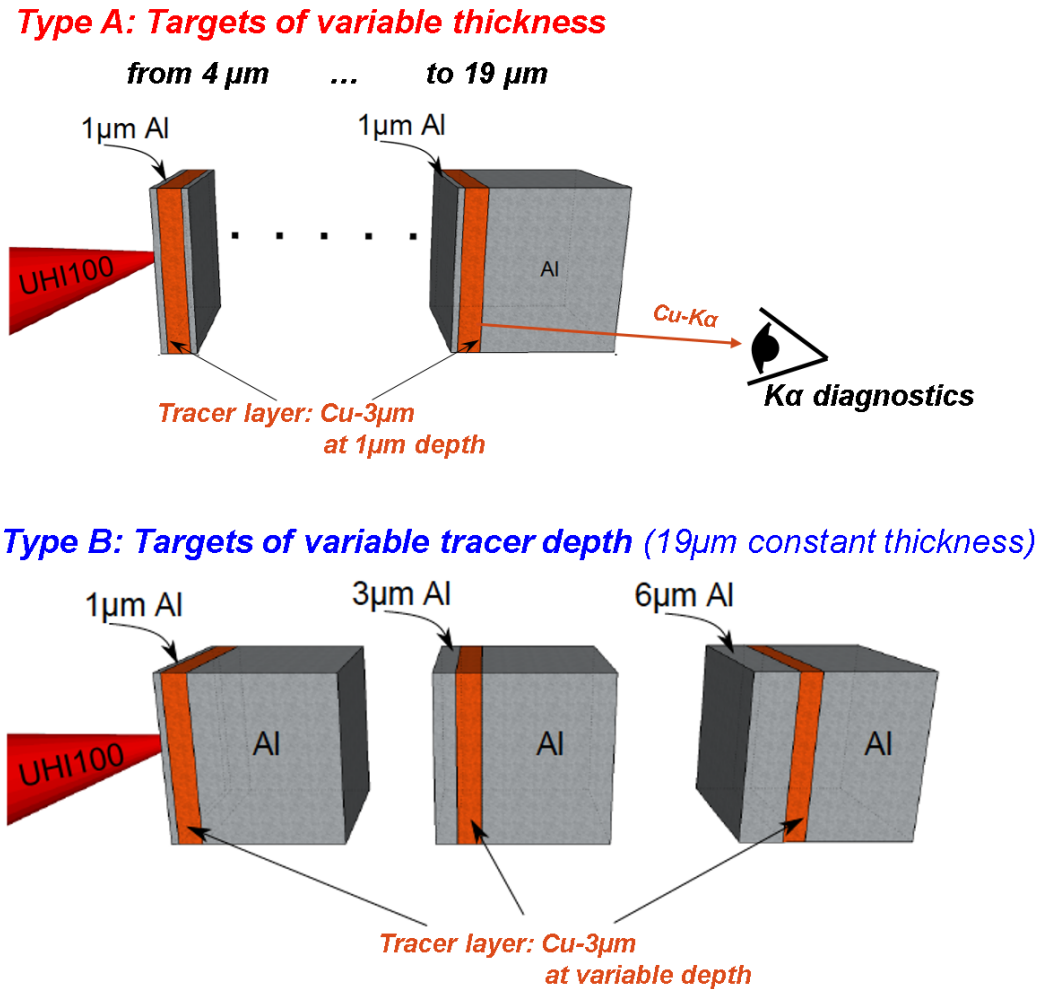


Figure 9.6: Scheme of the different targets irradiated by the UHI100 laser pulses in the experimental campaign conducted by [SANTOS et al., 2013]; courtesy of J. Santos.

In this section, we apply the model of $K\alpha_1$ photon emission (9.31), developed in the previous section 9.1.3, to the experiments conducted by [SANTOS et al., 2013] on the UHI100 laser facility, introduced in Chapter 8, section 2. As illustrated in Figure 9.6, an ultra high contrast laser pulse was focused at 45° on Aluminum targets with different thicknesses, and the hot electrons were detected in a $K\alpha$ Copper tracer layer of $3\ \mu\text{m}$ located at different depths. As already explained in Chapter 8, section 8.2.1, the hot electron source was calculated using Particle-In-Cell simulations performed by [Gremillet, 2012]. We may assume that these simulation results are close to the experimental reality thanks to the high contrast of the laser pulses, avoiding prepulse/preplasma effects on the laser solid interaction that are usually not well characterized. In addition, the laser pulses have been focused with a 45° angle of incidence. Thus, since the higher-energy fast electrons propagate mainly in the propagation direction of the laser pulse, the recirculation through the laser plasma interaction

zone and their deflections by strong local magnetic fields are minimized here. Therefore, we only take into account refluxing process due to the strong electric fields generated by the fast electrons at the target's rear and irradiated sides. The fast electron propagation is modeled with the M1 code accounting for two, forward and backward propagating groups, and assuming **specular reflections of the fast electrons at both target surfaces**. The time integrated Cu $K\alpha_1$ photon signal, emitted from the Copper tracer layer have been measured experimentally with a cylindrical quartz crystal Von Hamos spectrometer and another spherical quartz crystal completed by two cooled X-ray CCD camera [SANTOS et al., 2013] so that we can compare the time integrated $K\alpha_1$ photons signals obtained numerically and those obtained experimentally for all targets.

The M1 simulations presented in this **Chapter** are performed with the thermal capacities $C_{V,e}$ and $C_{V,i}$ presented in **Chapter 6, section 6.3.1**, the transport coefficients η and κ_e presented in **section 6.3.2** and the electron-lattice/ion coupling factor G presented in **section 6.3.3**. We start with a 2D-3V M1 simulation of the Al(1 μm)Cu(3 μm)Al(1 μm) target without refluxing but with these solid state physics corrections. It can be compared with the reference M1 simulation presented in **Chapter 8, section 8.2**, computed with the Eidmann-Chimier model for η and κ_e (see **Chapter 3, section 3.3.1**) and the hot plasma expressions for G , $C_{V,e}$ and $C_{V,i}$. Moreover, we will confirm that the assumption 2 made in the reference simulation is not verified for Copper and Aluminum. Secondly, we present the M1 simulation results with refluxing for the Al(1 μm)Cu(3 μm)Al(1 μm) and Al(1 μm)Cu(3 μm)Al(15 μm) targets. It allows us to highlight the dependence of refluxing effects upon the target thickness. Thirdly, we present the 2D-3V M1 simulation results with refluxing for all targets, focusing on the emission of $K\alpha_1$ photons. The simulations reproduce qualitatively the experimental data. Finally, three-dimensional effects are analyzed by considering the the 3D-3V M1 simulation results with refluxing for the Al(1 μm)Cu(3 μm)Al(1 μm) target.

Except for the 2D-3V M1 simulation presented in **9.2.1**, which uses the same numerical conditions as the simulation presented in **Chapter 8, section 8.2**, all others are performed with the same conditions. Firstly, in agreement with the experiments (\approx mm), the lateral size of the targets are taken sufficiently large ($L_x = L_y = 500 \mu\text{m}$) to avoid refluxing at the lateral target boundaries. We choose $\Delta x = \Delta y = \Delta z = 1 \mu\text{m}$ for the spatial mesh size and $\Delta \varepsilon = 30 \text{ keV}$ for the kinetic energy cells. This is a compromise between the numerical cost of the simulations and their accuracy, imposed by the available dynamic random access memory of the computer for the 3D-3V simulation. Indeed, with these conditions, we have to allocate at each time step the variables Φ , F_x , F_y , F_z , Γ_E , Γ_B and Γ_ν (see **Chapter 7, section 7.1** for the notations) while each one represents a $2 \times 4 \times 500 \times 500 \times 5 \times 100$ -dimensional table (2 for the two electron populations ⁽¹⁾ and ⁽²⁾, 4 for Ψ_0 , $\Psi_{1,x}$, $\Psi_{1,y}$ and $\Psi_{1,z}$, $500^2 \times 5$ for the spatial cells and 100 for the kinetic energy cells), that needs approximately 8 Go of available dynamic memory in double-precision floating-point format.

The fast electrons are initialized as in **Chapter 8, section 8.2**, except for the 3D-3V simulation

where the third spatial dimension is introduced as

$$\Psi_{\text{ini},0}(x, y, z = 0, \varepsilon, t) = N'_0(t)f_x(x, t)f_y(y, t)f_z(z = 0, t)f_\varepsilon(\varepsilon, t) \quad (9.32)$$

where

$$f_y(y, t) = \frac{1}{\sqrt{2\pi\frac{\Delta x(t)^2}{8\ln 2}}} \exp\left[-4\ln 2\left(\frac{y}{\Delta x(t)}\right)^2\right] \quad (9.33)$$

and

$$N'_0(t) = \nu_{L\rightarrow e}(t)\frac{E_L}{k_B T_{b0}(t)} \quad (9.34)$$

while

$$\Psi_{\text{ini},1}(x, y, z = 0, \varepsilon, t) = \Psi_{\text{ini},0}(x, y, z = 0, \varepsilon, t)\Omega_\varepsilon(x, z = 0, \varepsilon, t) \quad (9.35)$$

remains unchanged, following the notations introduced in **Chapter 8, section 8.2**. The computational time $L_t = 1.5$ ps is sufficient to let the fast electrons lose all their energy, thus ensuring that they do not contribute to the emission of $K\alpha$ photons anymore at the end of each simulation. The 2D simulations took from ≈ 2 to ≈ 11 hours on 20 CPU, depending on the target thickness compared to ≈ 4 days and 17 hours on 40 CPU for the 3D simulation. In what follows, we will talk about $K\alpha_1$ photons and $K\alpha$ photons interchangeably and we omit the emission of $K\alpha_2$ photons. The latter can be deduced from the $K\alpha_1$ emission and the contribution $F_{K\alpha_2}$ to the K-shell fluorescence.

9.2.1 Preliminary 2D-3V Simulation - Effects of Solid State Corrections

Firstly, let us present the 2D-3V simulation results for the thinnest target Al(1 μm)Cu(3 μm)Al(1 μm) without refluxing (absorbing conditions for 1 set of M1 equations) but with the target electron and ion parameters introduced in **Chapter 6, section 6.3** for the Copper and Aluminum layers and with the model of $K\alpha$ emission, described in **subsection 9.1.3**. By comparing it with the reference 2D-3V simulation presented in **Chapter 8, section 8.2**, one can evaluate the impact of the solid state physics corrections on the fast electron transport and the impact of the hole density dynamics on the emission of $K\alpha_1$ photons. Let us remind here that the reference simulation has been conducted without refluxing, with the Eidmann-Chimier model for η and κ_e , the plasma expressions for the thermal capacities $C_{V,e}^{\text{hot}}$ and $C_{V,i}^{\text{hot}}$, the Lee-More plasma electron-ion coupling factor G^{hot} (see **Chapter 6, section 6.3** for the notations) and the standard formula (9.19) for the $K\alpha$ emission.

The total energy is conserved within an accuracy about 1.7%, compared to the value of 0.5% obtained in the reference simulation. As illustrated in **Figures 8.9** and **9.7**, the energy injected in the target $U_{\text{inc}} \approx 70$ mJ, the energy escaping from the target rear side $U_{\text{out}} \approx 50$ mJ, the maximum instantaneous beam energy in the target $U_{b,\text{max}} \approx 4$ mJ and the total energy loss of the fast electron

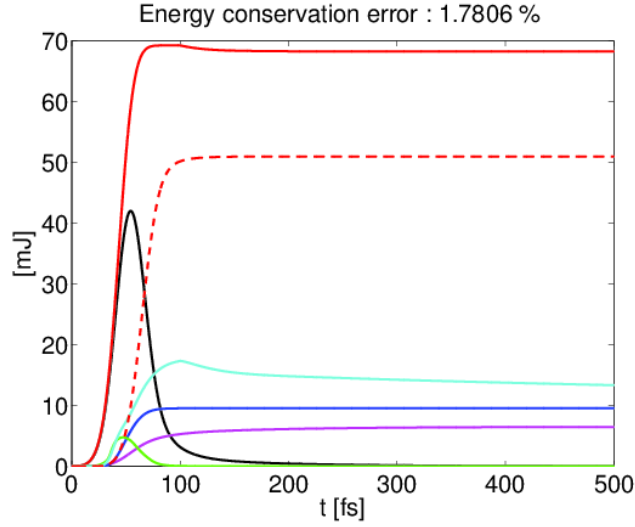


Figure 9.7: Instantaneous beam energy $U_b \times 10$ (solid black), integrated beam energy balanced between injected and escaping electrons at $z = 0$ U_{inc} (solid red), escaped energy U_{out} at $z = 5 \mu\text{m}$ (dashed red), total collisional energy loss U_{col} (solid magenta), total “collective” U_{res} energy loss (solid blue), instantaneous electric energy $U_E \times 10^3$ (solid green) and instantaneous magnetic energy $U_B \times 10^3$ (solid cyan).

beam $U_{\text{col}} + U_{\text{res}} \approx 20$ mJ are close to the reference results. However, the maximum of electric energy in the target $U_{E,\text{max}} \approx 5 \cdot 10^{-3}$ mJ is approximately twice less than the value obtained in the reference simulation, the maximum magnetic energy $U_B \approx 20 \cdot 10^{-3}$ mJ is less than the reference $U_{B,\text{max}} \approx 30 \cdot 10^{-3}$ mJ and the contributions of the collisional and collective losses are different : $U_{\text{res}} \approx 10$ mJ and $U_{\text{col}} \approx 8$ mJ while it has been obtained $U_{\text{res}} \approx 13$ mJ and $U_{\text{col}} \approx 6$ mJ in the reference case. Therefore, we conclude that the greater energy conservation error is due to the greater collisional losses of fast electrons, computed with the downwind scheme (1st order). The differences in the contributions of collective and collisional fast electron energy losses indicate a significant effect of solid state physics effects introduced in **Chapter 6, section 6.3**.

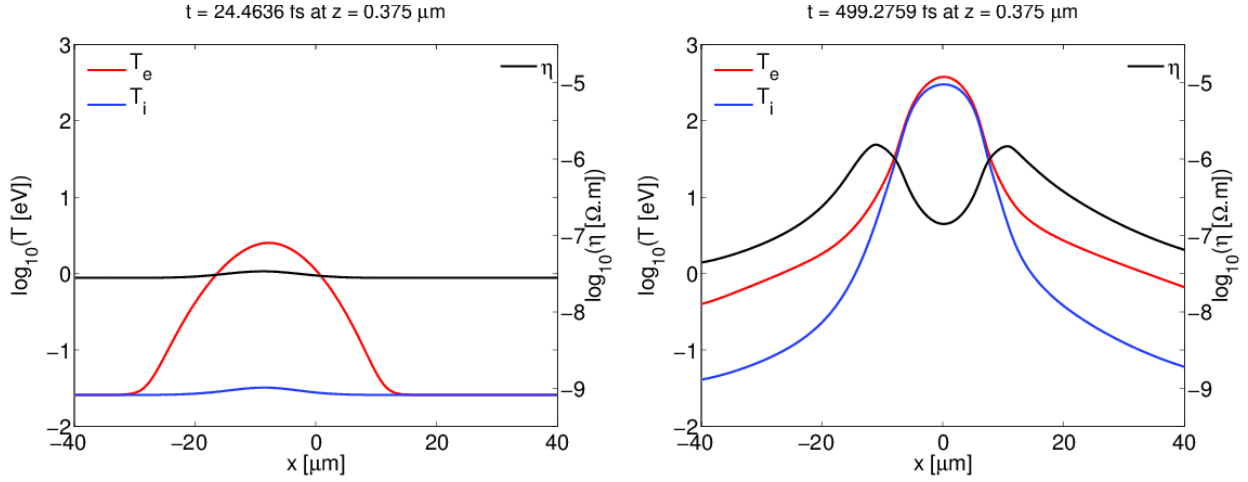


Figure 9.8: Slices at $z = 0.375 \mu\text{m}$ of the resistivity (black curve), the electron temperature (red curve) and the ion temperature (blue curve) at $t = 26.6 \text{ fs}$ (Left panel) and $t = 499.3 \text{ fs}$ (Right panel).

As illustrated in **Figure 9.10** (to be compared with **Figure 8.11**), the fast electrons reach the target rear side at approximately 100 fs in both simulations and the beam propagation do not differ too much. However, **Figure 9.11** (to be compared with **Figure 8.12**) shows differences in the target heating profile (a), that affects the electrical resistivity (b) and consequently the self-generated magnetic field (c). The maximum value of the self-generated magnetic field is less than 90 T while it exceeds 100 T in the reference case. Also, we observe a broader transverse profile (in the x -direction) of the heated Copper area compared to both Aluminum layers while we obtained exactly the opposite in the reference case. These discrepancies may be explained as follows. The Lee-More electron-ion coupling factor G^{hot} overestimates the electron-lattice coupling factor G^{cold} at solid/liquid/Warm Dense Matter (WDM) temperatures by one or two order of magnitudes (see **Figure 6.13**). Consequently, in the reference simulation, the ratios $G^{\text{hot}}/C_{V,e}$ and $G^{\text{hot}}/C_{V,i}$ were so huge that the target ion and electron temperature were instantaneously equilibrated ($T_e \approx T_i$), as illustrated in **Figure 8.13**. Therefore, the Eidmann-Chimier model led to electrical resistivity values close to those obtained with the Lee-More model that assumes $T_e = T_i$; see **Chapter 3, section 3.3.1**. Similar results were obtained with the Paris hybrid PIC simulation that uses the Lee-More electrical resistivity (see **Figure 8.14**). As illustrated in the left panel of **Figure 9.8**, this is not anymore the case here. The lower values of G^{cold} at solid/liquid/WDM temperatures imply a strongly non-equilibrium state, which impacts the target electrical resistivity η . Moreover, as illustrated in **Figure 6.8**, the electrical resistivity is higher in Aluminum than in Copper in the solid state regime with $T_i \ll T_e$ but it is much lower in the liquid/Warm Dense Matter (WDM) state. Since the Ohmic heating by the return current and the self-generated magnetic field generation strongly depend on the beam current and the electrical resistivity, the temperature decreases at both the Al/Cu and Cu/Al interfaces. By contrast, the reference simulation shows an increase in electron temperature at the Cu/Al interface (see **Figure 9.9**). This is due to the Eidmann-Chimer model predicting a greater

9.2. APPLICATION TO THE SACLAY UHI100 EXPERIMENT

electrical resistivity of Aluminum than the electrical resistivity of Copper in the liquid/WDM state with $T_i = T_e$.

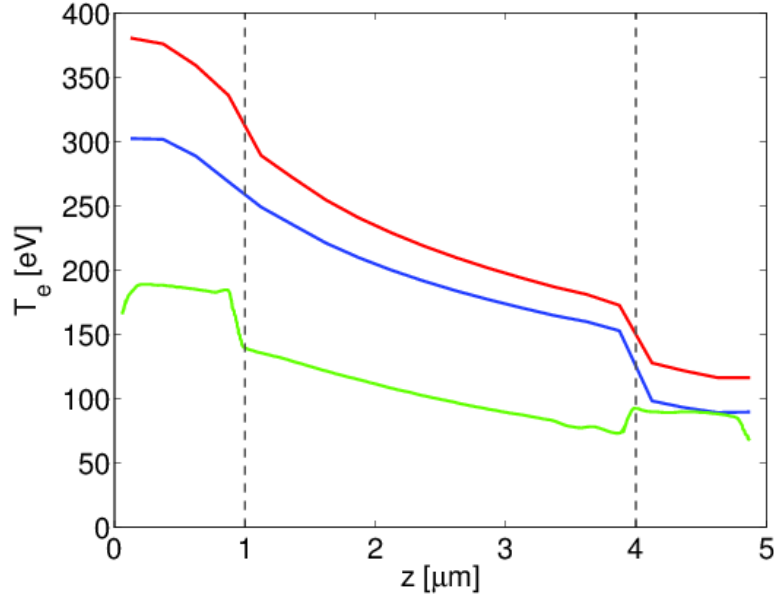


Figure 9.9: Comparison at $t = 500$ fs between the mean electron temperature $\langle T_e \rangle$ over $|x_{\max} - x| < 5 \mu\text{m}$ profile obtained with M1 (blue) and the one obtained with the hybrid PIC code Paris (green). x_{\max} is defined as the position where $T_e(x_{\max}, z)$ is the maximum electron temperature at a given depth z (red). Refluxing is neglected here.

As illustrated in the right panel of **Figure 9.8** (to be compared with the right panel of **Figure 8.13**), we observe the decrease of the electrical resistivity in the hot plasma regime, typical of the beam hollowing effect. This different Ohmic heating by the return current in the first target layers is therefore due to the introduction of the parameter B_ν that saturates the target electron-electron collision rate (6.113) in the liquid/WDM states. Thus, collisions of s-band electrons on d-band electrons may play a significant role in Copper. Due to the short time scale considered here, the target electron thermal conduction κ_e does not play any role. Also, $C_{V,i}$ does not impact the results since it weakly varies from the solid state to the plasma state according to the Einstein model.

Both simulations give approximately the same 2D distribution of the time-integrated number of emitted $K\alpha$ photons, as illustrated in **Figure 9.11 d**) (to be compared with **Figure 8.12 d**)). Both densities of time integrated Al and Cu $K\alpha_1$ photons are noted $n_{K\alpha}$ even if they are computed from different formulae depending on the atomic number of the material. It confirms the analytical estimates obtained for Copper and Aluminum, showing that the hole density dynamics plays an important role in the $K\alpha$ emission in cases where Δt_n is comparable to τ_K . Indeed, we obtain a maximum number of emitted of $K\alpha$ photons about $3 \cdot 10^{18} \text{ cm}^{-3} \cdot \text{sr}^{-1}$ from the Copper layer, which is four times less than the value of $12 \cdot 10^{18} \text{ cm}^{-3} \cdot \text{sr}^{-1}$, obtained in the reference case. In what follows, we will only discuss the $K\alpha_1$ and $K\beta$ emissions from the Copper layer.

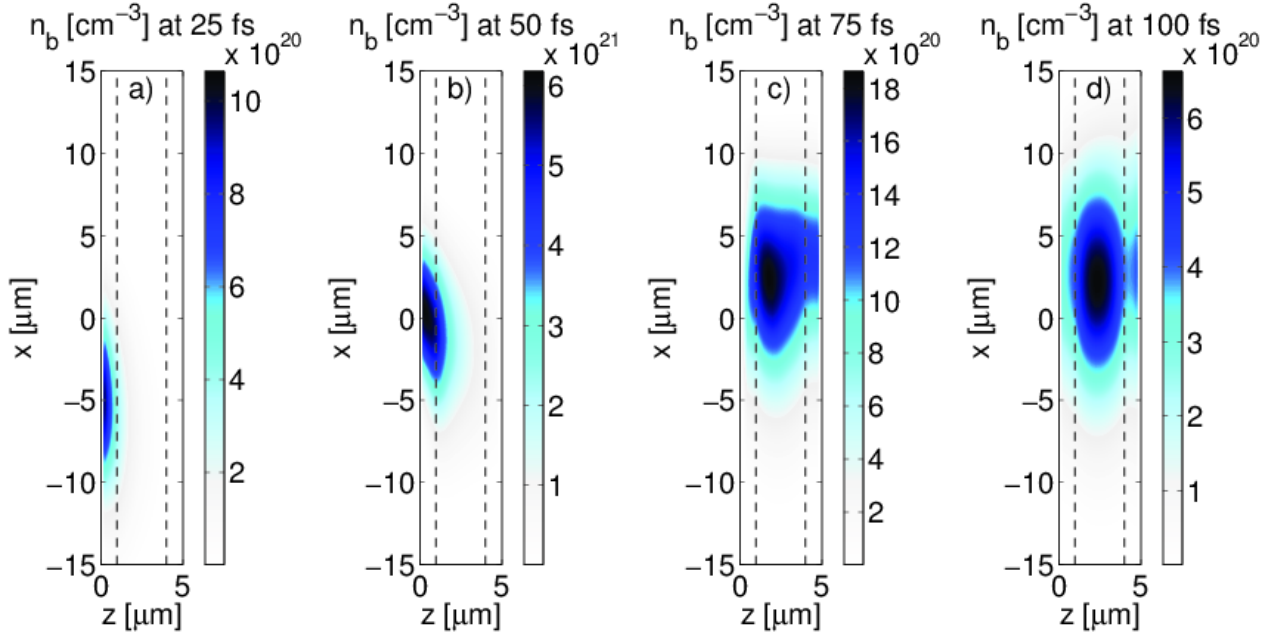


Figure 9.10: Electron beam density n_b [cm^{-3}] from the M1 simulation at $t = 25$ fs (a), $t = 50$ fs (b), $t = 75$ fs (c), and $t = 100$ fs (d). Refluxing is neglected here.

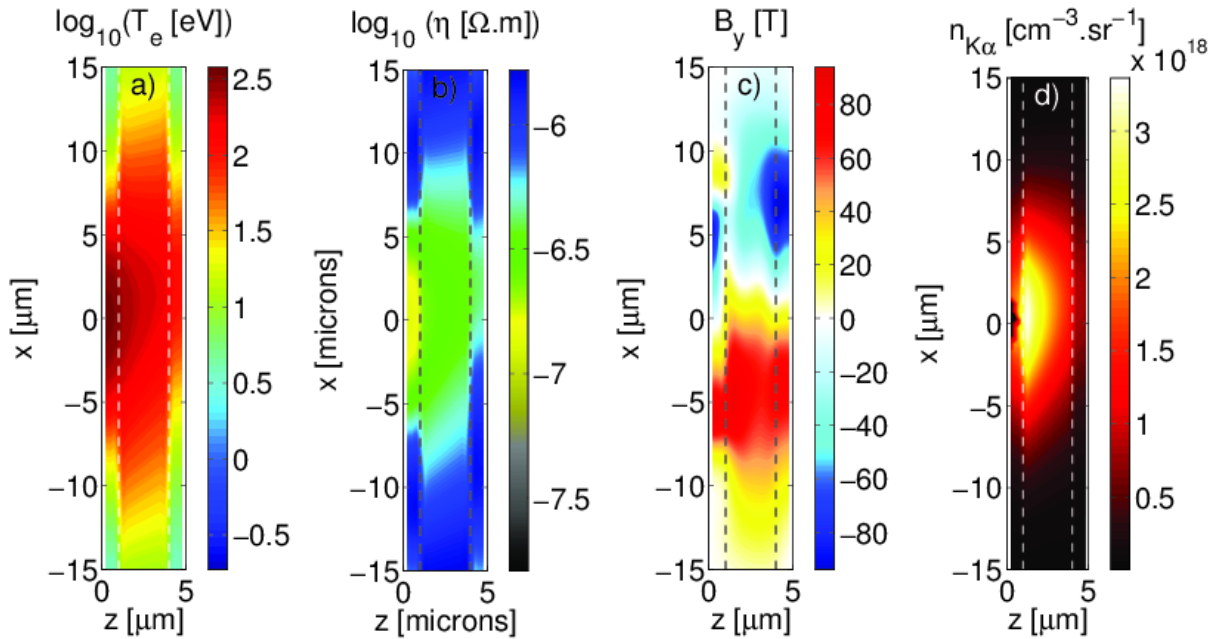


Figure 9.11: Plasma electron temperature T_e [eV] in a logarithmic scale (a), plasma electrical resistivity η [$\Omega\cdot\text{m}$] in a logarithmic scale (b), self-generated magnetic field B_y [T] (c) and the number of emitted $K\alpha$ photons $n_{K\alpha}$ [$\text{cm}^{-3}\cdot\text{sr}^{-1}$] (d) from the M1 simulation at $t = 500$ fs. Refluxing is neglected here.

9.2.2 Refluxing Dependence on the Target Thickness

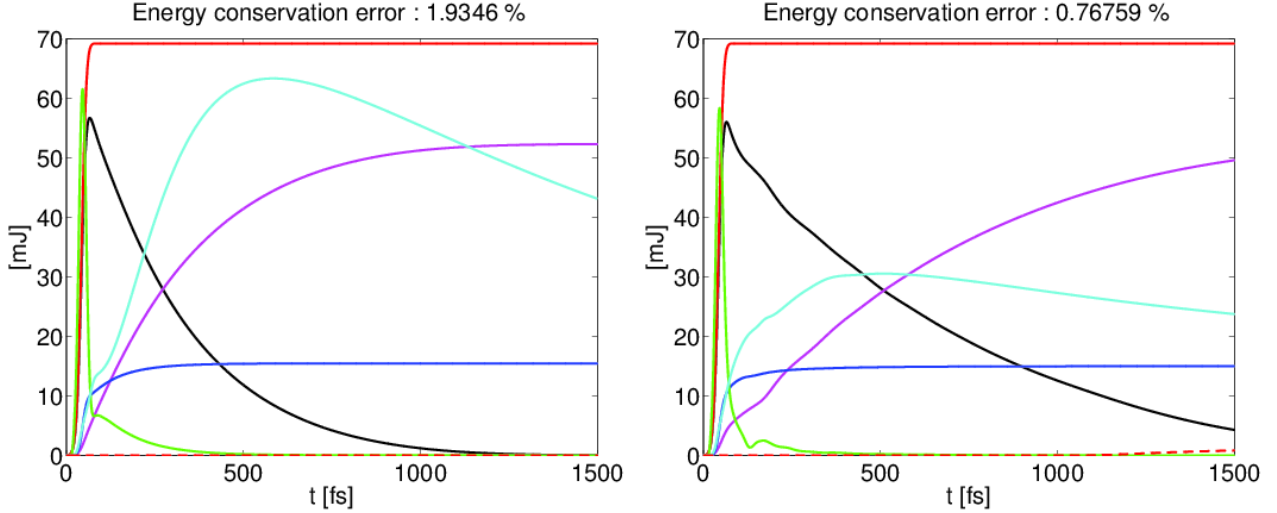


Figure 9.12: (Left panel) Al(1 μm)Cu(3 μm)Al(1 μm) target; (Right panel) Al(1 μm)Cu(3 μm)Al(15 μm) target; Instantaneous beam energy U_b (solid black), integrated beam energy injected at $z = 0$ U_{inc} (solid red), total collisional energy loss U_{col} (solid magenta), total “collective” energy loss U_{res} (solid blue), instantaneous electric energy $U_E \times 10^4$ (solid green) and instantaneous magnetic energy $U_B \times 10^3$ (solid cyan).

In this subsection, we consider the effects of refluxing on the fast electron transport. We present here the simulation results concerning the thinnest target Al(1 μm)Cu(3 μm)Al(1 μm) and the thickest target Al(1 μm)Cu(3 μm)Al(15 μm). Let us remind here that the **fast electron refluxing at the target-vacuum interfaces is modelled assuming their specular reflections.**

Figure 9.12, illustrates the time evolution of the injected fast electrons kinetic energy U_{inc} , the instantaneous fast electron’s energy in the target U_b , the collisional and collective losses of the fast electrons U_{col} and U_{res} and the self-generated electromagnetic energies U_E and U_B for both targets. The energy conservation errors in these two simulations are approximately 0.8 and 1.9%. A larger energy conservation error obtained for the thinner target is due to a greater collisional energy loss by the fast electrons, which is computed according to the downwind scheme (1st order consistency error). We can see that, contrary to the case without refluxing, the simulation must be run up to 1.5 ps in order to allow the fast electrons to lose all their energy and to ensure that they do not contribute anymore to the emission of $K\alpha$ photons. Actually, a simulation time of 1.5 ps is not sufficient for the thicker target ($U_b \approx 5$ mJ at this time). However, as indicated by the increasing fast electron energy escaping from the target transverse boundaries $x = \pm L_x/2$, the fast electrons still in the target at times $t > 1.5$ ps are located at the target transverse boundaries and do not contribute to the $K\alpha$ emission zone we are interested in. As soon as the fast electrons have completed their first recirculation in the target (at ≈ 200 fs for the thinner target and ≈ 250 fs for the thicker target), the fast electron’s energy losses are mostly due to collisions. Indeed, the recirculation of fast electrons

recirculation induces the presence of two counterpropagating beams of similar current densities in the z -direction. Thus, the background electron current and the self-generated electric field in the z -direction decrease rapidly ($j_{b,z}^{(1)} + j_{b,z}^{(2)} + j_{e,z} \approx 0$ implies $j_{e,z} \approx 0 \Rightarrow E_z = \eta j_{e,z} \approx 0$ if $j_{b,z}^{(1)} \approx -j_{b,z}^{(2)}$). This effect can be seen in **Figure 9.13** for the Al($1\ \mu\text{m}$)Cu($3\ \mu\text{m}$)Al($15\ \mu\text{m}$) target and in **Figure 9.14** for the Al($1\ \mu\text{m}$)Cu($3\ \mu\text{m}$)Al($1\ \mu\text{m}$) target. Indeed, we clearly see that the beam current density $|\mathbf{j}_b| = |\mathbf{j}_b^{(1)} + \mathbf{j}_b^{(2)}| \approx 0$ at $x \approx 10\ \mu\text{m}$ and $t \approx 240\ \text{fs}$ or $t \approx 490\ \text{fs}$, while there is a lot of fast electrons in these zones according to the corresponding beam density maps.

Figure 9.12 also shows that, for the thin target, the collective energy losses of the fast electrons are comparable with those obtained without refluxing ($U_{\text{res}} \approx 15\ \text{mJ}$ instead of $\approx 10\ \text{mJ}$). The fact that we observe the same amount of collective energy losses for the thick target ($U_{\text{res}} \approx 15\ \text{mJ}$) indicates that the decrease in the beam current density with depth is such that collisional losses of the fast electrons prevail for $z \gtrsim 4\ \mu\text{m}$. That is why we also obtain similar temperatures at the Aluminum rear side layer when comparing the simulations without refluxing in the previous **subsection**.

In **Figure 9.12**, we can see that the maximum of magnetic energy U_B in the target is greater for the thin target compared to the thick target by a factor ≈ 2 . This is a consequence of resistivity gradients at the Al/Cu and Cu/Al interfaces (see B_y at $t \approx 1.5\ \text{ps}$ in **Figure 9.13** and **9.14**). They are greater in the thin target compared to the thick target since the transverse component of the beam current density $j_{b,x}$ is greater. This results from the shorter propagation distance of the fast electrons, which have thus a larger density (see **Figure 9.13** and **9.14**). It must be emphasized here that we have to be careful concerning these self-generated magnetic fields induced by resistivity gradients at material interfaces: like all "hybrid" model, our model is based on the quasi-static approximation and the neglect of the target electron inertia, assuming time scales greater than the beam neutralization time. Consequently, it is valid on space scales much larger than the target skin depth $\lambda_e = c/\omega_p$. Therefore, the increase of these self-generated magnetic fields with decreasing spatial cell dimensions Δz must be mitigated in the case where Δz is chosen smaller than λ_e . Indeed, the temporal growth of this contribution to the self-generated magnetic field reads

$$\frac{\partial B_{y,\text{res}}}{\partial t} \approx j_{b,x} c \frac{\partial \eta}{\partial z} \Rightarrow \left| \frac{B_{y,\text{res}}^{n+1,i,k} - B_{y,\text{res}}^{n,i,k}}{\Delta t_n} \right| = \left| j_{b,x}^{n,i,k} c \frac{\eta^{i,k+1} - \eta^{i,k-1}}{2\Delta z} \right|. \quad (9.36)$$

Thus, if we fix $\eta^{i,k+1} = \eta_{\text{Cu}}$ and $\eta^{i,k-1} = \eta_{\text{Al}}$ or $\eta^{i,k+1} = \eta_{\text{Al}}$ and $\eta^{i,k-1} = \eta_{\text{Cu}}$, the B-field strongly depends on the value of Δz for a given beam current density $j_{b,x}$. Even if these huge magnetic fields are initially located over a few Δz , they subsequently diffuse inside the target, leading to unphysical magnetic energies. It is not the case for all the simulations presented in this thesis ($\Delta z = 0.25\ \mu\text{m}$ is the smaller spatial cell dimension that is used). However, additional simulations were conducted in the course of the thesis for the understanding of experiments using targets made of a Copper layer followed by a vitreous Carbon layer, for which the ratio $\eta_{\text{C}}/\eta_{\text{Cu}}$ was huge (see **Figure 3.9 c**). As a consequence, the obtained magnetic energy was found greater than the injected fast electron's kinetic

energy, which is clearly unphysical.

The maximum number of emitted $K\alpha$ photons in the thick target (see $n_{K\alpha}$ in **Figure 9.13**), is approximately equal to that obtained in the thin target without refluxing (see **Figure 9.11 d**). By contrast, the $K\alpha$ yield in the thin target with refluxing is increased by a factor > 8 (see **Figure 9.14**). We conclude that there is a strong dependence of refluxing effects on the fast electron transport with the target thickness and that the refluxing effects on the emission of $K\alpha$ photons decrease with the target thickness.

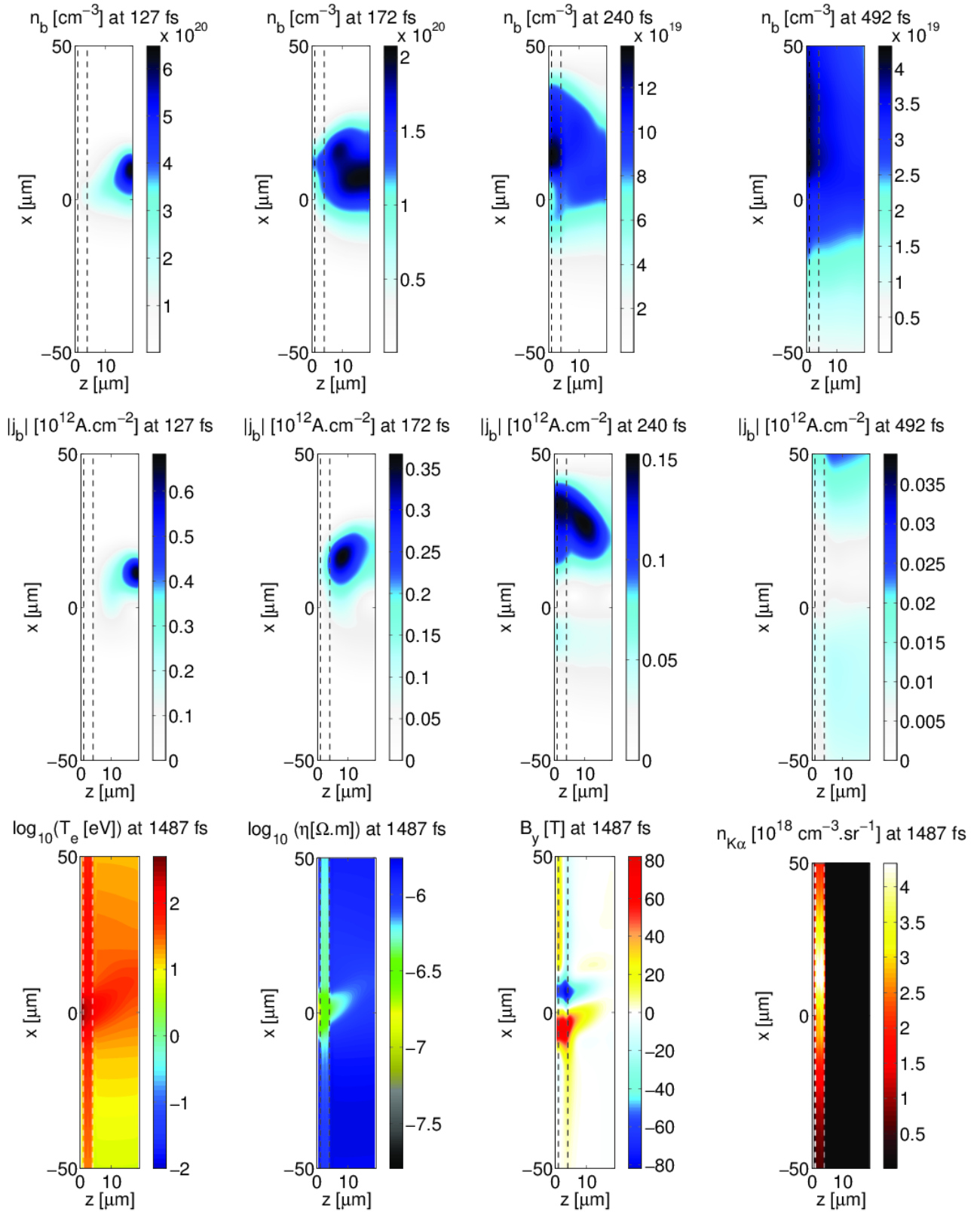


Figure 9.13: 2D maps of the beam density n_b [cm $^{-3}$] at $t = 127$ fs, $t = 172$ fs, $t = 240$ fs and $t = 492$ fs, corresponding 2D maps of the beam current density $|j_b|$ and target electron temperature T_e , self-generated magnetic field B_y and the number of $K\alpha$ and $K\beta$ photons $n_{K\alpha}$ and $n_{K\beta}$, emitted from the Copper tracer layer at $t = 1487$ fs.

9.2. APPLICATION TO THE SACLAY UHI100 EXPERIMENT

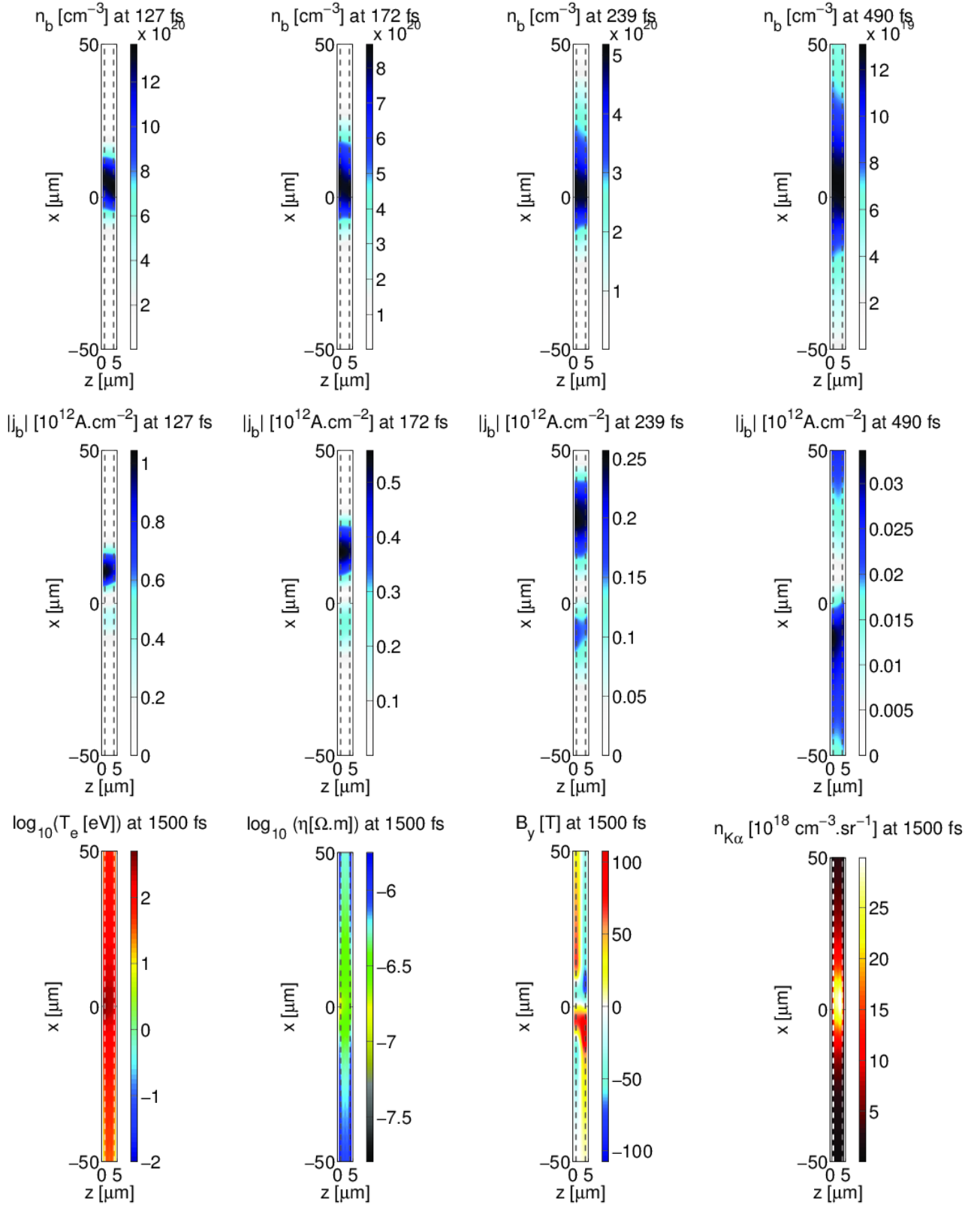


Figure 9.14: 2D maps of the beam density n_b [cm^{-3}] at $t = 127$ fs, $t = 172$ fs, $t = 240$ fs and $t = 492$ fs, corresponding 2D maps of the beam current density $|j_b|$ and target electron temperature T_e , self-generated magnetic field B_y and the number of $K\alpha$ and $K\beta$ photons $n_{K\alpha}$ and $n_{K\beta}$, emitted from the Copper tracer layer at $t = 1487$ fs.

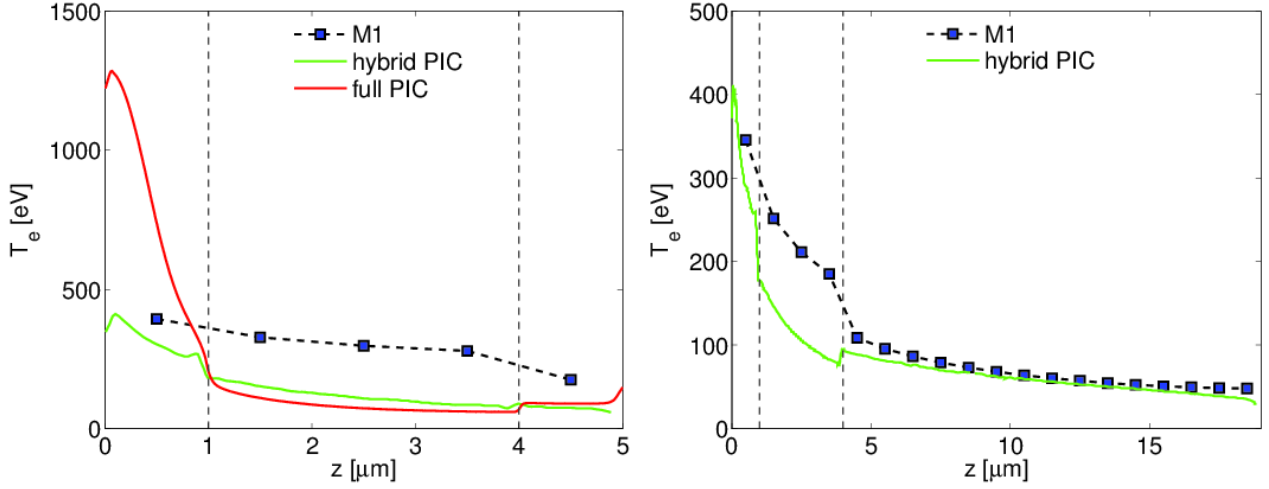


Figure 9.15: (Left panel) Longitudinal profiles of background electron temperature $\langle T_e \rangle$ (averaged over $|x_{\max} - x| < 5 \mu\text{m}$) obtained with the M1 code (blue points) with $\Delta z = 1 \mu\text{m}$, the hybrid PIC code PaRIS [Gremillet, 2014] (green curve) and the full collisional PIC code CALDER [Gremillet, 2014] (red curve) for the Al(1 μm)Cu(3 μm)Al(1 μm) target. (Right panel) Longitudinal profiles of $\langle T_e \rangle$ obtained with the M1 code (blue points) with $\Delta z = 1 \mu\text{m}$ and with the hybrid PIC code PaRIS [Gremillet, 2014] (green curve) for the Al(1 μm)Cu(3 μm)Al(15 μm) target. x_{\max} is defined as the position where $T_e(x_{\max}, z)$ is the maximum electron temperature at a given depth z .

We can see that in both thin and thick targets, far away from the first recirculation zone (from $x \approx -10$ to $x \approx 20 \mu\text{m}$), the Copper tracer layer is hotter than the Aluminum layers (see T_e in **Figures 9.13** and **9.14**). This is due to the greater density of background electrons (bound, free and screened free) in Copper, leading to greater collisional energy losses (see **Chapter 4, section 4.2, Figure 4.2**) compared to Aluminum. Besides, the Copper layer is hotter in the thin target due to the same reason as given for the explanation of the resistivity gradients contribution to the self-generated magnetic fields: the fast electrons recirculate more times through the Copper layer in the thin target and thus mainly deposit their energy through collisions. Also, in the M1 simulations, the Ohmic heating of the Copper layer by the return current is greater than the collisional heating of the Aluminum rear side layer during the first 100 fs due to solid state effects (**section 9.2.1**). Indeed, as illustrated in **Figure 9.15**, this is not the case for the simulation results obtained with the full collisional PIC code CALDER [Lefebvre et al., 2003] [Nuter et al., 2011] [Pérez et al., 2012] and the hybrid PIC code PARIS [Gremillet et al., 2002] conducted by [Gremillet, 2014]. The difference between the PIC methods (hybrid or not) and the M1 method concerning the spatial cell dimensions may be striking: $\Delta z = 1 \mu\text{m}$ for M1 while $\Delta z \leq \lambda_{D,b} = \sqrt{k_B T_b / 4\pi\gamma_b n_b e^2} \approx 7.43 \cdot 10^{-3} \mu\text{m} (T_b [\text{keV}] / \gamma_b n_b [10^{21} \text{cm}^{-3}])^{1/2}$ for the PIC codes. This is due to the conceptual difference between a PIC method and a "Vlasov-Fokker-Planck" method, like M1. For the latter, the whole space $500 \mu\text{m} (\times 500 \mu\text{m}) \times 5$ (or 19) μm is discretized in order to describe the distribution function, while for both PIC methods, this is the trajectories of the discretized macro particles following their position that are computed, only. Thus, the PIC method allows for a less expensive numerical cost concerning the space discretization by following

9.2. APPLICATION TO THE SACLAY UHI100 EXPERIMENT

the particles trajectories. The counterpart of this advantage is the interpolation and extrapolation of the electromagnetic fields that imposes $\Delta z \leq \lambda_{D,b}$ and constrains severely the computational cost. However, while we obtain a significant difference of heating in the Copper layer due to the solid state corrections mentioned above, we obtain the same temperature at the rear side Aluminum layer for the thick target, where the fast electron collisions dominate, is approximately the same (see **Figure 9.15**).

Besides, the full collisional PIC simulation predicts the temperature of the first Aluminum layer twice greater than the one predicted in both hybrid simulations. Let us try to explain such a discrepancy by the fact that the fast electron current is temporally modulated. For this, we solve the Maxwell equations coupled to the background electron hydrodynamic equations, assuming for simplicity

1. that the problem is one-dimensional,
2. a negligible pressure force of the plasma electrons,
3. a negligible electron thermal conductivity,
4. negligible collisional effects of fast electrons transport,
5. a negligible electron-ion energy exchange and
6. a rigid electron beam with a beam density

$$n_b(z, t) = n_{b0} + \delta n_b \text{ where } \delta n_b = -n_{b0} \sin^2\left(\frac{\omega_0}{2}t\right) \text{ such that } n_b(z, t) = n_{b0} \cos^2\left(\frac{\omega_0}{2}t\right). \quad (9.37)$$

$n_{b0} = n_{b0}(z - v_b t)$ represents the temporal/spatial envelope of the laser-generated beam density and δn_b accounts for the fast electron bunches injected in the target at the frequency $\omega_0 = \omega_L$ or $\omega_0 = 2\omega_L$ depending on the acceleration mechanisms (see **Chapter 8, section 8.2, Figure 8.7**). Here, due to the ultra high contrast of the laser pulse, we may expect that the $\mathbf{j} \times \mathbf{B}$ heating is the dominant acceleration mechanism so that we may consider $\omega_0 = 2\omega_L$. We note $j_{b0} = -n_{b0}ev_b$ the rigid beam current density envelope with v_b the beam velocity, assumed to be constant, and $\delta j_b = -\delta n_b ev_b$ the bunches component.

While assumptions 1 and 6 are made for simplicity in order to obtain analytical estimates, assumptions 2, 3, 4 and 5 are fully justified over simulation times of $t \approx 100$ fs. The equations that have to be solved are the Maxwell-Gauss equation

$$\frac{\partial E}{\partial z} = -4\pi e (n_e + n_b - Z^* n_i), \quad (9.38)$$

the Maxwell-Ampère equation

$$\frac{\partial E}{\partial t} = -4\pi (j_e + j_b) \quad (9.39)$$

the target electron continuity equation,

$$\frac{\partial n_e}{\partial t} + \frac{\partial}{\partial z} (n_e v_e) = 0 \quad (9.40)$$

the target electron momentum conservation equation

$$\frac{\partial j_e}{\partial t} + \frac{\partial}{\partial z} (v_e j_e) = \frac{n_e e^2}{m_e} (E - \eta j_e) = \frac{n_e e^2}{m_e} E - \nu j_e \quad (9.41)$$

and the target electron heat equation

$$C_{V,e} \left[\frac{\partial}{\partial t} + v_e \frac{\partial}{\partial z} \right] (T_e) = \eta j_e^2 = -\frac{m_e \nu v_e}{e} j_e. \quad (9.42)$$

The solutions n_{e0} , v_{e0} , j_{e0} , T_{e0} provided by hybrid models correspond to the quasi-static approximation: they neglect the target electron inertia, assuming times greater than the beam electromagnetic neutralization time. They read consequently

$$\left\{ \begin{array}{l} \frac{\partial E_0}{\partial z} = -4\pi e (n_{e0} + n_{b0} - Z^* n_i) = 0 \quad \text{with } n_{b0} \ll n_{e0} = Z^* n_i \\ \frac{\partial E_0}{\partial t} = -4\pi (j_{e0} + j_{b0}) = 0 \quad \text{implying } j_{e0} = -j_{b0} \text{ and } v_{e0} = -\frac{n_{b0}}{n_{e0}} v_b \\ \frac{\partial n_{e0}}{\partial t} + \frac{\partial}{\partial z} (n_{e0} v_{e0}) = 0 \\ E_0 = \eta_0 j_{e0} = -\frac{m_e \nu v_{e0}}{e} \quad \text{with } \eta_0 = \frac{m_e \nu}{n_{e0} e^2} = \frac{4\pi \nu}{\omega_p^2} \text{ and} \\ C_{V,e} \frac{\partial T_{e0}}{\partial t} = \eta_0 j_{e0}^2 = E_0 j_{e0}. \end{array} \right. \quad (9.43)$$

Let us estimate analytically the errors

$$\forall \xi \in \{n_e, v_e, j_e, T_e\}, \delta \xi = \xi - \xi_0 \quad (9.44)$$

done by hybrid codes. Assuming ξ_0 vary slowly compared to $\delta \xi$, we obtain, by injecting (10.56) and (10.60) in the previous equations :

$$\frac{\partial}{\partial z} \delta E = -4\pi e (\delta n_e + \delta n_b), \quad (9.45)$$

$$\frac{\partial}{\partial t} \delta E = -4\pi (\delta j_e + \delta j_b), \quad (9.46)$$

$$\left[\frac{\partial}{\partial t} + v_{e0} \frac{\partial}{\partial z} \right] \delta n_e = -n_{e0} \frac{\partial}{\partial z} \delta v_e - \frac{\partial}{\partial z} (\delta n_e \delta v_e) \quad \text{where } \delta v_e = -\frac{\delta j_e + \delta n_e e v_{e0}}{n_{e0} e \left(1 + \frac{\delta n_e}{n_{e0}} \right)}, \quad (9.47)$$

$$\left[\frac{\partial}{\partial t} + v_{e0} \frac{\partial}{\partial z} \right] \delta j_e = -\frac{\partial}{\partial z} (\delta v_e \delta j_e) - j_{e0} \frac{\partial}{\partial z} \delta v_e + \frac{\omega_p^2}{4\pi} \frac{\delta n_e}{n_{e0}} \delta E + \frac{\omega_p^2}{4\pi} \delta E + \frac{\omega_p^2}{4\pi} E_0 \frac{\delta n_e}{n_{e0}} - \nu \delta j_e \quad (9.48)$$

9.2. APPLICATION TO THE SACLAY UHI100 EXPERIMENT

and

$$C_{V,e} \left[\frac{\partial}{\partial t} + v_{e0} \frac{\partial}{\partial z} \right] \delta T_e = -C_{V,e} \delta v_e \frac{\partial}{\partial z} \delta T_e + E_0 \frac{\delta v_e}{v_{e0}} \delta j_e + E_0 \delta j_e - E_0 n_{e0} e \delta v_e. \quad (9.49)$$

We assume constant thermal capacity $C_{V,e}$ and electron relaxation time ν in space and time. In addition, $n_i = 6 \cdot 10^{22} \text{ cm}^{-3}$ and $n_{e0} = Z^* n_i \geq 3n_i$ in Aluminum so that the plasma frequency $\omega_p \geq 23 \text{ rad.fs}^{-1}$. The laser frequency is $\omega_L = 2\pi c/\lambda = 2.3 \text{ rad.fs}^{-1}$ ($\lambda = 800 \text{ nm}$). Consequently, we can consider $\omega_p \gg \omega_0$. Also, according to **Figure 6.9**, the background electron relaxation rate ν can be consider smaller than 10 fs^{-1} but larger than 1 fs^{-1} from $T_e \approx 10^{-1} \text{ eV}$ ($T_i = T_e$) to $T_e \approx 1 \text{ keV}$. Thus, we consider the scaling

$$\omega_p \gg \nu \gg \omega_0. \quad (9.50)$$

We assume in addition

7. the non-linear terms are negligible,
8. quasi neutrality $\delta n_e = -\delta n_b$ and
9. $(\partial \delta v_e / \partial z) = 0$.

Assumptions 8. and 9. can be justified by noting that the charge neutralization mainly takes place in the transverse direction leading rapidly to $\delta n_e = -\delta n_b$ with spatial variations of δv_e mainly in the x -direction. Assumption 7 serves to linearize the equations and to find analytical estimates. Under these last assumptions, by working in the frame where the target electron envelope is at rest : $\delta \hat{\xi}(\zeta, t) = \delta \xi(z, t)$ with $\zeta = z - v_{e0}t$ and by coupling (9.45) and (9.46), we obtain the coupled equations

$$\left\{ \begin{array}{l} \frac{\partial \delta \hat{E}}{\partial t} = -4\pi (\delta \hat{j}_e + \delta \hat{j}_b) \quad \text{a)} \\ \frac{\partial \delta \hat{n}_e}{\partial t} = 0 \quad \text{b)} \\ \frac{\partial \delta \hat{j}_e}{\partial t} = \frac{\omega_p^2}{4\pi} \delta \hat{E} + \frac{\omega_p^2}{4\pi} E_0 \frac{\delta \hat{n}_e}{n_{e0}} - \nu \delta \hat{j}_e \quad \text{c)} \end{array} \right. , \quad (9.51)$$

that finally gives

$$\frac{\partial^2 \delta \hat{j}_e}{\partial t^2} + \nu \frac{\partial \delta \hat{j}_e}{\partial t} + \omega_p^2 \delta \hat{j}_e = -\omega_p^2 \delta \hat{j}_b, \quad (9.52)$$

describing the error $\delta \hat{j}_e$ done by the hybrid methods. Considering the limit (9.50), assuming $\delta \hat{j}_e(\zeta, t = 0) = 0$ and $\partial_t \delta \hat{j}_e(\zeta, t = 0) = 0$, we find

$$\delta \hat{j}_e = -\frac{j_{b0}}{2} \left[1 - \cos(\omega_p t) \exp\left(-\frac{\nu}{2}t\right) \right]. \quad (9.53)$$

Solving then the heat equation (9.49) for the error in temperature, we find

$$C_{V,e} \frac{\partial \delta \widehat{T}_e}{\partial t} = 2E_0 \delta \widehat{j}_e + E j_{e0} \frac{\delta \widehat{n}_e}{n_{e0}}. \quad (9.54)$$

Following assumptions 7, 8 and 9, assuming $\delta \widehat{T}_e(\zeta, t = 0) = 0$, the ordering (9.50) and $n_{b0} \ll n_{e0}$ for neglecting of the second term in the right hand side of Equation (9.54), the solution reads

$$\delta \widehat{T}_e = -\frac{j_{b0} E_0}{C_{V,e}} \left[t - \frac{\sin(\omega_p t)}{\omega_p} \exp\left(-\frac{\nu}{2} t\right) \right]. \quad (9.55)$$

Finally, averaging over one electron bunch period $\tau_0 = 2\pi/\omega_0$, we deduce an estimate of the additive temperature component in the first Aluminum layer, obtained by the full PIC simulation and neglected by both hybrid models :

$$\langle \delta \widehat{T}_e \rangle_{1 \text{ bunch}} = \frac{1}{\tau_0} \int_0^{\tau_0} \delta \widehat{T}_e(\zeta, t) dt = -\frac{j_{b0} E_0}{C_{V,e}} \tau_0 = \langle T_{e0} \rangle_{1 \text{ bunch}}. \quad (9.56)$$

Thus, according to our simple model (9.51), each fast electron bunch generates a weak field of background electron plasma wave according to (9.51 a) and (9.51 c), which are damped due to collisions with the background ions and electrons, according to (9.51 c). This damping results in an additional target electron heating mechanism according to (9.54) that leads to a target electron temperature $T_e = T_{e0} + \delta T_e$, which is approximatively two times greater than the one predicted by the hybrid models T_{e0} according to (9.56). This is quite in good agreement with the simulation results, illustrated in the left panel of **Figure 9.16**. This additional electron heating mechanism was recently pointed out by [Sherlock et al., 2014]. They proposed therefore to replace the quasi-static Ohm's law $\mathbf{E} = -\eta \mathbf{j}_b$ by the dynamic equation

$$\frac{\partial^2 \mathbf{E}}{\partial t^2} + \nu \frac{\partial \mathbf{E}}{\partial t} + \omega_p^2 \mathbf{E} = -\frac{4\pi}{c} \left(\frac{\partial \mathbf{j}_b}{\partial t} + \nu \mathbf{j}_b \right) \quad (9.57)$$

for the electric field that takes into account the excitation of plasma waves and their collisional damping due to collisions.

9.2.3 Comparison of Time Integrated $K\alpha$ Emission of with the Experimental Data

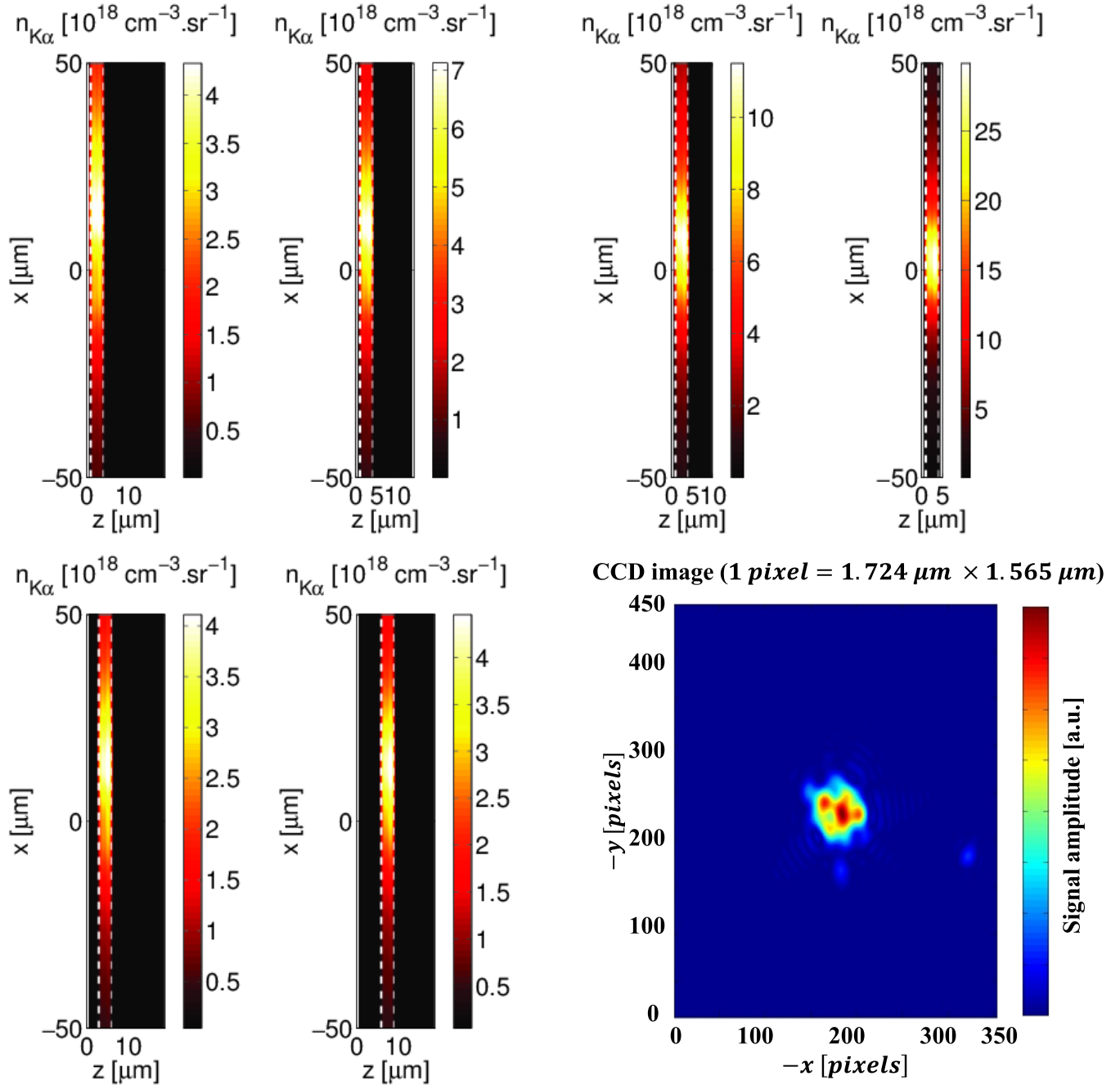


Figure 9.16: 2D maps of the number of emitted $K\alpha_1$ photons at $t = t_f = 1.5$ ps from the 2D-3V M1 simulations with refluxing and an example of CCD images obtained experimentally [Vauzour, 2014].

The 2D maps of the time integrated number of $K\alpha_1$ photons emitted per steradian at $t = 1.5$ ps from the 2D-3V M1 simulations with refluxing for all targets are plotted in **Figure 9.16**. We can see that the emission of $K\alpha_1$ photons from the Copper tracer layer increases with decreasing target thickness. Indeed, the maximum value of the $K\alpha_1$ emission reaches $\approx 30 \cdot 10^{18} \text{ cm}^{-3} \cdot \text{sr}^{-1}$ for the thinner target while this number decreases to $\approx 11 \cdot 10^{18} \text{ cm}^{-3} \cdot \text{sr}^{-1}$ for the Al($1 \mu\text{m}$)Cu($3 \mu\text{m}$)Al($6 \mu\text{m}$) target and $\approx 7 \cdot 10^{18} \text{ cm}^{-3} \cdot \text{sr}^{-1}$ for the Al($1 \mu\text{m}$)Cu($3 \mu\text{m}$)Al($10 \mu\text{m}$) target falling down to $4 \cdot 10^{18} \text{ cm}^{-3} \cdot \text{sr}^{-1}$ for the thickest target. Moreover, the location of maximum emission shifts to larger x with increasing target thickness. This is a clear signature of the fast electron's mean propagation direction that makes an angle of $\approx 25^\circ$ with the target normal.

Let us compare these 2D-3V M1 simulation results with the experimental $K\alpha_1$ signals received by the CCD camera and obtained thanks to the crystal spectrometers. An example of CCD image is shown in **Figure 9.16**. In order to decrease the effects of noise-to-signal ratios estimated around 10% according to [Santos, 2014], the experimental signals have been summed over several shots under the same conditions [Vauzour, 2014]. Therefore, we cannot directly compare the absolute values of the signals (since they depend on the number of shots conducted for each target). Rather, we renormalize the experimental signals according to our 2D-3V M1 simulation results:

$$n_{K\alpha, \text{exp}} \rightarrow n_{K\alpha, \text{exp}} \frac{\langle n_{K\alpha} \rangle_z^{\text{max}}}{n_{K\alpha, \text{exp}}^{\text{max}}}. \quad (9.58)$$

Here, $\langle n_{K\alpha} \rangle_z^{\text{max}}$ is the maximum value of the number of emitted $K\alpha_1$ photons from the 2D-3V M1 simulations, averaged over the Copper layer thickness

$$\langle n_{K\alpha} \rangle_z(x) = \frac{1}{L_{\text{Cu}}} \int_{z_1}^{z_2} n_{K\alpha}(x, z, t_f) dz. \quad (9.59)$$

Here, $L_{\text{Cu}} = 3 \mu\text{m}$, $t_f = 1.5$ ps, $z_1 = 1 \mu\text{m}$ and $z_2 = 4 \mu\text{m}$ or $z_1 = 3 \mu\text{m}$ and $z_2 = 6 \mu\text{m}$ or $z_1 = 6 \mu\text{m}$ and $z_2 = 9 \mu\text{m}$ depending on the targets. The resulting experimental signals averaged over 5 pixels ($8.6 \mu\text{m} \times 7.825 \mu\text{m}$) [Vauzour, 2014] are plotted in **Figure 9.17**. The panels **a**) and **b**) present the horizontal (x -axis) and vertical axis (y -axis) of the two-dimensional CCD image as shown in **Figure 9.16**. In order to make comparable plots, we add a uniform noise of 10% of the maximum value to the calculated $K\alpha$ profiles:

$$\langle n_{K\alpha} \rangle_z(x) \rightarrow \langle n_{K\alpha} \rangle_z(x) + b[x] \text{ where } b[x] = 0.1 \langle n_{K\alpha} \rangle_z^{\text{max}} 1_{x \in [-\infty, \infty]}[x]. \quad (9.60)$$

Also, we account for the average over 5 pixels ($8.62 \mu\text{m}$ in the x -direction) of $K\alpha_1$ signals by convolving (9.60) with a Gaussian function that has a Full Width at Half Maximum (FWHM) of $\Delta x_0 = 10 \mu\text{m}$

$$\langle n_{K\alpha} \rangle_z(x) = \int_{-\frac{L_x}{2}}^{\frac{L_x}{2}} \frac{\langle n_{K\alpha} \rangle_z(x_0)}{\sqrt{2\pi \frac{\Delta x_0^2}{8 \ln 2}}} \exp \left[-4 \ln 2 \left(\frac{x - x_0}{\Delta x_0} \right)^2 \right] dx_0. \quad (9.61)$$

9.2. APPLICATION TO THE SACLAY UHI100 EXPERIMENT

Finally, the offset implied by the artificial noise b is accounted for by subtracting $0.1\langle n_{K\alpha} \rangle_z^{\max}$ from (9.61). The processed numerical "signals" are plotted in **Figure 9.17 c)** for targets of variable thickness and in **Figure 9.17 d)** for targets of variable target depth.

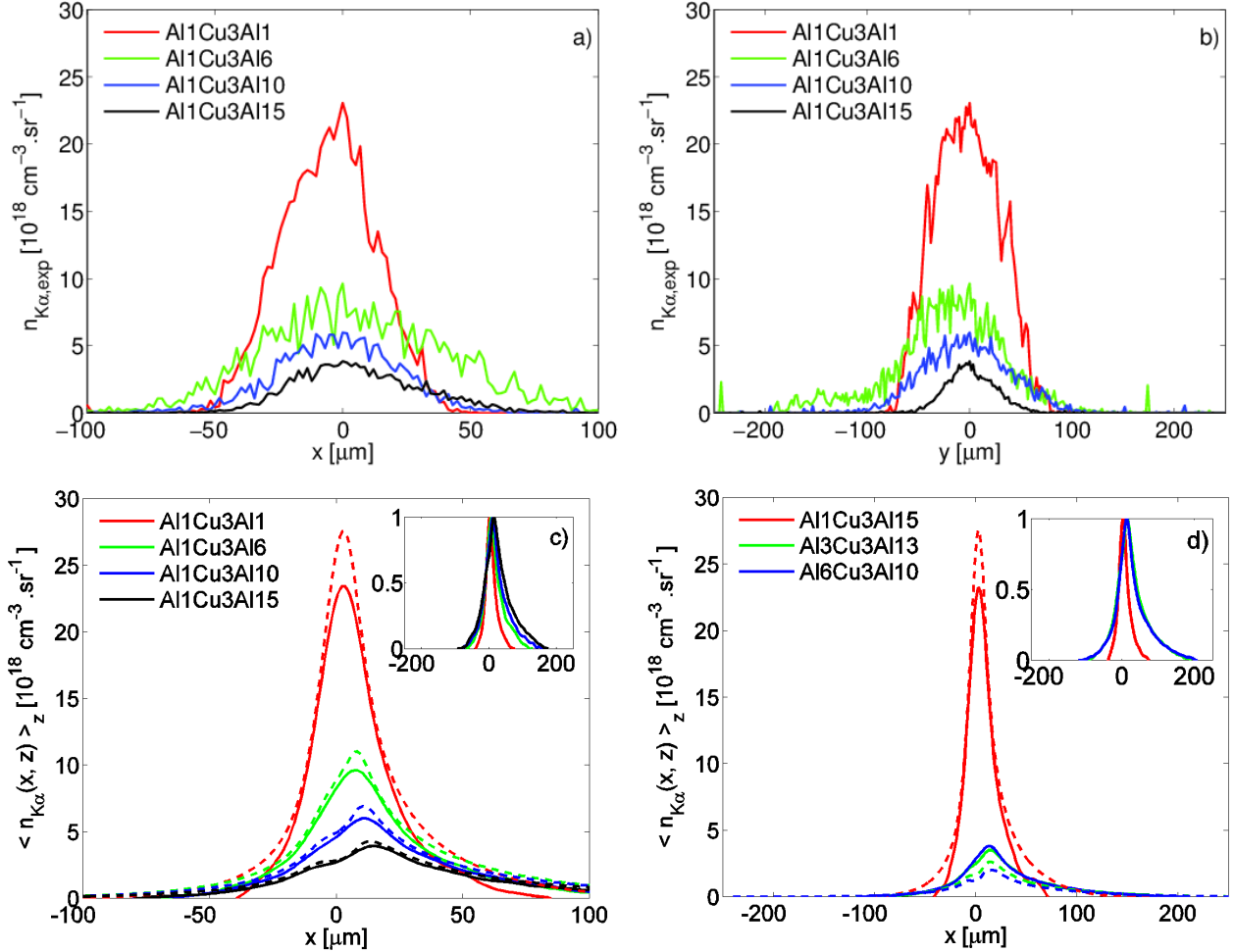


Figure 9.17: Experimental horizontal a) and vertical b) profiles of $K\alpha_1$ photon signals averaged over 5 pixels ($8.62 \mu\text{m} \times 7.825 \mu\text{m}$) [Vauzour, 2014] for targets of variable thickness (renormalized according to the corresponding 2D-3V M1 simulations). Horizontal profiles of the $K\alpha_1$ emission obtained from the simulations by averaging it over the whole Copper layer thickness (dashed curves), adding an uniform noise and convolving it with a Gaussian function of $10 \mu\text{m}$ FWHM (full curves) for targets of variable thickness c) and variable tracer depth d). Corresponding normalized profiles are plotted in the inserts of Figures c) and d).

According to the inset in **Figure 17 d)**, we can see that the $K\alpha_1$ emission spot size increases with the tracer depth. It is usually interpreted in experiments as a signature of a strong angular divergence of laser-generated electron beams. However, as already noticed by [Ovchinnikov et al., 2011], it is not so evident. The wings of the emission profiles are contaminated by the recirculation of fast electrons inside the target. For example, the normalized emission profiles plotted in the insert of **Figure 9.17 c)** would mean that the $K\alpha_1$ photon emission spot size increases with increasing target depth. It is false according to the non-normalized values as illustrated in **Figure 9.17 c)** : **due to the fast electron refluxing, the emission spot size increases with decreasing target thickness**. According to **9.17 b)**, the $K\alpha_1$ photon signals obtained experimentally are symmetric with respect to the y -axis in the plane $x = 0$. As illustrated in **Figure 9.17 a)**, it is not the case with respect to the x -axis in the plane $y = 0$ due to the incidence angle of the laser pulse in the plane $y = 0$.

Except for the thinner target, **Figures 9.17 a)** and **c)** show that the 2D-3V M1 simulations reproduce well the experimental results. However, these 2D-3V calculations must be revised with regard to three-dimensional effects. The right panel of **Figure 9.18** compares the 3D-3V simulation result and the experimental data. There is a strong discrepancy concerning the $K\alpha$ photon emission spot size, even worse than for the 2D-3V simulation. The comparison is conducted under the same conditions as in the 2D-3V simulations. Firstly, the experimental signal is renormalized to the 3D-3V M1 simulation according to (9.58). The maximum value of the $K\alpha_1$ emission is averaged over the Copper layer thickness

$$\langle n_{K\alpha} \rangle_z(x, y) = \frac{1}{L_{\text{Cu}}} \int_{z_1}^{z_2} n_{K\alpha}(x, y, z, t_f) dz \quad (9.62)$$

with $L_{\text{Cu}} = 3 \mu\text{m}$, $t_f = 1.5 \text{ ps}$, $z_1 = 1 \mu\text{m}$ and $z_2 = 4 \mu\text{m}$. A uniform noise of 10 % of the maximum value is added in x and y directions according to (9.60) and the result was convolved with two Gaussian functions of $\Delta x_0 = \Delta y_0 = 10 \mu\text{m}$ FWHM according to (9.61). The offset of $0.1 \langle n_{K\alpha} \rangle_z^{\text{max}}$ is then subtracted from the final result.

9.2.4 Three-Dimensional Effects

As illustrated in the inset of the right panel of **Figure 9.18**, the spot size on x -axis of the $K\alpha_1$ photon emission is almost twice less in 3D than in 2D. We explain this as follows. In the 2D simulations, we impose specular reflections of the fast electrons in the plane $y = 0$ since the third dimension is not taken into account. Therefore, the fast electrons are confined in this plane and the emission in the x -direction is enlarged. It is not the case in the 3D simulation where we allow the fast electrons to propagate in the y -direction. It is important to notice that this 3D effect also lead to a smaller maximum value of $K\alpha_1$ photon emission of $1.4 \cdot 10^{18} \text{ cm}^{-3} \cdot \text{sr}^{-1}$ even smaller than in the 2D case without refluxing (see $n_{K\alpha}$ in **Figure 9.11**). However, the effective surface of $K\alpha_1$ photon emission S_α is greater in 3D as we may expect. Indeed, we obtain a total number of $K\alpha_1$ photons emitted per

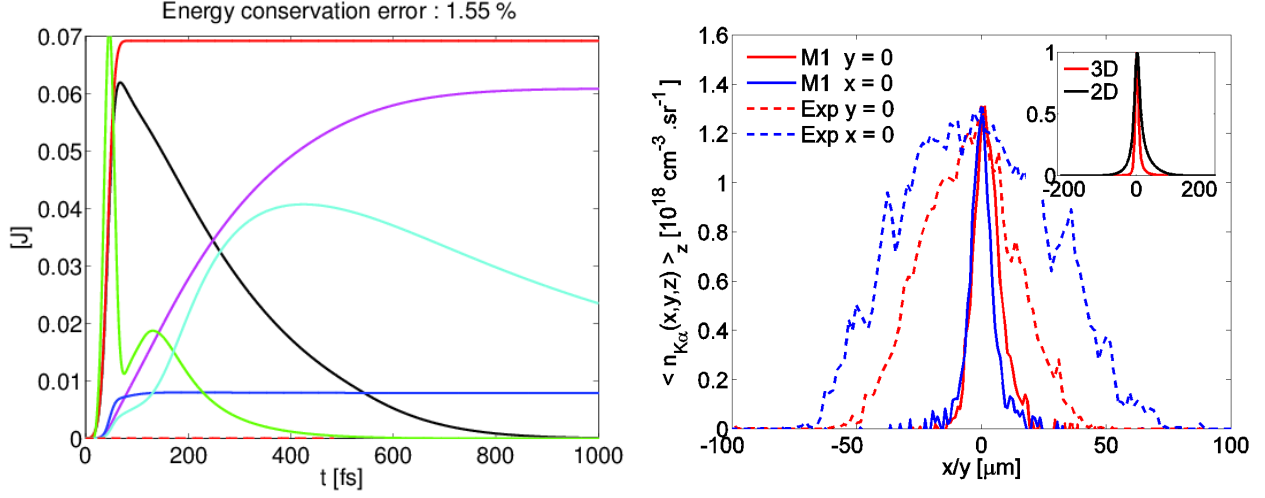


Figure 9.18: Left panel : Instantaneous beam energy U_b (solid black), integrated beam energy balanced between injected at $z = 0$ U_{inc} (solid red), total collisional energy loss U_{col} (solid magenta), total “collective” energy loss U_{res} (solid blue), instantaneous electric energy $U_E \times 10^4$ (solid green) and instantaneous magnetic energy $U_B \times 10^2$ (solid cyan) from the 3D-3V simulation for the thinner target. Right panel : Experimental horizontal and vertical profiles of $K\alpha_1$ photon signals averaged over 5 pixels ($8.62 \mu\text{m} \times 7.825 \mu\text{m}$) for the thinner target [Vauzour, 2014], renormalized according to the simulation (dashed curves) and corresponding horizontal and vertical profiles of the $K\alpha_1$ photon emission obtained from the 3D simulation (full curves). The horizontal profile is compared to the corresponding profile from the 2D simulation in the insert.

steradian

$$N_{K\alpha} = \begin{cases} \sqrt{2\pi} \frac{\Delta y^2}{8 \ln 2} \int_{-\frac{L_x}{2}}^{\frac{L_x}{2}} dx \int_{z_1}^{z_2} dz n_{K\alpha}(x, z, t_f) & \approx 7.8 \cdot 10^8 \text{ sr}^{-1} \text{ for the 2D-3V simulation} \\ \int_{-\frac{L_y}{2}}^{\frac{L_y}{2}} dy \int_{-\frac{L_x}{2}}^{\frac{L_x}{2}} dx \int_{z_1}^{z_2} dz n_{K\alpha}(x, y, z, t_f) & \approx 1.5 \cdot 10^9 \text{ sr}^{-1} \text{ for the 3D-3V simulation} \end{cases}, \quad (9.63)$$

an averaged emittance of $K\alpha_1$ photons per steradian

$$E_{K\alpha} = \begin{cases} \int_{-\frac{L_x}{2}}^{\frac{L_x}{2}} \frac{dx}{L_x} \int_{z_1}^{z_2} dz n_{K\alpha}(x, z, t_f) & \approx 4.3 \cdot 10^{13} \text{ cm}^{-2} \cdot \text{sr}^{-1} \text{ for the 2D-3V simulation} \\ \int_{-\frac{L_y}{2}}^{\frac{L_y}{2}} \frac{dy}{L_y} \int_{-\frac{L_x}{2}}^{\frac{L_x}{2}} \frac{dx}{L_x} \int_{z_1}^{z_2} dz n_{K\alpha}(x, y, z, t_f) & \approx 3.8 \cdot 10^{12} \text{ cm}^{-2} \cdot \text{sr}^{-1} \text{ for the 3D-3V simulation} \end{cases} \quad (9.64)$$

which results in an effective emission surface of

$$S_{K\alpha} = \frac{N_{K\alpha}}{E_{K\alpha}} \approx \begin{cases} 1.8 \cdot 10^3 \mu\text{m}^2 & \text{for the 2D-3V simulation} \\ 4.0 \cdot 10^4 \mu\text{m}^2 & \text{for the 3D-3V simulation} \end{cases}, \quad (9.65)$$

as we expected. The left panel of **Figure 9.18** illustrates the different energy balance for the 3D simulation. By comparing it with the left panel of **Figure 9.12** for the corresponding 2D simulation, one can clearly see strong 3D effects. While the maximum electric energy in the target weakly varies, the maximum magnetic energy $U_B \approx 40 \cdot 10^{-2}$ mJ (compared to $U_B \approx 60 \cdot 10^{-3}$ mJ) is greater than in the 2D simulation since the self-generated magnetic field diffuses in the third dimension. Also, since we let the fast electrons propagate in the third dimension, the longitudinal beam current density $j_{b,z}$ is lower in 3D during the first passage of the fast electrons through the target. Consequently, the Ohmic heating by the return current $U_{\text{res}} \approx 8$ mJ is smaller than in 2D, where $U_{\text{res}} \approx 15$ mJ. It also explains why the number of $K\alpha$ photons emitted in the 3D simulation is greater than in the 2D simulation. Indeed, fast electrons lose less energy due to their slowing down by the self-generated electric field compared to the 2D simulation. Therefore, the fast electrons are more energetic and ionize more K-shell electrons. This explains also why the 3D simulation shows greater collisional losses.

9.2. APPLICATION TO THE SACLAY UHI100 EXPERIMENT

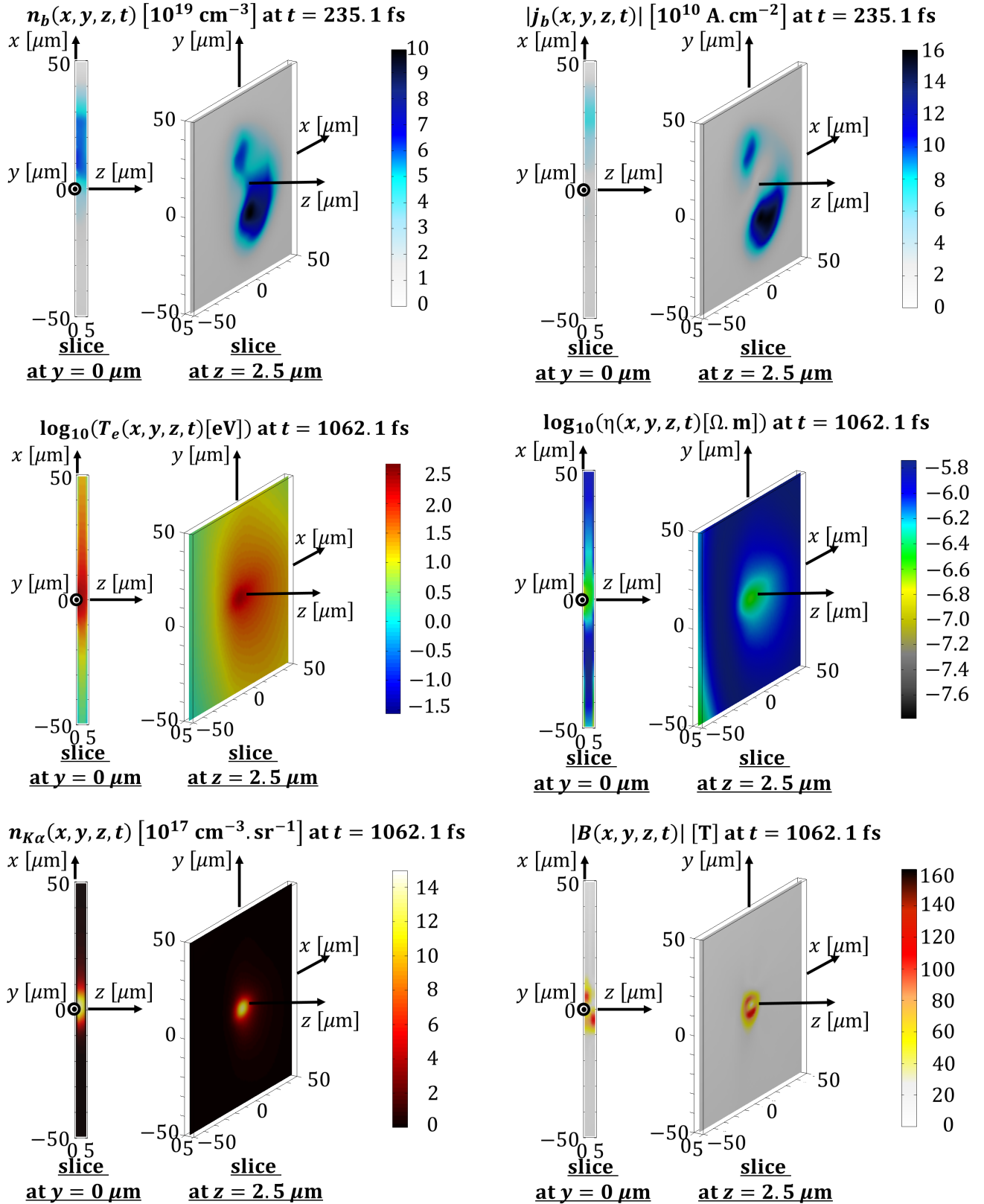


Figure 9.19: 3D-3V run : Slices of the beam density (Up Left) and current density at $t = 235.1$ fs (Up Right), target electron temperature (Middle Left), target electrical resistivity (Middle Right), time integrated density of $K\alpha_1$ photons emitted per steradian (Down Left) and magnetic fields at $t = 1062.1$ fs (Down Right); Slices are indicated in the Figure.

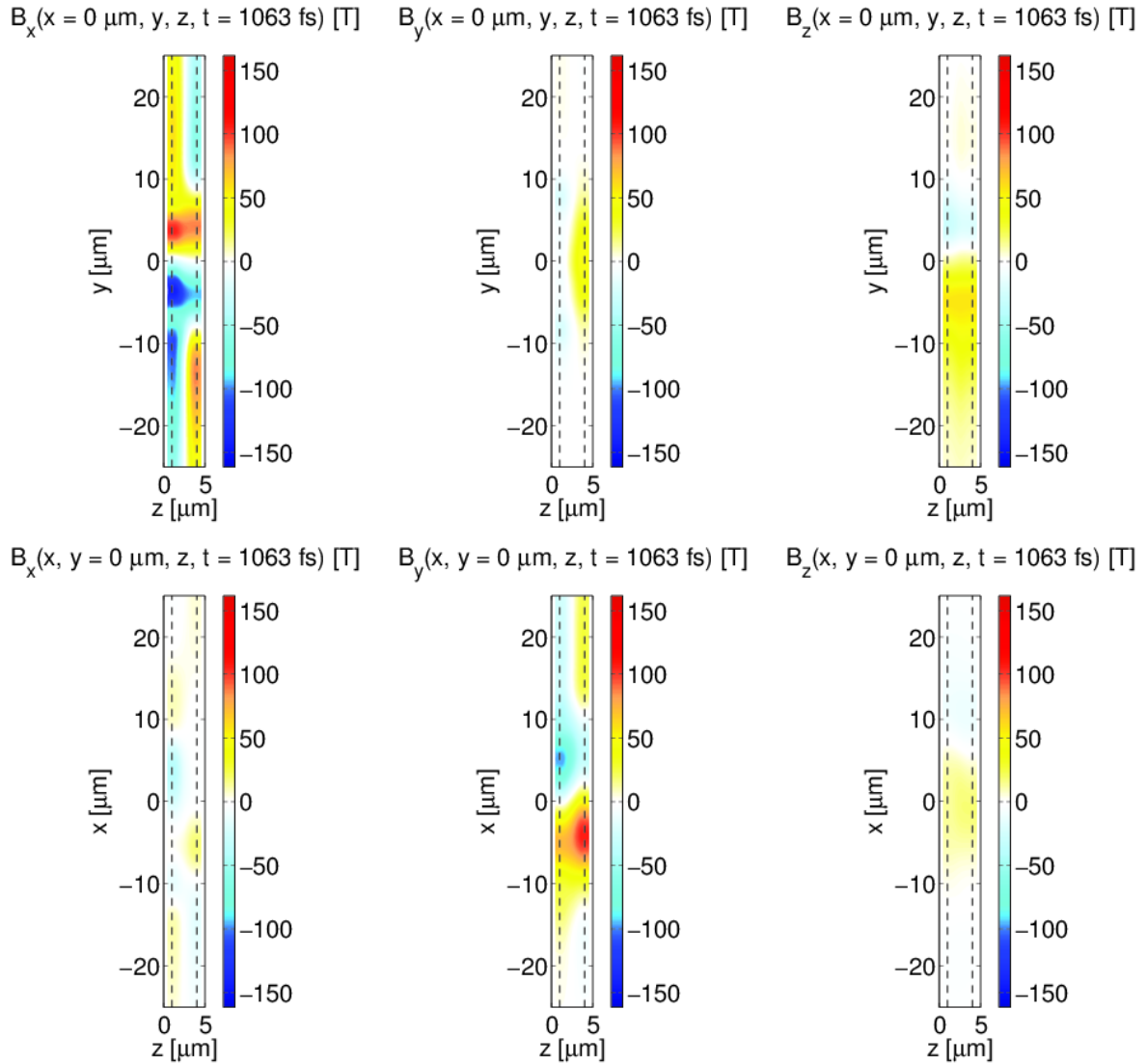


Figure 9.20: 3D-3V run : Slices at $x = 0 \mu\text{m}$ (Up) and $y = 0 \mu\text{m}$ of the x -component (Left), y -component (Middle) and z -component (Right) of the self-generated magnetic field \mathbf{B} .

9.2. APPLICATION TO THE SACLAY UHI100 EXPERIMENT

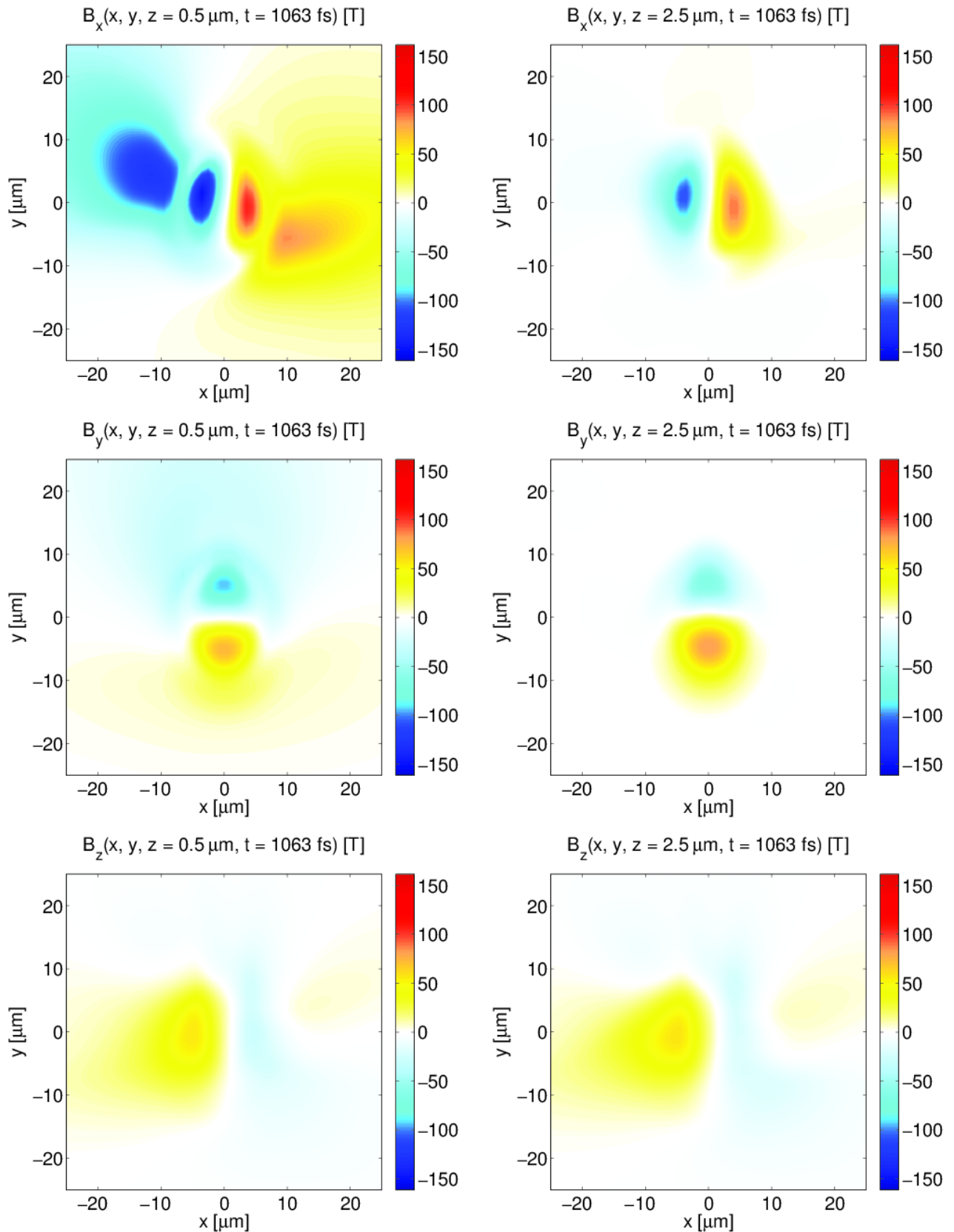


Figure 9.21: 3D-3V run : Slices at $z = 0.5 \mu\text{m}$ (Left) and $z = 2.5 \mu\text{m}$ (Right) of the x -component (Up), y -component (Middle) and z -component (Down) of the self-generated magnetic field \mathbf{B} .

The beam density n_b and the beam current $|\mathbf{j}_b|$ obtained from the 3D simulation for the thinner target at $t = 235.1$ fs are plotted in the upper panel of **Figure 9.19**. The slices at $y = 0$ can directly be compared with the corresponding 2D plots at $t = 239$ fs in **Figure 9.14**. These graphs confirm the conclusions drawn from the emission of $K\alpha$ photons : by allowing the fast electrons to propagate in the third dimension, the fast electron beam density and the maximum fast electron beam current density in the plane $y = 0$ are smaller in 3D. Indeed, the maximum beam density is $1 \cdot 10^{20} \text{ cm}^{-3}$ and the maximum beam current density is $1.6 \cdot 10^{11} \text{ A.cm}^{-2}$ compared to $5 \cdot 10^{20} \text{ cm}^{-3}$ and $2.5 \cdot 10^{11} \text{ A.cm}^{-2}$ obtained in 2D. That confirms the explanation of a lower $K\alpha$ emission in 3D. Due to their refluxing and the self-generated magnetic fields, the fast electrons propagate towards two opposite target corners instead of the x -direction as in the 2D case.

The electrical resistivity from the 3D simulation at $t = 1062.1$ fs is plotted in the middle right panel of **Figure 9.19**. The slice at $z = 2.5 \mu\text{m}$ illustrates the beam tendency towards hollowing in Copper. The norm of the self-generated magnetic field vector $|\mathbf{B}|$ is also plotted in the lower right panel of **Figure 9.19**. In order to understand its geometry, the different components of the self-generated magnetic field B_x , B_y and B_z are plotted in **Figures 9.20** and **9.21** showing the strong 3D effects. The magnetic field is mainly generated during the first passage of fast electrons through the target, then the magnetic field decreases due to the decrease of the resistivity entering the Spitzer regime and the decrease of beam currents. The plot of three magnetic field components in the plane $x = 0$ in the upper panel of **Figure 9.20** confirms the symmetry with respect to the y -axis in this plane. Since the electrons propagate mainly in the z -direction (with an angle $\approx 25^\circ$ compared to the z -axis), the z -component of the magnetic field is the smallest one. The y -component in the plane $y = 0$ is plotted in the lower middle panel of **Figure 9.20**. It can directly be compared with the corresponding B_y field obtained in the 2D simulation plotted in **Figure 9.14**. Except the contribution to B_y due to resistivity gradients and refluxing effects at the Al/Cu and Cu/Al interfaces, we do not observe too much differences between both simulations concerning the shape and the maximum value of B_y which is due to the curl of the beam current. However, we observe that B_x , which is totally omitted in the 2D simulation is actually the main component in the 3D simulation and reaches ≈ 150 T compared to ≈ 100 T for the B_y . In order to understand the shape of B_x , the contribution of resistivity gradients, curls of the beam current, target electron-density crossed gradients and 3-dimensional effects are plotted in **Figure 9.22**. The contribution due to the temperature-density crossed gradients is small and can be neglected while the 3D effects contribution has comparable values as the contribution of resistivity gradients. The major contribution to the x -component is mainly due to the curls of the beam current, in particular due to the term $\eta c(\partial j_{b,z}/\partial y)$. Similarly, B_y is mainly due to $-\eta c(\partial j_{b,z}/\partial x)$. However, since the fast electron beam propagate also in the x -direction, gradients in the x -direction are smoother so that B_x is greater than B_y .

9.2. APPLICATION TO THE SACLAY UHI100 EXPERIMENT

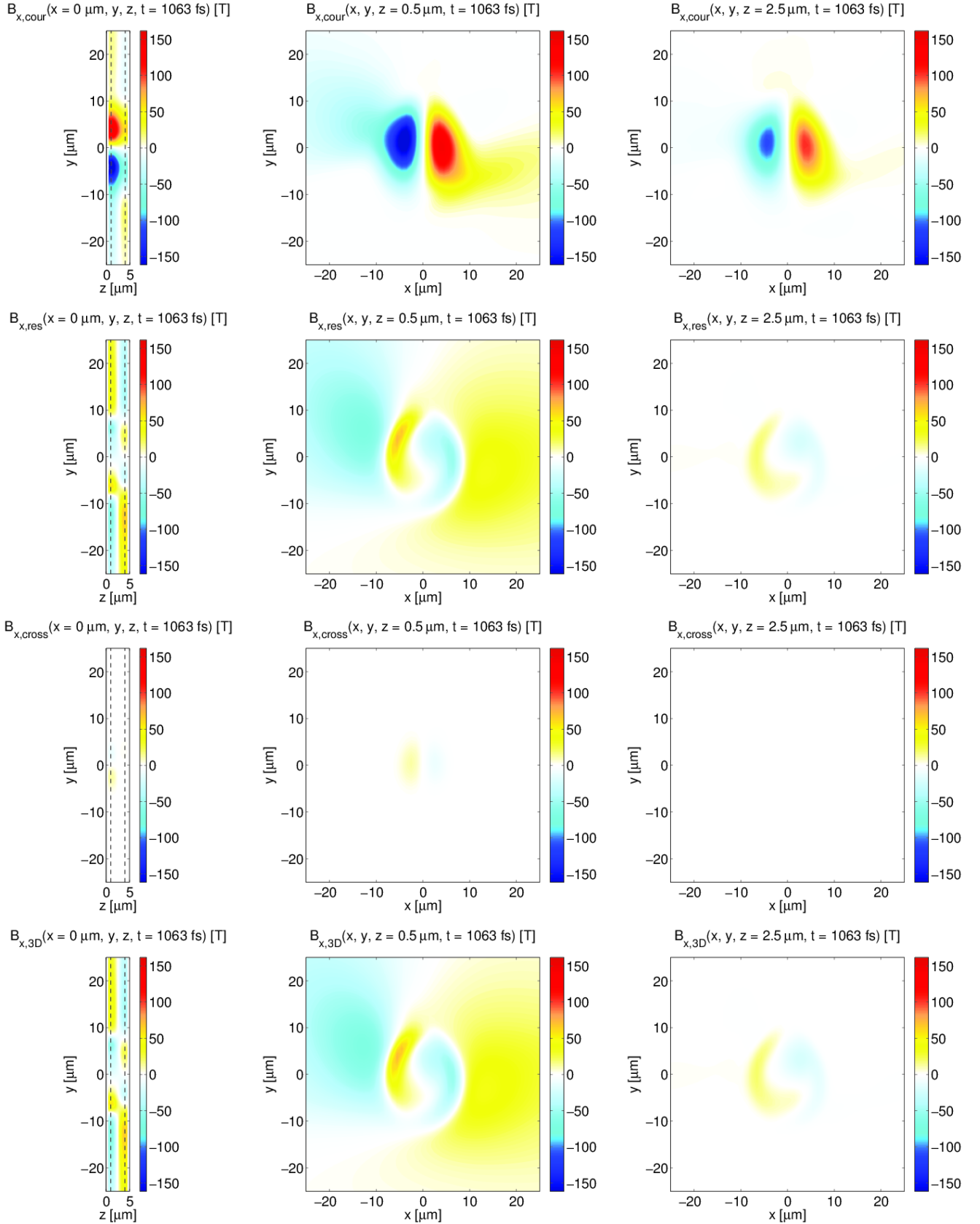


Figure 9.22: Slices of the contributions to B_x due to curls of the beam current density, resistivity gradients, temperature-density crossed gradients and 3D effects at $x = 0$ (Left), $z = 0.5 \mu\text{m}$ (Middle) and $z = 2.5 \mu\text{m}$ (Right).

9.2.5 Photoionization Effects

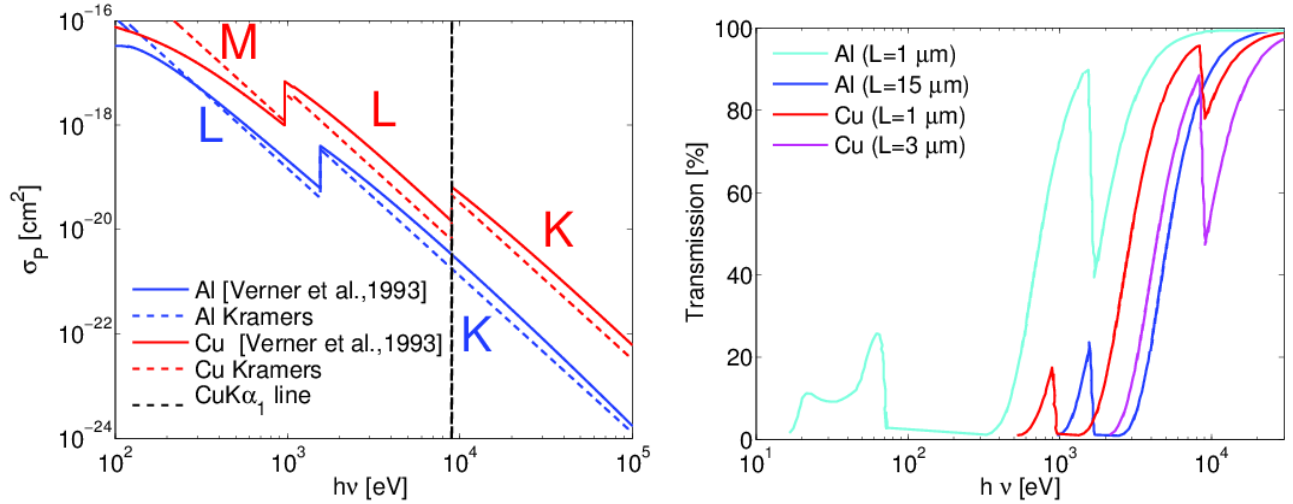


Figure 9.23: (Left panel) Photoionization cross section σ_P in Copper (red curves) and in Aluminum (blue curves) dependence on the photon energy $h\nu$ according to [Verner et al., 1993] (full curves) and the semiclassical formula (9.68) (dashed curves). $K\alpha_1$ photon energy from Copper is indicated by a vertical dashed line. (Right panel) Transparency of an Aluminum or Copper layer with a thickness L for a photon having the energy $h\nu$ according to [Henke et al., 1993] (http://henke.lbl.gov/optical_constants/).

In this subsection, we discuss the photoionization effects on the emission of $\text{Cu}K\alpha_1$ photons in order to check the assumptions 3 and 4 of our model in the **subsection 9.1.3**. According to [Verner et al., 1993] and [Verner and Yakovlev, 1995], the partial photoionization cross section for a photon with an energy $h\nu$, colliding with a (nl) atomic shell-electron, reads

$$\sigma_P^{(nl)}(h\nu) = \begin{cases} \sigma_0 \left[\left(\frac{h\nu}{E_0} - 1 \right)^2 + y_w^2 \right] \left(\frac{h\nu}{E_0} \right)^{-Q} \left(1 + \sqrt{\frac{h\nu}{y_a} \frac{h\nu}{E_0}} \right)^{-P} & \text{if } h\nu \geq E_{\text{th}} \\ 0 & \text{else} \end{cases} \quad (9.66)$$

where $Q = 5.5 + l - 0.5P$. This is an interpolation of a series of numerical calculations using the Hartree-Dirac-Slater method. [Verner et al., 1993] provide the tables for the photoionization threshold E_{th} and the parameters σ_0 , E_0 , y_w , y_a and P , depending on the quantum numbers n and l , that fit their numerical results for atomic numbers $Z, Z^* \leq 30$ and photon energies $h\nu \leq 50$ keV. $n = 1$ for K-shell electrons, $n = 2$ for L-shell electrons, $n = 3$ for M-shell electrons and $n = 4$ for N-shell electrons while $l = 0$ for s-band electrons, $l = 1$ for p-band electrons, $l = 2$ for d-band electrons and $l = 3$ for f-band electrons. The total photoionization cross section

$$\sigma_p(h\nu) = \sum_{n=1}^{n_{\text{max}}} \sum_{l=0}^{n-1} N_e^{(nl)} \sigma_P^{(nl)}(h\nu) \quad (9.67)$$

9.2. APPLICATION TO THE SACLAY UHI100 EXPERIMENT

is plotted in the left panel of **Figure 9.23** for Aluminum and Copper in the worst case, that is to say : for cold solid atoms ($Z^* = Z_c$). Therefore, $n_{\max} = 3$, $N_e^{(10)} = N_e^{(20)} = N_e^{(30)} = 2$, $N_e^{(21)} = 6$ and $N_e^{(31)} = 1$ for Aluminum while $n_{\max} = 4$, $N_e^{(10)} = N_e^{(20)} = N_e^{(30)} = 2$, $N_e^{(21)} = N_e^{(31)} = 6$, $N_e^{(32)} = 10$ and $N_e^{(40)} = 1$ for Copper. We find a good agreement with the total photoionization cross section computed according to the simpler semi-classical Kramers formula

$$\sigma_P^{(nl)}(h\nu) = \begin{cases} \frac{64}{3\sqrt{3}} \frac{\pi^4 m_e e^{10} Z^4}{h^3 c} \frac{1}{n^5} \frac{1}{(h\nu)^3} & \text{if } h\nu \geq E_{th} \\ 0 & \text{else} \end{cases} \quad (9.68)$$

However, the Hydrogen-like approximation for the estimates of E_{th} is too rough. Knowing the photoionization cross section, one may deduce the attenuation length $1/n_i \sigma_P$ of a photon $h\nu$ propagating in Aluminum ($n_i = 6.0 \cdot 10^{22} \text{ cm}^{-3}$) or Copper ($n_i = 8.5 \cdot 10^{22} \text{ cm}^{-3}$). The transmission of a photon beam propagating through Aluminum or Copper of a thickness L is plotted in the right panel of **Figure 9.23** according to [Henke et al., 1993] (http://henke.lbl.gov/optical_constants/).

The photoionization threshold for Cu K-shell electrons is $E_{th} = 8.972 \text{ keV}$. According to formula (1.8), the temperature T_I of electrons in the conditions of the UHI100 experiment is around 7 keV. Photons with energies greater than the Cu K-shell photoionization threshold E_{th} are thus emitted from the laser plasma interaction zone. In addition, according to the right panel of **Figure 9.23**, the first Aluminum layer is fully transparent for photons with energy greater than 10 keV. Therefore, the bremsstrahlung photons emitted from the laser plasma interaction zone may ionize some Cu K-shell electrons. However, their density is too small to play a significant role in the Cu K-shell hole dynamic (9.22) compared to the collisional ionization of K-shell electrons by the laser-generated fast electrons. Indeed, the radiative stopping power $(d\varepsilon/ds)_{\text{brem}} \approx 10^{-8} \text{ keV}/\mu\text{m}$ for electrons with a kinetic energy of $\varepsilon \approx 10 \text{ keV}$ in Aluminum according to [Heitler and Sauter, 1933]; see **Figure 4.1**. This is 8 orders of magnitude smaller than the collisional stopping power. Therefore, we can neglect the photoionization of K-shell electrons by X-ray bremsstrahlung photons compared to the collisional ionization by the laser-generated fast electrons. Also, X-ray photons may be emitted due to the presence of impurities in the laser plasma interaction zone such as hydrocarbons; see **Chapter 2, section 2.1**. However, for the same reason as for bremsstrahlung photons, the photoionization of CuK-shell electrons by these transition line photons can also be neglected compared to the collisional ionization by the laser-generated fast electrons. As a conclusion, the assumption 4 is fully justified.

According to the right panel of **Figure 9.2.4**, the assumption 3 must be mitigated, and the re-absorption of $K\alpha$ photons might be important. Indeed, even if $K\alpha_1$ photons emitted from the Copper tracer layer cannot ionize Cu K-shell electrons since $h\nu_{\alpha_1} = 8047.78 \text{ eV} < E_{th}$, they may ionize L-shell, M-shell or N-shell electrons of the Copper tracer layer and K-shell, L-shell or M-shell electrons of the Aluminum layers; , see the left panel of **Figure 9.23**. Consequently, according to the right panel of **Figure 9.23**, only $\approx 90\%$ of $K\alpha_1$ photons are transmitted through $\approx 3 \mu\text{m}$ of Copper or $\approx 15 \mu\text{m}$

of Aluminum. This effect is omitted in our model. Moreover, the ionization of CuL-shell electrons by $\text{Cu}K\alpha_1$ photons may be responsible for a decrease of the emission of $K\alpha_1$ photons. However, an error around 10% is not sufficient to explain a strong discrepancy between our simulations and the experimental data concerning the size of the $K\alpha$ emission zone..

9.2.6 Summary and Conclusion

The refluxing of fast electrons in the target may strongly affect the emission of $K\alpha$ photons. This effect must be taken into account when comparing numerical simulations of the $K\alpha$ emission with experimental data. In our model, this effect is accounted for by imposing specular reflection of fast electrons at the target-vacuum interfaces and adding a second population in the M1 equations. The first one describes the laser-generated electron population ⁽¹⁾ propagating in the laser pulse propagation direction while the second one describes the counterpropagating fast electron population ⁽²⁾. The model of calculation of the emission of $K\alpha$ photons is revised. It is demonstrated that the numerical time step of the fast electron transport calculation Δt_n may be comparable to the K-hole lifetime τ_K in the case of Aluminum and Copper targets. Therefore, we have implemented the self-consistent model proposed by [Thomas et al., 2013] describing the K-shell holes dynamic.

Simulations of fast electron transport in solid targets are compared with the experiments conducted on the UHI100 laser facility, introduced in **Chapter 8, section 8.2**. By comparing the simulations with different models for the target parameters such as the electron and ion thermal capacities, their temperature equilibration parameter and the transport coefficients, we demonstrated that solid state physics effects must be taken into account. In particular, the electron-ion temperature equilibration time and collisions of d-band with s-band electrons may affect the magnetic field distribution in the Copper target.

By comparing our simulations with refluxing with corresponding hybrid PIC and/or full PIC simulations conducted by [Gremillet, 2014], we confirmed the results obtained by [Sherlock et al., 2014] concerning the error made in the quasi-static hybrid models neglecting the target electron inertia in the Ohm's law and the displacement current. However, this effect is restricted to the first thin Aluminum layer. Here, the laser-generated bunches of electrons are injected into the target at the laser frequency or twice the laser frequency. each bunch generates an electric field that excites a weak field of background electron plasma waves. These plasma oscillations are damped due to collisions with target electrons and ions, resulting in an additive target electron heating component that is taken into account by full PIC simulations but neglected by hybrid models. The hybrid quasi-static model agrees well with the full PIC simulation in the following Copper tracer layer. This may be explained by the fast electron collisions in Copper ($Z = 29$) which degrades the coherence of the fast electron bunches and the decrease of the Ohmic heating by the return current with the target depth.

The profiles of $K\alpha_1$ photon emission from the Copper tracer layers obtained in to 2D and 3D

9.2. APPLICATION TO THE SACLAY UHI100 EXPERIMENT

simulations are compared to the experimental signals. Except for the thinnest target, the 2D simulation qualitatively reproduce the experiments. However, we found significant differences between 2D and 3D simulations, especially in what concerns the self-generated magnetic fields, the size of the $K\alpha$ emission zone and the absolute value of the local number of photons emitted per unit of volume. The simulation predicts a $K\alpha_1$ emission spot size 2-3 times smaller than the experimentally measured. We analyzed the assumptions of our model concerning the $K\alpha$ emission. The photon re-absorption may introduce an error of $\approx 10\%$ in our computations but it cannot explain the discrepancy concerning the $K\alpha_1$ spot size. We also checked the effective surface of $K\alpha$ emission. Even if the 3D simulation predicts a smaller spot size in the x -direction, it predicts a larger effective surface of emission of about $\approx 200\ \mu\text{m} \times 200\ \mu\text{m}$, as compared to $\approx 40\ \mu\text{m} \times 40\ \mu\text{m}$ obtained in the 2D case. This apparent paradox comes from simple geometrical reasons. Let us note r_{3D} the mean radius of the $K\alpha$ spot size obtained in 3D, r_{2D} the radius obtained in 2D (x -axis) and $l = \sqrt{2\pi\Delta y^2/8\ln 2}$ the thickness of the slice $y = 0$ of the 2D simulations. Even if r_{2D} is greater than r_{3D} , l is so small compared to r_{3D} that finally $\pi r_{3D}^2 > r_{2D}l$.

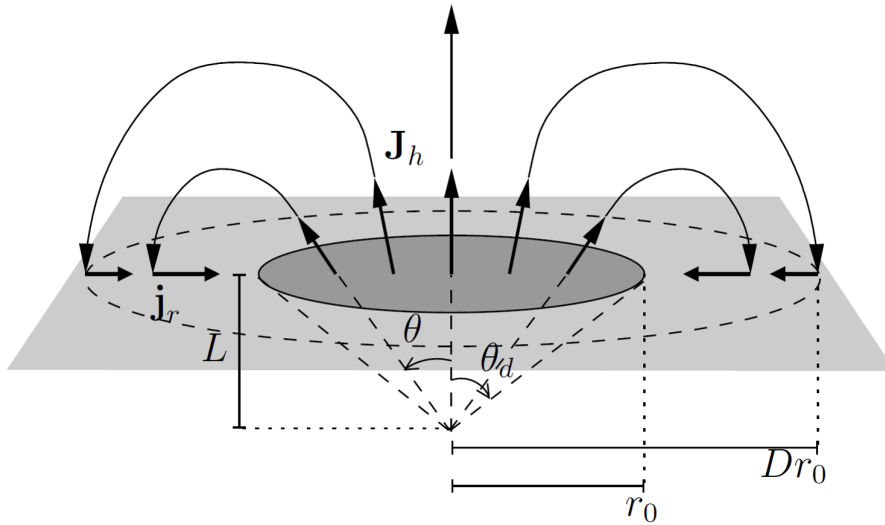


Figure 9.24: Sketch of the toy model by [Macchi, 2012].

The neglect of secondary electrons in our model may explain the discrepancy between the experimental data and our simulations. However, I think that the main critical assumption in our model concerns the specular reflection of fast electrons at the target-vacuum interfaces. **The local magnetic fields generated at the target-vacuum interfaces may deviate strongly the reflxed fast electrons, thus enhancing the off-axis $K\alpha_1$ signal.** Such magnetic fields have already been observed in experiments [Sarri et al., 2012] and in PIC simulations [Pukhov, 2001] with the laser parameters in the range of the UHI100 experiments. Similar observations have also been reported in the context of the resonant absorption [Sakagami et al., 1979] [Kolodner and Yablonovitch, 1979] (see **Chapter 1, section 1.1.2**). [Macchi, 2012] proposed a simple model called "toy model of the fountain effect", allowing to estimate the value of the magnetic field generated by the fast electrons

escaping from the target and reaccelerated back. The term "fountain" comes from the analogy with a fountain of water (electrons) where the water (electrons) fall to the floor (to the target) due to gravity (electrostatic field). The "toy model of fountain" is based on many simplifying assumptions such as non-relativistic electrons, small beam divergence, uniform electric field and many others. However, according to [Macchi, 2012], it provides an order of magnitude of the magnetic field generated at the target-vacuum interfaces. For example, this simple model provides an estimate of ≈ 10 kT in agreement with the experiment by [Sarri et al., 2012] and a corresponding PIC simulation. According to [Macchi, 2012], the magnetic field generated at the target-vacuum interface may be estimated as

$$B \approx \frac{8k_B T_b}{eEr_0} \theta_d \frac{2I_b}{r_0 c}. \quad (9.69)$$

The notations are illustrated in **Figure 9.24**. In order to apply this formula to our case, let us firstly estimate the maximum value of the electrostatic field at the target edge. Assuming that fast electrons escaping from the target form a Boltzmann distribution with a temperature $k_B T_b$ in the electrostatic potential, we may estimate the maximum electrostatic field as

$$E \approx \frac{k_B T_b \sqrt{2}}{\lambda_{D,b} e} \text{ where } \lambda_{D,b} = \sqrt{\frac{k_B T_b}{4\pi\gamma_{b0} n_{b0} e^2}} \text{ is the relativistic Debye screening length.} \quad (9.70)$$

The electron divergence angle θ_d can be roughly estimated by the angle $\approx 25^\circ$ of the fast electron propagation direction during their first passage in the target and the "fountain" beam radius r_0 by $L_z \arctan \theta_d \approx 2.1 \mu\text{m}$. According to our simulation, $\langle \varepsilon \rangle(z = L_z) \approx 70$ keV ($\rightarrow \gamma_{b0} \approx 1.13$), $n_b \approx 10^{20} \text{ cm}^{-3}$ and $I_b \approx -2$ MA at the target rear side at $t \approx 75$ fs. Then, assuming roughly $k_B T_b \approx \langle \varepsilon \rangle(z = L_z)$, we obtain

$$\lambda_{D,b} \approx 0.18 \mu\text{m}, E \approx 7.6 \cdot 10^{11} \text{ V/m and } B \approx 30 \text{ kT.} \quad (9.71)$$

We deduce that fast electrons has a Larmor radius of

$$\rho_L = \frac{\gamma v m_e c}{eB} \approx 0.056 \gamma \beta \mu\text{m.} \quad (9.72)$$

In agreement with the PIC simulation performed by [Pukhov, 2001], who obtains magnetic fields ≈ 1 kT, the main part of fast electrons with low kinetic energies are trapped by the magnetic field while only fast electrons with a momentum greater than

$$p > 3.3 m_e c \text{ such that } \rho_L > \lambda_{D,b} \quad (9.73)$$

may escape from the magnetized electron cloud and are reaccelerated inside the target with a strong angular deviation. It exactly corresponds to fast electrons with kinetic energies greater than

$$\varepsilon > 2.5 m_e c^2 \approx 1.2 \text{ MeV} \quad (9.74)$$

9.2. APPLICATION TO THE SACLAY UHI100 EXPERIMENT

that are responsible for the emission of $\text{Cu}K\alpha_1$ photons. We thus lose this physics by assuming the specular reflection of fast electrons at the target edges and it may explain why we obtain discrepancies with the experimental $K\alpha$ signals.

Chapter 10

Application to the Generation of Shock Waves by Fast Electron Energy Deposition

"We knew the world would not be the same. A few people laughed, a few people cried, most people were silent. I remembered the line from the Hindu scripture, the Bhagavad-Gita. Vishnu is trying to persuade the Prince that he should do his duty and to impress him takes on his multi-armed form and says, "Now, I am become Death, the destroyer of worlds." I suppose we all thought that one way or another."

J. Robert Oppenheimer

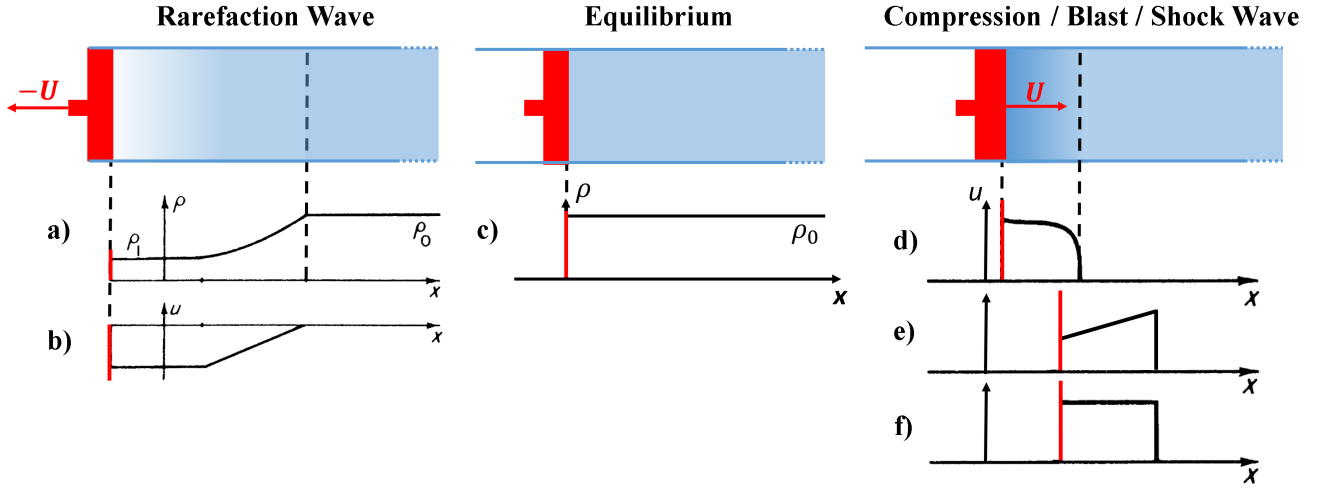


Figure 10.1: (Left panel) Schematic view of a rarefaction wave arising from the motion of a piston and corresponding distributions of the density (a) and gas velocity (b). (Middle panel) Schematic view of the equilibrium between the gas and the ambient pressure and corresponding distribution of the density (c). (Right panel) Schematic view of a compression wave generated by an accelerated piston : (d) is the distribution of the gas velocity of a compression wave arising from the slow motion of the piston, (e) is the distribution of the gas velocity of a blast wave arising from an instantaneous and rapid motion of the piston and (f) is the distribution of the gas velocity of a shock wave arising from a continuous and rapid motion of the piston.

In order to define what is a shock, let us conduct the following thought experiment. A semi-infinite tube is filled of a gas and a piston allows for expanding or compressing the gas, as illustrated in **Figure 10.1**. As a fluid, the gas can be described by the Navier-Stokes equations (B.60), (B.61) and (B.63) with $\rho_c = 0$ and $\mathbf{j} = 0$ complemented by the specific entropy conservation equation (B.65), derived in **Appendix B, section B.3.1** for charged fluids, i.e., for plasmas where $\rho_c \neq 0$ and $\mathbf{j} \neq 0$. If in addition, we neglect the fluid viscosity, the equations in one dimension read:

$$\frac{\partial \rho}{\partial t} + \frac{\partial}{\partial x}(\rho u) = 0, \quad (10.1)$$

$$\rho \left[\frac{\partial}{\partial t} + u \frac{\partial}{\partial x} \right] (u) = -\frac{\partial P}{\partial x}, \quad (10.2)$$

$$C_V \left[\frac{\partial}{\partial t} + u \frac{\partial}{\partial x} \right] (T) = -\frac{\partial q}{\partial x} + W_e \quad (10.3)$$

and

$$\rho \left[\frac{\partial}{\partial t} + u \frac{\partial}{\partial x} \right] (H) = -\frac{1}{T} \frac{\partial q}{\partial x}. \quad (10.4)$$

The notations are explained in **Appendix B, section B.3.1**. We have omitted the subscript "m" for brevity. Compression waves generated when pushing the piston, as illustrated **Figure 10.1 c)**, can be described by assuming a perturbation of the equilibrium $\rho = \rho_0$, $u = 0$, $T = T_0$, $H = H_0$. By

noting $\delta\rho$ and u the 1st order perturbation terms of this equilibrium and

$$c_s = \sqrt{\left(\frac{\partial P}{\partial \rho}\right)_H} \quad (10.5)$$

the velocity of sound in the gas, the 1st order linearized equations (10.1) and (10.2) give

$$\left(\frac{\partial}{\partial t} - c_s \frac{\partial}{\partial x}\right) \left(\frac{\partial}{\partial t} + c_s \frac{\partial}{\partial x}\right) (\delta\rho) = 0. \quad (10.6)$$

This equation describes compression waves propagating at the velocity of sound in the gas filling the tube, as illustrated in **Figure 10.1 d**).

When the perturbation is strong enough ($\delta\rho \sim \rho_0$), we cannot anymore linearize the equations assuming $\delta\rho$ is a perturbation of the equilibrium ρ_0 . A powerful theoretical tool when studying such non-linear equations is the search for self-similar solutions. It consists in looking for solutions of the equations in the form $\rho(x, t) = \rho_0 F(x^a t^b)$ where the scalar parameters a and b may be found according to dimensional reasoning depending on the invariant quantities of the problem, while the function F may be found by injecting the assumed form $F(x^a t^b)$ in the equations; see for example the self-similar rarefaction waves in a plasma found by [Gurevich et al., 1966] [Manheimer et al., 1982] [Fabbro et al., 1985] and illustrated in **Figure 10.1 a**). When studying the nonlinear equations of conservation (10.1), (10.2), (10.3) and (10.4), neglecting the thermal energy flux q and the source term W_e , B. Riemann discovered in the second half of the XIXth century thanks to a self-similar solution that the development of singularities may be possible, in the form of shock waves, as illustrated in **Figure 10.1 f**). Actually, if we zoom in on this hydrodynamic density discontinuity to the kinetic scale, i.e. at the spatial scale of the order of the particle mean free path, this discontinuity disappears. A few years later, starting from the same conservation equations (10.1), (10.2), (10.3) and (10.4) on the jump

$$\begin{cases} \rho_0 D & = \rho_1 (D - U) \\ P_1 - P_0 & = \rho_0 D U \\ \rho_0 D \left(\varepsilon_1 - \varepsilon_0 + \frac{U^2}{2} \right) & = P_1 U \\ h_1 - h_0 + \frac{U^2}{2} & = D U \end{cases} \quad (10.7)$$

in such a configuration **f**), W. J. M. Rankine and H. Hugoniot found the relations between the specific internal energies $\varepsilon_i = C_V T_i / \rho_i$, the pressures P_i , the specific enthalpies $h_i = \varepsilon_i + P_i V_i$ and the specific volumes $V_i = 1/\rho_i$ of the shocked ($i = 1$) and unperturbed gas ($i = 0$). These so-called Rankine-Hugoniot relations read

$$\begin{cases} \varepsilon_1 - \varepsilon_0 & = \frac{1}{2} (P_1 + P_0) (V_0 - V_1) \\ h_1 - h_0 & = \frac{1}{2} (P_1 - P_0) (V_0 + V_1) \end{cases}. \quad (10.8)$$

Here, U and D are the velocities of the piston and the shock front, respectively. The velocities of the

shocked and unperturbed gas have been taken equal to $u_0 = 0$ and $u_1 = U$. Let us apply Equation (10.8) to the case of an ideal gas filling the tube with the specific internal energy and enthalpy read

$$\varepsilon = \frac{C_V}{\rho} T = \frac{1}{\gamma - 1} \frac{P}{\rho} \quad \text{and} \quad h = \frac{C_P}{\rho} T = \frac{\gamma}{\gamma - 1} \frac{P}{\rho} \quad (10.9)$$

where $\gamma = C_P/C_V = 1 + (2/d)$ is the adiabatic index depending on the number d of degrees of freedom of particles. In this particular case, if we push the piston such that $U \gg c_s$, a strong shock is generated that propagates in the tube with the velocity

$$D = \sqrt{\frac{\gamma + 1}{2} \frac{P_1}{\rho_0}} \quad (10.10)$$

($P_1 \gg P_0$) and compresses the gas downstream up to the density

$$\frac{\rho_1}{\rho_0} = \frac{\gamma + 1}{\gamma - 1}. \quad (10.11)$$

according to (10.7), (10.8) and (10.9). Therefore, maximum density ratio for a monoatomic ideal gas with $\gamma = 5/3$ is equal to 4. In reality, at high temperatures and pressures, the specific heats and the specific heat ratio are no longer constant because of molecular dissociation and of ionization. However, the density ratio (10.11) remains finite and does not increase without limits : generally, it does not exceed 11-13 according to [Zel'dovich and Raizer, 1966].

When a large amount of energy is quasi-instantaneously deposited in a very small volume, we talk about blast waves instead of shock waves. Even if it presents a leading front discontinuity, as in shock waves, a blast wave is followed by a blast wind of negative pressure gradients. For example, the outcome from supernova-explosions may be described as a blast wave. Indeed, when a star has consumed all its thermonuclear fuel (see the **section 0.1.2** of the **Introduction**), the star internal pressure decreases and does not counterbalance anymore the star gravitational force. As a result, the equilibrium is broken, the star implodes and its plasma density increases. Depending on its mass according to [Chandrasekhar, 1931], it may reach the degeneracy pressure and a sudden re-ignition of nuclear fusions in the degenerate core may lead to its explosion. The subsequent expansion phase, called supernova and illustrated in **Figure 10.2**, may be described by the adiabatic self-similar blast wave obtained by [Sedov, 1946] and confirmed by [Taylor G., 1950], according to numerical simulations. It allows us to illustrate the "dimensional reasoning" mentioned above concerning the self-similar solutions of the non-linear and coupled equations of conservation (10.1), (10.2), (10.3) and (10.4) that must be expressed here in 3 dimensions, assuming a spherical symmetry and neglecting the thermal energy flux q as well as eventual source terms W_e . Indeed, let us try to find out the expression of the radius r [cm] of such an expanding spherical supernova according to the dimensional reasoning. We expect that r depends on the energy released quasi-instantaneously, let us say at $t = 0$, by the star explosion E_0 [erg]. It may thus be considered as the self-similar invariant quantity. We expect also

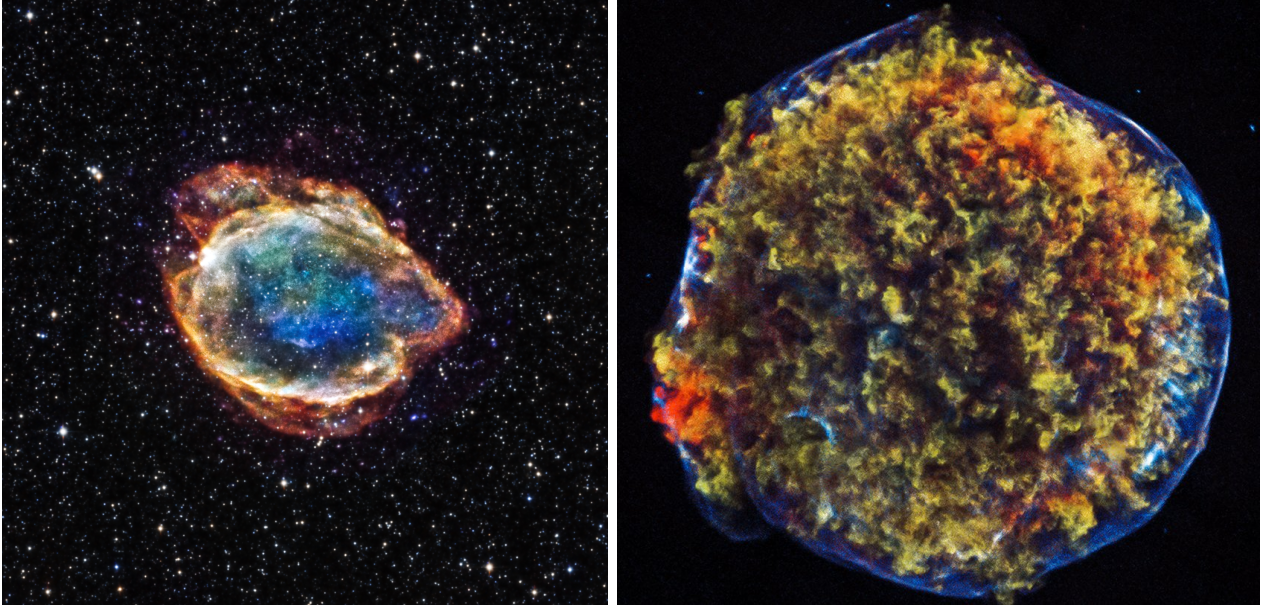


Figure 10.2: Supernovae G299 (Left panel) and SN 1572, also called Tycho's Supernova because of Tycho Brahe's extensive work [Tycho, 1573] (Right panel). Both are expected to be supernovae of Type Ia i.e. from a thermonuclear explosion of a white dwarf star in a tight orbit with a companion star. Pictures are taken from the NASA's telescope Chandra X-ray Observatory, called *Chandra* to pay homage to the astrophysicist and mathematician S. Chandrasekhar. *Chandra* orbits above Earth's atmosphere at an altitude of 139,000 km. The Smithsonian's Astrophysical Observatory in Cambridge, MA (USA), hosts the Chandra X-ray Center which operates the satellite, processes the data, and distributes it to scientists around the world for analysis.

that r depends on the surrounding medium density ρ_0 [g/cm^{-3}] and the age of the supernova t [s]. Therefore, let us look for an expression of the radius with the form

$$r [\text{cm}] = \xi_0 (E_0 [\text{erg}])^a (\rho_0 [\text{g}/\text{cm}^3])^b (t [\text{s}])^c \quad (10.12)$$

where ξ_0 , a , b and c are dimensionless constants to be determined. Since $1 \text{ erg} = 1 \text{ g}\cdot\text{cm}^2/\text{s}^2$, we deduce that we must have necessarily

$$\begin{cases} (a + b) & \text{kg} & = & 0 \text{ kg} \\ (2a - 3b) & \text{cm} & = & 1 \text{ cm} \\ (-2a + c) & \text{s} & = & 0 \text{ s} \end{cases} \quad (10.13)$$

for dimensional reasons. It thus gives the self-similar variable found by [Sedov, 1946]

$$r = \xi_0 \left(\frac{E_0}{\rho_0} \right)^{1/5} t^{2/5} \quad (10.14)$$

and the blast wave properties can be found by looking for the function $F(r)$, solution of the non-linear and coupled equations (10.1), (10.2), (10.3) and (10.4) expressed in 3 dimensions, assuming a

spherical symmetry and neglecting q as well as W_e . Applying this procedure for an ideal gas (10.9), [Taylor G., 1950] found that $\xi_0 \approx 1.11$ for $\gamma = 5/3$ ($d = 3$). Concerning our thought experiment of a piston compressing a gas filling a semi-infinite tube, a blast wave can be generated by applying a strong hit of hammer to the piston. The resulting blast wave is illustrated in **Figure 10.1 e**). It has this particular triangular shape due to the fact that the piston is not continuously pushed like in the case of shock waves. The X-ray photographs of the supernovae G299 and Tycho, illustrated in **Figure 10.2**, are obtained thanks to the strong emission of the hot expanding plasma behind the front.

The first direct observation of a laser-driven shock wave was reported by [van Kessel and Sigel, 1974]. A planar solid hydrogen target was irradiated with a 10 J, 5 ns, Nd laser (1.06 μm wavelength) and the propagation of the laser-driven shock wave was measured using a high-speed photography. The estimated pressure in this pioneering experiment was 2 Mbar. Twenty years after the first published experiment, the Nova laser at the Livermore laboratories in the United States of America (USA) created a pressure of 750 ± 200 Mbar [Cauble et al., 1994]. This was achieved in a collision of two gold foils, where the flyer (Au foil) was accelerated by a high-intensity x-ray flux created by the laser-plasma interaction. As explained above, a shock or a blast wave is created in a medium that suffers a sudden impact or in a medium where a large amount of energy is released in a short period of time. As already explained in the **section 0.2.1** of the **Introduction** concerning the conventional schemes of Inertial Confinement Fusion (ICF), a high-power laser pulse creates a very hot plasma at the target surface. This plasma exerts a high pressure on the surrounding material, acting like the piston of our thought experiment, that leads to the formation of an intense shock wave, moving into the interior of the target. The momentum of the out-flowing plasma balances the momentum imparted to the compressed medium behind the shock front. The thermal pressure together with the momentum of the ablated material drives the shock wave.

Energetic electrons are commonly considered to be a dangerous effect for ICF; see the **section 0.2.2** of the **Introduction**. Having a long mean free path, they penetrate through the solid shell and deposit their energy in the ablator and Deuterium-Tritium (DT) fuel. This process significantly increases the target entropy H , thus degrading its implosion. The phenomenon of target preheat was the major reason for several milestone events [Lindl, 1998] : cessation of the ICF program based on the CO₂ laser in the 1980s, switching to the third harmonic in the Nd:glass ICF lasers, and limiting the "useful" laser intensities to a few PW/cm². All these limitations significantly reduce the ICF operational domain. However, matching the mean free path of fast electrons with the target size may suppress the negative effect of preheat and open the possibility of using the energetic particles for creation of a high ablation pressure [Volosevich and Rozanov, 1981] [Gus'kov, 1983] [Evans, 1983] [Evans, 1986]. Fast ignition is an example of the application of energetic electrons in ICF. Here, a beam of relativistic electrons is supposed to create a small hot spot in the compressed

fuel [Tabak et al., 1994]; see the **section 0.2.3**. This scheme, nevertheless, faces serious difficulties related to tight focusing of an intense electron beam; see the **section 0.3.2**. Energetic electrons may play an important role in the creation of a high ablation pressure, which is interesting for ignition of fusion reactions in the laboratory [Betti et al., 2007] and in astrophysics concerning thermonuclear supernovae [Gamezo et al., 2004] or deflagration (subsonic)-to-detonation (supersonic) transition in premixed combustion wave front [Bychkov et al., 2008]. In the shock ignition scheme in ICF, the fuel is ignited by a strong shock launched by an intense laser spike at the end of the implosion process; see the **section 0.2.3**. The laser spike intensity is in the range of 10 PW/cm^2 , certainly well above the threshold of parametric instabilities, and a significant part of laser energy is expected to be deposited in the nonthermal, energetic electrons [Klimo et al., 2011]; see the **section 0.3.1**. It was suggested by [Betti et al., 2007] and [Ribeyre et al., 2009] that their deleterious effect on target implosion can be mitigated by the fact that, at the moment of spike arrival, the target has already passed halfway through the implosion phase, and its areal density is increased significantly, by a factor of 10-20 at least. If the target areal density would be larger than the range of fast electrons, the latter will be stopped in the imploding shell and may play a positive role by contributing to the ablation pressure.

In this **Chapter**, we study for the first time the generation of a shock wave by an ablation pressure driven by an energetic electron beam in a dense plasma. For this, we first present the theoretical predictions found by [Gus'kov et al., 2012]. Then, we describe the coupling of the reduced model for the fast electron transport in solids and dense plasmas presented in **Chapter 6** with the radiation hydrodynamic code CHIC, briefly described in **Appendix B, section B.3.2** and **B.3.3**. Finally, we compare the predictions of the theory with one-dimensional simulations of an electron beam energy deposition in a DT plasma with a step-like density profile. The parameters of these academic simulations correspond to typical values expected at the time of spike arrival in the shock ignition scheme. These simulations show a positive effect of energetic electrons in the shock ignition scheme, allowing to achieve the ablation pressures above 500 Mbar. Furthermore, in this section we consider another example of a blast wave generated by an ultrashort femtosecond laser pulse. The experimental campaign conducted by [SANTOS et al., 2013] was already described in **sections 8.2** and **9.2**. We demonstrate here by using analytical estimates and numerical radiation hydrodynamic simulations that a strong blast wave can be generated in a thin target due to strong temperature gradients induced by fast electron heating. This interpretation is confirmed by the observation of the shock breakout at the target rear side with a Streaked Optical Pyrometry.

10.1 Role of Laser-generated Fast electrons in the Shock Ignition Scheme

10.1.1 Theoretical predictions

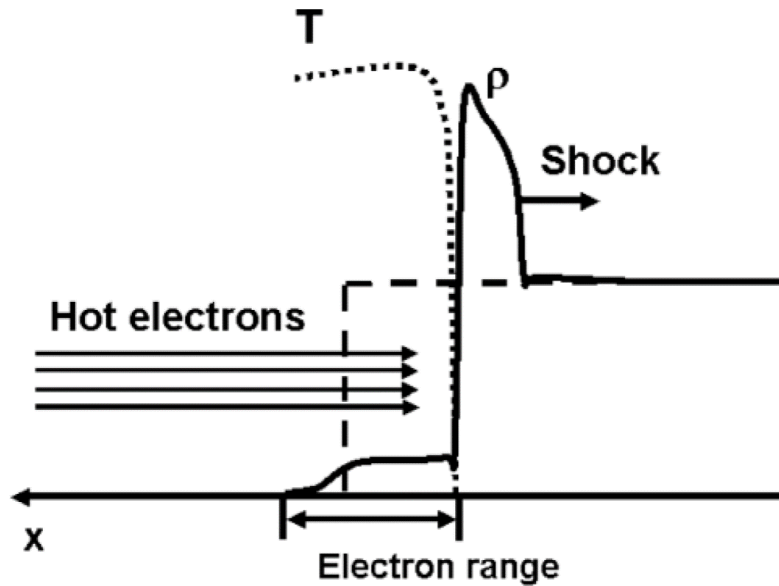


Figure 10.3: Schematic of the density and temperature profiles in the hot electron beam ablation non-stationary regime after the loading time.

There is no general model of pressure formation by an energetic particle beam. The model by [Gus'kov, 1983] applies for nanosecond electron beams where the heat conductivity of the thermal electrons plays an important role. In this case, the laser energy is deposited at the critical density and it is transported to the ablation zone by the thermal electrons. This is a stationary ablation process where the shock wave launched into the solid material is connected to the isothermal rarefaction wave [Gurevich et al., 1966] [Manheimer et al., 1982] [Fabbro et al., 1985], as it is schematically shown in the **Figure 8** of the **Introduction** and in **Figure 10.1 a)**. Formation of the ablation pressure by an energetic ion beam was considered by [Evans, 1983] [Evans, 1986]. A recent paper [Bell and Tzoufras, 2011] considers the regime of transition from the thermal electron diffusion to a nonlocal energy transport. However, the fast electron plasma heating is limited to a very short time scale, before the hydrodynamic separation takes place. The fast electrons, similarly to energetic x rays, propagate deeper in the target behind the ablation front created by the thermal electron conduction and produce a second ablation front. However, in contrast to x rays and thermal electrons, the range of fast electrons depends only weakly on the plasma temperature (only logarithmically; see **Chapter 4, section 4.2**). For this simple reason, the standard stationary isothermal model of plasma expansion does not apply to fast electrons. Fast electron-driven ablation is intrinsically a nonstationary process similar to the ion driven ablation [Evans, 1983] [Evans, 1986]. It can be described by a model

of heating and expansion of a finite mass defined by the fast electron range. Consequently, the shock is launched by the ablation pressure created by fast electrons during a finite time interval, **the loading time**, and after that, the shock transforms in a blast wave and its amplitude decreases slowly with time. **Figure 10.3** presents schematically the density and temperature profiles in this regime after the loading time. Thus, the fixed energy deposition range of fast particles implies an optimal time for fast electron beam injection : shorter beams will drive a smaller amplitude shock, while longer beams will be detached from the solid target and deposit their energy in the expanding plasma, thus decreasing the coupling efficiency. The fast electron ablation theoretical model GRT is presented here for a simple case of monoenergetic electrons and a plane geometry.

There are two classes of self-similar solutions of equations of ideal hydrodynamics that describe a rarefaction wave. One of them is the well-known stationary isothermal rarefaction wave, where the temperature is constant and the ablated mass increases linearly with time [Gurevich et al., 1966] [Manheimer et al., 1982] [Fabbro et al., 1985]. Another one describes an isothermal expansion of a given mass plasma with a temperature increasing with time [Imshennik, 1960] [Drake, 2011]. The former applies readily to the energy deposition of laser beams and thermal x rays [Fabbro et al., 1985] [Mora, 2003]. There, the plasma temperature is adjusted in a way that it accommodates the photon stopping length to the plasma density profile. This model, however, does not apply to fast electrons because their stopping power depends only on the fast electron energy $\varepsilon_0 = (\gamma_0 - 1)m_e c^2$. According to **section 8.1.3**, a monoenergetic and collimated electron beam deposits its energy over the distance

$$L_p = \xi R \quad (10.15)$$

where

$$R = \frac{(\gamma_0 - 1)^2}{\gamma_0} \frac{m_i (m_e c^2)^2}{4\pi Z \rho_0 e^4 (\ln \Lambda_{ee}^{\text{rel}})^*} \quad (10.16)$$

is the range of the beam electrons and

$$\xi = \left(\frac{\gamma_0 + 1}{\gamma_0 - 1} \right)^2 \frac{1}{\beta_0^2} \left(\beta_0^2 - 2 \frac{\ln \gamma_0}{\gamma_0} \right) \quad (10.17)$$

is the correction factor due to their angular scattering. For a fully ionized DT plasma with a density of $\rho_0 = 10 \text{ g/cm}^2$ and a temperature of 1 eV, the range R of a beam of collimated electrons is $0.878 \mu\text{m}$ for the electron energy $\varepsilon_0 = 30 \text{ keV}$ and $6.650 \mu\text{m}$ for $\varepsilon_0 = 100 \text{ keV}$ while the correction factor reaches the limiting value of $2/3$ so that

$$L_p = 0.5 \mu\text{m} \text{ for } \varepsilon_0 = 30 \text{ keV} \text{ and } L_p = 4.4 \mu\text{m} \text{ for } \varepsilon_0 = 100 \text{ keV}. \quad (10.18)$$

Collisions on screened free electrons (plasmons) provide the main contribution to the stopping power and the angular scattering correction factor in such a degenerate plasma; see **section 8.2**. Since the fast electron range depends only logarithmically on the plasma temperature, the electron beam

10.1. ROLE OF LASER-GENERATED FAST ELECTRONS IN THE SHOCK IGNITION SCHEME

will deposit its energy in the same mass even when this mass expands. This reasoning enables to introduce the following two-stage model of plasma expansion driven by a monoenergetic electron beam transporting the energy flux $I_b = n_b \varepsilon_0 v_0$, where v_0 is the initial electron velocity and n_b the beam density.

In the first stage, the plasma is heated by the incident beam of fast electrons and starts expanding. The plasma energy increases linearly with time. It is redistributed between the areal density of internal energy,

$$W_{\text{int}} = \frac{3}{2} \int \rho_0 c_s^2 dx \quad (10.19)$$

and the areal density of kinetic energy

$$W_{\text{kin}} = \frac{1}{2} \int \rho_0 u^2 dx \quad (10.20)$$

where c_s is the velocity of sound (10.22). The energy conservation of the process reads

$$W_{\text{int}} + W_{\text{kin}} = I_b t, \quad (10.21)$$

assuming that the energy flux I_b does not depend on time. In addition, it is assumed that the DT follows the relations (10.9) with $d = 3$, typical of a monoatomic ideal gas, so that the sound velocity (10.5) can be written

$$c_s = \sqrt{(Z + 1) \frac{k_B T}{m_i}}. \quad (10.22)$$

As a consequence, the repartition between the internal and kinetic energies in the heated layer, $W_{\text{kin}}/W_{\text{int}} = \zeta(t)$, increases with time. The duration of this stage t_h , called the loading time, is defined by the time of propagation of the rarefaction wave across the heated layer, $t_h \approx L_p/c_s$. The coefficient ζ can be evaluated by requesting a continuity of the plasma density and pressure at the time t_h with the self-similar solution. During the expansion phase, the absorbed energy is equally divided between the kinetic and internal energy. Thus, $\zeta(t_h) = 1$ at this stage, and the loading time and the pressure read consequently

$$t_h = 2 \frac{W_{\text{kin}}}{I_b} = \left(\frac{9}{2\pi} \right)^{1/3} \frac{L_p}{D_0} \quad (10.23)$$

and

$$P_m = P_h \frac{t}{t_h} \quad (10.24)$$

where

$$P_h = \left(\frac{1}{6\pi} \right)^{1/3} \frac{I_b}{D_0} \quad (10.25)$$

is the maximum pressure and

$$D_0 = \left(\frac{I_b}{\rho_0} \right)^{1/3} \quad (10.26)$$

CHAPTER 10. APPLICATION TO THE GENERATION OF SHOCK WAVES BY FAST ELECTRON ENERGY DEPOSITION

is the characteristic hydrodynamic velocity found according to the dimensional reasoning. Note that the maximum pressure depends only on the beam intensity and on the target density, while the loading time increases strongly with the electron energy in agreement with [Evans, 1983] [Evans, 1986].

For electron beam intensities in the range of few PW/cm², the heating proceeds so fast that the electron thermal conduction does not play a significant role, and the heated mass undergoes expansion without transferring the internal energy to the adjacent cold plasma. However, the pressure in the heated layer exerts a mechanical work and launches a shock wave in the cold plasma. Therefore, the second stage consists in the expansion of a heated layer of plasma continuously heated by an electron beam. It can be described by the isothermal rarefaction wave of a constant mass [Imshennik, 1960] [Drake, 2011]. It corresponds to the solution of hydrodynamics equations (10.1), (10.2), (10.3) and (10.4) with the energy deposition rate defined by the flux of fast electrons

$$W_e \approx \frac{I_b}{L_p} \quad (10.27)$$

in the right hand side of Equation (10.3) and neglecting the thermal energy flux q . Assuming the boundary conditions of zero flow velocity at $x = L_p$ and zero density at $x \rightarrow \infty$, this self-similar solution reads :

$$\left\{ \begin{array}{l} \rho = \frac{3}{\sqrt{2\pi I_b}} \left(\frac{\rho_0 L_p}{t} \right)^{3/2} \exp \left[-\frac{9\rho_0 L_p (L_p - x)^2}{8I_b t^3} \right] \quad \text{a)} \\ T = \frac{m_i I_b}{3(Z+1)\rho_0 k_B L_p} t \quad \text{b)} \\ u = \frac{3}{2} \frac{x - L_p}{t} \quad \text{b)} \end{array} \right. , \quad (10.28)$$

Here, the velocity increases linearly with the coordinate for $x < x_h$, the temperature increases linearly with time, and the density profile has a Gaussian-like shape with the characteristic scale length

$$\lambda_\rho(t) = \frac{1}{3\sqrt{L_p}} (2D_0 t)^{3/2} \quad (10.29)$$

increasing with time as $t^{3/2}$. As this self-similar solution corresponds to an infinitely thin initial heated layer, it formally diverges at $t = 0$, but it has a physical sense for times longer than the loading time t_h . We can check according to Equation (10.28 a) that the maximum of density ρ_m is obtained at $t = t_h$ and $x = L_p$ that gives the expression of the loading time (10.23). Also, we can check that, by injecting the sound velocity (10.22) expressed with the temperature (10.28 b) in the areal density of kinetic energy (10.19) at the loading time t_h , we find (10.23), as previously explained. The effect of expanding plasma on the shock wave formation depends on the values of plasma density

$$\rho_m = \rho_0 \left(\frac{t_h}{t} \right)^{3/2} \quad (10.30)$$

10.1. ROLE OF LASER-GENERATED FAST ELECTRONS IN THE SHOCK IGNITION SCHEME

and pressure

$$P_m = P_h \sqrt{\frac{t_h}{t}} \quad (10.31)$$

at the cold plasma interface at $x = L_p$ according to Equations (10.9), (10.23), (10.28 a and b). The pressure decreases as a square root of time at the second stage.

As an example, we consider an electron beam with an energy $\varepsilon_0 = 30$ keV and intensity $I_b = 1$ PW/cm² incident on a DT plasma with a density $\rho_0 = 10$ g/cm³. Then, the maximum pressure P_h rises to the value of 380 Mbar according to Equations (10.24) and (10.25). The loading time $t_h \approx 6$ ps ($D_0 = 10^7$ cm/s and $L_p = 0.5$ μ m) is relatively short according to (10.23). However, for longer times, the pressure decreases rather slowly according to (10.31). Knowing the pressure, it is straightforward to evaluate the shock wave velocity in the strong pressure limit. According to Equation (10.10), it reads

$$D_{sh}(t) = \sqrt{\frac{4 P_m}{3 \rho_0}} = \begin{cases} D_{sh}(t_h) \left(\frac{t}{t_h}\right)^{1/2} & \text{if } t < t_h \\ D_{sh}(t_h) \left(\frac{t_h}{t}\right)^{1/4} & \text{if } t \geq t_h \end{cases} \quad (10.32)$$

where

$$D_{sh}(t_h) = \sqrt{\frac{4 P_h}{3 \rho_0}} = \left(\frac{32}{81\pi}\right)^{1/6} D_0 \quad (10.33)$$

according to (10.26) and (10.25).

10.1.2 Coupling of the Reduced Model for Fast Electron Transport with the Radiation Hydrodynamic CHIC code

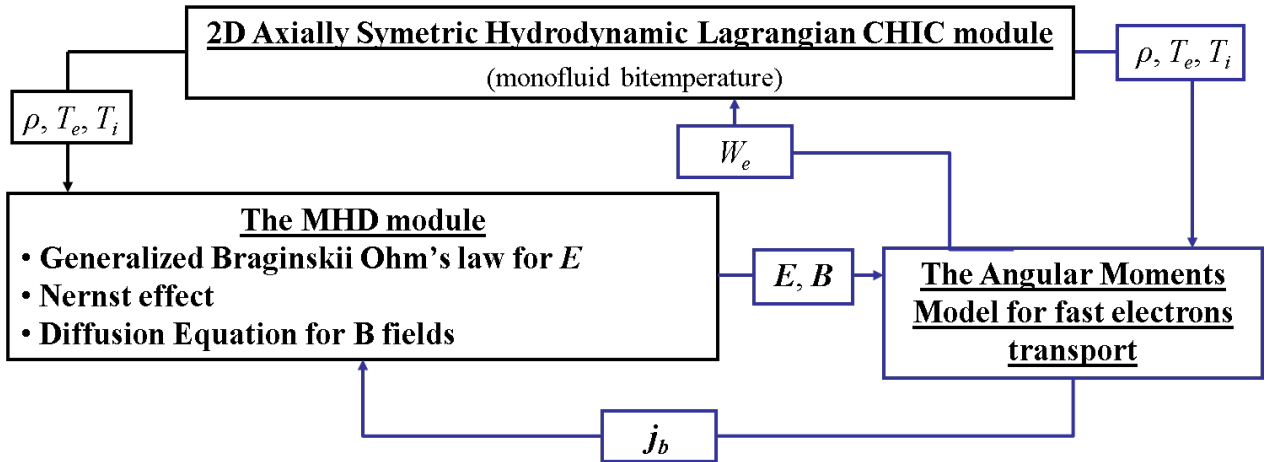


Figure 10.4: Schematic view of the coupling between the reduced model for fast electron transport and the radiation hydrodynamic CHIC code.

In this section, we present the coupling of the reduced model for the fast electron transport

in dense plasmas, described in **Chapter 6**, with the radiation MagnetoHydrodynamic CHIC code [Breil et al., 2011], described in **Appendix B**, sections **B.3.2** and **B.3.3**. This code is currently used to simulate laser-plasma interaction experiments. It includes thermal coupling of electrons and ions, classical or nonlocal electron heat conduction, and a detailed radiation transport with the tabulated ionization and the opacity data. Equations (6.34) and (6.35) completed with the M1 closure (6.61) of the reduced model for fast electron transport have already been implemented in CHIC by [Regan, 2010] [Regan et al., 2011] [Regan, 2011] for fast ion or electron beam transport in dense plasmas, without electromagnetic fields. An option allows for projecting or not the different quantities from the hydrodynamic Lagrangian grid of the code CHIC to a regular Eulerian grid for the fast particle transport, and vice-versa, at each hydrodynamic time step Δt_n . In the case where there are no projections, the resolution of the fast particle transport has been extended to irregular Eulerian grids, allowing to propagate the fast particles in the Lagrangian CHIC grid [Feugeas, 2011]. The self-generated magnetic fields have been implemented by [Nicolai et al., 2011] by adding the source terms $\eta(\partial/\partial\mathbf{r})\times\mathbf{j}_b$ and $(\partial\eta/\partial\mathbf{r})\times\mathbf{j}_b$ of Equation (6.24) into the magnetic field equation (B.81) [Nicolai, 2011]. The numerical scheme used to solve the resulting M1 equations

$$\frac{\partial}{\partial\varepsilon}\left(S\widehat{\Psi}_0\right) - \frac{\partial}{\partial\mathbf{r}}\cdot\widehat{\Psi}_1 = \frac{\partial\widehat{\Psi}_0}{v\partial t}, \quad (10.34)$$

$$\frac{\partial}{\partial\varepsilon}\left(S\widehat{\Psi}_1\right) - \frac{\partial}{\partial\mathbf{r}}\cdot\widehat{\Psi}_2 = \frac{\partial\widehat{\Psi}_1}{v\partial t} + k\widehat{\Psi}_1 + \frac{e}{pc}\widehat{\Psi}_1 \times \mathbf{B} \quad (10.35)$$

and

$$\widehat{\Psi}_2 = \frac{1}{3}\widehat{\Psi}_0\mathbf{I} + \mu\widehat{\Psi}_0\left(\frac{\widehat{\Psi}_1 \otimes \widehat{\Psi}_1}{|\widehat{\Psi}_1|^2} - \frac{1}{3}\mathbf{I}\right) \quad (10.36)$$

has been implemented by [Regan, 2010] in 1 or 2D Cartesian or axisymmetric and cylindrical geometry. Here, $\forall i \in \{0, 1, 2\}$, $\widehat{\Psi}_i = v\Psi_i$ and $k = \nu/v$ is the inverse of the beam electrons mean free path (8.11). This fully implicit numerical scheme reads

$$\frac{S^{n+1,l+1}\widehat{\Phi}^{n+1,l+1} - S^{n+1,l}\widehat{\Phi}^{n+1,l}}{\Delta\varepsilon_l} - \left[\frac{\partial}{\partial\mathbf{r}}\cdot\widehat{\mathbf{F}}\right]^{n+1,l+1} = \frac{\widehat{\Phi}^{n+1,l} - \widehat{\Phi}_0^{n,l}}{v_l\Delta t_n} + \widehat{\Gamma}_\nu^{n+1,l} + \widehat{\Gamma}_B^{n+1,l} \quad (10.37)$$

where the kinetic energy derivative is computed according to the 1st order downwind scheme and the spatial derivative according to the 2nd order HLL scheme described in **section 7.1.1**. It considers the kinetic energy derivative as a "time derivative" and it allows to deduce the angular moments $\widehat{\Phi}^{n+1,l}$ at kinetic energy ε_l from the knowledge of the angular moments $\widehat{\Phi}^{n+1,l+1}$ at kinetic energy ε_l . Here, $\widehat{\Phi}^{n,l} = v_l\Phi^{n,l}$, $\widehat{\mathbf{F}}^{n,l} = (F_x^{n,l}, F_y^{n,l}, F_z^{n,l})$,

$$\widehat{\Gamma}_\nu^{n+1,l} = k \begin{pmatrix} 0 \\ \widehat{\Psi}_{1,x}^{n+1,l} \\ \widehat{\Psi}_{1,y}^{n+1,l} \\ \widehat{\Psi}_{1,z}^{n+1,l} \end{pmatrix} \quad \text{and} \quad \widehat{\Gamma}_B^{n+1,l} = \frac{e}{pc} \begin{pmatrix} 0 \\ \widehat{\Psi}_{1,y}^{n+1,l}B_z^n - \widehat{\Psi}_{1,z}^{n+1,l}B_y^n \\ \widehat{\Psi}_{1,z}^{n+1,l}B_x^n - \widehat{\Psi}_{1,x}^{n+1,l}B_z^n \\ \widehat{\Psi}_{1,x}^{n+1,l}B_y^n - \widehat{\Psi}_{1,z}^{n+1,l}B_x^n \end{pmatrix},$$

10.1. ROLE OF LASER-GENERATED FAST ELECTRONS IN THE SHOCK IGNITION SCHEME

following the notations introduced in **section 7.1**. The CFL condition reads

$$\Delta\varepsilon_l < \frac{\min_{\mathbf{r}} \left\{ S^{n+1,l+1}(\mathbf{r}) \right\}}{\frac{1}{\Delta x} + \frac{1}{\Delta y} + \frac{1}{\Delta z}}. \quad (10.38)$$

Here, we introduce the self-generated electric field in the electron transport equations. For this, we consider only the main term of Equation (6.23) i.e. we assume the simpler Ohm's law

$$\mathbf{E} = -\eta\mathbf{j}_b. \quad (10.39)$$

In order to solve Equations (6.34) and (6.35) with the self-generated electric field according to the numerical scheme (10.37), we introduce the resistive stopping power

$$S_{\text{res}} = e\mathbf{E} \cdot \mathbf{\Omega}_\varepsilon, \quad (10.40)$$

the resistive slowing down frequency

$$\nu_{\text{res}} = \frac{S_{\text{res}}}{p} \quad (10.41)$$

and the inverse of the fast electrons resistive mean free path

$$k_{\text{res}} = \frac{\nu_{\text{res}}}{v}. \quad (10.42)$$

Then Equations (6.34), (6.35) and (6.61) multiplied by p read

$$\frac{\partial}{\partial\varepsilon} \left(S_{\text{tot}} \widehat{\Psi}_0 \right) - \frac{\partial}{\partial\mathbf{r}} \cdot \widehat{\Psi}_1 = \frac{\partial \widehat{\Psi}_0}{v\partial t} + (k_{\text{res}} + k_d) \widehat{\Psi}_0, \quad (10.43)$$

$$\frac{\partial}{\partial\varepsilon} \left(S_{\text{tot}} \widehat{\Psi}_1 + \widehat{\Pi}_\varepsilon \cdot \mathbf{E} \right) - \frac{\partial}{\partial\mathbf{r}} \cdot \widehat{\Psi}_2 = \frac{\partial \widehat{\Psi}_1}{v\partial t} + (k + k_d) \widehat{\Psi}_1 + \frac{e}{pv} \widehat{\Psi}_0 \mathbf{E} + \frac{e}{pc} \widehat{\Psi}_1 \times \mathbf{B} \quad (10.44)$$

and

$$\widehat{\Psi}_2 = \frac{1}{3} \widehat{\Psi}_0 \mathbf{I} + \mu \widehat{\Psi}_0 \left(\frac{\widehat{\Psi}_1 \otimes \widehat{\Psi}_1}{|\widehat{\Psi}_1|^2} - \frac{1}{3} \mathbf{I} \right) \quad (10.45)$$

where it has been noted $\forall i \in \{0, 1, 2\}$, $\widehat{\Psi}_i = p\widehat{\Psi}_i = pv\Psi_i$, $\nu_d = S/p$ the collisional slowing down frequency (5.2), $k_d = \nu_d/v$ the corresponding mean free path,

$$S_{\text{tot}} = S_{\text{res}} + S \quad (10.46)$$

the total stopping power due to both collective and collisional effects and

$$\widehat{\Pi}_\varepsilon = \widehat{\Psi}_2 - \widehat{\Psi}_1 \otimes \widehat{\Psi}_1 = pv\Pi_\varepsilon = \frac{1-\mu}{3}\widehat{\Psi}_0\mathbf{I} + \widehat{\Psi}_0\left(\mu - |\Omega_\varepsilon|^2\right)\frac{\widehat{\Psi}_1 \otimes \widehat{\Psi}_1}{|\widehat{\Psi}_1|^2} \quad (10.47)$$

the "angular pressure tensor" that has already been introduced in (8.10). These notations allow to make appearing the term $\widehat{\Psi}_2 \cdot \mathbf{E}$ only in the kinetic energy derivative of the 1st order equation (10.44). Then, by noticing that $\widehat{\Pi}_\varepsilon \cdot \mathbf{E} = \mathbf{0}$ in both anisotropic ($\widehat{\Pi}_\varepsilon = \mathbf{0}$) and isotropic ($\mathbf{E} = \mathbf{0}$ since $\mathbf{j}_b = \mathbf{0}$ for monoenergetic electron beam) limits, we assume

$$\widehat{\Pi}_\varepsilon \cdot \mathbf{E} = \mathbf{0} \quad (10.48)$$

in all cases. As a consequence, we can use the same numerical scheme as (10.37), by replacing S by S_{tot} in (10.37) and by adding the new source terms expressed at t_{n+1} for ε_l of Equations (10.43) and (10.44) in the the right hand side of the discretized Equation (10.37). The terms depending on the self-generated electric field in Equations (10.43) and (10.44) are discretized semi-implicitly i.e. they are expressed with the electric field \mathbf{E}^n at time t_n . It may happen that the resistive stopping power (10.40) changes sign and transforms into a "resistive pushing power" ($S_{\text{res}} < 0$) for some electron energy groups ε_l . However, it does not lead to numerical issues with the downwind scheme in the following simulations since we consider cases where $S_{\text{res}} \ll S$ so that the total stopping power (10.46) in the CFL condition (10.38) is always positive. Finally, we use the absorbing boundary conditions, described in **section 7.1.6**.

10.1.3 Electron driven shock waves

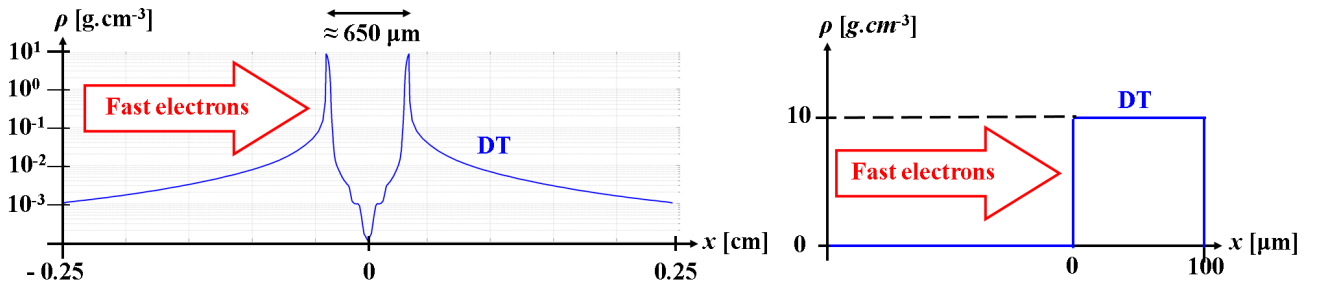


Figure 10.5: (Left panel) DT plasma density profile at the moment of spike arrival obtained from a CHIC simulation [Ribeyre et al., 2009]; Courtesy of X. Ribeyre. (Right panel) Initialization of the 1D academic simulations assuming an idealized target density profile at the time of ignitor spike arrival.

The geometry corresponding to the shock excitation in the shock ignition scheme is presented in the left panel of **Figure 10.5**. The distribution of the DT plasma density at the moment of spike

10.1. ROLE OF LASER-GENERATED FAST ELECTRONS IN THE SHOCK IGNITION SCHEME

arrival corresponds to a thin shell converging to the center. It is obtained from a CHIC simulation conducted by [Ribeyre et al., 2009] with the HiPER baseline target designed by [Atzeni et al., 2009a]. The initial dimensions of the capsule are 1044 μm of external radius and 211 μm of shell thickness. It is supposed to be imploded at a constant in-flight adiabat $\alpha \approx 1$. At the moment of the spike launch the shell is already compressed by a factor of 40. Consequently, we model here the shell as a DT plasma layer of a steplike profile with a maximum density of $\rho_0 = 10 \text{ g/cm}^3$, a temperature of $T_0 = 10 \text{ eV}$ and a thickness of 100 μm . This idealized target density profile is illustrated in the right panel of **Figure 10.5**. The plasma thickness is much larger than the fast electron range, thus allowing us to observe the creation and propagation of the shock wave for a sufficiently long time of the order of $t_f = 1 \text{ ns}$. The energy flux of monoenergetic and collimated electron beams is maintained constant in time during the simulation. Two representative cases with $I_b = 1 \text{ PW/cm}^2$ and $\varepsilon_0 = 30 \text{ keV}$ (case 1) and $I_b = 10 \text{ PW/cm}^2$ and $\varepsilon_0 = 100 \text{ keV}$ (case 2) have been tested. In both cases, because of a high plasma density, the resistive losses (10.40) are small and the electron energy deposition is due to the collisional effects of in a dense plasma. The fast electrons propagate in the Lagrangian CHIC grid, as explained in **section 10.1.2**. The initialized angular moments of the beam distribution function thus read

$$\Psi_{1,x}(x=0, \varepsilon, t) = \Psi_0(x=0, \varepsilon, t) = N f_\varepsilon(\varepsilon) F_z(t) \quad (10.49)$$

where

$$F_z(t) = \Pi(t) - \Pi(t - t_f) \quad (10.50)$$

(Π is the Heaviside distribution function),

$$f_\varepsilon(\varepsilon) = \begin{cases} \frac{1}{2\delta\varepsilon} & \text{if } |\varepsilon - \varepsilon_0| \leq \delta\varepsilon \\ 0 & \text{else} \end{cases} \quad (10.51)$$

with $\delta\varepsilon = 1 \text{ keV}$ and

$$N = \frac{I_b}{\varepsilon_0 v_0}. \quad (10.52)$$

The kinetic energy boundaries are $\varepsilon_{\min} = 1 \text{ keV}$ and $L_\varepsilon = \varepsilon_0 + 5 \text{ keV}$.

The left panel in **Figure 10.6** shows the power density W_e deposited by the electron beam, the plasma pressure and the density profiles for case 1. The mean free path of fast electrons is initially of the order of $L_p \approx 1 \mu\text{m}$, that is, twice the theoretical estimate (10.18). This difference is due to the assumption $(\ln \lambda_e + \ln \lambda_{ei}^{\text{rel}})/2 \ln \lambda_e \approx 1$, which allows us to find an analytical estimate for the correction factor (8.17) due to angular scattering of fast electrons. However, the characteristic hydrodynamic velocity $D_0 \approx 100 \mu\text{m/ns}$ and the corresponding loading time $t_h \approx 11 \text{ ps}$ are not so far from the predicted values. The maximum pressure P_h rises to 400 Mbar in agreement with the theoretical prediction and the density increases by a factor of 2.7 after the loading time. The assumption of a homogeneous energy deposition, $W_e \approx I_b/L_p$, seems to be reasonable even if the beam energy flux evolves in time according to **Figure 10.6 a**). Then, as time goes on, the pressure drops down to

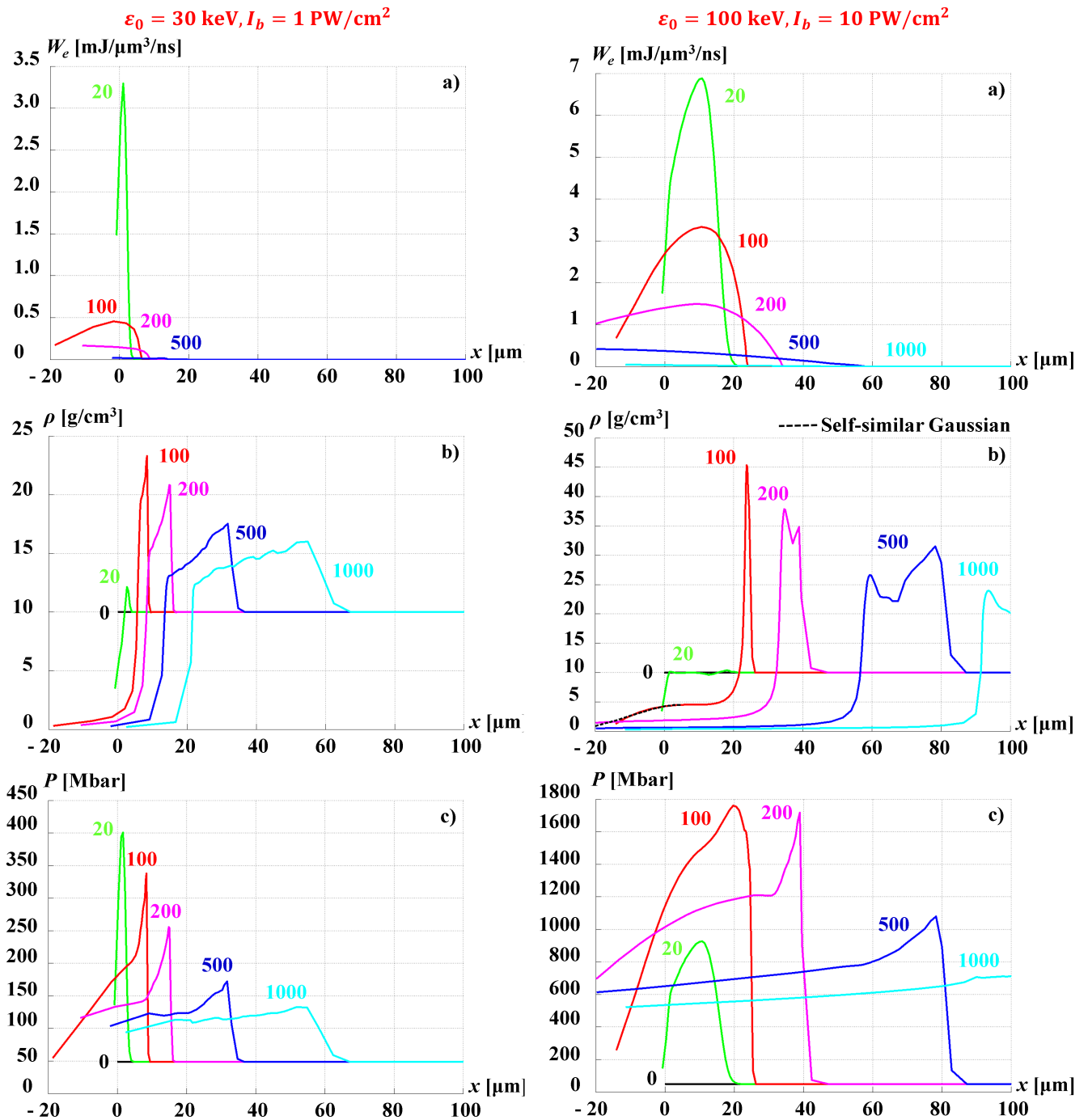


Figure 10.6: Distributions of the deposited power density W_e (a), the plasma density ρ (b) and DT plasma pressure P (c) from the simulations of a shock drive by a monoenergetic and collimated beam of electrons with a kinetic energy and an energy flux of 30 keV, 1 PW/cm 2 (Left panel) and 100 keV, 10 PW/cm 2 (Right panel). The numbers near the curves indicate the time in ps. The dashed line in the right panel b shows the self-similar solution (10.28 a).

$P_{sh} \approx 120$ Mbar, and the shock takes a triangular shape characteristic for a blast wave. It propagates with a velocity $D_{sh} \approx 60 \mu\text{m/ns}$. Consequently, the shock wave power $I_{sh} = P_{sh}D_{sh}$ is about 70 TW/cm^2 . The driver efficiency is thus about $I_{sh}/I_b \approx 7\%$. The fast electron energy deposition does not follow the shock front, but instead moves out and spreads over the expanding plasma. The front edge of the energy deposition zone coincides with the rear edge of the density compression. Thus, the deposited energy becomes decoupled from the shock, so the shock pressure drops down with time. A comparison of the runs with and without electron thermal conductivity shows that its role is negligible at the loading stage as the plasma temperature in the shock is rather low, just a few eV. Later in time, after ≈ 600 ps, the thermal wave from the hot corona catches up to the shock and broadens the pressure profile.

The electron beams of higher energy and intensity may create even much stronger blast waves. For the case 2 shown in the right panel of **Figure 10.6**, the loading time is ≈ 80 ps and the shock pressure rises to 1800 Mbar at the time of 100 ps. It reduces then to 700 Mbar after 1 ns. The shock velocity is about $120 \mu\text{m/ns}$ and the shock power is about 0.7 PW/cm^2 . The Gaussian-like density profile corresponding to the self-similar solution (10.28 a) with $\lambda_p = 20 \mu\text{m}$ for $t = 100$ ps is shown in **Figure 10.6 b** with a dashed line. It agrees rather well with the numerical solution shown with a red line corresponding to the time of 100 ps. The density profile in the shock in the later time, $t > 200$ ps, takes a two-humps shape. The second hump is driven by the thermal wave catching up the shock at the time of 1 ns. The driving efficiency of the beam remains at the same level of 7 % as in case 1.

10.1.4 Conclusion

The limits of the model are threefold. First, the target thickness should be larger than the electron beam stopping length. In practice, having in mind the electron energies of several tens of keV and the stopping lengths L_p of a few microns, the target density needs to be in the range of 10 g/cm^3 or more. Second, the planar model is limited by the two or three-dimensional effects. Thus, the thickness of the expanding plasma layer, $\approx (D_0 t^{3/2} / \sqrt{L_p})$, according to Equation (10.29), should be smaller than the characteristic distance in the second dimension r (the shell radius for a spherical target or the electron beam radius for a planar target). This condition limits the time to $t < t_h (r/L_p)^{2/3}$. Considering the shell radius of $200 \mu\text{m}$, this condition allows the time intervals of a few hundred ps in the examples discussed above. Third, a strong plane shock may become unstable with respect to front modulations if the target is accelerated. However, this effect needs a global description of the target dynamics.

The theory of the fast electron driven shock wave in dense solids has been confirmed by numerical simulations. It shows a possibility to achieve extremely high shock pressures in high density solid materials with the coupling efficiency up to 10 %. The case presented in the left panel of **Figure 10.6** corresponds to the fast electron current of 30 GA/cm^2 , which can be generated with high power laser pulses. The numerical simulations of laser plasma interaction [Klimo et al., 2011] predict the

efficiency of laser absorption more than 70 % with 90 % conversion in fast electrons for the laser intensities exceeding 10 PW/cm^2 at the wavelength $0.351 \mu\text{m}$. The laser accelerated electrons with energies less than 100 keV could be efficient drivers of strong shocks for ignition of ICF targets and for other high energy density applications. Such drivers could invest about 10 % of energy in the shock wave in solids with a pressure amplitude at the level of several hundred Mbar or more. However, the electron energy distribution, angular aperture and the target density profile may affect the shock amplitude or the preheat of the imploding shell. The simulations similar to those presented in this section have been conducted with more realistic electron energy spectrum and more realistic density profiles [Nicolai et al., 2014]. It has been shown that the fast electron beam may preheat the DT shell and jeopardizes its compression.

Since this work, another model developed by [Piriz et al., 2012] for the description of ablation driven by hot electrons generated during the ignitor laser pulse in shock ignition have been proposed. However, contrary to the model presented here, it assumes the process to be quasi-stationary, which does not agree with our numerical simulations. The possibility to launch shocks of several-hundred Mbar in spherical targets has been recently demonstrated on the OMEGA laser facility [Theobald et al., 2013] [Nora et al., 2015]. The ablation pressure has been inferred from the time of shock propagation to the target center by using radiation-hydrodynamic simulations. Peak ablation pressures exceeding 300 Mbar are inferred at absorbed laser intensities of $\approx 3 \cdot 10^{15} \text{ W/cm}^2$. It has been demonstrated that the shock strength is significantly enhanced by the coupling of suprathermal electrons with a total converted energy of up to 8 % of the incident laser energy. At the end of the laser pulse, the shock pressure is estimated to exceed $\approx 1 \text{ Gbar}$ because of convergence effects.

10.2 Blast Wave generation in solid targets by the quasi-isochoric heating by laser-generated Electron Beam

10.2.1 Analytical Estimates

Here, we consider another example of a blast wave driven by an intense short laser pulse. The experimental campaign conducted by [SANTOS et al., 2013], was described in **sections 8.2** and **9.2**. As illustrated in **Figure 10.7 a**), a Streaked Optical Pyrometry (SOP) at the wavelengths $\lambda = 405$ and 532 nm have been used to diagnose the targets rear side temperature [Vauzour, 2012]. It was estimated from the signal intensity assuming a Planckian-type emission (Black body radiations). The estimates of the target rear side temperature are in good agreement with the M1 and PaRIS simulations illustrated in **Figure 9.15**. A strong increase in visible light emission has been observed for the thick targets with a delay of $\approx 500 \text{ ps}$ after a 50 fs laser pulse **Figure 10.7 b**), but not the thinner targets. This effect is interpreted as a blast wave formation in a sufficiently thick target. From 2D

10.2. BLAST WAVE GENERATION IN SOLID TARGETS BY THE QUASI-ISOTHERMIC HEATING BY LASER-GENERATED ELECTRON BEAM

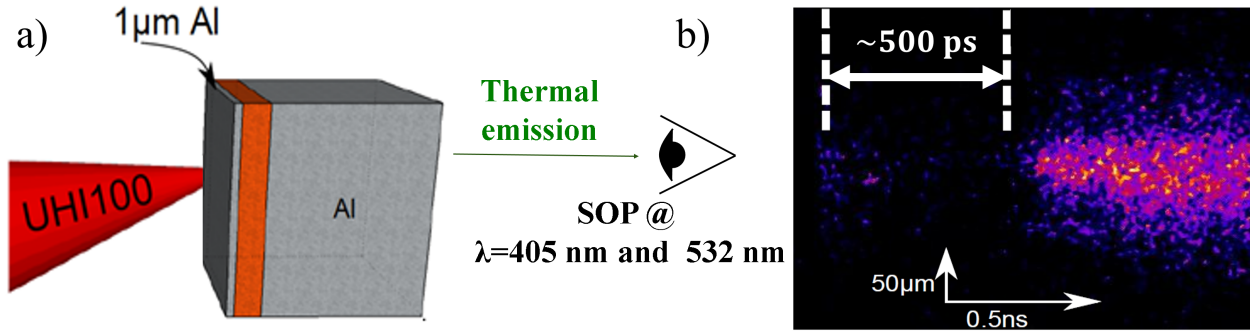


Figure 10.7: Schematic view of the laser-irradiated target and the Streaked Optical Pyrometry (SOP) diagnostic a) and a SOP image of SOP result at $\lambda = 532$ nm for the Al(1 μm)Cu(3 μm)Al(15 μm) target b); Courtesy of J. Santos.

PIC simulations of laser-solid interaction with a laser pulse intensity of $I_L = 7.5 \cdot 10^{17}$ W/cm² and a duration of 500 fs, [Sentoku et al., 2007] showed that the quasi-isochoric heating of the target by the laser-generated fast electrons may excite shock waves that compress the plasma beyond solid density and to keV temperatures. According to their simulations, shocks with pressures up to gigabar can be launched inside the target with ultrashort laser pulses.

Therefore, in order to explain this increase of visible light emission in the experiments conducted by [SANTOS et al., 2013], we developed a model of a blast wave generation by strong temperature gradients induced by a fast target heating. For this, we solve Equations (10.1), (10.2), (10.3) and (10.4) with a nonlinear heat flux

$$\mathbf{q} = -\kappa_0 T^n \frac{\partial T}{\partial x} \quad (10.53)$$

induced by an instantaneous energy deposition

$$W_e \propto \delta(t). \quad (10.54)$$

Indeed, according to **section 9.2.2**, the target heating by the laser-generated fast electrons lasts $\approx 1 - 2$ ps; see **Figure 9.12**. On the hydrodynamic time scale, this heating may thus be considered as instantaneous and isochoric due to the large ion inertia. Actually, some ions are accelerated on the ps time scale, but they do not affect the target dynamics. The main part of ions may be considered as immobile. Since in our conditions the electron and radiation heat fluxes are comparable

$$\frac{\kappa_{\text{rad}}}{\kappa_{\text{SH}}} \approx 5 \cdot 10^{18} \frac{(k_B T_e [\text{eV}])^{5/2}}{n_e [\text{cm}^{-3}]} > 1 \quad (10.55)$$

according to [Ditmire et al., 1996], we do not specify the values of n and κ_0 in the thermal energy flux (10.53). Here, κ_{SH} is the Spitzer-Harm thermal electron conductivity (see **Appendix B, section B.2.1** and **B.2.2**). Indeed, thermal waves are driven by radiation transport for solids ($n_e \approx 10^{23}$

CHAPTER 10. APPLICATION TO THE GENERATION OF SHOCK WAVES BY FAST ELECTRON ENERGY DEPOSITION

cm^{-3}) at temperatures greater than $k_B T_e \approx 100$ eV, according to the Ditmire criterion (10.55).

Let us assume that at the time $t = 0$ after the end of the laser pulse, the electron heating resulted in an exponential temperature profile

$$T(x, t = 0) = T_m \exp(-x/d_0), \quad (10.56)$$

with $T_m = 400$ eV and $d_0 = 5 \mu\text{m}$; see **Figure 9.15**. Contrary to the explanation given by [Sentoku et al., 2007], the blast wave generation is not related to the Copper tracer layer in our case. Therefore, we assume a simple target made of Aluminum, only ($\rho = 2.69 \text{ g/cm}^3$ and $n_i = 6 \cdot 10^{22} \text{ cm}^{-3}$). We model therefore the thermal capacity as

$$C_V = \frac{3}{2} n_e k_B = C^{\text{st}} \text{ with } n_e = Z^* n_i \quad (10.57)$$

and the velocity of sound as

$$c_s = \sqrt{Z^* \frac{k_B T}{m_i}}. \quad (10.58)$$

The ionization state may be estimated by its averaged value :

$$Z^* = \frac{1}{L_x} \int_0^{L_x} Z_m^* \exp\left(-\frac{x}{d_0}\right) dx \approx 5 \quad (10.59)$$

with L_x being the target thickness and $Z_m^* = 10$ the ionization state in the first micron of Aluminum. Due to the high temperature T_m , the plasma expands rapidly in vacuum at the irradiated side of the target with the velocity $c_s(T_m) = \sqrt{Z_m^* k_B T_m / m_i} \mathbf{e}_x$ corresponding to few hundreds of $\mu\text{m/ns}$, in agreement with the self-similar rarefaction wave expanding in vacuum [Gurevich et al., 1966]. Due to the plasma expansion, the temperature at $x = 0$ decreases rapidly to low temperatures in agreement with the 1D academic simulation so that we can consider the boundary condition

$$\forall t > 0, T(x = 0, t) = 0. \quad (10.60)$$

This boundary condition corresponds to the *dipole-type* solution found by [Barenblatt and Zel'dovich, 1957] when studying the self-similar process of gas filtration in a porous medium. Here, the invariant quantities are the heat diffusivity

$$a = \frac{\kappa_0}{C_V} [\text{cm}^2 \cdot \text{s}^{-1} \cdot \text{K}^{-n}] \quad (10.61)$$

and

$$P [\text{K} \cdot \text{cm}^2] = \int_0^\infty z T(z, t = 0) dz = T_m d_0^2 \approx 1.16 \text{ K} \cdot \text{cm}^2 \quad (10.62)$$

with $T_m = 400$ eV and $d_0 = 5 \mu\text{m}$ instead of a [$\text{cm}^2 \cdot \text{s}^{-1} \cdot \text{K}^{-n}$] and T_0 [K] for the self-similar solution

10.2. BLAST WAVE GENERATION IN SOLID TARGETS BY THE QUASI-ISOTHERMIC HEATING BY LASER-GENERATED ELECTRON BEAM

with a constant temperature T_0 at $x = 0$. Consequently, we can construct the two self-similar variables

$$x_f(t) [cm] = \xi_1 (aP^n t)^{\frac{1}{2(n+1)}} \quad (10.63)$$

and the effective initial heating depth

$$\tau(t) [s] = M \left(\frac{P}{at} \right)^{\frac{1}{n+1}}. \quad (10.64)$$

Here, ξ_1 and M are dimensionless constants while $a \approx 4.7 \cdot 10^{-14} \text{ cm}^2 \cdot \text{s}^{-1} \cdot \text{K}^{-5/2}$ for the electron thermal conductivity ($C_V = 6.2 \cdot 10^7 \text{ erg} \cdot \text{K}^{-1} \cdot \text{cm}^{-3}$ and $\ln \Lambda_{ei} = 3$) and $a \approx 8.5 \cdot 10^{-29} \text{ cm}^2 \cdot \text{s}^{-1} \cdot \text{K}^{-5}$ for the radiation thermal conductivity assuming

$$\kappa_{\text{rad}} = \frac{16\sigma_{\text{SB}}\lambda_R T^3}{3} \quad (10.65)$$

and the Rosseland mean free path for Hydrogen-like plasmas

$$\lambda_R \approx 8.7 \cdot 10^6 \frac{T^2}{Z^* n_i} \quad (10.66)$$

according to [Eliezer, 2002]. By looking for the function F such that

$$T(x, t) = \tau(t) \cdot F \left(\frac{x}{x_f(t)} \right) \quad (10.67)$$

is solution of (10.3), we find according to [Barenblatt and Zel'dovich, 1957]

$$F(\xi) = \xi^{1/(n+1)} \left(1 - \xi^{(n+2)/(n+1)} \right), \quad (10.68)$$

$$M = \left[\frac{n}{2(n+2)} \right]^{1/n} \approx \begin{cases} 0.599 & \text{if } n = 5/2 \\ 0.814 & \text{if } n = 5 \end{cases} \quad (10.69)$$

and

$$\xi_0 = (n+2)^{1/2} \left\{ \frac{2}{n} \left[(n+1) B \left(1 + \frac{1}{n}, \frac{n+1}{n+2} + 1 \right) \right]^{-n} \right\}^{\frac{1}{2(n+1)}} \approx \begin{cases} 1.918 & \text{if } n = 5/2 \\ 1.680 & \text{if } n = 5 \end{cases}. \quad (10.70)$$

The *dipole-type* solution is illustrated in **Figure 10.8**.

Knowing the temperature profile, let us now estimate the target depth and the time at which the blast wave is generated. A criterion called *hydrodynamic separation* consists in estimating the time needed for compression waves to "overshoot" the thermal wave front. According to Equation (10.6) that describes the propagation of compression waves, we estimate the propagation velocity of

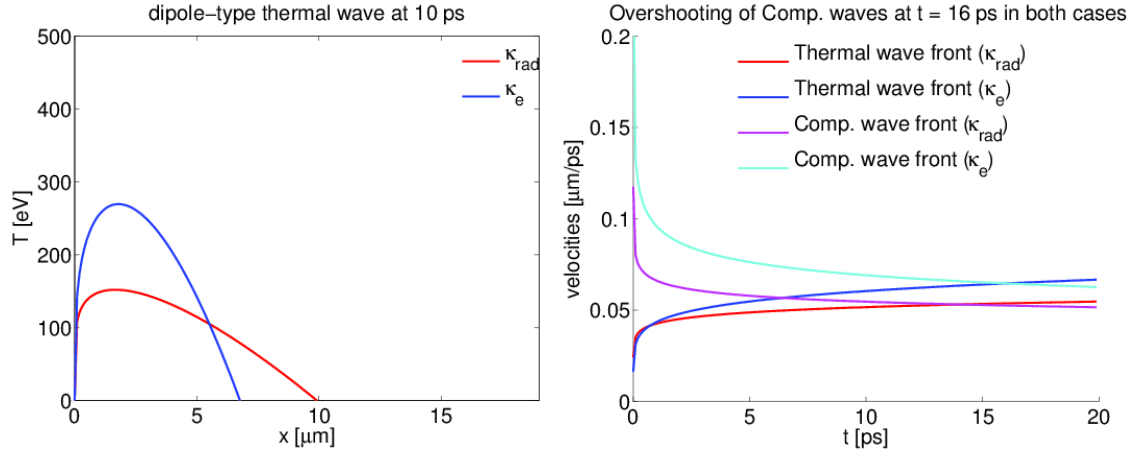


Figure 10.8: (Left panel) Dipole-type solution profile for the heat equation at 10 ps. (Right panel) Plots of the thermal wave front and compression wave velocities versus time.

compression waves that propagate towards the target rear side as

$$c_s(t) \approx \sqrt{\frac{Z^* k_B \langle T \rangle(t)}{m_i}} \quad (10.71)$$

where

$$\langle T \rangle(t) = \tau(t) \frac{n}{n+2} \quad (10.72)$$

is the mean temperature in the *dipole-type* profile illustrated in **Figure 10.8**. Then, by equating the compression wave velocity at the steepening time with the thermal wave front velocity

$$c_s(t_s) \approx \frac{dx_f}{dt}(t_s) = \frac{x_f(t_s)}{2(n+1)t_s}, \quad (10.73)$$

we obtain

$$t_s \approx \left(\frac{\xi_1^2 (n+2)}{4Mn(n+1)^2} \cdot \frac{m_i}{Z^* k_B P} \right)^{(n+1)/2n} (aP^n)^{1/n} \approx \begin{cases} 16 \left(\frac{T_m}{400 \text{ eV}} \right)^{3/10} \left(\frac{d_0}{5 \mu\text{m}} \right)^{3/5} \text{ ps} & \text{if } n = 5/2 \\ 16 \left(\frac{T_m}{400 \text{ eV}} \right)^{3/5} \left(\frac{d_0}{5 \mu\text{m}} \right)^{6/5} \text{ ps} & \text{if } n = 5 \end{cases} \quad (10.74)$$

Knowing the steepening time, we can also estimate the steepening depth as the thermal wave front position at the steepening time t_s . It reads

$$x_s \approx x_f(t_s) \approx \begin{cases} 7 \left(\frac{T_m}{400 \text{ eV}} \right)^{2/5} \left(\frac{d_0}{5 \mu\text{m}} \right)^{4/5} \mu\text{m} & \text{if } n = 5/2 \\ 10 \left(\frac{T_m}{400 \text{ eV}} \right)^{9/20} \left(\frac{d_0}{5 \mu\text{m}} \right)^{9/10} \mu\text{m} & \text{if } n = 5 \end{cases} \quad (10.75)$$

10.2. BLAST WAVE GENERATION IN SOLID TARGETS BY THE QUASI-ISOTHERMIC HEATING BY LASER-GENERATED ELECTRON BEAM

This expression explains why a strong increase in visible light emission has been observed experimentally for the thickest target and not for the thinnest target. This is due to the fact that the thin target does not have a sufficient thickness to allow for the blast wave generation. Interestingly, we obtain the same steepening time of 16 ps in both regimes of thermal conduction for the set of parameters corresponding to the experiment. However, the compression waves steepening depth is slightly larger in the case of radiation thermal transport. Since the heat transport regime changes with depth, we estimate between 7 and 10 μm the value of the steepening depth.

We have demonstrated analytically that the target temperature gradients, due to the isochoric and instantaneous target heating by the laser-generated fast electrons, may be responsible for the generation of a blast wave in the thicker target. The blast wave breakout at the target rear side is in turn responsible for a rapid increase of the temperature at the target rear side. It thus increases the visible light emission from the target rear side that has been observed in the experiment. Let us estimate now the time t_{bo} needed for the blast wave to reach the target rear side. By estimating the energy released in the target, **responsible for the blast wave generation** as

$$E_0 = \int_0^\infty 2\pi r dr \int_0^{L_x} dx C_V T(x, t=0) \exp\left[-4 \ln 2 \left(\frac{r}{\Delta r}\right)^2\right] \approx 16 \text{ mJ} \quad (10.76)$$

with $\Delta r = 10 \mu\text{m}$ according to the hybrid simulation results (see $\log_{10}(T_e)$ in **Figure 9.13**) but assuming an axisymmetry for simplicity, we may estimate t_{bo} according to the Sedov law (10.14) with $\gamma = 5/3$. It reads

$$t_{bo} = t_s + \left(\frac{L_x - x_s}{\xi_0}\right)^{5/2} \left(\frac{\rho_0}{E_0}\right)^{1/2} \approx \begin{cases} 174 \text{ ps} & \text{if } n = 5/2 \\ 93 \text{ ps} & \text{if } n = 5/2 \end{cases}. \quad (10.77)$$

We thus obtain the same order of magnitude of a few hundreds of ps as observed in the experiment for the thicker target. The target rear side temperature of $\approx 10 \text{ eV}$ that drives a rarefaction wave may explain the discrepancy between the analytical estimate and the experiment as we are going to explain in the next section. For example, if we conduct the same estimate with $L_x = 19 \mu\text{m}$ instead of $L_x - x_s$, we obtain $t_{b0} = 514 \text{ ps}$.

10.2.2 Radiation Hydrodynamic Simulations

We have performed hydrodynamic simulations with the hydrodynamic code CHIC, which described the radiative transfer in the diffusive approximation and the visible light emission at $\lambda = 405 \text{ nm}$ from the target rear side. Opacities were computed according to the approximate method proposed by [Tsakiris and Eidmann, 1987]. The blast wave was generated with or without accounting for the radiation thermal conduction, confirming the results obtained in **section 10.2.1**. In order to account for the 3-dimensional effects of the blast wave propagation, the simulations are conducted in the 2D-

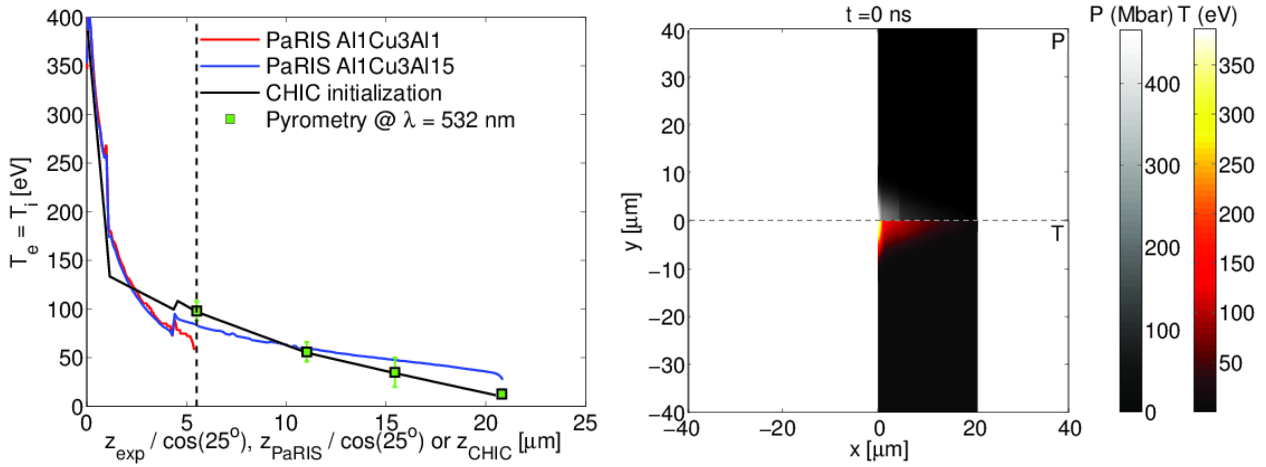


Figure 10.9: Comparison between the temperature profile obtained with the hybrid PIC simulation conducted by [Gremillet, 2012] and the initialization of the Radiation Hydrodynamic simulation for the thinner and thicker targets with the Copper traer layer at $z = 1 \mu\text{m}$.

axisymmetric geometry. The initial temperature profile was deduced from the graph in the left panel of **Figure 10.9** in agreement with the simulation results obtained by [Gremillet, 2012] with the hybrid PIC code PaRIS. The longitudinal profile of the fast electron transport energy deposition was obtained by projecting into the axisymmetric geometry of the hydrodynamic codethe energy deposition along the main direction of fast electron propagation in the M1 simulation, $L_x = L_z / \cos(25^\circ)$. The radial profile Δr_0 at $x = 0$ is the same as in Equation (10.76). However, in order to model the effects of the departure from axisymmetry of the target around the fast electron propagation direction, the FWHM was decreased with the target depth as $\Delta r = \Delta r_0 - 6(x \cos(25^\circ) / 19 \mu\text{m})$.

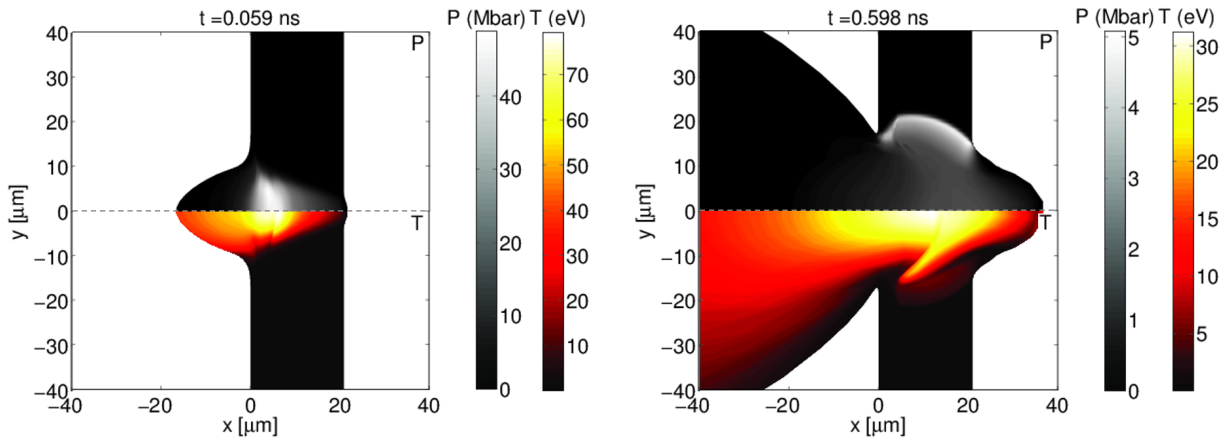


Figure 10.10: Distribution of the plasma temperature and pressure at $t = 60$ (Left panel) and 600 ps (Right panel).

The initial 2D map of the temperature and the pressure are plotted in the right panel of **Figure 10.9**. The pressure rises up to 400 Mbar over the first micron. Snapshots of the plasma density, temperature and pressure at $t = 39, 239$ ps, 499 and 1000 ps are illustrated in **Figure 10.10** for the thinner target and in **Figure 10.11** for the thicker target. We can see that the high temperature

10.2. BLAST WAVE GENERATION IN SOLID TARGETS BY THE QUASI-ISOTHERMIC HEATING BY LASER-GENERATED ELECTRON BEAM

and pressure produce a rapid plasma expansion in vacuum at the target boundaries. At the laser-irradiated side of the target, the temperature is much higher so that the expansion is stronger and a rapid decrease of the temperature corresponds well to our theoretical model (10.60). The gradients of the temperature and the pressure drive both a thermal wave and a compression wave inside the target. The thermal wave front is caught up by the compression wave for the thicker target, producing a blast wave. It is not the case for the thinner target, which simply explodes. A shock is formed at a depth of $x_s \approx 10 \mu\text{m}$ (in agreement with our theoretical predictions) at a time between 20 and 60 ps for the thicker target. It is not evident to distinguish between the expansion of the Copper tracer layer in the rear side Aluminum layer and the shock front at these times. The pressure at the shock front is ≈ 50 Mbar at 60 ps as illustrated in the left panel of **Figure 10.10** and decreases with time, as illustrated in **Figure 10.12**. The downstream plasma temperature behind it is more or less homogeneous and on the level of $T \approx 50$ eV. We can see that the plasma expansion at the target rear side drives a rarefaction wave that decreases strongly the blast wave strength on-axis. As a result, we deduce that the increase of visible light observed experimentally is mainly due to the blast wave front breakout far away from the fast electron propagation axis. It may also explain why using $L_x = 19 \mu\text{m}$ in (10.77) instead of $L_x - x_s$ allows for a better agreement with the experimental observations.

CHAPTER 10. APPLICATION TO THE GENERATION OF SHOCK WAVES BY FAST ELECTRON ENERGY DEPOSITION

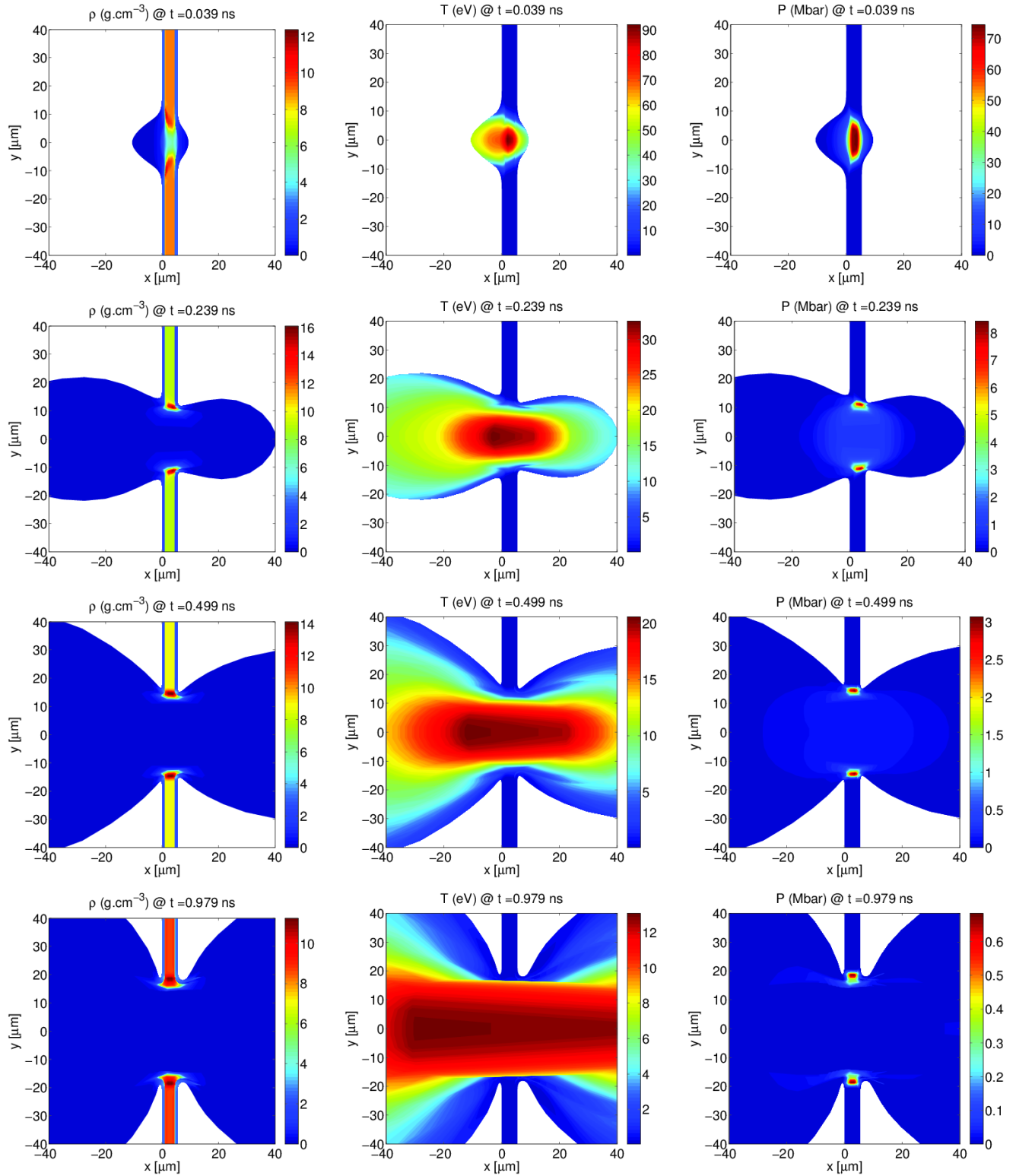


Figure 10.11: Distributions of the target density ρ (Left), temperature T (Middle) and pressure P (Right) from the CHIC simulation at $t = 39, 239, 499$ and 979 ps for the 5-microns thick target.

10.2. BLAST WAVE GENERATION IN SOLID TARGETS BY THE QUASI-ISOCHORIC HEATING BY LASER-GENERATED ELECTRON BEAM

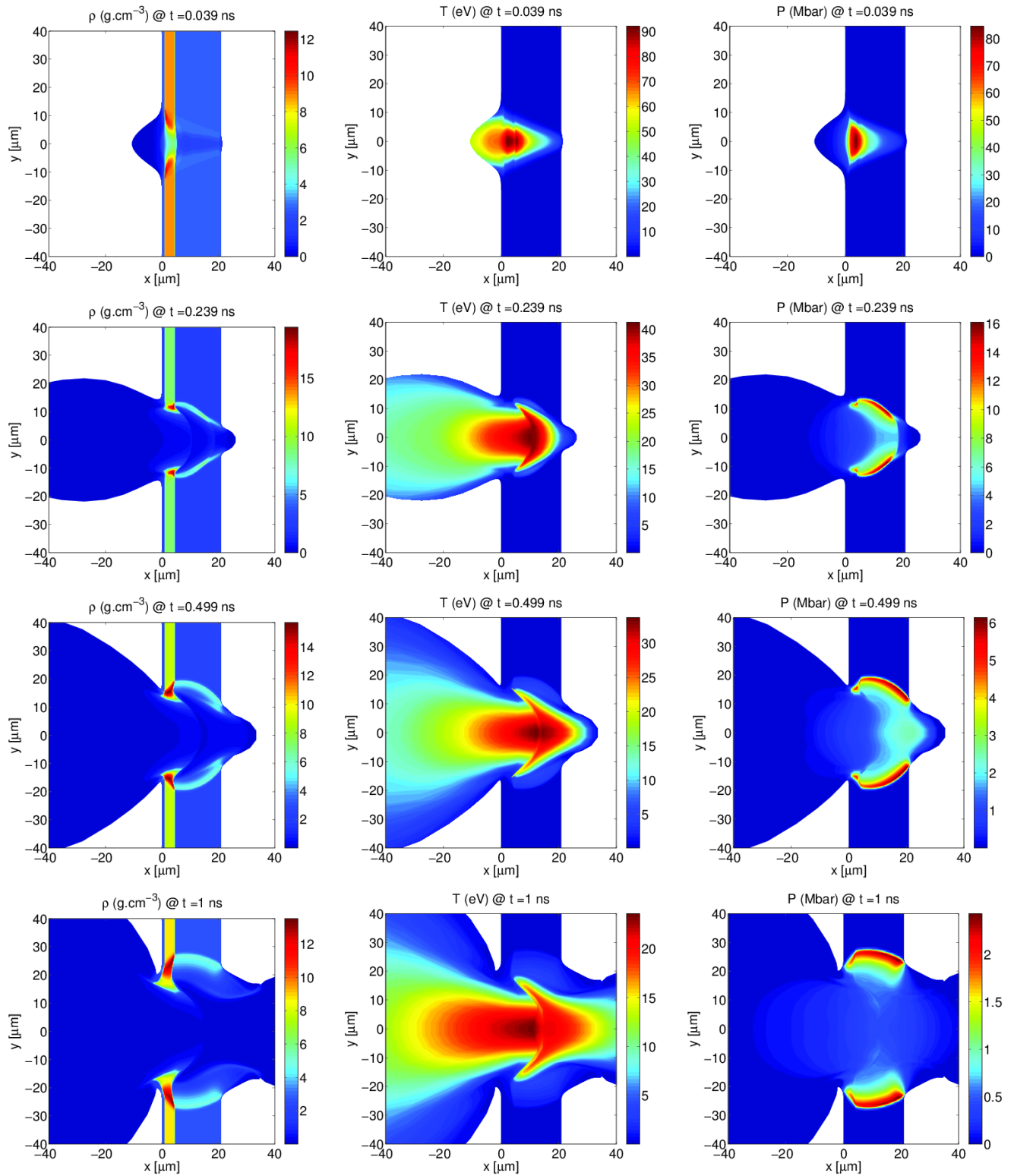


Figure 10.12: Distributions of the target density ρ (Left) and temperature T_e (Middle) and pressure P (Right) from the CHIC simulation at $t = 39, 239, 499$ and 1000 ps for the 19-microns thick target.

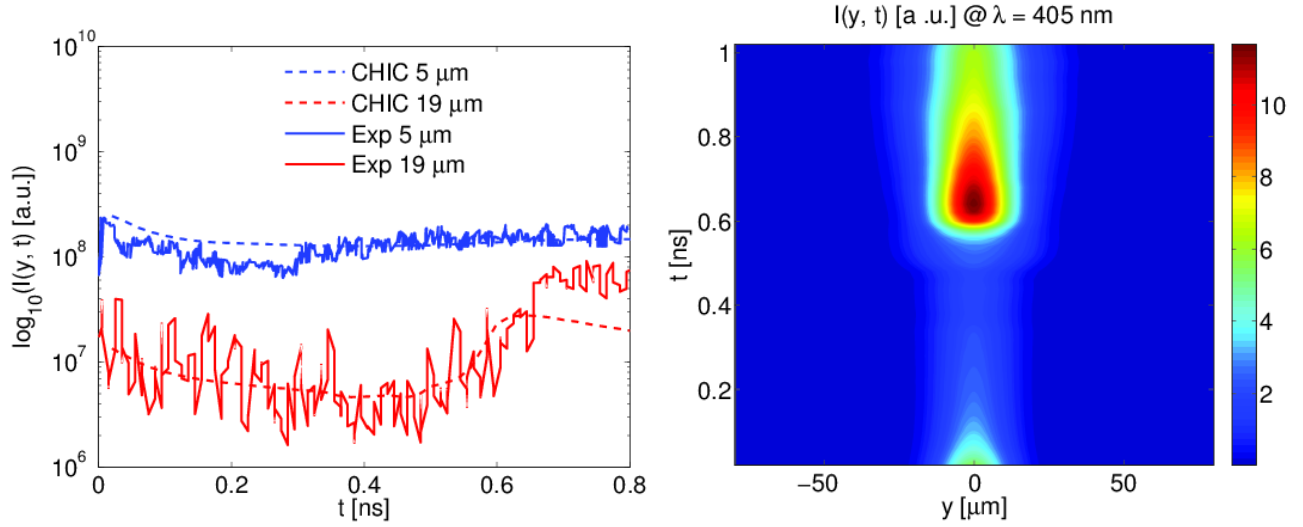


Figure 10.13: (Left panel) Comparison between the experimental signals and the simulation results for both targets. (Right panel) Streak camera-like images from the CHIC simulation for the thicker target.

The chronometry of the shock breakout at $L_z = 19 \mu\text{m}$ (the rear surface) is shown in the right panel of **Figure 10.13**. In order to make a comparison with the experimental SOP image as illustrated in **Figure 10.7 b**), we convolve the signal obtained numerically by the Gaussian function in time with a FWHM of 20 ps and in space with a FWHM of 20 μm . The resulting signal obtained in the hydrodynamic simulation is renormalized by the value of the maximum emission obtained experimentally for the thinner target. The signals summed over the y -axis are plotted versus time in the left panel of **Figure 10.13**. At $t_{bo} \approx 600$ ps, we observe a large increase by a factor ≈ 10 of the visible light emitted from the thicker target. It can be directly compared with the simulation result conducted for the thinner target where no such increase of temperature occurs.

As a conclusion, the hydrodynamic simulations confirm the explanation given in **section 9.2.1** concerning the generation of a blast wave in the thicker target due to the large temperature gradients induced by the laser energy deposition. When the the blast wave arrives at the target rear side, the temperature increases by a factor ≈ 6 and the emission of visible light is enhanced. No blast wave is generated in the thinner target due to the absence of hydrodynamic separation.

10.2. BLAST WAVE GENERATION IN SOLID TARGETS BY THE QUASI-ISOTHERMIC HEATING BY LASER-GENERATED ELECTRON BEAM

Chapter 11

Conclusion

” We need science education to produce scientists, but we need it equally to create literacy in the public. Man has a fundamental urge to comprehend the world about him, and science gives today the only world picture which we can consider as valid. It gives an understanding of the inside of the atom and of the whole universe, or the peculiar properties of the chemical substances and of the manner in which genes duplicate in biology. An educated layman can, of course, not contribute to science, but can enjoy and participate in many scientific discoveries which are constantly made. Such participation was quite common in the 19th century, but has unhappily declined. Literacy in science will enrich a person’s life.”

Hans Bethe

The goal of this PhD thesis was to develop a new reduced 3D-3V hybrid relativistic Vlasov-Fokker-Planck model, which must be as accurate and as time efficient as possible for the study of fast electron transport in solids and dense plasmas in the context of ICF. For this, we have linearized the Belyaev-Budker collision tensor by applying it to the study of laser-generated fast electron beam transport in solids or dense plasmas, assuming a small momentum transfer in a collision. The production of secondary electrons is neglected, assuming the residual energy of background electrons after a collision with a beam electron is smaller than the exchanged momentum of a consecutive collision with another beam electron. These assumptions allowed us to obtain a simpler Landau-like collision operator. Moreover, it allowed us to relate the angular scattering collision frequency by colliding with background particles (free electrons, bound electrons, screened free electrons/plasmons or ion nuclei) to the corresponding stopping powers according to an Einstein-like relation, similar to the one obtained for Brownian motion of particles. This allows us to obtain more accurate expressions compared to the angular scattering theories usually used, by retaining all terms in the Moller relativistic Coulomb logarithm instead of the relativistic generalization of Rutherford term, only. However, our model is limited to low density beams $n_b \ll n_e$ since the collisions of beam electrons with themselves and the production of secondary electrons are neglected.

The analysis of existing numerical methods for solving the Vlasov-Fokker-Planck equation (V-F-P) oriented our choice towards a hybrid and expanded "Vlasov-Fokker-Planck" method. In order to make numerical computations as fast as possible, we limited ourselves to the first two angular moments. The "hybrid" assumption consists in separating the beam electron population and the background electron population. Contrary to the widely used P1 approximation, also usually called the "diffusion approximation", our M1 model accounts for an arbitrary degree of anisotropy. The closure relation is deduced from the Minerbo maximum angular entropy criterion depending on the anisotropy vector. Such a closure is exact for fully isotropic local (in space and kinetic energy) angular distribution function and for fully anisotropic local angular distribution function. While the first order expansion reduces the information concerning the local angular distribution function, it provides a sufficient accuracy for the laser-generated fast electron beam transport. Such a closure is fully justified in the collisional limit. Besides, a comparison of the full kinetic and the M1 approach for the analysis of the resistive filamentation instability shows that our model describes the instability growth rate with an error of a few 10s of % in the case of collisionless fast electrons.

Our model assumes time scales greater than the electromagnetic neutralization time of the beam and that the beam is not modified during its electromagnetic neutralization. This is a strong assumption in the case of propagation through insulators since the ionization processes occur in this time scale, implying additional energy losses of the electron beam that are omitted here. In our hybrid model, the self-generated magnetic field verifies the diffusion equation with source terms depending on the resistivity gradients, curls of the beam current and temperature-density crossed gradients while the self-generated electric field is given by the quasi-static Ohm's law. Thus, we have neglected the

magnetization effects, the background electron viscosity, the collisional friction of the background electrons due to collisions with beam electrons, the displacement current in the Maxwell-Ampere equation (quasi-static approximation), the background electron inertia and we have considered the ideal gas expression for the equation of state of background electrons. These assumptions are justified in the case of laser-generated electron beam transport in dense targets. The self-generated electromagnetic fields depend on the electrical resistivity of the material and its spatial gradients, which depend on the electron and ion temperatures of the material. Thus, the electron temperature evolution needs to be described self-consistently according to the electron heat equation. Also, the background ion heating is described self-consistently according to a simplified heat equation. In our model, we neglect the ion motion and the ion thermal conductivity, considering times scales smaller than 10-100s of ps. We also proposed new expressions for the heat capacities, the electrical resistivity, the electron thermal conductivity and the electron-ion coupling factor, allowing to describe metals from the solid state at the room temperature ≈ 300 K through the liquid and Warm and Dense Matter (WDM) states to the hot plasma state with temperatures ≈ 10 keV. The collisions of background free electrons with d-band bound electrons are taken into account according to recent studies showing the importance of this relaxation process.

The numerical schemes used for the solution of the M1 equations have been described. The M1 equations are computed with second order explicit schemes except for the fast electron collisional slowing down, which is computed according to the 1st order downwind scheme. The advection terms are computed according to the HLL schemes allowing to ensure a positive number of electrons and a norm of the mean propagation vector less than 1. Implicit schemes have also been implemented in order relax the CFL condition in case of fast electron transport in a very dense plasma. The self-generated electromagnetic fields are computed according to 2nd order schemes except the self-generated magnetic diffusion that is resolved semi-implicitly thanks to 2nd order discretizations and a conjugated gradients algorithm. Finally, both heat equations are computed according to explicit numerical schemes. The numerical schemes used to solve the equations of the model have been validated thanks to a 2D-3V academic case of a monoenergetic and collimated fast electron beam propagating in a warm and dense hydrogen plasma. Also, it allowed to demonstrate the major features of the M1 approximation and to derive analytical expressions for the various quantities computed by the code such as the fast electrons penetration-depth-to-the-range ratio due to their angular scattering.

A realistic simulation of a laser-generated fast electron beam transport in a thin Aluminum target has been conducted and compared to a hybrid PIC simulation. It shows that the M1 approximation is sufficiently accurate to reproduce the hybrid PIC simulation results. We have applied the model to the study of the emission of $K\alpha$ photons. The refluxing of fast electrons is accounted for by imposing the specular reflection of fast electrons at the target-vacuum interfaces and adding a second population in the M1 equations. The first one describes the laser-generated electron population propagating in the laser direction, while the second one describes the counterpropagating fast electrons. The model

of calculation of the emission of $K\alpha$ photons is revised. The conclusion of this study are manifold. Firstly, we demonstrated that the numerical time step of the fast electron transport calculation may be comparable to the K-hole lifetime in the case of Aluminum and Copper targets. Therefore, we have implemented the K-shell hole dynamics in our model. Secondly, we demonstrated that the solid state corrections must be taken into account. In particular, the electron-ion temperature equilibration time and collisions of d-band with s-band electrons may affect the magnetic field distribution in the Copper target. Thirdly, we confirmed with a simple analytical model, the result obtained by [Sherlock et al., 2014] concerning the effect of the target electron inertia in the Ohm's law and the displacement current. Each laser-generated bunch of electrons, injected in the target at the laser frequency or twice the laser frequency excites a weak field of background electron plasma waves. Collisional damping of these plasma oscillations results in an additional target electron heating, which is not accounted for in hybrid models. Fourthly, we confirmed a strong contribution of refluxing electrons in the $K\alpha$ photon emission. The thinner the target is, the stronger the refluxing electrons contribute to the $K\alpha$ photon emission. Fifthly, we demonstrated significant differences between 2D and 3D simulations, especially in what concerns the self-generated magnetic fields, the size of the $K\alpha$ emission zone and the local density of emitted photons. In particular, the size of the $K\alpha$ emission zone is underestimated in our calculations as compared to the experimental data. We analyzed the assumptions of our model concerning the $K\alpha$ emission that may explain this discrepancy. The photon re-absorption may introduce an error of only $\approx 10\%$ in our computations. Another candidate is the contribution of the secondary electrons. However, it seems to me that the main critical assumption in our model is concerned with the specular reflection of fast electrons at the target-vacuum interfaces. A simple estimate of the magnetic field generated by the "fountain" effect indicates that these local fields may significantly deviate the refluxed fast electrons, thus enhancing the $K\alpha_1$ signal spotsize.

We coupled our reduced model for fast electron transport with a radiation hydrodynamic code and investigated the generation of strong shock by energetic electron beam. One example concerns the fast electron driven shock wave in dense plasmas in the shock ignition conditions. It confirms the theoretical estimates by [Gus'kov et al., 2012] and shows a possibility to achieve Gbar shock pressures in high density solid materials with the coupling efficiency up to 10%. In contrast, we disapprove another model developed by [Piriz et al., 2012] as the quasi-stationary assumption of that paper does not agree with our numerical simulations. Another example concerns the excitation of a blast wave with a femtosecond laser pulse. We have demonstrated analytically and numerically that a blast wave is generated due to the temperature gradients induced by the laser-generated fast electron energy deposition in the target tens of picoseconds after the end of the laser pulse. The analytical estimates and hydrodynamic simulations showed a good agreement with the experimental data.

The hybrid model of fast electron transport developed in this thesis has been already used in several other studies. More realistic simulations of the ablation pressure driven by an electron beam in the context of shock ignition by [Nicolai et al., 2014] show that an exponential electron energy

spectrum and a more realistic target density profiles may reduce the ablation pressure and preheat the target thus reducing the shock strength. The model have been applied by [Volpe et al., 2014] for studies of the multiple pulse scheme proposed by [Robinson et al., 2008] [Scott et al., 2012] to control the divergence of laser-generated electron beam in the context of fast ignition. It is shown that a sequence of three ps laser pulses allows to improve the collimation of the beam at least by a factor 2 compared to the double pulse scheme. Another series of simulations has been performed for the understanding of a laser-generated transport experiment reported by [Vaisseau, 2014]. In this experiment, a collimation of the fast electron beam in a planar Carbon target has been demonstrated and explained with hybrid numerical simulations. Finally, we conducted estimates of the emission of $K\alpha$ photons in future PETAL laser pulse experiments for radiography applications. Simulations with the M1 code have been compared with 3D Monte Carlo simulations conducted by [Boutoux, 2014] with the codes GEANT4 [Agostinelli et al., 2003] and PENELOPE [Sempau et al., 1997].

The perspectives of this work are manifold. Firstly, the wake field losses of modulated electron beams may be implemented in the hybrid code. This will allow to resolve the laser-generated electron bunches and to implement the CTR diagnostic in the code. The secondary electrons and the magnetic field generated at the target edges by the escaping electrons can also be taken into account. However, these physical effects require resolving very small spatial scales of the order of the fast electron Larmor radius and, therefore, represent an important investment in terms of vectorization and parallelization of codes. Also, it would be interesting to compute self-consistently the fast electron and $K\alpha$ photon transport in the target in order to account for opacity effects that are usually neglected. Concerning the application of fast electron transport to the generation of shocks in ICF, more realistic simulations must be conducted combining both laser-and-electron-generated shocks in a convergent geometry. Concerning fast ignition, the interaction of the petawatt laser pulse with the cone is still an intense field of research [Kemp et al., 2014]. The M1 model may be useful to perform a parametric study of the target density and temperature conditions and the properties of the ignitor electron beam. Different ways to collimate the fast electron beam can be also considered. For example, simulations at the ignition scale of the fast ignition of fusion pellets with an engineered cone-in-shell [Robinson and Schmitz, 2013] or with an external magnetic field [Fujioka S. et al., 2013] can be performed with plasma magnetization and three-dimensional effects taken into account.

Part IV

Résumé en Français

Chapter 12

Étude du transport d'Électrons Rapides pour la Fusion par Confinement Inertiel

"I do not know what I may appear to the world, but to myself I seem to have been only like a boy playing on the sea-shore, and diverting myself in now and then finding a smoother pebble or a prettier shell than ordinary, whilst the great ocean of truth lay all undiscovered before me."

Isaac Newton

Toutes les expériences et les observations menées jusqu'à aujourd'hui montrent qu'il existe une quantité universelle qui est conservée au cours de toutes évolutions et/ou transformations de la matière et des champs : l'Énergie. En d'autres termes, cela signifie que les lois de la Physique ne changent pas au cours du temps. Tous les développements de la physique moderne sont liés à ce principe de conservation de l'énergie et consiste en l'étude des différentes manières de convertir l'énergie existante sous une forme donnée en une autre forme d'énergie. Par exemple, les réactions nucléaires de fission de 0.01 g d'uranium fournissent approximativement 1 kWh (1 kWh = 3.6 MJ) d'énergie thermique dans une centrale nucléaire. La même quantité d'énergie thermique peut être obtenue par combustion d'approximativement 100 g de pétrole, de charbon ou de gaz (1 million de tonnes de pétrole ou équivalent pétrole produit environ 4,4 TWh d'électricité dans une centrale électrique moderne), par condensation de 1,6 kg de vapeur d'eau ou en capturant le rayonnement solaire sur un panneau d'une surface de 1 m² pendant une heure (l'intensité de la lumière du soleil sur la Terre est d'environ 0,1 W/cm² lors d'une journée ensoleillée). 1 kWh représente aussi l'énergie potentielle gravitationnelle de 3 tonnes d'eau chutant de plus de 100 m d'altitude dans une centrale hydroélectrique, l'énergie cinétique de 20000 m³ d'air se déplaçant à une vitesse de 60 km/h poussant une pale d'éolienne ou encore l'énergie nécessaire pour un être humain de 65 kg pour grimper jusqu'à un sommet de montagne situé à une altitude de 3000 m.

Depuis le XIXe siècle, la croissance exponentielle des connaissances technologiques et scientifiques, rendue possible grâce à ce concept de conservation d'énergie, a conduit à une incroyable amélioration de la qualité de vie de l'Homme sur Terre ainsi qu'une augmentation fulgurante de la population mondiale. A titre d'exemple, il est frappant de constater la forte corrélation qu'il existe entre le produit national brut d'un pays et la consommation en énergie de ses habitants à l'heure actuelle. Cependant, la combustion de ressources fossiles tels que le pétrole, le gaz et le charbon qui est toujours majoritairement utilisée aujourd'hui afin de produire de l'énergie. Ils représentent à eux seuls environ 90 % des ressources en énergie consommées dans le monde. Le nucléaire et l'énergie hydroélectrique ne représentent que seulement 6 % de la consommation mondiale en énergie. Même si d'autres énergies renouvelables tels que l'éolien, la combustion de biomasse ou de déchets, l'énergie solaire ou encore les centrales géothermiques sont de plus en plus utilisés grâce aux subventions gouvernementales, leurs contributions restent toutefois négligeables. Comme toute fonction continue positive partant de zéro et arrivant à zéro, on peut montrer que l'extraction de chaque ressource naturelle terrestre atteindra tôt ou tard un maximum à un moment donné de notre Histoire, puis diminuera jusqu'à ce que la ressource ait totalement disparu de la surface de la Terre. On estime ainsi que nous disposons de 50 ans de réserves en gaz et en pétrole ainsi que d'environ 100 ans de réserves en charbon avant d'avoir consommé tout ce qu'il en reste sur Terre. Ces évaluations sont probablement sous-estimées pour des raisons financières. Cependant, elles sont fondées sur des données datant de 2013 concernant le nombre d'être humains sur Terre alors que l'on s'attend à être plus de 11 milliards en 2100 (par rapport à environ 7,1 milliards en 2013). En outre, cette forte croissance démographique devrait se produire dans les pays où les demandes en ressources naturelles seront les plus élevés. On comprend donc facilement que, si nous

ne trouvons pas d'alternatives, le coût financier de notre consommation en charbon, gaz ou pétrole sera en perpétuelle augmentation jusqu'à ce que chacune de ces ressources disparaissent. Même si l'utilisation de centrales nucléaires reste à l'heure actuelle la solution la plus efficace et la moins nocive pour l'environnement, on peut s'attendre à ce que la politique des gouvernements tende à limiter leur utilisation en raison de la grande durée de vie des déchets radioactifs qu'elles produisent ainsi que l'opposition croissante du public à son utilisation en raison des catastrophes telles que Fukushima en 2011, Tchernobyl en 1986 ou encore Three Mile Island en 1979.

Depuis 1965, l'émission de dioxyde de carbone dans notre atmosphère, connue pour être l'un des principaux facteurs responsables de l'effet de serre et donc de l'augmentation de la température moyenne sur Terre, est passé d'environ 3500 kg/an/habitant à environ 5000 kg/an/habitant aujourd'hui. Par conséquent, même si l'hydroélectricité reste le moyen le plus efficace pour produire de l'énergie parmi les méthodes les plus écologiques, son utilisation sera également affectée par les sécheresses induites par cette augmentation de température. Par exemple, l'Europe devrait perdre entre 20 et 30 % de ces précipitations d'ici à 2100 conduisant ainsi à une efficacité de production hydroélectrique beaucoup plus faible (La majorité des centrales hydroélectriques européennes ne fonctionnent déjà pas très bien en été). Enfin, d'autres 'énergies renouvelables', comme les centrales éoliennes ou les panneaux photovoltaïques sont insuffisantes pour satisfaire la demande mondiale et en particulier la demande industrielle. En conclusion, l'humanité va faire face au XXI^e siècle à d'importantes pénuries d'énergie si nous ne trouvons pas d'alternatives pour la production d'énergie (ou si nous ne réduisons pas notre consommation; ce qui suppose une prise de conscience collective pour contrôler l'insatiable désir de consommation imposé par nos sociétés pour des raisons économiques).

Dans les années 1950, l'idée de contrôler la combustion thermonucléaire d'atomes légers pour produire de l'énergie est née peu de temps après le développement par H. Bethe d'un modèle théorique de réactions de fusion permettant d'expliquer la conversion de l'énergie de liaison nucléaire en chaleur dans les Étoiles. Dès lors, "reproduire l'énergie des Étoiles sur Terre" est devenu le rêve de nombreux physiciens et semble être aujourd'hui une solution prometteuse pour résoudre le problème de la production et de la consommation de l'énergie dans le monde au XXI^e siècle. Cependant, contrairement à la force gravitationnelle et à la force électromagnétique qui agissent sur des distances potentiellement infinies, les deux autres forces nucléaires forte et faible agissent sur des distances subatomiques minuscules et sont beaucoup plus difficiles d'accès avec la technologie actuelle. Selon la théorie de l'Électromagnétisme, une énergie d'environ 1 MeV ($1 \text{ eV} = 1.6022 \cdot 10^{-19} \text{ J}$) est nécessaire afin de vaincre la barrière d'énergie Coulombienne d'un atome afin de le faire fusionner avec un autre. En réalité, une énergie d'environ 10 keV est suffisante grâce à l'effet tunnel quantique découvert par G. Gamow. La seule manière possible de produire de l'énergie grâce à de telles réactions de fusion d'atomes légers consiste à créer un plasma thermonucléaire ayant des conditions de température et de densité proche de celles de certaines Étoiles. Cela permettrait en effet d'atteindre des taux de réaction de fusion nucléaire suffisamment élevés et donc des gains de conversion d'énergie élevés pour

la production d'électricité. Cependant, en plus de ces contraintes de températures et de densités, la réaction de fusion nucléaire choisie doit être exothermique. Pour cela, il faut donc que la réaction consomme des noyaux atomiques les plus légers possibles afin d'avoir à vaincre une barrière Coulombienne moins énergétique. Aussi, la section efficace de la réaction de fusion (ou probabilité de réaction de fusion) doit être la plus grande possible. Cela implique par conséquent une réaction nucléaire consommant seulement deux noyaux, conservant le nombre de protons et de neutrons afin de limiter la force nucléaire faible et, enfin, produisant au moins un neutron en plus du noyau plus lourd produit afin de chauffer le liquide caloporteur circulant dans la couverture de la chambre de la centrale, permettant ainsi de chauffer de l'eau pour la production d'électricité à l'aide d'une turbine. 80 réactions de fusion nucléaire satisfont à ces critères. Cependant, la réaction la plus probable compte tenu de la technologie actuelle est la réaction de fusion des deux isotopes de l'atome d'Hydrogène



en raison de l'existence d'un état intermédiaire résonant lors de la réaction. D'un point de vue pratique concernant la production d'énergie électrique, il existe sur Terre une quantité quasi-infinie de Deutérium (D) avec une concentration de 33 g par tonne d'eau de mer; C'est pour cette raison que la production d'énergie par fusion d'un plasma de DT s'appelle l'*énergie bleue*. Le Tritium (T) peut être produit directement dans la centrale à l'aide d'une seconde réaction de fusion entre les neutrons (n), s'échappant du plasma thermonucléaire, et des noyaux de Lithium (Li), eux aussi très abondants sur Terre, préalablement placés dans la couverture de la chambre de la centrale. Ainsi, contrairement aux centrales nucléaires de fission préexistantes, qui utilisent des ressources limitées comme l'Uranium, le Plutonium ou le Thorium, l'*énergie bleue* ne fait face à aucun problème de limitation de ressources. En outre, la fusion d'un plasma thermonucléaire de DT ne présente aucun risque d'emballement des réactions en chaîne et ne produit que des déchets radioactifs à courte durée de vie (moins de 10 ans). En conclusion, une éventuelle centrale à fusion thermonucléaire aurait donc tous les avantages des centrales à fission nucléaire sans ses inconvénients, c'est-à-dire, sans polluer l'environnement, sans provoquer d'éventuelles catastrophes nucléaires ou encore sans problèmes liés à la limitation des ressources terrestres. Seule la radioactivation éventuelle de matériaux environnant peut poser problème.

Du fait du mouvement chaotique des particules chargées portées à de grandes températures $T \approx 10$ keV ($1 \text{ eV} = 11600 \text{ K}$), un plasma thermonucléaire tend naturellement à s'expandre et il est difficile de le maintenir confiné pendant le temps nécessaire τ_c avec une densité suffisamment élevée n_e . En effet, d'après le critère de J. Lawson, la température T ainsi que le temps de confinement τ_c d'un plasma thermonucléaire sont reliés par la densité n_e du plasma si on veut pouvoir extirper du plasma plus d'énergie de fusion que d'énergie investie pour le créer et le maintenir confiné. Dans les Étoiles, le confinement du plasma est accompli naturellement par l'attraction gravitationnelle de l'Étoile sur elle-même. Par exemple, la masse du Soleil d'environ 10^{30} kg est suffisamment élevée pour attirer et

compresser le plasma stellaire à des densités pouvant aller jusqu'à $n_e \approx 10^{32} / \text{cm}^3$ et des températures de l'ordre de $T \approx 10$ keV pendant toute sa durée de vie d'à peu près $\tau_c \approx 10$ milliards d'années. Du fait que, dans un plasma, les particules sont chargées électriquement, les physiciens soviétiques I. Tamm et A. Sakharov ont proposé dans les années 1950 l'idée d'utiliser de puissants champs magnétiques afin de confiner le plasma thermonucléaire. Ce dispositif expérimental appelé *tokamak* se présente sous la forme d'un tore. Il permet de confiner le plasma thermonucléaire grâce à un champ magnétique toroïdal produit par des bobines magnétiques supraconductrices entourant le tore alors qu'un autre champ magnétique poloïdal est créé par un courant électrique à l'intérieur du tore permettant ainsi le chauffage du plasma. Le projet internationale ITER planifie la construction d'un tel dispositif sur le site du CEA (Commissariat à l'Énergie Atomique et aux Énergies Alternatives) à Cadarache, en France, d'ici quelques années.

La Fusion par Confinement Inertiel (FCI) est un autre moyen de produire et contrôler de l'énergie de fusion thermonucléaire. Suivant cette approche, les conditions de densités extrêmes (jusqu'à 1000 g/cm^3) sont obtenues grâce à la compression rapide d'une capsule sphérique solide de dimension millimétrique remplie d'un mélange de D et de T gazeux et cryogénisé. La conversion de l'énergie cinétique de l'implosion en énergie interne à la fin de la phase de compression entraîne le chauffage de la zone centrale, communément appelé "point chaud", jusqu'à une température $T > 5$ keV. Les réactions de fusion du combustible de DT sont ainsi initiés en accord avec le critère de J. Lawson. Contrairement à la Fusion par Confinement Magnétique (FCM), le plasma thermonucléaire est ici confiné par l'inertie de sa propre masse et non grâce à des champs magnétiques extérieurs. En outre, l'implosion des cibles ne dure que quelques nanosecondes. Par conséquent, cette approche entraîne des difficultés technologiques supplémentaires dues au taux de répétition du processus à 10 Hz, imposé par la production continue d'électricité. Cependant, en atteignant des densités n_e si élevées pendant un temps de confinement τ_c si bref, l'approche FCI est beaucoup plus efficace en termes de gain de production par rapport à la FCM qui, elle, vise à fusionner les isotopes de D et T à de faibles densités n_e mais sur des temps de confinement τ_c beaucoup plus longs. Les schémas FCI conventionnels impliquent l'allumage d'un point chaud central de manière isobarique où le combustible de DT atteint une température de $T \approx 7$ keV et une densité surfacique ρR d' environ $0,25 \text{ g/cm}^2$, où R est le rayon de la coquille solide, pendant un temps de confinement τ_c d'environ 40 ps. Afin d'atteindre ces conditions extrêmes, de nombreuses impulsions laser nanosecondes représentant une énergie totale de $E_L \approx 1$ MJ peuvent être utilisées afin d'irradier uniformément la coquille solide renfermant le combustible de DT. L'irradiation de la coquille peut se faire directement avec les impulsions laser (Attaque directe) ou par des rayons X produits par interaction laser-matière (Attaque indirecte). Dans les deux cas, les couches externes du solide irradié sont ablatés par la lumière. Cette ablation de matière entraîne ensuite l'implosion de la cible par *effet fusée*, i.e. par conservation de la quantité de mouvement. L'évolution temporelle des impulsions laser de Nuckolls-Kidder est choisie de telle sorte que la pression d'ablation de la coquille génère une onde de choc suivie d'une succession continue d'ondes de compression sphériques convergentes dans la cible. Au moment précis où les ondes de

compression arrivent au même instant au niveau de la surface interne de la coquille, une onde de choc est transmise dans le DT gazeux, tandis qu'une onde de raréfaction est réfléchi dans la coquille. Lorsque cette dernière arrive à la surface d'ablation, la coquille est mise en vol et subit une forte accélération centripète. Du fait de sa symétrie sphérique, la capsule implose et le combustible de DT est alors comprimé à la densité souhaitée. La conversion de l'énergie cinétique de l'implosion en énergie interne à la fin de la phase de compression entraîne la création d'un point chaud central isobare à la température voulue. Des réactions de fusion auto-entretenues entre les atomes de D et de T sont alors initiées, générant une onde de combustion thermonucléaire sphérique divergente suivie d'une détonation, qui brûle la partie dense du combustible dans la coquille. Le temps de confinement τ_{c} correspond à la durée de vie du point chaud centrale juste avant son explosion hydrodynamique. Les processus de compression et de chauffage de la cible imposent de nombreuses contraintes sur la rugosité et la symétrie sphérique des cibles ainsi que sur l'uniformité de l'irradiation par les impulsions laser pour l'attaque directe ou du rayonnement X pour l'attaque indirecte.

Ces contraintes sont multifactorielles. Tout d'abord, les instabilités paramétriques liées à l'interaction des impulsions lasers avec le plasma en expansion, appelé "couronne", peuvent réduire l'efficacité de conversion de l'énergie laser en pression d'ablation de la coquille ainsi qu'entraîner des inhomogénéités de la surface d'ablation. D'autres part, la génération d'électrons rapides inhérent à l'interaction laser-plasma dans la couronne entraîne un préchauffage de la cible. Cela conduit à l'augmentation de l'entropie de cette dernière et limite par conséquent la bonne compression du combustible. Enfin, du fait d'une vitesse d'implosion élevée et de la non-uniformité de la surface d'ablation, les instabilités hydrodynamiques peuvent briser la coquille pendant son implosion et entraîner le mélange du combustible chaud avec le combustible froid. Afin de relaxer ces contraintes liées à la compression et au chauffage simultanés du combustible, M. Tabak a proposé en 1994 de séparer la phase de compression de la phase de chauffage. Dans ce schéma qualifié d'allumage rapide, la coquille est implosée et le combustible est densifié de manière analogue aux schémas conventionnels de FCI. Cependant, l'allumage des réactions de fusion est amorcé dans un second temps en focalisant une impulsion laser relativiste sur la cible. L'impulsion laser relativiste génère alors un faisceau d'électrons rapides qui va déposer son énergie en profondeur dans la partie plus dense du combustible juste à la fin de la phase de compression, créant ainsi un point chaud latéral isochore. La densité centrale requise est donc beaucoup plus faible (300 g/cm^3 au lieu de 1000 g/cm^3) que dans les schémas classiques d'allumage et les contraintes sur la convergence de l'onde de choc, la vitesse et la symétrie de l'implosion sont réduits. Notamment, la vitesse d'implosion étant plus faible, les contraintes imposées sur la cible et les impulsions laser vis-à-vis des instabilités hydrodynamiques se retrouvent amoindries et le risque de briser la coquille lors de l'implosion est réduit. Aussi, un faisceau d'électrons relativistes accéléré par laser peut fournir un chauffage beaucoup plus efficace de la matière dense et des gains beaucoup plus élevés peuvent être obtenus comparé aux scénarios classiques. En outre, la phase de compression a besoin de beaucoup moins d'énergie (200 - 300 kJ) comparée aux schémas conventionnels et le coût d'une éventuelle centrale à fusion thermonucléaire par allumage rapide serait donc

plus faible. Toutefois, l'allumage rapide présente toujours de nombreux problèmes à résoudre. En raison du fait que l'impulsion laser ultra-intense, utilisée pour générer le faisceau d'électrons, ne peut pas pénétrer les zones de la couronne ayant une densité supérieure à la densité critique du plasma, il est difficile de focaliser le faisceau d'électrons rapides d'allumage sur une toute petite zone de la partie dense du combustible. De plus, il a été démontré expérimentalement et numériquement que les faisceaux d'électrons relativistes accélérés par laser présentent nécessairement un angle de divergence important. Depuis, de nombreuses méthodes ont alors été proposées pour tenter de collimater le faisceaux d'électrons d'allumage. Cependant, de nombreuses expériences et simulations numériques sont toujours nécessaires afin de pouvoir les confirmer et les valider.

Plus récemment en 2006, une autre méthode séparant les phases de compression et d'allumage du combustible de DT a été proposé par R. Betti. Il s'agit du schéma d'allumage par choc qui consiste à allumer un point chaud central à la fin de la phase de compression en générant un fort choc à l'aide d'une pression d'ablation supérieure à 300 Mbar. En convergeant ensuite vers le centre de la coquille en implosion, la force du choc va en augmentant. Lorsque ce dernier entre en collision avec sa propre réflexion au centre de la coquille, le point chaud central est boosté, libérant ainsi l'énergie de fusion thermonucléaire. Pour ce schéma d'allumage, des coquilles cryogéniques de grande masses ainsi qu'une faible vitesse d'implosion et un faible adiabat (quantité physique mesurant l'entropie de la cible) peuvent aussi être utilisés. Par conséquent, le combustible de DT atteint de grandes densités surfaciques et permet d'atteindre l'allumage des réactions de fusion avec une énergie inférieure à celle de l'allumage central isobarique conventionnel. Le choc d'allumage peut être lancé par une puissance laser compatible avec les lasers existants pour l'étude de la FCI comme le NIF (National Ignition Facility) du LLNL (Lawrence Livermore National Laboratory) aux Etats-Unis d'Amérique ou le LMJ (Laser MegaJoule) du CEA-Cesta près de Bordeaux, en France. Aussi, le gain thermonucléaire obtenu par allumage par choc peut être significativement plus grand que dans le cas isobare classique pour une énergie laser donnée. Enfin, vu qu'il implique des implosions de cible à faible vitesse de même que pour l'allumage rapide, le schéma d'allumage par choc est aussi plus robuste en ce qui concerne les instabilités hydrodynamiques au cours de l'accélération de la coquille. La puissance laser nécessaire pour générer une pression d'ablation de 300 Mbar dépend du matériau de la coquille et de ses dimensions. Néanmoins, elle peut être estimée à 120-200 TW. Cela représente une puissance laser un ordre de grandeur inférieure à la puissance requise par l'impulsion laser d'allumage rapide. Ainsi, contrairement à l'allumage rapide, l'allumage par choc présente l'avantage qu'il ne nécessite pas d'installation laser de ultra forte puissance. Cependant, le couplage de l'impulsion laser d'allumage avec la cible en implosion présente plusieurs problèmes toujours non résolus tels que les instabilités paramétriques dans la couronne, les instabilités hydrodynamiques de la coquille et le rôle des électrons rapides accélérés dans la couronne sur l'ablation de la coquille dans ce régime particulier d'interaction laser-plasma.

Cette thèse s'inscrit directement dans ce contexte. Elle a en effet consisté à développer un nouveau

modèle hybride 3D-3V de type "Vlasov-Fokker-Planck" pour le transport d'électrons rapides accélérés par laser. Afin de pouvoir étudier le transport de ces électrons dans des solides ou des plasmas denses du même type que ceux de la FCI, le modèle devait être à la fois le plus précis et le plus économe en temps de calcul possible. Pour cela, nous avons donc tout d'abord linéarisé le tenseur de collisions relativistes de Belyaev-Budker en l'appliquant à l'étude du transport de faisceaux d'électrons relativistes accélérés par laser dans des solides ou des plasmas denses. Dans ce cas, le transfert de quantité de mouvement est supposé faible lors de chaque collision avec une particule cible du milieu dans lequel se propagent le faisceau. De plus, la production d'électrons secondaires est négligée, supposant que l'énergie résiduelle des électrons cibles après une collision avec un électron du faisceau est plus petite que l'énergie échangé lors d'une collision consécutive avec un autre électron du faisceau. Ces hypothèses nous ont permis d'obtenir un opérateur de collision relativiste plus simple et du même type que celui obtenu par L. Landau dans le cas non relativiste. En outre, cela nous a permis de relier la fréquence de diffusion angulaire des électrons du faisceau due à leurs collisions avec des électrons libres, des électrons liés, des électrons libres écrantés (plasmons) ou des noyaux atomiques du milieu dans lequel se propage le faisceau avec les pouvoirs d'arrêts correspondants selon une formule de type de celle obtenue par A. Einstein lors de son étude du mouvement Brownien des particules. Ainsi, en conservant tous les termes du logarithme Coulombien relativiste que l'on a déduit du pouvoir d'arrêt de C. Möller, nous avons pu obtenir une équation cinétique relativiste plus précise que celle utilisée généralement ne prenant en compte que le logarithme Coulombien de E. Rutherford. Cependant, notre modèle est limité à des faisceaux de basse densité et nous avons négligé les collisions des électrons du faisceau entre eux.

L'analyse des méthodes numériques existantes pour résoudre l'équation Vlasov-Fokker-Planck (VFP) obtenue a orienté notre choix vers un modèle de transport d'électrons relativistes hybride basé sur la décomposition de la fonction de distribution en produits scalaires-tensoriels. Afin d'être en mesure de résoudre numériquement les équations le plus rapidement possible, nous limitons cette expansion angulaire au 1er ordre. Nous avons donc déduit les deux premières équations de la hiérarchie des modèles aux moments angulaires MN en intégrant l'équation VFP sur la sphère unité de l'espace des quantités de mouvement des électrons du faisceau. Contrairement à la décomposition strictement équivalente de la fonction de distribution sur les harmoniques sphériques limitée au même ordre dans le même espace, la densité du faisceau ainsi que sa densité de courant sont directement liées aux moments angulaires de la fonction de distribution, solutions des équations M1. L'hypothèse "hybride" consiste à ne considérer dans l'équation cinétique uniquement la population des électrons du faisceau en introduisant une valeur d'énergie cinétique seuil $\varepsilon \geq \varepsilon_{\min}$ afin de les distinguer avec la population d'électrons du milieu dans lequel se propage le faisceau $\varepsilon < \varepsilon_{\min}$. Contrairement à l'approximation P1 couramment utilisée, aussi appelé "approximation de la diffusion", notre modèle M1 permet de considérer des faisceaux se propageant de manière totalement anisotrope. En effet, la relation de fermeture utilisée est obtenue en appliquant le critère de maximisation de l'entropie angulaire proposé par G. N. Minerbo dans le cadre de la théorie du transport radiatif. Une telle fermeture est exacte pour des distributions angulaires isotropes locales, i.e. à une position de l'espace, à un instant et pour une

énergie cinétique des électrons donnés, ainsi que pour des distributions angulaires locales totalement anisotropes. Un paramètre dépendant de la direction moyenne locale de propagation des électrons du faisceau permet de relier ces deux régimes extrêmes. De manière évidente, le fait d'arrêter l'expansion de la fonction de distribution du faisceau d'électrons à l'ordre 1 entraîne nécessairement une perte d'informations concernant la distribution angulaire locale des électrons du faisceau. Par conséquent, nous avons dérivé l'équation d'évolution de l'entropie angulaire du faisceau afin d'étudier le critère que nous avons choisi. Notre analyse montre que le critère de G. N. Minerbo est justifié pour le transport de faisceaux d'électrons rapides accélérés par laser en raison de la diffusion angulaire des électrons du faisceau et de la propagation anisotrope des électrons les plus énergétiques. En outre, l'étude menée sur l'instabilité faisceau-plasma de filamentation résistive, pour laquelle il n'y a aucune raison de maximiser localement l'entropie angulaire, montre que notre modèle décrit le taux de croissance de l'instabilité avec une erreur de l'ordre de 10 particulier d'un faisceau d'électrons monoénergétique.

Dans notre modèle, nous considérons des échelles de temps grandes devant le temps caractéristique de la neutralisation électromagnétique du faisceau d'électrons. Par conséquent, de même que les autres modèles hybrides, notre modèle suppose que le faisceau ne subit pas de modifications importantes durant sa neutralisation en charge et en courant électriques. Ceci est une hypothèse grossière dans le cas particulier du transport de faisceau d'électrons accélérés par laser dans des matériaux isolants du fait des processus d'ionisation qui se produisent à cette échelle de temps et qui impliquent une perte en énergie supplémentaire pour le faisceau. Dans notre modèle hybride, le champ magnétique auto-généré par le faisceau vérifie l'équation de diffusion couramment utilisée avec les différents termes sources dus aux gradients de résistivité électrique du milieu, au rotationnel du courant électrique du faisceau ainsi qu'aux gradients croisés de température et de densité des électrons du milieu tandis que le champ électrique auto-généré par le faisceau est donné par la loi d'Ohm quasi-statique classique. Ainsi, nous avons négligé l'aimantation du milieu, la viscosité des électrons du milieu, leur friction sur les électrons du faisceau, le courant de déplacement dans l'équation de Maxwell-Ampère (approximation quasi-statique), l'inertie des électrons du milieu et nous avons considéré l'expression de la pression d'un gaz parfait d'électrons. Ces hypothèses sont justifiées dans le cas du transport de faisceaux d'électrons accélérés par laser dans des cibles denses ainsi que dans le cas où la fréquence cyclotron des électrons du milieu est négligeable devant leur fréquence de collisions. Les champs électromagnétiques auto-générés dépendent donc de la résistivité électrique du matériau dans lequel se propage le faisceau ainsi que de ses gradients spatiaux. Ces derniers dépendent fortement de la température des électrons et du réseau cristallin/ions du matériau. Par conséquent, l'évolution des températures électronique et du réseau/ions du matériau sont aussi décrites de manière auto-cohérente suivant les équations bien connues de la chaleur. Dans notre modèle, nous négligeons le mouvement des ions et la conductivité thermique ionique, considérant des échelles de temps plus petites que la dizaine ou la centaine de picosecondes. Par ailleurs, les équations de la chaleur résolues sont en accord avec les hypothèses faites à l'égard des champs électromagnétiques auto-générés (pas de viscosités, aucune aimantation, pas d'inertie et pas de friction sur les électrons du faisceau), sauf en ce qui concerne les dérivées temporelles

de la température dans les équations de la chaleur qui, ici, ne sont pas négligées. Nous avons également proposé de nouvelles expressions pour les capacités thermiques, la résistivité électrique, la conductivité thermique électronique ainsi que le facteur de couplage des températures électronique et ionique, dans le cas particulier des métaux. En effet, sous l'action de son chauffage par le faisceau d'électrons accélérés par l'impulsion laser, un métal initialement à l'état solide à température ambiante (≈ 300 K) devient rapidement liquide avant de devenir un plasma avec des températures pouvant aller jusqu'à plusieurs keV. Les collisions des électrons du matériau avec les vibrations (phonons) et les électrons libres du réseau cristallin ainsi qu'avec les électrons liés aux atomes sont pris en compte, en accord avec des études récentes montrant l'importance de ces processus de relaxation.

Les schémas numériques utilisés pour la résolution des équations M1 sont décrits en détail. Elles sont résolues avec des schémas explicites du second ordre, sauf pour le terme d'advection en énergie dû au ralentissement collisionnel des électrons rapides qui est résolu par le schéma d'advection décentré d'ordre 1. Concernant les termes d'advection spatiale et d'advection en énergie dûs au champ électrique auto-généré, nous avons utilisés les schémas HLL (A. Harten, P. Lax et B. Van Leer) permettant d'assurer un nombre positif d'électrons et une norme du vecteur d'anisotropie (vecteur associé à la direction moyenne locale de propagation des électrons) inférieure à l'unité. Des schémas implicites ont également été développés pour les effets collisionnels afin de diminuer la contrainte sur le pas de temps numérique imposée par la condition CFL (R. Courant, K. Friedrich et H. Lewy) dans le cas d'un transport de faisceau d'électrons rapides dans des plasmas très denses. Les équations d'évolution des champs électromagnétiques auto-générés sont résolues à l'aide de schémas explicites du second ordre sauf en ce qui concerne le terme de diffusion magnétique qui est résolu semi-implicitement grâce à une discrétisation de l'opérateur de diffusion au second ordre ainsi qu'à l'inversion de la matrice de diffusion obtenue par la méthode des gradients conjugués. Enfin, les deux équations de la chaleur sont discrétisées à l'aide de schémas numériques explicites du second ordre. L'ensemble de ces schémas numériques utilisés pour résoudre les équations du modèle ont été validées grâce à leur application à un cas d'école de transport de faisceau d'électrons rapides mono énergétique et collimaté dans un plasma dense et tiède d'Hydrogène pour lequel nous avons pu déterminer des solutions analytiques afin de les comparer aux différentes quantités physiques calculées par le code. Par exemple, l'expression analytique de la distance de pénétration d'un électron relativiste dans un plasma dense et tiède d'Hydrogène que nous avons trouvé reproduit bien les résultats de la simulation.

Dans un second temps, une simulation plus réaliste de transport d'électrons rapides accélérés par laser dans une cible mince d'aluminium a été comparée à une simulation PIC (Particle-In-Cell) hybride. Elle montre que le modèle M1 pour le transport de faisceaux d'électrons relativistes est suffisamment précis pour reproduire les résultats de la simulation PIC hybride. Une fois le modèle théorique et numérique validé, nous avons pu appliqué le modèle à l'étude de l'émission de photons $K\alpha$ induit par le transport d'électrons relativistes dans des cibles solides ou des plasmas denses. Lors des expériences d'interaction laser-matière, ce processus est en effet souvent utilisé pour diagnostiquer le passage des

électrons accélérés par le laser dans la cible irradiée. Dans notre modèle, la recirculation des électrons rapides dans la cible est prise en compte en imposant la réflexion spéculaire des électrons rapides au niveau des interfaces cible-vide ainsi qu'une seconde population d'électrons rapides décrite par un second système d'équations M1. La première population décrit les électrons rapides se propageant dans la direction de propagation de l'impulsion laser et la seconde population décrit les électrons rapides se propageant en sens contraire, réaccélérés dans la cible par les forts champs électriques de charge d'espace générés aux interfaces cible-vide lorsque la première population tente de s'échapper de la cible. Le modèle de calcul de l'émission de photons $K\alpha$ est ensuite révisé. Les conclusions de cette étude sont multiples. Tout d'abord, nous avons montré que, dans le cas de cibles faites d'Aluminium ou de Cuivre, le pas de temps numérique imposé par la résolution des équations du transport d'électrons rapides peut être comparable à la durée de vie des absences électroniques ou "trous" du niveau d'énergie K des électrons atomiques, responsables de l'émission $K\alpha$. Par conséquent, nous avons pris en compte dans notre modèle la dynamique des trous en couche K des atomes du solide irradié par le laser. Deuxièmement, nous avons démontré que les propriétés du solide à basses températures doivent être prises en compte. En particulier, le facteur de couplage entre la température électronique et la température du réseau cristallin du solide ainsi que les collisions des électrons de la bande s de conduction sur les électrons de la bande d sont susceptibles d'affecter la distribution des champs magnétiques dans des cibles de Cuivre. En troisième lieu, nous avons confirmé, à l'aide un modèle analytique simple, le résultat obtenu par M. Sherlock (2014) en ce qui concerne les effets de l'inertie des électrons dans la loi d'Ohm ainsi que du courant de déplacement dans l'équation de Maxwell-Ampère sur le chauffage de la cible. Les paquets d'électrons accélérés par l'impulsion laser son injectés dans la cible à la fréquence du laser ou deux fois la fréquence du laser. Chaque paquet excite dans son sillage des ondes plasma électroniques. L'amortissement de ces oscillations plasma du fait des collisions entraîne un chauffage supplémentaire des électrons de la cible qui n'est pas pris en compte dans les modèles hybrides de transport électronique. Quatrièmement, nous avons confirmé une forte contribution de la recirculation des électrons dans la cible sur la tâche d'émission de photons $K\alpha$. Plus la cible est fine, plus la tâche d'émission $K\alpha$ de la cible est contaminée par la recirculation des électrons. En cinquième lieu, nous avons trouvé des différences significatives entre des simulations bidimensionnelles et tridimensionnelles, en particulier en ce qui concerne les champs magnétiques auto-générés mais aussi en ce qui concerne la taille de la tache d'émission $K\alpha$ ainsi que la valeur absolue du nombre de photons émis localement par unité de volume. Néanmoins, la taille de la tâche d'émission $K\alpha$ obtenue reste beaucoup plus petite que celle déduite des données expérimentales même dans la simulation tridimensionnelle beaucoup plus réaliste. Nous avons donc analysé toutes les hypothèses de notre modèle concernant l'émission de photons $K\alpha$ afin de déterminer qu'est ce qui pourrait expliquer cette différence. L'opacité de la cible peut introduire une erreur de seulement $\approx 10\%$ dans nos calculs. Une autre possibilité serait que les électrons secondaires, négligés dans notre modèle, influent sur l'émission $K\alpha$. Aussi, la forte augmentation de la température pourrait éventuellement jouer sur la physique atomique de l'émission de photons $K\alpha$. Cependant, il me semble que l'hypothèse la plus critique dans

le modèle est d'avoir supposé une réflexion spéculaire des électrons rapides au niveau des interfaces cible-vide. En effet, une simple estimation du champ magnétique généré par l'effet "fontaine" indique que des champs magnétiques locaux générés au niveau des interfaces cible-vide peuvent dévier de façon significative les électrons rapides réaccélérés dans la cible par les champs électriques de charge d'espace, et peuvent donc être responsables d'un agrandissement de la taille de la tâche d'émission de photons $K\alpha$.

Nous avons aussi couplé notre modèle réduit de transport d'électrons rapides avec un code Lagrangien d'hydrodynamique radiative. Cela nous a permis d'étudier la génération de choc par le dépôt d'énergie d'un faisceau d'électrons rapides. Un exemple traite de la génération d'une onde de choc dans un plasma dense d'Hydrogène dans les conditions typiques du schéma d'allumage par choc. Il confirme les estimations théoriques établies par S. Gus'kov (2012) qui montrent qu'il est possible d'atteindre des pressions de choc de l'ordre du Gbar par le dépôt d'énergie d'un faisceau d'électrons rapides dans une cible dense avec une efficacité de couplage pouvant aller jusqu'à 10%. Une autre application concerne la génération d'une onde de choc avec une impulsion laser femtoseconde. Nous avons démontré analytiquement et numériquement que les gradients de température induits dans une cible solide par le dépôt d'énergie des électrons accélérés par une impulsion laser femtoseconde peut générer une onde de choc dans la cible au bout de plusieurs dizaines de picosecondes, bien après la fin du dépôt d'énergie par les électrons rapides. Les estimations analytiques ainsi que les simulations hydrodynamiques sont en bon accord avec les données expérimentales.

Les perspectives de ce travail sont multiples. Tout d'abord, les pertes énergétiques du faisceau d'électrons dues au champ de sillage d'ondes plasma électroniques doivent être pris en compte dans le code. Cela permettrait de résoudre correctement la propagation des paquets d'électrons accélérés par l'impulsion laser et de développer un diagnostic de l'émission CTR (Coherent Transition Radiation) des électrons dans le code. En ce qui concerne l'émission de photons $K\alpha$, les électrons secondaires ainsi le champ magnétique généré au niveau des bords de la cible doivent également être pris en compte. Toutefois, ce dernier nécessite de résoudre les équations sur une très petite échelle spatiale de l'ordre des rayons électroniques de Larmor et ce, sur des durées de l'ordre de la picoseconde et sur des distances de l'ordre de la centaine de microns. Cela représente un investissement important en termes de vectorisation et de parallélisation de codes. En outre, il serait intéressant de coupler de manière auto-cohérente le transport des photons $K\alpha$ émis avec le transport des électrons rapides afin de prendre en compte l'opacité des cibles irradiées par impulsion laser. En ce qui concerne l'application du transport des électrons rapides à la génération de chocs dans le contexte de l'allumage par choc, des simulations plus réalistes doivent être menées combinant à la fois la génération de choc par ablation laser et par dépôt d'électrons rapides accélérés par les instabilités paramétriques dans la couronne; le tout dans une géométrie tridimensionnelle sphérique convergente. Concernant l'allumage rapide, l'interaction de l'impulsion laser petawatt avec la cible est toujours un domaine intense de recherche A. Kemp (2014). Le modèle M1 peut être utile pour effectuer une étude paramétrique des conditions

de densité et de température optimales de la cible au moment de l'allumage ainsi que les propriétés optimales du faisceau d'électrons lui-même. Par ailleurs, différentes méthodes ont déjà été proposées afin de collimater le faisceau d'électrons rapides d'allumage. Par exemple, des simulations à l'échelle de l'allumage rapide d'une cible de FCI avec un cône préalablement inséré dans la coquille et présentant des gradients de résistivités du type de ceux proposés par A. Robinson (2013) ou encore avec un champ magnétique externe comme proposé par S. Fujioka (2013) peuvent être réalisées en prenant en compte l'aimantation de la cible ainsi que les effets tridimensionnels.

Part V

Appendix

Appendix A

Classical Plasma Kinetic Theory

” When you ask what are electrons and protons I ought to answer that this question is not a profitable one to ask and does not really have a meaning. The important thing about electrons and protons is not what they are but how they behave, how they move. I can describe the situation by comparing it to the game of chess. In chess, we have various chessmen, kings, knights, pawns and so on. If you ask what chessman is, the answer would be that it is a piece of wood, or a piece of ivory, or perhaps just a sign written on paper, or anything whatever. It does not matter. Each chessman has a characteristic way of moving and this is all that matters about it. The whole game of chess follows from this way of moving the various chessmen.”

Paul A.M. Dirac

A plasma is an ensemble of a large number of charged particles which are interacting collectively through long distance Electromagnetic forces. In order to describe physical processes in plasmas, one has to take into account the electromagnetic fields (\mathbf{E} , \mathbf{B}) generated by the charged particles. According to the Electromagnetic Theory, they are described by the Maxwell's equations

$$\begin{aligned}\frac{\partial \mathbf{E}}{\partial t} &= c \frac{\partial}{\partial \mathbf{r}} \times \mathbf{B} - 4\pi \mathbf{j} \quad , \quad \frac{\partial}{\partial \mathbf{r}} \cdot \mathbf{E} = 4\pi \rho, \\ \frac{\partial \mathbf{B}}{\partial t} &= -c \frac{\partial}{\partial \mathbf{r}} \times \mathbf{E} \quad , \quad \frac{\partial}{\partial \mathbf{r}} \cdot \mathbf{B} = 0.\end{aligned}\tag{A.1}$$

where ρ is the plasma electric charge density and \mathbf{j} the electric current density. In a quantum approach, which is out of scope in this thesis, the electromagnetic fields are considered as an ensemble of photons with quantized energy $h\nu$ described by the Klein-Gordon equation for bosons.

The retroaction of these electromagnetic fields on the charged particles must be also resolved. For a very diluted classical gas consisting of N_i ions and $N_e = Z^*n_i$ electrons, one can solve directly the dynamic equations for all $N = N_i + N_e$ particles

$$\begin{aligned}\frac{d\mathbf{p}_{\alpha,n}}{dt} &= q_\alpha \left\{ \mathbf{E}_{\text{ext}}(\mathbf{r}_{\alpha,n}, t) + \mathbf{E}(\mathbf{r}_{\alpha,n}, t) + \frac{\mathbf{v}_{\alpha,n}}{c} \times [\mathbf{B}_{\text{ext}}(\mathbf{r}_{\alpha,n}, t) + \mathbf{B}(\mathbf{r}_{\alpha,n}, t)] \right\} \\ \frac{d\mathbf{r}_{\alpha,n}}{dt} &= \mathbf{v}_{\alpha,n} = \frac{\mathbf{p}_{\alpha,n}}{\gamma_{\alpha,n} m_\alpha}\end{aligned}\tag{A.2}$$

with given initial conditions $\mathbf{p}_{\alpha,n}(t=0) = \mathbf{p}_{\alpha,n,0}$ and $\mathbf{r}_{\alpha,n}(t=0) = \mathbf{r}_{\alpha,n,0}$ where $\mathbf{r}_{\alpha,n}$ and $\mathbf{p}_{\alpha,n}$ are the position and the momentum at time t of the particle denoted by (α, n) . Here, $\alpha = e$ for electrons, $\alpha = i$ for ions and $n \in [1..N_\alpha]$. Thus, the particle charges read $q_e = -e$ while $q_i = Z^*e$. Also, it has been noted $\gamma_{\alpha,n} = \sqrt{1 + (\mathbf{p}_{\alpha,n}/m_\alpha c)^2}$ the Lorentz factor of the particle (α, n) and $\mathbf{v}_{\alpha,n}$ its velocity. Finally, $(\mathbf{E}_{\text{ext}}, \mathbf{B}_{\text{ext}})$ are eventual external electromagnetic fields. The plasma generated electromagnetic fields (\mathbf{E}, \mathbf{B}) can be deduced by solving self-consistently the Maxwell's equations (A.1) with the source terms

$$\begin{aligned}\mathbf{j}(\mathbf{r}, t) &= -e \sum_{n=1}^{N_e} \mathbf{v}_{e,n}(t) \delta^3[\mathbf{r} - \mathbf{r}_{e,n}(t)] + Z^*e \sum_{n=1}^{N_i} \mathbf{v}_{i,n}(t) \delta^3[\mathbf{r} - \mathbf{r}_{i,n}(t)] \\ \rho(\mathbf{r}, t) &= -e \sum_{n=1}^{N_e} \delta^3[\mathbf{r} - \mathbf{r}_{e,n}(t)] + Z^*e \sum_{n=1}^{N_i} \delta^3[\mathbf{r} - \mathbf{r}_{i,n}(t)].\end{aligned}\tag{A.3}$$

For example, in the static approach i.e. by neglecting the time delay terms in the Maxwell's equations (A.1), the electromagnetic fields read

$$\begin{aligned}\mathbf{E}(\mathbf{r}, t) &= -\frac{\partial \Phi}{\partial \mathbf{r}}(\mathbf{r}, t) \\ \mathbf{B}(\mathbf{r}, t) &= c \frac{\partial}{\partial \mathbf{r}} \times \mathbf{A}(\mathbf{r}, t)\end{aligned}\tag{A.4}$$

with

$$\Phi(\mathbf{r}, t) = -4\pi e \sum_{n=1}^{N_e} \frac{\delta^3[\mathbf{r} - \mathbf{r}_{e,n}(t)]}{|\mathbf{r} - \mathbf{r}_{e,n}(t)|} + 4\pi Z^* e \sum_{m=1}^{N_i} \frac{\delta^3[\mathbf{r} - \mathbf{r}_{i,n}(t)]}{|\mathbf{r} - \mathbf{r}_{i,n}(t)|}$$

and

$$\mathbf{A}(\mathbf{r}, t) = 4\pi e \sum_{n=1}^{N_e} \frac{\mathbf{v}_{e,n}(t) \delta^3[\mathbf{r} - \mathbf{r}_{e,n}(t)]}{c|\mathbf{r} - \mathbf{r}_{e,n}(t)|} - 4\pi Z^* e \sum_{n=1}^{N_i} \frac{\mathbf{v}_{i,n}(t) \delta^3[\mathbf{r} - \mathbf{r}_{i,n}(t)]}{c|\mathbf{r} - \mathbf{r}_{i,n}(t)|}.$$

In the Copenhagen quantum approach, electrons trajectories does not exist anymore and one has to solve the Dirac equation for fermions, verified by the N_e -body wave function. Also, the electron dynamics cannot be resolved without considering the electron antiparticles namely the positrons. However, in the De Broglie-Bohm quantum approach, also usually called the pilot wave approach, developed in the non relativistic case, one can solve Newton-like particle trajectory equations with a quantum force depending on the N_e -body wavefunction, which is a solution of the Schrodinger equation [Bohm, 1952a] [Bohm, 1952b]. It can be done exactly with the same technique as one uses to solve the Lorentz-equation depending on the electromagnetic field (respectively the wave function) which are the solution of the Maxwell's equations (respectively the Schrodinger equation). In this approach, which is mathematically strictly equivalent to the Copenhagen approach, particles trajectories remains true, \mathbf{r} and \mathbf{p} not being hidden variables [Bell et al., 1964]. This quantum approach is however out of scope in this thesis and we will only consider the Classical and not Quantum Physics.

The resolution of the N -body problem could be the more accurate method for plasma studies. However, it is impossible to solve it analytically and it can be done numerically only for a small number of particles $N = N_e + N_i$. In the usual plasma physics cases of a very large number of N_e electrons and N_i ions, one may adopt a statistical approach. In this case, the electron and ion populations are described by the N_α -body distribution functions

$$\begin{aligned} f_{\alpha, N_\alpha} &= f_{\alpha, N_\alpha}(\mathbf{r}_1, \mathbf{p}_1, \dots, \mathbf{r}_n, \mathbf{p}_n, \dots, \mathbf{r}_{N_\alpha}, \mathbf{p}_{N_\alpha}, t) \\ &= \sum_{n=1}^{N_\alpha} \delta^3[\mathbf{r}_n - \mathbf{r}_{\alpha, n}(t)] \delta^3[\mathbf{p}_n - \mathbf{p}_{\alpha, n}(t)] \end{aligned} \quad (\text{A.5})$$

where \mathbf{r}_n is the random variable for the position in space of the particle (α, n) and \mathbf{p}_n is the random variable for its momentum.

This **Appendix** is dedicated to the Classical Plasma Kinetic Theory (without Relativistic effects), allowing to estimate the distribution functions f_{α, N_α} . For simplicity, we neglect external electromagnetic fields and assume that the ions are immobile.

A.1 BBGKY Hierarchy

A.1.1 Vlasov Equation

In a first attempt, let us neglect collisions between electrons and between electrons and ions. In this particular case, one can assume that all electrons are independent. It follows from the Theory of Probability that

$$f_{e,N_e}(\mathbf{r}_1, \mathbf{p}_1, \dots, \mathbf{r}_n, \mathbf{p}_n, \dots, \mathbf{r}_{N_e}, \mathbf{p}_{N_e}, t) = N_e \prod_{n=1}^{N_e} \widehat{f}_{e,1}(\mathbf{r}_n, \mathbf{p}_n, t) \quad (\text{A.6})$$

and the problem is reduced to study of the 1-body distribution function

$$\begin{aligned} f_{e,1}(\mathbf{r}_1, \mathbf{p}_1, t) &= N_e \widehat{f}_{e,1}(\mathbf{r}_n, \mathbf{p}_n, t) \\ &= N_e \prod_{n=2}^{N_e} \int d^3\mathbf{r}_n \int d^3\mathbf{p}_n f_{e,N_e}(\mathbf{r}_1, \mathbf{p}_1, \mathbf{r}_2, \mathbf{p}_2, \dots, \mathbf{r}_n, \mathbf{p}_n, \dots, \mathbf{r}_{N_e}, \mathbf{p}_{N_e}, t). \end{aligned} \quad (\text{A.7})$$

The 1-body electron distribution function $f_{e,1}(\mathbf{r}, \mathbf{p}, t)$ is the probable number of electrons per unit of the phase-space infinitesimal volume $d^6V_1 = d^3\mathbf{r}d^3\mathbf{p}$ located between (\mathbf{r}, \mathbf{p}) and $(\mathbf{r} + d^3\mathbf{r}, \mathbf{p} + d^3\mathbf{p})$ with a given initial condition $f_{e,1}(t = 0)$. Indeed, since all electrons evolve in the same way according to (A.6), it is sufficient to characterize their properties in the 6-dimensional phase space (\mathbf{r}, \mathbf{p}) . By assuming that the total number N_e of electrons is conserved in this 6-dimensional infinitesimal phase space (no chemical reactions, no quantum electrodynamic effects, no radiation losses, ...), one obtains the Vlasov equation

$$\frac{df_{e,1}}{dt} = \frac{\partial f_{e,1}}{\partial t} + \mathbf{v} \cdot \frac{\partial f_{e,1}}{\partial \mathbf{r}} + \mathbf{F} \cdot \frac{\partial f_{e,1}}{\partial \mathbf{p}} = 0. \quad (\text{A.8})$$

Here, $\mathbf{v} = \mathbf{p}/m_e$ is the the velocity random variable of the electrons and

$$\mathbf{F} = -e \left(\mathbf{E} + \frac{\mathbf{v}}{c} \times \mathbf{B} \right)$$

is the Lorentz force acting on the electrons deduced from the self-consistent Maxwell's equation (A.1) with the source terms

$$\begin{aligned} \rho &= -e \int_{\mathbb{R}^3} f_{e,1}(\mathbf{r}, \mathbf{p}, t) d^3\mathbf{p} + Z^*en_i \\ \mathbf{j} &= -e \int_{\mathbb{R}^3} f_{e,1}(\mathbf{r}, \mathbf{p}, t) \mathbf{v} d^3\mathbf{p} + \mathbf{0} \end{aligned} \quad (\text{A.9})$$

where n_i is the ion density. It can be shown that the Vlasov equation (A.8) remains true in the relativistic regime [Weibel, 1967b]. The only difference is that, one has to account for the relativistic relation between the velocity and momentum $\mathbf{v} = \mathbf{p}/\gamma m_e$ in (A.8) and (A.9) where $\gamma = \sqrt{1 + (\mathbf{p}/m_e c)^2}$ is the Lorentz factor.

A.1.2 Liouville Theorem

The N_e -body electron distribution function $f_{e,N_e} = f_{e,N_e}(\mathbf{r}_1, \mathbf{p}_1, \dots, \mathbf{r}_n, \mathbf{p}_n, \dots, \mathbf{r}_{N_e}, \mathbf{p}_{N_e}, t)$ is the density of probability of all electrons in the the phase space infinitesimal volume $d^{6N_e}V$ located between $(\mathbf{r}_1, \mathbf{p}_1, \dots, \mathbf{r}_n, \mathbf{p}_n, \dots, \mathbf{r}_{N_e}, \mathbf{p}_{N_e})$ and $(\mathbf{r}_1 + d^3\mathbf{r}_1, \mathbf{p}_1 + d^3\mathbf{p}_1, \dots, \mathbf{r}_n + d^3\mathbf{r}_n, \mathbf{p}_n + d^3\mathbf{p}_n, \dots, \mathbf{r}_{N_e} + d^3\mathbf{r}_{N_e}, \mathbf{p}_{N_e} + d^3\mathbf{p}_{N_e})$ with a given initial condition $f_{e,N_e}(t = 0)$. \mathbf{r}_n is the random position variable of the electron denoted by n and \mathbf{p}_n its random momentum variable. Assuming the conservation of the total number of particles, one has

$$\forall t, \prod_{n=1}^{N_e} \int d^3\mathbf{r}_n \int d^3\mathbf{p}_n f_{e,N_e}(\mathbf{r}_1, \mathbf{p}_1, \dots, \mathbf{r}_n, \mathbf{p}_n, \dots, \mathbf{r}_{N_e}, \mathbf{p}_{N_e}, t) = 1. \quad (\text{A.10})$$

One can also consider that the $6N_e$ -dimensional infinitesimal phase space volume is incompressible. Then, the conservation of N_e electrons between t and $t + dt$ in the infinitesimal phase-space volume

$$d^{6N_e}V = \prod_{n=1}^{N_e} d^6V_n$$

where $d^6V_n = d^3\mathbf{r}_n d^3\mathbf{p}_n$ leads to the Liouville equation

$$\frac{df_{e,N_e}}{dt} = \frac{\partial f_{e,N_e}}{\partial t} + \sum_{n=1}^{N_e} \left\{ \mathbf{v}_n \frac{\partial f_{e,N_e}}{\partial \mathbf{r}_n} + \mathbf{F}_n \frac{\partial f_{e,N_e}}{\partial \mathbf{p}_n} \right\} = 0, \quad (\text{A.11})$$

which also describes the conservation of the number of particles but this time in the $6N_e$ -dimensional phase space. Here, for all $n \in [1..N_e]$, $\mathbf{v}_n = \mathbf{p}_n/m_e$ is the the velocity random variable of the electron n and

$$\mathbf{F}_n = -e \left(\mathbf{E} + \frac{\mathbf{v}_n}{c} \times \mathbf{B} \right)$$

is the Lorentz force acting on the electron n deduced from (A.2). The Liouville theorem (A.11) means that the electron N_e -body distribution function f_{e,N_e} is constant along the electron trajectories (A.2) expressed with the variables \mathbf{r}_n and \mathbf{p}_n .

A.1.3 BBGKY Hierarchy

In this section, we assume the static approximation (A.4) and neglect the magnetic force in order to simplify the presentation. Equation (A.11) can be reduced to the to 6-dimensional phase space by integrating it over $6(N_e - 1)$ phase coordinates i.e. over $\mathbf{r}_2, \mathbf{p}_2, \dots, \mathbf{r}_{N_e}, \mathbf{p}_{N_e}$:

$$\frac{\partial f_1}{\partial t} + \mathbf{v}_1 \cdot \frac{\partial f_1}{\partial \mathbf{r}_1} = - \int d^3\mathbf{r}_2 \int d^3\mathbf{p}_2 \left(e^2 \frac{\mathbf{r}_1 - \mathbf{r}_2}{|\mathbf{r}_1 - \mathbf{r}_2|^3} \right) \cdot \frac{\partial f_{e,2}}{\partial \mathbf{p}_1}. \quad (\text{A.12})$$

A.1. BBGKY HIERARCHY

This equation depends on the 2-body distribution function

$$\begin{aligned}
 & f_{e,2}(\mathbf{r}_1, \mathbf{p}_1, \mathbf{r}_2, \mathbf{p}_2, t) \\
 = & N_e(N_e - 1) \prod_{n=3}^{N_e} \int d^3\mathbf{r}_n \int d^3\mathbf{p}_n f_{e,N_e}(\mathbf{r}_1, \mathbf{p}_1, \mathbf{r}_2, \mathbf{p}_2, \dots, \mathbf{r}_n, \mathbf{p}_n, \dots, \mathbf{r}_{N_e}, \mathbf{p}_{N_e}, t).
 \end{aligned} \tag{A.13}$$

The equation for this function can be obtained by integrating the Liouville Equation (A.11) over the $6(N_e - 2)$ phase coordinates. It reads

$$\begin{aligned}
 \frac{\partial f_{e,2}}{\partial t} & + \left[\mathbf{v}_1 \cdot \frac{\partial}{\partial \mathbf{r}_1} + \mathbf{v}_2 \cdot \frac{\partial}{\partial \mathbf{r}_2} \right] (f_{e,2}) \\
 & + \left[\left(e^2 \frac{\mathbf{r}_1 - \mathbf{r}_2}{|\mathbf{r}_1 - \mathbf{r}_2|^3} \right) \cdot \left(\frac{\partial}{\partial \mathbf{p}_1} - \frac{\partial}{\partial \mathbf{p}_2} \right) \right] (f_{e,2}) \\
 = & - \int d^3\mathbf{r}_3 \int d^3\mathbf{p}_3 \left[\left(e^2 \frac{\mathbf{r}_1 - \mathbf{r}_3}{|\mathbf{r}_1 - \mathbf{r}_3|^3} \right) \cdot \frac{\partial}{\partial \mathbf{p}_1} + \left(e^2 \frac{\mathbf{r}_2 - \mathbf{r}_3}{|\mathbf{r}_2 - \mathbf{r}_3|^3} \right) \cdot \frac{\partial}{\partial \mathbf{p}_2} \right] (f_{e,3})
 \end{aligned} \tag{A.14}$$

And one can continue that procedure until $s = N_e - 1$ with

$$\begin{aligned}
 & \forall s \in [3, N_e - 1], f_{e,s}(\mathbf{r}_1, \mathbf{p}_1, \dots, \mathbf{r}_s, \mathbf{p}_s, t) \\
 = & \frac{N_e!}{(N_e - s)!} \prod_{n=s+1}^{N_e} \int d^3\mathbf{r}_n \int d^3\mathbf{p}_n f_{e,N_e}(\mathbf{r}_1, \mathbf{p}_1, \mathbf{r}_2, \mathbf{p}_2, \dots, \mathbf{r}_n, \mathbf{p}_n, \dots, \mathbf{r}_{N_e}, \mathbf{p}_{N_e}, t).
 \end{aligned} \tag{A.15}$$

This chain of equations is called the **BBGKY hierarchy** (from the name of its founders N.N. Bogoliubov, M. Born, H.S. Green, J.G. Kirkwood and J. Yvon). It formally simplifies the N_e -body problem by approaching the solution. In practice, it allows to evaluate the right hand side of Equation (A.12) that accounts for collisions by evaluating the two-body distribution function $f_{e,2}$ from Equation (A.14).

A.1.4 Vlasov-Boltzmann Equation

In order to find an expression for the right hand side of Equation (A.12), we consider the BBGKY hierarchy at the 1st order. Thus, one has to simplify the second order equation (A.14) to express the right hand side of the first order equation of the hierarchy (A.12). Let us introduce the normalized distribution functions $\widehat{f}_{e,1} = f_{e,1}/N_e$ and $\widehat{f}_{e,2} = f_{e,2}/N_e(N_e - 1)$. If electrons 1 and 2 were independent, one has $\widehat{f}_{e,2}(\mathbf{r}_1, \mathbf{p}_1, \mathbf{r}_2, \mathbf{p}_2, t) = \widehat{f}_{e,1}(\mathbf{r}_1, \mathbf{p}_1, t)\widehat{f}_{e,1}(\mathbf{r}_2, \mathbf{p}_2, t)$. The binary collisions between electrons 1 and 2 can be accounted for by the correlation function g_2

$$\widehat{f}_{e,2}(\mathbf{r}_1, \mathbf{p}_1, \mathbf{r}_2, \mathbf{p}_2, t) = \widehat{f}_{e,1}(\mathbf{r}_1, \mathbf{p}_1, t)\widehat{f}_{e,1}(\mathbf{r}_2, \mathbf{p}_2, t) + g_2(\mathbf{r}_1, \mathbf{p}_1, \mathbf{r}_2, \mathbf{p}_2, t). \tag{A.16}$$

Obviously, g_2 is particle-symmetric, i.e. it has the same values by permuting the two electrons. By injecting (A.16) in the first order equation (A.12), we obtain

$$\frac{\partial \widehat{f}_{e,1}}{\partial t} + \mathbf{v}_1 \cdot \frac{\partial \widehat{f}_{e,1}}{\partial \mathbf{r}_1} + \mathbf{F}_1 \cdot \frac{\partial \widehat{f}_{e,1}}{\partial \mathbf{p}_1} = \left(\frac{\partial \widehat{f}_{e,1}}{\partial t} \right)_{\text{col}} \quad (\text{A.17})$$

where

$$\mathbf{F}_1 = e \frac{\partial \Phi}{\partial \mathbf{r}_1}(\mathbf{r}_1, t) = \int d^3 \mathbf{r}_2 \int d^3 \mathbf{p}_2 \left(e^2 \frac{\mathbf{r}_1 - \mathbf{r}_2}{|\mathbf{r}_1 - \mathbf{r}_2|^3} \right) f_{e,1}(\mathbf{r}_2, \mathbf{p}_2, t)$$

is the Coulomb electrostatic force averaged over the momenta and positions of the electron 2 and

$$\left(\frac{\partial \widehat{f}_{e,1}}{\partial t} \right)_{\text{col}} = -\frac{1}{N_e} \int d^3 \mathbf{r}_2 \int d^3 \mathbf{p}_2 \left(e^2 \frac{\mathbf{r}_1 - \mathbf{r}_2}{|\mathbf{r}_1 - \mathbf{r}_2|^3} \right) \cdot \frac{\partial g_2}{\partial \mathbf{p}_1}$$

is the collision integral that has to be estimated according to the second order Equation (A.14). In a first attempt, we neglect the right hand side of Equation (A.14) accounting for 3-body correlations. Also, assuming that \widehat{f}_2 evolves in time mainly due to changes in \widehat{f}_1 , rather than to changes in the pair correlations g_2 , we neglect the time derivative of \widehat{f}_2 in (A.14) to get

$$\left[\mathbf{v}_1 \cdot \frac{\partial}{\partial \mathbf{r}_1} + \mathbf{v}_2 \cdot \frac{\partial}{\partial \mathbf{r}_2} \right] [\widehat{f}_{e,2}] + \left[\left(e^2 \frac{\mathbf{r}_1 - \mathbf{r}_2}{|\mathbf{r}_1 - \mathbf{r}_2|^3} \right) \cdot \left(\frac{\partial}{\partial \mathbf{p}_1} - \frac{\partial}{\partial \mathbf{p}_2} \right) \right] [\widehat{f}_{e,2}] = 0. \quad (\text{A.18})$$

Again, by assuming that \widehat{f}_2 evolves in space mainly due to changes in \widehat{f}_1 , rather than to changes in the pair correlations g_2 , we neglect the space derivative of \widehat{g}_2 in the first term of (A.18). One expects that $\widehat{f}_{e,2}(\mathbf{r}_1, \mathbf{p}_1, \mathbf{r}_{e,2}, \mathbf{p}_2, t)$ is varying slowly in the binary collision center of mass coordinates $\mathbf{R}_{12} = (\mathbf{r}_1 + \mathbf{r}_2)/2$ while it exhibits fast variations over the relative coordinates $\mathbf{r}_{12} = \mathbf{r}_2 - \mathbf{r}_1$. Therefore, $(\partial \widehat{f}_{e,2} / \partial \mathbf{r}_{12}) \gg (\partial \widehat{f}_{e,2} / \partial \mathbf{R}_{12})$ and $(\partial \widehat{f}_{e,2} / \partial \mathbf{r}_{12}) = (\partial \widehat{f}_{e,2} / \partial \mathbf{r}_2) = -(\partial \widehat{f}_{e,2} / \partial \mathbf{r}_1)$. Thus, by integrating (A.18) over the positions \mathbf{r}_2 and momenta \mathbf{p}_2 of the electron 2, we make appearing the collision integral of Equation (A.17)

$$\begin{aligned} \left(\frac{\partial \widehat{f}_{e,1}}{\partial t} \right)_{\text{col}} &= -\frac{1}{N_e} \int d^3 \mathbf{r}_2 \int d^3 \mathbf{p}_2 \left(e^2 \frac{\mathbf{r}_1 - \mathbf{r}_2}{|\mathbf{r}_1 - \mathbf{r}_2|^3} \right) \cdot \frac{\partial g_2}{\partial \mathbf{p}_1} \\ &= \frac{1}{N_e} \int d^3 \mathbf{p}_2 \int d^3 \mathbf{r}_{12} (\mathbf{v}_2 - \mathbf{v}_1) \cdot \frac{\partial}{\partial \mathbf{r}_{12}} \cdot [\widehat{f}_{e,1}(\mathbf{r}_1, \mathbf{p}_1, t) \widehat{f}_{e,1}(\mathbf{r}_2, \mathbf{p}_2, t)] \end{aligned} \quad (\text{A.19})$$

By renormalizing the distribution functions and performing the integration of this last equation, introducing the differential cross section $d^2 \sigma$ and the exchanged momentum $\Delta \mathbf{p}$ in such a electron-electron binary collision, we finally obtain the **Boltzmann equation**

$$\frac{\partial f_{e,1}}{\partial t} + \mathbf{v}_1 \cdot \frac{\partial f_{e,1}}{\partial \mathbf{r}_1} + \mathbf{F}_1 \cdot \frac{\partial f_{e,1}}{\partial \mathbf{p}_1} = \left(\frac{\partial f_{e,1}}{\partial t} \right)_{\text{col}} \quad (\text{A.20})$$

where the Boltzmann collision integral reads

$$\left(\frac{\partial f_{e,1}}{\partial t}\right)_{\text{col}} = - \int d^3\mathbf{p}_2 \int d^2\sigma |\mathbf{v}_2 - \mathbf{v}_1| \cdot \left[f_{e,1}(\mathbf{r}_1, \mathbf{p}_1, t) f_{e,1}(\mathbf{r}_1, \mathbf{p}_2, t) - f_{e,1}(\mathbf{r}_1, \mathbf{p}_1 - \Delta\mathbf{p}, t) f_{e,1}(\mathbf{r}_1, \mathbf{p}_2 + \Delta\mathbf{p}, t) \right] \quad (\text{A.21})$$

By generalizing this result to the electron-ion collisions and by taking into account all terms in the one-body force \mathbf{F}_1 as in the Vlasov equation (A.8), we obtain the **Vlasov-Boltzmann equation**

$$\begin{aligned} & \frac{\partial f_{e,1}}{\partial t} + \frac{\partial}{\partial \mathbf{r}_1} (\mathbf{v}_1 f_{e,1}) - \frac{\partial}{\partial \mathbf{p}_1} \left\{ e \left[\mathbf{E}(\mathbf{r}_1, t) + \frac{\mathbf{v}_1}{c} \times \mathbf{B}(\mathbf{r}_1, t) \right] f_{e,1} \right\} \\ &= \left(\frac{\partial f_{e,1}}{\partial t}\right)_{\text{col}} = C_{ee}^{\text{B}} [f_{e,1}, f_{e,1}](\mathbf{r}_1, \mathbf{p}_1, t) + C_{ei}^{\text{B}} [f_{e,1}, f_{i,1}](\mathbf{r}_1, \mathbf{p}_1, t) \end{aligned} \quad (\text{A.22})$$

where

$$\begin{aligned} C_{ee}^{\text{B}} [f_{e,1}, f_{e,1}](\mathbf{r}_1, \mathbf{p}_1, t) &= - \int_{\mathbb{R}^3} d^3\mathbf{p}_2 \int_{\mathbb{R}^3} d^2\sigma_{ee} |\mathbf{v}_2 - \mathbf{v}_1| \cdot \left[f_{e,1}(\mathbf{r}_1, \mathbf{p}_1, t) f_{e,1}(\mathbf{r}_1, \mathbf{p}_2, t) \right. \\ &\quad \left. - f_{e,1}(\mathbf{r}_1, \mathbf{p}_1 - \Delta\mathbf{p}_{ee}, t) f_{e,1}(\mathbf{r}_1, \mathbf{p}_2 + \Delta\mathbf{p}_{ee}, t) \right], \end{aligned} \quad (\text{A.23})$$

is the electron-electron Boltzmann collision integral and

$$\begin{aligned} C_{ei}^{\text{B}} [f_{e,1}, f_{i,1}](\mathbf{r}_1, \mathbf{p}_1, t) &= - \int_{\mathbb{R}^3} d^3\mathbf{p}_2 \int_{\mathbb{R}^3} d^2\sigma_{ei} |\mathbf{v}_1 - \mathbf{v}_2| \cdot \left[f_{e,1}(\mathbf{r}_1, \mathbf{p}_1, t) f_{i,1}(\mathbf{r}_1, \mathbf{p}_2, t) \right. \\ &\quad \left. - f_{e,1}(\mathbf{r}_1, \mathbf{p}_1 - \Delta\mathbf{p}_{ei}, t) f_{i,1}(\mathbf{r}_1, \mathbf{p}_2 + \Delta\mathbf{p}_{ei}, t) \right] \end{aligned} \quad (\text{A.24})$$

is the electron-ion Boltzmann collision integral. Similarly to the **Vlasov equation** (A.8), the electromagnetic fields (\mathbf{E}, \mathbf{B}) verify the Maxwell equations (A.1) with the plasma charge and current densities

$$\begin{aligned} \rho(\mathbf{r}, t) &= -e \int_{\mathbb{R}^3} f_{e,1}(\mathbf{r}, \mathbf{p}_1, t) d^3\mathbf{p}_1 + Z^* e n_i \\ \mathbf{j}(\mathbf{r}, t) &= -e \int_{\mathbb{R}^3} f_{e,1}(\mathbf{r}, \mathbf{p}_1, t) \mathbf{v}_1 d^3\mathbf{p}_{e,1} + \mathbf{0}. \end{aligned} \quad (\text{A.25})$$

A.1.5 Properties of the Boltzmann equation

Boltzmann integral invariants

Firstly, one can easily notice that for $\alpha = e$ or i ,

$$\begin{aligned} & \int_{\mathbb{R}^3} C_{\alpha\alpha}^{\text{B}} [f_{\alpha,1}, f_{\alpha,1}](\mathbf{r}, \mathbf{p}_{\alpha,1}, t) \quad 1 \quad d^3\mathbf{p}_{\alpha,1} = 0 \\ & \int_{\mathbb{R}^3} C_{\alpha\alpha}^{\text{B}} [f_{\alpha,1}, f_{\alpha,1}](\mathbf{r}, \mathbf{p}_{\alpha,1}, t) \quad \mathbf{p}_{\alpha,1} \quad d^3\mathbf{p}_{\alpha,1} = 0 \\ & \int_{\mathbb{R}^3} C_{\alpha\alpha}^{\text{B}} [f_{\alpha,1}, f_{\alpha,1}](\mathbf{r}, \mathbf{p}_{\alpha,1}, t) \quad \frac{\mathbf{p}_{\alpha,1}^2}{2m_\alpha} \quad d^3\mathbf{p}_{\alpha,1} = 0 \end{aligned} \quad (\text{A.26})$$

by doing the change of variables $\mathbf{p}_{\alpha,1} - \Delta\mathbf{p}_{\alpha\alpha} \rightarrow \mathbf{p}_{\alpha,1}$ and $\mathbf{p}_{\alpha,2} + \Delta\mathbf{p}_{\alpha\alpha} \rightarrow \mathbf{p}_{\alpha,2}$ in the second double integral

$$\begin{aligned}
 & \int d^3\mathbf{p}_{\alpha,1} \int_{\mathbb{R}^3} d^3\mathbf{p}_{\alpha,2} \int_{\mathbb{R}^3} d^2\sigma_{\alpha\alpha} |\mathbf{v}_{\alpha,2} - \mathbf{v}_{\alpha,1}| f_{\alpha,1}(\mathbf{p}_{\alpha,1} - \Delta\mathbf{p}_{\alpha\alpha}) f_{\alpha,1}(\mathbf{p}_{\alpha,2} + \Delta\mathbf{p}_{\alpha\alpha}) \mathbf{A}(\mathbf{p}_{\alpha,1}) \\
 = & \int d^3\mathbf{p}_{\alpha,1} \int_{\mathbb{R}^3} d^3\mathbf{p}_{\alpha,2} \int_{\mathbb{R}^3} d^2\sigma_{\alpha\alpha} |\mathbf{v}_{\alpha,2} - \mathbf{v}_{\alpha,1}| f_{\alpha,1}(\mathbf{p}_{\alpha,1}) f_{\alpha,1}(\mathbf{p}_{\alpha,2}) \mathbf{A}(\mathbf{p}_{\alpha,1} + \Delta\mathbf{p}_{\alpha\alpha})
 \end{aligned}$$

where

$$\mathbf{A}(\mathbf{p}_{\alpha,1}) = 1, \mathbf{p}_{\alpha,1} \text{ or } \mathbf{p}_{\alpha,1}^2/2m_{\alpha}.$$

The case $\mathbf{A}(\mathbf{p}_{\alpha,1}) = 1$ is obvious because the double integral of the second term cancels directly the double integral of the first term of (A.24) or (A.23). The demonstration for $\mathbf{A}(\mathbf{p}_{\alpha,1}) = \mathbf{p}_{\alpha,1}$ and $\mathbf{A}(\mathbf{p}_{\alpha,1}) = \mathbf{p}_{\alpha,1}^2/2m_{\alpha}$ is also evident. These three functions $\mathbf{A}(\mathbf{p}_{\alpha,1})$ are called the Boltzmann integral invariants. These conservation properties come from the fact that each binary collision conserves the number (1), momentum ($\mathbf{p}_{\alpha,1}$) and kinetic energy $\mathbf{p}_{\alpha,1}^2/2m_{\alpha}$ of the particles. For the same mathematical reasons, one can also show that

$$\begin{aligned}
 & \int_{\mathbb{R}^3} C_{ei}^B [f_{e,1}, f_{i,1}] (\mathbf{r}, \mathbf{p}_{e,1}, t) \quad 1 \quad d^3\mathbf{p}_{e,1} = \int_{\mathbb{R}^3} C_{ie}^B [f_{i,1}, f_{e,1}] (\mathbf{r}, \mathbf{p}_{i,1}, t) \quad 1 \quad d^3\mathbf{p}_{i,1} = 0 \\
 & \int_{\mathbb{R}^3} C_{ei}^B [f_{e,1}, f_{i,1}] (\mathbf{r}, \mathbf{p}_{e,1}, t) \quad \mathbf{p}_{e,1} \quad d^3\mathbf{p}_{e,1} + \int_{\mathbb{R}^3} C_{ie}^B [f_{i,1}, f_{e,1}] (\mathbf{r}, \mathbf{p}_{i,1}, t) \quad \mathbf{p}_{i,1} \quad d^3\mathbf{p}_{i,1} = 0 \\
 & \int_{\mathbb{R}^3} C_{ei}^B [f_{e,1}, f_{i,1}] (\mathbf{r}, \mathbf{p}_{e,1}, t) \quad \frac{\mathbf{p}_{e,1}^2}{2m_e} \quad d^3\mathbf{p}_{e,1} + \int_{\mathbb{R}^3} C_{ie}^B [f_{i,1}, f_{e,1}] (\mathbf{r}, \mathbf{p}_{i,1}, t) \quad \frac{\mathbf{p}_{i,1}^2}{2m_i} \quad d^3\mathbf{p}_{i,1} = 0
 \end{aligned} \tag{A.27}$$

It was demonstrated that the Vlasov-Boltzmann equation has only these three integral invariants [Decoster et al., 1997]. Thus, any other functions which is Boltzmann integral invariant, is a linear combination of these three functions.

H-Theorem

The Boltzmann collision operator property is that for any $\mathbf{A}(\mathbf{p}_{e,1})$

$$\begin{aligned}
 & \int_{\mathbb{R}^3} \mathbf{A}(\mathbf{p}_{e,1}) C_{e\alpha}^B [f_{e,1}, f_{\alpha,1}] d^3\mathbf{p}_{e,1} \\
 = & \frac{1}{4} \int_{\mathbb{R}^3} [\mathbf{A}(\mathbf{p}_{e,1}) + \mathbf{A}(\mathbf{p}_{e,2}) - \mathbf{A}(\mathbf{p}_{e,1} - \Delta\mathbf{p}_{e\alpha}) - \mathbf{A}(\mathbf{p}_{e,2} - \Delta\mathbf{p}_{e\alpha})] C_{e\alpha}^B [f_{e,1}, f_{\alpha,1}] d^3\mathbf{p}_{e,1}.
 \end{aligned} \tag{A.28}$$

This equality can be demonstrated similarly to the Boltzmann integrals by performing the change of variables $\mathbf{p}_{e,1} - \Delta\mathbf{p}_{e\alpha} \rightarrow \mathbf{p}_{e,1}$ and $\mathbf{p}_{\alpha,2} + \Delta\mathbf{p}_{e\alpha} \rightarrow \mathbf{p}_{\alpha,2}$ in the integrals. Then, starting from the Boltzmann equation (A.22), one can also show that the function defined as

$$H(\mathbf{r}_{e,1}, t) = - \int_{\mathbb{R}^3} (f_{e,1} \ln f_{e,1} - f_{e,1}) d^3\mathbf{p}_{e,1} \tag{A.29}$$

is the solution of the equation

$$\frac{dH}{dt} = \frac{\partial H}{\partial t} + \frac{\partial}{\partial \mathbf{r}_{e,1}} \cdot \left[- \int_{\mathbb{R}^3} \mathbf{v}_{e,1} (f_{e,1} \ln f_{e,1} - f_{e,1}) d^3 \mathbf{p}_{e,1} \right] = - \sum_{\alpha=e,i} \int_{\mathbb{R}^3} \ln f_{e,1} C_{e\alpha}^B [f_{e,1}, f_{\alpha,1}] d^3 \mathbf{p}_{e,1} \quad (\text{A.30})$$

since for all $\mu \in [t, \mathbf{r}_{e,1}, \mathbf{p}_{e,1}]$

$$\frac{\partial}{\partial \mu} (f_{e,1} \ln f_{e,1} - f_{e,1}) = \frac{\partial f_{e,1}}{\partial \mu} \ln f_{e,1}.$$

According to (A.28), one gets so

$$\begin{aligned} \frac{dH}{dt} = \sum_{\alpha=e,i} \frac{1}{4} \int_{\mathbb{R}^3} d^3 \mathbf{p}_\alpha \int_{\mathbb{R}^3} d^3 \mathbf{p}_e \int d^2 \sigma |\mathbf{v}_\alpha - \mathbf{v}_e| \ln \left(\frac{f_e(\mathbf{p}_e) f_\alpha(\mathbf{p}_\alpha)}{f_e(\mathbf{p}_e - \Delta \mathbf{p}_{e\alpha}) f_\alpha(\mathbf{p}_\alpha + \Delta \mathbf{p}_{e\alpha})} \right) \\ \times \left[f_e(\mathbf{p}_e) f_\alpha(\mathbf{p}_\alpha) - f_e(\mathbf{p}_e - \Delta \mathbf{p}_{e\alpha}) f_\alpha(\mathbf{p}_\alpha + \Delta \mathbf{p}_{e\alpha}) \right] \end{aligned} \quad (\text{A.31})$$

for which the subscript "1" and "2" have been omitted for brevity. Thus, if $f_e(\mathbf{p}_e) f_\alpha(\mathbf{p}_\alpha) > f_e(\mathbf{p}_e - \Delta \mathbf{p}_{e\alpha}) f_\alpha(\mathbf{p}_\alpha + \Delta \mathbf{p}_{e\alpha})$, the logarithm is positive and in the opposite case where it is negative, the logarithm is also negative. As a conclusion, as Boltzmann has noticed, the function H so called the plasma electrons **Entropy** is such that

$$\frac{dH}{dt} \geq 0. \quad (\text{A.32})$$

This property is called the H-theorem and it is at the origin of the 2nd principle of Thermodynamics.

Maxwell-Boltzmann distribution function

According to the H-theorem (A.32), the entropy H of any closed system will asymptotically reach its maximum value. Let us find the distribution function f_M which maximizes the entropy H under the constraints of the definition of the electron density

$$n_e(\mathbf{r}, t) = \int_{\mathbb{R}^3} f_e d^3 \mathbf{p}_e, \quad (\text{A.33})$$

the mean electron flux

$$n_e \mathbf{u}_e(\mathbf{r}, t) = \int_{\mathbb{R}^3} f_e \mathbf{v}_e d^3 \mathbf{p}_e. \quad (\text{A.34})$$

and the internal energy

$$\frac{3}{2} n_e k_B T_e(\mathbf{r}, t) = \int_{\mathbb{R}^3} f_e \frac{m_e (\mathbf{v}_e - \mathbf{u}_e)^2}{2} d^3 \mathbf{p}_e. \quad (\text{A.35})$$

By following the standard procedure of maximization problems, one introduces the Lagrange multipliers α_0 , α_1 and α_2 associated with these three constraints, respectively. Then, in order to find f_M , one has to solve

$$\frac{dL}{df_e} [f_M] = 0 \quad (\text{A.36})$$

where L is the Lagrangian of this maximization problem :

$$\begin{aligned}
 L[f_e] = H[f_e] &+ \alpha_0 \left(n_e - \int_{\mathbb{R}^3} f_e d^3 \mathbf{p}_e \right) \\
 &+ \boldsymbol{\alpha}_1 \cdot \left(n_e \mathbf{u}_e - \int_{\mathbb{R}^3} f_e \mathbf{v}_e d^3 \mathbf{p}_e \right) \\
 &+ \alpha_2 \left(\frac{3}{2} n_e k_B T_e - \int_{\mathbb{R}^3} f_e \frac{m_e \mathbf{v}_e^2}{2} d^3 \mathbf{p}_e \right).
 \end{aligned} \tag{A.37}$$

The solution of (A.36) is an exponential function

$$f_M = \exp \left[- \left(\alpha_0 + \boldsymbol{\alpha}_1 \cdot \mathbf{v}_e + \alpha_2 \frac{m_e \mathbf{v}_e^2}{2} \right) \right]. \tag{A.38}$$

Injecting this expression in the definition of the electron density (A.33), the mean electron flux (A.34) and the mean electron kinetic energy (A.35), one finds respectively

$$\begin{aligned}
 n_e &= \exp \left(-\alpha_0 + \frac{\boldsymbol{\alpha}_1^2}{2\alpha_2 m_e} \right) m_e^3 \int_{\mathbb{R}^3} \exp \left[-\frac{\alpha_2 m_e}{2} \left(\mathbf{v} + \frac{\boldsymbol{\alpha}_1}{\alpha_2 m_e} \right)^2 \right] d^3 \mathbf{v}_e \\
 &= \exp \left(-\alpha_0 + \frac{\boldsymbol{\alpha}_1^2}{2\alpha_2 m_e} \right) m_e^3 \left(\frac{2\pi}{\alpha_2 m_e} \right)^{3/2}, \\
 n_e \mathbf{u}_e &= \exp \left(-\alpha_0 + \frac{\boldsymbol{\alpha}_1^2}{2\alpha_2 m_e} \right) m_e^3 \int_{\mathbb{R}^3} \mathbf{v}_e \exp \left[-\frac{\alpha_2 m_e}{2} \left(\mathbf{v} + \frac{\boldsymbol{\alpha}_1}{\alpha_2 m_e} \right)^2 \right] d^3 \mathbf{v}_e \\
 &= \exp \left(-\alpha_0 + \frac{\boldsymbol{\alpha}_1^2}{2\alpha_2 m_e} \right) m_e^3 \left(\frac{2\pi}{\alpha_2 m_e} \right)^{3/2} \left(-\frac{\boldsymbol{\alpha}_1}{\alpha_2 m_e} \right) \text{ and} \\
 \frac{3}{2} n_e k_B T_e &= \exp \left(-\alpha_0 + \frac{\boldsymbol{\alpha}_1^2}{2\alpha_2 m_e} \right) m_e^3 \int_{\mathbb{R}^3} \frac{m_e \mathbf{v}_e^2}{2} \exp \left[-\frac{\alpha_2 m_e}{2} \left(\mathbf{v} + \frac{\boldsymbol{\alpha}_1}{\alpha_2 m_e} \right)^2 \right] d^3 \mathbf{v}_e \\
 &= \exp \left(-\alpha_0 + \frac{\boldsymbol{\alpha}_1^2}{2\alpha_2 m_e} \right) m_e^3 \left(\frac{2\pi}{\alpha_2 m_e} \right)^{3/2} \frac{3}{2} \frac{1}{\alpha_2}
 \end{aligned}$$

which provides

$$\alpha_2 = \frac{1}{k_B T_e}, \quad \boldsymbol{\alpha}_1 = -\frac{m_e \mathbf{u}_e}{k_B T_e} \text{ and } \exp(-\alpha_0) = \frac{n_e}{(2\pi m_e k_B T_e)^{3/2}} \exp \left[-\frac{m_e \mathbf{u}_e^2}{2k_B T_e} \right] \tag{A.39}$$

and consequently

$$f_M(\mathbf{r}_e, \mathbf{p}_e, t) = \frac{n_e(\mathbf{r}_e, t)}{(2\pi m_e k_B T_e)^{3/2}} \exp \left[-\frac{m_e (\mathbf{v}_e - \mathbf{u}_e)^2}{2k_B T_e} \right] \tag{A.40}$$

called the Maxwell-Boltzmann distribution function. It is the stationary solution of the Boltzmann equation (A.22).

A.2 Vlasov-Fokker-Plank-Landau Equation

A.2.1 Differential Rutherford Cross Section

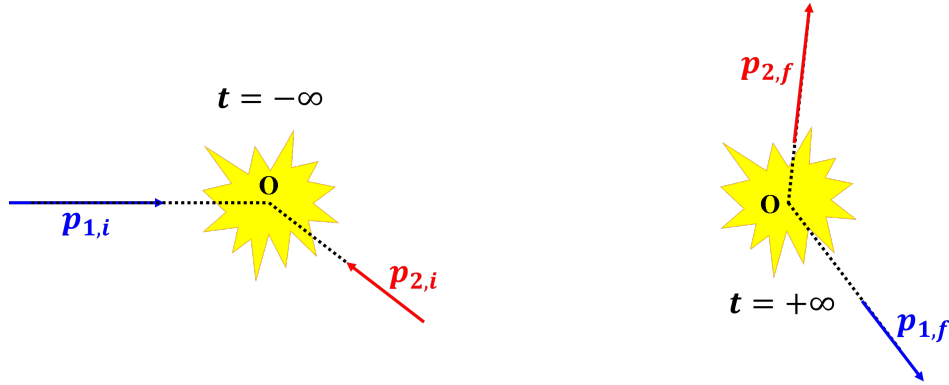


Figure A.1: Elastic collision in the laboratory frame

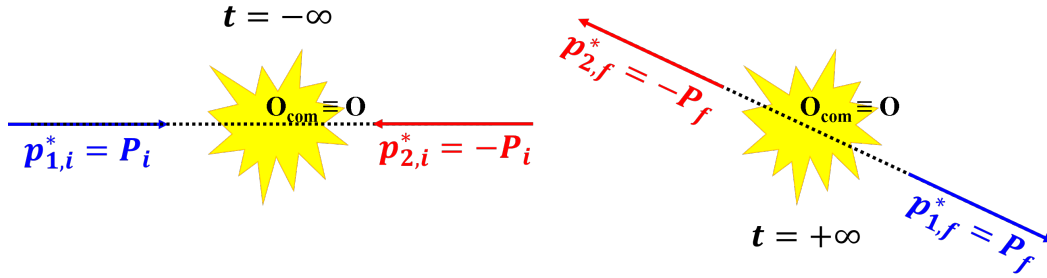


Figure A.2: Corresponding elastic collision in the center of mass frame

Let us consider the binary Coulomb collision between a non-relativistic charged particle (1) of mass m_1 and a charge q_1 moving with the velocity $\mathbf{v}_{1,i}$ before $t = 0$ with the momentum $\mathbf{p}_{1,i}$ and a non-relativistic charged particle (2) of mass m_2 and a charge q_2 moving with the velocity $\mathbf{v}_{2,i}$ before $t = 0$ with the momentum $\mathbf{p}_{2,i}$ in the laboratory frame. These particles collide at the time $t = 0$ at the origine O . Let us note $\mathbf{v}_{1 \text{ or } 2, f}$ and $\mathbf{p}_{1 \text{ or } 2, f}$ their velocities and momenta after the collision time $t = 0$. The system consisting of these two particles $\{(1) + (2)\}$ interacting with each other at $t = 0$ is equivalent to a system of one effective particle of mass $\mu = m_1 m_2 / (m_1 + m_2)$ with a velocity $\mathbf{v}_{\text{rel}} = \mathbf{v}_1 - \mathbf{v}_2$, a momentum $\mathbf{P} = \mu \mathbf{v}_{\text{rel}}$ and a charge q_1 interacting with a Coulomb potential $q_2 \mathbf{r} / |\mathbf{r}|^3$ located at the origine $O_{\text{com}} \equiv O$ in the center-of-mass frame moving at the velocity $\mathbf{v}_{\text{com}} = (m_1 \mathbf{v}_1 + m_2 \mathbf{v}_2) / (m_1 + m_2)$. It has been noted $\mathbf{r} = \mathbf{r}_1 - \mathbf{r}_2$. This equivalence follows from the conservation of the energy and momentum of the system, which means that the center of mass motion is not affected by the collision:

$$\forall t, \mathbf{p}_1^* = -\mathbf{p}_2^* = \mathbf{P} \text{ and } \varepsilon_1^* = \varepsilon_2^* = \frac{\mathbf{P}^2}{2\mu} = \frac{1}{2} \mu \mathbf{v}_{\text{rel}}^2 \quad (\text{A.41})$$

where it has been noted the values in the center of mass frame within the superscript * (see **Figure A.2**). According to the Newton's law expressed in the center of mass frame, the momentum variation of the fictitious particle reads

$$\Delta \mathbf{P} = \mathbf{P}_f - \mathbf{P}_i = \int_{-\infty}^{\infty} \frac{d\mathbf{P}}{dt} dt = \int_{-\infty}^{\infty} \frac{q_1 q_2 \mathbf{r}(t)}{|\mathbf{r}(t)|^3} dt = \Delta P \mathbf{u}. \quad (\text{A.42})$$

According to the law of conservation of angular momentum for a central force, one has necessarily $|\mu \mathbf{v}_{\text{rel}} \times \mathbf{r}| = \mu r^2 |d\varphi/dt| = |\mathbf{b}|$ where \mathbf{b} is a constant vector called the impact parameter and $\varphi(t)$ the angle between the vector \mathbf{u} and $\mathbf{r}(t)$ (see **Figure A.3**). It means that the binary collision occurs in the 2D plane $(\mathbf{P}_i, \mathbf{b})$. By projecting (A.42) on the \mathbf{u} -axis and by doing the change of variable $t \rightarrow \varphi$, one gets

$$\frac{\Delta P}{P_i} = \frac{\lambda_L}{b} \cos\left(\frac{\theta^*}{2}\right) \quad (\text{A.43})$$

where θ^* is the angle between the momenta of the fictitious particle before (\mathbf{P}_i) and after (\mathbf{P}_f) its diffusion while

$$\lambda_L = \frac{2q_1 q_2}{\mu \mathbf{v}_{\text{rel}}^2} \quad (\text{A.44})$$

is the Landau length i.e. the classical minimal distance between the fictitious particle and the diffusion center. According to the law of energy conservation for the fictitious particle (A.41), $|\mathbf{P}_f| = |\mathbf{P}_i + \Delta \mathbf{P}|$. It leads consequently to

$$\frac{\Delta P}{P_i} = 2 \sin\left(\frac{\theta^*}{2}\right). \quad (\text{A.45})$$

Finally, due to the fact that $\mathbf{u} = \cos(\theta^*/2)\mathbf{b}/b - \sin(\theta^*/2)\mathbf{P}_i/P_i$, one deduces from (A.43) and (A.45) the variation of the momentum of the fictitious scattered particle

$$\frac{\Delta \mathbf{P}}{P_i} = -\left(\frac{\Delta P}{P_i}\right)^2 \frac{\mathbf{P}_i}{2P_i} + \left(\frac{\Delta P}{P_i}\right)^2 \frac{\mathbf{b}}{\lambda_L} \quad \text{where} \quad \frac{\Delta P}{P_i} = \frac{2\frac{\lambda_L}{b}}{\sqrt{4 + \left(\frac{\lambda_L}{b}\right)^2}} \quad (\text{A.46})$$

and

$$b = \frac{\lambda_L}{2} \cot\left(\frac{\theta^*}{2}\right). \quad (\text{A.47})$$

By definition, the number of particles dN_{dif} scattered into the solid angle $d^2\Omega^* = d\varphi^* \sin\theta^* d\theta^*$ per time dt is equal to the number of incident fictitious particles $dN_{\text{inc}} = n_1 |\mathbf{v}_{1,i} - \mathbf{v}_{2,i}| d^2S dt$. That defines the differential cross section

$$d^2\sigma = \frac{d^2\sigma}{d^2\Omega^*} d^2\Omega^* = \frac{dN_{\text{dif}}/dt}{dN_{\text{inc}}/dt/d^2S} = d\varphi^* b db. \quad (\text{A.48})$$

Thus, one deduces from (A.47)

$$\frac{d^2\sigma}{d^2\Omega^*} = \frac{b}{\sin\theta^*} \left| \frac{db}{d\theta^*} \right| = \left(\frac{\lambda_L}{4} \right)^2 \frac{1}{\sin^4\left(\frac{\theta^*}{2}\right)} \quad (\text{A.49})$$

called the Rutherford differential Coulomb collision cross-section. Coming back to the laboratory frame, one finds the exchange momentum in the collision

$$\begin{aligned} \Delta\mathbf{p} &= \mathbf{p}_{1,i} - \mathbf{p}_{1,f} = \mathbf{p}_{2,f} - \mathbf{p}_{2,i} = \Delta\mathbf{P} \\ &= \frac{m_1 m_2}{m_1 + m_2} |\mathbf{v}_{1,i} - \mathbf{v}_{2,i}| \left[\sin\theta^* \frac{\mathbf{b}}{b} - (1 - \cos\theta^*) \frac{\mathbf{v}_{1,i} - \mathbf{v}_{2,i}}{|\mathbf{v}_{1,i} - \mathbf{v}_{2,i}|} \right]. \end{aligned} \quad (\text{A.50})$$

A.2.2 Small-angle Collisions

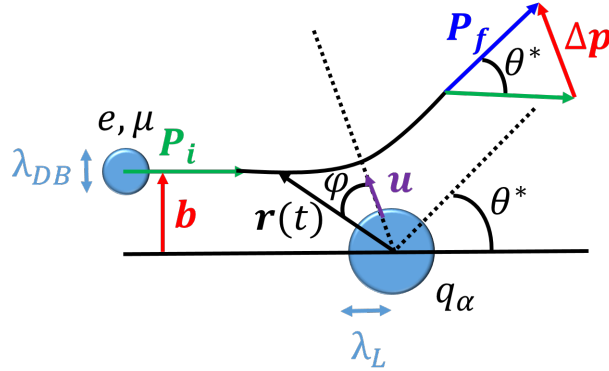


Figure A.3: Schematic view of the diffusion of the fictitious particle of charge e and mass μ by the Coulomb diffusion center q_α .

According to (A.47) and (A.49), the effective cross section increases with the impact parameter. This is a consequence of the long range electrostatic interaction. Therefore, one can neglect the large angle binary collisions and account only for the collisions at large impact parameters $b \gg \lambda_L$. Assuming so $\theta^* \rightarrow 0$ in (A.46) and (A.50), one finds as far as the second order term

$$\Delta\mathbf{p} = \frac{m_e m_\alpha}{m_e + m_\alpha} |\mathbf{v}_e - \mathbf{v}_\alpha| \left[\frac{\lambda_L}{b} \frac{\mathbf{b}}{b} - \frac{1}{2} \left(\frac{\lambda_L}{b} \right)^2 \frac{\mathbf{v}_e - \mathbf{v}_\alpha}{|\mathbf{v}_e - \mathbf{v}_\alpha|} \right] + o(\theta^{*2}) \quad \text{with } \frac{\lambda_L}{b} \ll 1. \quad (\text{A.51})$$

Thus, under the small angle assumption, the change of momentum of the particles in the binary collision $\Delta\mathbf{p}$ is perpendicular to their relative velocity $\mathbf{v}_{\text{rel}} = \mathbf{v}_e - \mathbf{v}_\alpha$ and is small compared to the initial momentum of the particles \mathbf{p}_e and \mathbf{p}_α . Applying this small angle assumption in the Boltzmann

equation (A.22), one obtains

$$\begin{aligned}
 & f_e(\mathbf{p}_e) f_\alpha(\mathbf{p}_\alpha) - f_e(\mathbf{p}_e - \Delta\mathbf{p}) f_\alpha(\mathbf{p}_\alpha + \Delta\mathbf{p}) \\
 = & -(\Delta\mathbf{p}^{(1)} + \Delta\mathbf{p}^{(2)}) \left[\frac{\partial}{\partial \mathbf{p}_e} - \frac{\partial}{\partial \mathbf{p}_\alpha} \right] (f_e(\mathbf{p}_e) f_\alpha(\mathbf{p}_\alpha)) \\
 - & \frac{\Delta\mathbf{p}^{(1)} \otimes \Delta\mathbf{p}^{(1)}}{2} \cdot \left[\frac{\partial}{\partial \mathbf{p}_e} - \frac{\partial}{\partial \mathbf{p}_\alpha} \right] \left[\frac{\partial}{\partial \mathbf{p}_e} - \frac{\partial}{\partial \mathbf{p}_\alpha} \right] (f_e(\mathbf{p}_e) f_\alpha(\mathbf{p}_\alpha)) + o(\theta^{*2}).
 \end{aligned} \tag{A.52}$$

Here,

$$\Delta\mathbf{p}^{(1)} = \mu v_{\text{rel}} \frac{\lambda_L}{b} \frac{\mathbf{b}}{b}$$

is the first order term $\sim \theta^*$ of the exchanged momentum and

$$\Delta\mathbf{p}^{(2)} = -\frac{\mu v_{\text{rel}}}{2} \left(\frac{\lambda_L}{b} \right)^2 \frac{\mathbf{v}_{\text{rel}}}{v_{\text{rel}}}$$

is the second order term $\sim \theta^{*2}$. By noticing that

$$\frac{\partial}{\partial \mathbf{p}_e} - \frac{\partial}{\partial \mathbf{p}_\alpha} = \frac{1}{\mu} \frac{\partial}{\partial \mathbf{v}_{\text{rel}}}, \tag{A.53}$$

expressing the differential cross section as $d^2\sigma = d\varphi^* b db$ and injecting the resulting Taylor expansion (A.52) in the Coulomb collision operator of the Boltzmann equation (A.22), one obtains

$$\begin{aligned}
 C_{e\alpha}^{\text{B}}[f_e, f_\alpha] = & \int_{\mathbb{R}^3} d^3\mathbf{p}_\alpha \int_0^{2\pi} d\varphi^* \int b db \\
 v_{\text{rel}} \left[& \frac{\Delta\mathbf{p}^{(1)} + \Delta\mathbf{p}^{(2)}}{\mu} \cdot \frac{\partial}{\partial \mathbf{v}_{\text{rel}}} (f_e f_\alpha) + \frac{\Delta\mathbf{p}^{(1)} \otimes \Delta\mathbf{p}^{(1)}}{2\mu^2} \cdot \frac{\partial}{\partial \mathbf{v}_{\text{rel}}} \cdot \frac{\partial}{\partial \mathbf{v}_{\text{rel}}} (f_e f_\alpha) \right].
 \end{aligned} \tag{A.54}$$

Firstly, one has

$$\int b db \int_0^{2\pi} d\varphi^* \Delta\mathbf{p}^{(1)} = \int \mu v_{\text{rel}} \frac{\lambda_L}{b} \int_0^{2\pi} \frac{\mathbf{b}}{b} d\varphi^* b db = 0$$

due to the axisymetry around the \mathbf{v}_{rel} -axis of the binary collisions,

$$\int b db \int_0^{2\pi} d\varphi^* \Delta\mathbf{p}^{(2)} = -\int_0^{2\pi} d\varphi^* \frac{\mu v_{\text{rel}}}{2} \lambda_L^2 \frac{\mathbf{v}_{\text{rel}}}{v_{\text{rel}}} \int \frac{db}{b} = -2\pi \frac{\mu}{2} \lambda_L^2 \mathbf{v}_{\text{rel}} \ln \Lambda_{e\alpha}$$

where it has been noted $\ln \Lambda_{e\alpha} = \int db/b$ the Coulomb logarithm which is discussed in the next section

A.3.3 and

$$\begin{aligned}
 \int b db \int_0^{2\pi} d\varphi^* \Delta\mathbf{p}^{(1)} \otimes \Delta\mathbf{p}^{(1)} & = \int \mu^2 v_{\text{rel}}^2 \left(\frac{\lambda_L}{b} \right)^2 \int_0^{2\pi} \frac{\mathbf{b} \otimes \mathbf{b}}{b^2} d\varphi^* b db \\
 & = \int \mu^2 v_{\text{rel}}^2 \left(\frac{\lambda_L}{b} \right)^2 \pi \frac{v_{\text{rel}}^2 \mathbf{I} - \mathbf{v}_{\text{rel}} \otimes \mathbf{v}_{\text{rel}}}{v_{\text{rel}}^2} b db \\
 & = \pi \mu^2 \lambda_L^2 (v_{\text{rel}}^2 \mathbf{I} - \mathbf{v}_{\text{rel}} \otimes \mathbf{v}_{\text{rel}}) \ln \Lambda_{e\alpha}.
 \end{aligned}$$

A.2. VLASOV-FOKKER-PLANK-LANDAU EQUATION

Secondly, noticing that

$$\frac{\partial}{\partial \mathbf{v}_{\text{rel}}} \cdot \frac{v_{\text{rel}}^2 \mathbf{I} - \mathbf{v}_{\text{rel}} \otimes \mathbf{v}_{\text{rel}}}{2v_{\text{rel}}^3} = -\frac{\mathbf{v}_{\text{rel}}}{v_{\text{rel}}^3} \quad (\text{A.55})$$

where \mathbf{I} is the unity tensor, the Boltzmann collision operator under the small angle assumption becomes

$$C_{e\alpha}^{\text{B}}[f_e, f_\alpha] = \frac{2\pi e^2 q_\alpha^2 \ln \Lambda_{e\alpha}}{\mu^2} \int_{\mathbb{R}^3} \frac{\partial}{\partial \mathbf{v}_{\text{rel}}} \cdot \left[\frac{v_{\text{rel}}^2 \mathbf{I} - \mathbf{v}_{\text{rel}} \otimes \mathbf{v}_{\text{rel}}}{v_{\text{rel}}^3} \cdot \frac{\partial}{\partial \mathbf{v}_{\text{rel}}} (f_e f_\alpha) \right] d^3 \mathbf{p}_\alpha. \quad (\text{A.56})$$

Finally, due to the fact that the distribution function f_α and its derivatives tend to zero when $|\mathbf{p}_\alpha| \rightarrow \pm\infty$, one finally gets the Landau collision operator according to the relationship (A.53)

$$C_{e\alpha}^{\text{L}}[f_e, f_\alpha] = \frac{\partial}{\partial \mathbf{p}_e} \cdot \int_{\mathbb{R}^3} \mathbf{U}_{e\alpha} \cdot \left[f_\alpha \frac{\partial f_e}{\partial \mathbf{p}_e} - f_e \frac{\partial f_\alpha}{\partial \mathbf{p}_\alpha} \right] d^3 \mathbf{p}_\alpha \quad (\text{A.57})$$

with

$$\mathbf{U}_{e\alpha} = U_{e\alpha,0} \frac{|\mathbf{v}_e - \mathbf{v}_\alpha|^2 \mathbf{I} - (\mathbf{v}_e - \mathbf{v}_\alpha) \otimes (\mathbf{v}_e - \mathbf{v}_\alpha)}{2|\mathbf{v}_e - \mathbf{v}_\alpha|^2} \quad \text{and} \quad U_{e\alpha,0} = 4\pi \frac{e^2 q_\alpha^2 \ln \Lambda_{e\alpha}}{|\mathbf{v}_e - \mathbf{v}_\alpha|} \quad (\text{A.58})$$

which is called the Landau collision tensor. This expression has been derived using the Rutherford differential cross section (A.49) but in the more general case,

$$U_{e\alpha,0} = \int d^2 \sigma_{e\alpha} \frac{\Delta \mathbf{p}^2}{2} |\mathbf{v}_e - \mathbf{v}_\alpha|. \quad (\text{A.59})$$

The structure of the Landau collision kernel $\mathbf{U}_{e\alpha}$ is originated from the small angle assumption. By integrating by part the second term in the integrand of the Landau collision operator (A.57), one can write it using the fact that the distribution functions f_e (and f_α) as well as its derivatives tend to 0 when $|\mathbf{p}_e| \rightarrow \pm\infty$ (respectively when $|\mathbf{p}_\alpha| \rightarrow \pm\infty$) as follows :

$$C_{e\alpha}^{\text{L}}[f_e, f_\alpha] = -\frac{\partial}{\partial \mathbf{p}} \cdot \left[\frac{\langle \Delta \mathbf{p} \rangle_\alpha}{\Delta t} f_e - \frac{\langle \Delta \mathbf{p} \otimes \Delta \mathbf{p} \rangle_\alpha}{2\Delta t} \cdot \frac{\partial f_e}{\partial t} \right] \quad (\text{A.60})$$

where the friction vector term can be written in the general case

$$\frac{\langle \Delta \mathbf{p} \rangle_\alpha}{\Delta t} = \int_{\mathbb{R}^3} d^3 \mathbf{p}_\alpha f_\alpha \frac{\partial}{\partial \mathbf{p}_\alpha} \cdot \mathbf{U}_{e\alpha} \quad (\text{A.61})$$

and the diffusion tensor term

$$\frac{\langle \Delta \mathbf{p} \otimes \Delta \mathbf{p} \rangle_\alpha}{2\Delta t} = \int_{\mathbb{R}^3} d^3 \mathbf{p}_\alpha f_\alpha \mathbf{U}_{e\alpha}. \quad (\text{A.62})$$

Using the Rutherford differential cross section (A.49), it reads

$$\frac{\langle \Delta \mathbf{p} \rangle_\alpha}{\Delta t} = -4\pi \frac{e^2 q_\alpha^2 \ln \Lambda_{e\alpha}}{m_\alpha} \int_{\mathbb{R}^3} \frac{\mathbf{v}_e - \mathbf{v}_\alpha}{|\mathbf{v}_e - \mathbf{v}_\alpha|^3} f_\alpha d^3 \mathbf{p}_\alpha \quad (\text{A.63})$$

and

$$\frac{\langle \Delta \mathbf{p} \otimes \Delta \mathbf{p} \rangle_\alpha}{2\Delta t} = 4\pi e^2 q_\alpha^2 \ln \Lambda_{e\alpha} \int_{\mathbb{R}^3} \frac{|\mathbf{v}_e - \mathbf{v}_\alpha|^2 \mathbf{I} - (\mathbf{v}_e - \mathbf{v}_\alpha) \otimes (\mathbf{v}_e - \mathbf{v}_\alpha)}{2|\mathbf{v}_e - \mathbf{v}_\alpha|^3} f_\alpha d^3 \mathbf{p}_\alpha. \quad (\text{A.64})$$

These friction and diffusion terms are also called the Spitzer-Chandrasekhar coefficients. The expression (A.60) is a **Fokker-Planck**-like expression verified by any Markovian stochastic process. Indeed, as explained in [Chandrasekhar, 1943], the Landau collision operator (??) can also be derived assuming that the distribution function $f_e(\mathbf{p}_e, t)$ is a stochastic process which does not depend at $t = t_0$ on its whole history $t < t_0$ but only on the infinitesimal time interval $t_0 - \Delta t$ with $\Delta t \ll t_0$ which however, is sufficiently large compared to the time between two consecutive electron- α collisions (definition of a Markovian stochastic process). In the textbook by [Balescu, 1963], a similar approach is presented to derive (A.57) from the Boltzmann collision operator while [Landau and Lifshitz, 1981] derived it by using physical considerations on the electron fluxes in the momentum space. Equation (A.57) can also be derived from the Lenard-Balescu equation, as done in the textbook by [Decoster et al., 1997], assuming the permittivity $\epsilon(\mathbf{k}, \omega) = 1 + (1/3k^2 \lambda_D^2)$ that takes into account electron plasma waves with thermal corrections. The Landau collision integral can be extended to degenerate electrons by replacing the Debye length λ_D by a more general expression evaluated in the Debye-Huckel theory

$$\lambda_D = \left[\frac{4\pi n_e e^2}{k_B \sqrt{T_e^2 + T_F^2}} + \frac{4\pi n_i (Z^* e) r}{k_B T_i} \right]^{-1/2}. \quad (\text{A.65})$$

Here, the electron temperature T_e has been replaced by $\sqrt{T_e^2 + T_F^2}$ [Lee and More, 1984] where

$$T_F = \frac{\hbar^2}{2m_e k_B} (3\pi^2 n_e)^{2/3} \quad (\text{A.66})$$

is the Fermi temperature and Z^* the ionization state which can be evaluated using the formula

$$Z^* = g \left(\frac{T_e}{Z^{4/3}}, \frac{\rho}{ZA} \right) Z \quad (\text{A.67})$$

where g is an analytical fit of numerical Thomas-Fermi calculations provided by [More, 1985].

A.2.3 Coulomb Logarithm $\ln \Lambda_{e\alpha}$

The integral defined in the previous section as the Coulomb logarithm

$$\ln \Lambda_{e\alpha} = \int_{b_{\min}}^{b_{\max}} \frac{db}{b}$$

diverges at both the lower and upper boundaries of integration if $b_{\min} = 0$ and $b_{\max} = \infty$. These limits need to be defined separately. As the Landau collision operator (A.57) is valid only for small angle

A.2. VLASOV-FOKKER-PLANK-LANDAU EQUATION

collisions $\theta^* \ll 1$ or $b \gg \lambda_L$ according to (A.47), the low boundary has to be defined by $b_{\min} = \lambda_L$. Moreover, the Landau collision operator must be cut at the screening length $b_{\max} = \lambda_D$. This also explains why assuming $k\lambda_D \gg 1$ ($k \sim b^{-1}$), the Lenard-Balescu collision operator also allows to describe this Debye screening effect. Thus, the Coulomb logarithm can be evaluated as

$$\ln \Lambda_{e\alpha} = \int_{\lambda_L}^{\lambda_D} \frac{db}{b} = \ln \left(\frac{\lambda_D}{\lambda_L} \right).$$

This classical expression is valid only if the relative collision velocity is sufficiently small so that the Landau length is larger than the effective De Broglie length

$$\lambda_{\text{DB}} = \frac{\hbar}{2\mu v_{\text{rel}}} \quad (\text{A.68})$$

(see **Figure A.3**). In this case, the lower limit must be chosen by $b_{\min} = \lambda_{\text{DB}}$. This quantum limit must be chosen for the electron energies larger than 10 eV. Concerning collisions of electrons on ions, in the case of dense plasmas, the Debye-Huckel treatment of screening breaks down due to strong ion-ion correlation effects. If the Debye length λ_D becomes less than interparticle distance

$$r_i = \left(\frac{3}{4\pi n_i} \right)^{1/3}, \quad (\text{A.69})$$

the screening length must be evaluated by r_i [Lee and More, 1984]. The Coulomb logarithm depends on the colliding particles velocities \mathbf{v}_e and \mathbf{v}_α . In a plasma at the thermal equilibrium, the particles follow a Maxwell-Boltzmann distribution function and the effective lengths in the Coulomb logarithm can be replaced by their average values $\sqrt{3k_B T_e / m_e}$. Finally, one can write the Coulomb logarithm as (the minimum value of 2 accounts for the non-ideal plasma effects)

$$\ln \Lambda_{e\alpha} = \max \left\{ 2, \frac{1}{2} \ln \left(1 + \frac{b_{\max}^2}{b_{\min}^2} \right) \right\} \quad (\text{A.70})$$

where

$$b_{\max} = \max \{ r_i, \lambda_D \} \text{ and } b_{\min} = \max \{ \overline{\lambda_L}, \overline{\lambda_{\text{DB}}} \}$$

with

$$\overline{\lambda_L} = \frac{2eq_\alpha}{\frac{m_e m_\alpha}{m_e + m_\alpha} \sqrt{\frac{3k_B T_e}{m_e}}} \text{ and } \overline{\lambda_{\text{DB}}} = \frac{\hbar}{2 \frac{m_e m_\alpha}{m_e + m_\alpha} \sqrt{\frac{3k_B T_e}{m_e}}}.$$

A.2.4 Properties of the Landau equation

One can check that the Landau equation preserves the properties of the Boltzmann equation. The functions 1 , $\mathbf{p}_{\alpha,1}$ and $\mathbf{p}_{\alpha,1}^2/2m_\alpha$ are still integral invariant i.e. for $\alpha = e$ or i ,

$$\begin{aligned} \int_{\mathbb{R}^3} C_{\alpha\alpha}^L [f_{\alpha,1}, f_{\alpha,1}] (\mathbf{r}, \mathbf{p}_{\alpha,1}, t) \quad 1 \quad d^3\mathbf{p}_{\alpha,1} &= 0 \\ \int_{\mathbb{R}^3} C_{\alpha\alpha}^L [f_{\alpha,1}, f_{\alpha,1}] (\mathbf{r}, \mathbf{p}_{\alpha,1}, t) \quad \mathbf{p}_{\alpha,1} \quad d^3\mathbf{p}_{\alpha,1} &= 0 \\ \int_{\mathbb{R}^3} C_{\alpha\alpha}^L [f_{\alpha,1}, f_{\alpha,1}] (\mathbf{r}, \mathbf{p}_{\alpha,1}, t) \quad \frac{\mathbf{p}_{\alpha,1}^2}{2m_\alpha} \quad d^3\mathbf{p}_{\alpha,1} &= 0 \end{aligned} \quad (\text{A.71})$$

and

$$\begin{aligned} \int_{\mathbb{R}^3} C_{ei}^L [f_{e,1}, f_{i,1}] (\mathbf{r}, \mathbf{p}_{e,1}, t) \quad 1 \quad d^3\mathbf{p}_{e,1} &= \int_{\mathbb{R}^3} C_{ie}^L [f_{i,1}, f_{e,1}] (\mathbf{r}, \mathbf{p}_{i,1}, t) \quad 1 \quad d^3\mathbf{p}_{i,1} = 0 \\ \int_{\mathbb{R}^3} C_{ei}^L [f_{e,1}, f_{i,1}] (\mathbf{r}, \mathbf{p}_{e,1}, t) \quad \mathbf{p}_{e,1} \quad d^3\mathbf{p}_{e,1} &+ \int_{\mathbb{R}^3} C_{ie}^L [f_{i,1}, f_{e,1}] (\mathbf{r}, \mathbf{p}_{i,1}, t) \quad \mathbf{p}_{i,1} \quad d^3\mathbf{p}_{i,1} = 0 \\ \int_{\mathbb{R}^3} C_{ei}^L [f_{e,1}, f_{i,1}] (\mathbf{r}, \mathbf{p}_{e,1}, t) \quad \frac{\mathbf{p}_{e,1}^2}{2m_e} \quad d^3\mathbf{p}_{e,1} &+ \int_{\mathbb{R}^3} C_{ie}^L [f_{i,1}, f_{e,1}] (\mathbf{r}, \mathbf{p}_{i,1}, t) \quad \frac{\mathbf{p}_{i,1}^2}{2m_i} \quad d^3\mathbf{p}_{i,1} = 0. \end{aligned} \quad (\text{A.72})$$

Secondly, one can show that if $f_{e,1}$ is the solution of the **Landau equation**

$$\begin{aligned} \frac{\partial f_{e,1}}{\partial t} + \frac{\partial}{\partial \mathbf{r}_{e,1}} (\mathbf{v}_{e,1} f_{e,1}) + \frac{\partial}{\partial \mathbf{p}_{e,1}} \left\{ e \left[\mathbf{E}_{\text{ext}} + \mathbf{E}_p(\mathbf{r}_{e,1}, t) + \frac{\mathbf{v}_{e,1}}{c} \times (\mathbf{B}_{\text{ext}} + \mathbf{B}_p(\mathbf{r}_{e,1}, t)) \right] f_{e,1} \right\} \\ = \left(\frac{\partial f_{e,1}}{\partial t} \right)_{\text{coll}} = C_{ee}^L [f_{e,1}, f_{e,1}] (\mathbf{r}_{e,1}, \mathbf{p}_{e,1}, t) + C_{ei}^L [f_{e,1}, f_{i,1}] (\mathbf{r}_{e,1}, \mathbf{p}_{e,1}, t), \end{aligned} \quad (\text{A.73})$$

thus, the entropy defined as

$$H(\mathbf{r}_{e,1}, t) = - \int_{\mathbb{R}^3} (f_{e,1} \ln f_{e,1} - f_{e,1}) d^3\mathbf{p}_{e,1} \quad (\text{A.74})$$

verifies the H-theorem

$$\frac{dH}{dt} \geq 0. \quad (\text{A.75})$$

Finally, it can be shown that the Maxwell-Boltzmann distribution, maximizing the entropy H ,

$$f_M(\mathbf{r}_e, \mathbf{p}_e, t) = \frac{n_e(\mathbf{r}_e, t)}{(2\pi m_e k_B T_e)^{3/2}} \exp \left[-\frac{m_e(\mathbf{v}_e - \mathbf{u}_e)^2}{2k_B T_e} \right] \quad (\text{A.76})$$

is still the stationary solution of the Landau equation (A.73).

A.3 Simplified Forms of the Collision Integral

A.3.1 BGK Approximation

A simplified form of the collision term was proposed by P. L. Bhatnagar, E. P. Gross and M. Krook. It reads

$$\left(\frac{\partial f_{e,1}}{\partial t}\right)_{\text{col}} = -\nu(f_{e,1} - f_M) \quad (\text{A.77})$$

where ν is a velocity-dependent effective collision frequency which characterize the time needed by $f_{e,1}$ to reach the maximum-entropy equilibrium distribution function f_M [Bhatnagar et al., 1954]. This is called the BGK approximation from the names of its founders. It describes the relaxation of the distribution function to the Maxwell-Boltzmann distribution in agreement with the H-theorem. The parameters in the function f_M (A.40) are defined according to the conservation of the number of particles, the total momentum and energy.

A.3.2 Lorentzian Plasmas

The Lorentz assumption concerns only the electron-ion collision term (??). Because of the large mass ratio $m_i/m_e \gg 1$, the friction term (A.61) is much smaller than the diffusion term (A.62). By assuming that the distribution function of particles α is given by $f_\alpha(\mathbf{r}, \mathbf{p}_\alpha, t) = n_\alpha(\mathbf{r}, t)\delta[\mathbf{p}_\alpha]$, where δ is the Dirac distribution, in order to account for only small α particle velocities, the diffusion term (A.62) reads :

$$\frac{\langle \Delta \mathbf{p} \otimes \Delta \mathbf{p} \rangle_\alpha}{2\Delta t} = \nu_{e\alpha}(\mathbf{v}_e) \frac{|\mathbf{p}_e|^2 \mathbf{I} - \mathbf{p}_e \otimes \mathbf{p}_e}{2} \quad (\text{A.78})$$

where

$$\nu_{e\alpha}(\mathbf{v}_e) = 4\pi n_\alpha \frac{e^2 q_\alpha^2 \ln \Lambda_{e\alpha}}{m_e^2 |\mathbf{v}_e|^3}. \quad (\text{A.79})$$

One can directly notice that the ratio of the two isotropization rates

$$\frac{\nu_{ei}}{\nu_{ee}} = \frac{Z^* \ln \Lambda_{ei}}{\ln \Lambda_{ee}} \gg 1. \quad (\text{A.80})$$

for material with $Z^* \gtrsim 10$ assuming $\ln \Lambda_{ei}$ and $\ln \Lambda_{ee}$ have approximatively the same order of magnitude. Thus, the omission of the electron-electron diffusion term compared to the electron-ion one is fully justified for a plasma with $Z^* \gtrsim 10$ and the Lorentz approximation leads to

$$\begin{aligned} \left(\frac{\partial f_e}{\partial t}\right)_{\text{col}} &= \nu_{ei}(\mathbf{v}_e) |\mathbf{v}_e|^3 \frac{\partial}{\partial \mathbf{p}_e} \cdot \frac{|\mathbf{p}_e|^2 \mathbf{I} - \mathbf{p}_e \otimes \mathbf{p}_e}{2|\mathbf{v}_e|^3} \cdot \frac{\partial f_e}{\partial \mathbf{p}_e} \\ &= \frac{\nu_{ei}(\mathbf{v}_e)}{2} \left[\frac{1}{\sin \theta_e} \frac{\partial}{\partial \theta_e} \left(\sin \theta_e \frac{\partial f_e}{\partial \theta_e} \right) + \frac{1}{\sin^2 \theta_e} \frac{\partial^2 f_e}{\partial \varphi_e^2} \right] \end{aligned} \quad (\text{A.81})$$

expressed in the spherical coordinates in the electron momentum space $(p_e, \theta_e, \varphi_e)$.

The Lorentz assumption neglects the electron-electron collisions and therefore describes only the isotropization of the electron distribution function. The Lorentz approximation is particularly useful for estimating the electron-ion collision friction expressed with the frequency $\bar{\nu}_{ei}$ averaged over the whole electron velocity distribution function $f_e(\mathbf{v}_e)$. It is defined by the relation

$$-n_e m_e \bar{\nu}_{ei} \mathbf{u}_e = m_e \int_{\mathbb{R}^3} \left(\frac{\partial f_e}{\partial t} \right)_{\text{col}} \mathbf{v}_e d^3 \mathbf{p}_e \quad (\text{A.82})$$

where

$$n_e \mathbf{u}_e = \int_{\mathbb{R}^3} f_e \mathbf{v}_e d^3 \mathbf{p}_e$$

is the hydrodynamic electron flux. By injecting (A.81) in (A.82) and by assuming the electrons follow the Maxwell-Boltzmann distribution function (A.40), we obtain

$$\bar{\nu}_{ei} = \frac{1}{3} \sqrt{\frac{2}{\pi}} 4\pi n_i \frac{Z^{*2} e^4 \ln \Lambda_{ei}}{m_e^2 v_{T,e}^3} \quad (\text{A.83})$$

where

$$v_{T,e} = \sqrt{\frac{k_B T_e}{m_e}}$$

is the electron thermal velocity.

Appendix B

Classical Plasma Hydrodynamic Theory

*” Classical thermodynamics ... is the only physical theory of universal content which I am convinced
... will never be overthrown. ”*

Albert Einstein

According to **Appendix A, section A.2.**, plasma electrons can be described on the kinetic scale according to the Vlasov-Fokker-Planck-Landau equation for the electron distribution function $f_e = f_e(\mathbf{r}, \mathbf{p}, t)$. It reads

$$\frac{\partial f_e}{\partial t} + \frac{\partial}{\partial \mathbf{r}} \cdot (\mathbf{v} f_e) - \frac{\partial}{\partial \mathbf{p}} \cdot \left\{ e \left[\mathbf{E}(\mathbf{r}, t) + \frac{\mathbf{v}}{c} \times \mathbf{B}(\mathbf{r}, t) \right] f_e \right\} = \left(\frac{\partial f_e}{\partial t} \right)_{\text{col}} \quad (\text{B.1})$$

with

$$\left(\frac{\partial f_e}{\partial t} \right)_{\text{coll}} = C_{ee}^{\text{L}}[f_e, f_e](\mathbf{r}, \mathbf{p}, t) + C_{ei}^{\text{L}}[f_e, f_i](\mathbf{r}, \mathbf{p}, t)$$

where for $\alpha = i$ or e ,

$$C_{e\alpha}^{\text{L}}[f_e, f_\alpha](\mathbf{r}, \mathbf{p}, t) = -\frac{\partial}{\partial \mathbf{p}} \cdot \left[\frac{\langle \Delta \mathbf{p} \rangle_\alpha}{\Delta t} f_e - \frac{\langle \Delta \mathbf{p} \otimes \Delta \mathbf{p} \rangle_\alpha}{2\Delta t} \cdot \frac{\partial f_e}{\partial t} \right] \quad (\text{B.2})$$

with

$$\frac{\langle \Delta \mathbf{p} \rangle_\alpha}{\Delta t} = -4\pi \frac{e^2 q_\alpha^2 \ln \Lambda_{e\alpha}}{m_e} \int_{\mathbb{R}^3} \frac{\mathbf{v} - \mathbf{v}_\alpha}{|\mathbf{v} - \mathbf{v}_\alpha|^3} f_\alpha(\mathbf{r}, \mathbf{p}_\alpha, t) d^3 \mathbf{p}_\alpha \quad (\text{B.3})$$

and

$$\frac{\langle \Delta \mathbf{p} \otimes \Delta \mathbf{p} \rangle_\alpha}{2\Delta t} = 4\pi e^2 q_\alpha^2 \ln \Lambda_{e\alpha} \int_{\mathbb{R}^3} \frac{|\mathbf{v} - \mathbf{v}_\alpha|^2 \mathbf{I} - (\mathbf{v} - \mathbf{v}_\alpha) \otimes (\mathbf{v} - \mathbf{v}_\alpha)}{2|\mathbf{v} - \mathbf{v}_\alpha|^3} f_\alpha(\mathbf{r}, \mathbf{p}_\alpha, t) d^3 \mathbf{p}_\alpha. \quad (\text{B.4})$$

According to the H-theorem (cf **Appendix A, section A.1.5**), there is a time $t \sim \nu^{-1}$ needed for the electrons and ions to reach the maximum entropy equilibrium where their distribution functions are close to the Maxwell-Boltzmann distribution function

$$f_\alpha(\mathbf{r}, \mathbf{p}_\alpha, t) = \frac{n_\alpha(\mathbf{r}, t)}{(2\pi m_\alpha k_B T_\alpha)^{3/2}} \exp \left[-\frac{m_\alpha (\mathbf{v}_\alpha - \mathbf{u}_\alpha)^2}{2k_B T_\alpha} \right]. \quad (\text{B.5})$$

The kinetic time scale ν^{-1} can be estimated by the averaged electron-ion collision frequency (A.83)

$$\nu \approx \bar{\nu}_{ei} = \frac{1}{3} \sqrt{\frac{2}{\pi}} 4\pi n_i \frac{Z^{*2} e^4 \ln \Lambda_{ei}}{m_e^2 v_{T,e}^3}. \quad (\text{B.6})$$

Thus, the distribution function f_e being assumed to be locally a Maxwell-Boltzmann distribution in the considered time scales $t \gg \bar{\nu}_{ei}^{-1}$, we only need to find the electron density n_e , the mean electron velocity \mathbf{u}_e and the electron temperature T_e in order to fully characterize the electron distribution function f_e . This approximation is called the **Local Thermodynamic Equilibrium**.

This **Appendix** is dedicated to the Classical Plasma Hydrodynamic Theory (without Relativistic effects) based on this **Local Thermodynamic Equilibrium**, quoted throughout this thesis. It also presents the radiation hydrodynamic code CHIC that has been used in this work. For simplicity, we neglect external electromagnetic fields (except in the derivation of the Spitzer, Lee-More or Braginskii transport coefficients) and assume that the plasma consists of two species -electrons and ions.

B.1 Two fluids Hydrodynamic Equations

B.1.1 Definitions

Knowing the distribution function $f_\alpha = f_\alpha(\mathbf{r}, \mathbf{p}_\alpha, t)$ for the particles α , one defines the following quantities

Name	Notation	Definition
Particles density	$n_\alpha(\mathbf{r}, t)$	$\int_{\mathbb{R}^3} f_\alpha d^3\mathbf{p}_\alpha$
Mean particles flux	$n_\alpha \mathbf{u}_\alpha(\mathbf{r}, t)$	$\int_{\mathbb{R}^3} f_\alpha \mathbf{v}_\alpha d^3\mathbf{p}_\alpha$
Mean particles kinetic energy	$K_\alpha(\mathbf{r}, t)$	$\frac{1}{n_\alpha} \int_{\mathbb{R}^3} f_\alpha \frac{m_e \mathbf{v}_\alpha^2}{2} d^3\mathbf{p}_\alpha$
Internal kinetic energy	$U_\alpha(\mathbf{r}, t)$	$\int_{\mathbb{R}^3} f_\alpha \frac{m_e (\mathbf{v}_\alpha - \mathbf{u}_\alpha)^2}{2} d^3\mathbf{p}_\alpha$
Particles temperature	$T_\alpha(\mathbf{r}, t)$	$\frac{m_\alpha}{3k_B} \frac{1}{n_\alpha} \int_{\mathbb{R}^3} f_\alpha (\mathbf{v}_\alpha - \mathbf{u}_\alpha)^2 d^3\mathbf{p}_\alpha$
Mean particles momentum flux tensor	$\mathbf{\Pi}_\alpha(\mathbf{r}, t)$	$m_\alpha \int_{\mathbb{R}^3} f_\alpha \mathbf{v}_\alpha \otimes \mathbf{v}_\alpha d^3\mathbf{p}_\alpha$
Kinetic pressure tensor	$\mathbf{P}_\alpha(\mathbf{r}, t)$	$m_\alpha \int_{\mathbb{R}^3} f_\alpha (\mathbf{v}_\alpha - \mathbf{u}_\alpha) \otimes (\mathbf{v}_\alpha - \mathbf{u}_\alpha) d^3\mathbf{p}_\alpha$
Scalar kinetic pressure	$P_\alpha(\mathbf{r}, t)$	$\frac{m_\alpha}{3} \int_{\mathbb{R}^3} f_\alpha (\mathbf{v}_\alpha - \mathbf{u}_\alpha)^2 d^3\mathbf{p}_\alpha$
Kinetic energy flux	\mathbf{Q}_α	$n_\alpha \int_{\mathbb{R}^3} f_\alpha \frac{m_\alpha \mathbf{v}_\alpha^2}{2} \mathbf{v}_\alpha d^3\mathbf{p}_\alpha$
Thermal energy flux	\mathbf{q}_α	$\int_{\mathbb{R}^3} f_\alpha \frac{m_\alpha (\mathbf{v}_\alpha - \mathbf{u}_\alpha)^2}{2} (\mathbf{v}_\alpha - \mathbf{u}_\alpha) d^3\mathbf{p}_\alpha$

Under these definitions, one can relate the internal kinetic energy U_α with the mean particles kinetic energy K_α , the mean particle velocity \mathbf{u}_α and the temperature T_α as follows

$$U_\alpha(\mathbf{r}, t) = n_\alpha K_\alpha - n_\alpha \frac{m_\alpha \mathbf{u}_\alpha^2}{2} = C_{V,\alpha} T_\alpha \quad (\text{B.7})$$

where it has been noted $C_{V,\alpha} = (3/2)n_\alpha k_B$ the α particles thermal capacity. Also, the kinetic pressure tensor \mathbf{P}_α is related with the scalar kinetic pressure P_α , the temperature T_α and the viscosity tensor

$$\boldsymbol{\tau}_\alpha = \mathbf{\Pi}_\alpha - P_\alpha \mathbf{I} - n_\alpha m_\alpha \mathbf{u}_\alpha \otimes \mathbf{u}_\alpha \quad (\text{B.8})$$

as follows

$$\mathbf{P}_\alpha = P_\alpha \mathbf{I} - \boldsymbol{\tau}_\alpha \quad (\text{B.9})$$

with

$$P_\alpha(\mathbf{r}, t) = \frac{1}{3} \text{Tr}[\mathbf{P}_\alpha] = n_\alpha k_B T_\alpha. \quad (\text{B.10})$$

The thermal energy flux \mathbf{q}_α can be related with the kinetic energy flux \mathbf{Q}_α , the mean particles velocity

B.1. TWO FLUIDS HYDRODYNAMIC EQUATIONS

\mathbf{u}_α , the scalar pressure P_α and the viscosity tensor $\boldsymbol{\tau}_\alpha$ as follows

$$\mathbf{q}_\alpha = \mathbf{Q}_\alpha - \frac{m_\alpha \mathbf{u}_\alpha^2}{2} n_\alpha \mathbf{u}_\alpha - \frac{5}{2} P_\alpha \mathbf{u}_\alpha - \boldsymbol{\tau}_\alpha \cdot \mathbf{u}_\alpha. \quad (\text{B.11})$$

B.1.2 Local Thermodynamic Equilibrium

By integrating (B.1) over the momentum space $\int d^3\mathbf{p}$, one gets the hydrodynamic particles conservation equation

$$\frac{\partial n_e}{\partial t} + \frac{\partial}{\partial \mathbf{r}} \cdot (n_e \mathbf{u}_e) = 0 \quad (\text{B.12})$$

in agreement with the Landau collision integral property of the section **A.3.4** of **Appendix A**

$$\int_{\mathbb{R}^3} C_{e\alpha}^L[f_e, f_\alpha](\mathbf{r}, \mathbf{p}, t) d^3\mathbf{p} = 0.$$

By integrating (B.1) multiplied by the particles momentum $m_e \mathbf{v}$ over the momentum space $\int d^3\mathbf{p} \mathbf{v}$, one gets the hydrodynamic particle momentum conservation equation

$$\begin{aligned} & m_e \left[\frac{\partial}{\partial t} (n_e \mathbf{u}_e) + \frac{\partial}{\partial \mathbf{r}} \cdot (n_e \mathbf{u}_e \otimes \mathbf{u}_e) \right] \\ &= -n_e e \left[\mathbf{E} + \frac{\mathbf{u}_e}{c} \times \mathbf{B} \right] - \frac{\partial}{\partial \mathbf{r}} \cdot (P_e \mathbf{I} - \boldsymbol{\tau}_e) + \mathbf{R}_{ei}. \end{aligned} \quad (\text{B.13})$$

Indeed, according to the Landau collision integral property (see **Appendix A, section A.2.4**), one has

$$\int_{\mathbb{R}^3} \mathbf{v} C_{ee}^L[f_e, f_e](\mathbf{r}, \mathbf{p}, t) d^3\mathbf{p} = 0.$$

Concerning electron-ion collisions, we define the friction force

$$\mathbf{R}_{ei}(\mathbf{r}, t) = \int_{\mathbb{R}^3} m_e \mathbf{v} C_{ei}^L[f_e, f_i](\mathbf{r}, \mathbf{p}, t) d^3\mathbf{p}. \quad (\text{B.14})$$

By developing (B.13) and simplifying it using (B.12), one can also deduce the hydrodynamic electron fluid velocity equation

$$\begin{aligned} & m_e n_e \left[\frac{\partial}{\partial t} + \left(\mathbf{u}_e \cdot \frac{\partial}{\partial \mathbf{r}} \right) \right] (\mathbf{u}_e) \\ &= -n_e e \left[\mathbf{E} + \frac{\mathbf{u}_e}{c} \times \mathbf{B} \right] - \frac{\partial}{\partial \mathbf{r}} \cdot (P_e \mathbf{I} - \boldsymbol{\tau}_e) + \mathbf{R}_{ei}. \end{aligned} \quad (\text{B.15})$$

By integrating (B.1) multiplied by the electron kinetic energy $m_e \mathbf{v}^2/2$ over the momentum space $\int d^3\mathbf{p} (m_e \mathbf{v}^2/2)$, one gets the hydrodynamic electron energy conservation equation

$$\begin{aligned} & \frac{\partial}{\partial t} \left(\frac{1}{2} n_e m_e \mathbf{u}_e^2 + \frac{3}{2} n_e k_B T_e \right) + \frac{\partial}{\partial \mathbf{r}} \cdot \left[\left(\frac{3}{2} n_e k_B T_e + \frac{1}{2} n_e m_e \mathbf{u}_e^2 \right) \cdot \mathbf{u}_e \right] \\ &= -\frac{\partial}{\partial \mathbf{r}} \cdot [(P_e \mathbf{I} - \boldsymbol{\tau}_e) \cdot \mathbf{u}_e] - \frac{\partial}{\partial \mathbf{r}} \cdot \mathbf{q}_e - n_e e \mathbf{u}_e \cdot \mathbf{E} + W_{ei} \end{aligned} \quad (\text{B.16})$$

Indeed, according to the Landau collision integral property (see **Appendix A, section A.2.4**), one has

$$\int_{\mathbb{R}^3} \frac{m_e \mathbf{v}^2}{2} C_{ee}^L[f_e, f_e](\mathbf{r}, \mathbf{p}, t) d^3\mathbf{p} = 0.$$

Concerning electron-ion collisions, we define the energy exchange rate

$$W_{ei}(\mathbf{r}, t) = \int_{\mathbb{R}^3} \frac{m_e \mathbf{v}^2}{2} C_{ei}^L[f_e, f_i](\mathbf{r}, \mathbf{p}, t) d^3\mathbf{p}. \quad (\text{B.17})$$

By subtracting the work of the friction force, one gets the relation

$$W_{ei}(\mathbf{r}, t) = Q_{ei} + \mathbf{R}_{ei} \cdot \mathbf{u}_e \quad (\text{B.18})$$

where

$$Q_{ei}(\mathbf{r}, t) = \int_{\mathbb{R}^3} \frac{m_e (\mathbf{v} - \mathbf{u}_e)^2}{2} C_{ei}^L[f_e, f_i](\mathbf{r}, \mathbf{p}, t) d^3\mathbf{p}$$

is the thermal electron-ion equilibration power. By developing (B.16) and using the hydrodynamic electron momentum conservation equation (B.13), one finds the electron hydrodynamic electron energy equation in the form

$$\begin{aligned} & n_e \left[\frac{\partial}{\partial t} + \left(\mathbf{u}_e \cdot \frac{\partial}{\partial \mathbf{r}} \right) \right] \left(\frac{1}{2} m_e \mathbf{u}_e^2 + \frac{3}{2} k_B T_e \right) \\ &= - \frac{\partial}{\partial \mathbf{r}} \cdot [(P_e \mathbf{I} - \boldsymbol{\tau}_e) \cdot \mathbf{u}_e] - \frac{\partial}{\partial \mathbf{r}} \cdot \mathbf{q}_e - n_e e \mathbf{E} \cdot \mathbf{u}_e + \mathbf{R}_{ei} \cdot \mathbf{u}_e + Q_{ei} \end{aligned} \quad (\text{B.19})$$

By multiplying (B.15) by $m_e \mathbf{u}_e$, one can find the hydrodynamic electron kinetic energy conservation equation

$$\begin{aligned} & n_e \left[\frac{\partial}{\partial t} + \left(\mathbf{u}_e \cdot \frac{\partial}{\partial \mathbf{r}} \right) \right] \left(\frac{1}{2} m_e \mathbf{u}_e^2 \right) \\ &= -n_e e \mathbf{E} \cdot \mathbf{u}_e - \mathbf{u}_e \cdot \frac{\partial}{\partial \mathbf{r}} \cdot (P_e \mathbf{I} - \boldsymbol{\tau}_e) + \mathbf{R}_{ei} \cdot \mathbf{u}_e. \end{aligned} \quad (\text{B.20})$$

Subtracting (B.19) by (B.20), one gets the hydrodynamic electron internal energy equation

$$C_{V,e} \left[\frac{\partial}{\partial t} + \left(\mathbf{u}_e \cdot \frac{\partial}{\partial \mathbf{r}} \right) \right] (T_e) + \frac{\partial}{\partial \mathbf{r}} \cdot \mathbf{q}_e = -P_e \frac{\partial}{\partial \mathbf{r}} \cdot \mathbf{u}_e + \boldsymbol{\tau}_e \odot \left(\frac{\partial}{\partial \mathbf{r}} \otimes \mathbf{u}_e \right) + Q_{ei}. \quad (\text{B.21})$$

By performing the same calculi for the ions starting from the Vlasov-Fokker-Planck-Landau equation for the ion distribution function $f_i = f_i(\mathbf{r}, \mathbf{p}, t)$, one gets respectively

$$\frac{\partial n_i}{\partial t} + \frac{\partial}{\partial \mathbf{r}} \cdot (n_i \mathbf{u}_i) = 0, \quad (\text{B.22})$$

$$\begin{aligned} & m_i \left[\frac{\partial}{\partial t} (n_i \mathbf{u}_i) + \frac{\partial}{\partial \mathbf{r}} \cdot (n_i \mathbf{u}_i \otimes \mathbf{u}_i) \right] \\ &= n_i Z^* e \left[\mathbf{E} + \frac{\mathbf{u}_i}{c} \times \mathbf{B} \right] - \frac{\partial}{\partial \mathbf{r}} \cdot (P_i \mathbf{I} - \boldsymbol{\tau}_i) + \mathbf{R}_{ie} \end{aligned} \quad (\text{B.23})$$

which consequently provides the non conservative form

$$\begin{aligned} & m_i n_i \left[\frac{\partial}{\partial t} + \left(\mathbf{u}_i \cdot \frac{\partial}{\partial \mathbf{r}} \right) \right] (\mathbf{u}_i) \\ &= n_i Z^* e \left[\mathbf{E} + \frac{\mathbf{u}_i}{c} \times \mathbf{B} \right] - \frac{\partial}{\partial \mathbf{r}} \cdot (P_i \mathbf{I} - \boldsymbol{\tau}_i) + \mathbf{R}_{ie}. \end{aligned} \quad (\text{B.24})$$

Also, one obtains

$$\begin{aligned} & \frac{\partial}{\partial t} \left(\frac{1}{2} n_i m_i \mathbf{u}_i^2 + \frac{3}{2} n_i k_B T_i \right) + \frac{\partial}{\partial \mathbf{r}} \cdot \left[\left(\frac{3}{2} n_i k_B T_i + \frac{1}{2} n_i m_i \mathbf{u}_i^2 \right) \cdot \mathbf{u}_i \right] \\ &= - \frac{\partial}{\partial \mathbf{r}} \cdot [(P_i \mathbf{I} - \boldsymbol{\tau}_i) \cdot \mathbf{u}_i] - \frac{\partial}{\partial \mathbf{r}} \cdot \mathbf{q}_i + n_i Z^* e \mathbf{u}_i \cdot \mathbf{E} + W_{ie} \end{aligned} \quad (\text{B.25})$$

which provides the non conservative form

$$C_{V,i} \left[\frac{\partial}{\partial t} + \left(\mathbf{u}_i \cdot \frac{\partial}{\partial \mathbf{r}} \right) \right] (T_i) + \frac{\partial}{\partial \mathbf{r}} \cdot \mathbf{q}_i = -P_i \frac{\partial}{\partial \mathbf{r}} \cdot \mathbf{u}_i + \boldsymbol{\tau}_i \odot \left(\frac{\partial}{\partial \mathbf{r}} \otimes \mathbf{u}_i \right) + Q_{ie} \quad (\text{B.26})$$

where obviously

$$\mathbf{R}_{ie} = -\mathbf{R}_{ei}, W_{ie} = -W_{ei} \text{ and thus } Q_{ie} = -Q_{ei} + \mathbf{R}_{ei} \cdot (\mathbf{u}_e - \mathbf{u}_i). \quad (\text{B.27})$$

B.2 Plasma Transport Coefficients

The system consisting of the hydrodynamic equations $\{(B.12), (B.15, B.21), (B.22), (B.24), (B.26)\}$ forms a set of 10 equations with 10 hydrodynamic unknowns $n_e, \mathbf{u}_e, T_e, n_i, \mathbf{u}_i, T_i$ assuming that the hydrodynamic fluxes $\mathbf{P}_e, \mathbf{q}_e, \mathbf{P}_i, \mathbf{q}_i, Q_{ei}$ and \mathbf{R}_{ei} are known. Considering the time scales much less than ~ 100 ps, we neglect the ion conductivity \mathbf{q}_i and the ion velocity \mathbf{u}_i in the ion conservation equations. Also, the viscosity tensors $\boldsymbol{\tau}_i$ and $\boldsymbol{\tau}_e$ and the mechanical work $-P_e(\partial/\partial \mathbf{r}) \cdot \mathbf{u}_e$ of (B.26) are neglected. In what follows, we evaluate the transport coefficients allowing to express the friction force \mathbf{R}_{ei} , the electron-ion energy exchange Q_{ei} and the electron thermal flux \mathbf{q}_e in order to close this set of 10 equations.

B.2.1 Lorentz Approximation

The hydrodynamic fluxes are found from the kinetic equation by evaluating the deviation of the electron distribution function δf_e from the local equilibrium Maxwellian function f_M . Here, we account only for the electron-ion collisions in the electron kinetic equation and also neglect the magnetic component of the Lorentz force. Then, the electron kinetic equation takes the following form (see

Appendix A, section A.3.2)

$$\frac{\partial f_e}{\partial t} + \frac{\partial}{\partial \mathbf{r}} \cdot (\mathbf{v} f_e) - \frac{\partial}{\partial \mathbf{p}} \cdot (e \mathbf{E} f_e) = \frac{\nu_{ei}(\mathbf{v})}{2} \left[\frac{1}{\sin \theta} \frac{\partial}{\partial \theta} \left(\sin \theta \frac{\partial f_e}{\partial \theta} \right) + \frac{1}{\sin^2 \theta} \frac{\partial^2 f_e}{\partial \varphi^2} \right]. \quad (\text{B.28})$$

Also, the electric field \mathbf{E} is assumed to be homogeneous, not varying with time and with a value $|\mathbf{E}| \ll E_{\text{run}} \sim m_e \bar{\nu}_{ei} v_{T,e} / e$ sufficiently small such that the electric field \mathbf{E} can be seen as a perturbation of the maximum entropy equilibrium $f_e^{(0)} = f_M$ with $\mathbf{u}_e^{(0)} = \mathbf{0}$ (see **Appendix A, section A.2.4**). By noting so

$$f_e(\mathbf{r}, \mathbf{p}, t) = f_M(\mathbf{r}, \mathbf{p}, t) + \delta f_e(\mathbf{r}, \mathbf{p}), \quad (\text{B.29})$$

one can linearize the equation assuming the electric field is a first order term $\mathbf{E} = \delta \mathbf{E}$ to get

$$-e \mathbf{E} \cdot \frac{\partial f_M}{\partial \mathbf{p}} = \frac{\nu_{ei}(\mathbf{v})}{2} \left[\frac{1}{\sin \theta} \frac{\partial}{\partial \theta} \left(\sin \theta \frac{\partial \delta f_e}{\partial \theta} \right) + \frac{1}{\sin^2 \theta} \frac{\partial^2 \delta f_e}{\partial \varphi^2} \right]. \quad (\text{B.30})$$

By expanding δf_e on the Legendre polynomial basis and by noticing that the left hand side of this equation does not depend on the azimuthal angle φ , one deduces δf_e and consequently

$$\delta \mathbf{j}_e = \mathbf{j}_e = -e \int_{\mathbb{R}^3} \mathbf{v} \delta f_e d^3 \mathbf{p} = \sigma_L \mathbf{E} \quad (\text{B.31})$$

(because $\mathbf{u}_e = \mathbf{0}$) with

$$\sigma_L = \frac{32}{3\pi} \frac{n_e e^2}{m_e \bar{\nu}_{ei}} \quad (\text{B.32})$$

called the plasma electron electrical conductivity and expressed with the averaged electron-ion collision frequency (see **Appendix A, section A.3.2**).

Recalling that the electric current is proportional to the electron mean velocity, one can find from (B.31) the expression for the friction force in the electron momentum hydrodynamic equation :

$$\mathbf{R}_{ei} = e n_e \eta_L \mathbf{j}_e \quad (\text{B.33})$$

with

$$\eta_L = \frac{1}{\sigma_L} = \frac{\pi^{3/2} m_e^{1/2} Z^* e^2 \ln \Lambda_{ei}}{(k_B T_e)^{3/2}} \quad (\text{B.34})$$

called the plasma electrical resistivity. It does not depend on the plasma density (in this approximation) but only on the plasma temperature.

To obtain an expression for the electron heat flux, one has to solve the linearized equation

$$\mathbf{v} \cdot \frac{\partial f_M}{\partial \mathbf{r}} - e \mathbf{E} \cdot \frac{\partial f_M}{\partial \mathbf{p}} = \frac{\nu_{ei}(\mathbf{v})}{2} \left[\frac{1}{\sin \theta} \frac{\partial}{\partial \theta} \left(\sin \theta \frac{\partial \delta f_e}{\partial \theta} \right) + \frac{1}{\sin^2 \theta} \frac{\partial^2 \delta f_e}{\partial \varphi^2} \right]. \quad (\text{B.35})$$

One can express the electron current density $\delta \mathbf{j}_e$ and the electron heat flux $\delta \mathbf{q}_e$ as a function of the moments of δf_e which depend on $(\partial T_e / \partial \mathbf{r})$ and \mathbf{E} . One gets the expression of the electric field \mathbf{E} by

B.2. PLASMA TRANSPORT COEFFICIENTS

considering $\delta \mathbf{j}_e = \mathbf{0}$ in order to avoid charge accumulations. Injecting the obtained expression of the electric field in the expression of $\delta \mathbf{q}_e$, one finally obtains

$$\mathbf{q}_e = \delta \mathbf{q}_e = \int_{\mathbb{R}^3} \frac{m_e \mathbf{v}_e^2}{2} \mathbf{v}_e \delta f_e d^3 \mathbf{p}_e = -\kappa_L \frac{\partial T_e}{\partial \mathbf{r}} \quad (\text{B.36})$$

with

$$\kappa_L = \frac{128}{3\pi} \frac{n_e k_B^2 T_e}{m_e \bar{\nu}_{ei}} = 0.4 \frac{20 (2/\pi)^{3/2} k_B^{7/2} T_e^{5/2}}{m_e^{1/2} Z^* e^4 \ln \Lambda_{ei}} \quad (\text{B.37})$$

the plasma electron thermal conductivity. Besides, one can easily notice that the ratio

$$\gamma_L = \frac{\kappa_L}{\sigma_L T_e} = 4 \left(\frac{k_B}{e} \right)^2 \quad (\text{B.38})$$

is a constant called the Lorenz constant.

Concerning the electron-ion energy exchange Q_{ei} , it can be obtained directly by using the Maxwell-Boltzmann distribution function (B.5) and the full Landau electron-ion collision integral, i.e. without neglecting the term $\propto m_e/m_i$ (see for example [Landau and Lifshitz, 1981] p.173). It reads

$$\begin{aligned} Q_{ie}(\mathbf{r}, t) &= \int_{\mathbb{R}^3} \frac{m_i (\mathbf{v} - \mathbf{u}_i)^2}{2} C_{ie}^L[f_i, f_e](\mathbf{r}, \mathbf{p}, t) d^3 \mathbf{p} \\ &= 2 \frac{m_e}{m_i} C_{V,e} \bar{\nu}_{ei} (T_e - T_i) \\ &= -Q_{ei}(\mathbf{r}, t) - \mathbf{R}_{ei}(\mathbf{u}_e - \mathbf{u}_i). \end{aligned} \quad (\text{B.39})$$

B.2.2 Electron-electron Collision Contribution to the Hydrodynamic Fluxes

By taking into account the electron-electron collision term, the linearized equation (B.35) becomes

$$\begin{aligned} &\mathbf{v} \cdot \frac{\partial f_M}{\partial \mathbf{r}} - e \mathbf{E} \cdot \frac{\partial f_M}{\partial \mathbf{p}} \\ &= C_{ee}^L[f_M, \delta f_e] + C_{ee}^L[\delta f_e, f_M] + \frac{\nu_{ei}(\mathbf{v})}{2} \left[\frac{1}{\sin \theta} \frac{\partial}{\partial \theta} \left(\sin \theta \frac{\partial \delta f_e}{\partial \theta} \right) + \frac{1}{\sin^2 \theta} \frac{\partial^2 \delta f_e}{\partial \varphi^2} \right]. \end{aligned} \quad (\text{B.40})$$

[Spitzer and Härm, 1953] have shown that the electron-electron collision contribution to the electrical and thermal conductivities can be expressed as follows

$$\sigma_{Sp} = \gamma_E \sigma_L \quad \text{and} \quad \kappa_{Sp} = \frac{\epsilon \delta_T}{0.4} \kappa_L \quad (\text{B.41})$$

where γ_E and $\epsilon \delta_T$ are correction factors, which can be fitted by functions of the ionization state Z^* from the tabulations provided by [Spitzer and Härm, 1953]. They read

$$\gamma_E \approx \frac{Z^* + 0.9833}{Z^* + 2.4101}$$

and

$$\frac{\epsilon\delta_T}{0.4} \approx \frac{Z^*}{Z^* + 0.2 \ln Z^* + 3.44}.$$

The expression proposed by [Brysk et al., 1975] for $\epsilon\delta_T$ is less accurate than the expression proposed here because it does not reproduce the Spitzer results $(\kappa_{Sp}/\sigma_{Sp}T_e) \rightarrow (\kappa_L/\sigma_L T_e) = 4(k_B/e)^2$ when $Z^* \rightarrow \infty$ [Ribeyre, 2014]. The parameters δ_T and δ_E account for the electron-electron collisions while ϵ accounts for the reduction of the heat flux due the electrostatic field induced by temperature gradients in a steady state.

One may ask himself why electron-electron collisions modify the electric conductivity since the hydrodynamic moments of the electron-electron collision terms vanish, giving $\mathbf{R}_{ee} = \mathbf{0}$ and $Q_{ee} = 0$, according to the properties of the Landau collision integral. This is actually a purely kinetic effect due to the "rearrangement" of the electron momentum spectrum, due to electron-electron collisions, such that the electron-ion collisions ($\propto 1/v^3$) are enhanced leading to larger slowing downs of the electrons by colliding the ions. Indeed, in the limit $Z^* \rightarrow \infty$ where electron-electron collisions are negligible compared to electron-ion collisions, one can notice that $\sigma_{Sp} \rightarrow \sigma_L$, $\kappa_{Sp} \rightarrow \kappa_L$ and that the Lorenz factor $(\kappa_{Sp}/\sigma_{Sp}T_e) \rightarrow (\kappa_L/\sigma_L T_e) = 4(k_B/e)^2$. For other specific values of Z^* , one gets according to [Spitzer and Härm, 1953] :

$$\frac{\kappa_{Sp}}{\sigma_{Sp}T_e} \approx 1.6 \left(\frac{k_B}{e} \right)^2 \text{ for } Z^* = 1$$

$$\frac{\kappa_{Sp}}{\sigma_{Sp}T_e} \approx 2.2 \left(\frac{k_B}{e} \right)^2 \text{ for } Z^* = 2$$

$$\frac{\kappa_{Sp}}{\sigma_{Sp}T_e} \approx 2.7 \left(\frac{k_B}{e} \right)^2 \text{ for } Z^* = 4$$

$$\frac{\kappa_{Sp}}{\sigma_{Sp}T_e} \approx 3.5 \left(\frac{k_B}{e} \right)^2 \text{ for } Z^* = 16$$

B.2.3 Transport Coefficients in an External Magnetic Field

The transport in the external homogeneous magnetic field was considered by [Braginskii, 1965]. The magnetic field may strongly affect the electron fluxes if the electron cyclotron frequency $\omega_{ce} = |e\mathbf{B}|/m_e c$ is of the same order of magnitude than the electron-ion collision frequency $\bar{\nu}_{ei}$. The electron kinetic equation in the external magnetic field \mathbf{B} (B.40) reads

$$\begin{aligned} & \mathbf{v} \cdot \frac{\partial f_M}{\partial \mathbf{r}} - e\mathbf{E} \cdot \frac{\partial f_M}{\partial \mathbf{p}} - e \frac{\mathbf{v}}{c} \times \mathbf{B} \cdot \frac{\partial \delta f_e}{\partial \mathbf{p}} \\ & = C_{ee}^L[f_M, \delta f_e] + C_{ee}^L[\delta f_e, f_M] + \frac{\nu_{ei}(\mathbf{v})}{2} \left[\frac{1}{\sin \theta} \frac{\partial}{\partial \theta} \left(\sin \theta \frac{\partial \delta f_e}{\partial \theta} \right) + \frac{1}{\sin^2 \theta} \frac{\partial^2 \delta f_e}{\partial \varphi^2} \right]. \end{aligned} \quad (\text{B.42})$$

B.2. PLASMA TRANSPORT COEFFICIENTS

The magnetic field introduces an anisotropy of the fluxes that are not parallel to the generalized forces any more. Consequently, transport coefficients become tensors :

$$\mathbf{R}_{ei} = \mathbf{R}_u + \mathbf{R}_T \quad (\text{B.43})$$

with

$$\mathbf{R}_u = en_e \boldsymbol{\eta} \cdot \mathbf{j} = en_e \eta_{\parallel} j_{\parallel} + en_e \eta_{\perp} j_{\perp} + en_e \eta_{\wedge} \frac{\mathbf{B}}{|\mathbf{B}|} \times \mathbf{j}$$

and

$$\mathbf{R}_T = -k_B \boldsymbol{\beta} \cdot \frac{\partial T_e}{\partial \mathbf{r}} = -\beta_{\parallel} k_B \left(\frac{\partial T_e}{\partial \mathbf{r}} \right)_{\parallel} - \beta_{\perp} k_B \left(\frac{\partial T_e}{\partial \mathbf{r}} \right)_{\perp} - \beta_{\wedge} k_B \frac{\mathbf{B}}{|\mathbf{B}|} \times \frac{\partial T_e}{\partial \mathbf{r}}.$$

The notations \parallel and \perp define the components for the generalized forces (current and temperature gradient) parallel and perpendicular to the magnetic field direction. The first term \mathbf{R}_u is due to the friction of electrons on the ions as already presented in the previous section while \mathbf{R}_T is due to the temperature gradient effect. Here, \mathbf{j} is the plasma current density evaluated in the quasineutral approximation :

$$\mathbf{j} = -en_e \mathbf{u}_e + Z^* en_i \mathbf{u}_i = \rho_c \mathbf{u} - en_e (\mathbf{u}_e - \mathbf{u}_i) = -en_e (\mathbf{u}_e - \mathbf{u}_i).$$

Analogously, the electron heat flux consists of two parts

$$\mathbf{q}_e = \mathbf{q}_u + \mathbf{q}_T \quad (\text{B.44})$$

with

$$\mathbf{q}_u = \frac{k_B T_e}{n_e e} \boldsymbol{\beta} \cdot \mathbf{j} = \beta_{\parallel} \frac{k_B T_e}{n_e e} j_{\parallel} + \beta_{\perp} \frac{k_B T_e}{n_e e} j_{\perp} + \beta_{\wedge} \frac{k_B T_e}{n_e e} \frac{\mathbf{B}}{|\mathbf{B}|} \times \mathbf{j}$$

and

$$\mathbf{q}_T = -\boldsymbol{\kappa}_e = -\kappa_{\parallel} \left(\frac{\partial T_e}{\partial \mathbf{r}} \right)_{\parallel} - \kappa_{\perp} \left(\frac{\partial T_e}{\partial \mathbf{r}} \right)_{\perp} - \kappa_{\wedge} \frac{\mathbf{B}}{|\mathbf{B}|} \times \frac{\partial T_e}{\partial \mathbf{r}}.$$

The components of the tensors are

$$\begin{aligned} \kappa_{\perp} &= \frac{n_e k_B^2 T_e}{m_e \bar{\nu}_{ei}} \frac{\gamma_1' x^2 + \gamma_0'}{\Delta} \\ \kappa_{\wedge} &= \frac{n_e k_B^2 T_e}{m_e \bar{\nu}_{ei}} \frac{x (\gamma_1'' x^2 + \gamma_0'')}{\Delta} \\ \eta_{\perp} &= \frac{1}{\sigma_{\perp}} = \frac{m_e \bar{\nu}_{ei}}{n_e e^2} \left(1 - \frac{\alpha_1' x^2 + \alpha_0'}{\Delta} \right) \\ \eta_{\wedge} &= \frac{1}{\sigma_{\wedge}} = \frac{m_e \bar{\nu}_{ei}}{n_e e^2} \frac{x (\alpha_1'' x^2 + \alpha_0'')}{\Delta} \\ \beta_{\parallel} &= n_e \frac{\beta_0'}{\delta_0} \end{aligned}$$

$$\beta_{\perp} = n_e \frac{\beta'_1 x^2 + \beta'_0}{\Delta}$$

and $\beta_{\parallel} = n_e \frac{x(\beta''_1 x^2 + \beta''_0)}{\Delta}$

where $\Delta = x^4 + \delta_1 x^2 + \delta_0$ and $x = \omega_{ce}/\bar{v}_{ei}$ while the transport coefficients η_{\parallel} and κ_{\parallel} in the \parallel direction are defined by equations (B.41). The parameters in these expressions depend only on the ionization state Z^* :

$$\delta_0 \approx \left(\left(\frac{1.3008}{Z^*} + 1.5956 \right) \frac{1}{Z^*} + 0.7778 \right) \frac{1}{Z^*} + 0.0961$$

$$\delta_1 \approx \left(\frac{1.35}{Z^*} + 5.958 \right) \frac{1}{Z^*} + 7.482$$

$$\alpha'_0 \approx \left(\left(\frac{0.3008}{Z^*} + 0.976 \right) \frac{1}{Z^*} + 0.4924 \right) \frac{1}{Z^*} + 0.0678$$

$$\alpha''_0 \approx \left(\frac{0.3714}{Z^*} + 0.3142 \right) \frac{1}{Z^*} + 0.094$$

$$\alpha'_1 \approx \frac{1.786}{Z^*} + 4.630$$

$$\alpha''_1 \approx 1.704$$

$$\beta'_0 \approx \left(\left(\frac{0.3768}{Z^*} + 1.2998 \right) \frac{1}{Z^*} + 0.8583 \right) \frac{1}{Z^*} + 0.146$$

$$\beta''_0 \approx \left(\frac{0.7215}{Z^*} + 1.4545 \right) \frac{1}{Z^*} + 0.877$$

$$\beta'_1 \approx \frac{1.303}{Z^*} + 3.798$$

$$\beta''_1 \approx 1.50$$

$$\gamma'_0 \approx \left(\left(\frac{0.909}{Z^*} + 4.405 \right) \frac{1}{Z^*} + 5.406 \right) \frac{1}{Z^*} + 1.20$$

$$\gamma''_0 \approx \left(\frac{2.31}{Z^*} + 9.31 \right) \frac{1}{Z^*} + 10.23$$

$$\gamma'_1 \approx \frac{1.414}{Z^*} + 3.250$$

$$\gamma''_1 \approx 2.50$$

B.2.4 Electron Degeneracy Corrections

The transport coefficients in the case of degenerated electrons were considered by [Lee and More, 1984]. They considered a linearized kinetic equation in the BGK approximation (see **Appendix A section**

B.2. PLASMA TRANSPORT COEFFICIENTS

A.4.1) with the Fermi-Dirac distribution function

$$f_{\text{FD}}(\mathbf{r}, \mathbf{p}, t) = \frac{1}{1 + \exp\left[\frac{m_e(\mathbf{v} - \mathbf{u}_e)^2}{2k_B T_e} - \frac{\mu}{k_B T_e}\right]} \quad (\text{B.45})$$

instead of the Maxwell-Boltzmann distribution function (B.5). The chemical potential μ is defined by the normalization of Fermi-Dirac distribution function to the electron density n_e

$$n_e(\mathbf{r}, t) = \int_{\mathbb{R}^3} f_{\text{FD}}(\mathbf{r}, \mathbf{p}_\alpha, t) d^3 \mathbf{p}_e.$$

The transport coefficients in the case without external magnetic read

$$\eta = \frac{m_e \bar{\nu}_{ei}}{n_e e^2} \frac{1}{A^\alpha \left(\frac{\mu}{k_B T_e}\right)} \quad (\text{B.46})$$

and

$$\kappa = \frac{n_e k_B^2 T_e}{m_e \bar{\nu}_{ei}} A^\beta \left(\frac{\mu}{k_B T_e}\right) \quad (\text{B.47})$$

where the averaged electron-ion collision frequency is given by

$$\bar{\nu}_{ei} = \frac{2\sqrt{2}\pi(Z^*)^2 n_i e^4 \ln \Lambda_{ei}}{3\sqrt{m_e}(k_B T_e)^{3/2} \left[1 + \exp\left(-\frac{\mu}{k_B T_e}\right)\right] F_{1/2}\left(\frac{\mu}{k_B T_e}\right)}. \quad (\text{B.48})$$

The expression of the electron-ion coupling power Q_{ei} (B.39) depending on $\bar{\nu}_{ei}$ is therefore also modified by the electron degeneracy according to (B.48). Here,

$$A^\alpha \left(\frac{\mu}{k_B T_e}\right) = \frac{4}{3} \frac{F_2\left(\frac{\mu}{k_B T_e}\right)}{\left[1 + \exp\left(-\frac{\mu}{k_B T_e}\right)\right] \left[F_{1/2}\left(\frac{\mu}{k_B T_e}\right)\right]^2}$$

and

$$A^\beta \left(\frac{\mu}{k_B T_e}\right) = \frac{20}{9} \frac{F_4\left(\frac{\mu}{k_B T_e}\right) \left[1 - \frac{16F_4\left(\frac{\mu}{k_B T_e}\right)^2}{15F_2\left(\frac{\mu}{k_B T_e}\right) F_4\left(\frac{\mu}{k_B T_e}\right)}\right]}{\left[1 + \exp\left(-\frac{\mu}{k_B T_e}\right)\right] \left[F_{1/2}\left(\frac{\mu}{k_B T_e}\right)\right]^2}$$

where

$$F_j \left(\frac{\mu}{k_B T_e}\right) = \int_0^\infty \frac{t^j}{1 + \exp\left(t - \frac{\mu}{k_B T_e}\right)} dt$$

are the Fermi-Dirac integrals (There is a mistake in the original paper [Lee and More, 1984] concerning the numerator of A^α , it is F_2 and not F_3). Thus, according to [Lee and More, 1984] the Lorenz factor reads

$$\gamma_L = \frac{A^\alpha \left(\frac{\mu}{k_B T_e} \right)}{A^\beta \left(\frac{\mu}{k_B T_e} \right)} \left(\frac{k_B}{e} \right)^2.$$

In the non-degenerate limit i.e. when $\mu/k_B T_e \rightarrow -\infty$, one has $A^\alpha \rightarrow 32/3\pi$ and $A^\beta \rightarrow 128/3\pi$ which reproduces the transport coefficients in the non-degenerate case considered by [Spitzer and Härm, 1953] without the electron-electron correction factors. At the complete degeneracy limit i.e. when $\mu/k_B T_e \rightarrow \infty$, the conductivities of totally degenerated plasmas are recovered. Indeed, one has $A^\alpha \rightarrow 1$, $A^\beta \rightarrow \pi^2/3$ and $\bar{\nu}_{ei} \rightarrow 3\pi\hbar^3/2m_e Z^* e^4 \ln \Lambda_{ei}$ (second mistake in [Lee and More, 1984] where it is written 4 and not 2 in the denominator) which agree with the results given by [Hubbard, 1966]

$$\kappa_H = \frac{2^{1/2}\pi k_B (k_B T_e) (k_B T_F)^{3/2}}{3 m_e^{1/2} e^4 Z^* \ln \Lambda_{ei}} \text{ and } \eta_H = \gamma_L \frac{T_e}{\kappa_e}. \quad (\text{B.49})$$

Here, the empirical Wiedemann–Franz law for metals $\gamma_L = (\pi^2/3)(k_B/e)^2$ [Franz and Wiedemann, 1853] is also recovered. The only difference with the results found by [Hubbard, 1966] is the Coulomb logarithm which is defined in [Hubbard, 1966] as $\ln \Lambda_{ei} = 1/G_\Gamma(\kappa_F)$ where $\Gamma = Z^{*2} e^4 / k_B r_i T_i$ is the ion-ion coupling parameter and $\kappa_F = r_i (2m_e k_B T_F)^{1/2} / \hbar$ the Fermi wavenumber. [Hubbard, 1966] provides a tabulation of G_Γ depending on Γ and κ_F .

B.3 Radiation Hydrodynamic Code CHIC

B.3.1 Monofluid Hydrodynamic Equations

For a plasma consisting of electrons and one ion species, one can define the mass density

$$\rho_m = n_e m_e + n_i m_i, \quad (\text{B.50})$$

the momentum flux

$$\rho_m \mathbf{u} = m_e n_e \mathbf{u}_e + m_i n_i \mathbf{u}_i \quad (\text{B.51})$$

where \mathbf{u} is the mean velocity, the charge density

$$\rho_c = -en_e + Z^* en_i, \quad (\text{B.52})$$

the current density

$$\mathbf{j} = -en_e \mathbf{u}_e + Z^* en_i \mathbf{u}_i = \rho_c \mathbf{u}_i + en_e (\mathbf{u}_i - \mathbf{u}_e), \quad (\text{B.53})$$

B.3. RADIATION HYDRODYNAMIC CODE CHIC

the scalar plasma pressure

$$P = P_e + P_i \quad (\text{B.54})$$

and a plasma viscosity tensor

$$\boldsymbol{\tau} = \boldsymbol{\tau}_e + \boldsymbol{\tau}_i, \quad (\text{B.55})$$

the specific internal energy

$$U_m = \frac{U_e + U_i}{\rho_m} = \varepsilon_e + \varepsilon_i \text{ with } \forall \alpha \in \{i, e\}, \varepsilon_\alpha = U_\alpha / \rho_m, \quad (\text{B.56})$$

and the heat flux

$$\mathbf{q} = \mathbf{q}_e + \mathbf{q}_i. \quad (\text{B.57})$$

With these definitions, one can obtain the monofluid hydrodynamic continuity equation from (B.12) and (B.22) :

$$\frac{\partial \rho_m}{\partial t} + \frac{\partial}{\partial \mathbf{r}} \cdot (\rho_m \mathbf{u}) = 0 \quad (\text{B.58})$$

and the charge continuity equation

$$\frac{\partial \rho_c}{\partial t} + \frac{\partial}{\partial \mathbf{r}} \cdot \mathbf{j} = 0. \quad (\text{B.59})$$

The monofluid conservation equation for the particles momentum is obtained by adding Equation (B.13) and Equation (B.23) :

$$\frac{\partial}{\partial t} (\rho_m \mathbf{u}) + \frac{\partial}{\partial \mathbf{r}} \cdot (\rho_m \mathbf{u} \otimes \mathbf{u}) = \rho_c \mathbf{E} + \frac{\mathbf{j}}{c} \times \mathbf{B} - \frac{\partial}{\partial \mathbf{r}} \cdot (P \mathbf{I} - \boldsymbol{\tau}). \quad (\text{B.60})$$

Substracting (B.58) from (B.60), one obtains

$$\rho_m \left[\frac{\partial}{\partial t} + \left(\mathbf{u} \cdot \frac{\partial}{\partial \mathbf{r}} \right) \right] (\mathbf{u}) = \rho_c \mathbf{E} + \frac{\mathbf{j}}{c} \times \mathbf{B} - \frac{\partial}{\partial \mathbf{r}} \cdot (P \mathbf{I} - \boldsymbol{\tau}). \quad (\text{B.61})$$

By adding (B.16) and (B.25), one obtains the monofluid energy conservation equation

$$\begin{aligned} \frac{\partial}{\partial t} \left[\rho_m \left(U_m + \frac{\mathbf{u}^2}{2} \right) \right] + \frac{\partial}{\partial \mathbf{r}} \cdot \left\{ \left[\rho_m \left(U_m + \frac{\mathbf{u}^2}{2} \right) + P \right] \cdot \mathbf{u} \right\} \\ = \frac{\partial}{\partial \mathbf{r}} \cdot (\boldsymbol{\tau} \cdot \mathbf{u}) - \frac{\partial}{\partial \mathbf{r}} \cdot \mathbf{q} + \mathbf{j} \cdot \mathbf{E} \end{aligned} \quad (\text{B.62})$$

which provides by taking into account (B.58) and (B.60) the monofluid specific internal energy conservation equation

$$\rho_m \left[\frac{\partial}{\partial t} + \left(\mathbf{u} \cdot \frac{\partial}{\partial \mathbf{r}} \right) \right] (U_m) + \frac{\partial}{\partial \mathbf{r}} \cdot \mathbf{q} = -P \frac{\partial}{\partial \mathbf{r}} \cdot \mathbf{u} + \boldsymbol{\tau} \odot \left(\frac{\partial}{\partial \mathbf{r}} \otimes \mathbf{u} \right) + \mathbf{j} \cdot \mathbf{E}. \quad (\text{B.63})$$

It is usually assumed that the plasma is quasi-neutral ($\rho_c = 0$). In this case, (B.58), (B.61) and (B.63) are commonly called the **Navier-Stokes equations**. In the particular case where the electron and

ion populations have thermalized ($T_e = T_i = T$) in addition to the quasi-neutrality assumption, one can write Equation (B.63) as

$$C_V \left[\frac{\partial}{\partial t} + \left(\mathbf{u} \cdot \frac{\partial}{\partial \mathbf{r}} \right) \right] (T) + \frac{\partial}{\partial \mathbf{r}} \cdot \mathbf{q} = -P \frac{\partial}{\partial \mathbf{r}} \cdot \mathbf{u} + \boldsymbol{\tau} \odot \left(\frac{\partial}{\partial \mathbf{r}} \otimes \mathbf{u} \right) + \mathbf{j} \cdot \mathbf{E} \quad (\text{B.64})$$

where

$$C_V dT = \rho_m dU_m \text{ and } C_V = \frac{3}{2} k_B (Z^* + 1) n_i$$

is the plasma thermal capacity. Still under the same assumption, according to the first principle of Thermodynamics, one has

$$dU_m = \delta Q_m - P d \left(\frac{1}{\rho_m} \right)$$

while according to the second principle of Thermodynamics

$$\delta Q_m = T dH_m \geq 0$$

where it has been noted δQ_m the infinitesimal specific heat energy exchange and H_m the specific entropy (usually noted s but we prefer H_m to relate it with the Boltzmann kinetic theory, see **Appendix A, section A.1.5**), one can obtain the time evolution of the plasma specific entropy according to (B.63)

$$\rho_m \left[\frac{\partial}{\partial t} + \mathbf{u} \cdot \frac{\partial}{\partial \mathbf{r}} \right] (H_m) = \frac{1}{T} \left[\boldsymbol{\tau} \odot \left(\frac{\partial}{\partial \mathbf{r}} \otimes \mathbf{u} \right) - \frac{\partial}{\partial \mathbf{r}} \cdot \mathbf{q} \right]. \quad (\text{B.65})$$

By making the assumption $\boldsymbol{\tau} = \mathbf{0}$, $\mathbf{j} = \mathbf{0}$ and $\mathbf{q} = \mathbf{0}$, one gets **Euler's equations** from fluid mechanics:

$$\frac{\partial \rho_m}{\partial t} + \frac{\partial}{\partial \mathbf{r}} \cdot (\rho_m \mathbf{u}) = 0, \quad (\text{B.66})$$

$$\rho_m \left[\frac{\partial}{\partial t} + \left(\mathbf{u} \cdot \frac{\partial}{\partial \mathbf{r}} \right) \right] (\mathbf{u}) = -\frac{\partial P}{\partial \mathbf{r}} \quad (\text{B.67})$$

and

$$\rho_m \left[\frac{\partial}{\partial t} + \left(\mathbf{u} \cdot \frac{\partial}{\partial \mathbf{r}} \right) \right] (U_m) = -P \frac{\partial}{\partial \mathbf{r}} \cdot \mathbf{u}. \quad (\text{B.68})$$

B.3.2 Radiation Hydrodynamic Code CHIC

The Hydrodynamic CHIC code solves the monofluid two temperatures hydrodynamic equations under the assumption of zero tensor viscosity ($\boldsymbol{\tau} = \mathbf{0}$) and small current density $|\mathbf{j}| \ll n_e e c$ for a quasi neutral plasma ($\rho_c = 0$). The code solves the following equations (B.58) and (B.61) :

$$\begin{aligned} \frac{\partial \rho_m}{\partial t} + \frac{\partial}{\partial \mathbf{r}} \cdot (\rho_m \mathbf{u}) &= 0, \\ \rho_m \left[\frac{\partial}{\partial t} + \left(\mathbf{u} \cdot \frac{\partial}{\partial \mathbf{r}} \right) \right] (\mathbf{u}) &= -\frac{\partial}{\partial \mathbf{r}} (P_e + P_i) \end{aligned}$$

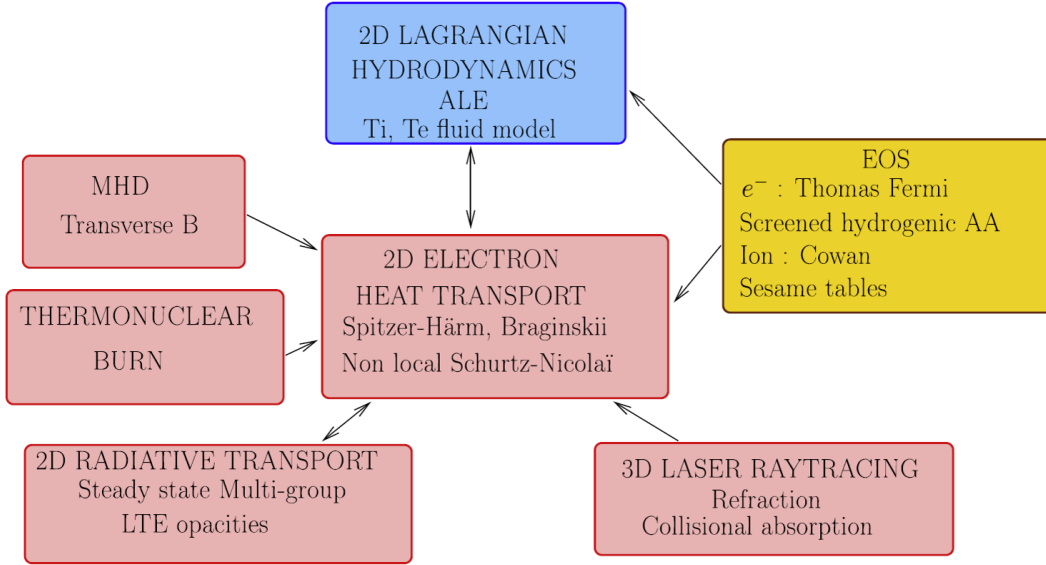


Figure B.1: CHIC main packages [Breil et al., 2011]

and Equation (B.63) which is split in two equations. One for the plasma electrons

$$\rho_m \left[\frac{\partial}{\partial t} + \left(\mathbf{u} \cdot \frac{\partial}{\partial \mathbf{r}} \right) \right] (\varepsilon_e) + \frac{\partial}{\partial \mathbf{r}} \cdot \mathbf{q}_e = -P_e \frac{\partial}{\partial \mathbf{r}} \cdot \mathbf{u} - Q_{ie} + W_{e,\text{ext}}$$

for which the collisional term $-\mathbf{R}_{ei}(\mathbf{u}_e - \mathbf{u}_i)$ from Q_{ei} has been neglected (since in practice, \mathbf{u}_e and \mathbf{u}_i are unknown here) and another one for the plasma ions

$$\rho_m \left[\frac{\partial}{\partial t} + \left(\mathbf{u} \cdot \frac{\partial}{\partial \mathbf{r}} \right) \right] (\varepsilon_i) + \frac{\partial}{\partial \mathbf{r}} \cdot \mathbf{q}_i = -P_i \frac{\partial}{\partial \mathbf{r}} \cdot \mathbf{u} + Q_{ie}$$

where it has been noted $W_{e,\text{ext}} = W_{\text{las}} + W_{\text{rad}} + W_{\text{fus}} + W_{\text{fe}}$ the source terms due to laser plasma interaction W_{las} , radiation heating W_{rad} , nuclear fusion reactions heating W_{fus} or fast electron beam heating W_{fe} (cf. **Chapter 10, section 10.2**). Each heating source term is computed with a special package, as shown in **Figure B.1**. $P_e = P_e(\rho_m, T_e)$, $P_i = P_i(\rho, T_i)$, $\varepsilon_e = \varepsilon_e(\rho, T_e)$ and $\varepsilon_i = \varepsilon_i(\rho, T_i)$ are given by the material Equation of State (Thomas-Fermi for the electrons, Cowan for the ions and/or Sesame tables). \mathbf{q}_e can be computed with the Spitzer, the Braginskii or the Non Local Schurtz-Nicolaï-Busquet model [Schurtz et al., 2000] while Q_{ie} is given by (B.39). These hydrodynamic equations are solved by using the **Lagrangian formalism** i.e. by presenting the transport terms with a derivative along the fluid trajectories

$$\frac{d}{dt} = \frac{\partial}{\partial t} + \mathbf{u} \cdot \frac{\partial}{\partial \mathbf{r}}.$$

By noting with a superscript i the index of the fluid streamline denoted by i , $V_m = 1/\rho_m$ and $\forall \xi \in \{\rho_m, V_m, \mathbf{u}, P_e, P_i, P, T_e, T_i, \varepsilon_e, \varepsilon_i, Q_{ei}, W_{e,\text{ext}}, Q_{ie}\}$, $\widehat{\xi}^i(t) = \xi(\widehat{\mathbf{r}}^i, t)$ where

$$\frac{d\widehat{\mathbf{r}}^i}{dt} = \widehat{\mathbf{u}}^i(t) = \mathbf{u}(\widehat{\mathbf{r}}^i, t) \text{ knowing the initial condition } \widehat{\mathbf{r}}^i(t=0),$$

these equations read

$$\widehat{\rho}_m^i \frac{d\widehat{V}_m^i}{dt} - \left[\frac{\partial}{\partial \mathbf{r}} \cdot \mathbf{u} \right] (\widehat{\mathbf{r}}^i, t) = 0, \quad (\text{B.69})$$

$$\widehat{\rho}_m^i \frac{d\widehat{\mathbf{u}}^i}{dt} + \left[\frac{\partial}{\partial \mathbf{r}} (P_e + P_i) \right] (\widehat{\mathbf{r}}^i, t) = 0, \quad (\text{B.70})$$

$$\widehat{\rho}_m^i \left[\frac{d\widehat{\varepsilon}_e^i}{dt} + \widehat{P}_e^i \frac{d\widehat{V}_m^i}{dt} \right] - \left[\frac{\partial}{\partial \mathbf{r}} \cdot \left(\kappa_e \frac{\partial T_e}{\partial \mathbf{r}} \right) \right] (\widehat{\mathbf{r}}^i, t) = -\widehat{Q}_{ie}^i + \widehat{W}_{e,\text{ext}}^i \quad (\text{B.71})$$

and

$$\widehat{\rho}_m^i \left[\frac{d\widehat{\varepsilon}_i^i}{dt} + \widehat{P}_i^i \frac{d\widehat{V}_m^i}{dt} \right] - \left[\frac{\partial}{\partial \mathbf{r}} \cdot \left(\kappa_i \frac{\partial T_i}{\partial \mathbf{r}} \right) \right] (\widehat{\mathbf{r}}^i, t) = \widehat{Q}_{ie}^i. \quad (\text{B.72})$$

Indeed, as mentioned, the time derivative of ξ following a fluid particle reads

$$\frac{d\widehat{\xi}^i}{dt} = \frac{\partial \xi}{\partial t} (\widehat{\mathbf{r}}^i, t) + \mathbf{u}(\widehat{\mathbf{r}}^i, t) \cdot \frac{\partial \xi}{\partial \mathbf{r}} (\widehat{\mathbf{r}}^i, t).$$

Also, for numerical reasons which will be explained further, Equation (B.62) is simplified according to (B.58) and expressed in the **Lagrangian formalism** to give

$$\widehat{\rho}_m^i \frac{d\widehat{E}^i}{dt} + \left[\frac{\partial}{\partial \mathbf{r}} \cdot (P\mathbf{u}) \right] (\widehat{\mathbf{r}}^i, t) = - \left[\frac{\partial}{\partial \mathbf{r}} \cdot (\mathbf{q}) \right] (\widehat{\mathbf{r}}^i, t) \quad (\text{B.73})$$

where $E = U_m + (\mathbf{u}^2/2)$ (There is a mistake in [Breil et al., 2011] concerning the second term of the left hand side of this equation [?]). These equations are solved in 2D Cartesian (x, y) or in 2D cylindrical (z, r) assuming an axial symmetry (azimuthal invariance assumption).

Numerical Schemes :

The numerical computation of Equations (B.69), (B.70), (B.71) and (B.72) is split in two steps

1. On the interval between the time step t_n and $t_* = t_n + \Delta t^*$, the system of Equations (B.69), (B.70) and (B.73) is solved without taking into account the thermal conduction according to a cell-centered discretization of each fluid mesoparticle i [Maire et al., 2007] and a high order Lagrangian finite volume scheme based on the acoustic generalized Riemann problem solved

using a least squares procedure followed by a slope limitation procedure [Maire, 2009]

$$\begin{cases} \tilde{\rho}_m^{i,n} \left[\frac{\widehat{V}_m^* - \widehat{V}_m^n}{\Delta t^*} \right]^i - \left[\frac{\partial}{\partial \mathbf{r}} \cdot \mathbf{u} \right]^{n,i} = 0 \\ \tilde{\rho}_m^{i,n} \left[\frac{\widehat{\mathbf{u}}^* - \widehat{\mathbf{u}}^n}{\Delta t^*} \right]^i + \left[\frac{\partial}{\partial \mathbf{r}} \cdot (P\mathbf{I}) \right]^{i,n} = 0 \\ \tilde{\rho}_m^{i,n} \left[\frac{E^* - E^n}{\Delta t^*} \right]^i + \left[\frac{\partial}{\partial \mathbf{r}} \cdot (P\mathbf{u}) \right]^{n,i} = 0 \end{cases} \quad (\text{B.74})$$

Then, by assuming that the electron evolution at this time step is isentropic in such a way that the entropy is deposited into the ion internal energy, one has to solve

$$\tilde{\rho}_m^i \left[\frac{d\widehat{\varepsilon}_e^i}{dt} + \widehat{P}_e^i \frac{d\widehat{V}_m^i}{dt} \right] = 0$$

which gives numerically

$$\left[\frac{\widehat{\varepsilon}_e^* - \widehat{\varepsilon}_e^n}{\Delta t^*} \right]^i + \widehat{P}_e^{i,n} \left[\frac{\widehat{V}_m^* - \widehat{V}_m^n}{\Delta t^*} \right]^i = 0. \quad (\text{B.75})$$

It allows to deduce $\widehat{\varepsilon}_e^{i,*} = \widehat{E}^{i,*} - \widehat{\varepsilon}_e^{i,*} - [(\widehat{\mathbf{u}}^{i,*})^2/2]$.

2. Then, the energy transfer between ions and electrons and the electron heating is solved on the interval between t_* and t_{n+1} using a Newton algorithm while the non linear conduction is solved implicitly with the discretization of the thermal diffusion operator [Breil and Maire, 2007]

$$\begin{cases} \tilde{\rho}_m^i \widehat{C}_{V,e,m}^i \frac{d\widehat{T}_e^i}{dt} - \left[\frac{\partial}{\partial \mathbf{r}} \cdot \left(\kappa_e \frac{\partial T_e}{\partial \mathbf{r}} \right) \right] (\widehat{\mathbf{r}}^i, t) = -\widehat{Q}_{ie}^i + \widehat{W}_{e,\text{ext}}^i \\ \tilde{\rho}_m^i \widehat{C}_{V,i,m}^i \frac{d\widehat{T}_i^i}{dt} - \left[\frac{\partial}{\partial \mathbf{r}} \cdot \left(\kappa_i \frac{\partial T_i}{\partial \mathbf{r}} \right) \right] (\widehat{\mathbf{r}}^i, t) = \widehat{Q}_{ie}^i \end{cases} \quad (\text{B.76})$$

where it has been noted $\forall \alpha \in \{e, i\}$, $C_{V,\alpha,m} = d\varepsilon_\alpha/dT_\alpha$ the specific thermal capacity.

B.3.3 CHIC MHD Package

In order to study the effects of the magnetic fields on the thermal conduction according to the Braginskii expression for the thermal conduction coefficient κ_e , a MHD package has been implemented in CHIC by [Schurtz et al., 2007] and [Breil et al., 2008]. This has been motivated by an experimental campaign on the LIL facility of CEA. This section is devoted to the description of this package. By neglecting the viscosity tensor ($\boldsymbol{\tau} = \mathbf{0}$), the plasma electrons inertia ($n_e m_e (\partial \mathbf{u}_e / \partial t) + n_e m_e (\mathbf{u}_e \cdot \partial / \partial \mathbf{r})(\mathbf{u}_e)$) and by assuming that the plasma is quasineutral ($\rho_c = 0$), the hydrodynamic conservation equation

of electron momentum (B.24) is written with the Braginskii collisional terms as

$$\mathbf{E} - \frac{\mathbf{j}}{n_e e c} \times \mathbf{B} + \frac{\mathbf{u}_i}{c} \times \mathbf{B} + \frac{k_B}{e n_e} \boldsymbol{\beta} \cdot \frac{\partial T_e}{\partial \mathbf{r}} - \boldsymbol{\eta} \cdot \mathbf{j} + \frac{1}{n_e e} \frac{\partial P_e}{\partial \mathbf{r}} = \mathbf{0}. \quad (\text{B.77})$$

This equation is called the generalized Ohm's law. The term

$$\mathbf{E}_{\text{Hall}} = \frac{\mathbf{j}}{n_e e c} \times \mathbf{B} \quad (\text{B.78})$$

accounts for the Hall effect and will be neglected since $|\mathbf{j}| \ll n_e e c$ while in the 2D Cartesian or 2D axisymmetric configuration, one can write

$$\frac{k_B}{e n_e} \boldsymbol{\beta} \cdot \frac{\partial T_e}{\partial \mathbf{r}} = \frac{\mathbf{u}_{\text{Nernst}}}{c} \times \mathbf{B} \quad (\text{B.79})$$

where

$$u_{\text{Nernst}, \perp} = \frac{k_B c}{n_e e |\mathbf{B}|} \boldsymbol{\beta}_{\perp} \cdot \left(\frac{\partial T_e}{\partial \mathbf{r}} \right)_{\perp}$$

and

$$u_{\text{Nernst}, \wedge} = \frac{k_B c}{n_e e |\mathbf{B}|} \boldsymbol{\beta}_{\wedge} \cdot \frac{\mathbf{B}}{|\mathbf{B}|} \times \frac{\partial T_e}{\partial \mathbf{r}}$$

which accounts for the Nernst effect. Coupled to the Maxwell equations in the quasi-static approximation, the generalized Braginskii Ohm's law gives

$$\begin{aligned} \frac{\partial \mathbf{B}}{\partial t} &+ \frac{\partial}{\partial \mathbf{r}} \times \left(\frac{\eta c^2}{4\pi} \cdot \frac{\partial}{\partial \mathbf{r}} \times \mathbf{B} \right) \\ &- \frac{\partial}{\partial \mathbf{r}} \times [(\mathbf{u}_i + \mathbf{u}_{\text{Nernst}}) \times \mathbf{B}] \\ &= - \frac{k_B c}{n_e e} \frac{\partial n_e}{\partial \mathbf{r}} \times \frac{\partial T_e}{\partial \mathbf{r}}. \end{aligned} \quad (\text{B.80})$$

The first line of this equation accounts for the magnetic diffusion, the second line accounts for its advection by the plasma ions (\mathbf{u}_i) and the plasma heat flux via the Nernst effect ($\mathbf{u}_{\text{Nernst}}$) and the third line accounts for the magnetic field generation due to electron temperature-density crossed gradients. Focused on the heat-conduction phenomena, the electrical resistivity has been assumed isotropic, such that $\boldsymbol{\eta} = \eta \mathbf{I}$ with $\eta^{-2} = \eta_{\text{Hubbard}}^{-2} + \eta_{\text{Spitzer}}^{-2}$. Also, due to the huge ion mass, the electron contribution to the plasma fluid velocity is neglected $\mathbf{u} = \mathbf{u}_i$. Thus, Equation (B.80) can be written in the Lagrangian form (in the 2D Cartesian or 2D axisymmetric geometry!)

$$\begin{aligned} \frac{d\widehat{\mathbf{B}}^i}{dt} &+ \left[\frac{\partial}{\partial \mathbf{r}} \times \left(\frac{\eta c^2}{4\pi} \cdot \frac{\partial}{\partial \mathbf{r}} \times \mathbf{B} \right) \right] (\widehat{\mathbf{r}}^i, t) \\ &- \left[\frac{\partial}{\partial \mathbf{r}} \times (\mathbf{u}_{\text{Nernst}} \times \mathbf{B}) \right] (\widehat{\mathbf{r}}^i, t) \\ &= - \left[\frac{k_B c}{n_e e} \frac{\partial n_e}{\partial \mathbf{r}} \times \frac{\partial T_e}{\partial \mathbf{r}} \right] (\widehat{\mathbf{r}}^i, t). \end{aligned} \quad (\text{B.81})$$

B.3. RADIATION HYDRODYNAMIC CODE CHIC

Numerical scheme : The numerical computation of Equation (B.81) is presented here in the 2D axisymmetric case :

$$\begin{aligned}
 \frac{d}{dt} \left(\widehat{\mathbf{r}}^i \widehat{B}_\theta^i \right) &= \left\{ \frac{\partial}{\partial z} \left[\frac{\eta c^2}{4\pi} \frac{\partial}{\partial z} (r B_\theta) \right] \right\} (\widehat{\mathbf{r}}^i, t) - \left\{ \frac{\partial}{\partial r} \left[\frac{\eta c^2}{4\pi} \frac{\partial}{\partial r} (r B_\theta) \right] \right\} (\widehat{\mathbf{r}}^i, t) \\
 &+ \left\{ \frac{\partial}{\partial z} [u_{\text{Nernst},z} (r B_\theta)] \right\} (\widehat{\mathbf{r}}^i, t) + \left\{ \frac{\partial}{\partial r} [u_{\text{Nernst},r} (r B_\theta)] \right\} (\widehat{\mathbf{r}}^i, t) \\
 &= \left[\frac{1}{r} u_{\text{Nernst},r} (r B_\theta) \right] (\widehat{\mathbf{r}}^i, t) - \left[\frac{1}{r} \frac{\eta c^2}{4\pi} \frac{\partial}{\partial r} (r B_\theta) \right] (\widehat{\mathbf{r}}^i, t) \\
 &- \left[\frac{k_{BC}}{n_e e} \frac{\partial n_e}{\partial \mathbf{r}} \times \frac{\partial T_e}{\partial \mathbf{r}} \right] (\widehat{\mathbf{r}}^i, t) .
 \end{aligned}$$

The 2D Cartesian case can be obtained in the same way by removing all terms $\propto 1/r$ in the right hand side of this equation, by replacing z by x , r by y and $r B_\theta$ by B_y . The computation is split in two steps

1. Firstly, the magnetic field generation due to density-temperature crossed gradients and the Nernst advection are solved explicitly using a finite volume method. Let us note

$$S_B^n = \left(\widehat{\mathbf{r}}^i \widehat{B}_\theta^i \right)^n - \Delta t \left[\frac{k_{BC}}{n_e e} \frac{\partial n_e}{\partial \mathbf{r}} \times \frac{\partial T_e}{\partial \mathbf{r}} \right]^{i,n} - \Delta t \left\{ \frac{\partial}{\partial z} [u_{\text{Nernst},z} (r B_\theta)] \right\}^{i,n} - \Delta t \left\{ \frac{\partial}{\partial r} [u_{\text{Nernst},r} (r B_\theta)] \right\}^{i,n}$$

the results of this computation.

2. Secondly, the diffusion of the magnetic field is solved in the same way as the thermal diffusion [Breil and Maire, 2007] to deduce $\left(\widehat{\mathbf{r}}^i \widehat{B}_\theta^i \right)^{n+1}$ from

$$\begin{aligned}
 \left(\widehat{\mathbf{r}}^i \widehat{B}_\theta^i \right)^{n+1} &- \Delta t \left\{ \frac{\partial}{\partial z} \left[\frac{\eta c^2}{4\pi} \frac{\partial}{\partial z} (r B_\theta) \right] \right\}^{n+1} - \Delta t \left\{ \frac{\partial}{\partial r} \left[\frac{\eta c^2}{4\pi} \frac{\partial}{\partial r} (r B_\theta) \right] \right\}^{n+1} \\
 &= S_B^n + \Delta t \left[\frac{1}{r} u_{\text{Nernst},r} (r B_\theta) \right]^{i,n} - \Delta t \left[\frac{1}{r} \frac{\eta c^2}{4\pi} \frac{\partial}{\partial r} (r B_\theta) \right]^{i,n} .
 \end{aligned}$$

Bibliography

- [Abramowitz and Stegun, 1965] Abramowitz, M. and Stegun, I. (1965). *Handbook of Mathematical Functions*. Dover, New York.
- [Adam et al., 2006] Adam, J. C., Héron, A., Laval, G., et al. (2006). Dispersion and Transport of Energetic Particles due to the Interaction of Intense Laser Pulses with Overdense Plasmas. *Phys. Rev. Lett.*, 97:205006.
- [Agostinelli et al., 2003] Agostinelli, S., Allison, J., Amako, K., Apostolakis, J., Araujo, H., Arce, P., Asai, M., Axen, D., Banerjee, S., Barrand, G., Behner, F., Bellagamba, L., Boudreau, J., Broglia, L., Brunengo, A., Burkhardt, H., Chauvie, S., Chuma, J., Chytracsek, R., Cooperman, G., Cosmo, G., Degtyarenko, P., Dell'Acqua, A., Depaola, G., Dietrich, D., Enami, R., Feliciello, A., Ferguson, C., Fesefeldt, H., Folger, G., Foppiano, F., Forti, A., Garelli, S., Giani, S., Giannitrapani, R., Gibin, D., Cadenas, J. G., González, I., Abril, G. G., Greeniaus, G., Greiner, W., Grichine, V., Grossheim, A., Guatelli, S., Gumplinger, P., Hamatsu, R., Hashimoto, K., Hasui, H., Heikkinen, A., Howard, A., Ivanchenko, V., Johnson, A., Jones, F., Kallenbach, J., Kanaya, N., Kawabata, M., Kawabata, Y., Kawaguti, M., Kelner, S., Kent, P., Kimura, A., Kodama, T., Kokoulin, R., Kossov, M., Kurashige, H., Lamanna, E., Lampén, T., Lara, V., Lefebure, V., Lei, F., Liendl, M., Lockman, W., Longo, F., Magni, S., Maire, M., Medernach, E., Minamimoto, K., de Freitas, P. M., Morita, Y., Murakami, K., Nagamatu, M., Nartallo, R., Nieminen, P., Nishimura, T., Ohtsubo, K., Okamura, M., O'Neale, S., Oohata, Y., Paech, K., Perl, J., Pfeiffer, A., Pia, M., Ranjard, F., Rybin, A., Sadilov, S., Salvo, E. D., Santin, G., Sasaki, T., Savvas, N., Sawada, Y., Scherer, S., Sei, S., Sirotenko, V., Smith, D., Starkov, N., Stoecker, H., Sulkimo, J., Takahata, M., Tanaka, S., Tcherniaev, E., Tehrani, E. S., Tropeano, M., Truscott, P., Uno, H., Urban, L., Urban, P., Verderi, M., Walkden, A., Wander, W., Weber, H., Wellisch, J., Wenaus, T., Williams, D., Wright, D., Yamada, T., Yoshida, H., Zschesche, D., et al. (2003). Geant4—a simulation toolkit. *Nuclear Instruments and Methods in Physics Research Section A: Accelerators, Spectrometers, Detectors and Associated Equipment*, 506(3):250–303.
- [Akhiezer and Polovin, 1956] Akhiezer, A. and Polovin, R. V. (1956). Theory of wave motion of an electron plasma. *Sov. Phys. JETP*, 3:696–705.

BIBLIOGRAPHY

- [Alfvén, 1939] Alfvén, H. (1939). On the Motion of Cosmic Rays in Interstellar Space. *Phys. Rev.*, 55:425–429.
- [Andrews et al., 1970] Andrews, M. L., Davitian, H., Hammer, D. A., Fleischmann, H. H., Nation, J. A., and Rostoker, N. (1970). ON THE PROPAGATION OF HIGH CURRENT BEAMS OF RELATIVISTIC ELECTRONS IN GASES. *Applied Physics Letters*, 16(3):98–100.
- [ANTIA, 1993] ANTIA, H. M. (1993). Rational function approximations for Fermi-Dirac integrals. *Astrophysical Journal Supplement Series*, 84:101–108.
- [Atzeni, 1999] Atzeni, S. (1999). Inertial fusion fast ignitor: Igniting pulse parameter window vs the penetration depth of the heating particles and the density of the precompressed fuel. *Physics of Plasmas (1994-present)*, 6(8):3316–3326.
- [Atzeni, 2009] Atzeni, S. (2009). Laser driven inertial fusion: the physical basis of current and recently proposed ignition experiments. *Plasma Physics and Controlled Fusion*, 51(12):124029.
- [Atzeni et al., 2009a] Atzeni, S., Davies, J., Hallo, L., Honrubia, J., Maire, P., Olazabal-Loumé, M., Feugeas, J., Ribeyre, X., Schiavi, A., Schurtz, G., Breil, J., and Nicolai, P. (2009a). Studies on targets for inertial fusion ignition demonstration at the HiPER facility. *Nuclear Fusion*, 49(5):055008.
- [Atzeni et al., 2009b] Atzeni, S., Schiavi, A., and Davies, J. R. (2009b). Stopping and scattering of relativistic electron beams in dense plasmas and requirements for fast ignition. *PFCF*, 51(1):015016.
- [Aymerich-Humet et al., 1983] Aymerich-Humet, X., Serra-Mestres, F., and Millan, J. (1983). A generalized approximation of the Fermi Dirac integrals. *Journal of Applied Physics*, 54(5):2850–2851.
- [Balescu, 1963] Balescu, R. (1963). *Statistical mechanics of charged particles*. Interscience publishers.
- [Bambynek, 1984] Bambynek, W. (1984). A new evaluation of K-Shell Fluorescence Yields. *X-84 Proc. X-Ray and Inner-Shell Processes in Atoms, Molecules and Solids, Leipzig*.
- [BAMBYNEK et al., 1972] BAMBYNEK, W., CRASEMANN, B., FINK, R. W., FREUND, H. U., MARK, H., SWIFT, C. D., PRICE, R. E., and RAO, P. V. (1972). X-Ray Fluorescence Yields, Auger, and Coster-Kronig Transition Probabilities. *Rev. Mod. Phys.*, 44:716–813.
- [Barenblatt and Zel'dovich, 1957] Barenblatt, G. I. and Zel'dovich, Y. B. (1957). On the dipole-type solution in problems of unsteady gas filtration in the polytropic regime. *Prikl. Mat. i Mekh*, 21:718–720.
- [Basov et al., 1968] Basov, N., Kriukov, P., Zakharov, S., Senatsky, Y., Tchekalin, S., et al. (1968). Experiments on the observation of neutron emission at a focus of high-power laser radiation on a lithium deuteride surface. *Quantum Electronics, IEEE Journal of*, 4(11):864–867.

BIBLIOGRAPHY

- [Baton et al., 2008] Baton, S. D., Koenig, M., Fuchs, J., Benuzzi-Mounaix, A., Guillou, P., Loupias, B., Vinci, T., Gremillet, L., Rousseaux, C., Drouin, M., Lefebvre, E., Dorchie, F., Fourment, C., Santos, J. J., Batani, D., Morace, A., Redaelli, R., Nakatsutsumi, M., Kodama, R., Nishida, A., Ozaki, N., Norimatsu, T., Aglitskiy, Y., Atzeni, S., Schiavi, A., et al. (2008). Inhibition of fast electron energy deposition due to preplasma filling of cone-attached targets. *Physics of Plasmas (1994-present)*, 15(4):–.
- [Baton et al., 2003] Baton, S. D., Santos, J. J., Amiranoff, F., Popescu, H., Gremillet, L., Koenig, M., Martinolli, E., Guilbaud, O., Rousseaux, C., Rabec Le Gloahec, M., Hall, T., Batani, D., Perelli, E., Scianitti, F., Cowan, T. E., et al. (2003). Evidence of Ultrashort Electron Bunches in Laser-Plasma Interactions at Relativistic Intensities. *Phys. Rev. Lett.*, 91:105001.
- [Bauer and Mulser, 2007] Bauer, D. and Mulser, P. (2007). Vacuum heating versus skin layer absorption of intense femtosecond laser pulses. *Physics of Plasmas (1994-present)*, 14(2):–.
- [Bauer et al., 1995] Bauer, D., Mulser, P., Steeb, W. H., et al. (1995). Relativistic Ponderomotive Force, Uphill Acceleration, and Transition to Chaos. *Phys. Rev. Lett.*, 75:4622–4625.
- [Beg et al., 1997] Beg, F. N., Bell, A. R., Dangor, A. E., Danson, C. N., Fews, A. P., Glinsky, M. E., Hammel, B. A., Lee, P., Norreys, P. A., Tatarakis, M., et al. (1997). A study of picosecond laser–solid interactions up to 10^{19} W cm $^{-2}$. *Physics of Plasmas (1994-present)*, 4(2):447–457.
- [Bell et al., 1981] Bell, A. R., Evans, R. G., and Nicholas, D. J. (1981). Electron Energy Transport in Steep Temperature Gradients in Laser-Produced Plasmas. *Phys. Rev. Lett.*, 46:243–246.
- [Bell and Kingham, 2003] Bell, A. R. and Kingham, R. J. (2003). Resistive Collimation of Electron Beams in Laser Produced Plasmas. *Phys. Rev. Lett.*, 91:035003.
- [Bell et al., 2006] Bell, A. R., Robinson, A. P. L., Sherlock, M., Kingham, R. J., and Rozmus, W. (2006). Fast electron transport in laser-produced plasmas and the KALOS code for solution of the Vlasov–Fokker–Planck equation. *Plasma Physics and Controlled Fusion*, 48(3):R37.
- [Bell and Tzoufras, 2011] Bell, A. R. and Tzoufras, M. (2011). Electron transport and shock ignition. *Plasma Physics and Controlled Fusion*, 53(4):045010.
- [Bell et al., 1964] Bell, J. S. et al. (1964). On the Einstein Podolsky Rosen paradox. *Physics*, 1(3):195–200.
- [Bellei et al., 2012] Bellei, C., Davies, J. R., Chauhan, P. K., and Najmudin, Z. (2012). Coherent transition radiation in relativistic laser–solid interactions. *Plasma Physics and Controlled Fusion*, 54(3):035011.
- [Bellei et al., 2013] Bellei, C., Divol, L., Kemp, A. J., Key, M. H., Larson, D. J., Strozzi, D. J., Marinak, M. M., Tabak, M., and Patel, P. K. (2013). Fast ignition: Dependence of the ignition energy

BIBLIOGRAPHY

- on source and target parameters for particle-in-cell-modelled energy and angular distributions of the fast electrons. *Physics of Plasmas (1994-present)*, 20(5):–.
- [Belyaev and Budker, 1956] Belyaev, S. T. and Budker, G. I. (1956). *Sov. Phys. Doklady*, 1(218).
- [Beretstetskii et al., 1982] Beretstetskii, V. B., Lifshitz, E. M., and Pitaevskii, L. P. (1982). *Quantum Electrodynamics*, volume 4 of *A Course of Theoretical Physics*. Pergamon press, second edition edition.
- [Berger and Seltzer, 1964] Berger, M. J. and Seltzer, S. M. (1964). Tables of energy losses and ranges of electrons and positrons. *NASA technical report SP-3012*.
- [Berthon et al., 2010] Berthon, C., Dubois, J., Dubroca, B., Nguyen-Bui, T.-H., and Turpault, R. (2010). A Free Streaming Contact Preserving Scheme for the M1 Model. *Adv. Appl. Math. Mech.*, 2(3):259–285.
- [Bethe, 1932] Bethe, H. (1932). Bremsformel für elektronen relativistischer geschwindigkeit. *Z. f. Physik*, 76:293.
- [Bethe and Heitler, 1934] Bethe, H. and Heitler, W. (1934). On the Stopping of Fast Particles and on the Creation of Positive Electrons. *Proc. R. Soc. Lond. A*, 146:83–112.
- [Bethe, 1939] Bethe, H. A. (1939). Energy Production in Stars. *Phys. Rev.*, 55:434–456.
- [Bethe, 1953] Bethe, H. A. (1953). Molière’s Theory of Multiple Scattering. *Phys. Rev.*, 89:1256–1266.
- [Betti et al., 2007] Betti, R., Zhou, C. D., Anderson, K. S., Perkins, L. J., Theobald, W., and Solodov, A. A. (2007). Shock Ignition of Thermonuclear Fuel with High Areal Density. *Phys. Rev. Lett.*, 98:155001.
- [Bévilion et al., 2014] Bévilion, E., Colombier, J. P., Recoules, V., and Stoian, R. (2014). Free-electron properties of metals under ultrafast laser-induced electron-phonon nonequilibrium: A first-principles study. *Phys. Rev. B*, 89:115117.
- [Bhabha, 1936] Bhabha, H. J. (1936). The Scattering of Positrons by Electrons with Exchange on Dirac’s Theory of the Positron. *Proc. R. Soc. Lond. A*, 154:195–206.
- [Bhatnagar et al., 1954] Bhatnagar, P. L., Gross, E. P., and Krook, M. (1954). A Model for Collision Processes in Gases. I. Small Amplitude Processes in Charged and Neutral One-Component Systems. *Phys. Rev.*, 94:511–525.
- [Birdsall and Fuss, 1969] Birdsall, C. K. and Fuss, D. (1969). Clouds in clouds, clouds in cells physics for many body plasma simulation. *Journal of Computational Physics*, 3(4):494.

BIBLIOGRAPHY

- [Birdsall and Langdon, 1991] Birdsall, C. K. and Langdon, A. B. (1991). *Plasma Physics via Computer Simulation*. The Adam Hilger Series on Plasma Physics. Adam Hilger Bristol, Philadelphia and New York.
- [Bludman et al., 1960] Bludman, S. A., Watson, K. M., and Rosenbluth, M. N. (1960). Statistical Mechanics of Relativistic Streams. II. *Physics of Fluids (1958-1988)*, 3(5):747–757.
- [Bobylev and Chuyanov, 1976] Bobylev, A. and Chuyanov, V. (1976). On the numerical solution of Landau’s kinetic equation. *{USSR} Computational Mathematics and Mathematical Physics*, 16(2):121–130.
- [Bohm, 1952a] Bohm, D. (1952a). A Suggested Interpretation of the Quantum Theory in Terms of ”Hidden” Variables. I. *Phys. Rev.*, 85:166–179.
- [Bohm, 1952b] Bohm, D. (1952b). A Suggested Interpretation of the Quantum Theory in Terms of ”Hidden” Variables. II. *Phys. Rev.*, 85:180–193.
- [Bohm and Gross, 1949] Bohm, D. and Gross, E. P. (1949). Theory of Plasma Oscillations. B. Excitation and Damping of Oscillations. *Phys. Rev.*, 75:1864–1876.
- [Bosch and Hale, 1992] Bosch, H.-S. and Hale, G. (1992). Improved formulas for fusion cross-sections and thermal reactivities. *Nuclear Fusion*, 32(4):611.
- [Bourdier et al., 2005] Bourdier, A., Patin, D., Lefebvre, E., et al. (2005). Stochastic heating in ultra high intensity laser plasma interaction. *Physica D: Nonlinear Phenomena*, 206(1):1.
- [Boutoux, 2014] Boutoux, G. (2014). Private communication.
- [Braams and Karney, 1987] Braams, B. J. and Karney, C. F. F. (1987). Differential form of the collision integral for a relativistic plasma. *Phys. Rev. Lett.*, 59:1817–1820.
- [Braginskii, 1965] Braginskii, S. (1965). *Reviews of Plasmas Physics*. Consultants Bureau, New York, ed. by m. leontovitch edition.
- [Breil et al., 2011] Breil, J., Galera, S., and Maire, P.-H. (2011). Multi-material {ALE} computation in inertial confinement fusion code {CHIC}. *Computers & Fluids*, 46(1):161–167. 10th {ICFD} Conference Series on Numerical Methods for Fluid Dynamics (ICFD 2010).
- [Breil and Maire, 2007] Breil, J. and Maire, P.-H. (2007). A cell-centered diffusion scheme on two-dimensional unstructured meshes. *Journal of Computational Physics*, 224(2):785–823.
- [Breil et al., 2008] Breil, J., Maire, P.-H., Nicolai, P., and Schurtz, G. (2008). Modelling of the magnetic field effects in hydrodynamic codes using a second order tensorial diffusion scheme. *Journal of Physics: Conference Series*, 112(2):022035.

BIBLIOGRAPHY

- [Bret et al., 2010a] Bret, A., Gremillet, L., and Bénisti, D. (2010a). Exact relativistic kinetic theory of the full unstable spectrum of an electron-beam-plasma system with Maxwell-Jüttner distribution functions. *Phys. Rev. E*, 81:036402.
- [Bret et al., 2010b] Bret, A., Gremillet, L., and Dieckmann, M. E. (2010b). Multidimensional electron beam plasma instabilities in the relativistic regime. *Physics of Plasmas (1994-present)*, 17(12):–.
- [Brice, 1985] Brice, D. K. (1985). Stopping powers for electrons and positrons (ICRU report 37; International commission on radiation units and measurements, Bethesda, Maryland, USA, 1984). *Nuclear Instruments and Methods in Physics Research Section B: Beam Interactions with Materials and Atoms*, 12(1):187–188.
- [Brunel, 1987] Brunel, F. (1987). Not-so-resonant, resonant absorption. *Phys. Rev. Lett.*, 59:52.
- [Brunel, 1988] Brunel, F. (1988). Anomalous absorption of high intensity subpicosecond laser pulses. *Physics of Fluids (1958-1988)*, 31(9):2714–2719.
- [Brysk et al., 1975] Brysk, H., Campbell, P. M., and Hammerling, P. (1975). Thermal conduction in laser fusion. *Plasma Phys.*, 17(6):473.
- [Bychkov et al., 2008] Bychkov, V., Valiev, D., and Eriksson, L.-E. (2008). Physical Mechanism of Ultrafast Flame Acceleration. *Phys. Rev. Lett.*, 101:164501.
- [Cai et al., 2011] Cai, H.-b., Zhu, S.-p., He, X. T., Wu, S.-z., Chen, M., Zhou, C., Yu, W., and Nagatomo, H. (2011). Magnetic collimation of fast electrons in specially engineered targets irradiated by ultraintense laser pulses. *Physics of Plasmas (1994-present)*, 18(2):–.
- [Campbell and Hogan, 1999] Campbell, E. M. and Hogan, W. J. (1999). The National Ignition Facility - applications for inertial fusion energy and high-energy-density science. *Plasma Phys. Control. Fusion*, 41:B39–B56.
- [Catto and More, 1977] Catto, P. J. and More, R. M. (1977). Sheath inverse bremsstrahlung in laser produced plasmas. *Physics of Fluids (1958-1988)*, 20(4):704–705.
- [Cauble et al., 1994] Cauble, R., Phillion, D., Lee, R., and Hoover, T. (1994). X-ray driven flyer foil experiments near 1.0 Gbar. *Journal of Quantitative Spectroscopy and Radiative Transfer*, 51(1–2):433–437. Special Issue Radiative Properties of Hot Dense Matter.
- [Cerchez et al., 2008] Cerchez, M., Jung, R., Osterholz, J., Toncian, T., Willi, O., Mulser, P., Ruhl, H., et al. (2008). Absorption of Ultrashort Laser Pulses in Strongly Overdense Targets. *Phys. Rev. Lett.*, 100:245001.
- [Champion, 1932] Champion, F. C. (1932). The Scattering of Fast β -Particles by Electrons. *Proc. R. Soc. Lond. A*, 137:688–695.

BIBLIOGRAPHY

- [Chandrasekhar, 1931] Chandrasekhar, S. (1931). The highly collapsed configurations of a stellar mass. *Monthly Notices of the Royal Astronomical Society*, 91:456–466.
- [Chandrasekhar, 1943] Chandrasekhar, S. (1943). Stochastic Problems in Physics and Astronomy. *Rev. Mod. Phys.*, 15:1–89.
- [Chen et al., 2009] Chen, C. D., Patel, P. K., Hey, D. S., Mackinnon, A. J., Key, M. H., Akli, K. U., Bartal, T., Beg, F. N., Chawla, S., Chen, H., Freeman, R. R., Higginson, D. P., Link, A., Ma, T. Y., MacPhee, A. G., Stephens, R. B., Van Woerkom, L. D., Westover, B., Porkolab, M., et al. (2009). Bremsstrahlung and $K\alpha$ fluorescence measurements for inferring conversion efficiencies into fast ignition relevant hot electrons. *Physics of Plasmas (1994-present)*, 16(8):–.
- [Chen et al., 2005] Chen, J. K., Latham, W. P., and Beraun, J. E. (2005). The role of electron–phonon coupling in ultrafast laser heating. *Journal of Laser Applications*, 17(1):63–68.
- [Chimier et al., 2007] Chimier, B., Tikhonchuk, V. T., and Hallo, L. (2007). Heating model for metals irradiated by a subpicosecond laser pulse. *Phys. Rev. B*, 75:195124.
- [Cohen et al., 2010] Cohen, B., Kemp, A., and Divol, L. (2010). Simulation of laser–plasma interactions and fast-electron transport in inhomogeneous plasma. *Journal of Computational Physics*, 229(12):4591–4612.
- [Cohen et al., 1982] Cohen, B. I., Langdon, A., and Friedman, A. (1982). Implicit time integration for plasma simulation. *Journal of Computational Physics*, 46(1):15–38.
- [Cohen et al., 1950] Cohen, R. S., Spitzer, L., and Routly, P. M. (1950). The Electrical Conductivity of an Ionized Gas. *Phys. Rev.*, 80:230–238.
- [Colin et al., 1968] Colin, C., Durand, Y., Floux, F., Guyot, D., Langer, P., Veyrie, P., et al. (1968). Laser Produced Plasmas from Solid Deuterium Targets. *Journal of Applied Physics*, 39(7):2991–2993.
- [Cox and Bennett, 1970] Cox, J. L. and Bennett, W. H. (1970). Reverse Current Induced by Injection of a Relativistic Electron Beam into a Pinched Plasma. *Physics of Fluids (1958-1988)*, 13(1):182–192.
- [Daido et al., 1986] Daido, H., Miki, F., Mima, K., Fujita, M., Sawai, K., Fujita, H., Kitagawa, Y., Nakai, S., and Yamanaka, C. (1986). Generation of a strong magnetic field by an intense CO₂ laser pulse. *Phys. Rev. Lett.*, 56:846.
- [Davies, 2003] Davies, J. (2003). Electric and magnetic field generation and target heating by laser-generated fast electrons. *Phys. Rev. E*, 68(056404).
- [Davies, 2002] Davies, J. R. (2002). How wrong is collisional Monte Carlo modeling of fast electron transport in high-intensity laser-solid interactions? *Phys. Rev. E*, 65:026407.

BIBLIOGRAPHY

- [Davies, 2009] Davies, J. R. (2009). Laser absorption by overdense plasmas in the relativistic regime. *Plasma Physics and Controlled Fusion*, 51(1):014006.
- [Davies et al., 1997] Davies, J. R., Bell, A. R., Haines, M. G., and Guérin, S. M. (1997). Short-pulse high-intensity laser-generated fast electron transport into thick solid targets. *Phys. Rev. E*, 56:7193–7203.
- [Davies et al., 2013] Davies, J. R., Betti, R., Nilson, P. M., and Solodov, A. A. (2013). Copper K-shell emission cross sections for laser–solid experiments. *Physics of Plasmas (1994-present)*, 20(8):–.
- [Davies et al., 2006] Davies, J. R., Green, J. S., and Norreys, P. A. (2006). Electron beam hollowing in laser–solid interactions. *PPCF*, 48(8):1181.
- [Dawson and Oberman, 1962] Dawson, J. and Oberman, C. (1962). High Frequency Conductivity and the Emission and Absorption Coefficients of a Fully Ionized Plasma. *Physics of Fluids (1958-1988)*, 5(5):517–524.
- [Debayle et al., 2013] Debayle, A., Gremillet, L., Honrubia, J. J., and d’Humières, E. (2013). Reduction of the fast electron angular dispersion by means of varying resistivity structured targets. *Physics of Plasmas (1994-present)*, 20(1):–.
- [Debayle et al., 2010] Debayle, A., Honrubia, J. J., d’Humières, E., Tikhonchuk, V. T., et al. (2010). Divergence of laser driven relativistic electron beams. *Phys. Rev. E*, 82:036405.
- [Debayle and Tikhonchuk, 2007] Debayle, A. and Tikhonchuk, V. T. (2007). Target ionization by a high current relativistic monoenergetic electron beam. *Physics of Plasmas (1994-present)*, 14(7):–.
- [Decoster et al., 1997] Decoster, A., Markowich, P. A., and B., P. (1997). *Modeling of collisions*. Masson, raviart, p.-a. edition.
- [Desjarlais, 2001] Desjarlais, M. (2001). Practical Improvements to the Lee-More Conductivity Near the Metal-Insulator Transition. *Contributions to Plasma Physics*, 41(2-3):267–270.
- [Ding et al., 2009] Ding, W.-J., Sheng, Z.-M., Zhang, J., Yu, M. Y., et al. (2009). Bulk resonance absorption induced by relativistic effects in laser-plasma interaction. *Physics of Plasmas (1994-present)*, 16(4):–.
- [Ditmire et al., 1996] Ditmire, T., Gumbrell, E. T., Smith, R. A., Mountford, L., and Hutchinson, M. H. R. (1996). Supersonic Ionization Wave Driven by Radiation Transport in a Short-Pulse Laser-Produced Plasma. *Phys. Rev. Lett.*, 77:498–501.
- [Drake, 2011] Drake, R. P. (2011). Isothermal, mass-limited rarefactions in planar and spherical geometry. *Physics of Plasmas (1994-present)*, 18(10):–.

BIBLIOGRAPHY

- [Dubois et al., 2014] Dubois, J.-L., Lubrano-Lavaderci, F., Raffestin, D., Ribolzi, J., Gazave, J., Fontaine, A. C. L., d’Humières, E., Hulin, S., Nicolai, P., Poyé, A., and Tikhonchuk, V. T. (2014). Target charging in short pulse laser plasma experiments. *Phys. Rev. E*, 89:013102.
- [Dubroca, 2012] Dubroca, B. (2012). Private communication.
- [Dubroca and Feugeas, 1999] Dubroca, B. and Feugeas, J.-L. (1999). Etude théorique et numérique d’une hiérarchie de modèles aux moments pour le transfert radiatif. *C. R. Sci. Paris*, t. 329(Série I):915–920.
- [Dubroca et al., 2010] Dubroca, B., Feugeas, J.-L., and Franck, M. (2010). Angular moment model for the Fokker-Planck equation. *Eur. Phys. J. D*, 60:301–307.
- [Duclous et al., 2009] Duclous, R., Dubroca, B., Filbet, F., and Tikhonchuk, V. (2009). High order resolution of the Maxwell-Fokker-Planck-Landau model intended for ICF applications. *J. Comput. Phys.*, 228:5072–5100.
- [Ebrahim et al., 1980] Ebrahim, N. A., Baldis, H. A., Joshi, C., and Benesch, R. (1980). Hot Electron Generation by the Two Plasmon Decay Instability in the Laser Plasma Interaction at 10.6 μm . *Phys. Rev. Lett.*, 45:1179.
- [Eddington, 1926] Eddington, A. (1926). *The internal constitution of the Stars*. Dover, new york edition.
- [Eidmann et al., 2000] Eidmann, K., Meyer-ter Vehn, J., Schlegel, T., and Hüller, S. (2000). Hydrodynamic simulation of subpicosecond laser interaction with solid-density matter. *Phys. Rev. E*, 62:1202–1214.
- [Eliezer, 2002] Eliezer, S. (2002). *The Interaction of High Power Lasers with Plasmas*. CRC Press.
- [Evans, 1983] Evans, R. G. (1983). A simple model of ion beam heated ICF targets. *Laser and Particle Beams*, 1:231–239.
- [Evans, 1986] Evans, R. G. (1986). Laser generation of ultra high pressure. *Plasma Physics and Controlled Fusion*, 28(1A):157.
- [Fabbro et al., 1985] Fabbro, R., Max, C., and Fabre, E. (1985). Planar laser driven ablation: Effect of inhibited electron thermal conduction. *Physics of Fluids (1958-1988)*, 28(5):1463–1481.
- [Fermi, 1940] Fermi, E. (1940). The Ionization Loss of Energy in Gases and in Condensed Materials. *Phys. Rev.*, 57:485–493.
- [Feugeas, 2011] Feugeas, J.-L. (2011). Private communication.
- [Feynman et al., 1963] Feynman, R., Leighton, R., and Sands, M. (1963). *The Feynman Lectures on Physics*, volume 1. Addison-Wesley, Boston, second edition.

BIBLIOGRAPHY

- [Fill, 2001] Fill, E. E. (2001). Relativistic electron beams in conducting solids and dense plasmas: Approximate analytical theory. *Physics of Plasmas (1994-present)*, 8(4):1441–1444.
- [FIORE et al., 2010] FIORE, M., FIÚZA, F., MARTI, M., FONSECA, R. A., and SILVA, L. O. (2010). Relativistic effects on the collisionless–collisional transition of the filamentation instability in fast ignition. *Journal of Plasma Physics*, 76:813–832.
- [Forslund et al., 1977] Forslund, D. W., Kindel, J. M., Lee, K., et al. (1977). Theory of Hot-Electron Spectra at High Laser Intensity. *Phys. Rev. Lett.*, 39:284–288.
- [Forslund et al., 1975] Forslund, D. W., Kindel, J. M., Lee, K., Lindman, E. L., Morse, R. L., et al. (1975). *Phys. Rev. A*, 11:679–683.
- [Forslund et al., 1985] Forslund, D. W., Kindel, J. M., Mori, W. B., Joshi, C., Dawson, J. M., et al. (1985). Two Dimensional Simulations of Single Frequency and Beat Wave Laser Plasma Heating. *Phys. Rev. Lett.*, 54:558.
- [Fourment et al., 2014] Fourment, C., Deneuille, F., Descamps, D., Dorchie, F., Petit, S., Peyrusse, O., Holst, B., and Recoules, V. (2014). Experimental determination of temperature-dependent electron-electron collision frequency in isochorically heated warm dense gold. *Phys. Rev. B*, 89:161110.
- [Franz and Wiedemann, 1853] Franz, R. and Wiedemann, G. (1853). Ueber die Wärme-Leitungsfähigkeit der Metalle. *Annalen der Physik*, 165(8):497–531.
- [Freidberg et al., 1972] Freidberg, J. P., Mitchell, R. W., Morse, R. L., Rudsinski, L. I., et al. (1972). Resonant Absorption of Laser Light by Plasma Targets. *Phys. Rev. Lett.*, 28:795.
- [Fried, 1959] Fried, B. D. (1959). Mechanism for Instability of Transverse Plasma Waves. *Physics of Fluids (1958-1988)*, 2(3):337–337.
- [Fujioka S. et al., 2013] Fujioka S., Zhang Zhe, Ishihara Kazuhiro, Shigemori Keisuke, Hironaka Youichiro, Johzaki Tomoyuki, Sunahara Atsushi, Yamamoto Naoji, Nakashima Hideki, Watanabe Tsuguhiro, Shiraga Hiroyuki, Nishimura Hiroaki, Azechi Hiroshi, et al. (2013). Kilot Tesla Magnetic Field due to a Capacitor Coil Target Driven by High Power Laser. *Sci. Rep.*, 3. 10.1038/srep01170.
- [Gamezo et al., 2004] Gamezo, V. N., Khokhlov, A. M., and Oran, E. S. (2004). Deflagrations and Detonations in Thermonuclear Supernovae. *Phys. Rev. Lett.*, 92:211102.
- [Gamow, 1928] Gamow, G. (1928). Zur Quantentheorie des Atomkernes. *Zeitschrift für Physik*, 51(3-4):204–212.
- [Gibbon, 2005] Gibbon, P. (2005). *Short Pulse Laser Interactions with Matter*. Imperial College Press.

BIBLIOGRAPHY

- [Gibbon and Bell, 1992] Gibbon, P. and Bell, A. R. (1992). Collisionless absorption in sharp edged plasmas. *Phys. Rev. Lett.*, 68:1535.
- [Ginzburg, 1961] Ginzburg, V. I. (1961). *Propagation of Electromagnetic Waves in Plasma*. Gordon & Breach Science Publishers Ltd.
- [Gradshteyn and Ryzhik, 1965] Gradshteyn, I. and Ryzhik, I. (1965). *Table of Integrals, Series and Products*. Academic, New York.
- [Graybill and Nablo, 1966] Graybill, S. E. and Nablo, S. V. (1966). OBSERVATIONS OF MAGNETICALLY SELF FOCUSING ELECTRON STREAMS. *Applied Physics Letters*, 8(1):18–20.
- [Green et al., 2008] Green, J. S., Ovchinnikov, V. M., Evans, R. G., Akli, K. U., Azechi, H., Beg, F. N., Bellei, C., Freeman, R. R., Habara, H., Heathcote, R., Key, M. H., King, J. A., Lancaster, K. L., Lopes, N. C., Ma, T., MacKinnon, A. J., Markey, K., McPhee, A., Najmudin, Z., Nilson, P., Onofrei, R., Stephens, R., Takeda, K., Tanaka, K. A., Theobald, W., Tanimoto, T., Waugh, J., Van Woerkom, L., Woolsey, N. C., Zepf, M., Davies, J. R., Norreys, P. A., et al. (2008). Effect of Laser Intensity on Fast Electron Beam Divergence in Solid-Density Plasmas. *Phys. Rev. Lett.*, 100:015003.
- [Gremillet, 2012] Gremillet, L. (2012). Private communication.
- [Gremillet, 2014] Gremillet, L. (2014). Private communication.
- [Gremillet et al., 2002] Gremillet, L., Bonnaud, G., and Amiranoff, F. (2002). Filamented transport of laser-generated relativistic electrons penetrating a solid target. *Phys. Plasmas*, 9(3):941–948.
- [Gryziński, 1965a] Gryziński, M. (1965a). Two-Particle Collisions. I. General Relations for Collisions in the Laboratory System. *Phys. Rev.*, 138:A305–A321.
- [Gryziński, 1965b] Gryziński, M. (1965b). Two-Particle Collisions. II. Coulomb Collisions in the Laboratory System of Coordinates. *Phys. Rev.*, 138:A322–A335.
- [Guérin et al., 1995] Guérin, S., Laval, G., Mora, P., Adam, J. C., Héron, A., Bendib, A., et al. (1995). Modulational and Raman instabilities in the relativistic regime. *Physics of Plasmas (1994-present)*, 2(7):2807–2814.
- [Guérin et al., 1996] Guérin, S., Mora, P., Adam, J. C., Héron, A., Laval, G., et al. (1996). Propagation of ultraintense laser pulses through overdense plasma layers. *Physics of Plasmas (1994-present)*, 3(7):2693–2701.
- [Gurevich et al., 1966] Gurevich, A. V., Pariiskaya, L. V., and Pitaevskii, L. P. (1966). Self-similar Motion of Rarefied Plasma. *JETP*, 22(2):449.

BIBLIOGRAPHY

- [Gus'kov et al., 2012] Gus'kov, S., Ribeyre, X., Touati, M., Feugeas, J.-L., Nicolai, P., and Tikhonchuk, V. (2012). Ablation Pressure Driven by an Energetic Electron Beam in a Dense Plasma. *Phys. Rev. Lett.*, 109:255004.
- [Gus'kov, 1983] Gus'kov, S. Y. (1983). Steady-state model of the corona of spherical laser targets allowing for energy transfer by fast electrons. *Sov. J. Quant. Elec.*, 13(4):498.
- [Hammer and Rostoker, 1970] Hammer, D. A. and Rostoker, N. (1970). Propagation of High Current Relativistic Electron Beams. *Phys. Fluids*, 13:1831.
- [Hao et al., 2012] Hao, B., Ding, W. J., Sheng, Z. M., Ren, C., Kong, X., Mu, J., and Zhang, J. (2012). Collisional effects on the oblique instability in relativistic beam-plasma interactions. *Physics of Plasmas (1994-present)*, 19(7):-.
- [Harten et al., 1983] Harten, A., Lax, P. D., and van Leer, B. (1983). On Upstream Differencing and Godunov-Type Schemes for Hyperbolic Conservation Laws. *SIAM Review*, 25(1):35–61.
- [Hatchett et al., 2000] Hatchett, S. P., Brown, C. G., Cowan, T. E., Henry, E. A., Johnson, J. S., Key, M. H., Koch, J. A., Langdon, A. B., Lasinski, B. F., Lee, R. W., Mackinnon, A. J., Pennington, D. M., Perry, M. D., Phillips, T. W., Roth, M., Sangster, T. C., Singh, M. S., Snavely, R. A., Stoyer, M. A., Wilks, S. C., Yasuike, K., et al. (2000). Electron, photon, and ion beams from the relativistic interaction of Petawatt laser pulses with solid targets. *Physics of Plasmas (1994-present)*, 7(5):2076–2082.
- [Heitler and Sauter, 1933] Heitler, W. and Sauter, F. (1933). Stopping of Fast Particles with Emission of Radiation and the Birth of Positive Electrons. *Nature*, 132:892.
- [Henke et al., 1993] Henke, B., Gullikson, E., and Davis, J. (1993). X-Ray Interactions: Photoabsorption, Scattering, Transmission, and Reflection at $E = 50\text{--}30,000$ eV, $Z = 1\text{--}92$. *Atomic Data and Nuclear Data Tables*, 54(2):181–342.
- [Hombourger, 1998] Hombourger, C. (1998). An empirical expression for K-shell ionization cross section by electron impact. *Journal of Physics B: Atomic, Molecular and Optical Physics*, 31(16):3693.
- [Hubbard, 1966] Hubbard, W. B. (1966). Studies in stellar evolution. V. transport coefficients of degenerate stellar matter. *Astrophys. J.*, 146(858).
- [Hurricane O. A. et al., 2014] Hurricane O. A., Callahan D. A., Casey D. T., Celliers P. M., Cerjan C., Dewald E. L., Dittrich T. R., Doppner T., Hinkel D. E., Hopkins L. F., Berzak, Kline J. L., Le Pape S., Ma T., MacPhee A. G., Milovich J. L., Pak A., Park H.-S., Patel P. K., Remington B. A., Salmonson J. D., Springer P. T., Tommasini R., et al. (2014). Fuel gain exceeding unity in an inertially confined fusion implosion. *Nature*, 506(7488):343–348.

BIBLIOGRAPHY

- [Imshennik, 1960] Imshennik, V. S. (1960). The Isothermal Scattering of a Gas Cloud. *Sov. Phys. Dokl.* 5, 263, 5:263.
- [Inogamov and Petrov, 2010] Inogamov, N. and Petrov, Y. (2010). Thermal conductivity of metals with hot electrons. *Journal of Experimental and Theoretical Physics*, 110(3):446–468.
- [Jackson, 1975] Jackson, J. D. (1975). *Classical Electrodynamics*. (Wiley, New York), p. 426 (Problem 12.6).
- [Johnston, 1960] Johnston, T. W. (1960). Cartesian Tensor Scalar Product and Spherical Harmonic Expansions in Boltzmann’s Equation. *Phys. Rev.*, 120(4).
- [Johzaki et al., 2011] Johzaki, T., Nagatomo, H., Sunahara, A., Cai, H.-B., Sakagami, H., Nakao, Y., and Mima, K. (2011). Pre plasma effects on core heating and enhancing heating efficiency by extended double cone for FIREX. *Nuclear Fusion*, 51(7):073022.
- [Jones et al., 1983] Jones, S. E., Anderson, A. N., Caffrey, A. J., Walter, J. B., Watts, K. D., Bradbury, J. N., Gram, P. A. M., Leon, M., Maltrud, H. R., Paciotti, M. A., et al. (1983). Experimental Investigation of Muon-Catalyzed $d - t$ Fusion. *Phys. Rev. Lett.*, 51:1757–1760.
- [Jung et al., 2005] Jung, R., Osterholz, J., Löwenbrück, K., Kiselev, S., Pretzler, G., Pukhov, A., Willi, O., Kar, S., Borghesi, M., Nazarov, W., Karsch, S., Clarke, R., and Neely, D. (2005). Study of Electron-Beam Propagation through Preionized Dense Foam Plasmas. *Phys. Rev. Lett.*, 94:195001.
- [Jüttner, 1911] Jüttner, F. (1911). Das Maxwellsche Gesetz der Geschwindigkeitsverteilung in der Relativtheorie. *Annalen der Physik*, 339(5):856–882.
- [Kaganov et al., 1957] Kaganov, M. I., Lifshitz, I. M., and Tanatarov, L. V. (1957). Relaxation between electrons and the crystalline lattice. *Sov. Phys. JETP*, 4:173–178.
- [Kahoul A. et al., 2011] Kahoul A., Abassi A., Deghfel B., and Nekkab M. (2011). K-shell fluorescence yields for elements with $6 \leq Z \leq 99$. *Radiation Physics and Chemistry*, 80(3):369–377.
- [Kalashnikov et al., 1994] Kalashnikov, M. P., Nickles, P. V., Schlegel, T., Schnuerer, M., Billhardt, F., Will, I., Sandner, W., Demchenko, N. N., et al. (1994). Dynamics of Laser Plasma Interaction at 10^{18} W/cm². *Phys. Rev. Lett.*, 73:260–263.
- [Karmakar et al., 2008] Karmakar, A., Kumar, N., Pukhov, A., Polomarov, O., and Shvets, G. (2008). Three-dimensional filamentary structures of a relativistic electron beam in fast ignition plasmas. *Physics of Plasmas (1994-present)*, 15(12):–.
- [Kaw and Dawson, 1970] Kaw, P. and Dawson, J. (1970). Relativistic Nonlinear Propagation of Laser Beams in Cold Overdense Plasmas. *Physics of Fluids (1958-1988)*, 13(2):472–481.

BIBLIOGRAPHY

- [Keldysh, 1965] Keldysh, L. V. (1965). Ionization in the field of a strong electromagnetic wave. *Sov. Phys. JETP*, 20(5):1307.
- [Kemp et al., 2014] Kemp, A., Fiuza, F., Debayle, A., Johzaki, T., Mori, W., Patel, P., Sentoku, Y., Silva, L., et al. (2014). Laser plasma interactions for fast ignition. *Nuclear Fusion*, 54(5):054002.
- [Kemp et al., 2009] Kemp, A. J., Sentoku, Y., Tabak, M., et al. (2009). *Phys. Rev. E*, 79:066406.
- [Klimo et al., 2014] Klimo, O., Psikal, J., Tikhonchuk, V. T., Weber, S., et al. (2014). Two-dimensional simulations of laser–plasma interaction and hot electron generation in the context of shock-ignition research. *Plasma Physics and Controlled Fusion*, 56(5):055010.
- [Klimo et al., 2011] Klimo, O., Tikhonchuk, V. T., Ribeyre, X., Schurtz, G., Riconda, C., Weber, S., and Limpouch, J. (2011). Laser plasma interaction studies in the context of shock ignition—Transition from collisional to collisionless absorption. *Physics of Plasmas (1994-present)*, 18(8):–.
- [Klimo et al., 2010] Klimo, O., Weber, S., Tikhonchuk, V. T., Limpouch, J., et al. (2010). Particle-in-cell simulations of laser–plasma interaction for the shock ignition scenario. *Plasma Physics and Controlled Fusion*, 52(5):055013.
- [Kodama R. et al., 2001] Kodama R., Norreys P. A., Mima K., Dangor A. E., Evans R. G., Fujita H., Kitagawa Y., Krushelnick K., Miyakoshi T., Miyanaga N., Norimatsu T., Rose S. J., Shozaki T., Shigemori K., Sunahara A., Tampo M., Tanaka K. A., Toyama Y., Yamanaka T., Zepf M., et al. (2001). Fast heating of ultrahigh-density plasma as a step towards laser fusion ignition. *Nature*, 412(6849):798–802. 10.1038/35090525.
- [Kodama R. et al., 2002] Kodama R., Shiraga H., Shigemori K., Toyama Y., Fujioka S., Azechi H., Fujita H., Habara H., Hall T., Izawa Y., Jitsuno T., Kitagawa Y., Krushelnick K. M., Lancaster K. L., Mima K., Nagai K., Nakai M., Nishimura H., Norimatsu T., Norreys P. A., Sakabe S., Tanaka K. A., Youssef A., Zepf M., Yamanaka T., et al. (2002). Nuclear fusion: Fast heating scalable to laser fusion ignition. *Nature*, 418(6901):933–934.
- [Kolodner and Yablonovitch, 1979] Kolodner, P. and Yablonovitch, E. (1979). Two-Dimensional Distribution of Self-Generated Magnetic Fields near the Laser-Plasma Resonant- Interaction Region. *Phys. Rev. Lett.*, 43:1402–1403.
- [Krause, 1979] Krause, M. O. (1979). Atomic radiative and radiationless yields for K and L shells. *Journal of Physical and Chemical Reference Data*, 8(2):307–327.
- [Krause and Oliver, 1979] Krause, M. O. and Oliver, J. H. (1979). Natural widths of atomic K and L levels, $K\alpha$ X ray lines and several KLL Auger lines. *Journal of Physical and Chemical Reference Data*, 8(2):329–338.

BIBLIOGRAPHY

- [Kruer and Estabrook, 1985] Kruer, W. L. and Estabrook, K. (1985). J×B heating by very intense laser light. *Physics of Fluids (1958-1988)*, 28(1):430–432.
- [Lambert et al., 2011] Lambert, F., Recoules, V., Decoster, A., Cl  rouin, J., and Desjarlais, M. (2011). On the transport coefficients of hydrogen in the inertial confinement fusion regime a). *Phys. Plasmas*, 18(5):–.
- [Landau and Lifshitz, 1981] Landau, L. D. and Lifshitz, E. M. (1981). *Physical kinetics*, volume 10 of *A Course of Theoretical Physics*.
- [Lawson, 1957] Lawson, J. D. (1957). Some Criteria for a Power Producing Thermonuclear Reactor. *Proceedings of the Physical Society. Section B*, 70(1):6.
- [Lawson, 1959] Lawson, J. D. (1959). On the classification of electron streams. *Journal of Nuclear Energy. Part C, Plasma Physics, Accelerators, Thermonuclear Research*, 1(1):31.
- [Ledingham et al., 2000] Ledingham, K. W. D., Spencer, I., McCanny, T., Singhal, R. P., Santala, M. I. K., Clark, E., Watts, I., Beg, F. N., Zepf, M., Krushelnick, K., Tatarakis, M., Dangor, A. E., Norreys, P. A., Allott, R., Neely, D., Clark, R. J., Machacek, A. C., Wark, J. S., Cresswell, A. J., Sanderson, D. C. W., Magill, J., et al. (2000). Photonuclear Physics when a Multiterawatt Laser Pulse Interacts with Solid Targets. *Phys. Rev. Lett.*, 84:899–902.
- [Lee et al., 1977] Lee, K., Forslund, D. W., Kindel, J. M., Lindman, E. L., et al. (1977). Theoretical derivation of laser induced plasma profiles. *Physics of Fluids (1958-1988)*, 20(1):51–54.
- [Lee and Sudan, 1971] Lee, R. and Sudan, R. N. (1971). Return Current Induced by a Relativistic Beam Propagating in a Magnetized Plasma. *Phys. Fluids*, 14:1213.
- [Lee and More, 1984] Lee, Y. T. and More, R. M. (1984). An electron conductivity model for dense plasmas. *Physics of Fluids (1958-1988)*, 27(5):1273–1286.
- [Lefebvre and Bonnaud, 1995] Lefebvre, E. and Bonnaud, G. (1995). Transparency/Opacity of a Solid Target Illuminated by an Ultrahigh Intensity Laser Pulse. *Phys. Rev. Lett.*, 74.
- [Lefebvre et al., 2003] Lefebvre, E., Cochet, N., Fritzier, S., Malka, V., Al  onard, M.-M., Chemin, J.-F., Darbon, S., Disdier, L., Faure, J., Fedotoff, A., Landoas, O., Malka, G., M  ot, V., Morel, P., Gloahec, M. R. L., Rouyer, A., Rubbelynck, C., Tikhonchuk, V., Wrobel, R., Audebert, P., Rousseaux, C., et al. (2003). Electron and photon production from relativistic laser–plasma interactions. *Nucl. Fusion*, 43(7):629.
- [Levermore, 1979] Levermore, C. D. (1979). A Chapman-Enskog approach to flux-limited diffusion theory. Technical report.
- [Levermore, C.D., 1984] Levermore, C.D. (1984). Relating Eddington factors to flux limiters. *Journal of Quantitative Spectroscopy and Radiative Transfer*, 31(2):149–160.

BIBLIOGRAPHY

- [Lewis, 1950] Lewis, H. W. (1950). Multiple Scattering in an Infinite Medium. *Phys. Rev.*, 78:526–529.
- [Li et al., 2011] Li, Y. Y., Gu, Y. J., Zhu, Z., Li, X. F., Ban, H. Y., Kong, Q., and Kawata, S. (2011). Direct laser acceleration of electron by an ultra intense and short pulsed laser in under-dense plasma. *Physics of Plasmas (1994-present)*, 18(5):–.
- [Lin et al., 2008] Lin, Z., Zhigilei, L. V., and Celli, V. (2008). Electron-phonon coupling and electron heat capacity of metals under conditions of strong electron-phonon nonequilibrium. *Phys. Rev. B*, 77:075133.
- [Lindl, 1995] Lindl, J. (1995). Development of the indirect drive approach to inertial confinement fusion and the target physics basis for ignition and gain. *Physics of Plasmas (1994-present)*, 2(11):3933–4024.
- [Lindl, 1998] Lindl, J. (1998). *Inertial Confinement Fusion*. AIP-Press.
- [Macchi, 2012] Macchi, A. (2012). Toy model of the “fountain effect” for magnetic field generation in intense laser-solid interactions. *arXiv*, 1202(0389).
- [Macchi et al., 2013] Macchi, A., Borghesi, M., and Passoni, M. (2013). Ion acceleration by superintense laser plasma interaction. *Rev. Mod. Phys.*, 85:751–793.
- [MacLellan et al., 2013] MacLellan, D. A., Carroll, D. C., Gray, R. J., Booth, N., Burza, M., Desjarlais, M. P., Du, F., Gonzalez-Izquierdo, B., Neely, D., Powell, H. W., Robinson, A. P. L., Rusby, D. R., Scott, G. G., Yuan, X. H., Wahlström, C.-G., McKenna, P., et al. (2013). Annular Fast Electron Transport in Silicon Arising from Low-Temperature Resistivity. *Phys. Rev. Lett.*, 111:095001.
- [Maiman, 1960] Maiman, T. H. (1960). Stimulated Optical Radiation in Ruby. *Nature*, 187(4736):493–494.
- [Maire et al., 2007] Maire, P., Abgrall, R., Breil, J., and Ovardia, J. (2007). A Cell-Centered Lagrangian Scheme for Two-Dimensional Compressible Flow Problems. *SIAM Journal on Scientific Computing*, 29(4):1781–1824.
- [Maire, 2009] Maire, P.-H. (2009). A high-order cell-centered Lagrangian scheme for two-dimensional compressible fluid flows on unstructured meshes. *Journal of Computational Physics*, 228(7):2391–2425.
- [Mallet et al., 2014] Mallet, J., Brull, S., and Dubroca, B. (2014). An Entropic Scheme for an Angular Moment Model for the Classical Fokker-Planck-Landau Equation of Electrons. *Commun. Comput. Phys*, 15:422.
- [Manheimer et al., 1982] Manheimer, W. M., Colombant, D. G., and Gardner, J. H. (1982). Steady state planar ablative flow. *Physics of Fluids (1958-1988)*, 25(9):1644–1652.

BIBLIOGRAPHY

- [Marburger and Tooper, 1975] Marburger, J. H. and Tooper, R. F. (1975). Nonlinear Optical Standing Waves in Overdense Plasmas. *Phys. Rev. Lett.*, 35:1001–1004.
- [Martinolli et al., 2006] Martinolli, E., Koenig, M., Baton, S. D., Santos, J. J., Amiranoff, F., Batani, D., Perelli-Cippo, E., Scianitti, F., Gremillet, L., Mélizzi, R., Decoster, A., Rousseaux, C., Hall, T. A., Key, M. H., Snavely, R., MacKinnon, A. J., Freeman, R. R., King, J. A., Stephens, R., Neely, D., Clarke, R. J., et al. (2006). Fast electron transport and heating of solid targets in high intensity laser interactions measured by $K\alpha$ fluorescence. *Phys. Rev. E*, 73:046402.
- [Mason, 1981] Mason, R. J. (1981). Implicit moment particle simulation of plasmas. *Journal of Computational Physics*, 41(2):233–244.
- [Matte et al., 1984] Matte, J. P., Johnston, T. W., Delettrez, J., and McCrory, R. L. (1984). Electron Heat Flow with Inverse Bremsstrahlung and Ion Motion. *Phys. Rev. Lett.*, 53:1461–1464.
- [May et al., 2011] May, J., Tonge, J., Fiuza, F., Fonseca, R. A., Silva, L. O., Ren, C., and Mori, W. B. (2011). Mechanism of generating fast electrons by an intense laser at a steep overdense interface. *Phys. Rev. E*, 84:025401.
- [McGuire, 1982] McGuire, E. J. (1982). Subshell stopping power of the elements for protons in the Born approximation. *Phys. Rev. A*, 26:1858–1870.
- [McKenna et al., 2011] McKenna, P., Robinson, A. P. L., Neely, D., Desjarlais, M. P., Carroll, D. C., Quinn, M. N., Yuan, X. H., Brenner, C. M., Burza, M., Coury, M., Gallegos, P., Gray, R. J., Lancaster, K. L., Li, Y. T., Lin, X. X., Tresca, O., Wahlström, C.-G., et al. (2011). Effect of Lattice Structure on Energetic Electron Transport in Solids Irradiated by Ultraintense Laser Pulses. *Phys. Rev. Lett.*, 106:185004.
- [Mendonça, 1983] Mendonça, J. T. (1983). Threshold for electron heating by two electromagnetic waves. *Phys. Rev. A*, 28:3592–3598.
- [Minerbo, 1977] Minerbo, G. (1977). Maximum Entropy Eddington factors. Technical Report UC-32.
- [Minerbo, 1978] Minerbo, G. N. (1978). Maximum entropy Eddington factors. *Journal of Quantitative Spectroscopy and Radiative Transfer*, 20(6):541–545.
- [Moliere, 1948] Moliere, G. (1948). Theorie der Streuung schneller geladener Teilchen II Mehrfach- und Vielfachstreuung. *Z Naturforschung A*, 3(2).
- [Möller, 1932] Möller, C. (1932). Zur Theorie des durchgangs schneller electronen durch materie. *Ann. Phys.*, 14(531).
- [Molvig, 1975] Molvig, K. (1975). Filamentary Instability of a Relativistic Electron Beam. *Phys. Rev. Lett.*, 35:1504–1507.

BIBLIOGRAPHY

- [Mora, 1982] Mora, P. (1982). Theoretical model of absorption of laser light by a plasma. *Physics of Fluids (1958-1988)*, 25(6):1051–1056.
- [Mora, 2003] Mora, P. (2003). Plasma Expansion into a Vacuum. *Phys. Rev. Lett.*, 90:185002.
- [More, 1985] More, R. (1985). Pressure ionization, resonances and the continuity of bound and free states. *Adv. At. Mol. Phys.*, 21:305–356.
- [Moses, 2009] Moses, E. I. (2009). Ignition on the National Ignition Facility: a path towards inertial fusion energy. *Nuclear Fusion*, 49(10):104022.
- [Mott, 1932] Mott, N. F. (1932). The polarization of electrons by double scattering. *Proc. R. Soc. Lond. A*, 135:429–458.
- [Mulser et al., 2008] Mulser, P., Bauer, D., Ruhl, H., et al. (2008). Collisionless Laser-Energy Conversion by Anharmonic Resonance. *Phys. Rev. Lett.*, 101:225002.
- [Mulser et al., 2012] Mulser, P., Weng, S. M., and Liseykina, T. (2012). Analysis of the Brunel model and resulting hot electron spectra. *Physics of Plasmas (1994-present)*, 19(4):–.
- [Nanbu, 1997] Nanbu, K. (1997). Momentum relaxation of a charged particle by small angle Coulomb collisions. *Phys. Rev. E*, 56:7314–7314.
- [Nardi and Zinamon, 1978] Nardi, E. and Zinamon, Z. (1978). Energy deposition by relativistic electrons in high-temperature targets. *Phys. Rev. A*, 18:1246–1249.
- [Nicolai, 2011] Nicolai, P. (2011). Private communication.
- [Nicolai et al., 2011] Nicolai, P., Feugeas, J.-L., Regan, C., Olazabal-Loumé, M., Breil, J., Dubroca, B., Morreeuw, J.-P., Tikhonchuk, V., et al. (2011). Effect of the plasma-generated magnetic field on relativistic electron transport. *Phys. Rev. E*, 84:016402.
- [Nicolai et al., 2014] Nicolai, P., Feugeas, J.-L., Touati, M., Ribeyre, X., Gus'kov, S., and Tikhonchuk, V. (2014). Deleterious effects of nonthermal electrons in shock ignition concept. *Phys. Rev. E*, 89:033107.
- [Nicolai et al., 2006] Nicolai, P. D., Feugeas, J.-L. A., and Schurtz, G. P. (2006). A practical nonlocal model for heat transport in magnetized laser plasmas. *Physics of Plasmas (1994-present)*, 13(3):–.
- [Nora et al., 2015] Nora, R., Theobald, W., Betti, R., Marshall, F. J., Michel, D. T., Seka, W., Yaakobi, B., Lafon, M., Stoeckl, C., Delettrez, J., Solodov, A. A., Casner, A., Reverdin, C., Ribeyre, X., Vallet, A., Peebles, J., Beg, F. N., and Wei, M. S. (2015). Gigabar Spherical Shock Generation on the OMEGA Laser. *Phys. Rev. Lett.*, 114:045001.

BIBLIOGRAPHY

- [Norreys et al., 2014] Norreys, P., Batani, D., Baton, S., Beg, F. N., Kodama, R., Nilson, P., Patel, P., Pérez, F., Santos, J., Scott, R., Tikhonchuk, V., Wei, M., Zhang, J., et al. (2014). Fast electron energy transport in solid density and compressed plasma. *Nuclear Fusion*, 54(5):054004.
- [Norreys et al., 2006] Norreys, P. A., Green, J. S., Davies, J. R., Tatarakis, M., Clark, E. L., Beg, F. N., Dangor, A. E., Lancaster, K. L., Wei, M. S., Zepf, M., and Krushelnick, K. (2006). Observation of annular electron beam transport in multi-TeraWatt laser-solid interactions. *Plasma Physics and Controlled Fusion*, 48(2):L11.
- [Nuckolls et al., 1973] Nuckolls, J., Emmet, J., Wood, L., et al. (1973). Laser induced thermonuclear fusion. *Phys. Today*, 26(46).
- [Nuter et al., 2011] Nuter, R., Gremillet, L., Lefebvre, E., Lévy, A., Ceccotti, T., and Martin, P. (2011). Field ionization model implemented in Particle In Cell code and applied to laser-accelerated carbon ions. *Physics of Plasmas (1994-present)*, 18(3):-.
- [Ovchinnikov et al., 2011] Ovchinnikov, V. M., Kemp, G. E., Schumacher, D. W., Freeman, R. R., and Van Woerkom, L. D. (2011). How well do time-integrated $K\alpha$ images represent hot electron spatial distributions? *Physics of Plasmas (1994-present)*, 18(7):-.
- [Peano et al., 2009] Peano, F., Marti, M., Silva, L. O., and Coppa, G. (2009). Statistical kinetic treatment of relativistic binary collisions. *Phys. Rev. E*, 79:025701.
- [Pérez et al., 2012] Pérez, F., Gremillet, L., Decoster, A., Drouin, M., and Lefebvre, E. (2012). Improved modeling of relativistic collisions and collisional ionization in particle-in-cell codes. *Physics of Plasmas (1994-present)*, 19(8):-.
- [Pérez et al., 2013] Pérez, F., Kemp, A. J., Divol, L., Chen, C. D., Patel, P. K., et al. (2013). Deflection of MeV Electrons by Self-Generated Magnetic Fields in Intense Laser Solid Interactions. *Phys. Rev. Lett.*, 111:245001.
- [Petrov et al., 2013] Petrov, Y., Inogamov, N., and Migdal, K. (2013). Thermal conductivity and the electron-ion heat transfer coefficient in condensed media with a strongly excited electron subsystem. *JETP Letters*, 97(1):20–27.
- [Pines and Bohm, 1952] Pines, D. and Bohm, D. (1952). A collective description of electron interactions : II. Collective vs individual particle aspects of the interactions. *Phys. Rev.*, 85(2).
- [Ping et al., 2012] Ping, Y., Kemp, A. J., Divol, L., Key, M. H., Patel, P. K., Akli, K. U., Beg, F. N., Chawla, S., Chen, C. D., Freeman, R. R., Hey, D., Higginson, D. P., Jarrott, L. C., Kemp, G. E., Link, A., McLean, H. S., Sawada, H., Stephens, R. B., Turnbull, D., Westover, B., and Wilks, S. C. (2012). Dynamics of Relativistic Laser-Plasma Interaction on Solid Targets. *Phys. Rev. Lett.*, 109:145006.

BIBLIOGRAPHY

- [Ping et al., 2008] Ping, Y., Shepherd, R., Lasinski, B. F., Tabak, M., Chen, H., Chung, H. K., Fournier, K. B., Hansen, S. B., Kemp, A., Liedahl, D. A., Widmann, K., Wilks, S. C., Rozmus, W., Sherlock, M., et al. (2008). Absorption of Short Laser Pulses on Solid Targets in the Ultrarelativistic Regime. *Phys. Rev. Lett.*, 100:085004.
- [Piriz et al., 2012] Piriz, A. R., Rodriguez Prieto, G., Tahir, N. A., Zhang, Y., Liu, S. D., and Zhao, Y. T. (2012). Ablation driven by hot electrons generated during the ignitor laser pulse in shock ignition. *Physics of Plasmas (1994-present)*, 19(12):-.
- [Pisani et al., 2000] Pisani, F., Bernardinello, A., Batani, D., Antonicci, A., Martinolli, E., Koenig, M., Gremillet, L., Amiranoff, F., Baton, S., Davies, J., Hall, T., Scott, D., Norreys, P., Djaoui, A., Rousseaux, C., Fewes, P., Bandulet, H., and Pepin, H. (2000). Experimental evidence of electric inhibition in fast electron penetration and of electric-field-limited fast electron transport in dense matter. *Phys. Rev. E*, 62:R5927–R5930.
- [Pomeraning, 1981] Pomeraning, G. C. (1981). Flux limiters and Eddington factors. Technical Report UCRL-86561.
- [Pratt et al., 1977] Pratt, R., Tseng, H., Lee, C., Kissel, L., MacCallum, C., and Riley, M. (1977). Bremsstrahlung energy spectra from electrons of kinetic energy $1 \text{ keV} \leq \{T1\} \leq 2000 \text{ keV}$ incident on neutral atoms $2 \leq Z \leq 92$. *Atomic Data and Nuclear Data Tables*, 20(2):175–209.
- [Pukhov, 2001] Pukhov, A. (2001). Three-Dimensional Simulations of Ion Acceleration from a Foil Irradiated by a Short-Pulse Laser. *Phys. Rev. Lett.*, 86:3562–3565.
- [Pukhov et al., 1999] Pukhov, A., Sheng, Z.-M., Meyer-ter Vehn, J., et al. (1999). Particle acceleration in relativistic laser channels. *Physics of Plasmas (1994-present)*, 6(7):2847.
- [Rax, 1992] Rax, J. M. (1992). Compton harmonic resonances, stochastic instabilities, quasilinear diffusion, and collisionless damping with ultra high intensity laser waves. *Physics of Fluids B: Plasma Physics (1989-1993)*, 4(12):3962–3972.
- [Regan, 2010] Regan, C. (2010). *Modèles réduits pour le transport de particules rapides dans le cadre de la Fusion par Confinement Inertiel*. PhD thesis.
- [Regan, 2011] Regan, C. (2011). Private communication.
- [Regan et al., 2011] Regan, C., Schlegel, T., Tikhonchuk, V. T., Honrubia, J. J., Feugeas, J.-L., and Nicolai, P. (2011). Cone-guided fast ignition with ponderomotively accelerated carbon ions. *Plasma Physics and Controlled Fusion*, 53(4):045014.
- [Ribeyre, 2014] Ribeyre, X. (2014). Private communication.
- [Ribeyre et al., 2009] Ribeyre, X., Schurtz, G., Lafon, M., Galera, S., and Weber, S. (2009). Shock ignition: an alternative scheme for HiPER. *Plasma Physics and Controlled Fusion*, 51(1):015013.

BIBLIOGRAPHY

- [Roberts and Bennett, 1968] Roberts, T. G. and Bennett, W. H. (1968). The pinch effect in pulsed streams at relativistic energies. *Plasma Physics*, 10(4):381.
- [Robiche et al., 2010] Robiche, J., Rax, J.-M., Bonnaud, G., and Gremillet, L. (2010). Fast electron energy deposition in a magnetized plasma: Kinetic theory and particle-in-cell simulation. *Phys. Plasmas*, 17(3):–.
- [Robinson et al., 2014] Robinson, A., Strozzi, D., Davies, J., Gremillet, L., Honrubia, J., Johzaki, T., Kingham, R., Sherlock, M., and Solodov, A. (2014). Theory of fast electron transport for fast ignition. *Nuclear Fusion*, 54(5):054003.
- [Robinson et al., 2012] Robinson, A. P. L., Key, M. H., and Tabak, M. (2012). Focusing of Relativistic Electrons in Dense Plasma Using a Resistivity Gradient-Generated Magnetic Switchyard. *Phys. Rev. Lett.*, 108:125004.
- [Robinson and Schmitz, 2013] Robinson, A. P. L. and Schmitz, H. (2013). Elliptical magnetic mirror generated via resistivity gradients for fast ignition inertial confinement fusion. *Physics of Plasmas (1994-present)*, 20(6):–.
- [Robinson et al., 2008] Robinson, A. P. L., Sherlock, M., and Norreys, P. A. (2008). Artificial Collimation of Fast-Electron Beams with Two Laser Pulses. *Phys. Rev. Lett.*, 100:025002.
- [Rohrlich and Carlson, 1954] Rohrlich, F. and Carlson, B. C. (1954). Positron-Electron Differences in Energy Loss and Multiple Scattering. *Phys. Rev.*, 93:38–44.
- [Rosenbluth et al., 1957] Rosenbluth, M. N., MacDonald, W. M., and Judd, D. L. (1957). Fokker-Planck Equation for an Inverse-Square Force. *Phys. Rev.*, 107:1–6.
- [Rozmus and Tikhonchuk, 1990] Rozmus, W. and Tikhonchuk, V. T. (1990). Skin effect and interaction of short laser pulses with dense plasmas. *Phys. Rev. A*, 42:7401–7412.
- [Rozmus et al., 1996] Rozmus, W., Tikhonchuk, V. T., Cauble, R., et al. (1996). A model of ultrashort laser pulse absorption in solid targets. *Physics of Plasmas (1994-present)*, 3(1):360–367.
- [Sakagami et al., 1979] Sakagami, Y., Kawakami, H., Nagao, S., and Yamanaka, C. (1979). Two-Dimensional Distribution of Self-Generated Magnetic Fields near the Laser-Plasma Resonant-Interaction Region. *Phys. Rev. Lett.*, 42:839–842.
- [Santos, 2014] Santos, J. (2014). Private communication.
- [Santos et al., 2002] Santos, J. J., Amiranoff, F., Baton, S. D., Gremillet, L., Koenig, M., Martinolli, E., Rabec Le Gloahec, M., Rousseaux, C., Batani, D., Bernardinello, A., Greison, G., and Hall, T. (2002). Fast Electron Transport in Ultraintense Laser Pulse Interaction with Solid Targets by Rear-Side Self-Radiation Diagnostics. *Phys. Rev. Lett.*, 89:025001.

BIBLIOGRAPHY

- [SANTOS et al., 2013] SANTOS, J. J., BATANI, D., BATON, S. D., BEG, F. N., CECCOTTI, T., DEBAYLE, A., DORCHIES, F., FEUGEAS, J.-L., FOURMENT, C., GREMILLET, L., HONRUBIA, J. J., HULIN, S., MORACE, A., NICOLAÏ, P., PÉREZ, F., SAWADA, H., SCHLENVOIGT, H.-P., TIKHONCHUK, V. T., VAISSEAU, X., VAUZOUR, B., WEI, M., et al. (2013). Supra-thermal electron beam stopping power and guiding in dense plasmas. *Journal of Plasma Physics*, 79:429–435.
- [Sanz et al., 2012] Sanz, J., Debayle, A., and Mima, K. (2012). Model for ultraintense laser-plasma interaction at normal incidence. *Phys. Rev. E*, 85:046411.
- [Sarri et al., 2012] Sarri, G., Macchi, A., Cecchetti, C. A., Kar, S., Liseykina, T. V., Yang, X. H., Dieckmann, M. E., Fuchs, J., Galimberti, M., Gizzi, L. A., Jung, R., Kourakis, I., Osterholz, J., Pegoraro, F., Robinson, A. P. L., Romagnani, L., Willi, O., and Borghesi, M. (2012). Dynamics of Self-Generated, Large Amplitude Magnetic Fields Following High-Intensity Laser Matter Interaction. *Phys. Rev. Lett.*, 109:205002.
- [Sauerbrey et al., 1994] Sauerbrey, R., Fure, J., Le Blanc, S. P., van Wonterghem, B., Teubner, U., Schäfer, F. P., et al. (1994). Reflectivity of laser produced plasmas generated by a high intensity ultrashort pulse*. *Physics of Plasmas (1994-present)*, 1(5):1635–1642.
- [Schmitz et al., 2012a] Schmitz, H., Lloyd, R., and Evans, R. G. (2012a). Collisional particle-in-cell modelling of the generation and control of relativistic electron beams produced by ultra-intense laser pulses. *Plasma Physics and Controlled Fusion*, 54(8):085016.
- [Schmitz et al., 2012b] Schmitz, H., Lloyd, R., and Evans, R. G. (2012b). Collisional particle in cell modelling of the generation and control of relativistic electron beams produced by ultra intense laser pulses. *Plasma Physics and Controlled Fusion*, 54(8):085016.
- [Schroeder et al., 2004] Schroeder, C. B., Esarey, E., van Tilborg, J., and Leemans, W. P. (2004). Theory of coherent transition radiation generated at a plasma-vacuum interface. *Phys. Rev. E*, 69:016501.
- [Schurtz et al., 2007] Schurtz, G., Gary, S., Hulin, S., Chenais-Popovics, C., Gauthier, J.-C., Thais, F., Breil, J., Durut, F., Feugeas, J.-L., Maire, P.-H., Nicolai, P., Peyrusse, O., Reverdin, C., Soullie, G., Tikhonchuk, V., Villette, B., Fourment, C., et al. (2007). Revisiting Nonlocal Electron-Energy Transport in Inertial Fusion Conditions. *Phys. Rev. Lett.*, 98(095002).
- [Schurtz et al., 2000] Schurtz, G. P., Nicolai, P. D., and Busquet, M. (2000). A nonlocal electron conduction model for multidimensional radiation hydrodynamics codes. *Physics of Plasmas*, 7(10):4238–4249.
- [Scott et al., 2012] Scott, R. H. H., Beaucourt, C., Schlenvoigt, H.-P., Markey, K., Lancaster, K. L., Ridgers, C. P., Brenner, C. M., Pasley, J., Gray, R. J., Musgrave, I. O., Robinson, A. P. L., Li,

BIBLIOGRAPHY

- K., Notley, M. M., Davies, J. R., Baton, S. D., Santos, J. J., Feugeas, J.-L., Nicolai, P., Malka, G., Tikhonchuk, V. T., McKenna, P., Neely, D., Rose, S. J., Norreys, P. A., et al. (2012). Controlling Fast-Electron Beam Divergence Using Two Laser Pulses. *Phys. Rev. Lett.*, 109:015001.
- [Sedov, 1946] Sedov, L. I. (1946). Propagation of strong shock waves. *Prikl. Mat. i Mekh*, 10:241–250.
- [Seltzer and Berger, 1985] Seltzer, S. M. and Berger, M. J. (1985). Bremsstrahlung spectra from electron interactions with screened atomic nuclei and orbital electrons. *Nuclear Instruments and Methods in Physics Research Section B: Beam Interactions with Materials and Atoms*, 12(1):95–134.
- [Sempau et al., 1997] Sempau, J., Acosta, E., Baro, J., Fernández-Varea, J., and Salvat, F. (1997). An algorithm for Monte Carlo simulation of coupled electron-photon transport. *Nuclear Instruments and Methods in Physics Research Section B: Beam Interactions with Materials and Atoms*, 132(3):377–390.
- [Sentoku and Kemp, 2008] Sentoku, Y. and Kemp, A. (2008). Numerical methods for particle simulations at extreme densities and temperatures: Weighted particles, relativistic collisions and reduced currents. *Journal of Computational Physics*, 227(14):6846–6861.
- [Sentoku et al., 2007] Sentoku, Y., Kemp, A. J., Presura, R., Bakeman, M. S., and Cowan, T. E. (2007). Isochoric heating in heterogeneous solid targets with ultrashort laser pulses. *Physics of Plasmas (1994-present)*, 14(12):–.
- [Sheng et al., 2002] Sheng, Z., Mima, K., Sentoku, Y., Jovanović, M. S., Taguchi, T., Zhang, J., Meyer-ter Vehn, J., et al. (2002). Stochastic Heating and Acceleration of Electrons in Colliding Laser Fields in Plasma. *Phys. Rev. Lett.*, 88:055004.
- [Sheng et al., 2000] Sheng, Z. M., Sentoku, Y., Mima, K., Zhang, J., Yu, W., Meyer-ter Vehn, J., et al. (2000). Angular Distributions of Fast Electrons, Ions, and Bremsstrahlung x/ γ Rays in Intense Laser Interaction with Solid Targets. *Phys. Rev. Lett.*, 85:5340.
- [Sherlock, 2009] Sherlock, M. (2009). Universal scaling of the electron distribution function in one-dimensional simulations of relativistic laser-plasma interactions. *Physics of Plasmas (1994-present)*, 16(10):–.
- [Sherlock et al., 2014] Sherlock, M., Hill, E. G., Evans, R. G., Rose, S. J., and Rozmus, W. (2014). In-depth Plasma-Wave Heating of Dense Plasma Irradiated by Short Laser Pulses. *Phys. Rev. Lett.*, 113:255001.
- [Shiraga et al., 2011] Shiraga, H., Fujioka, S., Nakai, M., Watari, T., Nakamura, H., Arikawa, Y., Hosoda, H., Nagai, T., Koga, M., Kikuchi, H., Ishii, Y., Sogo, T., Shigemori, K., Nishimura, H., Zhang, Z., Tanabe, M., Ohira, S., Fujii, Y., Namimoto, T., Sakawa, Y., Maegawa, O., Ozaki, T., Tanaka, K., Habara, H., Iwawaki, T., Shimada, K., Nagatomo, H., Johzaki, T., Sunahara, A.,

BIBLIOGRAPHY

- Murakami, M., Sakagami, H., Taguchi, T., Norimatsu, T., Homma, H., Fujimoto, Y., Iwamoto, A., Miyanaga, N., Kawanaka, J., Jitsuno, T., Nakata, Y., Tsubakimoto, K., Morio, N., Kawasaki, T., Sawai, K., Tsuji, K., Murakami, H., Kanabe, T., Kondo, K., Sarukura, N., Shimizu, T., Mima, K., Azechi, H., et al. (2011). Fast ignition integrated experiments with Gekko and LFEX lasers. *Plasma Physics and Controlled Fusion*, 53(12):124029.
- [Shkarofsky, 1963] Shkarofsky, I. P. (1963). CARTESIAN TENSOR EXPANSION OF THE FOKKER-PLANCK EQUATION. *Canadian Journal of Physics*, 41(11):1753–1775.
- [Siminos et al., 2012] Siminos, E., Grech, M., Skupin, S., Schlegel, T., and Tikhonchuk, V. T. (2012). Effect of electron heating on self-induced transparency in relativistic-intensity laser-plasma interactions. *Phys. Rev. E*, 86:056404.
- [Solodov and Betti, 2008] Solodov, A. A. and Betti, R. (2008). Stopping power and range of energetic electrons in dense plasmas of fastignition fusion targets. *Phys. Plasmas*, 15(042707).
- [Spitzer and Härm, 1953] Spitzer, L. and Härm, R. (1953). Transport Phenomena in a Completely Ionized Gas. *Phys. Rev.*, 89:977–981.
- [Stephens et al., 2004] Stephens, R. B., Snavely, R. A., Aglitskiy, Y., Amiranoff, F., Andersen, C., Batani, D., Baton, S. D., Cowan, T., Freeman, R. R., Hall, T., Hatchett, S. P., Hill, J. M., Key, M. H., King, J. A., Koch, J. A., Koenig, M., MacKinnon, A. J., Lancaster, K. L., Martinolli, E., Norreys, P., Perelli-Cippo, E., Rabec Le Gloahec, M., Rousseaux, C., Santos, J. J., and Scianitti, F. (2004). $K\alpha$ fluorescence measurement of relativistic electron transport in the context of fast ignition. *Phys. Rev. E*, 69:066414.
- [Sternheimer, 1952] Sternheimer, R. M. (1952). The Density Effect for the Ionization Loss in Various Materials. *Phys. Rev.*, 88:851–859.
- [Sternheimer et al., 1982] Sternheimer, R. M., Seltzer, S. M., and Berger, M. J. (1982). Density effect for the ionization loss of charged particles in various substances. *Phys. Rev. B*, 26:6067–6076.
- [Storm et al., 2009] Storm, M., Solodov, A. A., Myatt, J. F., Meyerhofer, D. D., Stoeckl, C., Mileham, C., Betti, R., Nilson, P. M., Sangster, T. C., Theobald, W., and Guo, C. (2009). High-Current, Relativistic Electron-Beam Transport in Metals and the Role of Magnetic Collimation. *Phys. Rev. Lett.*, 102:235004.
- [Strickland and Mourou, 1985] Strickland, D. and Mourou, G. (1985). Compression of amplified chirped optical pulses. *Optics Communications*, 55(6):447–449.
- [Stroschio et al., 1978] Stroschio, M. A., Lee, K., Lindman, E. L., et al. (1978). Relativistic derivation of laser induced plasma profiles. *Physics of Fluids (1958-1988)*, 21(9):1509–1512.

BIBLIOGRAPHY

- [Strozzi et al., 2012] Strozzi, D. J., Tabak, M., Larson, D. J., Divol, L., Kemp, A. J., Bellei, C., Marinak, M. M., and Key, M. H. (2012). Fast ignition transport studies: Realistic electron source, integrated particle in cell and hydrodynamic modeling, imposed magnetic fields. *Physics of Plasmas (1994-present)*, 19(7):–.
- [Tabak et al., 1994] Tabak, M., Hammer, J., Glinsky, M. E., Kruer, W. L., Wilks, S. C., Woodworth, J., Campbell, E. M., Perry, M. D., Mason, R. J., et al. (1994). Ignition and high gain with ultrapowerful lasers—f—. *Phys. Plasmas*, 1(1626).
- [Takizuka and Abe, 1977] Takizuka, T. and Abe, H. (1977). A binary collision model for plasma simulation with a particle code. *J. Comput. Phys.*, 25(3):205–219.
- [Taylor G., 1950] Taylor G. (1950). The Formation of a Blast Wave by a Very Intense Explosion. II. The Atomic Explosion of 1945. *Proceedings of the Royal Society of London A: Mathematical, Physical and Engineering Sciences*, 201(1065):175–186.
- [Theobald et al., 2013] Theobald, W., Nora, R., Lafon, M., Anderson, K. S., Davies, J. R., Hohenberger, M., Sangster, T. C., Seka, W., Solodov, A. A., Stoeckl, C., Yaakobi, B., Betti, R., et al. (2013). Demonstration of 200-Mbar Ablation Pressure for Shock Ignition. In *Bulletin of the American Physical Society*, volume 58, pages 161–167.
- [Theobald et al., 2011] Theobald, W., Solodov, A. A., Stoeckl, C., Anderson, K. S., Betti, R., Boehly, T. R., Craxton, R. S., Delettrez, J. A., Dorrer, C., Frenje, J. A., Glebov, V. Y., Habara, H., Tanaka, K. A., Knauer, J. P., Lauck, R., Marshall, F. J., Marshall, K. L., Meyerhofer, D. D., Nilson, P. M., Patel, P. K., Chen, H., Sangster, T. C., Seka, W., Sinenian, N., Ma, T., Beg, F. N., Giraldez, E., Stephens, R. B., et al. (2011). Initial cone-in-shell fast-ignition experiments on OMEGAa). *Physics of Plasmas (1994-present)*, 18(5):–.
- [Thomas et al., 2012] Thomas, A., Tzoufras, M., Robinson, A., Kingham, R., Ridgers, C., Sherlock, M., and Bell, A. (2012). A review of Vlasov–Fokker–Planck numerical modeling of inertial confinement fusion plasma. *J. Comput. Phys.*, 231(3):1051–1079.
- [Thomas et al., 2013] Thomas, A. G. R., Sherlock, M., Kuranz, C., Ridgers, C. P., and Drake, R. P. (2013). Hybrid Vlasov–Fokker–Planck–Maxwell simulations of fast electron transport and the time dependence of K-shell excitation in a mid-Z metallic target. *New Journal of Physics*, 15(1):015017.
- [Thomson et al., 2009] Thomson, A., Attwood, D., Gullikson, E., Howells, M., Kim, K.-J., Kirz, J., Kortright, J., Lindau, I., Liu, Y., Pianetta, P., Robinson, J., Scofield, J., Underwood, J., Williams, G., and Winick, H. (2009). X-RAY DATA BOOKLET. CA 94720.
- [Tikhonchuk, 2002] Tikhonchuk, V. T. (2002). Interaction of a beam of fast electrons with solids. *Physics of Plasmas (1994-present)*, 9(4):1416–1421.

BIBLIOGRAPHY

- [Tsakiris and Eidmann, 1987] Tsakiris, G. and Eidmann, K. (1987). An approximate method for calculating Planck and Rosseland mean opacities in hot, dense plasmas. *Journal of Quantitative Spectroscopy and Radiative Transfer*, 38(5):353–368.
- [Tycho, 1573] Tycho, B. (1573). *De nova et nullius aevi memoria prius visa stella*. primum conspecta, contemplatio mathematica.
- [Tzoufras et al., 2011] Tzoufras, M., Bell, A., Norreys, P., and Tsung, F. (2011). A Vlasov-Fokker-Planck code for high energy density physics. *J. Comput. Phys.*, 230:6475–6494.
- [Tzoufras et al., 2013] Tzoufras, M., Tableman, A., Tsung, F. S., Mori, W. B., and Bell, A. R. (2013). A multi-dimensional Vlasov-Fokker-Planck code for arbitrarily anisotropic high-energy-density plasma. *Physics of Plasmas (1994-present)*, 20(5):–.
- [Vaisseau, 2014] Vaisseau, X. (2014). *Experimental study of fast electron transport in dense plasmas*. PhD thesis.
- [van Kessel and Sigel, 1974] van Kessel, C. G. M. and Sigel, R. (1974). Observation of Laser-Driven Shock Waves in Solid Hydrogen. *Phys. Rev. Lett.*, 33:1020–1023.
- [Vauzour, 2012] Vauzour, B. (2012). *Etude expérimentale du transport d’électrons rapides dans le cadre de l’allumage rapide pour la fusion inertielle*. PhD thesis.
- [Vauzour, 2014] Vauzour, B. (2014). Private communication.
- [Verner et al., 1993] Verner, D., Yakovlev, D., Band, I., and Trzhaskovskaya, M. (1993). Subshell Photoionization Cross Sections and Ionization Energies of Atoms and Ions from He to Zn. *Atomic Data and Nuclear Data Tables*, 55(2):233–280.
- [Verner and Yakovlev, 1995] Verner, D. A. and Yakovlev, D. (1995). Analytical fits for partial photoionization cross sections. *Astron. Astrophys. Suppl. Ser.* 109, pages 125–133.
- [Villani, 2014] Villani, C. (2014). Particle systems and nonlinear Landau damping. *Physics of Plasmas (1994-present)*, 21(3):–.
- [Volosevich and Rozanov, 1981] Volosevich, P. P. and Rozanov, V. B. (1981). Conversion of laser radiation into fast electrons in the LTF problem. *JETP Letters*, 33(1):173–178.
- [Volpe et al., 2014] Volpe, L., Feugeas, J.-L., Nicolai, P., Santos, J. J., Touati, M., Breil, J., Batani, D., and Tikhonchuk, V. (2014). Controlling the fast electron divergence in a solid target with multiple laser pulses. *Phys. Rev. E*, 90:063108.
- [Wei et al., 2004] Wei, M. S., Beg, F. N., Clark, E. L., Dangor, A. E., Evans, R. G., Gopal, A., Ledingham, K. W. D., McKenna, P., Norreys, P. A., Tatarakis, M., Zepf, M., and Krushelnick, K. (2004). Observations of the filamentation of high-intensity laser-produced electron beams. *Phys. Rev. E*, 70:056412.

BIBLIOGRAPHY

- [Weibel, 1959] Weibel, E. S. (1959). Spontaneously Growing Transverse Waves in a Plasma Due to an Anisotropic Velocity Distribution. *Phys. Rev. Lett.*, 2:83–84.
- [Weibel, 1967a] Weibel, E. S. (1967a). Anomalous Skin Effect in a Plasma. *Physics of Fluids (1958-1988)*, 10(4):741–748.
- [Weibel, 1967b] Weibel, E. S. (1967b). L'équation de Vlasov dans la théorie spéciale de la relativité. *Plasma Physics*, 9(6):665.
- [Welch et al., 2004] Welch, D., Rose, D., Clark, R., Genoni, T., and Hughes, T. (2004). Implementation of a non-iterative implicit electromagnetic field solver for dense plasma simulation. *Computer Physics Communications*, 164(1–3):183–188. Proceedings of the 18th International Conference on the Numerical Simulation of Plasmas.
- [Westover et al., 2011] Westover, B., Chen, C. D., Patel, P. K., Key, M. H., McLean, H., Stephens, R., and Beg, F. N. (2011). Fast electron temperature and conversion efficiency measurements in laser-irradiated foil targets using a bremsstrahlung x-ray detector. *Physics of Plasmas (1994-present)*, 18(6):–.
- [Wilks et al., 1992] Wilks, S. C., Kruer, W. L., Tabak, M., Langdon, A. B., et al. (1992). Absorption of ultra intense laser pulses. *Phys. Rev. Lett.*, 69.
- [Wright and Hadley, 1975] Wright, T. P. and Hadley, G. R. (1975). Relativistic distribution functions and applications to electron beams. *Phys. Rev. A*, 12:686–697.
- [Yabuuchi et al., 2010] Yabuuchi, T., Paradkar, B. S., Wei, M. S., King, J. A., Beg, F. N., Stephens, R. B., Nakanii, N., Hatakeyama, M., Habara, H., Mima, K., Tanaka, K. A., and Larsen, J. T. (2010). Transport study of intense-laser-produced fast electrons in solid targets with a preplasma created by a long pulse laser. *Physics of Plasmas (1994-present)*, 17(6):–.
- [Yang et al., 1995] Yang, T. B., Kruer, W. L., More, R. M., Langdon, A. B., et al. (1995). Absorption of laser light in overdense plasmas by sheath inverse bremsstrahlung. *Physics of Plasmas (1994-present)*, 2(8):3146–3154.
- [Yokota et al., 2006] Yokota, T., Nakao, Y., Johzaki, T., and Mima, K. (2006). Two-dimensional relativistic Fokker-Planck model for core plasma heating in fast ignition targets. *Phys. Plasmas*, 13(2):–.
- [Yu et al., 2000] Yu, W., Bychenkov, V., Sentoku, Y., Yu, M. Y., Sheng, Z. M., and Mima, K. (2000). Electron Acceleration by a Short Relativistic Laser Pulse at the Front of Solid Targets. *Phys. Rev. Lett.*, 85:570–573.
- [Yu et al., 1998] Yu, W., Yu, M. Y., Sheng, Z. M., Zhang, J., et al. (1998). Model for fast electrons in ultrashort pulse laser interaction with solid targets. *Phys. Rev. E*, 58:2456.

BIBLIOGRAPHY

- [Zel'dovich and Raizer, 1966] Zel'dovich, Y. B. and Raizer, Y. P. (1966). *Physics of Shock Waves and High Temperature Phenomena*. Academic Press, New York.
- [Zheng et al., 2003] Zheng, J., Tanaka, K. A., Miyakoshi, T., Kitagawa, Y., Kodama, R., Kurahashi, T., and Yamanaka, T. (2003). Theoretical study of transition radiation from hot electrons generated in the laser–solid interaction. *Physics of Plasmas (1994-present)*, 10(7):2994–3003.
- [Zhou and Betti, 2005] Zhou, C. and Betti, R. (2005). High Density and High Areal Density Fuel Assembly for Fast Ignition Inertial Confinement Fusion. In *Bull. Am. Phys. Soc.*, volume 506, page 140.
- [Ziman, 1961] Ziman, J. M. (1961). A theory of the electrical properties of liquid metals. I: The monovalent metals. *Philosophical Magazine*, 6(68):1013–1034.

Titre : Étude du Transport d'Électrons Rapides pour la Fusion par Confinement Inertiel

Résumé :

Un nouveau modèle réduit pour le transport de faisceaux d'électrons relativistes dans des solide ou des plasma denses est proposé. Il est basé sur la résolution des deux premiers moments angulaires de l'équation cinétique relativiste, complétés par une relation de fermeture déduite du principe de maximisation de l'entropie angulaire de Minerbo. Le modèle prend en compte aussi bien les effets collectifs du transport avec les champs électromagnétiques auto générés que les effets collisionnels liés au ralentissement des électrons par collision sur les plasmons, les électrons liés et les électrons libres du milieu ainsi que leur diffusion angulaire par collisions sur les électrons et les ions. Le modèle permet une résolution numérique rapide des équations du transport de faisceau d'électrons rapides tout en décrivant l'évolution cinétique de leur fonction de distribution. Malgré le fait de travailler avec les grandeurs angulaires moyennes, le modèle a été validé par comparaison avec des solutions analytiques dérivées dans un cas académique de transport de faisceau mono énergétique et collimaté dans un plasma dense et chaud d'Hydrogène ainsi qu'avec une simulation PIC hybride dans un cas réaliste de transport d'électrons accélérés par laser dans une cible solide. Le modèle est appliqué à l'étude de l'émission de photons $K\alpha$ lors d'expériences laser-plasma ainsi qu'à la génération d'ondes de choc.

Mots clés : Plasmas, Fusion par Confinement Inertielle, Interaction Laser-Plasma (Relativiste), Transport de Faisceaux d'Électrons Relativistes, Entropie Angulaire, Théorie Cinétique, Théorie Hydrodynamique

Title : Fast Electron Transport Study For Inertial Confinement Fusion

Abstract :

A new hybrid reduced model for relativistic electron beam transport in solids and dense plasmas is presented. It is based on the two first angular moments of the relativistic kinetic equation completed with the Minerbo maximum angular entropy closure. It takes into account collective effects with the self-generated electromagnetic fields as well as collisional effects with the slowing down of the electrons in collisions with plasmons, bound and free electrons and their angular scattering on both ions and electrons. This model allows for fast computations of relativistic electron beam transport while describing the kinetic distribution function evolution. Despite the loss of information concerning the angular distribution of the electron beam, the model reproduces analytical estimates in the academic case of a collimated and monoenergetic electron beam propagating through a warm and dense Hydrogen plasma and hybrid PIC simulation results in a realistic laser-generated electron beam transport in a solid target. The model is applied to the study of the emission of $K\alpha$ photons in laser-solid experiments and to the generation of shock waves.

Key words : Plasmas, Inertial Confinement Fusion, (Relativistic) Laser-Plasma Interaction, Relativistic Electron Beam Transport, Angular Entropy, Kinetic Theory, Hydrodynamic Theory